Molecular-based hybrid materials for artificial photosynthesis: Exploring new horizons in sustainable energy solutions

Martina Salati

UNIVERSITAT ROVIRA i VIRGILI

Molecular-based hybrid materials for artificial photosynthesis: Exploring new horizons in sustainable energy solutions

Martina Salati

DOCTORAL THESIS
2024

UNIVERSITAT ROVIRA I VIRGILI
Molecular-based hybrid materials for artificial photosynthesis: Exploring new horizons in sustainable energy solutions
Martina Salati

UNIVERSITAT ROVIRA I VIRGILI
Molecular-based hybrid materials for artificial photosynthesis: Exploring new horizons in sustainable energy solutions
Martina Salati

Martina Salati

Molecular-based hybrid materials for artificial photosynthesis: Exploring new horizons in sustainable energy solutions

DOCTORAL THESIS

Supervised by

Prof. Antoni Llobet and Dr. Marcos Gil-Sepulcre

Institute of Chemical Research of Catalonia

Tarragona
2024

UNIVERSITAT ROVIRA I VIRGILI
Molecular-based hybrid materials for artificial photosynthesis: Exploring new horizons in sustainable energy solutions
Martina Salati

ICIQ - Institut Català d'Investigació Química

Avinguda Països Catalans 16,

43007 Tarragona (Spain)

Prof. Antoni Llobet, Group Leader at the Institute of Chemical Research of Catalonia, and Dr. Marcos Gil-Sepulcre, Assistant Professor at the Autonomous University of Barcelona,

We STATE that the present study, entitled "*Molecular-based hybrid materials for artificial photosynthesis: Exploring new horizons in sustainable energy solutions*" presented by Martina Salati for the award of the degree of Doctor, has been carried out under our supervision at the group of Antoni Llobet in the Institute of Chemical Research of Catalonia.

Tarragona, October 7, 2024

Doctoral Thesis Supervisors

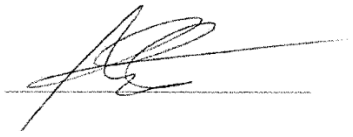

Prof. Antoni Llobet Dr. Marcos Gil-Sepulcre

Acknowledgements

Generally, this section is only a small part of the whole thesis book, but it actually represents one of the most important aspects of the full PhD doctorate process, since none of this was possible without the contribution of a great community.

First of all, I would like to thank my thesis supervisor, Toni, who gave me the opportunity to start this experience of PhD at ICIQ, and to Marcos, my co-supervisor. Thank you for guiding me in this challenging and exciting journey, from you I have learnt a lot from the scientific and professional perspective. I am particularly grateful to Marcos, who have taught me the importance of having a critical thinking and, especially at the beginning, directed me on every single step I was facing and when I had no idea how to deal with a problem. Later, even from the distant Germany, he has been determined to keep following my work, and he especially helped me when the time of writing came. You have been a great mentor, always stimulating me to go on and to not give up. I wish you all the best for your new position in Barcelona, I am sure you will definitely succeed also as professor.

During this experience I have had also the opportunity to share my work with several collaborators, who gave a great contribution to this work. In particular, I want to thank Prof. Menny Shalom for the warm welcoming and for the exceptional experience of short stay I was able to live in his research group at BGU in Beer Sheva, and especially to Dr. Sanjit Mondal, who was a great tutor and companion during those months. From you I have learnt a lot regarding the synthesis of carbon nitride polymers and different analysis techniques, and you always helped me with anything I needed. Fruitful collaborations were also obtained with Dr. Jia-Wei Wang, former member of our group, who helped me deal with CTF materials and conducted an amazing research on the complementary side of my work, focusing on the CO_2 reduction reaction. Marco Nicaso has been a great co-worker and colleague, who worked intensely on the computational side for the project of carbon nitrides, always keeping a critical thinking and being totally available for a positive dialogue. Furthermore, a great thank goes to our collaborators from ICL, MPI and UPV centers; and as well to my former mentors from UniFe in Italy, which were always available to give me support and guidance in different situations.

A single person can have a great talent for playing an instrument, but it takes a whole orchestra to create a symphony. I cannot be more grateful for the lab mates I have met during these four years. Thanks to Sergi, our great lab coordinator, who is so capable but so humble that always asks everyone if he is correctly doing his job. Your suggestions have always been useful and of great help, and you know how to hold a group together; this should be enough to make you a great friend and a great scientist. Thank you, Alisa, Elena, Paula, Josep, Marco and Zhi-Mei, the "Lab 1.5" team, and thank you Koushik, Jake, Pablo and Jing, the "Lab 1.2" team. Even if separated, it was always a pleasure meeting up for coffee time, cake time, chocolate time, the numerous birthdays and lunch time. Doing research has been wonderful in your company, and as well it was great to pass time with you outside the lab.

Last but not least, I want to thank my family and my relatives, who supported me during these long four years even with the distance, and my friends from the old times of the university, that always waited for me to have big reunions and celebrations.

Finally, the work performed in the present doctoral thesis has been possible thanks to the Institute of Chemical Research of Catalonia (ICIQ), Universitat Rovira i Virgili (URV) and the European Union for the financial support through grants PID2019-111617RB-I00, PRE2020-093789, and PID2022-140143OB-I00 financed by MCIN/AEI/ 10.13039/501100011033/ FEDER, UE. Financial support for scientific activities of Catalan research groups was also provided by AGAUR through the project 2021 SGR 01583.

List of Publications

(1) "Covalent Triazine-Based Frameworks with Covalently Anchored Ru-tda Based Catalyst for Photoinduced Water Oxidation" Salati, M.; Dorchies, F.; Wang, J.-W.; Ventosa, M.; González-Carrero, S.; Bozal-Ginesta, C.; Holub, J.; Rüdiger, O.; DeBeer, S.; Gimbert-Suriñach, C.; Durrant, J. R.; Ertem, M. Z.;* Gil-Sepulcre, M.;* Llobet, A.* *Small*, **2024**, e2406375.
DOI: 10.1002/smll.202406375

(2) "Supramolecular interaction of a molecular catalyst with a polymeric carbon nitride photoanode enhances photoelectrochemical activity and stability at neutral pH" Mondal, S.;† Salati, M.;† Nicaso, M.; Albero, J.; Segado-Centellas, M.; Volokh, M.; Bo, C.;* García, H.; Gil-Sepulcre, M.;* Llobet, A.;* Shalom, M.* *Chem. Sci.*, **2024**, 15, 16546-16553.
DOI: 10.1039/D4SC04678A

(3) "Molecular Catalyst Coordinatively Bonded to Organic Semiconductors for Selective Light-Driven CO_2 Reduction in Water" Wang, J.-W.;* Zhao, F.; Velasco, L.; Sauvan, M.; Moonshiram, D.; Salati, M.; Luo, Z.-M.; He, S.; Jin, T.; Mu, Y.-F.; Ertem, M. Z.; Lian, T.; Llobet, A.* *Nat. Comm.*, **2024**, accepted.
[Paper #NCOMMS-24-15315C]

Table of Contents

Graphical abstracts

Chapter 1. General introduction

This chapter focuses on the motivation for the research discussed in the present thesis, providing general information about the artificial photosynthesis. In principle, the causes and effects of climate change are described, with a general overview on the principal solutions to adopt. A brief discussion on the natural photosynthesis is then provided, which gives the essential knowledge about the main artificial methodologies used to obtain solar fuels from chemical reactions. The principles of artificial photosynthesis and its components are thus disclosed, and the state-of-the-art of specific groups of organic-based semiconductors and molecular catalysts for water oxidations is finally presented, to anticipate the main systems employed in this thesis.

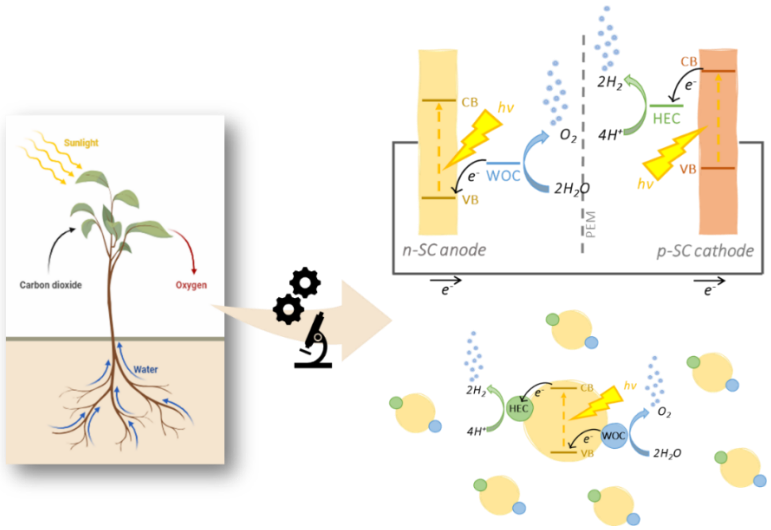

Chapter 2. Objectives

Following the review in the variety of scientific and technical solutions achieved in the field of artificial photosynthesis, the main objectives of this thesis are presented. The main purpose is to bridge the gap between homogeneous and heterogeneous catalysis for solar fuels production using organic-based semiconductors.

Chapter 3. Covalent triazine-based frameworks with covalently anchored Ru-tda based catalyst for photoinduced water oxidation

In this chapter we report the synthesis, characterization and photocatalytic performance of a novel hybrid material based on a CTF structure bearing dangling pyridyl groups that allow the anchoring of a Ru-based water oxidation catalyst (WOC) *via* covalent bonding. The assembly can carry out efficiently light-induced water oxidation (WO) at neutral pH, reaching values of TOF and TONs of 17 h^{-1} and 220, respectively, using sodium persulfate as a sacrificial electron acceptor.

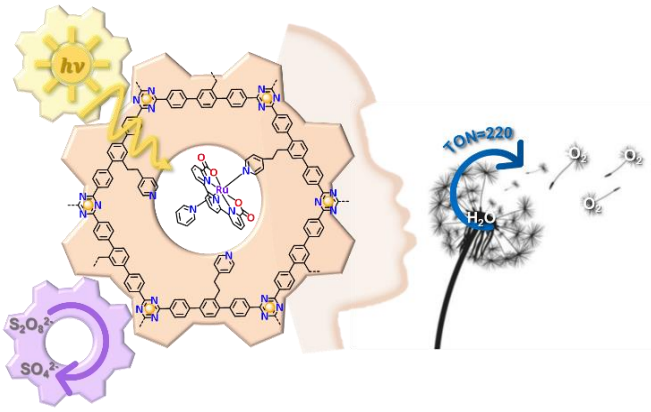

Chapter 4. Molecular catalyst coordinatively bonded to organic semiconductors for selective light-induced CO_2 reduction in water

In this chapter, the anchoring of discrete Co-based molecular catalysts on organic polymeric semiconductors *via* covalent bonding is presented, and the generated molecular hybrid materials are deeply studied for CO_2 photoreduction. The best molecular hybrid material achieves efficient and selective photoreduction of CO_2 to CO in aqueous buffer, giving high production rates in the range of 458 µmol g^{-1} h^{-1} and turnover numbers above 550 in 48 h, with no deactivation and no detectable H_2.

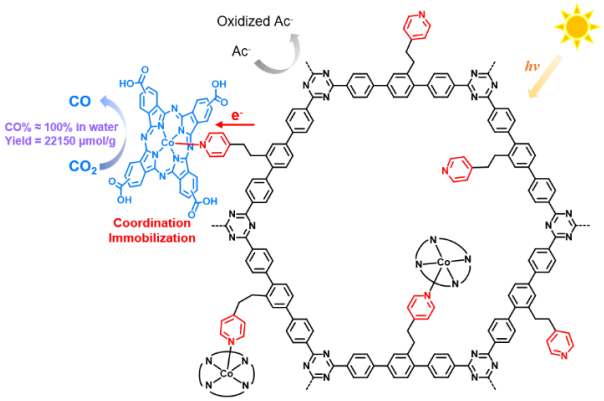

Chapter 5. Supramolecular interaction of molecular catalyst on a polymeric carbon nitride photoanode enhances PEC activity and stability at neutral pH

A carbon nitride (CN) photoanode connected to a highly active molecular Ru catalyst for water oxidation is analyzed in this chapter. The strong interaction by CH-π stacking within the assembly enables a strong connection and an efficient electronic communication. The optimized photoanode exhibits 89% faradaic efficiency for oxygen evolution with TONs in the range of 3300 and TOFs of 0.4 s^{-1}, and good stability up to 5 h.

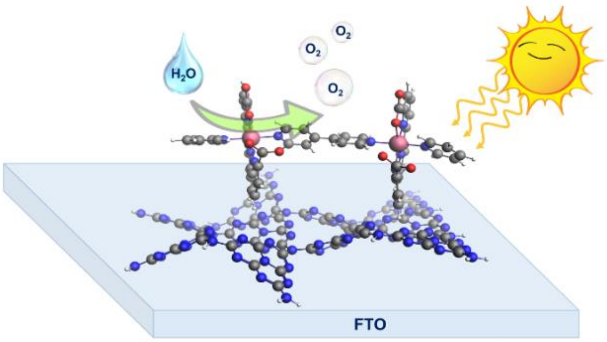

Chapter 6. Strategic functionalization of carbon nitride photoanodes for improved charge separation in the water oxidation process

In this work, we have successfully synthesized a carbon nitride (CN) photoanode with the covalent grafting of a Ru molecular catalyst *via* amidation reaction. The photoelectrochemical measurements were performed under 1 sun irradiation at neutral pH, achieving TONs and TOFs of 2 x 10^4 and 0.6 s^{-1}, respectively, improving the values obtained in Chapter 5. The photophysical study revealed an improved charge separation and transfer kinetics, and confirmed the efficiency of the catalyst to promote the WO.

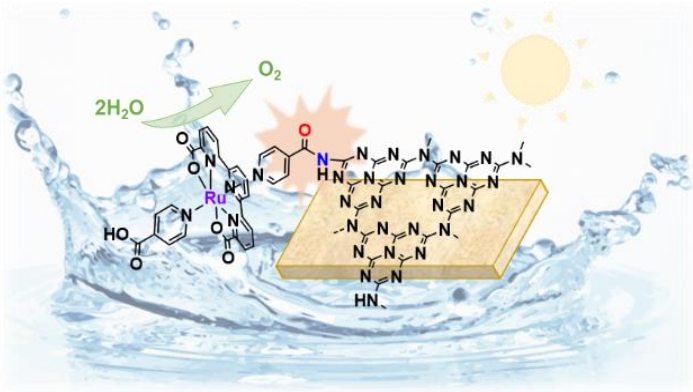

Chapter 7. General conclusions

Considering the initial objectives and the results obtained, this chapter establishes the main conclusions and outcomes of the present doctoral thesis.

Glossary of terms and abbreviations

Abs	Absorbance
AQY	Apparent Quantum Yield
bda^{2-}	[2,2'-bipyridine]-6,6'-dicarboxylate
bpy	2,2'-bipyridine
BE	Bulk electrolysis
BET	Brunauer Emmett Teller
COSY	Correlation Spectroscopy
CB	Conduction Band
CV	Cyclic Voltammetry
CE	Counter Electrode
CN	Carbon Nitride
CTF	Covalent Triazine-based Frameworks
δ (NMR)	Chemical shift
δ (FT-IR)	Bending mode
DCM	Dichloromethane
DLS	Dinamic Light Scattering
DFT	Density Functional Theory
DMSO	Dimethyl sulfoxide
DPV	Differential Pulse Voltammetry
DRS	Diffuse Reflectance Spectroscopy
DSPEC	Dye-Sensitized Photoelectrochemical Cell
ΔG°	Gibbs free energy
E	Potential
E°	Standard potential
$E_{½}$	Thermodynamic redox potential calculated as $(E_{p,a} + E_{p,c})/2$
$E_{p,a}$	Anodic peak potential
$E_{p,c}$	Cathodic peak potential
E_F	Fermi level
E_{fb}	Flatband potential
ε	Extinction coefficient
EC	Electrochemical Cell (electrolyzer)
EtOH	Ethanol
EXAFS	Extended X-ray Absorption Fine Structure
ϕ_{chem}	Chemical efficiency
FE	Faradaic Efficiency
FT-IR	Fourier Transform Infrared Spectroscopy
FTO	Fluorine-doped Tin Oxide
GC	Glassy Carbon
HER	Hydrogen Evolution Reaction
HMBC	Heteronuclear Multiple Bond Correlation
HSQC	Heteronuclear Single Quantum Coherence
hv	Light
λ	Wavelength
LSV	Linear Sweep Voltammetry

M	Molar
i	Current
I	Ionic strength
I2M	Interaction of two M-O groups
ICP-OES	Induced Coupled Plasma Optical Emission Spectroscopy
j	Current density
m/z	Mass-to-charge ratio
MLCT	Metal to Ligand Charge Transfer
MS	Mass Spectrometry
M-S	Mott-Schottky
MSE	Mercury Sulfate Electrode
MeOH	Methanol
h	Overpotential
ν (FT-IR)	Stretching mode
NHE	Normal Hydrogen Electrode
NMR	Nuclear Magnetic Resonance
NPs	Nanoparticles
ω	frequency
OEC	Oxygen-Evolving Center
PCET	Proton Coupled Electron Transfer
PEC	Photoelectrochemical cell
PL	Photoluminescence
ppm	Parts per million
PS	Photosensitizer
PSI	Photosystem I
PSII	Photosystem II
PV	Photovoltaic
PXRD	Powder X-Ray Diffraction
py	Pyridine
phbf	Phosphate buffer
RE	Reference Electrode
RHE	Reversible Hydrogen Electrode
RT	Room Temperature
SA_{BET}	Surface area obtained *via* N_2 sorption/desorption tests
SEA	Sacrificial Electron Acceptor
SEM	Scanning Electron Microscopy
τ	lifetime
TAS	Transient Absorption Spectroscopy
TCSPC	Time-Correlated Single-Photon Counting
tda^{2-}	[2,2’:6’,2’’-terpyridine]-6,6’’-dicarboxylate
tPa^{4-}	[2,2':6',2''-terpyridine]-6,6''-diphosphonate
TEM	Transmission Electron Microscopy
TFE	Trifluoroethanol
TOF	Turnover Frequency
TON	Turnover Number
trpy	2,2’:6’,2’’-terpyridine
UV-Vis	Ultraviolet-Visible Spectroscopy

VB	Valance Band
vs.	*versus*
WE	Working Electrode
WNA	Water Nucleophilic attack
WOC	Water Oxidation Catalyst
WOR	Water Oxidation Reaction
XANES	X-ray Absorption Near Edge Spectroscopy
XAS	X-ray Absorption Spectroscopy
XPS	X-ray Photoelectron Spectroscopy
XRD	X-Ray Diffraction

Chapter 1

General introduction


1

1.1. The right direction towards sustainability

Since the First Industrial Revolution at the end of the 18th century, we have experienced significant changes that have transformed the way we live, work and relate to one another. The Fourth and current revolution we are facing, according to the World Economic Forum,[1,2] is a new chapter in human development that builds on previously optimized technologies, and is expected to bring further advances in the interconnected fields of physics, technology and biology, creating an inclusive, human-centered future. This extraordinary progress, however, brings both great promise and potential peril. In fact, the improvement of the living conditions for a broader circle of people due to the spread of primary benefits is leading to an exponential growth in the world population, with the threshold of 8 billion people reached in the first half of 2022.[3] This growth leads to a constantly increasing demand for energy (up to 180,000 TWh; see Figure 1, top), with fossil fuels like oil and coal representing the most relevant energy sources still under use.[4] Currently, about 80% of our energy consumption is from the combustion of fossil fuels, which not only makes us dependent on a limited resource, but also continues to drive global warming. Indeed, the direct consequence of the employment of fossil fuels for energy is the rise of greenhouse gas (GHG) emissions, thus provoking consequential effects for the ecosystem.[5] The GHG (such as CO_2, CH_4 and water vapor) are gases naturally or artificially present in the atmosphere that, absorbing part of the infrared (IR) sunlight radiation, induce an increase of the overall temperature at the surface of the Earth.[6] Since the 1980s, however, the global temperature has experienced a constant rise[7] and in recent years, humanity is facing an increase in the occurrence of extreme weather conditions and climate events, directly or indirectly associated to issues with health, food and safety. Examples of these issues include heatwaves, cold waves, heavy precipitation, drought, tornadoes and tropical cyclones, which have been amplified in intensity, duration and spatial extent, of which has caused a large number of climate emigrants from the poorest and most affected areas.[8] This year we have exceeded average temperatures of 1.5°C greater than those seen in the pre-industrial era for a period of 10 months (Figure 1, bottom), of which has never been previously reached for such an extended period. Furthermore, the ocean acidification is also a direct consequence of the CO_2 increase in the atmosphere (at the current average of

423.6 ± 0.5 ppm),[9] which negatively affects the life of seawater organisms.[10] In summary, natural catastrophes derived from global warming threaten billions of living beings, with a disproportionate effect on the poorest and most vulnerable people. This may ultimately lead to a point of no return in terms of the balance of our ecosystem as we know it.

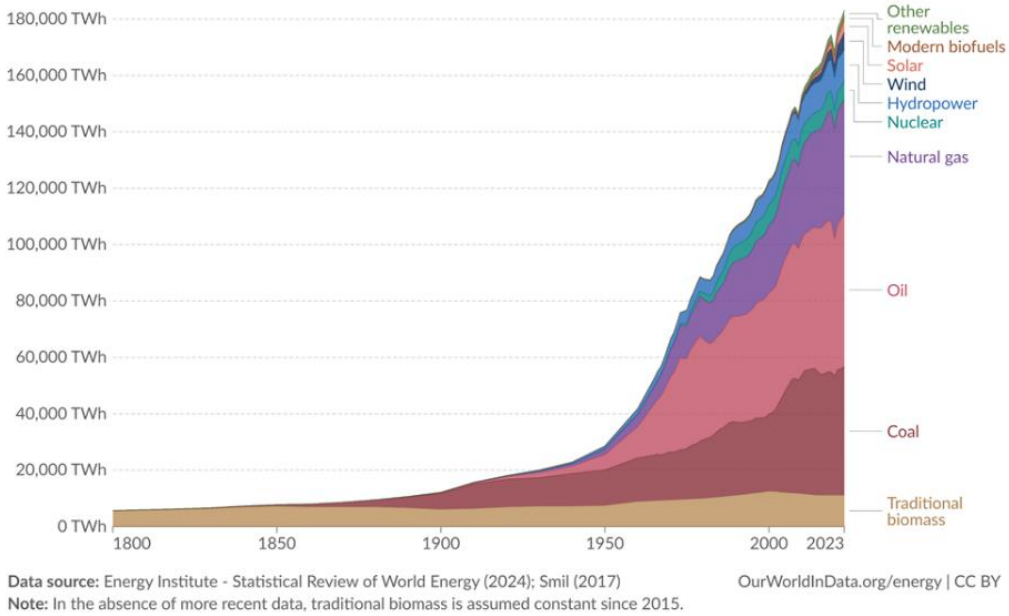

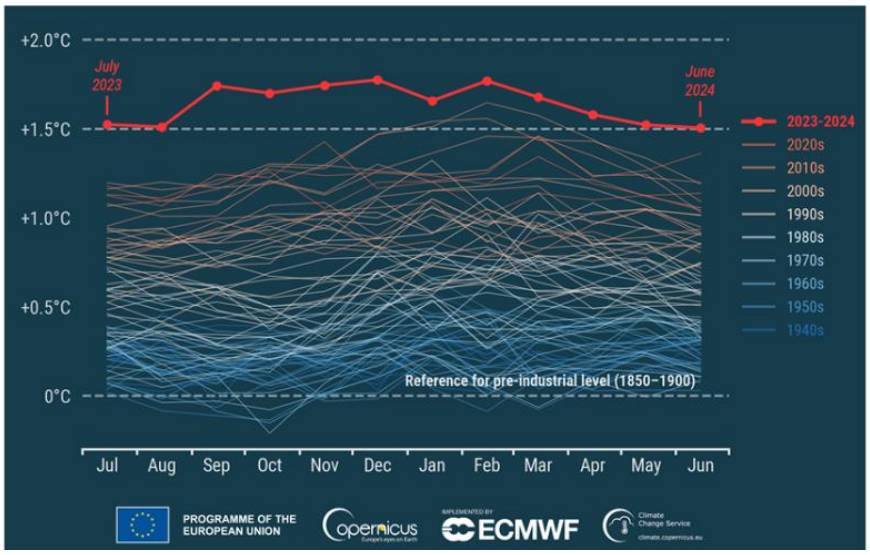

Figure 1. *(Top) Global primary energy consumption by source reported in terawatts per hour (TWh), which includes most known renewable energy sources, based on data reported by the Energy Institute – Statistical Review of World Energy (2024).*[4] *(Bottom) Monthly global surface air temperature anomalies (°C) relative to 1850–1900 from January 1940 to June 2024 (Credit: Copernicus Climate Change Service /ECMWF).*[11]

Within the objective of mitigating the effects of climate change and supplying the increasing energy demands of society, an immediate action from a social and political perspective is needed,[12] and most importantly, it is essential to research environmentally benign renewable energy sources as alternatives to fossil fuels.

From the social point of view, there should be a higher engagement in a more sustainable every-day lifestyle, improving individual action and promoting a better education worldwide.[13]

Political commitment is also important to establish limitations to the current global market's rules and set international common objectives. The Kyoto Protocol, approved by the United Nations (ONU, or UNFCCC) in 1997, was the first international treaty in which 41 countries, including the most industrialized ones, agreed to reduce the use of six greenhouse gases (CO_2, CH_4, N_2O, perfluorocarbons, hydrofluorocarbons and SF_6) to 5.2% below 1990 levels.[14] Another recent and successful negotiation was the Paris Agreement in 2015 which included a total of 196 countries, where each agreed on and designed a sustainable climate plan, and to regularly report on its own GHG emissions contribution.[15] Additionally, in 2015 the United Nations set a list of Sustainable Development Goals (SDGs)[16] for peace and prosperity for the planet and human beings to fulfill by 2030. Later on, the European Green Deal was launched by the European Commission at the end of 2019,[17] with a series of strategies to achieve climate neutrality, which means net-zero GHG emissions (NZE), by 2050. Finally, the Conference of the Parties (COP) is held every year to provide updates on the work of any single country part of the UNFCCC and to set new objectives.[18]

The scientific community has also attempted to face climate change by focusing on finding new sustainable energy sources in alternative to the combustion of fossil fuels. Among the most interesting and effective sources are biomass, hydroelectric, wind power and solar energy (Figure 2).

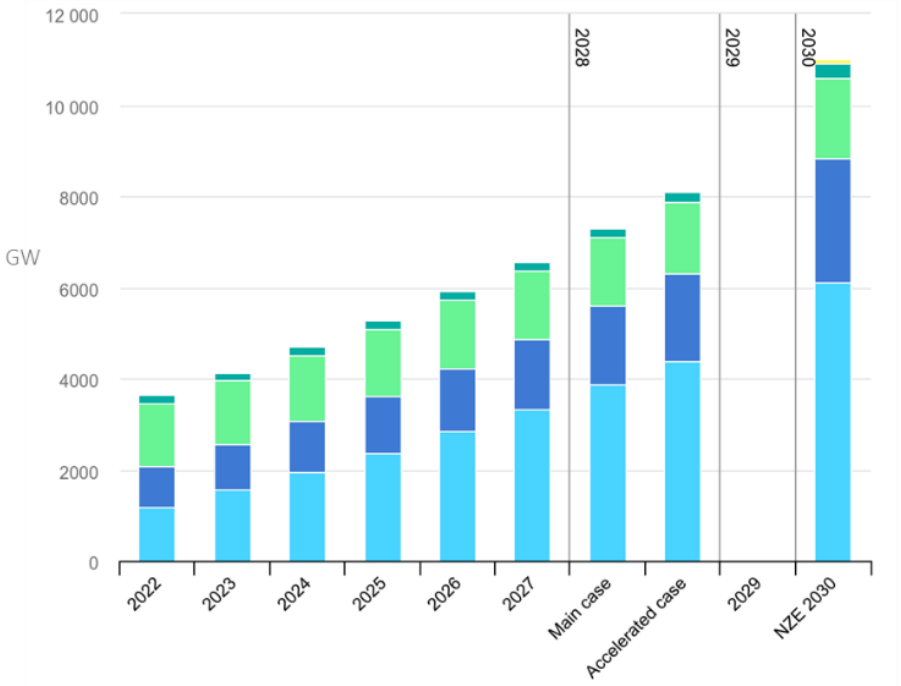

Figure 2. *Cumulative renewable electricity capacity in the main and accelerated cases and Net Zero Scenario, reported by IEA, including solar photovoltaic (PV, light-blue), wind (blue), hydropower (light-green), bioenergy (dark-green), and other renewables (yellow). Notes: solar PV and wind include capacity dedicated to hydrogen production. NZE = IEA Net Zero Scenario Emissions by 2050. 2022 are historical values, 2023 is an estimated value and 2023-2027 are main case values.*[19]

CO_2 removal technologies are also spreading in order to more easily reduce the CO_2 concentration in the atmosphere and help address the problem of GHG emissions.[20] However, most of these technologies are based on the direct conversion into electricity which has inherent problems for storage and transport.[21] Batteries are now widely commercialized since they are capable of accumulating a great amount of energy and don't release particulate or pollutants, since they are not based on combustion processes. However, the manufacturing of batteries also implies the use of non-abundant elements, such as cobalt, nickel, manganese and lithium, which have toxic procedures for extraction and processing that constitute a danger for the workers exploited by big lobbies and companies.[22,23]

Solar energy, instead, is particularly interesting and promising in this regard, since it represents an almost unlimited energy source (one hour of sunlight is comparable to the energy that humankind uses in one year), and is clean, sustainable and safe. During the last 50 years, many researches have paid attention in this field, yet so far most of the

studies have focused on the direct conversion of solar energy into electricity.[24] The need to investigate on the ulterior transformation of energy into more useful forms such as liquid or gas fuels, which can be easily stored and moved to different places, is therefore pivotal to achieve the net zero emission objective by 2050.

Nature in this case can lead us to understand mechanisms and processes behind chemical reactions that can help us to deal with climate change. In the next Section 1.2, an introduction about natural photosynthesis and the basis of solar energy conversion to useful chemical bonds is thus provided.

1.2. The solar energy conversion in Nature

The exploration of new renewable energy sources has been the focus of the scientific community for decades, and inspiration from nature has been pivotal for the understanding and the exploitation of different new technologies.[21] Considering solar energy, with its 120 000 TW of radiation reaching the surface of the Earth (ca. 70% of the solar energy delivered to the Earth), it has an enormous prospect as a clean, unlimited, sustainable and cheap energy source. However, despite its potential as an energy source, its use remains limited due to important factors, which are: (i) non-uniform distribution; (ii) light intermittency; and (iii) difficult storage. Light conversion into useful chemical fuels achieved through artificial photosynthesis represents thus a practical solution to these problems. It is therefore of humongous importance to comprehend the mechanism behind natural photosynthetic processes in order to mimic nature and efficiently obtain solar fuels to use as alternative energy source to non-renewable ones.

Natural photosynthesis performed by organisms like plants, cyanobacteria and algae allows for the storage of energy from sunlight as energy-rich hydrocarbons by utilizing H_2O and atmospheric CO_2 while producing O_2 gas as side-product. This process enabled the evolution of the primitive Earth to the current globe with an O_2-rich atmosphere.

The natural process comprises of several steps, which are divided into light absorption and subsequent oxidative and reductive reactions to obtain the final products afore

mentioned. The two complementary processes are happening in photosystem II (PSII) and photosystem I (PSI), respectively, both located in the thylakoid membrane of chloroplasts.[25] As shown schematically in Scheme 1, the process starts in PSII where the light is first absorbed by antenna systems (LH) consisting of pigment-proteins, then later the absorbed energy is directed in the form of electrons to the reaction-center chlorophyll P680 (λ = 680 nm), generating an exciton.[26] The charge separated state ($P680^{\bullet+}$) is stabilized by subsequent electron transfers to strong reducing agents, such as plastoquinone (PQ) and plastocyanin (PC). As soon as PQ gets reduced (PQH_2), protons can cross the membrane through the Cytochrome b_6f complex (Cyt b_6f), promoting a potential difference between the stroma and the lumen.[27,28]

Meanwhile, the positive charges coming from the oxidized P680 are stored and accumulated on a tetramanganese calcium complex (Mn_4CaO_4), the active site of the catalytic cluster named the Oxygen evolving center (OEC), which consequently follows an oxidation, leveling the potential difference previously described and allowing the four-electron water-splitting oxidation reaction to occur (Equation 1):[29,30]

$$2H_2O \xrightarrow{4h\nu} O_2 + 4e^- + 4H^+ \quad (1)$$

After the reduction of plastocyanin (PC), the electrons are directed to PSI, where light is collected by P700 (λ = 700 nm). The excited P700 continues the chain by transferring the electrons to ferredoxin-$NADP^+$ reductase (Fd), which catalyzes the reduction of nicotinamide adenine dinucleotide phosphate ($NADP^+$) to NADPH in the stroma (Eq. 2):

$$NADP^+ + H^+ + 2Fd^- \rightarrow NADPH + 2Fd \quad (2)$$

When NADPH is generated and adenosine triphosphate (ATP) is formed by condensation of adenosine diphosphate (ADP) and inorganic phosphate through the enzyme ATP synthase, a concomitant generation of proton motion is generated across the membrane, providing again the equilibration of pH between the two sides of the membrane. NADPH and ATP are finally used to fix carbon dioxide in the Calvin cycle, where it is ultimately converted into sugars and starches.

The entire process from the oxidation of water to the reduction of $NADP^+$ represents the so-called "Z-scheme",[31] and the overall reaction is the following (Eq.3):[32]

$$2H_2O + 2NADP^+ + 3ADP + 3\,P_i \rightarrow 2NADPH + 2H^+ + 3ATP + O_2 \qquad (3)$$

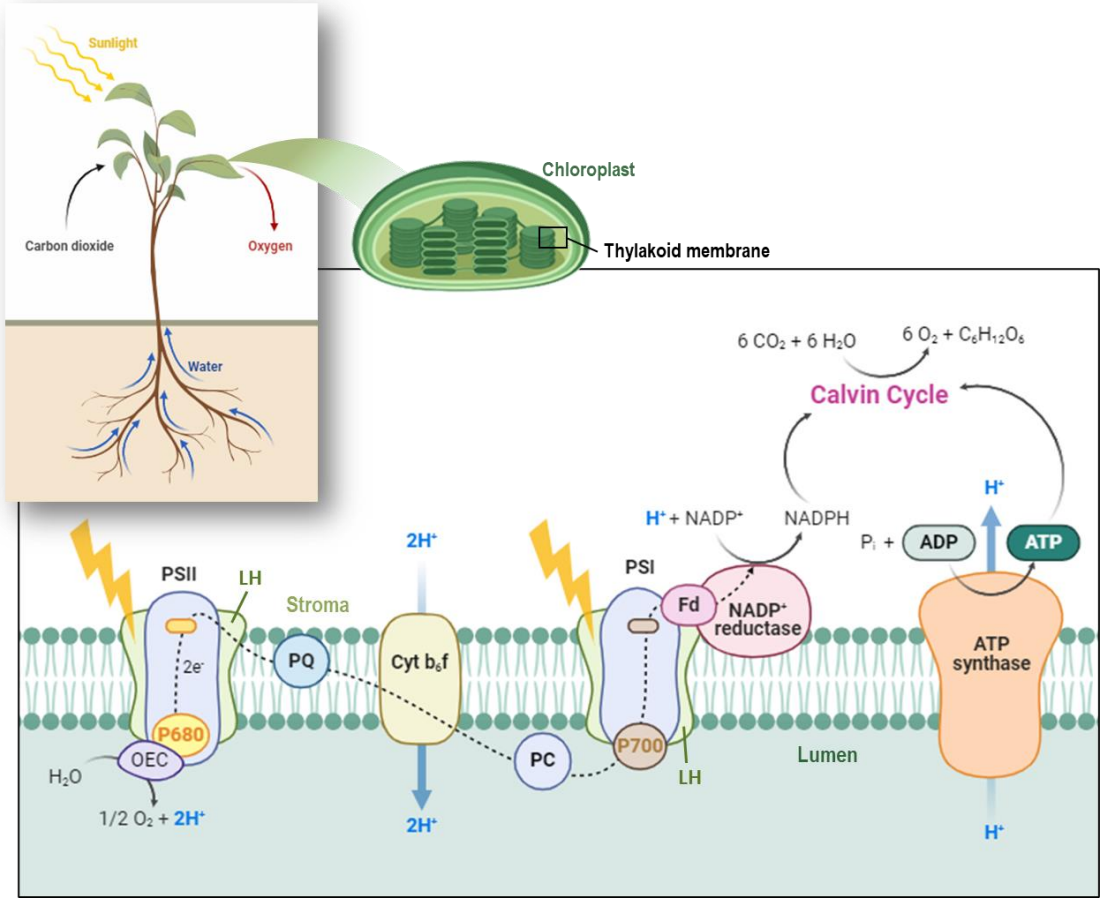

Scheme 1. *Simplified illustration of the mechanisms occurring during natural photosynthesis performed by plants in the chloroplasts. The image has been created using BioRender.com.*

Several studies regarding the single components and reactions included in the chloroplast's membrane have been carried out in order to fully understand the mechanism of natural photosynthesis.[33–37] The main contributors to this process which are used as inspiration for the mimicking of Nature in artificial photosynthesis are: (i) chlorophylls P680 and P700 absorbing one photon in the visible range of the solar spectrum, with an incredible almost unitary quantum efficiency under optimum conditions;[35] (ii) the catalytic center (OEC) in PSII that promotes water oxidation through

the accumulation and transfer of four holes and electrons; (iii) the reduction center in PSI where the reduction of $NADP^+$ to NADPH using two electrons and a proton takes place.

In this context, the Mn_4CaO_5 cluster has gained particular attention because of its ability to accumulate holes and perform the oxygen evolution reaction. The structure of the inorganic core is presented in Scheme 2, proposed by X-ray absorption spectroscopy (XAS), X-ray diffraction (XRD), and density functional theory (DFT) studies.[34] The structure resembles a cubane with three Mn atoms (Mn1, Mn2, Mn3) and one Ca atom (Ca1) linked by oxo-groups, whereas a fourth "outer" Mn atom (Mn4) is attached to the main structure via a corner μ_3-oxo (O5) and a μ-oxo bridge (O4) to Mn3. The surrounding area is formed by amino acid residues and water molecules, which provide a coordination framework around the cluster. The water oxidation process in the OEC follows a five-step mechanism, below simplified in Scheme 2, which comprehends successive oxidation of the Mn atoms after light irradiation *via* proton-coupled electron-transfer (PCET), meaning that there is a concerted transfer of one proton and one electron.[29,38,39] In summary, under sun-light irradiation the Mn atoms in the initial S_0 state undergo oxidation *via* three PCET until state S_4 (steps $S_0 \rightarrow S_1$, $S_2 \rightarrow S_3$, $S_3 \rightarrow S_4$). Step $S_1 \rightarrow S_2$ experiences only an electron transfer, while steps $S_2 \rightarrow S_3$ also sees the coordination of one H_2O molecule to the cluster. The step $S_4 \rightarrow S_0$, finally, involves the insertion of one water molecule and the production of O_2, closing the cycle and achieving the initial Mn oxidation states. However, the mechanism of the last step still remains uncertain.

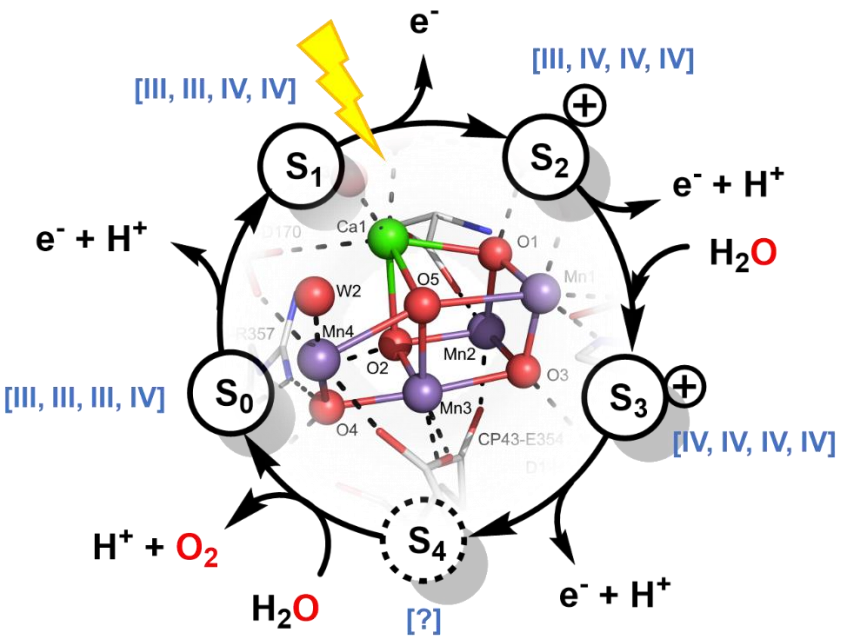

Scheme 2. *The S-state cycle proposed by Kok et al.,*[40] *showing the consequent release of electrons and protons through five S_i states, where the manganese centers change oxidation state after accumulation of holes (the Mn oxidation states are set in blue close to the S_i states). Inset: X-ray crystal structure of the Mn_4CaO_5 core of the oxygen evolving complex of Photosystem II at a resolution of 1.9 Å, where the position of all Mn ions and Ca^{2+} can be identified.*[34]

The exceptional aspect of this process, besides the PCET catalytic steps, is the ability to work at neutral pH while using only earth-abundant elements.

Inspired by Nature, artificial photosynthesis emerges as a promising technology to harvest sunlight energy and store it into so-called solar fuels.[33,41–43] This process uses sunlight to oxidize water to O_2 with the aim of employing the released H^+ and e for reducing either H^+, CO_2 or N_2 into H_2, hydrocarbons or NH_3, and therefore storing the energy of light in the form of chemical bonds (Table 1).[44]

Table 1. *Redox reactions and their respective potentials (V vs. RHE) suitable for solar fuel generation in artificial photosynthesis.*

	Reaction	*E°* / V *vs.* RHE or NHE (pH 0)
Water oxidation reactions (WOR)	$2\mathrm{H_2O} \rightarrow \mathrm{O_2} + 4\mathrm{H^+} + 4\mathrm{e^-}$	1.23
	$2H_2O \rightarrow H_2O_2 + 2H^+ + 2e^-$	1.77
Proton reduction reaction (PRR)	$4H^+ + 4e^- \rightarrow 2H_2$	0
Nitrogen reduction reaction (NRR)	$N_2 + 8H^+ + 6e^- \rightarrow 2NH_4^+$	0.275
CO_2 reduction reactions (CO2RR)	$CO_2 + 8H^+ + 8e^- \rightarrow CH_4 + 2H_2O$	0.18
	$CO_2 + 14H^+ + 14e^- \rightarrow C_2H_4 + 4H_2O$	0.14
	$CO_2 + 12H^+ + 12e^- \rightarrow C_2H_5OH + 4H_2O$	0.08
	$CO_2 + 6H^+ + 6e^- \rightarrow CH_3OH + H_2O$	0.03
	$CO_2 + 2H^+ + 2e^- \rightarrow CO + H_2O$	-0.1
	$CO_2 + 2H^+ + 2e^- \rightarrow HCOOH$	-0.17
	$CO_2 + 2H^+ + 2e^- \rightarrow H_2C_2O_4$	-0.45

Like in natural photosynthesis, the use of light-harvesting materials (also called photo-sensitizers) combined with an oxidation or reduction catalyst center is the basis for an efficient process. In the next Section 1.3, the state-of-the-art of the main technologies developed and exploited in the last decades will provide a broad knowledge on the artificial photosynthesis devices under study and in use so far.

1.3. Towards artificial photosynthesis: different approaches for energy production

In order to accelerate on the development of innovative technologies for water splitting and artificial photosynthesis and reduce global CO_2 emissions, there are several requirements that need to be fulfilled in order to meet national and international targets such as: commercialization, large-scale adoption of efficient, low-cost and durable technologies, and competitiveness with fossil fuels and incumbent technologies that are

currently in use. In the case of clean hydrogen, the US Department of Energy (DOE) stated that in order to develop affordable technologies, the cost for the production of hydrogen should be $2/kg by 2026, and $1/kg by 2031.[45] The efficiency towards hydrogen production is generally defined by the Solar-to-Hydrogen conversion efficiency (STH) parameter, explained through the Equation 4:

$$STH\ (\%) = \frac{output\ energy\ as\ H_2}{energy\ of\ incident\ solar\ light} = \frac{(mol\ H_2 \cdot s^{-1}) x\ (237000\ J \cdot mol^{-1})}{(100\ mW \cdot cm^{-2}) x\ area\ (cm^2)}\ x\ 100 \quad (4)$$

There are a large number of electrolyzer technologies currently under development which are divided into two groups: (i) low-temperature electrolysis technologies, which include proton exchange membrane (PEM) electrolyzers, liquid alkaline electrolyzers and alkaline exchange membrane (AEM) electrolyzers; and (ii), high-temperature electrolysis techniques, that include oxide-ion-conducting solid oxide electrolysis cell (O-SOEC) electrolyzers and proton-conducting solid oxide electrolysis cell (P-SOEC) electrolyzers.[45,46] Besides these devices, there are also advanced pathways for clean solar hydrogen production that are currently under study and development, some of which are here presented: photovoltaic-assisted (PV) electrolyzers, photoelectrochemical (PEC) cells and photocatalysts (PC) colloid suspensions (Figure 3). The idea of these advanced technologies is to couple oxidation and reduction reactions in a unique device that works in aqueous electrolytes and to use solar light as an energy source for overall water splitting.

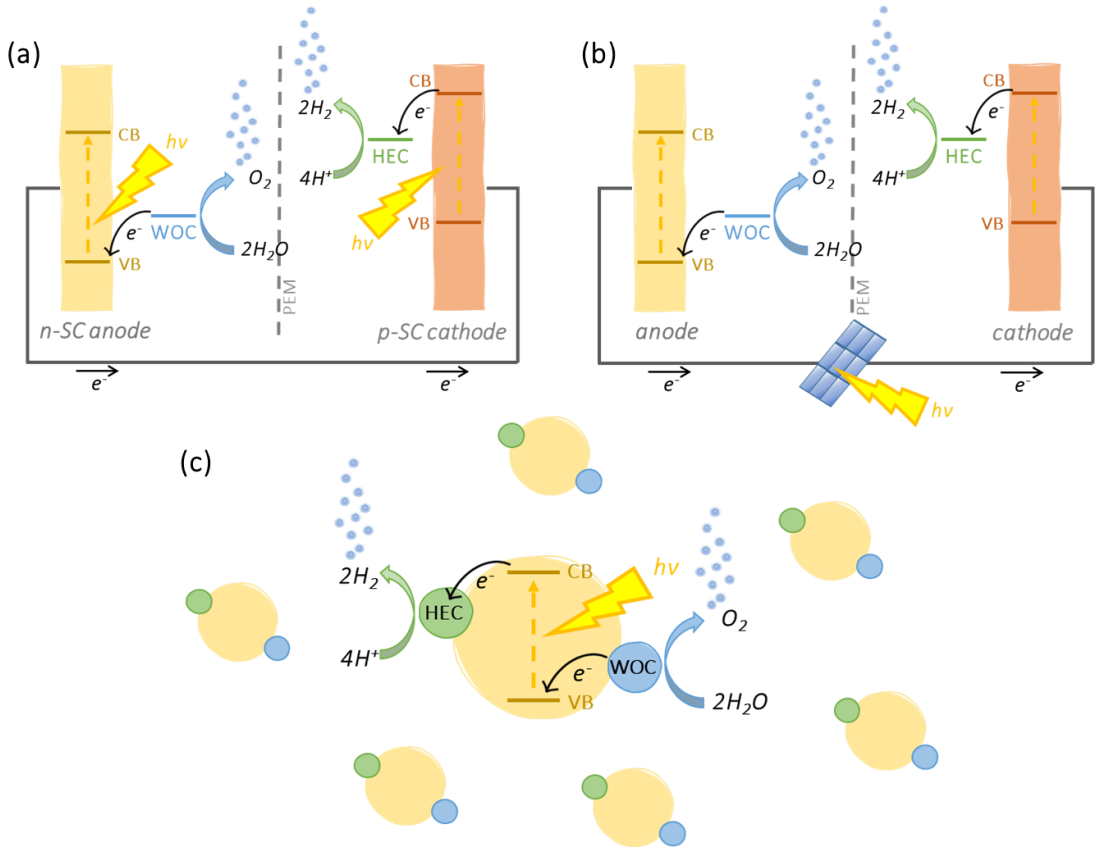

Figure 3. *Simplified design of different artificial photosynthetic approaches: (a) n/p tandem photoelectrochemical (PEC) cell, (b) photovoltaic-assisted electrolyzer (PV-EC), (c) photochemical (PC) colloidal suspension. PEM stands for proton exchange membrane, WOC is water oxidation catalyst, HEC is hydrogen evolution catalyst, and VB and CB stand for valence band and conduction band.*

All the approaches reported in Figure 3 show the production of H_2 and O_2 from water, but the technologies can be also coupled with the CO_2 reduction reaction (CO2RR) to convert it further to carbon-rich products, simulating natural photosynthetic systems.

Generally, any device designed for clean fuel production should fulfill three main requirements: (i) be stable at different pHs and under oxidative/reductive conditions; (ii) absorb a significant fraction of sunlight (as explained in section 1.4.1), thus the materials used need to have the suitable bandgap energy; (iii) possess band edges in an optimal position with respect to the redox thermodynamic potential for a specific oxidation or reduction process; and (iv) have efficient catalyst that speed up the reactions involved.

Here below the three methodologies are more precisely delineated with their main characteristics.

The PEC system (Figure 3a) consists of a cell with two photoelectrodes made of semiconductor materials functionalized with suitable catalysts for the desired oxidation and reduction reactions, and no energy supply other than solar light and a semi-permeable membrane (such as proton-exchange membrane, PEM) that can separate the half-reactions and thus the resulting gases.[47] The cell, as reported in the mentioned figure, can be a p/n tandem system, where both photoelectrodes are absorbing light and generating excitons for the subsequent charge separation and transfer, or alternatively can be constituted by only one photoelectrode absorbing light and a potential bias applied in order to equilibrate the system. This latter case is generally employed for primary studies of the half-reactions separately, in order to optimize them separately. Another common way to use PEC cells is with a dye-sensitized photoelectrochemical cell (DSPEC),[48] which are later mentioned in section 1.4.2. In this case a molecular dye-sensitizer is interfaced to the semiconductor material when the latter possesses a wide band-gap and is not able to absorb visible light (e.g. SnO_2, ZnO and TiO_2).

In order to be used as photoelectrodes in PEC devices, semiconductor materials should be supported on suitable substrates. These substrates consist of glass slides with one face covered with a highly doped semiconductor, e.g. fluorine-doped tin oxide (FTO) or indium-doped tin oxide (ITO), which are good conductors and are transparent to visible light due to their wide bandgap. This allows the collected electrons to migrate from the photoanode to the (photo)cathode through an external circuit.

The semiconductors are usually deposited in the form of nanostructured materials (generally from colloidal suspensions),[49–51] resulting thus in a porous network which allows for the permeation of the electrolytic solution such that it gets in contact with each particle. The enhanced surface area allows for a higher absorption of photons, however the single particles can hardly sustain the invoked charge separation, meaning that the presence of a catalyst is of major importance to avoid charge recombination.[52,53]

An advantage of PEC devices is that they require only intermediate STH efficiencies of 10-15% to be economically competitive.[24] In fact, assuming a 100% quantum yield (that is, the conversion of photons to products) for a material absorbing in the visible light region (400-700/1000 nm), the STH value obtained would be between 25% and 47%.[54]

PV-assisted electrolysis systems (Figure 3b), instead, are based on a PV cell connected to an electrolyzer (EC) composed of an anode and a cathode functionalized with heterogeneous catalysts and immersed in an electrolyte solution. In this system, the light absorption and the redox reactions are separated and completely independent, which gives the opportunity to optimize absorption and stability separately.[55,56] However for efficient performance, the materials employed are typically quite expensive. Furthermore, due to energy loss that can occur during the process or the several resistive processes that occur due to the separation of components, the STH efficiencies cannot reach high values. In order for the system to be economically competitive and to offset the high costs associated with manufacturing precious metal materials for both PV and EC, the STH achieved should be more than 25%.[24] In recent years, several studies have obtained major results even though still at laboratory scale.[56,57]

Finally, in the photocatalytic (PC) colloidal suspensions systems (Figure 3c), the light absorption and the redox reactions are integrated. The semiconductor particles are modified with catalysts for both redox reactions, such that following photoexcitation, the same semiconductor particle can induce OER and HER simultaneously.[58–60] In this case it is also possible to focus on one half-reaction at a time by using a sacrificial agent, specifically a sacrificial electron acceptor (SEA) when using a co-catalyst for oxidation, and a sacrificial electron donor (SED) when using a co-catalyst for reduction. PC based technologies are facing numerous problems in their development and thus are currently only being tested at laboratory scale, however, are highly promising due to their simplicity in reactor design, economic viability, and scalability. To be economically competitive, in fact, this system requires only small STH values (5-10%),[61] because of the low cost of plant installation. Generally, PC devices comprehend wide bandgap semiconductors, on top of which co-catalysts in the form of metal-oxide nanoparticles are deposited (e.g. RuO_x, IrO_x, NiO_x, CoO_x), while only few cases are reported of SC with

anchored molecular catalysts.[24,62] Considering the wide energy gap of the materials, it is thus a common consequence that they exhibit low STH value around 0.1-2%. In order to address this problem, numerous materials have been recently developed with the usual metal oxide SC doped with nitrogen or sulfur.[62] Particular attention was given lately to organic-based materials,[60,63–67] such as carbon-nitrides (g-C_3N_4), covalent organic frameworks (COFs), covalent-triazine based frameworks (CTFs) and carbon quantum dots (CQDs), which are synthetically versatile and possess a delocalized π-system. These characteristics allow improved light absorption in comparison with wide-bandgap SC, tunable electronic properties, and porous structures, which give them an increased surface area. However, several problems are generated by the very low-rate photocatalytic reactions, as well as the internal charge recombination that occurs when both oxidation and reduction reaction are taking place on the same material.[32,54] Nevertheless, photocatalyst colloidal suspensions are recent and promising materials, with just a few examples in the literature (*vide infra*, section 1.5), leaving the possibility for large improvements.

In the following sections, a theoretical overview will be given regarding each of the contributors for artificial photosynthesis, as well as the state-of-the-art technologies for various components employed in the whole work.

1.4. Primary elements in artificial photosynthetic devices

1.4.1. Light absorption and photo-sensitizers

Electromagnetic radiation occurs over an extremely broad range of wavelengths, from gamma rays (with wavelengths less than about 1×10^{-11} meter) to radio waves (measured in meters). Within this wide spectrum, the wavelengths visible to the human eye occupy a very narrow region, from about 700 nm for red light down to about 400 nm for violet light. The spectral regions adjacent to the visible band are often also referred to as light, infrared at one end and ultraviolet at the other (see Figure 4). Like all types of electromagnetic radiation, visible light propagates by massless elementary particles called photons (or *quanta*) with a speed of 299,792,458 m s^{-1} measured in vacuum. The main source of natural light on Earth is the Sun, which emits thermal

electromagnetic radiation (yellow spectrum in Fig. 4) like an ideal black-body, a body in thermodynamic equilibrium with its own environment, that consists of a continuous spectrum (black line in Fig. 4).

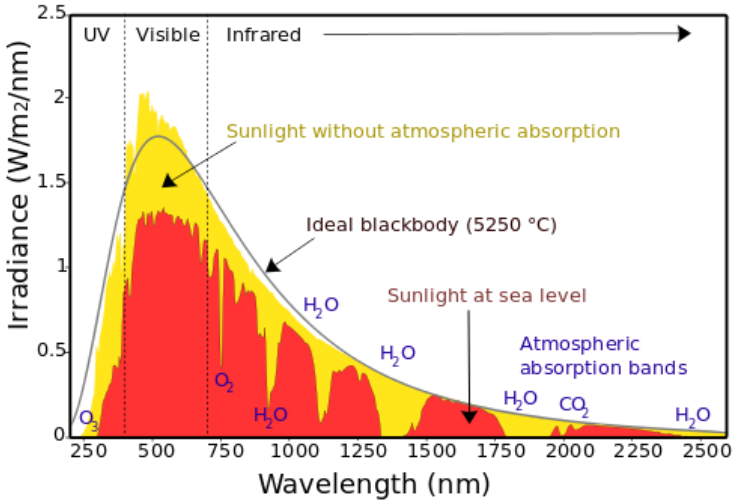

Figure 4. *Solar radiation spectrum for direct light from above the Earth's atmosphere (area in yellow) and at sea level (area in red). The sun produces light with a distribution similar to what would be expected from a 5525 K (5250 °C) blackbody, which is approximately the sun's surface temperature. As light passes through the atmosphere, some photons are absorbed by gases like water and CO_2. Additional light is redistributed by Rayleigh scattering, which is responsible for the atmosphere's blue color. Regions of ultraviolet, visible and infrared light are indicated. Figure without copyright prepared as part of the Global Warming Art project, Wikipedia.*

When photons pass through the atmosphere, part of the radiation is scattered from gases present, like H_2O, CO_2 and O_3, while the rest of the radiation reaches the Earth with the spectrum shown in red. Considering the final solar spectrum, it is evident how visible light is the most intense form of radiation, meaning that most of the photons own an energy between 1.77 and 3.1 eV, obtained from Equation 5:

$$\mathrm{E\ (eV)} = \frac{\mathrm{h\ (eV\ m)} \times \mathrm{c\ (m/s)}}{\lambda\ \mathrm{(m)}} = \frac{1.2398 \times 10^{-6}}{\lambda\ \mathrm{(m)}} \qquad (5)$$

where h is the Plank constant (eV m = kg m^2 s^{-1}), c is the speed of light (m s^{-1}) and λ is the photon's wavelength (m).

Photons in emitted light can interact with matter, producing different effects, like scattering, absorption, or transmission. In the first case, light is dispersed in different directions, depending on the phenomena occurring (reflection, refraction, diffraction), while in the second case photons react with the material itself, and in the last case photons pass through the matter, even though the first two effects can prevent it.

Whenever a photon is absorbed, depending on the energy it possesses, it generates the transition of an electron from the ground state (*gs*) to an excited state (*es*). The electron can later return to the *gs* through radiative (light or photons) or non-radiative (heat or phonons) decay by either undergoing a chemical reaction or interacting with another matter/molecule to provoke quenching (oxidative or reductive) through electron transfer. From the artificial photosynthesis perspective, it is important that the electrons are efficiently transferred from the light absorbers to the water oxidation, H_2 evolution or CO_2 reduction catalysts, avoiding the decay to the ground state and/or undergoing secondary processes. This electron transfer process can be controlled by strategic engineering of the system.

When designing a system for artificial photosynthesis for solar fuel production, the assembly should simulate the natural process. Since visible light constitute about 46% of the solar spectrum,[68] finding suitable light absorbing systems working in the visible light region is crucial for the efficient conversion of water to H_2, or for the reduction of CO_2 to C_xH_y products. Over the past decades, semiconductor (SC) materials and molecular photosensitizers (PS), mostly based on transition metals, have been deeply studied and optimized to get the best solar energy conversion efficiency,[69] although the cost of the components and the stability should be further improved.[70]

Considering PS, in order to be efficient, different qualities should be fulfilled: (i) strong visible light spectrum absorption; (ii) strong adhesion to the SC surface; (iii) alignment of energy levels for effective thermodynamic oxidation or reduction processes; (iv) effective charge separation; (v) fast electron transport rate; (vi) stability in different thermal and electrochemical conditions. Among all molecular photosensitizers, the most known example is the extensively described $[Ru(bpy)_3]^{2+}$, which has been widely used in combination with water oxidation catalysts, either in homogeneous phase or covalently linked between the two systems.[44,70–76] Porphyrin, protoporphyrin, and

phthalocyanines are instead among the natural chemicals and derivatives that make up the majority of photosensitizers for the reduction process.[69,77–80] Perylenes also represent another example of dye-sensitizers (DS) that have been deeply studied in the last years in combination with catalysts and semiconductors. Because perylenes have a completely organic composition, incredibly high absorption coefficient and stability in different conditions, they are a very interesting system to try to resemble nature.[50,81,82] Dye-sensitized photoelectrochemical cells (DSPEC) and dye-sensitized solar cells (DSSC), which contain both photosensitizers and semiconductors in the same system, are among the most investigated devices for artificial photosynthesis.[83–85] However, considerable effort should be dedicated to their improvement of stability, charge transfer and photocatalytic activity.

In the following section, a detailed explanation about semiconductor materials and their properties is provided.

1.4.2. Band theory and semiconductors properties

The element which is essential for efficient solar energy conversion to chemical fuels or electrical energy is, definitely, the semiconductor. Semiconductors (SC, as previously introduced) can absorb electromagnetic frequencies varying from the near-IR to the near-UV, including the visible region, achieving a quantum yield close to unity depending on their energy gap (*vide infra*). Semiconductor properties are indeed well described by the Band Theory, which is exclusively applicable to solids.[86,87]

Generally, in molecular systems, overlapping atomic orbitals produce a discrete system of molecular orbitals that can be either bonding or anti-bonding. In a different way, solids, due to the presence of a huge number of interacting atoms, have an electronic structure that is typically presented in terms of energy bands; indeed, with *N* atoms constituting a crystalline lattice, there will be *N* molecular orbitals generated that are placed very close to each other and can be described as a continuum of energy.

In solids, the highest energy level occupied with electrons, comparable to the highest occupied molecular orbital in molecules (HOMO), is called the Valence Band (VB), while the empty energy level, similarly to the lowest unoccupied molecular orbitals (LUMO) is named Conduction Band (CB). The energy separation between the bands is called the

Energy Bandgap (E_{gap}), which is the parameter that allows for the distinction of three classes of solids and defines the material's optical and electronic properties (Figure 5).

Metals, or alloys, (Figure 5, orange) are characterized by the absence of an energy gap between VB and CB, which are thus overlapping, that promotes the transfer of a huge number of electrons with energy as low as a thermal quantum k_bT (with k_b the Boltzmann constant and T the temperature) that ensures high conductivity in the material. Insulating materials (Figure 5, blue), with a very wide bandgap, do not allow for electron transfer between the two bands, leaving the conduction band completely empty. Finally, semiconductors (Figure 5, green) have a smaller bandgap with respect to insulators. Consequently, the electrons can be promoted to the CB after the absorption of an energetic input, whether thermal, electric or optical. The excitation of an electron to the CB leaves a positively charged electron hole in the VB, which can be filled with other electrons in nearby levels of the same band, thus promoting the mobility of holes in the opposite direction of electrons.

Semiconductors can be classified into two groups: intrinsic and extrinsic. The first case applies to those materials that possess a sufficient number of charge carriers without any dopant species (green blocks, Figure 5). The second, instead, refers to materials which are intentionally modified (i.e. doped). The doping methodology allows for a change in conductivity by reorganizing the electronic structure and consists of the addition of electron-rich or electron-deficient atoms into the crystalline lattice, which influences the resulting properties of the semiconductor. An example of this could be the insertion of phosphorous (P, group V) or boron (B, group III) in a silicon material (Si, group IV).

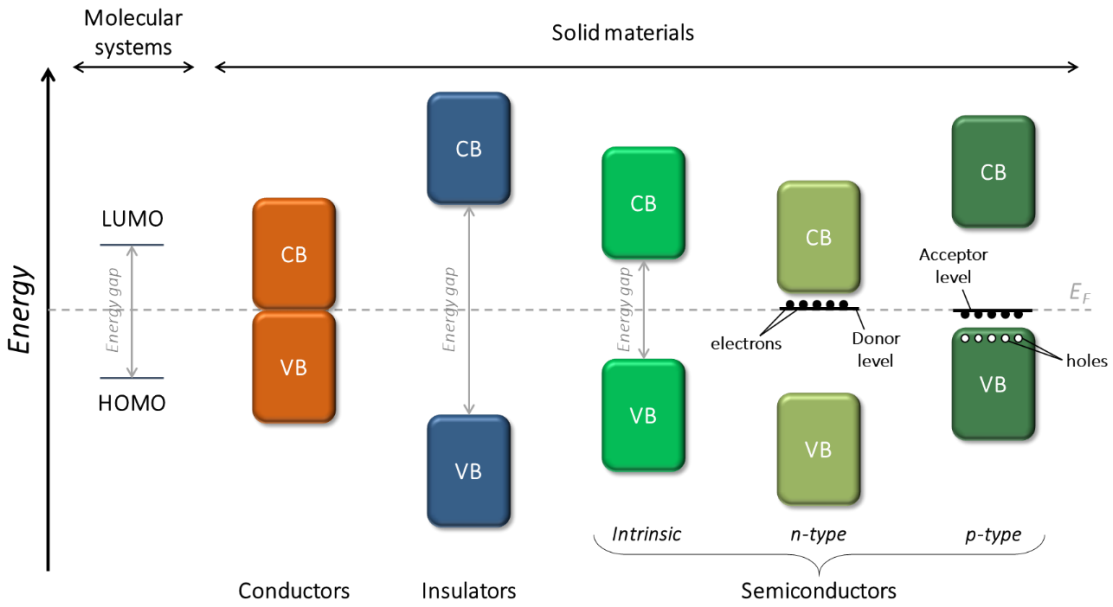

Figure 5. *Energy diagram schematically describing the Band Theory for conductors or metals (in orange), insulators (in blue) and semiconductors (in green), represented through the valence band (VB) and conduction band (CB), compared to molecular systems with HOMO and LUMO levels (on the left). On the right of the diagram, three types of semiconductors are shown: intrinsic semiconductors (in green), n-type semiconductors (in light-green) and p-type semiconductors (in dark-green).* E_F *stands for Fermi level (*vide infra *for further explanation).*

In the first type of doped semiconductors, the insertion of an electron-deficient atom in the crystalline lattice induces the formation of acceptor levels due to the presence of an empty orbital on the same atom, which can host electrons from the VB. These acceptor states are energetically close to the valence band and are centered on the foreign atom. These materials are called *p-type* semiconductors (dark-green blocks, Figure 5). Analogously for the other type, an electron-rich element is introduced, and the exceeding electron remains partially free, occupying the so-called donor states; states that are energetically close to the conduction band edge. A thermal excitation from these states to the CB results in improved conductivity of the material. This situation represents the condition of *n-type* semiconductors (light-green blocks, Figure 5).

Since in this thesis project the focus will be mostly on the water oxidation half-reaction, a detailed description of p-type semiconductors will not be provided, and attention will be given exclusively to n-type SC.

These donor states, also called *intra-bandgap states* or more simply *trap states*, can play different roles in controlling the charge recombination reactions, depending on their position in the E_{gap}. For the specific case of n-type SC, if these traps are shallow, which means that they are close to the CB, they can act as an electron stock. Otherwise, if they are near the VB, it is possible that some holes can be easily excited to these donor states and consequently facilitate recombination reactions.

There is another possible situation for extrinsic semiconductors, which is represented mainly by metallic oxides or amorphous materials where the stoichiometric ratio of the compounds is not well-defined, or the material lacks electrons. A very representative example could be the case of a TiO_2 lattice,[53] in which there could be some oxygen vacancies, particularly on the surface of the semiconductor. Titanium(IV) has a d^0 configuration, but the lack of a bonded oxygen or the presence of dangling bonds leads the metallic center to assume a different oxidation state (Ti^{3+}) in order to maintain the neutrality of the crystal. Thus, the formation of some electron-rich centers close to the CB is inevitable and the semiconductor will act like an n-type material. These trap states are well-described in the case of the first photochemical device for water splitting reported by Fujishima and Honda, where the TiO_2 photoanode presents states close to the CB which do not provide enough driving force to generate hydrogen at the counter electrode and thus induce a charge recombination.[52,88,89]

Considering that SC materials for artificial photosynthesis work under illumination immersed in an aqueous solution, an important point of study is the solid/electrolyte interface and its properties.

Taking n-type semiconductors as reference, the *Fermi level* (E_F) is typically present right below the conduction band edge (E_{CB}). Thermodynamically speaking, the Fermi level represents the electrochemical potential of electrons in the solid state, while, statistically, it is the energy where the probability of an electron occupying a level is 50%. Thus, the Fermi level describes the occupation of energy levels in a semiconductor at the thermodynamic equilibrium (Figure 6a).

When the semiconductor surface and electrolyte get in contact, E_F in the semiconductor adapts to the redox potential of the A/A^- couple in the solution ($E_{F,redox}$), which remains

basically constant due to the number of available states per unit energy in solution exceeding the analogous number in the solid. In the case of n-type SC, this equilibration occurs through the migration of electrons across the interface (Fig. 6b), leading to the formation of a space-charge layer, or *depletion layer*, where the surface area suffers a depletion of the majority carriers. The interface can hence be described as a parallel-plate capacitor (from equivalent circuits): the Helmholtz layer (C_H) in the solution is negatively charged and it is counterbalanced by a positive charge excess in the depletion layer (C_{SC}). To establish an equilibrium at the interface, electrons are transferred from the solid surface to the solution, inducing upward band bending (Fig. 6b).[48] Under particular conditions (e.g. polarizing the electrode by applying an external potential $\Delta\phi$), this energy difference can be removed and the bands become "flat" again. This condition identifies the *flatband* potential, E_{fb}, which lays close to the CB in n-type systems.[90]

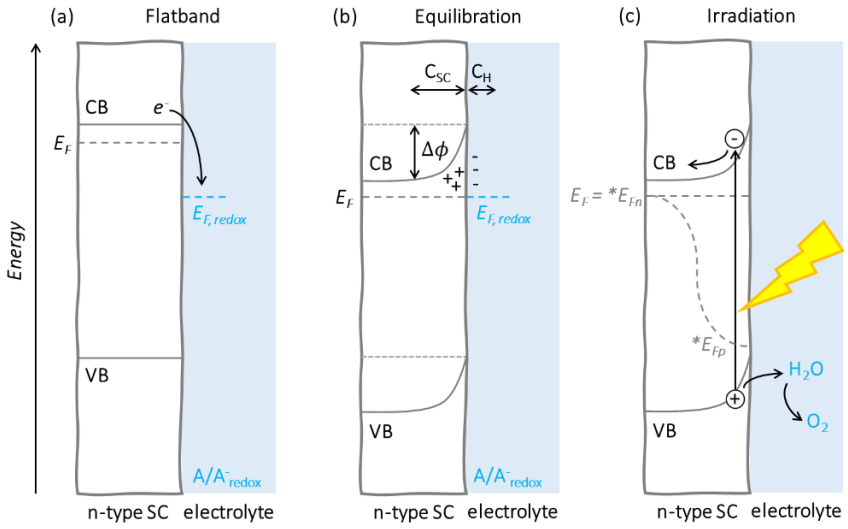

Figure 6. *Schematic energy model of the semiconductor/electrolyte interface, (a) before and (b) after the establishment of equilibrium. E_F, $E_{F,redox}$, CB and VB are, respectively, the Fermi level, the redox potential for the electrolyte, the conduction band and valence band, respectively. $\Delta\phi$, C_{SC} and C_H represent the potential bias, the depletion layer and the Helmholtz layer, respectively. (c) Representation of the mechanism of electron-hole couple generation and spatial separation. $^*E_{Fn}$ and $^*E_{Fp}$ correspond to the quasi-Fermi level for electrons and holes, respectively.*

The band bending generated at the interface is fundamental for the correct operational process of the system upon illumination. Indeed, when the material immersed in the electrolyte is irradiated with light of higher energy than that of its bandgap, electron-hole pairs (*excitons*) are generated and further separated by the potential gradient of the depletion layer. The hole created in the VB is attracted from the negatively-charged Helmholtz layer of the solution, while the electron in the CB suffers a repulsion effect from the same solution and is thus induced towards the inner part of the solid (Figure 6c). Therefore, using an illuminated n-type semiconductor, it is possible to convey holes to the electrolytic solution and take advantage of their oxidative power in order to perform water oxidation. Similarly, p-type SC can be used for proton or CO_2 reduction. In order to improve the hole transfer to the solution and prompt the reaction, the introduction of a catalyst in the device is then pivotal. For this reason, a detailed explanation about catalysts, their properties and functionalities is provided in the following sections (1.4.3 and 1.6).

It is also important to underline the effect of light on the Fermi level. In fact, when solar irradiation is provided to the system, the excess of photogenerated electrons and holes at the SC surface produces a variation in the population of CB and VB with respect to the equilibrium case. These non-equilibrium states are described as the *quasi*-Fermi level of electrons ($^*E_{Fn}$) and *quasi*-Fermi level of holes ($^*E_{Fp}$). In general, the density of the majority carriers (electrons in the case of n-type SC) does not increase significantly upon illumination, thus the quasi-Fermi level of electrons is almost equal to the Fermi level in the dark. In contrast, the density of the minority carriers (holes) increases significantly in the vicinity of the solid surface, resulting in a shift of $^*E_{Fp}$ towards the VB edge (Fig. 6c).[91] With the increasing generation of charges at the surface under constant illumination, $\Delta\phi$ get reduced until the *flatband* condition is obtained again (Figure 6a).

This phenomenon, however, is mainly occurring in compact n-type SC. When the dimension and morphology of the SC change (e.g. in the case of porous or nanostructured materials), new effects can be observed due to their new electronic, optical and physical properties, such as the plasmon effect.[92] Because of the small dimension of particles or the increased surface area in contact with the electrolyte when exposed to irradiation, the photogenerated charge separation is not controlled by the

potential gradient $\Delta\phi$ over the space-charge region and an effective depletion layer is not supported.[47]

A new class of semiconductors that have these properties are, for instance, the organic-based SC. These materials, which will be later better described in the following section 1.5, are organic polymers composed by repetitive units which provide an extended π-conjugation. Compared to inorganic SC, they are cost-effective, have an easy synthetic approach, a high chemical stability, mechanical flexibility and with tailorable optical properties, depending on their electronic structure.[93–95]

In this particular case, considering the low dielectric constant of organic SC,[96] the proper photogenerated charge separation occurs through the inclusion in the system of electron acceptor (A) and electron donor (D) groups. The A-D configuration can be (i) intrinsic to the organic polymer, e.g. by choosing a repetitive unit containing both, or (ii) extrinsic, by combining two different monomers. As well, the charge separation is facilitated by a fast reaction of holes at the surface with a suitable redox species in the electrolyte, but the inclusion of a catalyst in the system can favorably increase charge extraction, prolong the charge separation, provide active sites for specific reactions and thus improve the overall efficiency.[97] Further explanations of the mechanism and the role of the catalyst in the whole system are explained in the next paragraphs, where we will focus especially on the oxidative reaction from water to dioxygen, while only a brief overview of the reduction process characteristics will be provided.

1.4.3. Catalysts for oxidation and reduction processes

As previously reported in section 1.2, the artificial photosynthesis process can be divided into oxidation and reduction half-reactions and involves the oxidation of water (WOR) to dioxygen with the formation of $4H^+$ and $4e^-$, which are later used to produce H_2 from protons (HER) or reduce CO_2 to hydrocarbons (CO2RR) (see Table 1). One of the critical barriers that keep these processes from being of practical use is the highly demanding thermodynamic potential barriers and the sluggish reaction kinetics (Figure 7, left).[98] Thus, the use of catalysts capable of accumulating redox equivalents and operating close to the thermodynamic potential are necessary. Within this context, transition metal-based catalysts can store electrons *via* multiple redox states, hence they are considered as suitable candidates to efficiently drive the reactions while lowering the associated

activation energy barrier. Moreover, they are essential for reducing the occurrence of charge recombination and accelerating surface reactions, especially when using earth-abundant materials.[99] The catalysts are traditionally classified into two groups: (i) transition metal complexes; (ii) metal oxides.[100,101] In this PhD thesis, we will focus our attention on the molecular complexes, which usually include transition metals like Cu, Fe, Ni, Ir, Mn, Co or Ru.[73,102–105]

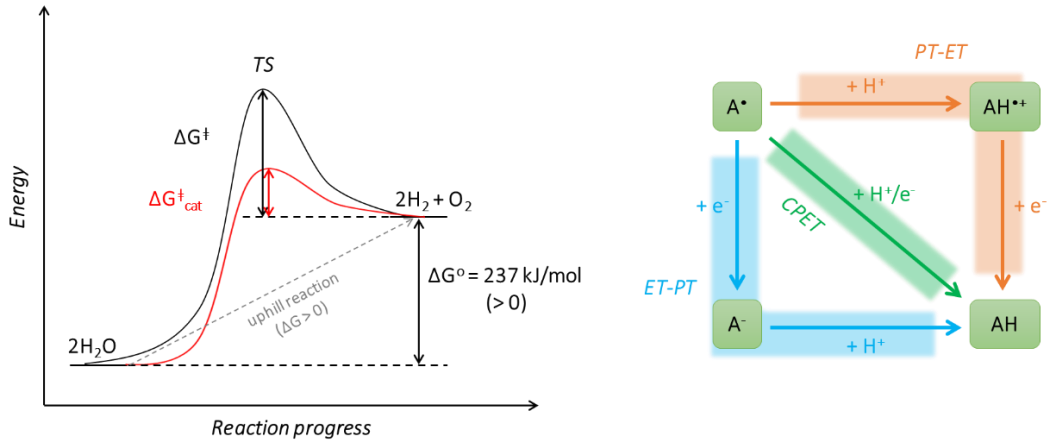

Figure 7. *On the left, schematic illustration of the thermodynamic (ΔG^{o}) and kinetic barriers ($\Delta G^{\ddagger}$) for water splitting (black arrows), with catalyst's effect in lowering the activation energy barrier ($\Delta G^{\ddagger}_{cat}$) (red arrow). On the right, simplified mechanism of proton-coupled electron redox reaction from an $A^{\bullet}$ species to an AH species, involving 1 H^{+} and 1 e^{-} in three different ways: consecutive proton-transfer electron-transfer (orange path), consecutive electron-transfer proton-transfer (ET-PT, blue path) and proton-coupled electron transfer (PCET) or concerted proton-electron transfer (CPET, green path).*

An interesting advantage of molecular catalysts is their rational design and the mechanistic information that can be obtained with intermediates involved in the catalytic cycle through several spectroscopic, electrochemical and computational techniques. A key process was observed when a water molecule got anchored to a metal center in transition metal complexes, and in 1970 the curious redox behavior led to the discovery of the Proton-coupled Electron Transfer (PCET) effect by Meyer's group.[106] PCET is a mechanism in which a proton and an electron are exchanged in a concerted manner, that occurs due to the acidic property of water when coordinated to the metal center (Figure 7, right). This process allows the complex to remain stable while the

oxidation state of the metal center is changing and thus avoids the generation of high-energy intermediates. Moreover, the potential to obtain highly oxidized/reduced species is decreases and is dependent on the pH of the solution following the Nernstian equation (Eq. 6):

$$\mathrm{E} = \mathrm{E}^{\circ} + \frac{\mathrm{RT}}{\mathrm{nF}} \ln \frac{[\mathrm{ox}]}{[\mathrm{red}]} = \mathrm{E}^{\circ} + 2.3026 \frac{\mathrm{RT}}{\mathrm{nF}} \log_{10} \frac{[\mathrm{ox}]}{[\mathrm{red}]} = \mathrm{E}^{\circ} - 0.059\ \mathrm{pH} \qquad (6)$$

where *E* is the reduction potential, E^o is the standard potential, *R* is the gas constant, *T* is the temperature, *n* is the number of electrons exchanged, *F* is the Faraday constant, *[ox]* is the concentration of oxidized species and *[red]* is the concentration of the reduced species. The *E vs.* pH dependence is represented in Pourbaix diagrams, and for $1e^-/1H^+$ transfer the potential slope variates with 59 mV per pH unit.[106]

In order to compare the different catalysts based on their performance, four main parameters are considered:

1. Faradaic Efficiency (FE, %): efficiency of charge transfer towards product (P) formation, given in percentage (Equation 7):

$$\mathrm{FE}\ (\%) = \frac{\exp \mathrm{mol_P}}{\mathrm{theo\ mol_P}} \cdot 100 = \frac{\mathrm{z \cdot F \cdot exp\ mol_P}}{\mathrm{I \cdot t}} \cdot 100 \qquad (7)$$

   where mol_P are the moles of product, obtained experimentally and theoretically, *z* is the number of electrons transferred (4 for OER, 2 for HER), *F* is the Faraday constant (96485 C mol^{-1}), *I* is the current (A) and *t* is the time (s).

2. Turnover Number (TON): number of chemical conversions per active site of the catalyst (Cat) before it deactivates (Equation 8). It is a dimensionless parameter that evaluates the robustness and stability of a molecular catalyst.

$$\mathrm{TON} = \frac{\mathrm{mols\ P}}{\mathrm{mols\ Cat}} \qquad (8)$$

3. Turnover Frequency (TOF, s^{-1}): activity rate defined by the number of catalytic cycles per catalytic center per unit of time (Equation 9). This parameter evaluates how fast a catalyst is, and normally is presented as the TON divided by time (s^{-1}).

$$\mathrm{TOF} = \frac{\mathrm{TON}}{\Delta \mathrm{t}} \qquad (9)$$

4. Electrochemical overpotential (η, V): extra potential required to overcome the kinetic barrier imposed by the reaction (Equation 10). Mathematically it is

defined as the difference between the thermodynamic potential in standard conditions (E^o) and the actual potential needed to perform the reaction (E).

$$\eta = E - E^o \quad (10)$$

With these considerations, we briefly introduce the basis for each of the half-reactions involved in artificial photosynthesis (WOR, HER and CO2RR), focusing on the reaction mechanisms proposed and main molecular catalysts used, with particular attention given to the oxidation half-reaction.

In the context of the reduction half-reaction, the HER involves a two-electron transfer process (Table 1). The mechanism is highly dependent on the environmental condition, i.e. on the pH of the electrolyte, and the thermodynamic redox potential registered as -0.41 V *vs.* NHE at pH 7.[107] To decrease the kinetic energy barrier, however, the most common catalysts employed are based on Rhodium and Platinum, because of their high reactivity to protons and their ability to form metal hydrides. A proposed mechanism for proton reduction, the so-called heterolytic pathway, at a generic metallic center M^{n+} is first the reduction to $H\text{-}M^{n+}$. This species can then be further protonated to evolve hydrogen and regenerate the starting metal catalyst. Alternatively, the $H\text{-}M^{n+}$ species can react with a second hydride molecule, forming $M^{(n-1)+}$ and releasing hydrogen (homolytic pathway). Otherwise, the intermediate can be further reduced to $H\text{-}M^{(n-1)+}$ and follow both heterolytic and homolytic pathways. Other more abundant metals have also been used, like Co, Ni, Fe and Mo, in order to provide a potential facile scalability.[42,98,105,108,109]

CO2RR to carbon-rich products is another challenging reduction process which requires a catalyst to efficiently work. In fact, the injection of one electron into CO_2 requires a lot of energy, since it leads to the formation of the $CO_2/CO_2^{\bullet-}$ redox couple, which has a particularly negative potential (-1.9 V *vs.* NHE at pH 7), due to the rearrangement of the molecule from linear to a bent configuration (Table 1). Hence, the inclusion of a catalyst allows the proton-coupled multielectron transfer to generate more thermodynamically stable molecules, avoiding high energy barriers and decreasing the overall overpotential. However, in most cases only the $2e^-$ reduction products are generated in molecular-based mediated CO2RR, i.e. carbon monoxide or formic acid, and furthermore HER compete with these processes, since it is thermodynamically

favoured.[110] A typical mechanistic process that was observed mainly in iron porphyrins, for example, considers first a reduction of the metal-based catalyst from M^{n+}-L to $M^{(n-2)+}$-L species, followed by CO_2 cleavage from the metal generally through a *σ*-bond formed with the carbon and the final release of CO.[111] However, as explained before, the $M^{(n-2)+}$-L species can also undergo the formation of the metal hydride using H^+, further promoting either H_2 formation or producing the desired formate (HCO_2^-) through CO_2 addition.[42] Some of the most efficient electrocatalytic species employed for CO2RR are Fe-porphyrins and other macrocyclic complexes with Co and Ni as the metal center.[112–118]

Finally, regarding the oxidation half-reaction, the formation of a molecule of O_2 from water (OER) is well-known to be hard to perform kinetically; indeed, it requires the removal of 4 electrons and 4 protons, typically occurring *via* PCET, and resulting in an exceedingly high activation barrier. The process is highly complex as well due to the breaking of an O-H bond and the formation of an O=O double bond (1.23 V *vs.* NHE at pH = 0, ΔG^o = 113.5 kcal mol^{-1}).[119,120] It is hence pivotal to optimize of suitable water oxidation catalysts (WOCs) that are able to promote the reaction by accumulating the 4 holes necessary for water oxidation. They must also remain stable in water under highly oxidative conditions.[120]

Two mechanistic processes unraveled *via* kinetics and spectroscopic studies were reported for OER, one is the interaction between two high-valent metal-oxo groups (I2M) and the other is water nucleophilic attack (WNA).[42] The I2M mechanism consists of two M-O groups interacting to form the O-O bond, which represents the rate-determining step, after which O_2 is released (Figure 8, left). In WNA, instead, a water molecule acts as a nucleophile and attacks the electrophilic high-valent M-O species, with the formation of M-O-O-H (metal hydroperoxide species), which ultimately releases molecular oxygen (Figure 8, right). This last mechanistic path is especially adopted by mononuclear catalysts and catalysts acting on a surface, under restricted mobility conditions.

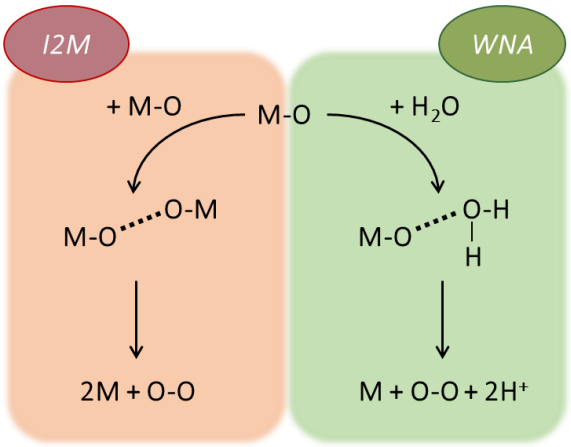

Figure 8. *Proposed mechanistic pathways for O=O bond formation in oxygen evolution catalysis through interaction between two metal-oxo groups (I2M, left) and water nucleophilic attack (WNA, right).*

Among the state-of-the-art molecular electrocatalysts for OER, we find several WOCs of different transition metals, such as those based on Co and Cu. However, the catalysts giving the best reported performances and with the most complete studies about their reaction mechanism are certainly Ru-based molecular complexes, known for their robustness in oxidative environments and for high rates of catalysis. These complexes represent a good alternative to the traditional metal oxides such as IrO_2 and RuO_2.[98,121,122]

A better explanation of these species, their performances and applications will be further provided in the next Section 1.6.

1.5. Employing organic based materials as semiconductors

As previously mentioned in section 1.4.2, 2D organic-based polymeric materials are a new class of semiconductors that were developed in recent years and that have interesting properties for the preparation of more sustainable devices for solar-to-chemical energy conversion.[63,93–95] The main reasons that they are attractive are: (i) the suitable electronic structures and band positions, which straddle the redox potentials for water reduction and oxidation, while the optical gap remains sufficiently narrow for visible light harvesting; (ii) excellent chemical and thermal stability; (iii) facility in the

synthesis from cost-effective, earth-abundant precursors. In a review paper by Thomas *et al.* published in 2010,[93] organic materials were defined as "functional materials", since they are a part of a range of compounds that are being prepared through a "target-motivated" approach, meaning that all properties are adjusted and optimized for a specific purpose.

Generally, the properties of the 2D organic-based polymeric materials can be tuned by rational design of the monomeric units to modify their chemical functionality, electrical conductivity and optical properties, as well as their final structure and morphology. The extended π-conjugation, due to the 2D structure of the organic polymers, provides with a well delocalized charge distribution, where charge transfer is mainly happening through hopping. Although organic-based polymeric materials have been in constant development over the past decades, they still suffer from low conductivity, which facilitates the formation of polarons and the presence of charge recombination processes.[123,124] To address this problem, several strategies have been employed to improve the system, such as atom or molecular integration,[95,125,126] the co-polymerization of different monomers (with a different length of phenyl chain or analogous structure with different atomic content, that does not change the terminal groups),[127] tailoring the particle edges and porosity,[128–130] the inclusion of electron acceptor (A) and electron donor (D) groups in the system[131,132] and functionalization with catalysts (either heterogeneous materials or molecular complexes).[97,133]

The degree of porosity of the material represents another important parameter to master. This property allows one to tune the active surface area, thus controlling the number of active sites available to perform the desired reaction. Some applications for porous materials are, for example, their use as catalysts or catalyst supports, such as with covalent organic frameworks (COFs) and carbon nitrides,[134,135] or for the sorption, purification and storage of gases, such as with metal-organic frameworks (MOF).[136–138] As well, the degree of crystallinity can influence the density of defects and performances of the system in terms of exciton dissociation and charge recombination.[139]

The most studied organic-based polymers are graphitic carbon nitrides (g-C_3N_4, or more simply CN), which are obtained through the polymerization of melamine or heptazine-based monomeric units (Figure 9a). The first time a heptazine was used to create

polymeric carbon nitrides was back in 1834,[140] and represents the oldest polymer synthesized of this type. After that, a broad set of diverse carbon- and nitrogen-rich starting compounds were used to prepare a wide range of CN polymers with lots of different characteristics.[66,100,128,141] Generally, the synthesis of CN relies on the thermal treatment of N-rich monomers after previously modifying them or providing them with supramolecular interaction by dispersing them in suitable solvents. The supramolecular interactions allow for a more ordered polymerization process and enhanced crystallinity, while the following calcination at high temperatures (normally > 400°C) eliminates the solvents and subproducts to obtain a pure final material.[128]

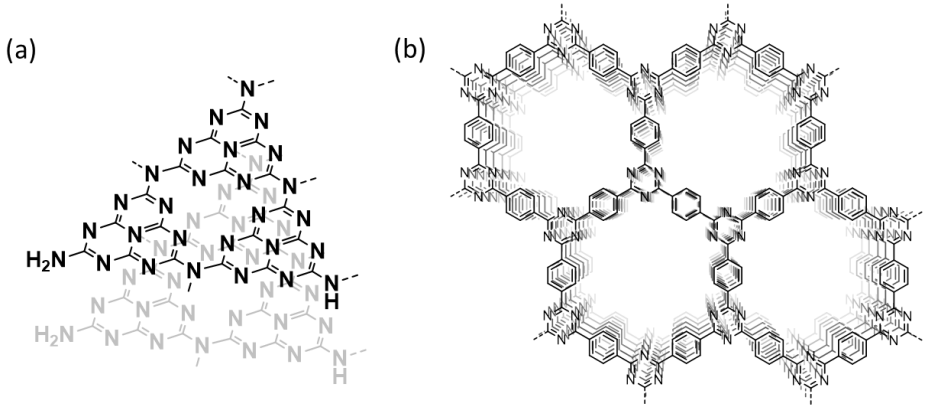

Figure 9. *General structure of (a) Carbon nitride (CN) materials and (b) Covalent triazine-based frameworks (CTFs), which are part of the "functional materials" and will be the main topic of this thesis.*

Several cases are also reported where a polymer is formed directly on a conductive support like FTO (fluorine-doped tin oxide) for the purpose of photo-electrocatalysis, employing methods like doctor blading, vapor transport, substrate immersion, powder deposition between flat surfaces or deposition on different surfaces by precursor melting/vaporization.[142,143] The final electrodes normally possess a bandgap between 2.9 and 2.5 eV and suitable band edges for OER and HER, being perfect candidates for overall water splitting, and have been used especially for the reduction half-reaction (Figure 10, right).[144] The intercalation of ions or atoms in the crystal structure of carbon nitrides has been suggested to have a substantial influence on photocatalytic activity, as well as on the bandgap energy. For example, sulfur or boron-doping has created a band-

edge shift to lower and higher energies, respectively, and the integration of barbituric acid (BA) has created a decrease in energy gap and extended light absorption in the visible region (see Figure 10, right).[145,146] However, considering the water oxidation half-reaction, these materials have poor charge separation and transfer properties, together with slow WO kinetics, and have a resultant PEC activity and instability, which strongly hinder their application into useful devices, especially in neutral aqueous medium.[142] The resultant instability of the CN layer is another significant obstacle in its long-term use, due to self-oxidation from the accumulation of long-lived photogenerated holes. To overcome the water oxidation kinetic barrier, co-catalysts are frequently used, mostly as metal oxides, with increased final performances.[97,147,148]

Covalent-triazine frameworks (CTFs) are another type of carbon and nitrogen-based materials (Figure 9b), which also have an extended π-conjugated system, due to triazine moieties present in the structure. They are a part of the more generic group of conjugated microporous polymers (CMP), along with covalent organic frameworks (COFs) and metal organic frameworks (MOFs). Unlike carbon nitrides, CTFs possess inherent micro- or meso-porosity, which can be altered during the synthetic pathway, and are mainly used for photocatalysis. Generally, Lewis-acids are used to catalyze the trimerization from a nitrile-functionalized monomer to the triazine moiety, and due to the high robustness of the triazine bridging group, the process is mostly non-reversible, such that high-temperature synthetic approaches are commonly used.[149] However, a big disadvantage of this reaction is that the high-temperatures cause functional-group intolerance, which thus limits the choice of monomers. Moreover, partial carbonization can occur, which is detrimental for the characterization and the photocatalytic applications of the material. One of the major procedures used is the polymerization in molten zinc chloride at 400°C, that allows for the attainment of CTFs with high porosity and crystallinity.[150] Other methodologies were also employed with milder conditions, such as room temperature and microwave-assisted reactions with strong acids,[151,152] or condensation reactions between an aldehyde and an amidine without-strong acids and at low (> 120°C) temperature, or even using cost-effective acids (like polyphosphoric acid) in combination with high temperatures under vacuum.[153] In most cases, the synthetic protocol led to amorphous structures, which consequently influences the

porosity of the material. Regarding the optical properties, the bandgap decreases with decreasing nitrogen content, as well as with longer chain length (Figure 10, left), since it generates bigger pores, and induces a less intense quantum-confinement effect, and allows for a higher light-absorption.[145] The stacking of layers can also influence the energy gap, similarly as for CN, increasing light-harvesting.[154] As a consequence, improved photocatalytic performances are achieved for water oxidation and proton reduction reactions, with special application in the reduction half-reaction. The inclusion of co-catalysts in CTFs to restrict the energy gap and enhance the activity is also commonly studied (Figure 10, left), and there are several cases that report the deposition of Pt nanoparticles for HER.[134,155–157] There are generally few cases where a molecular co-catalyst is anchored onto the material,[158–160] and should be better explored for a more controlled material hybridization.

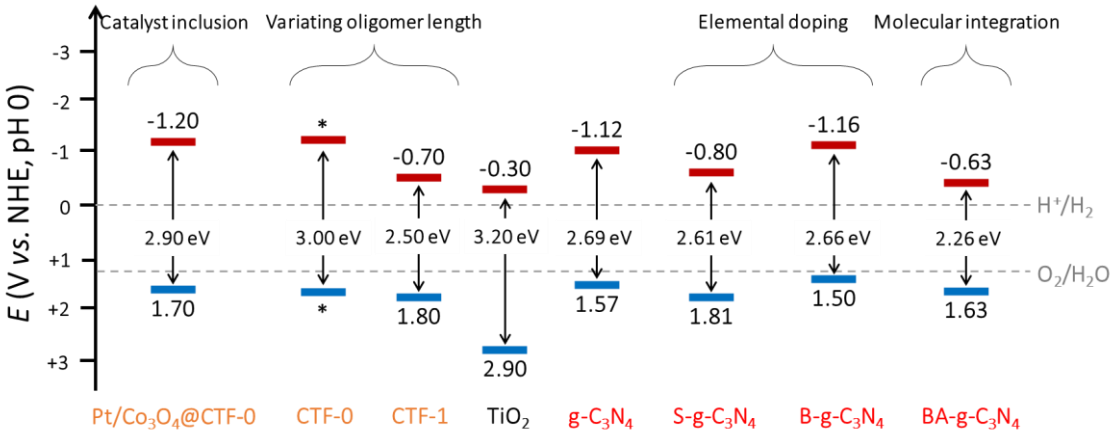

Figure 10. *Energy level band diagram of some examples of organic semiconductors based on carbon nitride (in red, on the right) and on covalent triazine-based frameworks (in orange, on the left), compared TiO_2 SC (in black, in the center). Created and adapted from literature.*[60,134,146,157]

1.6. Ru-based molecular catalysts for water oxidation

Ruthenium is a second-row transition metal with electronic configuration [Kr]$4d^7 5s^1$, and access to a wide range of oxidation states (from +8 to -2, respectively d^0 and d^{10} configurations). The majority of Ru complexes have an octahedral geometry and a

coordination environment that remains stable even under high oxidation states of the metal center.

The first example of a water oxidation catalyst reported in the literature was the dinuclear Ru-complex cis,cis-{[$Ru^{III}(H_2O)$-$(bpy)_2]_2(\mu$-$O)\}^{4+}$ (*bpy* = 2,2'-bipyridine) (**1**, Fig. 11), known as *blue dimer*, published by Meyer *et al.* in 1980s.[161,162] The dinuclear complex connects both metal centers through a Ru-O-Ru bridging bond and bears two bipyridyl (bpy) ligands and one water molecule per Ru^{III} center. The presence of the *μ*-oxo bridge promotes a strong electronic coupling between the two metallic centers and stabilizes the complex at high oxidation states through electronic delocalization. The catalytic cycle described by Meyer involves the accumulation of four oxidative equivalents by several proton-coupled electron transfer processes, finally leading to an active Ru^{V}-O-Ru^{V} complex. In the latter, one of the high-valent ruthenium centers can undergo a nucleophilic attack by a water molecule and form a hydroperoxide species, which in turn experiences an intramolecular oxidation by the second Ru center, releasing O_2 and closing the catalytic cycle.

The main issue associated with the blue dimer is the instability of the μ-oxo bridge, which can suffer cleavage and produce two inactive monomers. To overcome this problem, the system was redesigned to improve the stability of the bridging ligand, yielding the $\{[Ru^{II}(H_2O)(trpy)]_2(\mu$-$bpp)\}^{3+}$ (*bpp* = 3,5-bis(2-pyridyl)pyrazolate) (**2** in Fig. 11), which was reported by Llobet's group in the early 2000s.[163] The main difference between **2** and the *blue dimer* is the presence of an organic ligand acting as a bridging unit between the two metallic centers, and the coordination sphere is completed by a terpyridyl ligand and a water molecule. Upon successive oxidation steps *via* PCET, the complex can reach the oxidation state (IV) and form the highly oxidizing Ru(IV)=O unit. Then, the O-O bond is formed through an efficient intramolecular I2M mechanism, followed by the final release of molecular oxygen and regeneration of the initial species.

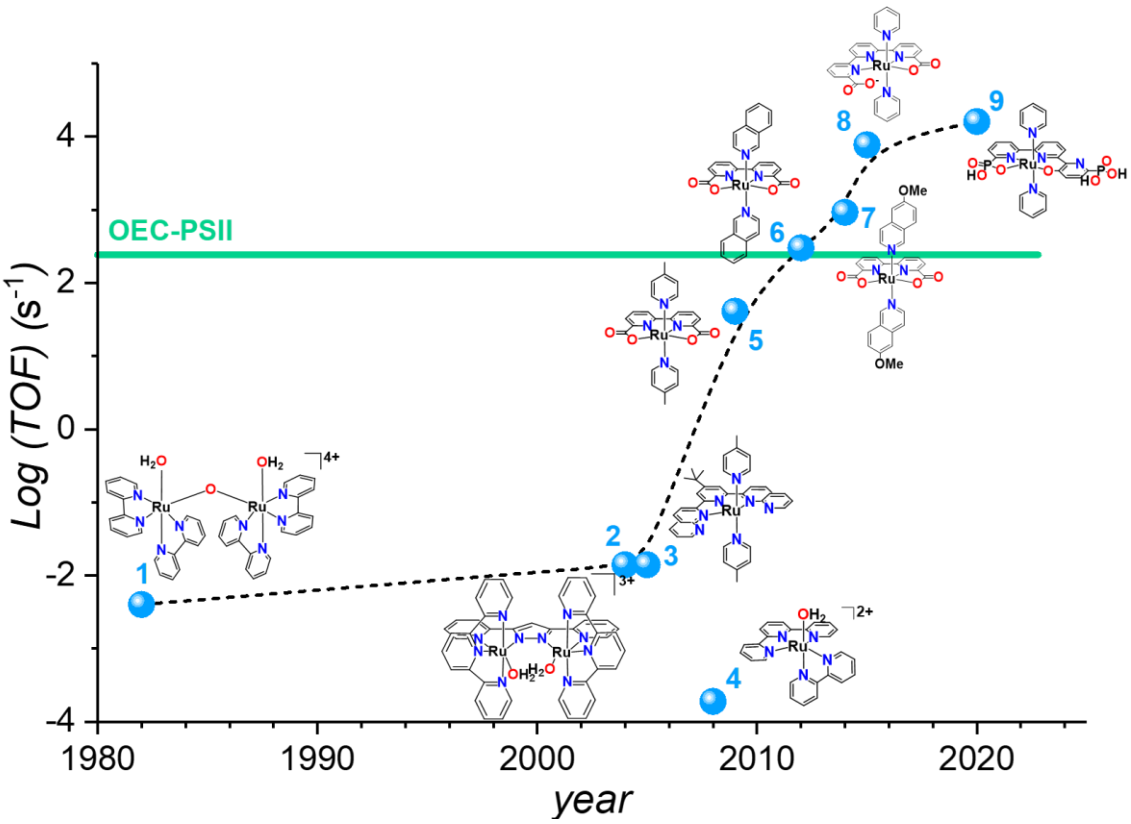

Figure 11. *Evolution of TOF values for molecular WOC in the last 40 years. The green line indicates the TOF (400 s^{-1}) of the oxygen evolution center (OEC) in photosystem II. TOF values for complexes **1**-**7** were determined at pH 1.0 using Ce^{IV} as a sacrificial oxidant, in the case of **8** and **9** TOFs were calculated through electrochemical measurements at pH 7.0.*

An important breakthrough came in 2005,[164] when Thummel *et al.* proposed that mononuclear complexes were capable of accumulating the four oxidative equivalents that could oxidize water to dioxygen. The reported catalyst, $[Ru^{II}(npm)(pic)_2(OH_2)]^{2+}$ (**3**, where *npm* is 4-t-butyl-2,6-di(1',8'-naphthyrid-2'-yl)pyridine and *pic* is 4-picoline), could reach a TOF of 0.014 s^{-1}. However, it was not until 2008 that Meyer and co-workers reported a thorough mechanistic study that demonstrated the mononuclear nature of the catalysis.[165] The proposed catalytic cycle has been later adapted for several catalysts, which are proposed to follow a WNA mechanism. The $[Ru^{II}(tpy)(bpm)(OH_2)]^{2+}$ complex (**4**, with *tpy* as 2,2';6',2''-terpyridine and *bpm* as 2,2'-bipyrimidine)[165,166] performed water oxidation catalysis and achieved a TOF value of 1.9 x 10^{-4} s^{-1}. The discovery of single-site water oxidation catalysis offered the possibility of straightforward

ligand/complex design, synthesis and characterization, and therefore a rapid expansion of the field.

Following, from 2009 to 2014 a new family of Ru complexes (**5**, **6**, **7** in Figure 11) containing the *bda* ligand (where bda^{2-} is 2,2'-bipyridine-6,6'-dicarboxylate) was described, which implements two carboxylate moieties at the equatorial position, were developed in order to increase the electron-donating property at the first coordination sphere and consequently stabilize the high oxidation states reached by the metal center.[167–169] Moreover, the Ru(bda) complexes can reach a seven-coordinated structure and work *via* the I2M catalytic mechanism. This new design led to even higher TOF values with respect to the OEC-PSII cluster (TOF = 400 s^{-1}). Among these catalysts, $[Ru(bda)(MeO\text{-}isoq)_2]$ (**7**, where bda^{2-} is 2,2'-bipyridine-6,6'-dicarboxylate and *isoq* is isoquinoline) showed an improved TOF_{max} of almost 1000 s^{-1}, due to stronger supramolecular interactions obtained with the axial ligand that improves the I2M mechanism and kinetics.[169]

The best WOC recorded to date is the $[Ru^{II}(tda)(py)_2]$ complex (**8**, where tda^{2-} is [2,2':6',2"-terpyridine]-6,6"-dicarboxylate), which was introduced in 2015 by Llobet *et al*.[170] The key for its superior performance is the *tda* equatorial ligand, which stabilizes the Ru center in its high oxidation states (IV or V), and allows the complex to acquire a seven-coordinated environment, while the pendant carboxylate assists the deprotonation of H_2O during its nucleophilic attack of the Ru(V)=O moiety, facilitating O=O bond formation.[171–173] The catalytic cycle was deeply studied by computational and experimental analysis. Overall, the system is capable of performing water oxidation to dioxygen with a TOF_{max} of 7,700 s^{-1} at pH 7 (50,000 s^{-1} at pH 10) and an overpotential of 400 mV.

The *bda* and *tda* ligands are included in the group of the FAME ligands (flexible, adaptative, multidentate and equatorial), and can benefit the molecular complexes to induce better efficiencies.[104,171,174] An example is the recently presented $[Ru^{II}(HtPa)(py)_2]^-$ (**9**, tPa^{4-} is [2,2':6',2''-terpyridine]-6,6''-diphosphonate) by Llobet and coworkers,[175] where the carboxylates have been substituted by phosphonate groups. These dangling phosphonates act as pendant bases enhancing intramolecular proton transfer and O-O bond formation, thus reducing the energy required to form the active

species of the catalyst to achieve a TOF_{max} of 16,000 s^{-1} and an overpotential of 530 mV at pH 7. One of the main problems, however, is the progressive transformation of the catalyst to form RuO_2, due to the facile oxidation of the phenoxo group to pyridine and the following reorganization of the equatorial ligand, which later can induce a complete ligand loss.[176]

The use of these complexes in homogeneous catalysis has been clearly an advantage for the elucidation of detailed catalytic mechanisms, including the detection of active intermediates for water oxidation. As a continuation of this investigation, the evolution from homogeneous to heterogeneous catalysts is fundamental to achieve practical applications, since the combination with materials like conductors or semi-conductors can lead to higher catalytic activity and an easier way to separate the products. The key parameter to take into account when passing to heterogeneous systems is the anchoring and deposition methodology, which can influence the O-O bond formation mechanism and consequently the performance of the final device.

The modulation of the pyridinyl axial ligands to achieve an optimal anchoring to the material surface, or the inclusion of the same catalyst in the latter, has brought several studies which have been reported in the literature.[49,177–182] Functionalization of the axial position brings an easy synthetic approach, and normally shows high stability in aqueous electrolytes thanks to hydrophobic effects. Three are the main anchoring strategies (see Figure 12) employed in heterogeneous catalysis: (i) supramolecular interactions; (ii) creation of an insoluble conductive polymer on the material; (iii) covalent linking.

The supramolecular interactions ((Figure 12, in the middle) comprise the generation of stable hybrid materials between the functional groups on the catalyst and the graphitic material. Highly developed in our research group, one exemplar case was the use of an extended-conjugated group at the axial position (such as in complex $[Ru(tda)(L^1)_2]$, where L^1 is 4-(pyren-1-yl)-N-(pyridin-4-ylmethyl)butanamide),[49,177,178] to enhance the interaction through non-covalent π-π stacking with any graphitic material or with semiconductor surfaces. Another strategy employed to achieve a good interaction with the material surface was the formation of oligomers, such as the $\{[Ru(tda)(4,4'\text{-bpy})]_{15}(4,4'\text{-bpy})\}$[179] and $\{[Ru(bda)(4,4'\text{-bpy})]_{10}(4,4'\text{-bpy})\}$[183] (where *4,4'-bpy* is 4,4'-bipyridine), starting from Ru molecular complexes previously reported as repetitive

units. In both cases, the equatorial ligands were found to interact with the graphitic surface through supramolecular CH-π stacking, which singularly are found to be weak interactions, but when working harmoniously they provide the catalyst with an overall better stability on the material. Moreover, the polymeric nature of the complex contributes to a higher surface coverage and an increased charge delocalization. Finally, another possibility is the generation of self-assembled bilayers interacting *via* allyl-alkyl chains using adequately functionalized oxides with alkyl phosphonates or silanes and the corresponding catalyst containing large alkyl chain.[184]

The second way to create heterogeneous systems is the creation of insoluble conductive polymers on the material surface (Figure 12, on the right). The strategy consists in the addition of thiophene functional groups on the catalyst, which will polymerize *in situ* under oxidative conditions to form the insoluble polymer. A recent work from Llobet *et al.*[185] reported the oxidative electro-polymerization of the thiophene groups of the complex [Ru(tda)(pyrS)$_2$] (where *pyrS* is 4-(2-(thiophen-3-yl)ethyl)pyridine) on top of a graphitic surface, which induced a high rate of water oxidation in neutral pH.

More demanding is, instead, the functionalization of the WOC with specific groups for covalent anchoring (Figure 12 on the left). This methodology can be more advantageous compared to supramolecular interactions, due to a more stable molecular-material assembly and a better electron/hole communication, but it can lead to a lower mass loading capacity with respect to the previous strategies. Normally, the covalent bonding is achieved by using diazonium groups coupling to graphitic surfaces, carboxylic acids for amide formation and phosphonic acid to bind to conductive metal oxide electrodes.[186] Thiol derivatives were also found to react with Cu or Au metallic electrodes. In this context, Ding et al.[187] used a synthesis *in situ* of a Ru-WOC to covalently bond the catalyst to a carbon nitride surface through the formation of an amide bridging group.[187] Ott and coworkers[180] reported instead a [Ru(tda)(PyCOOH)$_2$ complex (where *PyCOOH* is iso-nicotinic acid) which was incorporated into a metal-organic framework (MOF) structure.

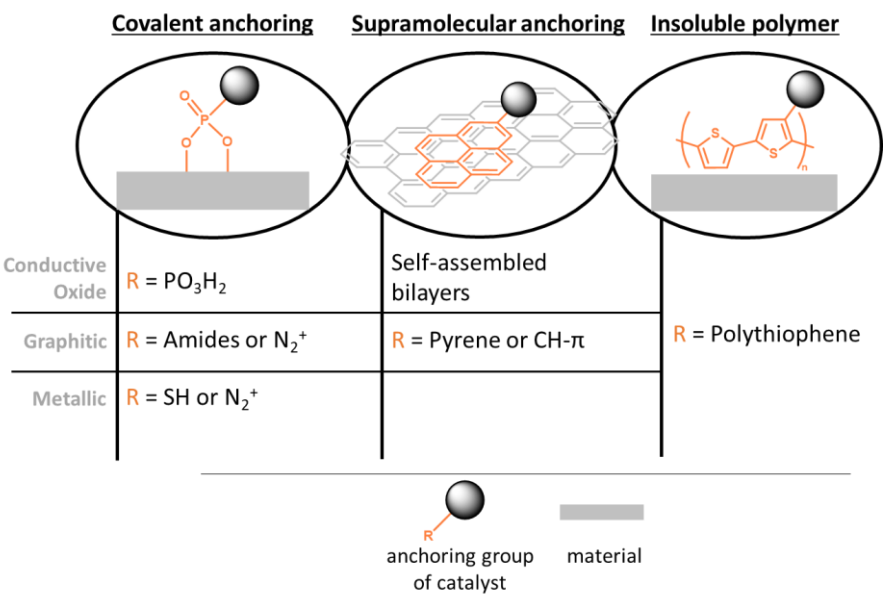

Figure 12. *Simplified scheme of three different anchoring strategies (covalent and supramolecular anchoring, and creation of insoluble polymers) used to incorporate Ru complexes into materials for heterogeneous catalysis, depending on the type of surface (conductive oxide, graphitic and metallic). R is the anchoring group (in orange), and the groups reported for each strategy correspond to the possible anchoring functionals used on top of different electrodes (in grey).*

With this solid background on the mechanistic studies and surface functionalization, it is thus of great interest to load molecular catalysts onto organic photoactive surfaces in order to improve the overall oxygen evolution reaction and study the mechanism, and thus move forward to more sustainable processes.

1.7. References

(1) World Economic Forum. *Fourth Industrial Revolution*. weforum.org. https://www.weforum.org/focus/fourth-industrial-revolution/.

(2) Park, H.-A. Are We Ready for the Fourth Industrial Revolution? *Yearb. Med. Inform.* **2016**, *1*, 1–3. https://doi.org/10.15265/IY-2016-052.

(3) Worldometer. *World Population*. worldometers.info. https://www.worldometers.info/world-population/#.

(4) Ritchie, H.; Rosado, P.; Roser, M. *Energy Production and Consumption*. OurWorldInData.org. https://ourworldindata.org/energy-production-consumption.

(5) IEA. *World Energy Balances: Overview*; Paris, 2021.

(6) United States Environmental Protection Agency (EPA). *Overview of Greenhouse Gases*. epa.gov. https://www.epa.gov/ghgemissions/overview-greenhouse-gases.

(7) Grantham Institute – Climate Change and the Environment. *How do we know climate change is happening?*. Imperial. https://www.imperial.ac.uk/grantham/publications/climate-change-faqs/how-do-we-know-climate-change-is-happening/#:~:text=Multiple independent data sets show,the Industrial Revolution in 1850.

(8) IPCC. *Climate Change 2022: Impacts, Adaptation and Vulnerability*; 2022.

(9) Betts, R. A.; Jones, C. D.; Knight, J. R.; Pope, J. O.; Sandford, C. *Mauna Loa Carbon Dioxide Forecast for 2024 : Atmospheric CO_2 Rise Predicted to Exceed IPCC 1.5°C Scenarios*; 2024.

(10) National Ocean and Atmospheric Administration (NOAA). *What is Ocean Acidification?*. oceanservice.noaa.gov. https://oceanservice.noaa.gov/facts/.

(11) Copernicus. Copernicus: June 2024 Marks 12th Month of Global Temperature Reaching 1.5°C above Pre-Industrial. *climate.copernicus.eu*. 2024.

(12) Roston, E.; Murray, P. The Best Way to Slow Global Warming? You Decide in This Climate Simulator. *Bloomberg*. 2020.

(13) Lomborg, B. *How to Spend $75 Billion to Make the World a Better Place*; Bjorn Lomborg, Ed.; Copenhagen Concensus Center USA, Inc., 2014.

(14) United Nations. *Kyoto Protocol*; 1998.

(15) United Nations. *The Paris Agreement*; 2016.

(16) United Nations. *Global Sustainable Development Report 2023: Key Messages*; 2023.

(17) The European Council. *The European Green Deal*. consilium.europa.eu. https://www.consilium.europa.eu/en/policies/green-deal/.

(18) United Nations. *Joint Statement on Climate Change*; 2023.

(19) International Energy Agency. *Cumulative Renewable Electricity Capacity in the Main and Accelerated Cases and Net Zero Scenario*; Paris, 2024.

(20) Honegger, M. Toward the Effective and Fair Funding of CO_2 Removal Technologies. *Nat. Commun.* **2023**, *14* (1), 2–4. https://doi.org/10.1038/s41467-023-36199-4.

(21) Armaroli, N.; Balzani, V. The Future of Energy Supply: Challenges and Opportunities. *Angew. Chemie - Int. Ed.* **2007**, *46* (1-2), 52–66. https://doi.org/10.1002/anie.200602373.

(22) Davie, M. Blood Cobalt. *ABC News*. 2022.

(23) UNICEF. *Child Labour*; 2024.

(24) Dumortier, M.; Tembhurne, S.; Haussener, S. Holistic Design Guidelines for Solar Hydrogen Production by Photo-Electrochemical Routes. *Energy Environ. Sci.* **2015**, *8* (12), 3614–3628. https://doi.org/10.1039/c5ee01821h.

(25) Bassham, J. A. *Photosynthesis*; 1998.

(26) Romero, E.; Novoderezhkin, V. I.; Van Grondelle, R. Quantum Design of Photosynthesis for Bio-Inspired Solar-Energy Conversion. *Nature* **2017**, *543* (7645), 355–365. https://doi.org/10.1038/nature22012.

(27) Zhang, J. Z.; Sokol, K. P.; Paul, N.; Romero, E.; Van Grondelle, R.; Reisner, E. Competing Charge Transfer Pathways at the Photosystem II-Electrode Interface. *Nat. Chem. Biol.* **2016**, *12* (12), 1046–1052. https://doi.org/10.1038/nchembio.2192.

(28) Minagawa, J. State Transitions-the Molecular Remodeling of Photosynthetic Supercomplexes That Controls Energy Flow in the Chloroplast. *Biochim. Biophys. Acta - Bioenerg.* **2011**, *1807* (8), 897–905. https://doi.org/10.1016/j.bbabio.2010.11.005.

(29) McEvoy, J. P.; Brudvig, G. W. Water-Splitting Chemistry of Photosystem II. *Chem. Rev.* **2006**, *106* (11), 4455–4483. https://doi.org/10.1021/cr0204294.

(30) Cox, N.; Pantazis, D. A.; Neese, F.; Lubitz, W. Biological Water Oxidation. *Acc. Chem. Res.* **2013**, *46* (7), 1588–1596. https://doi.org/10.1021/ar3003249.

(31) Merchant, S.; Sawaya, M. R. The Light Reactions: A Guide to Recent Acquisitions for the Picture Gallery. *Plant Cell* **2005**, *17* (3), 648–663. https://doi.org/10.1105/tpc.105.030676.

(32) Wang, L.; Yu, J. Principles of Photocatalysis. In *Interface Science and Technology*; Yu, J., Zhang, L., Wang, L., Zhu, B., Eds.; Science Direct, 2023; pp 35, 1–52. https://doi.org/10.1016/B978-0-443-18786-5.00002-0.

(33) Nocera, D. G. The Artificial Leaf. *Acc. Chem. Res.* **2012**, *45* (5), 767–776. https://doi.org/10.1021/ar2003013.

(34) Umena, Y.; Kawakami, K.; Shen, J. R.; Kamiya, N. Crystal Structure of Oxygen-Evolving Photosystem II at a Resolution of 1.9 Å. *Nature* **2011**, *473* (7345), 55–60. https://doi.org/10.1038/nature09913.

(35) Wraight, C. A.; Clayton, R. K. The Absolute Quantum Efficiency of Bacteriochlorophyll Photooxidation in Reaction Centres of Rhodopseudomonas Spheroides. *Biochim Biophys Acta* **1974**, *333* (2), 246–260. https://doi.org/0.1016/0005-2728(74)90009-7.

(36) Kornienko, N.; Zhang, J. Z.; Sokol, K. P.; Lamaison, S.; Fantuzzi, A.; Van Grondelle, R.; Rutherford, A. W.; Reisner, E. Oxygenic Photoreactivity in Photosystem II Studied by Rotating Ring Disk

Electrochemistry. *J. Am. Chem. Soc.* **2018**, *140* (51), 17923–17931. https://doi.org/10.1021/jacs.8b08784.

(37) Ferreira, K. N.; Iverson, T. M.; Maghlaoui, K.; Barber, J.; Iwata, S. Architecture of the Photosynthetic Oxygen-Evolving Center. *Science* **2004**, *303* (5665), 1831–1838. https://doi.org/10.1126/science.1093087.

(38) Britt, B. R. D.; Marchiori, D. A. Photosystem II, Poised for O_2 Formation. *Science* **2019**, *366* (6463), 305-306. https://science.org/doi/10.1126/science.aaz4522

(39) Askerka, M.; Brudvig, G. W.; Batista, V. S. The O_2-Evolving Complex of Photosystem II: Recent Insights from Quantum Mechanics/molecular Mechanics (QM/MM), Extended X-Ray Absorption Fine Structure (EXAFS), and Femtosecond X-Ray Crystallography Data. *Acc. Chem. Res.* **2017**, *50* (1), 41–48. https://doi.org/10.1021/acs.accounts.6b00405.

(40) Kok, B.; Forbush, B.; McGloin, M. Cooperation of Charges in Photosynthetic O_2 Evolution-1. A Linear Four Step Mechanism. *Photochem. Photobiol.* **1970**, *11* (6), 457–475. https://doi.org/10.1111/j.1751-1097.1970.tb06017.x.

(41) Montoya, J. H.; Seitz, L. C.; Chakthranont, P.; Vojvodic, A.; Jaramillo, T. F.; Nørskov, J. K. Materials for Solar Fuels and Chemicals. *Nat. Mater.* **2016**, *16* (1), 70–81. https://doi.org/10.1038/nmat4778.

(42) Berardi, S.; Drouet, S.; Francàs, L.; Gimbert-Suriñach, C.; Guttentag, M.; Richmond, C.; Stoll, T.; Llobet, A. Molecular Artificial Photosynthesis. *Chem. Soc. Rev.* **2014**, *43* (22), 7501–7519. https://doi.org/10.1039/c3cs60405e.

(43) Nocera, D. G. Solar Fuels and Solar Chemicals Industry. *Acc. Chem. Res.* **2017**, *50* (3), 616–619. https://doi.org/10.1021/acs.accounts.6b00615.

(44) Wang, X. S.; Li, L.; Li, D.; Ye, J. Recent Progress on Exploring Stable Metal–Organic Frameworks for Photocatalytic Solar Fuel Production. *Sol. RRL* **2020**, *4* (8), 1–34. https://doi.org/10.1002/solr.201900547.

(45) US Department of Energy (DOE). Hydrogen and Fuel Cell Technologies Office Multi-Year Program Plan. 2024, 32–54.

(46) Chi, J.; Yu, H. Water Electrolysis Based on Renewable Energy for Hydrogen Production. *Chinese J. Catal.* **2018**, *39* (0), 390–394. https://doi.org/10.1016/S1872-2067(17)62949-8.

(47) Hisatomi, T.; Domen, K. Introductory Lecture: Sunlight-Driven Water Splitting and Carbon Dioxide Reduction by Heterogeneous Semiconductor Systems as Key Processes in Artificial Photosynthesis. *Faraday Discuss.* **2017**, *198*, 11–35. https://doi.org/10.1039/c6fd00221h.

(48) Grätzel, M. Photoelectrochemical Cells. *Nature* **2001**, *414*, 338–344.

https://doi.org/10.1038/35104607.

(49) Grau, S.; Berardi, S.; Moya, A.; Matheu, R.; Cristino, V.; Vilatela, J. J.; Bignozzi, C. A.; Caramori, S.; Gimbert-Suriñach, C.; Llobet, A. A Hybrid Molecular Photoanode for Efficient Light-Induced Water Oxidation. *Sustain. Energy Fuels* **2018**, *2* (9), 1979–1985. https://doi.org/10.1039/c8se00146d.

(50) Berardi, S.; Cristino, V.; Canton, M.; Boaretto, R.; Argazzi, R.; Benazzi, E.; Ganzer, L.; Borrego Varillas, R.; Cerullo, G.; Syrgiannis, Z.; Rigodanza, F.; Prato, M.; Bignozzi, C. A.; Caramori, S. Perylene Diimide Aggregates on Sb-Doped SnO_2: Charge Transfer Dynamics Relevant to Solar Fuel Generation. *J. Phys. Chem. C* **2017**, *121* (33), 17737–17745. https://doi.org/10.1021/acs.jpcc.7b05928.

(51) Kay, A.; Grätzel, M. Dye-Sensitized Core-Shell Nanocrystals: Improved Efficiency of Mesoporous Tin Oxide Electrodes Coated with a Thin Layer of an Insulating Oxide. *Chem. Mater.* **2002**, *14* (7), 2930–2935. https://doi.org/10.1021/cm0115968.

(52) Qian, R.; Zong, H.; Schneider, J.; Zhou, G.; Zhao, T.; Li, Y.; Yang, J.; Bahnemann, D. W.; Pan, J. H. Charge Carrier Trapping, Recombination and Transfer during TiO_2 Photocatalysis: An Overview. *Catal. Today* **2019**, *335* (October 2018), 78–90. https://doi.org/10.1016/j.cattod.2018.10.053.

(53) Yan, H.; Wang, X.; Yao, M.; Yao, X. Band Structure Design of Semiconductors for Enhanced Photocatalytic Activity: The Case of TiO_2. *Prog. Nat. Sci. Mater. Int.* **2013**, *23* (4), 402–407. https://doi.org/10.1016/j.pnsc.2013.06.002.

(54) Wang, Q.; Domen, K. Particulate Photocatalysts for Light-Driven Water Splitting: Mechanisms, Challenges, and Design Strategies. *Chem. Rev.* **2020**, *120* (2), 919–985. https://doi.org/10.1021/acs.chemrev.9b00201.

(55) Jia, J.; Seitz, L. C.; Benck, J. D.; Huo, Y.; Chen, Y.; Ng, J. W. D.; Bilir, T.; Harris, J. S.; Jaramillo, T. F. Solar Water Splitting by Photovoltaic-Electrolysis with a Solar-to-Hydrogen Efficiency over 30%. *Nat. Commun.* **2016**, *7* (May), 1–6. https://doi.org/10.1038/ncomms13237.

(56) Tournet, J.; Lee, Y.; Karuturi, S. K.; Tan, H. H.; Jagadish, C. III-V Semiconductor Materials for Solar Hydrogen Production: Status and Prospects. *ACS Energy Lett.* **2020**, *5* (2). https://doi.org/10.1021/acsenergylett.9b02582.

(57) National Renewable Energy Laboratory. *Best Research-Cell Efficiencies*; 2024.

(58) Melchionna, M.; Fornasiero, P. Updates on the Roadmap for Photocatalysis. *ACS Catal.* **2020**, *10* (10), 5493–5501. https://doi.org/10.1021/acscatal.0c01204.

(59) Kosco, J.; Moruzzi, F.; Willner, B.; McCulloch, I. Photocatalysts Based on Organic Semiconductors with Tunable Energy Levels for Solar Fuel Applications. *Adv. Energy Mater.* **2020**, *10* (39). https://doi.org/10.1002/aenm.202001935.

(60) Liras, M.; Barawi, M.; De La Peña O'Shea, V. A. Hybrid Materials Based on Conjugated Polymers and Inorganic Semiconductors as Photocatalysts: From Environmental to Energy Applications. *Chem. Soc. Rev.* **2019**, *48* (22), 5454–5487. https://doi.org/10.1039/c9cs00377k.

(61) Fabian, D. M.; Hu, S.; Singh, N.; Houle, F. A.; Hisatomi, T.; Domen, K.; Osterloh, F. E.; Ardo, S. Particle Suspension Reactors and Materials for Solar-Driven Water Splitting. *Energy Environ. Sci.* **2015**, *8* (10), 2825–2850. https://doi.org/10.1039/c5ee01434d.

(62) Kong, D.; Zheng, Y.; Kobielusz, M.; Wang, Y.; Bai, Z.; Macyk, W.; Wang, X.; Tang, J. Recent Advances in Visible Light-Driven Water Oxidation and Reduction in Suspension Systems. *Mater. Today* **2018**, *21* (8), 897–924. https://doi.org/10.1016/j.mattod.2018.04.009.

(63) Vyas, V. S.; Lau, V. W. H.; Lotsch, B. V. Soft Photocatalysis: Organic Polymers for Solar Fuel Production. *Chem. Mater.* **2016**, *28* (15), 5191–5204. https://doi.org/10.1021/acs.chemmater.6b01894.

(64) Banerjee, T.; Podjaski, F.; Kröger, J.; Biswal, B. P.; Lotsch, B. V. Polymer Photocatalysts for Solar-to-Chemical Energy Conversion. *Nat. Rev. Mater.* **2021**, *6*, 168–190. https://doi.org/10.1038/s41578-020-00254-z.

(65) Fang, Y.; Hou, Y.; Fu, X.; Wang, X. Semiconducting Polymers for Oxygen Evolution Reaction under Light Illumination. *Chem. Rev.* **2022**, *122* (3), 4204–4256. https://doi.org/10.1021/acs.chemrev.1c00686.

(66) Wang, Y.; Wang, X.; Antonietti, M. Polymeric Graphitic Carbon Nitride as a Heterogeneous Organocatalyst: From Photochemistry to Multipurpose Catalysis to Sustainable Chemistry. *Angew. Chemie - Int. Ed.* **2012**, *51* (1), 68–89. https://doi.org/10.1002/anie.201101182.

(67) Fernando, K. A. S.; Sahu, S.; Liu, Y.; Lewis, W. K.; Guliants, E. A.; Jafariyan, A.; Wang, P.; Bunker, C. E.; Sun, Y. P. Carbon Quantum Dots and Applications in Photocatalytic Energy Conversion. *ACS Appl. Mater. Interfaces* **2015**, *7* (16), 8363–8376. https://doi.org/10.1021/acsami.5b00448.

(68) Liu, J.; Ma, N.; Wu, W.; He, Q. Recent Progress on Photocatalytic Heterostructures with Full Solar Spectral Responses. *Chem. Eng. J.* **2020**, *393* (March), 124719. https://doi.org/10.1016/j.cej.2020.124719.

(69) Khalkhali, F. S.; Kowsari, E.; Ramakrishna, S.; Eqbalpour, M.; Gheibi, M.; Esmaili, H. A Review on the Photosensitizers Used for Enhancing the Photoelectrochemical Performance of Hydrogen Production with Emphasis on a Novel Toxicity Assessment Framework. *Int. J. Hydrogen Energy* **2024**, *51*, 990–1022. https://doi.org/10.1016/j.ijhydene.2023.07.116.

(70) Zhu, Y.; Wang, D.; Huang, Q.; Du, J.; Sun, L.; Li, F.; Meyer, T. J. Stabilization of a Molecular Water Oxidation Catalyst on a Dye−sensitized Photoanode by a Pyridyl Anchor. *Nat. Commun.* **2020**, *11* (1), 1–8. https://doi.org/10.1038/s41467-020-18417-5.

(71) Francàs, L.; Matheu, R.; Pastor, E.; Reynal, A.; Berardi, S.; Sala, X.; Llobet, A.; Durrant, J. R. Kinetic Analysis of an Efficient Molecular Light-Driven Water Oxidation System. *ACS Catal.* **2017**, *7* (8), 5142–5150. https://doi.org/10.1021/acscatal.7b01357.

(72) Limburg, B.; Bouwman, E.; Bonnet, S. Rate and Stability of Photocatalytic Water Oxidation Using $[Ru(bpy)_3]^{2+}$ as Photosensitizer. *ACS Catal.* **2016**, *6* (8), 5273–5284. https://doi.org/10.1021/acscatal.6b00107.

(73) Sun, L.; Hammarström, L.; Åkermark, B.; Styring, S. Towards Artificial Photosynthesis: Ruthenium-Manganese Chemistry for Energy Production. *Chem. Soc. Rev.* **2001**, *30* (1), 36–49. https://doi.org/10.1039/a801490f.

(74) Lämmle, M.; Bagemihl, B.; Nauroozi, D.; Petermann, L.; Pannwitz, A.; Rau, S. Monosubstitution of 1*H*-Imidazo[4,5-*f*][1,10]phenanthroline Ligands Yields Maximum Luminescence Quantum Yield in Ruthenium Polypyridyl Complexes. *ChemPhotoChem* **2022**, *6* (7), e202200053. https://doi.org/10.1002/cptc.202200053.

(75) Meza-Chincha, A. L.; Schindler, D.; Natali, M.; Würthner, F. Effects of Photosensitizers and Reaction Media on Light-Driven Water Oxidation with Trinuclear Ruthenium Macrocycles. *ChemPhotoChem* **2021**, *5* (2), 173–183. https://doi.org/10.1002/cptc.202000133.

(76) Cancelliere, A. M.; Arrigo, A.; Galletta, M.; Nastasi, F.; Campagna, S.; La Ganga, G. Photo-Driven Water Oxidation Performed by Supramolecular Photocatalysts Made of Ru(II) Photosensitizers and Catalysts. *J. Chem. Phys.* **2024**, *160* (8). https://doi.org/10.1063/5.0189316.

(77) Wang, A.; Shen, X.; Ren, J.; Wang, Q.; Zhao, W.; Zhu, W.; Shang, D. Regulating the Type of Cobalt Porphyrins for Synergistic Promotion of Photoelectrochemical Water Splitting of $BiVO_4$. *Dye. Pigment.* **2021**, *192* (May), 109468. https://doi.org/10.1016/j.dyepig.2021.109468.

(78) Sudi, M. S.; Zhao, L.; Wang, Q.; Dou, Y.; Shen, X.; Wang, A.; Zhu, W. Efficient Photoelectrochemical Water Splitting of Metal-Porphyrin Decorated on $BiVO_4$ Photoanode. *Appl. Surf. Sci.* **2022**, *606* (September), 154753. https://doi.org/10.1016/j.apsusc.2022.154753.

(79) Bu, Q.; Liu, X.; Zhao, Q.; Lu, G.; Zhu, X.; Liu, Q.; Xie, T. Unveiling the Influence of 5,10,15,20-Tetrakis (4-Carboxyl Phenyl) Porphyrin on the Photogenerated Charge Behavior and Photoelectrochemical Water Oxidation of Hematite Photoanode. *J. Colloid Interface Sci.* **2022**, *626*, 345–354. https://doi.org/10.1016/j.jcis.2022.06.084.

(80) Yıldız, B.; Güzel, E.; Akyüz, D.; Arslan, B. S.; Koca, A.; Şener, M. K. Unsymmetrically Pyrazole-3-Carboxylic Acid Substituted Phthalocyanine-Based Photoanodes for Use in Water Splitting Photoelectrochemical and Dye-Sensitized Solar Cells. *Sol. Energy* **2019**, *191* (August), 654–662. https://doi.org/10.1016/j.solener.2019.09.043.

(81) Bonchio, M.; Syrgiannis, Z.; Burian, M.; Marino, N.; Pizzolato, E.; Dirian, K.; Rigodanza, F.; Volpato,

G. A.; La Ganga, G.; Demitri, N.; Berardi, S.; Amenitsch, H.; Guldi, D. M.; Caramori, S.; Bignozzi, C. A.; Sartorel, A.; Prato, M. Hierarchical Organization of Perylene Bisimides and Polyoxometalates for Photo-Assisted Water Oxidation. *Nat. Chem.* **2019**, *11* (2), 146–153. https://doi.org/10.1038/s41557-018-0172-y.

(82) Ronconi, F.; Syrgiannis, Z.; Bonasera, A.; Prato, M.; Argazzi, R.; Caramori, S.; Cristino, V.; Bignozzi, C. A. Modification of Nanocrystalline WO_3 with a Dicationic Perylene Bisimide: Applications to Molecular Level Solar Water Splitting. *J. Am. Chem. Soc.* **2015**, *137* (14), 4630–4633. https://doi.org/10.1021/jacs.5b01519.

(83) Swierk, J. R.; Mallouk, T. E. Design and Development of Photoanodes for Water-Splitting Dye-Sensitized Photoelectrochemical Cells. *Chem. Soc. Rev.* **2013**, *42* (6), 2357–2387. https://doi.org/10.1039/c2cs35246j.

(84) Grätzel, M. Recent Advances in Sensitized Mesoscopic Solar Cells. *Acc. Chem. Res.* **2009**, *42* (11), 1788–1798. https://doi.org/10.1021/ar900141y.

(85) O'Regan, B.; Grätzel, M. A Low-Cost, High-Efficiency Solar Cell Based on Dye-Sensitized Colloidal TiO_2 Films. *Nature* **1991**, *353*, 737–740. https://doi.org/https://doi.org/10.1038/353737a0.

(86) Memming, R. *Semiconductor Electrochemistry*, 2nd editio.; 2015. https://doi.org/10.1002/9783527688685.

(87) Rajeshwar, K. Fundamentals of Semiconductor Electrochemistry and Photoelectrochemistry. In *Encyclopedia of Electrochemistry*; 2007; 1–45. https://doi.org/10.1002/9783527610426.bard060001.

(88) Fujishima, A.; Honda, K. Electrochemical Photolysis of Water at a Semiconductor Electrode. *Nature* **1972**, *238*, 37–38. https://doi.org/10.1038/238037a0.

(89) Youngblood, J. W.; Lee, S. H. A.; Kobayashi, Y.; Hernandez-Pagan, E. A.; Hoertz, P. G.; Moore, T. A.; Moore, A. L.; Gust, D.; Mallouk, T. E. Photoassisted Overall Water Splitting in a Visible Light-Absorbing Dye-Sensitized Photoelectrochemical Cell. *J. Am. Chem. Soc.* **2009**, *131* (3), 926–927. https://doi.org/10.1021/ja809108y.

(90) Hankin, A.; Bedoya-Lora, F. E.; Alexander, J. C.; Regoutz, A.; Kelsall, G. H. Flat Band Potential Determination: Avoiding the Pitfalls. *J. Mater. Chem. A* **2019**, *7* (45), 26162–26176. https://doi.org/10.1039/c9ta09569a.

(91) Beranek, R. (Photo)electrochemical Methods for the Determination of the Band Edge Positions of TiO_2-Based Nanomaterials. *Adv. Phys. Chem.* **2011**, 1–14. https://doi.org/10.1155/2011/786759.

(92) Yu, H.; Peng, Y.; Yang, Y.; Li, Z. Y. Plasmon-Enhanced Light–matter Interactions and Applications. *npj Comput. Mater.* **2019**, *5* (1), 1–14. https://doi.org/10.1038/s41524-019-0184-1.

(93) Thomas, A. Functional Materials: From Hard to Soft Porous Frameworks. *Angew. Chemie - Int. Ed.* **2010**, *49* (45), 8328–8344. https://doi.org/10.1002/anie.201000167.

(94) Wang, X.; Blechert, S.; Antonietti, M. Polymeric Graphitic Carbon Nitride for Heterogeneous Photocatalysis. *Acs Catal.* **2012**, *2* (8), 1596–1606.

(95) Wang, X.; Maeda, K.; Thomas, A.; Takanabe, K.; Xin, G.; Carlsson, J. M.; Domen, K.; Antonietti, M. A Metal-Free Polymeric Photocatalyst for Hydrogen Production from Water under Visible Light. *Nat. Mater.* **2009**, *8*, 76–80.

(96) Brütting, W. Introduction to the Physics of Organic Semiconductors. *Phys. Org. Semicond.* **2006**, 1–14. https://doi.org/10.1002/3527606637.ch.

(97) Zhen, W.; Xue, C. Atomic- and Molecular-Level Functionalizations of Polymeric Carbon Nitride for Solar Fuel Production. *Sol. RRL* **2021**, *5* (2), 1–28. https://doi.org/10.1002/solr.202000440.

(98) Wang, S.; Lu, A.; Zhong, C. J. Hydrogen Production from Water Electrolysis: Role of Catalysts. *Nano Converg.* **2021**, *8* (1). https://doi.org/10.1186/s40580-021-00254-x.

(99) Dong, G.; Yan, L.; Bi, Y. Advanced Oxygen Evolution Reaction Catalysts for Solar-Driven Photoelectrochemical Water Splitting. *J. Mater. Chem. A* **2023**, *11* (8), 3888–3903. https://doi.org/10.1039/d2ta09479g.

(100) Gunawan, D.; Zhang, J.; Li, Q.; Toe, C. Y.; Scott, J.; Antonietti, M.; Guo, J.; Amal, R. Materials Advances in Photocatalytic Solar Hydrogen Production: Integrating Systems and Economics for a Sustainable Future. *Adv. Mater.* **2024**, *2404618*, 1–37. https://doi.org/10.1002/adma.202404618.

(101) Nakada, A.; Kumagai, H.; Robert, M.; Ishitani, O.; Maeda, K. Molecule/Semiconductor Hybrid Materials for Visible-Light CO_2 Reduction: Design Principles and Interfacial Engineering. *Accounts Mater. Res.* **2021**, *2* (6), 458–470. https://doi.org/10.1021/accountsmr.1c00060.

(102) Kärkäs, M. D.; Åkermark, B. Water Oxidation Using Earth-Abundant Transition Metal Catalysts: Opportunities and Challenges. *Dalt. Trans.* **2016**, *45* (37), 14421–14461. https://doi.org/10.1039/c6dt00809g.

(103) Garrido-Barros, P.; Gimbert-Suriñach, C.; Matheu, R.; Sala, X.; Llobet, A. How to Make an Efficient and Robust Molecular Catalyst for Water Oxidation. *Chem. Soc. Rev.* **2017**, *46* (20), 6088–6098. https://doi.org/10.1039/c7cs00248c.

(104) Vereshchuk, N.; Gil-Sepulcre, M.; Ghaderian, A.; Holub, J.; Gimbert-Suriñach, C.; Llobet, A. Metamorphic Oxygen-Evolving Molecular Ru and Ir Catalysts. *Chem. Soc. Rev.* **2022**, *52* (1), 196–211. https://doi.org/10.1039/d2cs00463a.

(105) Eckenhoff, W. T.; Eisenberg, R. Molecular Systems for Light Driven Hydrogen Production. *Dalt. Trans.* **2012**, *41* (42), 13004–13021. https://doi.org/10.1039/c2dt30823a.

(106) Weinberg, D. R.; Gagliardi, C. J.; Hull, J. F.; Murphy, C. F.; Kent, C. A.; Westlake, B. C.; Paul, A.; Ess, D. H.; Granville, D.; Meyer, T. J. Proton-Coupled Electron Transfer. *Chem. Rev.* **2012**, *112*, 4016-4093. https://doi.org/10.1021/cr200177j

(107) Ďurovič, M.; Hnát, J.; Bouzek, K. Electrocatalysts for the Hydrogen Evolution Reaction in Alkaline and Neutral Media. A Comparative Review. *J. Power Sources* **2021**, *493* (March). https://doi.org/10.1016/j.jpowsour.2021.229708.

(108) Kumar, S.; Kaur, R.; Sharma, S. Recent Reports on Hydrogen Evolution Reactions and Catalysis. *Results Chem.* **2022**, *4* (July), 100613. https://doi.org/10.1016/j.rechem.2022.100613.

(109) Hansen, J. N.; Prats, H.; Toudahl, K. K.; Mørch Secher, N.; Chan, K.; Kibsgaard, J.; Chorkendorff, I. Is There Anything Better than Pt for HER? *ACS Energy Lett.* **2021**, *6* (4), 1175–1180. https://doi.org/10.1021/acsenergylett.1c00246.

(110) Schneider, J.; Jia, H.; Muckerman, J. T.; Fujita, E. Thermodynamics and Kinetics of CO_2, CO, and H^+ Binding to the Metal Centre of CO_2 Reduction Catalysts. *Chem. Soc. Rev.* **2012**, *41* (6), 2036–2051. https://doi.org/10.1039/c1cs15278e.

(111) Costentin, C.; Drouet, S.; Passard, G.; Robert, M.; Savéant, J. M. Proton-Coupled Electron Transfer Cleavage of Heavy-Atom Bonds in Electrocatalytic Processes. Cleavage of a C-O Bond in the Catalyzed Electrochemical Reduction of CO_2. *J. Am. Chem. Soc.* **2013**, *135* (24), 9023–9031. https://doi.org/10.1021/ja4030148.

(112) Yamazaki, Y.; Takeda, H.; Ishitani, O. Photocatalytic Reduction of CO_2 Using Metal Complexes. *J. Photochem. Photobiol. C Photochem. Rev.* **2015**, *25* (4), 106–137. https://doi.org/10.1016/j.jphotochemrev.2015.09.001.

(113) Wu, Y.; Hu, G.; Rooney, C. L.; Brudvig, G. W.; Wang, H. Heterogeneous Nature of Electrocatalytic CO/CO_2 Reduction by Cobalt Phthalocyanines. *ChemSusChem* **2020**, *13* (23), 6296–6299. https://doi.org/10.1002/cssc.202001396.

(114) Thoi, V. S.; Kornienko, N.; Margarit, C. G.; Yang, P.; Chang, C. J. Visible-Light Photoredox Catalysis: Selective Reduction of Carbon Dioxide to Carbon Monoxide by a Nickel N-Heterocyclic Carbene-Isoquinoline Complex. *J. Am. Chem. Soc.* **2013**, *135* (38), 14413–14424. https://doi.org/10.1021/ja4074003.

(115) Wang, J. W.; Huang, H. H.; Sun, J. K.; Ouyang, T.; Zhong, D. C.; Lu, T. B. Electrocatalytic and Photocatalytic Reduction of CO_2 to CO by Cobalt(II) Tripodal Complexes: Low Overpotentials, High Efficiency and Selectivity. *ChemSusChem* **2018**, *11* (6), 1025–1031. https://doi.org/10.1002/cssc.201702280.

(116) Morikawa, T.; Sato, S.; Sekizawa, K.; Suzuki, T. M.; Arai, T. Solar-Driven CO_2 Reduction Using a Semiconductor/Molecule Hybrid Photosystem: From Photocatalysts to a Monolithic Artificial Leaf.

Acc. Chem. Res. **2022**, *55* (7), 933–943. https://doi.org/10.1021/acs.accounts.1c00564.

(117) Marianov, A. N.; Jiang, Y. Mechanism-Driven Design of Heterogeneous Molecular Electrocatalysts for CO_2 Reduction. *Accounts Mater. Res.* **2022**, *3* (6), 620–633. https://doi.org/10.1021/accountsmr.2c00041.

(118) Wang, J. W.; Gil-Sepulcre, M.; Huang, H. H.; Solano, E.; Mu, Y. F.; Llobet, A.; Ouyang, G. CH-π Interaction Boosts Photocatalytic CO_2 Reduction Activity of a Molecular Cobalt Catalyst Anchored on Carbon Nitride. *Cell Reports Phys. Sci.* **2021**, *2* (12), 100681. https://doi.org/10.1016/j.xcrp.2021.100681.

(119) Millet, P. Fundamentals of Water Electrolysis. In *Hydrogen Production: By Electrolysis*; Godula-Jopek, A., Ed.; Wiley-VCH verlag GmbH & Co. KGaA, 2015; 33–62. https://doi.org/10.1002/9783527676507.ch2.

(120) Schneider, J.; Bangle, R. E.; Swords, W. B.; Troian-Gautier, L.; Meyer, G. J. Determination of Proton-Coupled Electron Transfer Reorganization Energies with Application to Water Oxidation Catalysts. *J. Am. Chem. Soc.* **2019**, *141* (25), 9758–9763. https://doi.org/10.1021/jacs.9b01296.

(121) She, Z. W.; Kibsgaard, J.; Dickens, C. F.; Chorkendorff, I.; Nørskov, J. K.; Jaramillo, T. F. Combining Theory and Experiment in Electrocatalysis: Insights into Materials Design. *Science.* **2017**, *355* (6321). https://doi.org/10.1126/science.aad4998.

(122) McCrory, C. C. L.; Jung, S.; Ferrer, I. M.; Chatman, S. M.; Peters, J. C.; Jaramillo, T. F. Benchmarking Hydrogen Evolving Reaction and Oxygen Evolving Reaction Electrocatalysts for Solar Water Splitting Devices. *J. Am. Chem. Soc.* **2015**, *137* (13), 4347–4357. https://doi.org/10.1021/ja510442p.

(123) Guiglion, P.; Butchosa, C.; Zwijnenburg, M. A. Polymer Photocatalysts for Water Splitting: Insights from Computational Modeling. *Macromol. Chem. Phys.* **2016**, *217* (3), 344–353. https://doi.org/10.1002/macp.201500432.

(124) Franchini, C.; Reticcioli, M.; Setvin, M.; Diebold, U. Polarons in materials. *Nat. Rev. Mater.* **2021**, *6* (7), 560–586. https://doi.org/10.1038/s41578- 021-00289-w.

(125) Thomas, A.; Fischer, A.; Goettmann, F.; Antonietti, M.; Müller, J. O.; Schlögl, R.; Carlsson, J. M. Graphitic Carbon Nitride Materials: Variation of Structure and Morphology and Their Use as Metal-Free Catalysts. *J. Mater. Chem.* **2008**, *18* (41), 4893–4908. https://doi.org/10.1039/b800274f.

(126) Karjule, N.; Barrio, J.; Xing, L.; Volokh, M.; Shalom, M. Highly Efficient Polymeric Carbon Nitride Photoanode with Excellent Electron Diffusion Length and Hole Extraction Properties. *Nano Lett.* **2020**, *20* (6), 4618–4624. https://doi.org/10.1021/acs.nanolett.0c01484.

(127) Zhang, G.; Savateev, A.; Zhao, Y.; Li, L.; Antonietti, M. Advancing the n → π* Electron Transition of Carbon Nitride Nanotubes for H_2 Photosynthesis. *J. Mater. Chem. A* **2017**, *5* (25), 12723–12728. https://doi.org/10.1039/c7ta03777e.

(128) Barrio, J.; Shalom, M. Rational Design of Carbon Nitride Materials by Supramolecular Preorganization of Monomers. *ChemCatChem* **2018**, *10* (24), 5573–5586. https://doi.org/10.1002/cctc.201801410.

(129) Zhang, G.; Li, G.; Heil, T.; Zafeiratos, S.; Lai, F.; Savateev, A.; Antonietti, M.; Wang, X. Tailoring the Grain Boundary Chemistry of Polymeric Carbon Nitride for Enhanced Solar Hydrogen Production and CO_2 Reduction. *Angew. Chemie - Int. Ed.* **2019**, *58* (11), 3433–3437. https://doi.org/10.1002/anie.201811938.

(130) Tilford, R. W.; Mugavero, S. J.; Pellechia, P. J.; Lavigne, J. J. Tailoring Microporosity in Covalent Organic Frameworks. *Adv. Mater.* **2008**, *20* (14), 2741–2746. https://doi.org/10.1002/adma.200800030.

(131) Zhang, A.; Dong, P.; Wang, Y.; Gao, K.; Pan, J.; Yang, B.; Xi, X.; Zhang, J. Fabrication of Well-Dispersed Pt Nanoparticles onto the Donor-Acceptor Type Conjugated Polymers for High-Efficient Photocatalytic Hydrogen Evolution. *Appl. Catal. A Gen.* **2022**, *644* (July). https://doi.org/10.1016/j.apcata.2022.118793.

(132) Byun, J.; Zhang, K. A. I. Designing Conjugated Porous Polymers for Visible Light-Driven Photocatalytic Chemical Transformations. *Mater. Horizons* **2020**, *7* (1), 15–31. https://doi.org/10.1039/c9mh01071h.

(133) Kuriki, R.; Maeda, K. Development of Hybrid Photocatalysts Constructed with a Metal Complex and Graphitic Carbon Nitride for Visible-Light-Driven CO_2 Reduction. *Phys. Chem. Chem. Phys.* **2017**, *19* (7), 4938–4950. https://doi.org/10.1039/c6cp07973c.

(134) Kong, D.; Xie, J.; Guo, Z.; Yang, D.; Tang, J. Stable Complete Water Splitting by Covalent Triazine-Based Framework CTF-0. *ChemCatChem* **2020**, *12* (10), 2708–2712. https://doi.org/10.1002/cctc.201902396.

(135) Hu, X. L.; Li, H. G.; Tan, B. E. COFs-Based Porous Materials for Photocatalytic Applications. *Chinese J. Polym. Sci. (English Ed.* **2020**, *38* (7), 673–684. https://doi.org/10.1007/s10118-020-2394-x.

(136) Xu, W.; Yaghi, O. M. Metal-Organic Frameworks for Water Harvesting from Air, Anywhere, Anytime. *ACS Cent. Sci.* **2020**, *6* (8), 1348–1354. https://doi.org/10.1021/acscentsci.0c00678.

(137) Hanikel, N.; Prévot, M. S.; Yaghi, O. M. MOF Water Harvesters. *Nat. Nanotechnol.* **2020**, *15* (5), 348–355. https://doi.org/10.1038/s41565-020-0673-x.

(138) Li, Z.; Xu, X.; Sheng, X.; Lin, P.; Tang, J.; Pan, L.; Kaneti, Y. V.; Yang, T.; Yamauchi, Y. Solar-Powered

Sustainable Water Production: State-of-the-Art Technologies for Sunlight-Energy-Water Nexus. *ACS Nano* **2021**, *15* (8), 12535–12566. https://doi.org/10.1021/acsnano.1c01590.

(139) Rahman, M. Z.; Mullins, C. B. Understanding Charge Transport in Carbon Nitride for Enhanced Photocatalytic Solar Fuel Production. *Acc. Chem. Res.* **2019**, *52* (1), 248–257. https://doi.org/10.1021/acs.accounts.8b00542.

(140) Liebig, J. Uber Einige Stickstoff - Verbindungen. *European J. Org. Chem.* **1834**, *10* (1), 1–47. https://doi.org/10.1002/jlac.18340100102.

(141) Xia, J.; Karjule, N.; Abisdris, L.; Volokh, M.; Shalom, M. Controllable Synthesis of Carbon Nitride Films with Type-II Heterojunction for Efficient Photoelectrochemical Cells. *Chem. Mater.* **2020**, *32* (13), 5845–5853. https://doi.org/10.1021/acs.chemmater.0c01856.

(142) Volokh, M.; Shalom, M. Polymeric Carbon Nitride as a Platform for Photoelectrochemical Water-Splitting Cells. *Ann. N. Y. Acad. Sci.* **2023**, *1521* (1), 5–13. https://doi.org/10.1111/nyas.14963.

(143) Barrio, J.; Volokh, M.; Shalom, M. Polymeric Carbon Nitrides and Related Metal-Free Materials for Energy and Environmental Applications. *J. Mater. Chem. A* **2020**, *8* (22), 11075–11116. https://doi.org/10.1039/d0ta01973a.

(144) Liu, J.; Liu, Y.; Liu, N.; Han, Y.; Zhang, X.; Huang, H.; Lifshitz, Y.; Lee, S. T.; Zhong, J.; Kang, Z. Metal-Free Efficient Photocatalyst for Stable Visible Water Splitting via a Two-Electron Pathway. *Science* **2015**, *347* (6225), 970–974. https://doi.org/10.1126/science.aaa3145.

(145) Banerjee, T.; Podjaski, F.; Kröger, J.; Biswal, B. P.; Lotsch, B. V. Polymer Photocatalysts for Solar-to-Chemical Energy Conversion. *Nat. Rev. Mater.* **2021**, *6*, 168–190. https://doi.org/10.1038/s41578-020-00254-z.

(146) Cao, S.; Low, J.; Yu, J.; Jaroniec, M. Polymeric Photocatalysts Based on Graphitic Carbon Nitride. *Adv. Mater.* **2015**, *27* (13), 2150–2176.

(147) Karjule, N.; Singh, C.; Barrio, J.; Tzadikov, J.; Liberman, I.; Volokh, M.; Palomares, E.; Hod, I.; Shalom, M. Carbon Nitride-Based Photoanode with Enhanced Photostability and Water Oxidation Kinetics. *Adv. Funct. Mater.* **2021**, *31* (25). https://doi.org/10.1002/adfm.202101724.

(148) Zhen, W.; Yuan, X.; Shi, X.; Xue, C. Grafting Molecular Cobalt-Oxo Cubane Catalyst on Polymeric Carbon Nitride for Efficient Photocatalytic Water Oxidation. *Chem. - An Asian J.* **2020**, *15* (16), 2480–2486. https://doi.org/10.1002/asia.202000583.

(149) Ockwig, N. W.; Keeffe, M. O.; Matzger, A. J.; Yaghi, O. M. Porous , Crystalline , Covalent Organic Frameworks. **2005**, *310* (November), 1166–1170.

(150) Kuhn, P.; Antonietti, M.; Thomas, A. Porous, Covalent Triazine-Based Frameworks Prepared by Ionothermal Synthesis. *Angew. Chemie - Int. Ed.* **2008**, *47* (18), 3450–3453.

https://doi.org/10.1002/anie.200705710.

(151) Ren, S.; Bojdys, M. J.; Dawson, R.; Laybourn, A.; Khimyak, Y. Z.; Adams, D. J.; Cooper, A. I. Porous, Fluorescent, Covalent Triazine-Based Frameworks via Room-Temperature and Microwave-Assisted Synthesis. *Adv. Mater.* **2012**, *24* (17), 2357–2361. https://doi.org/10.1002/adma.201200751.

(152) Meier, C. B.; Sprick, R. S.; Monti, A.; Guiglion, P.; Lee, J. S. M.; Zwijnenburg, M. A.; Cooper, A. I. Structure-Property Relationships for Covalent Triazine-Based Frameworks: The Effect of Spacer Length on Photocatalytic Hydrogen Evolution from Water. *Polymer (Guildf).* **2017**, *126*, 283–290. https://doi.org/10.1016/j.polymer.2017.04.017.

(153) Sun, T.; Liang, Y.; Luo, W.; Zhang, L.; Cao, X.; Xu, Y. A General Strategy for Kilogram-Scale Preparation of Highly Crystal-Line Covalent Triazine Frameworks. *Angew. Chemie - Int. Ed.* **2022**, *61* (25). https://doi.org/10.1002/anie.202203327.

(154) Wu, X.; Han, X.; Liu, Y.; Liu, Y.; Cui, Y. Control Interlayer Stacking and Chemical Stability of Two-Dimensional Covalent Organic Frameworks via Steric Tuning. *J. Am. Chem. Soc.* **2018**, *140* (47), 16124–16133. https://doi.org/10.1021/jacs.8b08452.

(155) Yu Liang, Binbin Zhao, Qiong Tang, L. L. & J. D. Adjusting Pt Nanoparticle Size on SBA-15 by a Sol-Immobilisation Method Towards Naphthalene Hydrogenation. *Catal. Letters* **2022**, *152*, 3489–3497. https://doi.org/10.1007/s10562-021-03907-y.

(156) Kong, D.; Han, X.; Xie, J.; Ruan, Q.; Windle, C. D.; Gadipelli, S.; Shen, K.; Bai, Z.; Guo, Z.; Tang, J. Tunable Covalent Triazine-Based Frameworks (CTF-0) for Visible-Light-Driven Hydrogen and Oxygen Generation from Water Splitting. *ACS Catal.* **2019**, *9* (9), 7697–7707. https://doi.org/10.1021/acscatal.9b02195.

(157) Xie, J.; Shevlin, S. A.; Ruan, Q.; Moniz, S. J. A.; Liu, Y.; Liu, X.; Li, Y.; Lau, C. C.; Guo, Z. X.; Tang, J. Efficient Visible Light-Driven Water Oxidation and Proton Reduction by an Ordered Covalent Triazine-Based Framework. *Energy Environ. Sci.* **2018**, *11* (6), 1617–1624. https://doi.org/10.1039/c7ee02981k.

(158) Cheng, Y. Z.; Ji, W.; Hao, P. Y.; Qi, X. H.; Wu, X.; Dou, X. M.; Bian, X. Y.; Jiang, D.; Li, F. T.; Liu, X. F.; Yang, D. H.; Ding, X.; Han, B. H. A Fully Conjugated Covalent Organic Framework with Oxidative and Reductive Sites for Photocatalytic Carbon Dioxide Reduction with Water. *Angew. Chemie - Int. Ed.* **2023**, *62* (36). https://doi.org/10.1002/anie.202308523.

(159) He, Y.; Zhao, Y.; Wang, X.; Liu, Z.; Yu, Y.; Li, L. Multiple Heteroatom-Hydrogen Bonds Bridging Electron Transport in Covalent Organic Framework-Based Supramolecular System for Photoreduction of CO_2. *Angew. Chemie - Int. Ed.* **2023**, *62* (31), 1–7. https://doi.org/10.1002/anie.202307160.

(160) Watson, G.; Derakhshandeh, P. G.; Abednatanzi, S.; Schmidt, J.; Leus, K.; Der Voort, P. Van. A Ru-Complex Tethered to a N-Rich Covalent Triazine Framework for Tandem Aerobic Oxidation-Knoevenagel Condensation Reactions. *Molecules* **2021**, *26* (4). https://doi.org/10.3390/molecules26040838.

(161) Gilbert, J. A.; Eggleston, D. S.; Murphy, W. R.; Geselowitz, J. D. A.; Gersten, S. W.; Hodgson, D. J.; Meyer, T. J. Structure and Redox Properties of the Water-Oxidation Catalyst $[(bpy)_2(OH_2)RuORu(OH_2)(bpy)_2]^{4+}$. *J. Am. Chem. Soc.* **1985**, *107* (13), 3855–3864. https://doi.org/10.1021/ja00299a017.

(162) Gersten, S. W.; Samuels, G. J.; Meyer, T. J. Catalytic Oxidation of Water by an Oxo-Bridged Ruthenium Dimer. *J. Am. Chem. Soc.* **1982**, *104* (14), 4029–4030. https://doi.org/10.1021/ja00378a053.

(163) Sens, C.; Romero, I.; Rodríguez, M.; Llobet, A.; Parella, T.; Benet-Buchholz, J. A New Ru Complex Capable of Catalytically Oxidizing Water to Molecular Dioxygen. *J. Am. Chem. Soc.* **2004**, *126* (25), 7798–7799. https://doi.org/10.1021/ja0486824.

(164) Zong, R.; Thummel, R. P. A New Family of Ru Complexes for Water Oxidation. *J. Am. Chem. Soc.* **2005**, *127* (37), 12802–12803. https://doi.org/10.1021/ja054791m.

(165) Concepcion, J. J.; Jurss, J. W.; Templeton, J. L.; Meyer, T. J. One Site Is Enough. Catalytic Water Oxidation by $[Ru(tpy)(bpm)(OH_2)]^{2+}$ and $[Ru(tpy)(bpz)(OH_2)]^{2+}$. *J. Am. Chem. Soc.* **2008**, *130* (49), 16462–16463. https://doi.org/10.1021/ja8059649.

(166) Tong, L.; Thummel, R. P. Mononuclear Ruthenium Polypyridine Complexes That Catalyze Water Oxidation. *Chem. Sci.* **2016**, *7* (11), 6591–6603. https://doi.org/10.1039/c6sc02766k.

(167) Duan, L.; Bozoglian, F.; Mandal, S.; Stewart, B.; Privalov, T.; Llobet, A.; Sun, L. A Molecular Ruthenium Catalyst with Water-Oxidation Activity Comparable to that of Photosystem II. *Nat. Chem.* **2012**, *4* (5), 418–423. https://doi.org/10.1038/nchem.1301.

(168) Duan, L.; Fischer, A.; Xu, Y.; Sun, L. Isolated Seven-Coordinate Ru(IV) Dimer Complex with [HOHOH]- Bridging Ligand as an Intermediate for Catalytic Water Oxidation. *J. Am. Chem. Soc.* **2009**, *131* (30), 10397–10399. https://doi.org/10.1021/ja9034686.

(169) Richmond, C. J.; Matheu, R.; Poater, A.; Falivene, L.; Benet-Buchholz, J.; Sala, X.; Cavallo, L.; Llobet, A. Supramolecular Water Oxidation with Rubda-Based Catalysts. *Chem. - A Eur. J.* **2014**, *20* (52), 17282–17286. https://doi.org/10.1002/chem.201405144.

(170) Matheu, R.; Ertem, M. Z.; Benet-Buchholz, J.; Coronado, E.; Batista, V. S.; Sala, X.; Llobet, A. Intramolecular Proton Transfer Boosts Water Oxidation Catalyzed by a Ru Complex. *J. Am. Chem. Soc.* **2015**, *137* (33), 10786–10795. https://doi.org/10.1021/jacs.5b06541.

(171) Matheu, R.; Ertem, M. Z.; Gimbert-Suriñach, C.; Sala, X.; Llobet, A. Seven Coordinated Molecular Ruthenium-Water Oxidation Catalysts: A Coordination Chemistry Journey. *Chem. Rev.* **2019**, *119* (6), 3453–3471. https://doi.org/10.1021/acs.chemrev.8b00537.

(172) Matheu, R.; Ertem, M. Z.; Gimbert-Suriñach, C.; Benet-Buchholz, J.; Sala, X.; Llobet, A. Hydrogen Bonding Rescues Overpotential in Seven-Coordinated Ru Water Oxidation Catalysts. *ACS Catal.* **2017**, *7* (10), 6525–6532. https://doi.org/10.1021/acscatal.7b01860.

(173) Matheu, R.; Ertem, M. Z.; Pipelier, M.; Lebreton, J.; Dubreuil, D.; Benet-Buchholz, J.; Sala, X.; Tessier, A.; Llobet, A. The Role of Seven-Coordination in Ru-Catalyzed Water Oxidation. *ACS Catal.* **2018**, *8* (3), 2039–2048. https://doi.org/10.1021/acscatal.7b03638.

(174) Matheu, R.; Garrido-Barros, P.; Gil-Sepulcre, M.; Ertem, M. Z.; Sala, X.; Gimbert-Suriñach, C.; Llobet, A. The Development of Molecular Water Oxidation Catalysts. *Nat. Rev. Chem.* **2019**, *3* (5), 331–341. https://doi.org/10.1038/s41570-019-0096-0.

(175) Vereshchuk, N.; Matheu, R.; Benet-Buchholz, J.; Pipelier, M.; Lebreton, J.; Dubreuil, D.; Tessier, A.; Gimbert-Suriñach, C.; Ertem, M. Z.; Llobet, A. Second Coordination Sphere Effects in an Evolved Ru Complex Based on Highly Adaptable Ligand Results in Rapid Water Oxidation Catalysis. *J. Am. Chem. Soc.* **2020**, *142* (11), 5068–5077. https://doi.org/10.1021/jacs.9b11935.

(176) Vereshchuk, N.; Holub, J.; Gil-Sepulcre, M.; Benet-Buchholz, J.; Llobet, A. Fate of the Molecular Ru-Phosphonate Water Oxidation Catalyst under Turnover Conditions. *ACS Catal.* **2021**, *11* (9), 5240–5247. https://doi.org/10.1021/acscatal.0c05363.

(177) Creus, J.; Matheu, R.; Peñafiel, I.; Moonshiram, D.; Blondeau, P.; Benet-Buchholz, J.; García-Antón, J.; Sala, X.; Godard, C.; Llobet, A. A Million Turnover Molecular Anode for Catalytic Water Oxidation. *Angew. Chemie - Int. Ed.* **2016**, *55* (49), 15382–15386. https://doi.org/10.1002/anie.201609167.

(178) Matheu, R.; Moreno-Hernandez, I. A.; Sala, X.; Gray, H. B.; Brunschwig, B. S.; Llobet, A.; Lewis, N. S. Photoelectrochemical Behavior of a Molecular Ru-Based Water-Oxidation Catalyst Bound to TiO_2-Protected Si Photoanodes. *J. Am. Chem. Soc.* **2017**, *139* (33), 11345–11348. https://doi.org/10.1021/jacs.7b06800.

(179) Hoque, M. A.; Gil-Sepulcre, M.; de Aguirre, A.; Elemans, J. A. A. W.; Moonshiram, D.; Matheu, R.; Shi, Y.; Benet-Buchholz, J.; Sala, X.; Malfois, M.; Solano, E.; Lim, J.; Garzón-Manjón, A.; Scheu, C.; Lanza, M.; Maseras, F.; Gimbert-Suriñach, C.; Llobet, A. Water Oxidation Electrocatalysis Using Ruthenium Coordination Oligomers Adsorbed on Multiwalled Carbon Nanotubes. *Nat. Chem.* **2020**, *12* (11), 1060–1066. https://doi.org/10.1038/s41557-020-0548-7.

(180) Liseev, T.; Howe, A.; Hoque, M. A.; Gimbert-Suriñach, C.; Llobet, A.; Ott, S. Synthetic Strategies to Incorporate Ru-Terpyridyl Water Oxidation Catalysts into MOFs: Direct Synthesis *vs.* Post-

Synthetic Approach. *Dalt. Trans.* **2020**, *49* (39), 13753–13759. https://doi.org/10.1039/d0dt01890b.

(181) Dürr, R. N.; Chasvised, S.; Gil-Sepulcre, M.; Howe, A.; Hoque, M. A.; N'Guyen, V.; Sadeghi, S.; Reynaud, S.; Cugnet, C.; Authier, L.; Gimbert-Suriñach, C.; Bousquet, A.; Llobet, A.; Billon, L. Robust and Efficient Screen-Printed Molecular Anodes with Anchored Water Oxidation Catalysts. *ACS Appl. Energy Mater.* **2021**, *4* (10), 10534–10541. https://doi.org/10.1021/acsaem.1c01435.

(182) Schindler, D.; Gil-Sepulcre, M.; Lindner, J. O.; Stepanenko, V.; Moonshiram, D.; Llobet, A.; Würthner, F. Efficient Electrochemical Water Oxidation by a Trinuclear Ru(bda) Macrocycle Immobilized on Multi-Walled Carbon Nanotube Electrodes. *Adv. Energy Mater.* **2020**, *10* (43), 1–7. https://doi.org/10.1002/aenm.202002329.

(183) Gil-Sepulcre, M.; Lindner, J. O.; Schindler, D.; Velasco, L.; Moonshiram, D.; Rüdiger, O.; Debeer, S.; Stepanenko, V.; Solano, E.; Würthner, F.; Llobet, A. Surface-Promoted Evolution of Ru-Bda Coordination Oligomers Boosts the Efficiency of Water Oxidation Molecular Anodes. *J. Am. Chem. Soc.* **2021**, *143* (30), 11651–11661. https://doi.org/10.1021/jacs.1c04738.

(184) Wang, L.; Polyansky, D. E.; Concepcion, J. J. Self-Assembled Bilayers as an Anchoring Strategy: Catalysts, Chromophores, and Chromophore-Catalyst Assemblies. *J. Am. Chem. Soc.* **2020**, *141* (20), 8020–8027. https://doi.org/10.1021/jacs.9b01044.

(185) Ventosa, M.; Gil-Sepulcre, M.; Benet-Buchholz, J.; Gimbert-Suriñach, C.; Llobet, A. Anode Based on a Molecular Ru Water Oxidation Catalyst Covalently Bonded to Polythiophene. *ACS Appl. Energy Mater.* **2021**, *4* (9), 9775–9782. https://doi.org/10.1021/acsaem.1c01851.

(186) Wu, L.; Eberhart, M.; Nayak, A.; Brennaman, M. K.; Shan, B.; Meyer, T. J. A Molecular Silane-Derivatized Ru(II) Catalyst for Photoelectrochemical Water Oxidation. *J. Am. Chem. Soc.* **2018**, *140* (44), 15062–15069. https://doi.org/10.1021/jacs.8b10132.

(187) Feng, Y.; Sun, W.; Liang, X.; Dong, X.; Yang, X.; Hu, C.; Li, B.; Yang, J.; Ma, B.; Ding, Y. Mononuclear Ruthenium (II) Complex Covalently Anchored on Melem and g-C_3N_4 as Efficient Heterogeneous Catalysts for Chemical Water Oxidation. *J. Colloid Interface Sci.* **2023**, *643* (December 2022), 480–488. https://doi.org/10.1016/j.jcis.2023.04.053.


1

Chapter 2

Objectives


2

In Chapter 1, the development of molecular catalysts, particularly for oxygen evolution, and the advancements in organic materials for photo(electro)catalysis were introduced. The next step in the field involves integrating the light absorber and the catalysts in a single hybrid material ensuring a fast and efficient charge transfer toward artificial photosynthesis. Inspired by Nature, this doctoral thesis focuses on preparing, characterizing and investigating C- and N-based materials containing molecular-based water oxidation and CO_2 reduction catalysts. Particularly, this study explores different strategies for functionalizing photoactive carbon- and nitrogen-based polymers with molecular catalysts and their performance. Thus, the general goal of this work is to provide alternative solutions in the field of heterogeneous catalysis, examining the processes through the photocatalytic and photoelectrocatalytic approaches. This general aim can be divided into four specific objectives.

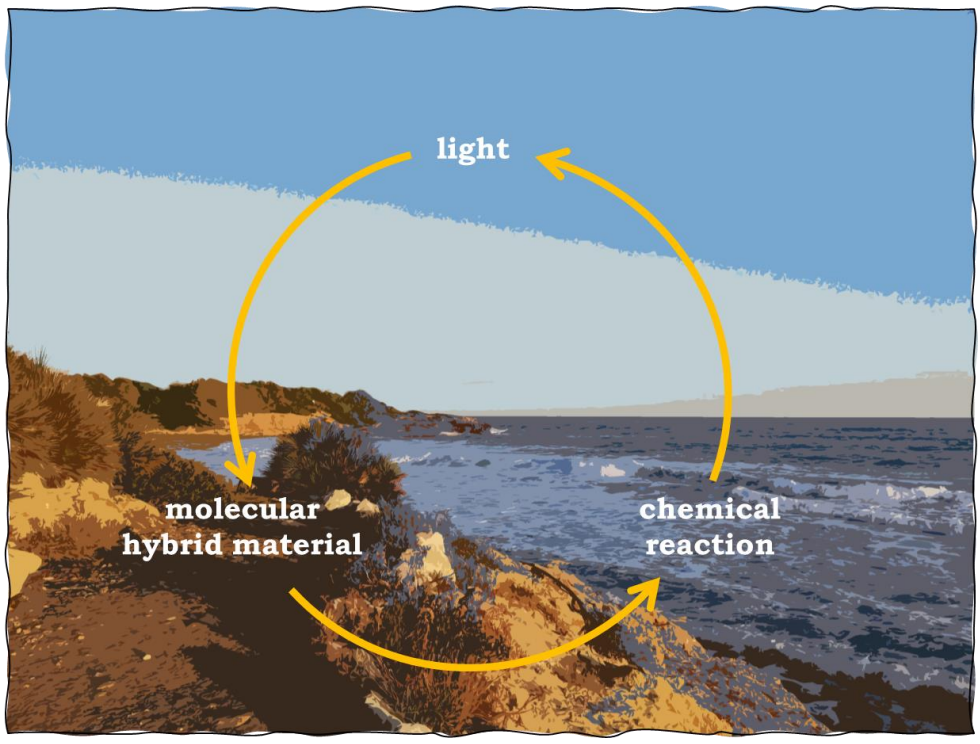

Objective 1

In the last decades, Covalent triazine-based frameworks (CTFs) have been deeply studied and developed as great tunable light-absorbing materials for the photocatalytic transformation of solar energy to chemicals. However, concerning especially the water oxidation (WO) to dioxygen, the use of a co-catalyst is pivotal to enhance the efficiency of the process and prevent an internal back-electron transfer. The target of this first project is thus the synthesis of a novel CTF material, *via* a trimerization reaction at room temperature, with a characteristic dangling pyridyl group included within the repetitive unit, and its further functionalization with a highly active Ru-based molecular complex for WO through covalent bonding. The aim is to improve the charge separation in the new molecular hybrid material (Ru-CTF) to prompt the water oxidation reaction in a photocatalytic suspension under irradiation, using sodium persulfate as sacrificial electron acceptor under neutral pH conditions.

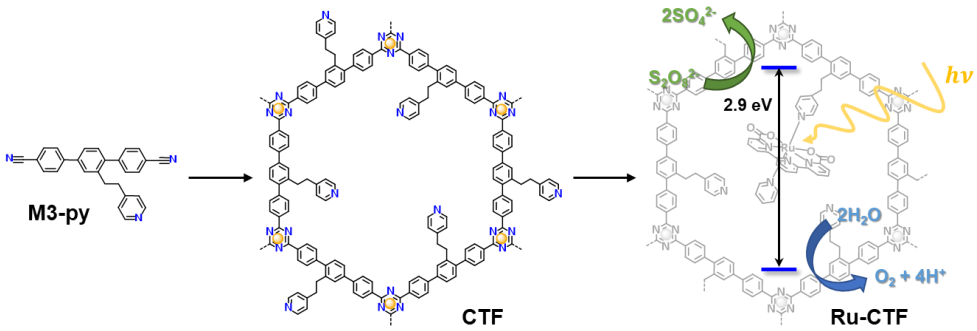

Objective 2

Within the same context of CTF materials for light-to-chemical reactions, the photocatalytic reduction of CO_2 to CO also represents a challenging process which requires the employment of co-catalysts to increase the active sites on the organic semiconductors. As well, most of the hybrid systems studied for this purpose work only with noble metals-based catalysts in organic solvents. Based on these considerations, the objective of this second project is the preparation and characterization of the CTF polymer already presented in the Objective 1, using a new synthetic approach, and to

functionalize it with a Co-based molecular catalyst for CO_2 reduction as complementary strategy for the first project. The aim is to show the potentiality of a covalently coordinated molecular catalyst based on abundant elements for selective CO formation from CO_2 in aqueous medium under irradiation and compare the properties, mechanism and efficiency with a parallel hybrid system with supramolecular interactions. The ultimate perspective would be thus the preparation of a bifunctional material based on the same CTF polymer working for both reactions of water oxidation and CO_2 reduction at a time.

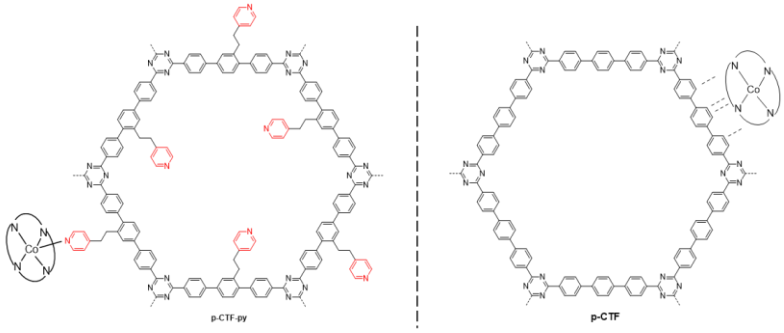

Objective 3

In the field of organic semiconductors, polymeric carbon nitride (CN) also constitutes a new class of functional materials, which has been investigated during the last decades and is currently one of the most studied organic semiconductors because of the tunable optical and electrochemical properties. However, when used for the purpose of water oxidation, most of the examples reported the used of alkaline or acidic pH electrolytes and the employment of metal-based nanoparticles. Herein, the third project aims to synthetize and analyze a novel molecular hybrid material composed by a Ru-tda based polymeric catalyst supramolecularly interacting with CN photoanodes for light-induced water oxidation in a photoelectrochemical (PEC) device. The objective comprehends the study of the novel system with its properties and catalytic activity and clarify the role of the molecular catalyst on the surface of the organic material when using a neutral pH medium.

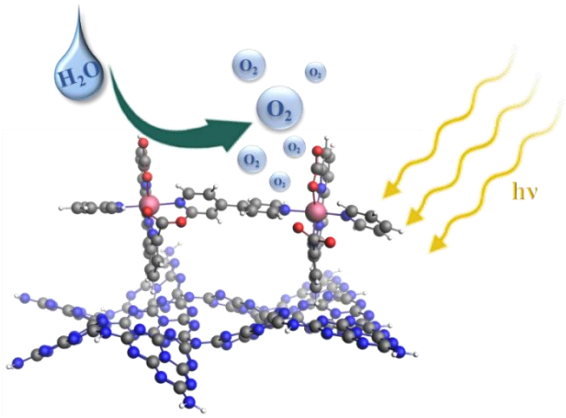

Objective 4

In the wake of the water oxidation performed with CN photoanodes with co-catalysts, there is no example among all the systems reported so far in PEC devices that shows the study of covalently anchored molecular catalysts on the semiconductor. Moreover, the use of high or low pH electrolytes is always adopted to enhance the stability. In the fourth and last project, the target is to investigate a new covalent anchoring procedure involving an amidation reaction at room temperature between the terminal NH_2 moieties of the carbon nitride and the carboxylate group of a molecular Ru-based catalyst. The aim is to further explore the efficiency and stability of a strategically designed hybrid system in neutral medium for oxygen evolution, considering the possible improvement of charge separation and transfer in the assembly.

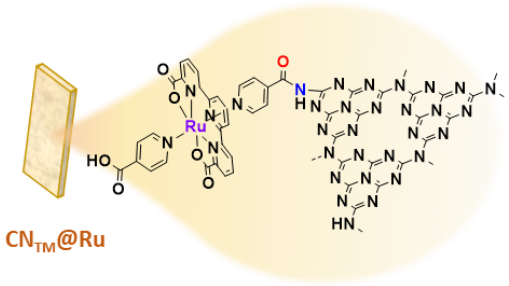

Chapter 3

Covalent triazine-based frameworks with covalently anchored Ru-tda based catalyst for photoinduced water oxidation


3

Covalent triazine-based frameworks with covalently anchored Ru-tda based catalyst for photoinduced water oxidation

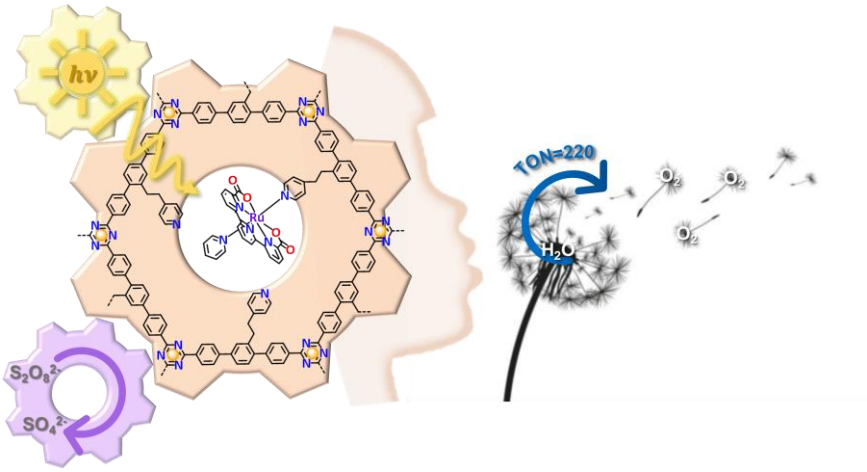

Abstract

Light-induced water splitting (*hv*-WS) for the production of hydrogen as a solar fuel is considered a promising sustainable strategy for the replacement of fossil fuels. An efficient system for *hv*-WS involves a photoactive material that, upon shining light, is capable of separating and transferring charges to catalysts for the hydrogen and oxygen evolution processes. Covalent triazine-based frameworks (CTFs) represent an interesting class of 2D organic light-absorbing materials that have recently emerged thanks to their tunable structural, optical and morphological properties. Typically, catalysts (Cat) are metallic nanoparticles generated *in situ* after photo(electro)reduction of metal precursors or directly drop-casted on top of the CTF material to generate Cat-CTF assemblies. In this work, we report the synthesis, characterization and photocatalytic performance of a novel hybrid material, **Ru-CTF**, based on a CTF structure featuring dangling pyridyl groups that allow to attach the Ru-tda (tda is [2,2':6',2''-terpyridine]-6,6''-dicarboxylic acid) water oxidation catalyst (WOC) unit via coordination covalent bond. The **Ru-CTF** molecular hybrid material can carry out the light-induced water oxidation reaction efficiently at neutral pH, reaching values of maximum TOF of 17 h^{-1} and TONs in the range of 220 using sodium persulfate as a sacrificial electron acceptor.

Contributions:

Martina Salati synthesized the [Ru(tda)(dmso)py] catalyst and precursors, **CTF** and **Ru-CTF**, as well as performed all the characterization measurements for the materials and the photocatalysis experiments.

3.1. Introduction

Photo-induced reactions are fundamental for the generation of solar fuels and for a large number of chemical processes generically known as light to chemistry.[1–4] A particular case of this is the light-induced water splitting (*hv*-WS) reaction for hydrogen production, which is considered one of the most promising strategies for the generation of renewable energy vectors without the formation of greenhouse gases or toxic side products. Three key elements are needed to achieve such a transformation: a light absorber, a water oxidation catalyst and a proton reduction catalyst. Further, for the *hv*-WS reaction to be useful from an applicative perspective, the redox potentials of catalysts need to be properly aligned with the energy band edges of the absorber, in order to provide the proper driving force for the charge transfer, as well as the chemical reactions need to be fast.[5] It is thus of paramount importance that the absorber and the catalyst have the right electronic communication so that the whole system works in a harmonious manner, avoiding undesired competitive back electron transfer and charge recombination processes. An additional hurdle that needs to be handled in light-induced reactions is the fact that general catalytic reactions involving proton and electron transfers, as well as bond breaking/formation, are orders of magnitude slower than those of the light induced processes.[6] As a result, back-electron transfer pathways become dominant and drastically reduce the quantum efficiency of the whole process, since it substantially decreases the productive reactions.

Photocatalytic systems for complete *hv*-WS in the absence of sacrificial reagents are based on materials or molecules or on a combination of both. However, the number of reported examples is very scarce, presenting low efficiencies and sometimes are difficult to reproduce.[7–10] In order to discover efficient systems, it is important to identify and understand the complex chemical reactions involved in the light-induced process.[11,12] For this purpose, the photo-induced oxidation and reduction reactions can be studied independently using large amounts of sacrificial reagents.[13–16]

Molecular-based systems, in principle, offer the possibility of a better in-depth characterization of the kinetics and reaction intermediates involved than the systems based on materials. Regarding the most challenging half-reaction of the WS process, which is represented from the light induced water oxidation reaction, there are a few

examples based on independent discrete molecules in homogeneous phase that have been described using invariably $[Ru(bpy)_3]^{2+}$ as light absorber in combination with a molecular water oxidation catalyst based on Ru and other transition metals.[6,10,17] There are also examples of dyads , again based on $[Ru(bpy)_3]^{2+}$ analogues, where the absorber and the catalyst are linked together *via* covalent bonds that have mainly been showing to work as a proof of principle systems with limited quantum efficiencies.[18–21]

Recently, transition metal-free polymeric organic absorbers such as Carbon dots,[22,23] Carbon nitrides (C_3N_4) [24–27] and Covalent triazine-based frameworks (CTFs) [13,28–31] have been developed showing promising properties for light to chemistry purposes.[14,32] In particular, CTFs are interesting materials because they present a high degree of synthetic versatility, that in turn can provide a fine tunability of their photochemical properties.[4] This allows preparing tailored CTF polymeric materials containing a dangling pyridyl group where a molecular catalyst can be covalently anchored. Herein, we report the synthesis and characterization of a CTF-based dyad containing Ru-tda (tda is [2,2':6',2''-terpyridine]-6,6''-dicarboxylic acid) water oxidation catalyst, **Ru-CTF**,[33,34] which is capable of carrying out the light induced water oxidation reaction in an efficient manner, achieving up to 220 catalytic cycles as well as 17 h^{-1} of max. TOF using a modest catalyst concentration in the system.

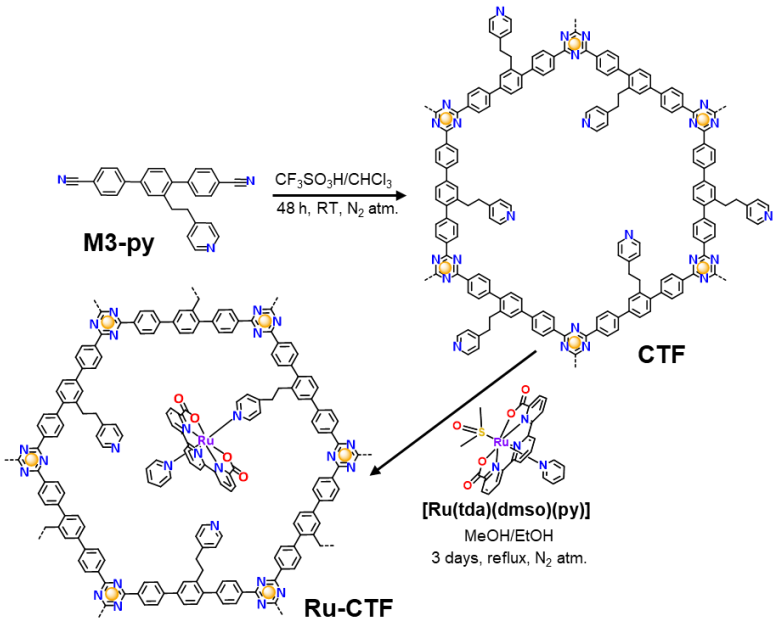

Scheme 1. *Synthetic strategy followed for the preparation of* ***CTF*** *and* ***Ru-CTF*** *starting from the* ***M3-py*** *monomer. Dashed lines indicate extension to a 2D structure.*

3.2. Results and discussion

3.2.1 Synthesis and Structure

The preparation of the dicyano monomer precursor 2'-(2-(pyridin-4-yl)ethyl)-[1,1':4',1''-terphenyl]-4,4''-dicarbonitrile, **M3-py** in Scheme 1, containing a dangling pyridine group used for the preparation of the triazine 2D polymer, involves a multistep organic synthesis using 2,5-dibromotoluene as starting material (See SI, Scheme S1). The reaction of **M3-py** with triflic acid in chloroform for 48 h at RT catalyzes its polymerization, generating a pale yellow powder of the corresponding covalent triazine framework (**CTF**) as shown in Scheme 1.[35] The latter reacts with the Ru water oxidation catalyst precursor [Ru(tda)(dmso)(py)] (py is pyridine), in MeOH/EtOH (1:1) at reflux temperature for 3 days, producing a purple powder of the desired **Ru-CTF** hybrid molecular material, whose structure is drawn in Scheme 1. All the intermediates and precursors have been characterized by the usual analytic and spectroscopic techniques and are reported in the SI (Figures S1-S4). The IR spectrum of the **CTF** material showed the absence of the $\nu_{C\equiv N}$ band at *ca.* 2220 cm^{-1}, which is indicative of a high degree of polymerization (Figure S5).[36] Further, powder X-ray diffraction (PXRD) for both **CTF** and

Ru-CTF shows a low degree of crystallinity, typical for this type of materials (Figure S6).[16,35,37] Nitrogen absorption-desorption experiments reveal that **CTF** has a low surface area with SA_{BET} = 11.2 m^2/g and low porosity (average pore diameter of 17.3 nm, associated to a non-uniform aggregation of particles) (Figure S7), supported by scanning electron microscopy (SEM) and transmission electron microscopy (TEM) techniques (Figures S8 and S9, respectively), which show disordered layers and agglomerated particles of different sizes. Related experiments were carried out also for **Ru-CTF,** giving similar results to **CTF** and showing a homogeneous distribution of the Ru in the material (See SI for a detailed explanation, Figures S5-S9). Additionally, electrochemical experiments were carried out for **Ru-CTF**, which showed similar redox properties as $[Ru(tda)(py)_2]$,further supporting the coordination of the Ru center into the dangling pyridine of the initial **CTF** framework (Figure S10 and Table S2).[33,38] This was also supported by Ru K-edge X-ray absorption (XAS) spectroscopy, including both the edge and the extended X-ray absorption fine structure (EXAFS) regions, which are sensitive to the oxidation state and the coordination environment around the metal center, Figure 1 (see also Figure S21 and Table S3). The Ru K-edge shows that the spectrum of **Ru-CTF** (black trace) is identical to that of the parent monomer $[Ru(tda)(py)_2]$ (purple trace) and clearly different from the Ru precursor complex [Ru(tda)(dmso)(py)] (yellow trace).[33,38] The experimental and simulated EXAFS region spectrum is in agreement with a typical octahedral coordination for Ru(II) in **Ru-CTF**, where fitted Ru-N/O distances at 1.92 and 2.08 Å are in good agreement with the X-ray structure of the monomer $[Ru(tda)(py)_2]$ (see Figure S21 and Table S3). Finally, ICP-OES analysis revealed a 1.05 ± 0.08% (in weight) of Ru content that is consistent with a substitution of about 14% of the dangling pyridines in the initial **CTF** material (Table S1), indicating a quite low uptake of catalyst probably influenced by the small SA_{BET} and the aggregated **CTF** particles.

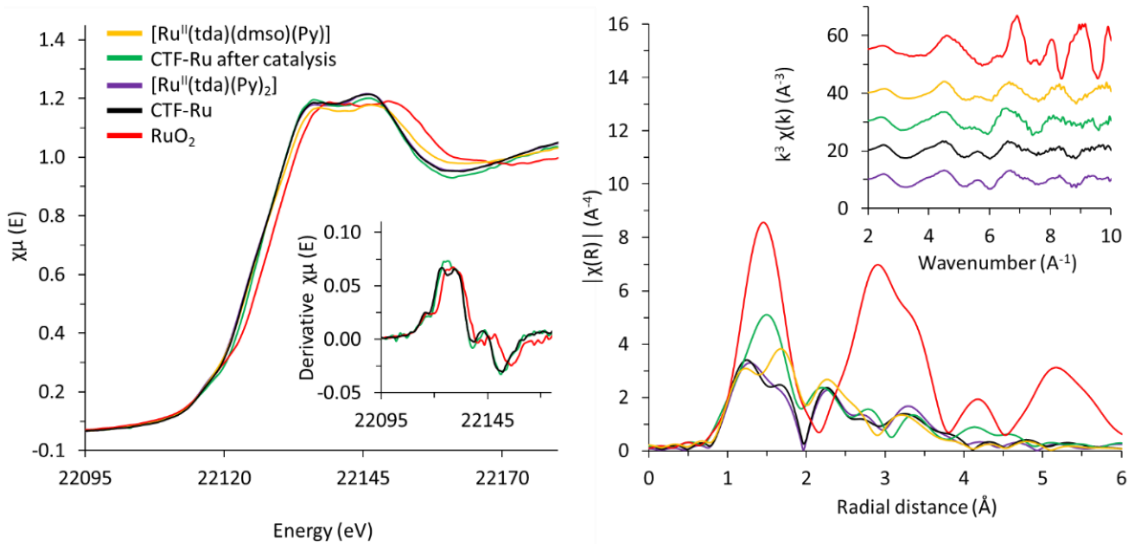

Figure 1. *Left, Normalized Ru K-edge spectra of [Ru(tda)(py)$_2$] (purple),* ***Ru-CTF*** *(black),* ***Ru-CTF*** *after photocatalysis (green), [Ru(tda)(dmso)(py)] (yellow) and RuO$_2$ (red). Inset: derivative Ru K-edge XANES spectra of the* ***Ru-CTF*** *(black),* ***Ru-CTF*** *after photocatalysis (green), and RuO$_2$ (red) samples. Right, Fourier transforms of the k^3-weighted Ru EXAFS spectra (same color code). Inset: EXAFS spectra. The green-line spectrum was recorded for* ***Ru-CTF*** *after photocatalysis experiment (1 mg/mL of* ***Ru-CTF*** *dispersed in 2 mL of 25 mM 7-phbf solution, 10 mM of SEA, under 3 suns illumination for 4 hours). The sample was washed with MeOH and dried before loading it onto FTO for the XAS analysis.*

3.2.2 Electronic Band Properties

The electronic properties of **CTF** and **Ru-CTF** hybrid materials were studied through UV-vis diffuse reflectance spectroscopy (DRS), Mott-Schottky (M-S) analysis (Figure 2) and Photoluminescence (PL) experiments (Figure 3). The Mott-Schottky experiments displayed in Figures 2a, 2b give a value of the Fermi level, E_F = -0.80 V (*vs*. NHE at pH 7) for both **CTF** and **Ru-CTF**, calculated at middle frequencies in the range of 0.5 - 2 MHz, that can be taken as an approximation for the conduction band energy (E_c) in *n*-type semiconductors.[39] The Tauc plots shown in Figure 2c give a band gap energy (E_g) of 2.90 eV again for both **CTF** and **Ru-CTF**, which is consistent with the absorbance spectra (Figures S12, S13). The absorption bands below 450 nm are associated with typical π-π* and n-π* electronic transitions of the polypyridyl ligands and the triazine units.[40,41] The **Ru-CTF** material shows an additional MLCT band at λ_{max} = 546 nm, indicative of the electronic transition between the Ru metal center and the tda ligand (Figure S13)[33].

From these values a valence band energy E_V = 2.1 V *vs.* NHE at pH 7 can be calculated as shown in Figure 2d.

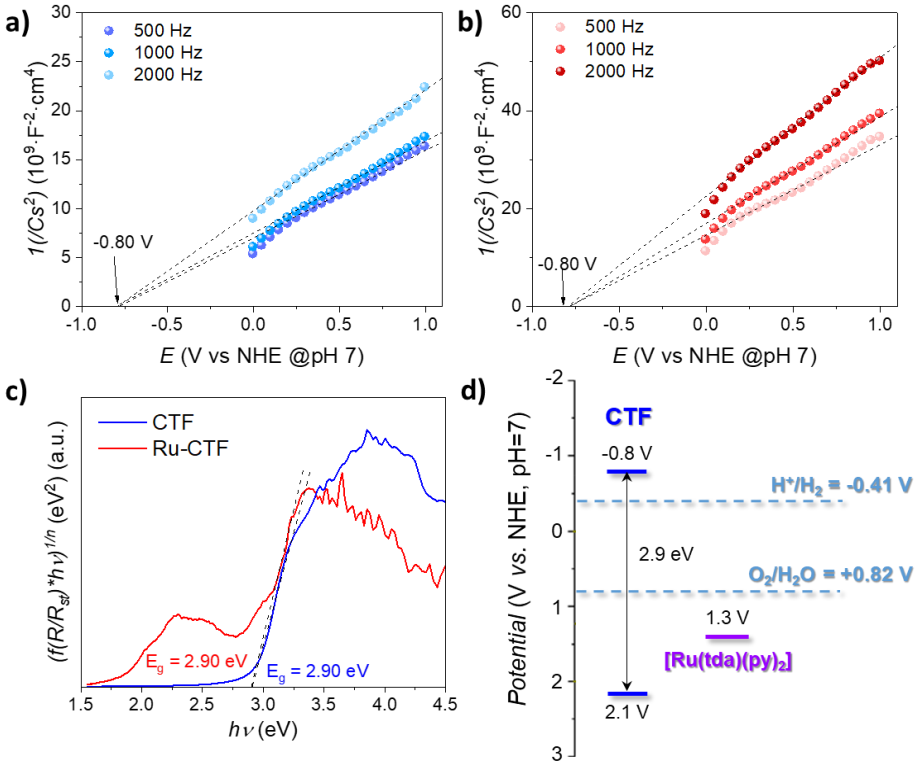

Figure 2. *Mott-Schottky plots performed for (a)* ***CTF*** *and (b)* ***Ru-CTF*** *in the potential range of 0.0 V – 1.0 V vs. NHE at pH 7 and at 500, 1000 and 2000 Hz as frequencies; (c) Tauc plot of* ***CTF*** *(blue line) and* ***Ru-CTF*** *(red line), with the corresponding band gap calculated; (d) energy diagram of* ***CTF****, compared to the thermodynamic potential for water oxidation and proton reduction half-reactions and the redox potential for the active species of the Ru-based catalyst.*

Photoluminescence (PL) and time resolved PL studies were carried out for the new hybrid materials **CTF** and **Ru-CTF** in the presence and absence of sodium persulfate as a sacrificial electron acceptor (SEA), as displayed in Figure 3. The PL intensity of **CTF** at 450 nm showed a quenching of 14 % in presence of sodium persulfate indicating slow electron transfer from the **CTF** to the SEA. In sharp contrast, the **Ru-CTF** hybrid material showed a nearly complete PL quenching (> 98 %), suppressing the exciton recombination (Figure 3a) due to very fast electron transfer from the Ru center to the electronically excited **CTF** moiety. Time-resolved single photon counting (TCSPC)

experiments (Figure 3b; Table S6 in the SI) show a similar decay kinetics lifetime of τ around 2 ns for **CTF** in the presence and absence of SEA, monitored at 450 nm, in agreement with the low capacity of excited state quenching by the SEA used here. On the other hand, the **Ru-CTF** PL decay is faster than our instrumental response and thus indicative of a charge separated state lifetime lower than 40 ps.[15,42] The fact that the catalyst reacts faster than the SEA with the excited state is in line with some examples described earlier in the literature that are termed anti-biomimetic.[43] The naming is based on the fact that the light excited chlorophyll in PSII interacts first with tyrosine (that can be considered as analogous to SEA) to generate a tyrosine radical cation that in turn reacts with the OEC (oxygen evolution catalyst) Mn cluster in the natural photosynthesis process.[43,44]

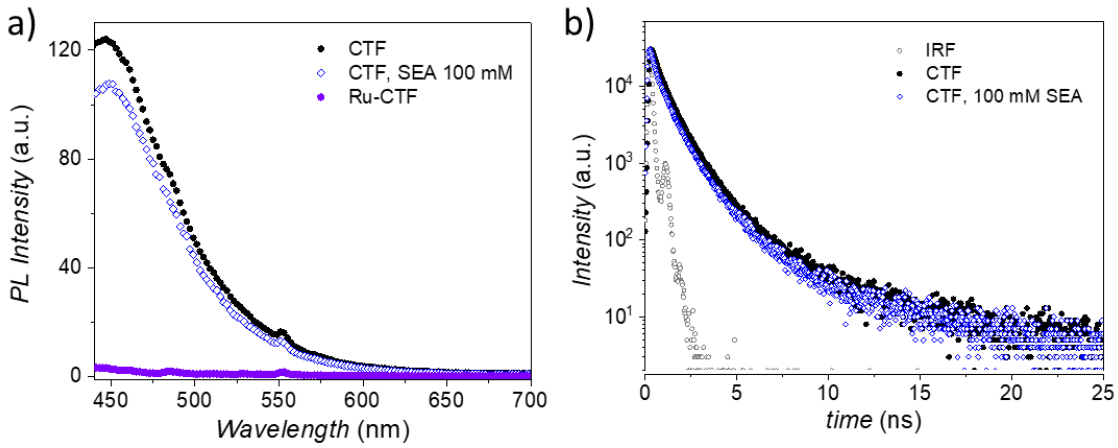

Figure 3. *(a) Steady-state photoluminescence spectra of **CTF** (black), **CTF** with SEA 100 mM (blue) and **Ru-CTF** (purple); (b) PL decays kinetics of **CTF** (black) and **CTF** with SEA 100 mM (blue). Excitation wavelength λ_{exc}= 404 nm, emission wavelength λ_{em}= 450 nm detected during PL decay experiment. IRF = instrument response function. The experiments were performed by dispersing 1 mg/mL of **CTF** or **Ru-CTF** in 7-phbf (25 mM) with and without 100 mM of SEA.*

3.2.3 Photocatalytic Water Oxidation

The photocatalytic water oxidation activity of the **Ru-CTF** molecular hybrid material was analyzed in the presence of persulfate as a SEA in aqueous buffered solution at pH 7. In a typical experiment, 1 mg (0.10 μmols of Ru) of **Ru-CTF** powder were dispersed in 1-6 mL of a 25 mM pH 7 phosphate buffer (7-phbf) solution containing 10 mM sodium

persulfate as a sacrificial electron acceptor, and placed in a jacketed quartz reactor maintained at 25ºC under Ar atmosphere (see SI for additional details). The dispersion was then irradiated over time in full arc with a Xenon lamp source (150 W) at 3 suns and the oxygen generated was measured in situ in the head space with a Clark electrode. A plot of O_2 generation *vs.* time under these conditions using 6 mL as the final volume, is presented in Figure 4, giving a TOF of 17 h^{-1} ($4.7x10^{-3}$ s^{-1}), a TON of 79 after approx. 8 h and with a chemical efficiency in the range of 80% and AQY of 1.4% (Table 1, entry 2). At the end of this experiment the **Ru-CTF** material is recovered by centrifugation rinsed with water and reused again giving practically the same the performance. Repeating this protocol three times gives and overall TON of 220 (See Figure S19). The recycling experiment indicates that the **Ru-CTF** hybrid material remain intact after the photocatalytic experiment and that the limiting factor is thus the concentration of the sacrificial agent, that is progressively depleted as the water oxidation reaction proceeds.

As can be observed in the graph, an induction period of approximately 10 minutes is observed, due to the need to activate the Ru molecular complex to reach its high oxidation states that lead to water oxidation catalysis and the need to saturate aqueous solution with oxygen.[38,45,46]

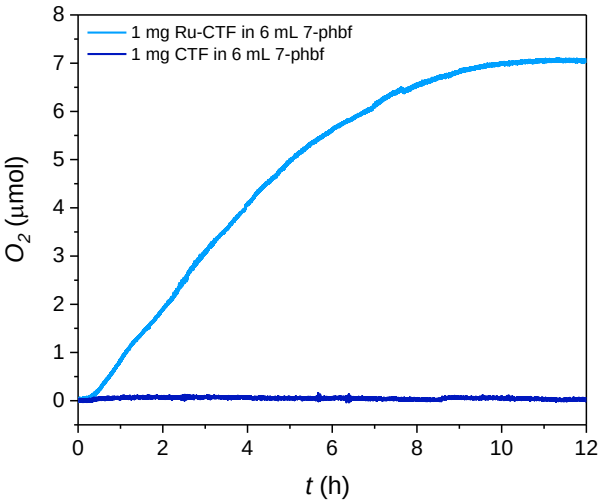

Figure 4. *Photoinduced oxygen detection experiments performed with a Clark-type electrode under 3 suns irradiation in 6 mL of 7-phbf (25 mM) with 10 mM of SEA and with: a) 1 mg of* ***Ru-CTF*** *(light-blue line) and b) 1 mg* ***CTF*** *(blue line).*

Related experiments under exactly the same conditions but using different total volumes (Figure S18) show that as the total volume decreases from 6 to 1 mL the generation of O_2 also decreases. We associate this phenomenon to the potential aggregation phenomenon that can occur as the photochemical water oxidation reaction proceeds. This decreases substantially the number of Ru-tda active sites in contact with the solution and thus a decrease of overall oxygen generation and rate. Indeed, a dynamic light scattering (DLS) experiment (See Fig. S22 and Table S4, S5) clearly reveals a progressive increase of particle size as the reaction proceeds. Finally, we also tested the effect of increasing the anionic strength up to 1 M pH 7 phbf resulting in a significant decrease of O_2 generation (See Figure S20). The photocatalytic experiment with **Ru-CTF** under lower irradiation intensity (1 sun) is shown in Figure S15. Under these conditions, the system reached a chemical efficiency close to unity (98%), and the TON and TOF values were 118 and 13 h^{-1} (3.1 x 10^{-3} s^{-1}), respectively, similar to those reported for the 3-sun experiment (Table 1, entry 3). The similarity in TOF values underlines the saturation of photon absorption already at 1 sun of illumination.

Finally, XAS analysis of **Ru-CTF** sample after 9 catalytic cycles is reported in Figure 1 (green trace) together with that of RuO_2 (red trace), confirming the absence of the latter and therefore the molecular integrity of the Ru complex active site. The edge position in the XANES spectrum indicates that the metal center oxidation state remains between Ru(II) and Ru(III).[47] The Fourier transformed EXAFS spectrum of **Ru-CTF** sample after 9 catalytic cycles provides evidence that the coordination environment of the Ru center has been rearranged with respect to the initial [Ru(tda)$(py)_2$] complex, consistent with the coordination of an H_2O ligand and the formation of the active form of the catalyst [Ru^{II}(tda-*k*-N^3O^0)$(py)_2(OH_2)$], responsible for water oxidation catalytic activity.[33,38]

3.2.4 Reaction Mechanism and Theoretical Calculations

We performed density functional theory (DFT) calculations at the MN15 level of theory[48] in conjunction with SMD aqueous continuum solvation model[49] on computational **Ru-CTF** model systems to investigate the mechanism of photocatalytic water oxidation reaction (see SI for further details on computational methods). The proposed water oxidation mechanism proceeds via three consecutive oxidation steps to generate reactive Ru^V=O species, followed by O-O bond formation and another oxidation step to

form the Ru^{IV}-OO species that leads to the evolution of O_2, similar to that of the discrete molecular analogue $[Ru(tda)(py)_2]$.[33] Our calculations demonstrate similar redox potentials and reaction energetics for the O_2 evolution mechanism of both **Ru-CTF** model and $[Ru(tda)(py)_2]$ indicating similar operating mechanisms (Figures S25, S26).

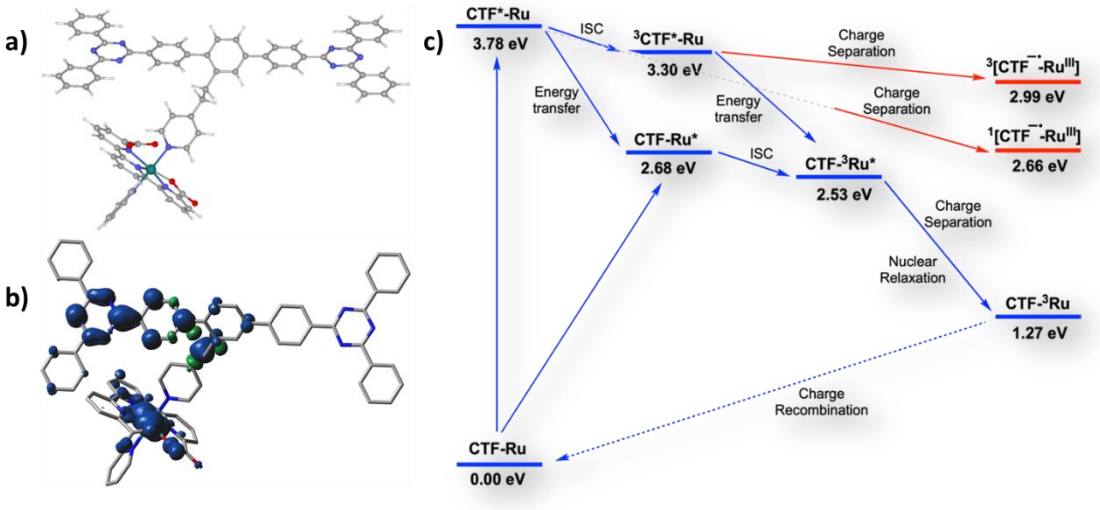

Figure 5. *(a) Optimized structure for **Ru-CTF** cluster model; (b) spin density distribution of the charge separated state 3[CTF•−-RuIII] calculated using constrained DFT (CDFT); (c) energy diagram generated via DFT/TDDFT (in blue) and CDFT (in red) calculations for the different species involved in the light induced reactions that occur at the first electron removal from **Ru-CTF** cluster model. The dash line represents the competing charge recombination reaction.*

Here we focus on charge and electron transfer steps for the activation of the **Ru-CTF**, which are critical for the overall photocatalytic performance. Both the low photoluminescence quenching efficiency of the SEA regarding **CTF** and the efficiency displayed by the **Ru-CTF** material indicate that, upon excitation, the primary reaction involves an intramolecular electron transfer (iET) from the excited states of CTF-moiety to the Ru center/complex bonded to the dangling pyridyl ligand in a time scale faster than 40 ps.

To probe this assertion further, we performed time-dependent density functional theory (TDDFT) and constrained DFT (CDFT)[50,51] calculations to model the electronic excitations and electron transfer steps (Figure 5).

The computed energy diagram indicates that electronic excitation in the singlet state followed by energy transfer and intersystem crossing (ISC) steps could lead to charge separated state localized on the [Ru(tda)(py)$_2$] complex moiety (Figure 5, **CTF-^{3}Ru** ΔE =1.27 eV; blue arrows in the diagram on the right) which could either be quenched by a SEA to generate **[CTF-Ru^{III}]$^+$** or to generate the initial state via a competing charge recombination reaction (dashed blue line). Closer inspection of **CTF-^{3}Ru** indicates that this state is essentially the metal-to-ligand charge-transfer state (MLCT) from the Ru center to the π* system of the tda moiety.

Alternatively, using CDFT calculations we probed charge separation via iET from the excited states of CTF-moiety to the [Ru(tda)(py)$_2$] fragment leading to formation of **^{1}[CTF$^{\bullet-}$-Ru^{III}]** (ΔE = 2.66 eV) and **^{3}[CTF$^{\bullet-}$-Ru^{III}]** (ΔE = 2.99 eV, Figures 5a, 5b) which can be quenched similarly by SEA to generate **[CTF-Ru^{III}]$^+$**. Theoretical modeling of the dynamics of these alternative pathways will be necessary to probe the kinetics, but this is beyond the scope of the current study. We also checked the potential oxidation pathway to generate **[CTF$^{\bullet+}$-Ru^{II}]$^+$** and found it to be less favorable by 1.16 eV compared to **[CTF-Ru^{III}]$^+$** (Figure S35). More interestingly it remains unfavorable by at least 0.22 eV even in the case of **[CTF$^{\bullet+}$-Ru^{IV}O]$^+$** *vs*. **[CTF-Ru^{V}O]$^+$** (Figure S37). It is important to realize here that the higher the oxidation state of the Ru center the larger will be the thermodynamic driving force for the recombination process. Thus, the recombination reaction of **[CTF$^{\bullet-}$-Ru^{V}=O]$^+$** to **[CTF-Ru^{IV}=O]** will be the most strongly competing reaction to SEA, for the overall O_2 evolution reaction. The independence of the oxygen generated from the ionic strength is also in agreement with this fast iET, indicating that ion pairs do not play a major role here as opposed to all the systems previously described in the literature.[6,52]

3.3. Discussion

We have described the preparation, spectroscopic and photocatalytic properties of a new polymeric covalent triazine framework containing a dangling pyridyl group labeled as **CTF**. The electronic properties of the **CTF** are similar to the unsubstituted one and also similar (a slightly lower CB energy) to the covalent triazine framework linked by 3 phenyls groups with no dangling pyridyl.[35]

Table 1. *Selected parameters describing the performance of key CTFs and other similar functional materials for the light induced water oxidation reaction.*

Entry	Material	Cat % [a]	pH [b]	SEA (mM)	µmol$_{Cat}$ /g$_s$ [c]	µmol O_2 /h g$_s$	µmol O_2 /h g$_{Cat}$	TOF (s^{-1}) [e]	TONs [e]	Irradiation conditions	AQY (%)	Ref.
1	CTF	-	7 (phbf)	10 (Na_2SO_8)	-	-	-	-	-	Full arc (300 mW/cm^2) [f]	-	tw
2	Ru-CTF	Ru / 1.1	7 (phbf)	10 (Na_2SO_8)	100 (Ru)	1220 [d]	1.2x10^5 [d]	4.7x10^{-3}	220 (3 runs)		1.4 (≥300 nm) [f]	tw
3	Ru-CTF	Ru / 1.1	7 (phbf)	10 ($Na_2S_2O_8$)	100 (Ru)	1020 [d]	9.7x10^5 [d]	3.1x10^{-3}	118 (1 run)	Full arc (100 mW/cm^2) [f]	0.82 (≥300 nm) [f]	tw
4	CTF-1	Ru / 3.0	7	200 ($AgNO_3$)	225 (Ru)	140	4.7x10^3	1.7x10^{-4}	-	≥420 nm [g]	4.0 (@400nm)	[16]
5	CTF-0-I	-	7	25 ($AgNO_3$)	-	226	-	-	-	Full arc [g]	15 (@365 nm)	[13]
6	CTF-0-I	-	7	25 ($AgNO_3$)	-	59	-	-	-	≥420 nm [g]	5.2 (@420 nm)	[13]
7	CTF-0	Co / 6.0	7	10 ($AgNO_3$)	83 (Co)	365	2.5x10^4	1.2x10^{-3}	593	Full arc [g]	-	[8]
8	CTF-HUST-A1	Ni / 4.5	7	-	N/A	13	-	-	-	≥420 nm (210 mW/cm^2)	0.8 (@420 nm)	[9]
9	CTP-2	Co / 3.0	7.8 (La_2O_3)	10 ($AgNO_3$)	509 (Co)	100	3.3x10^3	5.4x10^{-5}	0.8	>420 nm [g]	-	[15]
10	OCT (6.7 %)	-	7	N/A ($AgNO_3$)	-	102	-	-	-	Full arc [g]	2.6 (@400 nm)	[53]
11	P10	Co / 1.0	8.1 (La_2O_3)	10 ($AgNO_3$)	170 (Co)	102	-	-	-	Full arc [g]	-	[42]
12	P10	Co / 1.0	8.1 (La_2O_3)	10 ($AgNO_3$)	170 (Co)	332	3.3x10^4	5.4x10^{-4}	-	>420 nm [g]	-	[42]
13	Bpy-CTF-Co-3	Co / 2.5	7.8 (La_2O_3)	10 ($AgNO_3$)	509 (Co)	104	1.0x10^4	1.7x10^{-4}	-	>420 nm [g]	0.56 (@420 nm)	[54]
14	r-CTF NSs	Co / 3	7	10 ($AgNO_3$)	500 (Co)	247	1.7x10^3	1.4x10^{-4}	-	>420 nm [g]	5.6 (@420 nm)	[31]

[a] (grams of Cat metal/gram of sample) x 100. [b] Entries 1-3, 25 mM phosphate buffer solution (7-phbf); entries 4-8, 10 and 14, pure water with no buffer; entries 9, 11-13 La_2O_3 buffer. [c] µmols of Cat/gram of sample. [d] Measured at the first 0.5 h. [e] TON as mols of oxygen generated per mol of Cat; TOF as mols of oxygen generated per mol of Cat per second. [f] 150 W Xe lamp in full arc used for the photocatalysis experiments, as well as for AQY calculations. [g] 300 W Xe lamp used for the photocatalysis experiments.

The dangling pyridyl in **CTF** has been used as an axial ligand to coordinate the Ru-tda complex, which is one of the best molecular water oxidation catalysts (WOCs) available today in terms of both robustness and TOFs,[12] and is labelled as **Ru-CTF.** Upon light excitation and in the presence of persulfate as a sacrificial electron acceptor, the **Ru-CTF** hybrid material is capable of catalyzing the oxidation of water to dioxygen giving a max TOFs of 17 h^{-1} and TONs of 220 (cumulative of 3 repetitive runs, 3 suns) as indicated in Table 1 (entry 2), and TOFs of 13 h^{-1} and TONs of 118 using 1 sun (Table 1, entry 3). As it can be observed in the Table, the **Ru-CTF** performance is outperforming the best CTF functional materials reported so far. Further, it is also interesting to note here that persulfate is used as a SEA, in sharp contrast with most of the CTF systems reported up to now where the SEA is $AgNO_3$, that is known to possess rich luminescent properties and thus can potentially increase the complexity of the system also by generating Ag nanoparticles as the irradiation proceeds (See Table 1, entries 4-7 and 9-14).[53–55]

The TOF of the best system reported up to now, **CTF-0** [8] (Table 1, entry 7) is about 4 times smaller than that of **Ru-CTF** and again needs Ag to proceed**.** This points out the benefit of the molecular design using the dangling pyridyl to spatially control the anchoring of the WOC within the CTF absorber polymer as opposed to typical drop casting strategies where the catalyst is in contact with the whole polymeric structure that can produce undesired non-productive reactions. In addition, the ethyl linker from the axial pyridyl group of the Ru catalyst and the CTF absorber controls the distance between absorber and catalyst as well as their potential electronic coupling that dictates the kinetics of electron transfer between the catalyst and the absorber.

As proposed by theoretical calculations, upon excitation of the **Ru-CTF** material a series of steps could generate a long-lived charge separated state that can be singlet or triplet in nature and where negative charge is localized at the **CTF** moiety and the positive one is located at the Ru center, **[$CTF^{\bullet-}$-Ru^{III}]**. Since the ethyl units act as an electronically isolating unit, the back electron transfer needs to occur most likely through space. In addition, the negative charge in the triazine unit can be further delocalized over several triazine units, that do not have sufficiently close Ru centers to interact with, since the degree of functionalized pyridyl units in the **CTF-Ru** is only 14%. As a result of this electron density dilution effect and the very weak electronic coupling between the

catalyst and the absorber, the back electron transfer is sufficiently slow so that it can compete with the SEA for the charge separated state even at the highest Ru oxidation state, leading to the generation of O_2. This phenomenon highlights the synergistic effect of a localized charge at the Ru center of the molecular catalyst and the capacity of the 2D CTF polymeric structures to delocalize the negative charge over a large distance. This is reminiscent of the Z-scheme in photosynthesis in green plants and algae, where the positive charge is localized at the OEC-PSII but the negative charge is spatially removed away via series of chained electron transfer steps involving initially pheophytin (Pheo) and then quinones Q_a and Q_b.[44]

3.4. Conclusions

We have successfully synthesized a CTF functionalized with a molecular Ru(tda)-based catalyst through covalent linkage which is able to achieve light-induced water oxidation to dioxygen in the presence of sodium persulfate as sacrificial electron acceptor (SEA). The construct achieves turnover numbers and turnover frequencies of 220 and 17 h^{-1}, respectively, in the absence of $AgNO_3$. The assembly benefits of a dangling pyridyl to spatially control the anchoring of the WOC within the CTF polymer and avoid undesired reactions and back electron transfer phenomena. The present work represents the first example of an efficient molecular-based hybrid system for light-induced water oxidation reaction and it constitutes a step forward to efficient photocatalysts for water splitting using more sustainable and well-designed materials.

3.5. References

(1) Lewis, N. S. Research Opportunities to Advance Solar Energy Utilization. *Science (80-.).* **2016**, *351* (6271), aad1920. https://doi.org/10.1126/science.aad1920.

(2) Armaroli, N.; Balzani, V. The Future of Energy Supply: Challenges and Opportunities. *Angew. Chemie - Int. Ed.* **2007**, *46* (1-2), 52–66. https://doi.org/10.1002/anie.200602373.

(3) Nocera, D. G. Solar Fuels and Solar Chemicals Industry. *Acc. Chem. Res.* **2017**, *50* (3), 616–619. https://doi.org/10.1021/acs.accounts.6b00615.

(4) Banerjee, T.; Podjaski, F.; Kröger, J.; Biswal, B. P.; Lotsch, B. V. Polymer Photocatalysts for Solar-to-Chemical Energy Conversion. *Nat. Rev. Mater.* **2021**, *6*, 168–190.

https://doi.org/10.1038/s41578-020-00254-z.

(5) Walter, M. G.; Warren, E. L.; McKone, J. R.; Boettcher, S. W.; Mi, Q.; Santori, E. A.; Lewis, N. S. Solar Water Splitting Cells. *Chem. Rev.* **2010**, *110* (11), 6446–6473. https://doi.org/10.1021/cr1002326.

(6) Francàs, L.; Matheu, R.; Pastor, E.; Reynal, A.; Berardi, S.; Sala, X.; Llobet, A.; Durrant, J. R. Kinetic Analysis of an Efficient Molecular Light-Driven Water Oxidation System. *ACS Catal.* **2017**, *7* (8), 5142–5150. https://doi.org/10.1021/acscatal.7b01357.

(7) Bai, Y.; Li, C.; Liu, L.; Yamaguchi, Y.; Bahri, M.; Yang, H.; Gardner, A.; Zwijnenburg, M. A.; Browning, N. D.; Cowan, A. J.; Kudo, A.; Cooper, A. I.; Sprick, R. S. Photocatalytic Overall Water Splitting under Visible Light Enabled by a Particulate Conjugated Polymer Loaded with Iridium. *Angew. Chemie Int. Ed.* **2022**, *61* (26), e202201299. https://doi.org/10.1002/anie.202201299.

(8) Kong, D.; Xie, J.; Guo, Z.; Yang, D.; Tang, J. Stable Complete Water Splitting by Covalent Triazine-Based Framework CTF-0. *ChemCatChem* **2020**, *12* (10), 2708–2712. https://doi.org/10.1002/cctc.201902396.

(9) Zhang, S.; Cheng, G.; Guo, L.; Wang, N.; Tan, B.; Jin, S. Strong-Base-Assisted Synthesis of a Crystalline Covalent Triazine Framework with High Hydrophilicity via Benzylamine Monomer for Photocatalytic Water Splitting. *Angew. Chemie - Int. Ed.* **2020**, *59* (15), 6007–6014. https://doi.org/10.1002/anie.201914424.

(10) Liang, X.; Cao, X.; Sun, W.; Ding, Y. Recent Progress in Visible Light Driven Water Oxidation Using Semiconductors Coupled with Molecular Catalysts. *ChemCatChem* **2019**, *11* (24), 6190–6202. https://doi.org/10.1002/cctc.201901510.

(11) Kärkäs, M. D.; Åkermark, B. Water Oxidation Using Earth-Abundant Transition Metal Catalysts: Opportunities and Challenges. *Dalt. Trans.* **2016**, *45* (37), 14421–14461. https://doi.org/10.1039/c6dt00809g.

(12) Matheu, R.; Garrido-Barros, P.; Gil-Sepulcre, M.; Ertem, M. Z.; Sala, X.; Gimbert-Suriñach, C.; Llobet, A. The Development of Molecular Water Oxidation Catalysts. *Nat. Rev. Chem.* **2019**, *3* (5), 331–341. https://doi.org/10.1038/s41570-019-0096-0.

(13) Kong, D.; Han, X.; Xie, J.; Ruan, Q.; Windle, C. D.; Gadipelli, S.; Shen, K.; Bai, Z.; Guo, Z.; Tang, J. Tunable Covalent Triazine-Based Frameworks (CTF-0) for Visible-Light-Driven Hydrogen and Oxygen Generation from Water Splitting. *ACS Catal.* **2019**, *9* (9), 7697–7707. https://doi.org/10.1021/acscatal.9b02195.

(14) Fang, Y.; Hou, Y.; Fu, X.; Wang, X. Semiconducting Polymers for Oxygen Evolution Reaction under Light Illumination. *Chem. Rev.* **2022**, *122* (3), 4204–4256. https://doi.org/10.1021/acs.chemrev.1c00686.

(15) Lan, Z. A.; Fang, Y.; Zhang, Y.; Wang, X. Photocatalytic Oxygen Evolution from Functional Triazine-Based Polymers with Tunable Band Structures. *Angew. Chemie - Int. Ed.* **2018**, *57* (2), 470–474. https://doi.org/10.1002/anie.201711155.

(16) Xie, J.; Shevlin, S. A.; Ruan, Q.; Moniz, S. J. A.; Liu, Y.; Liu, X.; Li, Y.; Lau, C. C.; Guo, Z. X.; Tang, J. Efficient Visible Light-Driven Water Oxidation and Proton Reduction by an Ordered Covalent Triazine-Based Framework. *Energy Environ. Sci.* **2018**, *11* (6), 1617–1624. https://doi.org/10.1039/c7ee02981k.

(17) Limburg, B.; Bouwman, E.; Bonnet, S. Rate and Stability of Photocatalytic Water Oxidation Using $[Ru(bpy)_3]^{2+}$ as Photosensitizer. *ACS Catal.* **2016**, *6* (8), 5273–5284. https://doi.org/10.1021/acscatal.6b00107.

(18) Sun, L.; Hammarström, L.; Åkermark, B.; Styring, S. Towards Artificial Photosynthesis: Ruthenium-Manganese Chemistry for Energy Production. *Chem. Soc. Rev.* **2001**, *30* (1), 36–49. https://doi.org/10.1039/a801490f.

(19) Lämmle, M.; Bagemihl, B.; Nauroozi, D.; Petermann, L.; Pannwitz, A.; Rau, S. Monosubstitution of 1*H*-Imidazo[4,5-*f*][1,10]phenanthroline Ligands Yields Maximum Luminescence Quantum Yield in Ruthenium Polypyridyl Complexes. *ChemPhotoChem* **2022**, *6* (7), e202200053. https://doi.org/10.1002/cptc.202200053.

(20) Zhu, Y.; Wang, D.; Huang, Q.; Du, J.; Sun, L.; Li, F.; Meyer, T. J. Stabilization of a Molecular Water Oxidation Catalyst on a Dye–sensitized Photoanode by a Pyridyl Anchor. *Nat. Commun.* **2020**, *11* (1), 1–8. https://doi.org/10.1038/s41467-020-18417-5.

(21) Kawano, K.; Yamauchi, K.; Sakai, K. A cobalt–NHC Complex as an Improved Catalyst for Photochemical Hydrogen Evolution from Water. *Chem. Commun.* **2014**, *50* (69), 9872–9875. https://doi.org/10.1039/c4cc03493g.

(22) Yu, H.; Shi, R.; Zhao, Y.; Waterhouse, G. I. N.; Wu, L. Z.; Tung, C. H.; Zhang, T. Smart Utilization of Carbon Dots in Semiconductor Photocatalysis. *Adv. Mater.* **2016**, *28* (43), 9454–9477. https://doi.org/10.1002/adma.201602581.

(23) Fernando, K. A. S.; Sahu, S.; Liu, Y.; Lewis, W. K.; Guliants, E. A.; Jafariyan, A.; Wang, P.; Bunker, C. E.; Sun, Y. P. Carbon Quantum Dots and Applications in Photocatalytic Energy Conversion. *ACS Appl. Mater. Interfaces* **2015**, *7* (16), 8363–8376. https://doi.org/10.1021/acsami.5b00448.

(24) Barrio, J.; Volokh, M.; Shalom, M. Polymeric Carbon Nitrides and Related Metal-Free Materials for Energy and Environmental Applications. *J. Mater. Chem. A* **2020**, *8* (22), 11075–11116. https://doi.org/10.1039/d0ta01973a.

(25) Kuriki, R.; Maeda, K. Development of Hybrid Photocatalysts Constructed with a Metal Complex and Graphitic Carbon Nitride for Visible-Light-Driven CO_2 Reduction. *Phys. Chem. Chem. Phys.*

2017, *19* (7), 4938–4950. https://doi.org/10.1039/c6cp07973c.

(26) Ma, B.; Chen, G.; Fave, C.; Chen, L.; Kuriki, R.; Maeda, K.; Ishitani, O.; Lau, T. C.; Bonin, J.; Robert, M. Efficient Visible-Light-Driven CO_2 Reduction by a Cobalt Molecular Catalyst Covalently Linked to Mesoporous Carbon Nitride. *J. Am. Chem. Soc.* **2020**, *142* (13), 6188–6195. https://doi.org/10.1021/jacs.9b13930.

(27) Feng, Y.; Sun, W.; Liang, X.; Dong, X.; Yang, X.; Hu, C.; Li, B.; Yang, J.; Ma, B.; Ding, Y. Mononuclear Ruthenium (II) Complex Covalently Anchored on Melem and g-C_3N_4 as Efficient Heterogeneous Catalysts for Chemical Water Oxidation. *J. Colloid Interface Sci.* **2023**, *643* (December 2022), 480–488. https://doi.org/10.1016/j.jcis.2023.04.053.

(28) Kuhn, P.; Antonietti, M.; Thomas, A. Porous, Covalent Triazine-Based Frameworks Prepared by Ionothermal Synthesis. *Angew. Chemie - Int. Ed.* **2008**, *47* (18), 3450–3453. https://doi.org/10.1002/anie.200705710.

(29) Thomas, A. Functional Materials: From Hard to Soft Porous Frameworks. *Angew. Chemie - Int. Ed.* **2010**, *49* (45), 8328–8344. https://doi.org/10.1002/anie.201000167.

(30) Hug, S.; Tauchert, M. E.; Li, S.; Pachmayr, U. E.; Lotsch, B. V. A Functional Triazine Framework Based on N-Heterocyclic Building Blocks. *J. Mater. Chem.* **2012**, *22* (28), 13956–13964. https://doi.org/10.1039/c2jm31248d.

(31) Wang, C.; Zhang, H.; Luo, W.; Sun, T.; Xu, Y. Ultrathin Crystalline Covalent-Triazine-Framework Nanosheets with Electron Donor Groups for Synergistically Enhanced Photocatalytic Water Splitting. *Angew. Chemie - Int. Ed.* **2021**, *60* (48), 25381–25390. https://doi.org/10.1002/anie.202109851.

(32) Romero, N.; Bofill, R.; Francàs, L.; García-antón, J.; Sala, X. Light-driven Hydrogen Evolution Assisted by Covalent Organic Frameworks. *Catalysts* **2021**, *11* (6), 754. https://doi.org/10.3390/catal11060754.

(33) Matheu, R.; Ertem, M. Z.; Benet-Buchholz, J.; Coronado, E.; Batista, V. S.; Sala, X.; Llobet, A. Intramolecular Proton Transfer Boosts Water Oxidation Catalyzed by a Ru Complex. *J. Am. Chem. Soc.* **2015**, *137* (33), 10786–10795. https://doi.org/10.1021/jacs.5b06541.

(34) Matheu, R.; Ertem, M. Z.; Gimbert-Suriñach, C.; Sala, X.; Llobet, A. Seven Coordinated Molecular Ruthenium-Water Oxidation Catalysts: A Coordination Chemistry Journey. *Chem. Rev.* **2019**, *119* (6), 3453–3471. https://doi.org/10.1021/acs.chemrev.8b00537.

(35) Meier, C. B.; Sprick, R. S.; Monti, A.; Guiglion, P.; Lee, J. S. M.; Zwijnenburg, M. A.; Cooper, A. I. Structure-Property Relationships for Covalent Triazine-Based Frameworks: The Effect of Spacer Length on Photocatalytic Hydrogen Evolution from Water. *Polymer (Guildf).* **2017**, *126*, 283–290. https://doi.org/10.1016/j.polymer.2017.04.017.

(36) Ren, S.; Bojdys, M. J.; Dawson, R.; Laybourn, A.; Khimyak, Y. Z.; Adams, D. J.; Cooper, A. I. Porous, Fluorescent, Covalent Triazine-Based Frameworks via Room-Temperature and Microwave-Assisted Synthesis. *Adv. Mater.* **2012**, *24* (17), 2357–2361. https://doi.org/10.1002/adma.201200751.

(37) Wang, K.; Yang, L. M.; Wang, X.; Guo, L.; Cheng, G.; Zhang, C.; Jin, S.; Tan, B.; Cooper, A. Covalent Triazine Frameworks via a Low-Temperature Polycondensation Approach. *Angew. Chemie - Int. Ed.* **2017**, *56* (45), 14149–14153. https://doi.org/10.1002/anie.201708548.

(38) Hoque, M. A.; Gil-Sepulcre, M.; de Aguirre, A.; Elemans, J. A. A. W.; Moonshiram, D.; Matheu, R.; Shi, Y.; Benet-Buchholz, J.; Sala, X.; Malfois, M.; Solano, E.; Lim, J.; Garzón-Manjón, A.; Scheu, C.; Lanza, M.; Maseras, F.; Gimbert-Suriñach, C.; Llobet, A. Water Oxidation Electrocatalysis Using Ruthenium Coordination Oligomers Adsorbed on Multiwalled Carbon Nanotubes. *Nat. Chem.* **2020**, *12* (11), 1060–1066. https://doi.org/10.1038/s41557-020-0548-7.

(39) Bisquert, J.; Giménez, S.; Bertoluzzi, L.; Herraiz-Cardona, I. *Photoelectrochemical Solar Fuel Production: From Basic Principles to Advanced Devices*, 1st ed.; Giménez, S., Bisquert, J., Eds.; Springer Cham, 2016. https://doi.org/10.1007/978-3-319-29641-8.

(40) Zhang, G.; Savateev, A.; Zhao, Y.; Li, L.; Antonietti, M. Advancing the n → π^* Electron Transition of Carbon Nitride Nanotubes for H_2 Photosynthesis. *J. Mater. Chem. A* **2017**, *5* (25), 12723–12728. https://doi.org/10.1039/c7ta03777e.

(41) Suter, T. M.; Miller, T. S.; Cockcroft, J. K.; Aliev, A. E.; Wilding, M. C.; Sella, A.; Corà, F.; Howard, C. A.; McMillan, P. F. Formation of an Ion-Free Crystalline Carbon Nitride and Its Reversible Intercalation with Ionic Species and Molecular Water. *Chem. Sci.* **2019**, *10* (8), 2519–2528. https://doi.org/10.1039/c8sc05232h.

(42) Sprick, R. S.; Chen, Z.; Cowan, A. J.; Bai, Y.; Aitchison, C. M.; Fang, Y.; Zwijnenburg, M. A.; Cooper, A. I.; Wang, X. Water Oxidation with Cobalt-Loaded Linear Conjugated Polymer Photocatalysts. *Angew. Chemie* **2020**, *132* (42), 18854–18859. https://doi.org/10.1002/ange.202008000.

(43) Campagna, S.; Nastasi, F.; La Ganga, G.; Serroni, S.; Santoro, A.; Arrigo, A.; Puntoriero, F. Self-Assembled Systems for Artificial Photosynthesis. *Phys. Chem. Chem. Phys.* **2022**, *25* (3), 1504–1512. https://doi.org/10.1039/d2cp03655j.

(44) Klimov, V. V. Discovery of Pheophytin Function in the Photosynthetic Energy Conversion as the Primary Electron Acceptor of Photosystem II. *Photosynth. Res.* **2003**, *76*, 247–253. https://doi.org/10.1023/A:1024990408747.

(45) Creus, J.; Matheu, R.; Peñafiel, I.; Moonshiram, D.; Blondeau, P.; Benet-Buchholz, J.; García-Antón, J.; Sala, X.; Godard, C.; Llobet, A. A Million Turnover Molecular Anode for Catalytic Water Oxidation. *Angew. Chemie - Int. Ed.* **2016**, *55* (49), 15382–15386.

https://doi.org/10.1002/anie.201609167.

(46) Matheu, R.; Ertem, M. Z.; Gimbert-Suriñach, C.; Benet-Buchholz, J.; Sala, X.; Llobet, A. Hydrogen Bonding Rescues Overpotential in Seven-Coordinated Ru Water Oxidation Catalysts. *ACS Catal.* **2017**, *7* (10), 6525–6532. https://doi.org/10.1021/acscatal.7b01860.

(47) Levin, N.; Casadevall, C.; Cutsail, G. E.; Lloret-Fillol, J.; DeBeer, S.; Rüdiger, O. XAS and EPR in Situ Observation of Ru(V) Oxo Intermediate in a Ru Water Oxidation Complex**. *ChemElectroChem* **2022**, *9* (3), 8–11. https://doi.org/10.1002/celc.202101271.

(48) Yu, H. S.; He, X.; Li, S. L.; Truhlar, D. G. MN15: A Kohn-Sham Global-Hybrid Exchange-Correlation Density Functional with Broad Accuracy for Multi-Reference and Single-Reference Systems and Noncovalent Interactions. *Chem. Sci.* **2016**, *7* (8), 5032–5051. https://doi.org/10.1039/c6sc00705h.

(49) Marenich, A. V.; Cramer, C. J.; Truhlar, D. G. Universal Solvation Model Based on Solute Electron Density and on a Continuum Model of the Solvent Defined by the Bulk Dielectric Constant and Atomic Surface Tensions. *J. Phys. Chem. B* **2009**, *113* (18), 6378–6396. https://doi.org/10.1021/jp810292n.

(50) Wu, Q.; Van Voorhis, T. Direct Optimization Method to Study Constrained Systems within Density-Functional Theory. *Phys. Rev. A - At. Mol. Opt. Phys.* **2005**, *72* (2), 7–10. https://doi.org/10.1103/PhysRevA.72.024502.

(51) Kaduk, B.; Kowalczyk, T.; Van Voorhis, T. Constrained Density Functional Theory. *Chem. Rev.* **2012**, *112* (1), 321–370. https://doi.org/10.1021/cr200148b.

(52) Lewandowska-Andralojc, A.; Polyansky, D. E. Mechanism of the Quenching of the tris(bipyridine)ruthenium(II) Emission by Persulfate: Implications for Photoinduced Oxidation Reactions. *J. Phys. Chem. A* **2013**, *117* (40), 10311–10319. https://doi.org/10.1021/jp407573d.

(53) Kong, D.; Han, X.; Shevlin, S. A.; Windle, C.; Warner, J. H.; Guo, Z. X.; Tang, J. A Metal-Free Oxygenated Covalent Triazine 2-D Photocatalyst Works Effectively from the Ultraviolet to Near-Infrared Spectrum for Water Oxidation Apart from Water Reduction. *ACS Appl. Energy Mater.* **2020**, *3* (9), 8960–8968. https://doi.org/10.1021/acsaem.0c01153.

(54) Chen, H.; Gardner, A. M.; Lin, G.; Zhao, W.; Bahri, M.; Browning, N. D.; Sprick, R. S.; Li, X.; Xu, X.; Cooper, A. I. Covalent Triazine-Based Frameworks with Cobalt-Loading for Visible Light-Driven Photocatalytic Water Oxidation. *Catal. Sci. Technol.* **2022**, *12*, 5442–5452. https://doi.org/10.1039/d2cy00773h.

(55) Yam, V. W. W.; Lo, K. K. W. Luminescent Polynuclear d_{10} Metal Complexes. *Chem. Soc. Rev.* **1999**, *28* (5), 323–334. https://doi.org/10.1039/a804249g.

3.6. Supporting Information

3.6.1. Materials

All chemicals used in this work were obtained from Sigma Aldrich and have been used without further purification unless explicitly indicated. $RuCl_3 \cdot \times H_2O$ was purchased from Alfa-Aesar, [2,2':6',2''-terpyridine]-6,6''-dicarboxylic acid (H_2tda)[1] ligand and the precursors $[Ru^{II}Cl_2(dmso)_4]$[2] and $[Ru(tda\text{-}\kappa\text{-}N^3O)(py)(SO(CH_3)_2)]$[3] were prepared according to the literature. Solvents were dried with a SPS® system and degassed by bubbling nitrogen gas before starting the reactions. High purity de-ionized water used for the electrochemistry experiments was obtained by passing distilled water through a nanopore Milli-Q water purification system. For other spectroscopic and electrochemical studies HPLC grade solvents were used. FTO substrates for electrochemistry were purchased from XOP FÍSICA SL (FTO TEC 15, 12-15 Ω/sq).

3.6.2. Instrumentation

NMR spectroscopy

Bruker Advance 400 MHz and/or 500 MHz were used to carry out NMR spectroscopy. All the measurements were carried out at room temperature in the corresponding deuterated solvent using residual protons as internal reference.

Mass spectrometry

High-resolution electron spray ionization-mass spectra were recorded using micromass Q-TOF mass spectrometer in positive mode.

pH analysis

A METTLER TOLEDO InLab® Sensor was used for determining the pH of the solutions, calibrated before measurements through standard solutions at pH 2.00, 4.01, 7.00, 9.21 and 11.00.

Ball-Milling technique

The product was ground to a fine powder using a Retsch® MM200 Ball Mill instrument. CTF was milled over 1 hour at 30 Hz of frequency in a 5 mL closed jar, with two small (Ø=

5 - 6 mm) stainless-steel balls inside. The milling process was performed before the functionalization with the Ru catalyst.

Photocatalysis measurements

A 4 mL or 20 mL jacketed quartz cell maintained at 25 °C, closed with a septum, was equipped with a Clark-type oxygen sensor for O_2-detection in the headspace (Unisense® oxygen microsensor). Typically, 1 or 2 mg of previously degassed **Ru-CTF** (0.56 µmol), or **CTF** (0.78 µmol), and 10 mM $Na_2S_2O_8$ as sacrificial electron acceptor (SEA) were dispersed separately in 2 mL-6 mL total volume of purged 25 mM phosphate buffer solution (Na_2HPO_4/NaH_2PO_4, pH 7) and sonicated for 15 minutes. The resulting dispersion and solution were injected into the reactor, previously degassed as well under Ar for 30 minutes, and the suspension was let stirring at 1300 rpm, in order minimize bubble absorption. The sensor was inserted in the headspace and, after the baseline collection in total dark for 10 minutes, the solution was irradiated, leaving the experiment running until reaching a stable signal. The illumination was provided by a 150 W Xenon Arc Lamp (LS-150, ABET® technology) with no filter, calibrated to 1 sun (100 mW cm^{-2}) or 3 suns (300 mW cm^{-2}) by using a silicon photodiode for UV-vis light region. The calibration of the experiment was performed after each experiment by injecting air aliquots into the headspace of the cell (the calculations were performed considering a 21% of O_2 present in air-atmosphere. Repetitive runs were also performed by collecting the dispersion after catalysis, isolating the solid after washing it with MilliQ water by centrifugation (Eppendorf®, model 5702) and dispersing again the material in a new phosphate buffer (7-phbf) solution with 10 mM SEA, following the same procedure described above.

Electrochemistry

All electrochemical experiments were performed with an IJ-Cambria CHI-660 potentiostat using a one-compartment three-electrode cell. Cyclic voltammetry (CV) was carried out in 1 M pH 7 phosphate buffer (Na_2HPO_4/NaH_2PO_4) at a scan rate of 0.01 V/s. Differential pulse voltammetry (DPV) was performed in the same buffer conditions by using the following parameters: ΔE = 4 mV, amplitude = 50 mV, pulse width = 0.05 s, sampling width = 0.0167 s, pulse period = 0.2 s. The working electrode (WE) consisted of **Ru-CTF** spray-coated FTO electrode (FTO@**Ru-CTF**, 10 x 15 mm). The reference (RE)

and counter electrode (CE) were a $Hg/HgSO_4$ (K_2SO_4 sat.) and a platinum wire respectively. Before each electrochemical experiment, iR compensation was performed through the CHI660 Electrochemical workstation program. The resistance of the cell was typically 10-30 Ω and iR compensation was applied at 85 %. CVs of bare FTO were also recorded as blank. All the potentials reported in this work were converted to NHE by adding 0.65 V to the measured potential.

UV-vis diffuse reflectance spectroscopy (DRS)

UV-vis reflectance measurements for E_{gap} calculations were carried out on a Shimadzu UV2401PC spectrophotometer equipped with an integrating sphere. $BaSO_4$ was used as reflectance standard for the analysis, since it can reflect in high percentage in the whole range of UV-vis spectrum. In case of the characterization of **Ru-CTF** powder, $BaSO_4$ was also used as diluent of the sample, to avoid the saturation of the detector. The energy band-gap (E_g) of **CTF** and **Ru-CTF** were determined through Tauc plot. The Tauc method, specific for powder samples,[4] is based on the relationship between E_g and the ratio R_∞ of the reflectance of the sample (R_{sample}) and the reflectance of the standard ($R_{standard}$) according to Equation S1:

$$F(R_\infty)hv \propto (hv - E_g)^n \quad \text{(S1)}$$

where F is defined as in Eq. S2:

$$F(R_\infty = R_{sample}/R_{standard}) = (1 - R_\infty)^2/2R_\infty \quad \text{(S2)}$$

where hv (eV) is the energy of the incident photon and n is a coefficient that depends on the kind of electronic transition. In case of semiconductors, only direct allowed transitions were assumed (hence n = 1/2), since bandgap is not too wide. According to the Kubelka-Munk model, by plotting $(F(R_\infty)hv)^{1/n}$ against hv (with n = 1/2) and fitting the linear part of the curve, E_g can be found at the intersection of the x-axis and the fitting linear curve.

Powder X-Ray Diffraction (PXRD)

A Bruker D8 Advance Powder Diffractometer was used, with a vertical 2θ-θ goniometer in transmission configuration, with a Kα1 germanium monochromator for Cu radiation (λ = 1.5406 Å), fixed divergence slits and a diffracted beam radial Soller slit. The system

is equipped with a VÅNTEC single photon counting PSD detector with a 12º overture in 2θ, a ninety positions auto-charger sample stage.

Fourier Transform Infrared Spectroscopy (FT-IR)

FT-IR measurements were carried out on a Bruker Optics FT-IR Alpha spectrometer equipped with a DTGS detector, KBr beam-splitter at 4 cm^{-1} resolution using a one-bounce ATR accessory with diamond windows.

Mott-Schottky (M-S) analysis

For the Mott-Schottky experiments, an IJ-Cambria CHI-660D potentiostat was employed and a conventional three-electrode cell was used for the analysis in dark conditions. The working electrodes were prepared by homogeneously spray-coating **CTF** and **Ru-CTF** dispersed in MeOH (1 mg/mL) onto FTO slides. The RE and CE used were a $Hg/HgSO_4$ (K_2SO_4 sat.) and a platinum wire, respectively. For the calculation of the Fermi level, the potential was converted to NHE by applying the following formula (Eq. S3):

$$E\ (V\ vs\ NHE\ @pH\ 7)\ =\ E\ (V\ vs\ \mathrm{Hg/HgSO_4})\ +\ 0.654 \qquad \text{(S3)}$$

The experiments were performed by applying frequencies of 500, 1000 and 2000 Hz at a suitable DC potential range (-0.1 – 1.0 V vs NHE @pH 7) with an AC amplitude of 5 mV. The electrolyte used was a pH 7 phosphate buffer (I = 0.1 M). The extrapolation of the E_{CB} was obtained by selecting the linear region of the M-S curve and interpolating it with the x-axis (voltage).[5]

The frequencies employed for the extrapolation of the conduction band (in this case equalized to the Built-in voltage, V_{bi}, potential loss in the depletion layer of the semiconductor) were obtained from the constant capacitance plateau region observed in the capacitance spectrum, also known as 'Bode plot', performed before the Mott-Schottky.[5] The Bode plot has been performed through Electrochemical Impedance Spectroscopy (EIS), using the same potentiostat and the same set-up. The potential was places at 0 bias (V vs $Hg/HgSO_4$), with 5 mV amplitude of the sinusoidal perturbation and angular frequency ω ranged between 2 MHz and 10 Hz. The same experiment was also converted to Nyquist plot to consider and compare the resistance to charge transfer of the systems under study.

Induced Coupled Plasma Optical Emission Spectroscopy (ICP-OES)

ICP-OES measurements were performed with a Spectro Arcos, model FHS16. For the digestion of the sample, a Microwaves Digestor Milestone, model Ethos Easy was used, employing a mixture of HNO_3 (3 mL) and HCl (9 mL) concentrated acids for each duplicate. The conditions for the digestion were the following: i) ramp from r.t. to 120ºC in 10 minutes; ii) isotherm at 120ºC for 5 minutes; iii) ramp from 120 to 220ºC in 25 minutes; iv) isotherm at 220ºC for 15 minutes. After digesting, the samples were let to cool down to r.t. and diluted with Milli-Q water until 50 mL. The analysis is then performed, reproducing 3 times the measurement for each duplicate, and the average value is calculated, considering a standard solution of Ru metal for the calibration. Calculated percentage of the Ru metal per each duplicate could be found in Table S1.

Textural properties analysis

Physisorption experiments were performed with an Autosorb iQ (Quantachrome) instrument, to check the surface area and porosity of the material. Prior to the measurement, 40 mg of **CTF** and **Ru-CTF** materials were outgassed at 150ºC under vacuum for 15 h in order to get rid of the humidity or solvent traces trapped in the material. The adsorption-desorption isotherm was then recorded at 77 K with liquid nitrogen. The Brunauer Emmett Teller (BET) method [6] was applied to calculate the total surface area, and the t-plot method [7] was used to discriminate between micro- and meso-porosity. The Barrett Joyner Halenda (BJH) model [8] applied to the desorption branch of the isotherm provided information on the mesopore size distribution (2-50 nm).

Dynamics Light Scattering (DLS)

The experiments were performed analyzing the **Ru-CTF** dispersion during photocatalysis with a Mastersizer 2000 (Malvern Instruments). The hydrodynamic diameter of the particles in suspension was measured (range from 0.02 µm to 2000 µm) with a 635 nm laser beam, which irradiates an internal flow cell where the dispersion is passing. The particles scatter light at an angle that is inversely proportional to their size. The refraction index of the particles was set to 1.33 at an absorption of 0.02 (deduced from the diffuse reflectance spectrum of **Ru-CTF** at 635 nm). The angular intensity of the

scattered light was then measured by a series of photosensitive detectors, and the particles size was calculated through the Mastersizer 2000 software. An external sample dispersion unit was connected to the flow cell, and a stirring system was used to keep the suspension and let the solution flow in and outside the instrument. Each measurement was performed by injecting 3 mL of the sample suspension into the external unit and immediately analyzed by running 5 scans of 5 seconds each, without any pause in between. The measurement was performed immediately in order to avoid the reaggregation or the change of the size of the particles injected. For the entire experiment, 0.5 mg/mL **Ru-CTF** were dispersed in 20 mL of 25 mM 7-phbf solution with 10 mM SEA inside a quartz cell by 20 minutes sonication and, after the first measurement, the dispersion under stirring was irradiated with a Xe lamp applying 3 suns (same conditions as the photocatalysis experiments). The analyses were performed at t = 0 (right after sonication), at t = 60, 120 and 180 minutes after starting the irradiation under stirring.

Scanning Electron Microscopy (SEM)

The morphology and homogeneity of **CTF** was analyzed by SEM using a scanning electron microscope with focused ion beam (FESEM-FIB) for ultra-high resolution images. Cross-section analysis was performed on an FTO@CTF electrode (loading by drop-casting of a **CTF** dispersion), covered first with a layer of atomic Au by gold sputtering (90 seconds at 30 mA of current) in order to prevent the surface charging, and later with a Pt paste on the area of the cut, to protect the material from possible ion-beam damages.

Transmission Electron Microscopy (TEM)

The instrument FETEM 200 kV for high resolution transmission electron microscopy was used to check the morphology, like SEM, of **CTF** and **Ru-CTF**, as well as the homogeneity of the Ru distribution in **Ru-CTF** (EDS). Dispersions of 0.5 mg/mL of **CTF** and **Ru-CTF** in EtOH were drop-cast (1 drop) on standard TEM Cu-grids.

Time-Correlated Single-Photon Counting (TCSPC)

The TCSPC experiments were carried out using a commercial setup (Horiba DeltaFlex) equipped with a pulsed LED excitation source (404 nm, Horiba NanoLED series) and a fast rise-time photomultiplier detector (Horiba PPD-650). The instrument response function (IRF) was measured at the excitation wavelength. A suitable long-pass filter was

inserted between the sample and detector to block off scattered excitation light in all the measurements. The concentration of the **CTF** and **Ru-CTF** was 1 mg/mL, prepared in buffer phosphate pH 7 (25 mM) and 10 mM of SEA.

X-ray absorption spectroscopy

Ru K-edge XAS was used to measure **Ru-CTF** and **Ru-CTF** after catalysis, and the reference samples [Ru(tda)(py)(dmso)], [Ru(tda)(py_2)] and RuO_2 in fluorescence mode. All samples were prepared by dropcasting a suspension of the corresponding powder in EtOH on a previously cleaned FTO electrode. Afterwards, the prepared samples were placed in the sample holder and sealed with 30 µm Kapton tape. Measurements were carried out at beamline CLAESS (Static Ru K-edge XAS and EXAFS) at ALBA synchrotron with the collaboration of beamline scientist and ALBA staff. The incident energy was selected by a Si (311) double crystal monochromator. Incident flux was *ca.* 5 x 10^{11} ph/sec using a beam size of 250 µm × 500 µm. Samples were kept bellow 80 K in a N_2 LN_2-cryo cryostat. Incident energy was calibrated by assigning the first inflection point of Ru foil to 22117.2 eV. Fluorescence spectra were recorded using a Multichannel Silicon-drift fluorescence detector. A step size of 0.2 eV was used in the XANES and EXAFS regions (1 s integration time). Final spectra were processed and normalized using Athena program, included in the DEMETER package.[9]

3.6.3. Methods

Calculation of occupied pyridyl sites

The percentage of free dangling pyridyl groups was calculated starting from Equations S4 and S5:

$$\%\ occupied\ sites = \frac{\%\ Ru\ (ICP-OES)}{\%\ Ru\ theo} \times 100 \quad \text{(S4)}$$

$$\text{where: } \%\ Ru\ theo = \frac{MW\ Ru \times 3}{MW\ Ru-CTF} \times 100 \quad \text{(S5)}$$

Where $\%\ Ru\ (ICP-OES)$ is the value obtained from the ICP-OES analysis, $\%\ Ru\ theo$ is the theoretical percentage of Ru metal if all pyridyl groups are occupied, $MW\ Ru$ is the molecular weight of atomic Ru (multiplied by 3, as the Ru centers considered per each **CTF** repetitive unit) and $MW\ Ru-CTF$ is the theoretically calculated molecular weight for a repetitive unit of **Ru-CTF** with 3 Ru centers (4057.48 g/mol).

Calculation of TONs and TOFs

The turnover numbers (TONs) and the turnover frequencies (TOFs) were calculated following Equations S6 and S7:

$$TON = \frac{mol\ O_2}{mol\ Ru} \quad \text{(S6)}$$

$$TOF\ (s^{-1}) = \frac{mol\ O_2}{mol\ Ru \times time\ (s)} \quad \text{(S7)}$$

where $mmol\ O_2$ is the number of moles of oxygen detected during the photocatalytic experiment, $mmol\ Ru$ is the amount of Ru used for each photocatalytic experiment calculated from the % of Ru obtained experimentally from ICP-OES. In case of TOFs, calculations were performed during the first part of the experiment (0.45-0.50 h), where aggregation phenomena are not taking place.

Chemical efficiency

The efficiency of the electron extraction respect with the total SEA was calculated according to the following Equations:

$$\Phi_{chem} = \frac{mmolO_2}{mmolO_2(theo)} \times 100 \quad \text{(S8)}$$

$$mmol\ O_2(theo) = \frac{[S_2O_8]^{2-} \times V_{tot} \times n^e}{n^h} \quad \text{(S9)}$$

where $mmolO_2$ is the number of moles of oxygen detected during the photocatalytic experiment , $mmolO_2(theo)$ is the theoretical number of moles of O_2 that should be produced during the process with a efficiency of 100 %, $[S_2O_8]^{2-}$ is the concentration of SEA, V_{tot} is the total volume of the dispersion, n^e is the number of electrons given per molecule of persulfate, and n^h is the number of holes transferred to the catalyst to produce a molecule of O_2.

Apparent Quantum Yield (AQY)

The AQY (%) was estimated by using the following Equation:

$$AQY(\%) = \frac{n^o\ reacted\ electrons\ (n^e)}{n^o\ incident\ photons} \times 100$$

$$= \frac{4 \times (molecules\ O_2)_t}{Absorbed\ photons \times \Delta t \times Area} \times 100 =$$

$$= \frac{4 \times (N_A \times mol\ O_2)_t}{Absorbed\ photons \times \Delta t \times Area} \times 100 \quad \text{(S10)}$$

where $mol\ O_2$ is the number of moles of oxygen detected during the photocatalytic experiment, N_A is the Avogadro's number (6.022×10^{23} mol^{-1}), n^e is the number of electrons necessary to form a molecule of O_2, Δt is the time during the first 30 minutes of experiment, *A* is the area irradiated of the cell (2.41×10^{-4} m^2 in the case of 2 mL).[10,11] Absorbed photons were calculated starting from the irradiance power of the light source following Equations S11, S12 and S13:

$$\frac{P}{area \times \lambda_{inc}} = \left[\frac{W}{m^2 \times nm} = \frac{J}{s \times m^2 \times nm}\right] = \frac{E_{tot}}{t \times area \times \lambda_{inc}} \quad \text{(S11)}$$

$$E_{ph} = \frac{h \times c}{\lambda(nm)} = [J] \quad \text{(S12)}$$

$$\frac{E_{tot}}{E_{ph}} = \left[\frac{n^o photons\ absorbed}{s \times m^2 \times nm}\right] = \frac{n^o\ photons\ absorbed}{t \times area \times \lambda_{inc}} \quad \text{(S13)}$$

where *P* stands for irradiance power (W m^{-2}), *area* is the irradiated area (m^2), *t* (s) is the irradiation time (s), *h* the Planck constant ($6.26 \times 10^{-34}\ Js$) and *c* the light speed ($c = 3 \times 10^8\ m/s$), λ_{inc} is the incident wavelength (nm), E_{tot} is the total energy of incident monochromatic light and E_{ph} is the energy of one photon with wavelength λ_{inc}. The solar spectrum is thus plotted as *Absorbed photons* s^{-1} m^{-2} nm^{-1} vs *wavelength* (nm), and the AQY is calculated integrating the area in the range where CTF is absorbing mostly

(from 330 to 444.5 nm) (Fig. S17). The solar spectra were recorded for both 3 suns and 1 sun irradiation used for the photocatalytic experiments.

3.6.4. Synthetic procedures

Synthesis of M3-py

Synthesis of 1,4-dibromo-2-(bromomethyl)benzene (1): 15 g of 2,5-dibromotoluene (60 mmol), 11.76 g of NBS (66 mmol), 1.101 g of AIBN (6.7 mmol) were added in a 250 mL two-neck round bottom flask and the flask was vacuum-flushed with N_2. 150 ml of degassed benzene were added and the mixture was heated at reflux for 24 h. The resulting solution was cooled down to room temperature (RT) and washed with 5% sodium carbonate solution (4 x 50 mL) to remove succinimide and dried with $MgSO_4$. A pinkish orange solid was obtained and purified by flash column (cyclohexane, 1% NEt_3). **1** was obtained as a white solid (9.4 g, 48% yield).

^{1}H NMR (400 MHz, $CDCl_3$) δ: 7.59 (d, *J* = 2.4 Hz, 1H), 7.43 (d, *J* = 8.5 Hz, 1H), 7.29 (dd, *J* = 8.5, 2.4 Hz, 1H), 4.52 (s, 2H). ^{13}C NMR (101 MHz, $CDCl_3$) δ: 138.98, 134.67, 133.98, 133.08, 123.05, 121.47, 32.14.

Synthesis of 4-(2,5-dibromophenethyl)pyridine (2): To a dried 50 mL two-neck round bottom flask, a dried mixture of 15 mL of THF and 0.74 mL of previously distilled 4-picoline (7.6 mmol, 0.8 eq.) was added under inert atmosphere. The flask was then cooled down to -78ºC with an acetone/dry ice bath and the solution was kept stirring for 30 min. 4.4 mL of a 2 M LDA solution (32.4 mmol, 3.2 eq.) were then added dropwise, and the reaction was kept for other 2 hours under stirring at low temperature. Finally, 2.5 g of previously dried 1,4-dibromo-2-(bromomethyl)benzene (10 mmol, 1 eq.), **1**, were dissolved in 10 mL of dry THF and, after purging with N_2 flow for 10 minutes, the solution was added dropwise to the reaction flask, leaving it under stirring for 2 hours at low temperature and then overnight at room temperature. The color of the mixture gradually changed during addition from dark brown to bright yellow. The crude was dried under vacuum, extracted with EtOAc/water and the combined organic layers were dried over $MgSO_4$. After evaporating the solution, the product was washed with EtO_2, causing the precipitation of a black solid impurity that was separated by filtration. The

resulting purified product 4-(2,5-dibromophenethyl)pyridine (**2**) was obtained with a yield of 64% (1.66 g).

^{1}H NMR (500 MHz, CD_2CL_2) δ: 8.57 – 8.45 (m, 2H), 7.44 (d, *J* = 8.5 Hz, 1H), 7.34 (d, *J* = 2.4 Hz, 1H), 7.24 (dd, *J* = 8.5, 2.5 Hz, 1H), 7.18 – 7.10 (m, 2H), 3.04 – 2.96 (m, 2H), 2.96 – 2.86 (m, 2H). ^{13}C NMR (126 MHz, CD_2Cl_2) δ: 149.81, 142.37, 134.27, 133.21, 131.01, 123.80, 123.02, 121.18, 53.45, 36.88, 35.01. (+)-HRMS-ESI (MeOH). Calc. for [M+H$^+$], ($C_{13}H_{11}Br_2N$ + H$^+$): 339.9331, found 339.9335.

Synthesis of monomer 2'-(2-(pyridin-4-yl)ethyl)-[1,1':4',1''-terphenyl]-4,4''-dicarbonitrile (M3-py): 250 mg of **2** (0.8 mmol, 1 eq.), 323.1 mg of 4-cyanophenylboronic acid (2.2 mmol, 2.7 eq.), 466.2 mg of Na_2CO_3 (4.4 mmol, 5.5 eq.) and 80.5mg of $Pd(Cl_2)(dppf)$ (0.1 mmol, 0.13 eq.) were added in a 100 mL two-neck round bottom flask and the flask was vacuum-flushed with N_2. A degassed mixture of 20 mL of dioxane and 20 mL of water was added to the flask and the resulting solution was stirred under reflux for 20 h. The resulting mixture was cooled down to RT, the solvent was removed under vacuum and DCM was added. The organic layer was then washed thoroughly with water to remove Na_2CO_3. The organic layer was dried over $MgSO_4$ and the product purified by flash column with cyclohexane (containing 1% NEt_3)/ethyl acetate (ratio 8:2). The monomer **M3-py** is obtained as a yellowish solid (106 mg, 35% yield).

^{1}H NMR (500 MHz, CD_2Cl_2) δ: 8.43 – 8.34 (m, 2H), 7.80 – 7.70 (m, 6H), 7.56 (d, *J* = 7.6 Hz, 2H), 7.44 – 7.37 (m, 2H), 7.33 – 7.29 (m, 1H), 6.91 – 6.80 (m, 2H), 2.99 (dd, *J* = 9.1, 6.7 Hz, 2H), 2.76 (dd, *J* = 9.1, 6.7 Hz, 2H). ^{13}C NMR (126 MHz, CD_2Cl_2) δ: 149.67, 145.62, 144.78, 140.57, 139.24, 138.97, 132.70, 132.18, 130.57, 129.94, 128.54, 128.29, 127.64, 125.27, 123.72, 118.77, 118.71, 111.26, 111.25, 36.61, 33.92. (+)-HRMS-ESI (MeOH). Calc. for [M+H$^+$], ($C_{27}H_{19}N_3$ + H$^+$): 386.1652, found 386.1639.

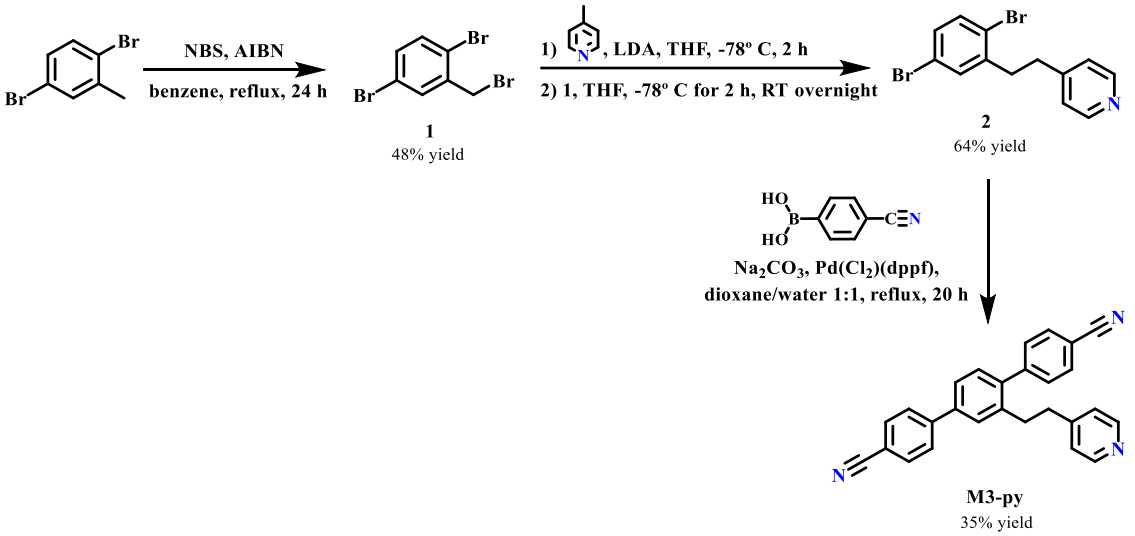

Scheme S1. *Schematic procedure for the synthesis of the monomer* ***M3-py****.*

Synthesis of CTF

CTF was synthesized following the paper of Meier et al.,[12] with a few modifications. 83 mg of **M3-py** (0.22 mol) dissolved in 0.6 mL of degassed $CHCl_3$ were slowly added to a 10 mL flask already containing trifluoromethanesulfonic acid (0.4 mL, 45 mmol) and chloroform (0.1 mL, 12.5 mmol), keeping the system under N_2 atmosphere and at RT. The solution changed immediately color from white to deep red, and the reaction was kept stirring for 2 days. The resulting solution was afterwards adjusted to pH 7 by adding drops of NH_3 (0.1 M) solution, giving a pale-yellow precipitate. The suspension was stirred for 1 hour, and the solid was filtered and washed with water, EtOH, DCM and MeOH. The product was finally dried at 100°C under vacuum for 8h, in order to get rid of possible water residue inside the cavities of the **CTF**, obtaining the product in a 92% yield (76 mg).

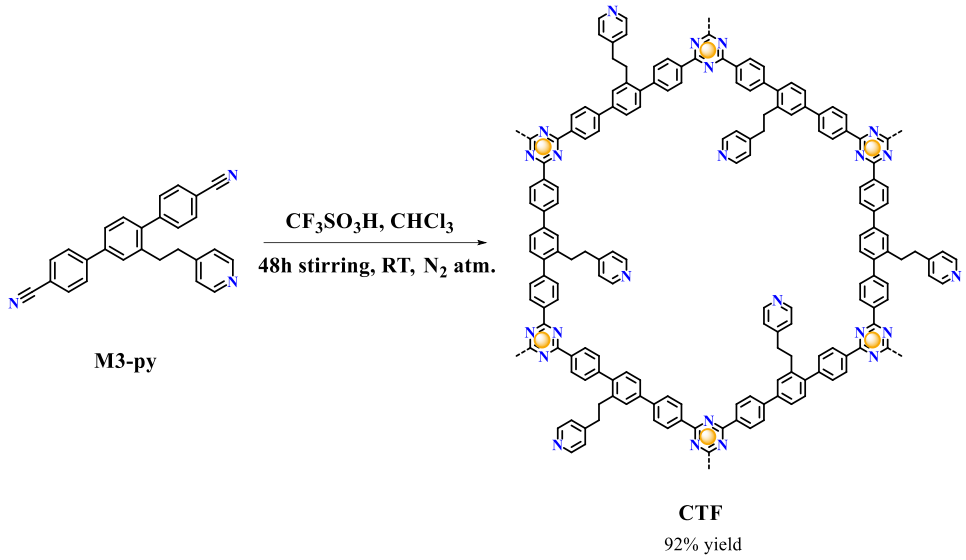

Scheme S2. *Schematic drawing of the synthesis of* ***CTF****.*

Synthesis of Ru-CTF

[Ru(tda)(py)(dmso)] (4.2 mg, 7.3 µmol) was covalently linked to **CTF** polymer (24.5 mg, 10 µmol) by reflux for 3 days under N_2 flow in a 10 mL mixture of EtOH/MeOH solvents (1:1 ratio). As a result, the yellow color of bare **CTF** changed to deep purple in the presence of Ru complex. After evaporating the solvent, the solid was washed with MeOH and centrifuged several times until the solution was colorless. The final compound **Ru-CTF** was dried under vacuum, obtaining 60% yield.

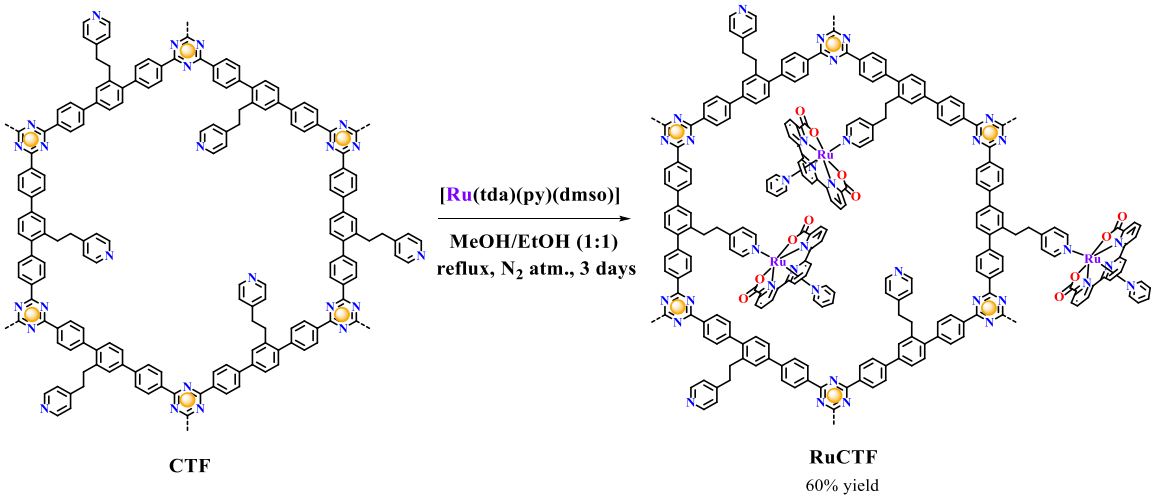

Scheme S3. *Schematic drawing of the synthesis of* ***Ru-CTF****.*

3.6.5. Results

NMR spectroscopy

a)

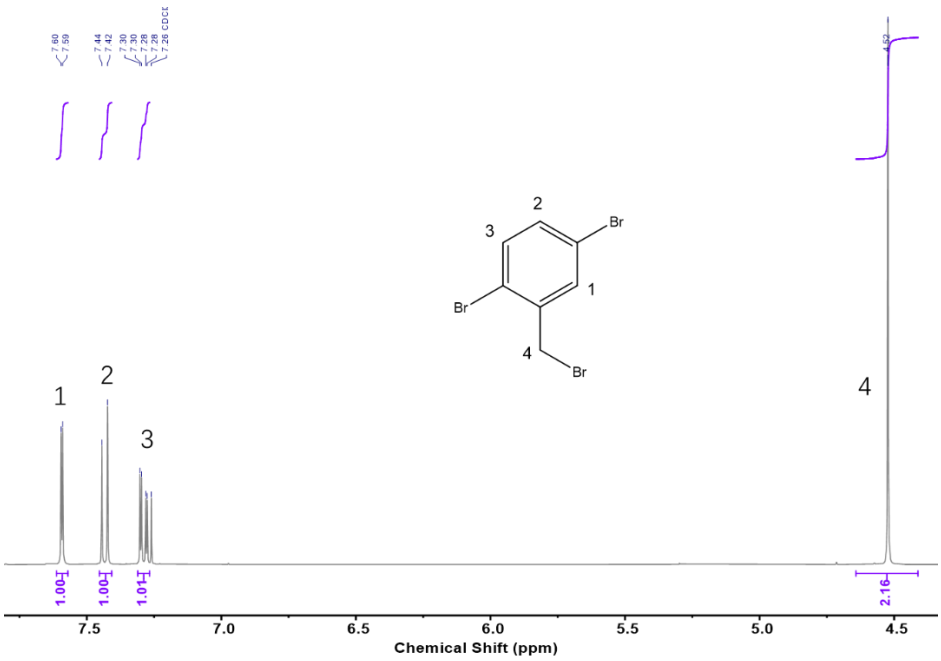

b)

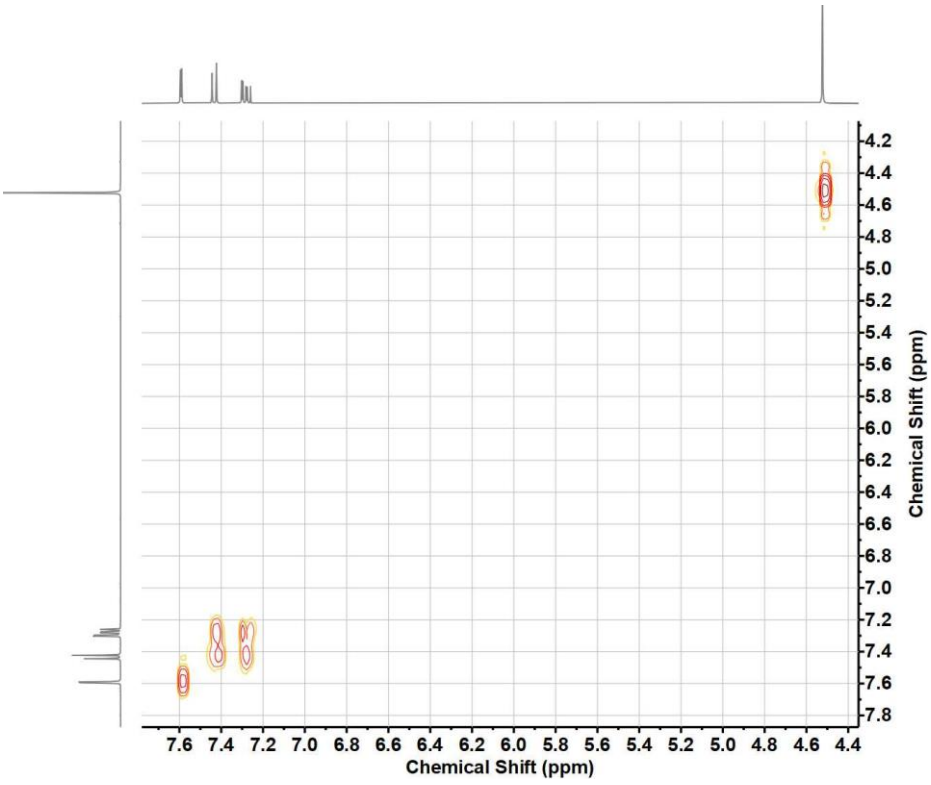

c)

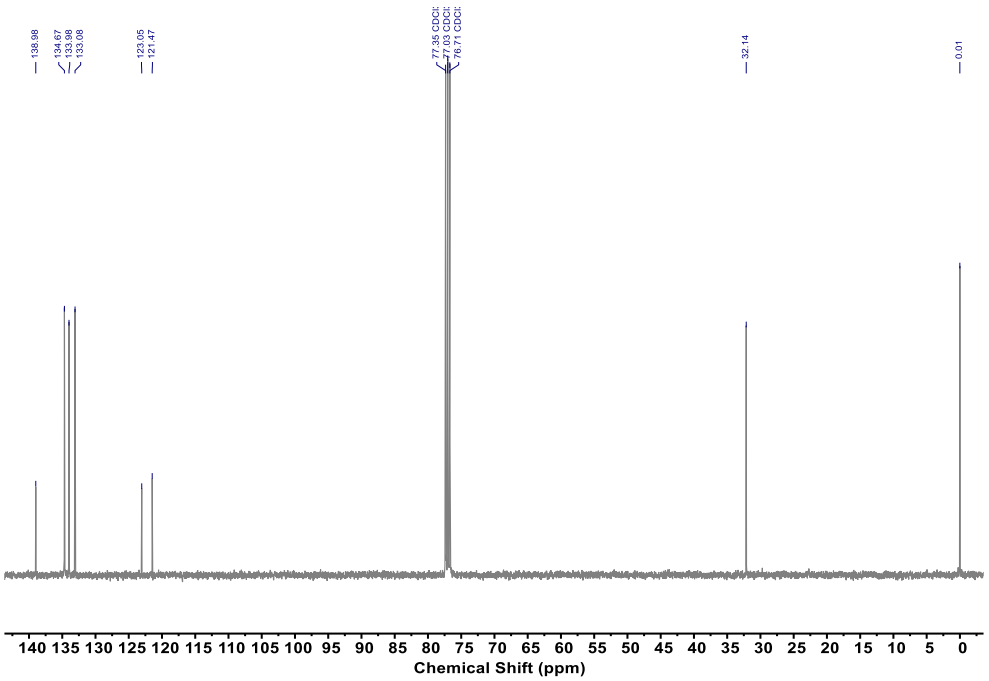

Figure S1. *NMR spectra (400 MHz, 298 K, Chloroform-d) for* ***1****. (a)* ^{1}H *NMR, (b) COSY and (c)* ^{13}C *NMR.*

a)

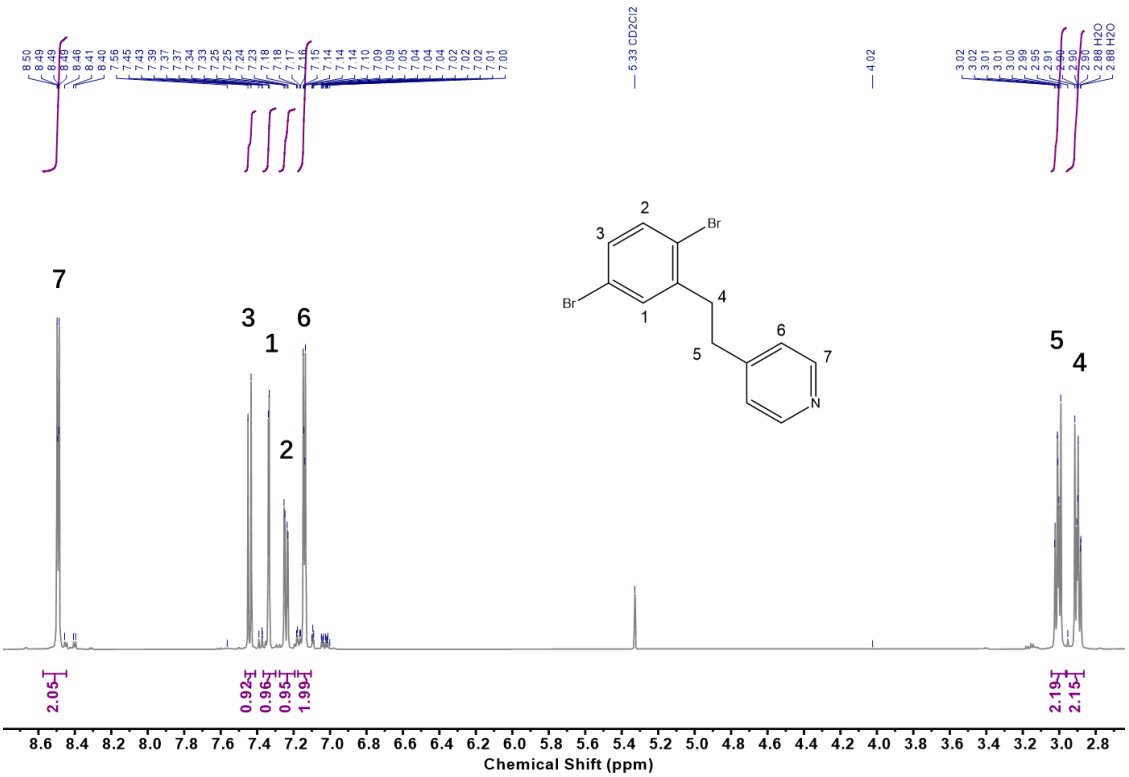
5.33 CD2Cl2
4.02
H2O
H2O
Br
Br
7
3
1
6
2
5
4
2.05
0.92
0.96
0.95
1.99
2.19
2.15
Chemical Shift (ppm)

b)

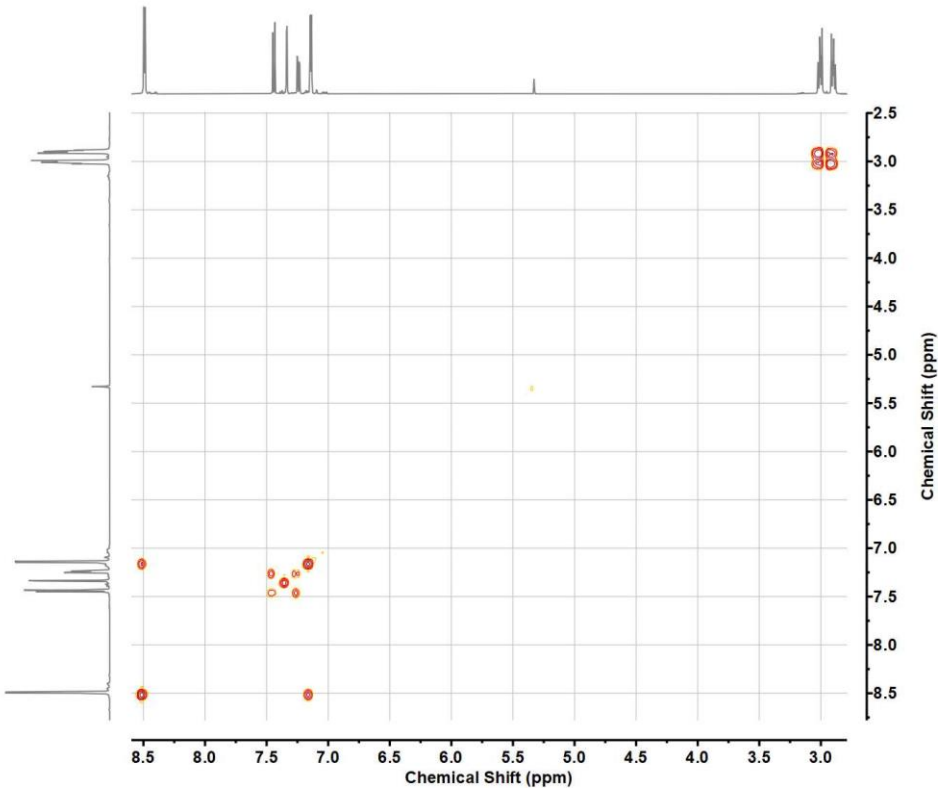
Chemical Shift (ppm)
Chemical Shift (ppm)

c)

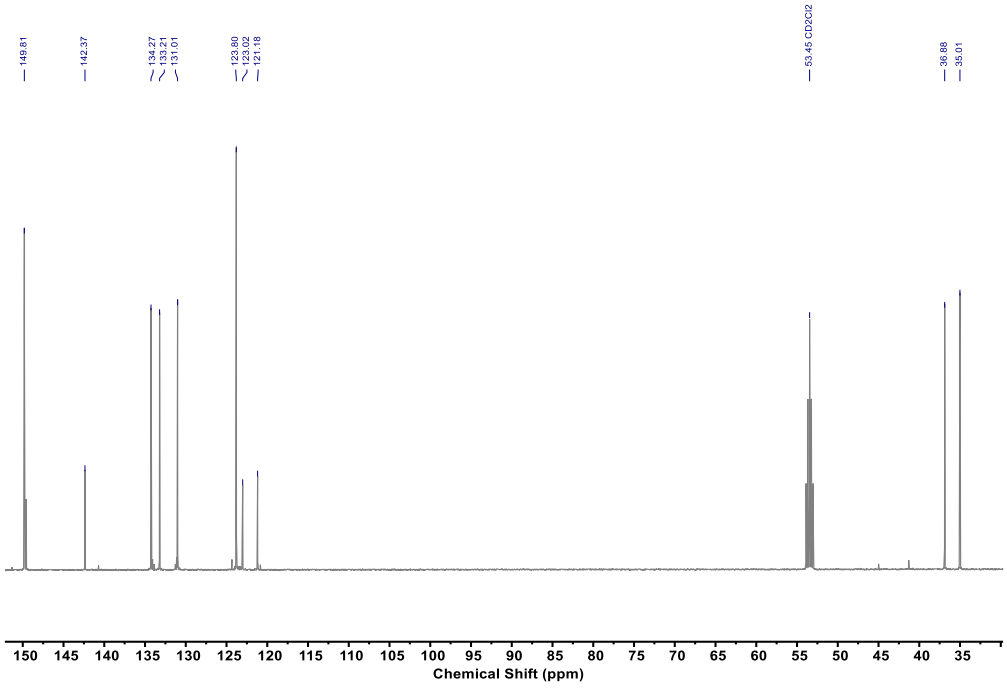

Figure S2. *NMR spectra (500 MHz, 298 K, Methylene Chloride-d_2) for* ***2****. (a)* ^{1}*H NMR, (b) COSY and (c)* ^{13}*C NMR.*

a)

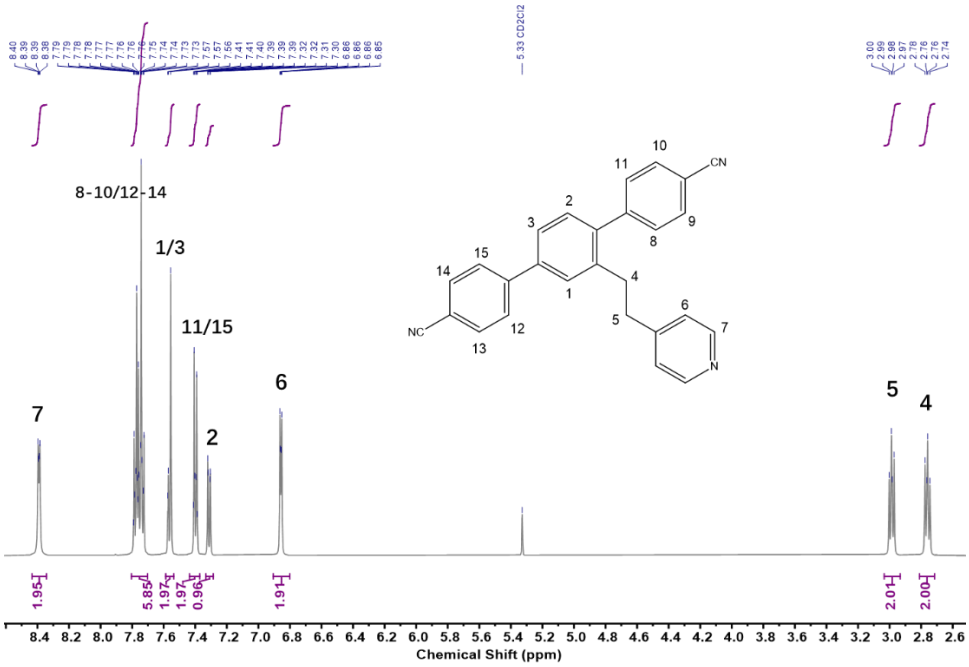
8-10/12-14
1/3
11/15
2
6
7
5
4
1.95
5.85
1.97
1.97
0.96
1.91
2.01
2.00
Chemical Shift (ppm)

b)

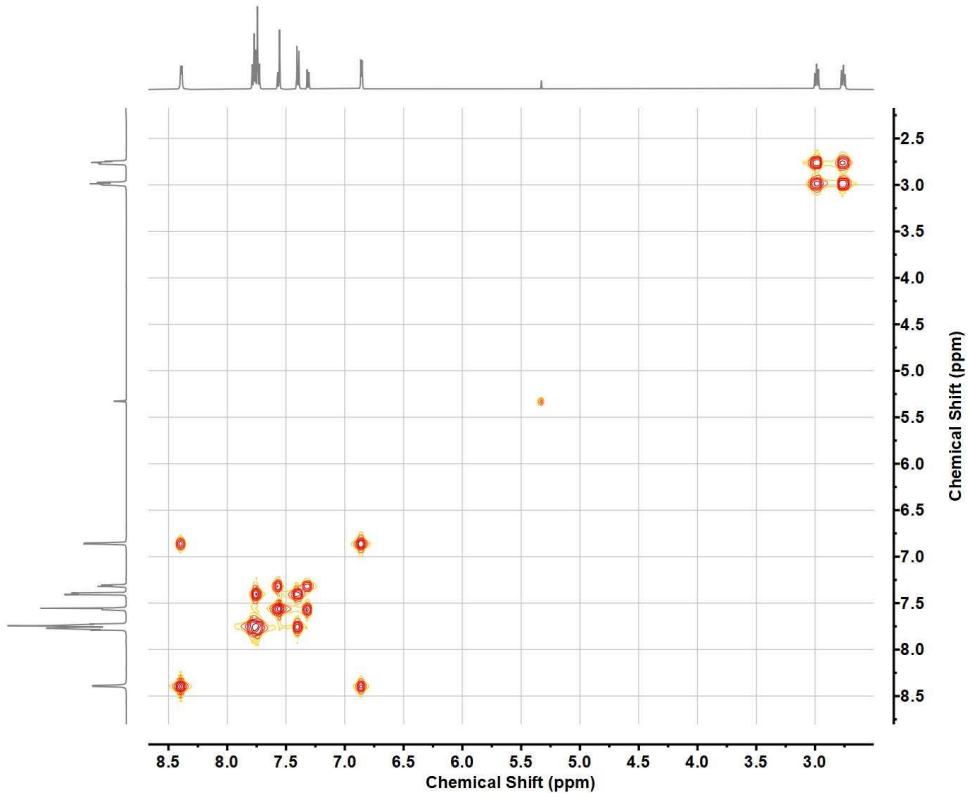
Chemical Shift (ppm)
Chemical Shift (ppm)

c)

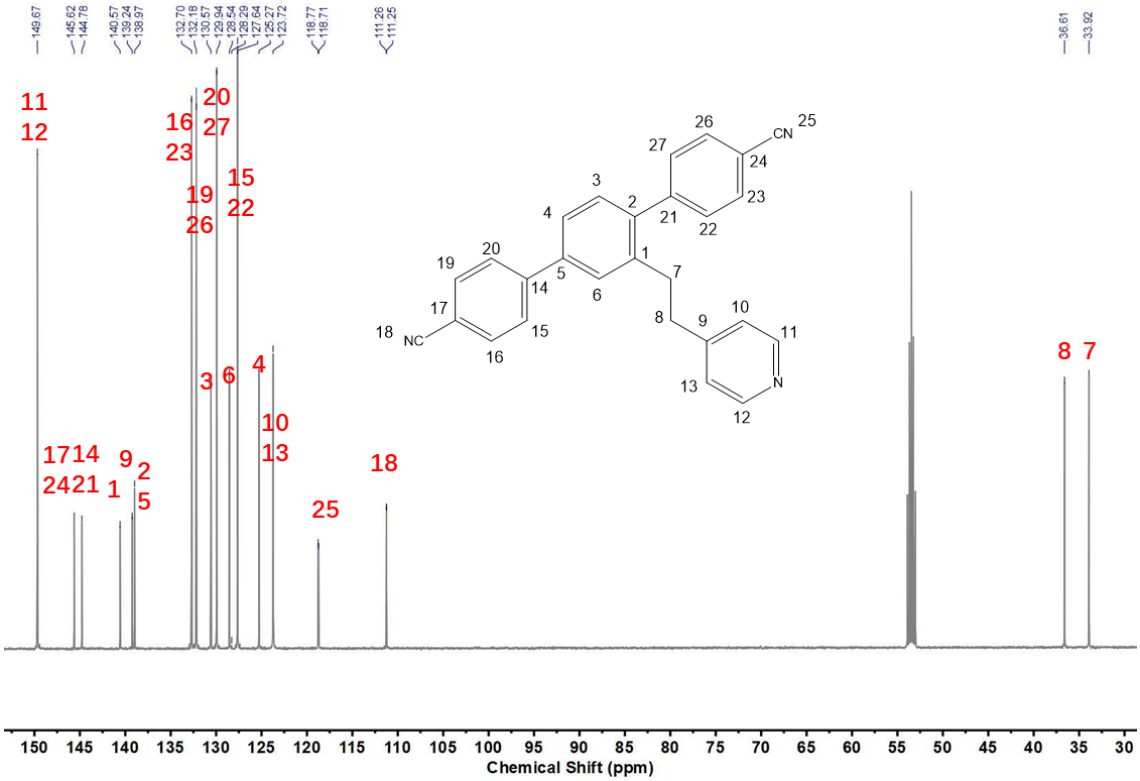
149.67
145.62
144.78
140.57
139.24
138.97
132.70
132.18
130.57
129.94
128.54
128.29
127.64
125.27
123.72
118.77
118.71
111.26
111.25
36.61
33.92
11
12
16
23
20
27
19
26
15
22
3
6
4
10
13
17
14
24
21
9
1
2
5
25
18
8
7
NC
CN
N
Chemical Shift (ppm)

d)

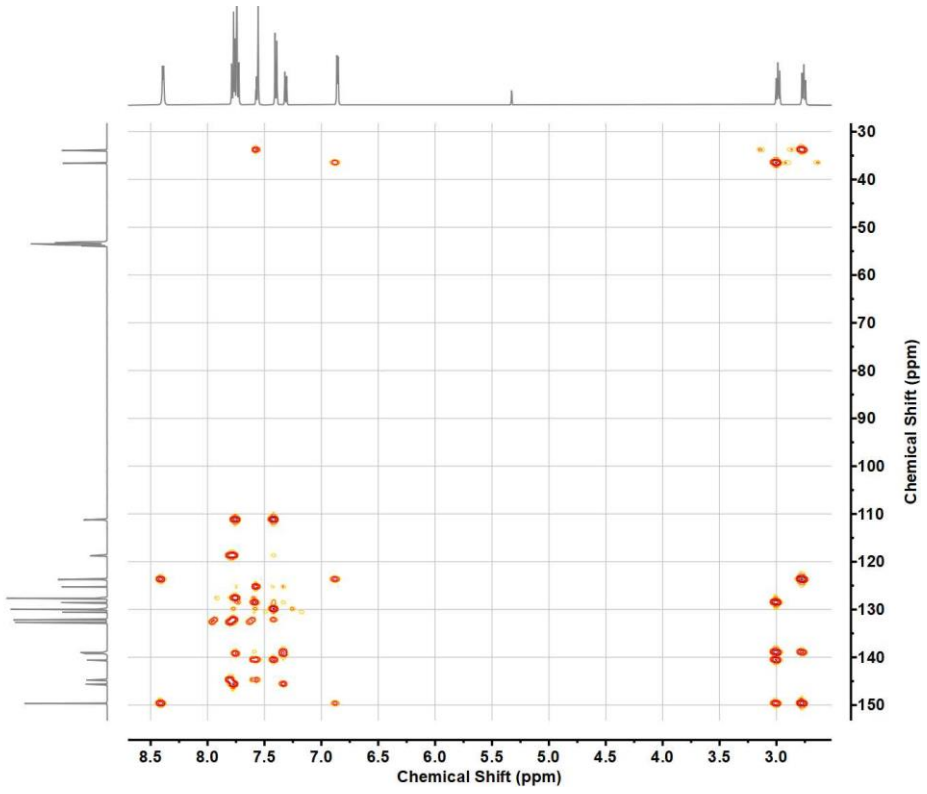
Chemical Shift (ppm)
Chemical Shift (ppm)

e)

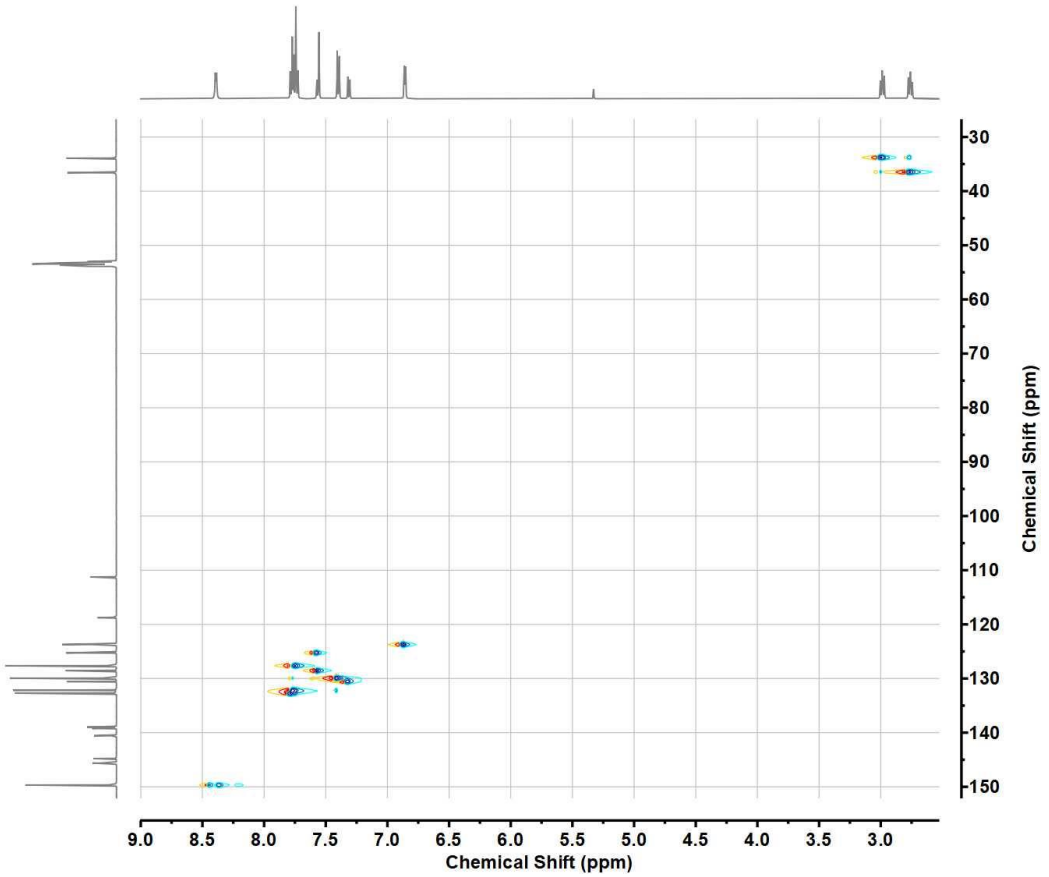

Figure S3. *NMR spectra (500 MHz, 298 K, Methylene Chloride-d_2) for* ***M3-Py****. (a) ^{1}H NMR, (b) COSY, (c) ^{13}C NMR, (d) HMBC and (e) HSQC.*

Mass Spectrometry (HRMS-ESI)

a)

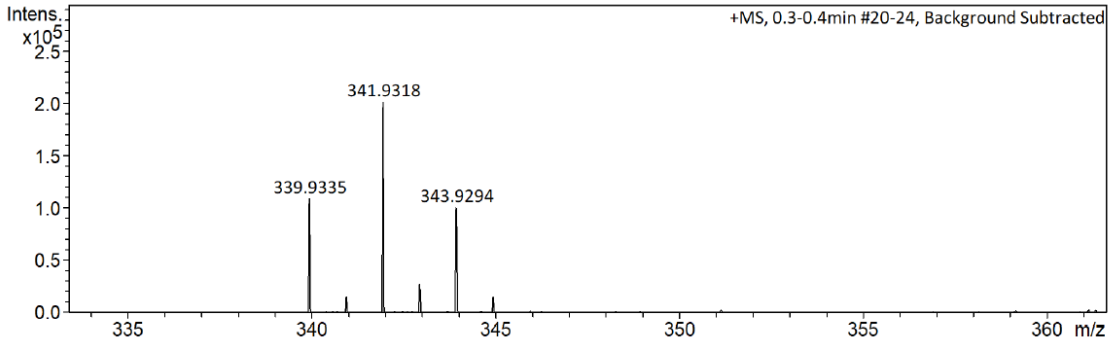

b)

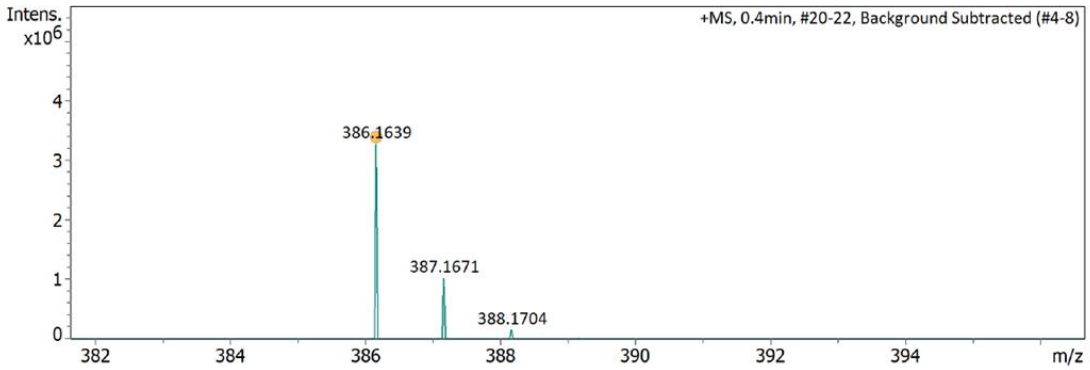

Figure S4. *HRMS-ESI for* ***2*** *(a) and* ***M3-Py*** *(b). Calc. for (a) [M+H⁺], ($C_{13}H_{11}Br_2N + H^+$): 339.9331, found 339.9335; calc. for (b) [M+H⁺], ($C_{27}H_{19}N_3 + H^+$): 386.1652, found 386.1639.*

Fourier Transform Infrared spectroscopy (FT-IR)

The IR spectrum of the **CTF** material (Figure S5) shows the absence of the $\nu_{C\equiv N}$ band at ca. 2220 cm^{-1}, which is indicative of a high degree of polymerization.[13] The formation of the triazine moieties is indicated by the appearance of the typical stretching and bending features of the triazine rings at ν = 1503, 1359 (C-N=C stretching) and δ = 810 cm^{-1} (C-N bending).[13,14] The presence of the pyridyl group is also confirmed by the peaks at around 1602 cm^{-1} and 1006 cm^{-1} attributed to the C-C stretching and C-N-C bending, while other characteristic peaks are overlapped to the triazine stretching modes of the same **CTF**.[15]

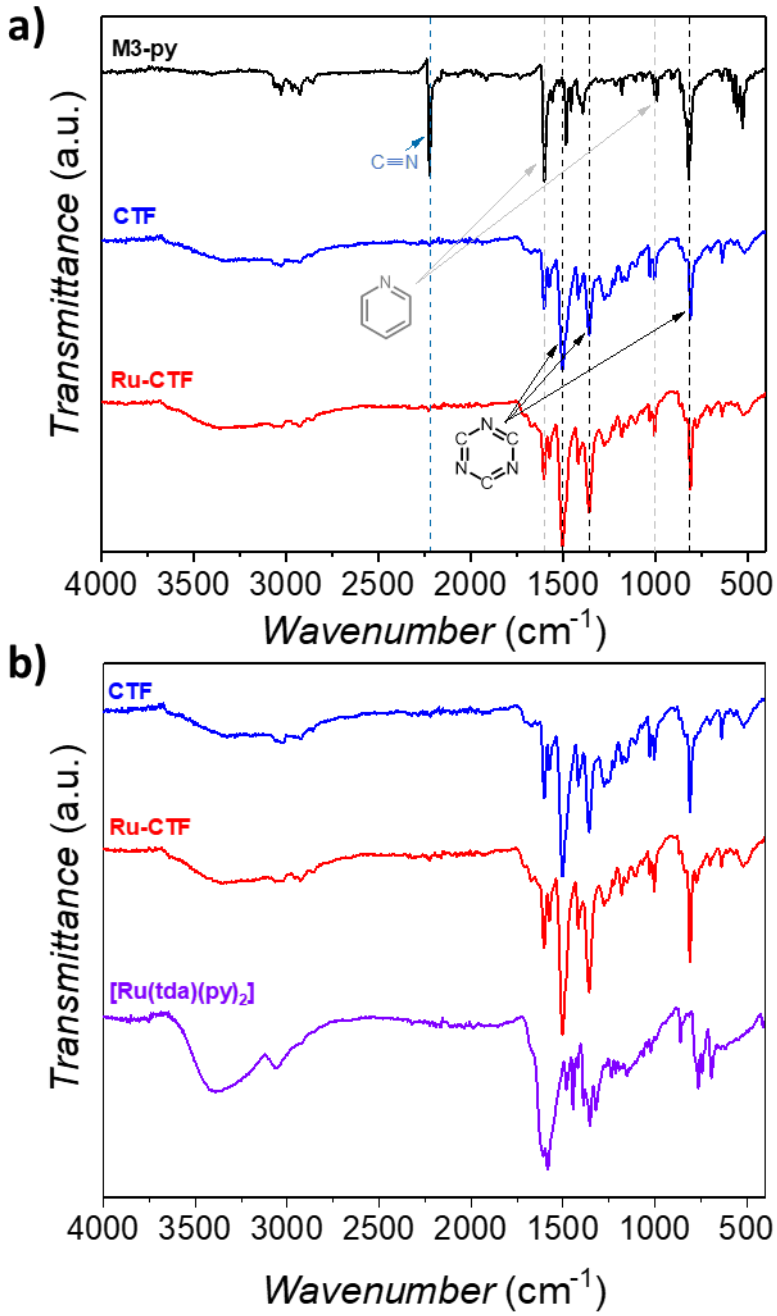

Figure S5. *(a) FT-IR spectra of* ***M3-py*** *(black line),* ***CTF*** *(blue line) and* ***Ru-CTF*** *(red line); (b) FT-IR spectra comparison of* ***CTF*** *and* ***Ru-CTF*** *with the [Ru(tda)(py)$_2$] complex (purple line). The dotted lines in figure (a) highlight the presence of the characteristic stretching and bending of pyridyl and triazine moieties.*

Powder X-ray diffraction (PXRD)

The diffractograms reported below in Figure S6 show the typical peak at 2θ = 24.5° characteristic of the (001) reflection for CTFs,[12,13,16–18] as well as a broad band at 18.5°, which can be tentatively attributed to a not complete eclipsed orientation of the **CTF** layers, having a so-called AB-stacking (interlayer coupling of C-N atoms).[16] Moreover, the (100) peak at 2θ = 7° is slightly visible in the spectrum of **Ru-CTF**, probably due to the redispersion of **CTF** during the reflux reaction which creates a partially more crystalline material. None of the signatures of the **Ru-CTF** are ascribable to the [Ru(tda)(dmso)(py)] precursor, meaning that no aggregates of this compound are present in the **Ru-CTF** material.

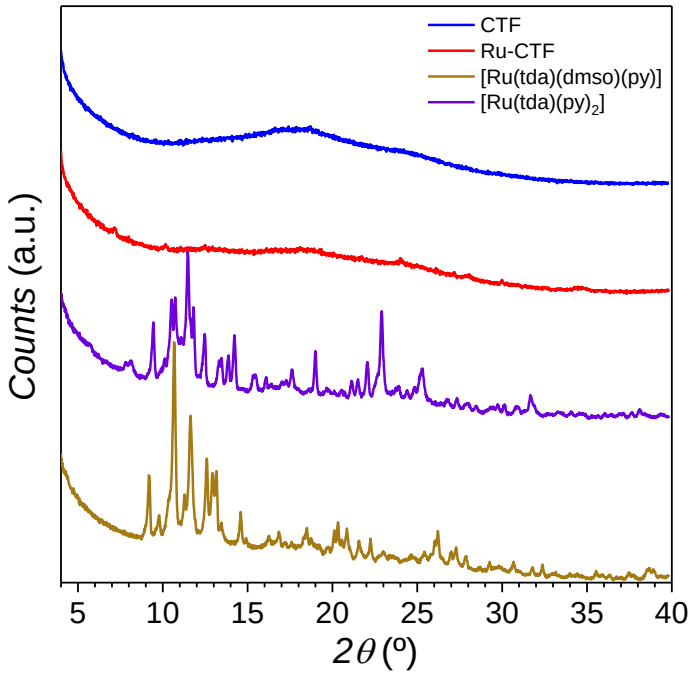

Figure S6. *PXRD pattern of* ***Ru-CTF*** *(red) and* ***CTF*** *(blue), compared to the precursor [Ru(tda)(dmso)(py)] (dark-yellow) and the reference catalyst [Ru(tda)(py)₂] (purple).*

Brunauer Emmett Teller (BET)

The type VI isotherms of both **CTF** and **Ru-CTF** represents stepwise multilayer adsorption on a non-porous or barely porous surface, meanwhile the hysteresis in the isotherms obtained shows a low mesoporous behavior in solid state.[19] The step-height represents the monolayer capacity for each adsorbed layer and, in the simplest case, remains nearly constant for two or three adsorbed layers. The lack of porosity is confirmed by the low surface area (SA_{BET} = 11.2 m^2/g and 21.7 m^2/g for **CTF** and **Ru-CTF**, respectively) obtained through the Brunauer Emmett Teller (BET) method (Figure S7a). The higher surface area detected for **Ru-CTF** could be due to the redispersion of the **CTF** during the reflux reaction, leading to increment of exposed surface. Additionally, application of the t-plot method revealed no microporosity,[7] in contrast with related CTFs reported in the literature.[12,13,17] Moreover, as detected through the Barrett Joyner Halenda (BJH) model, there is low nitrogen uptake indicative of a scarcely porous material (Figure S7b). Besides, in both cases the pore size distribution is not uniform, which is normally happening for purely amorphous systems,[18] and the pore diameter was calculated to be centered at around 17.3 nm and 18.3 nm for **CTF** and **Ru-CTF**, respectively. These results suggest the formation of compact aggregates when the **CTF** is in solid state, which was further confirmed by morphology studies by using scanning electron microscopy (SEM) and transmission electron microscopy (TEM) techniques, where disordered layers of the material and aggregated particles of different sizes were visible on a bare conductive surface (Figures S8-S9).

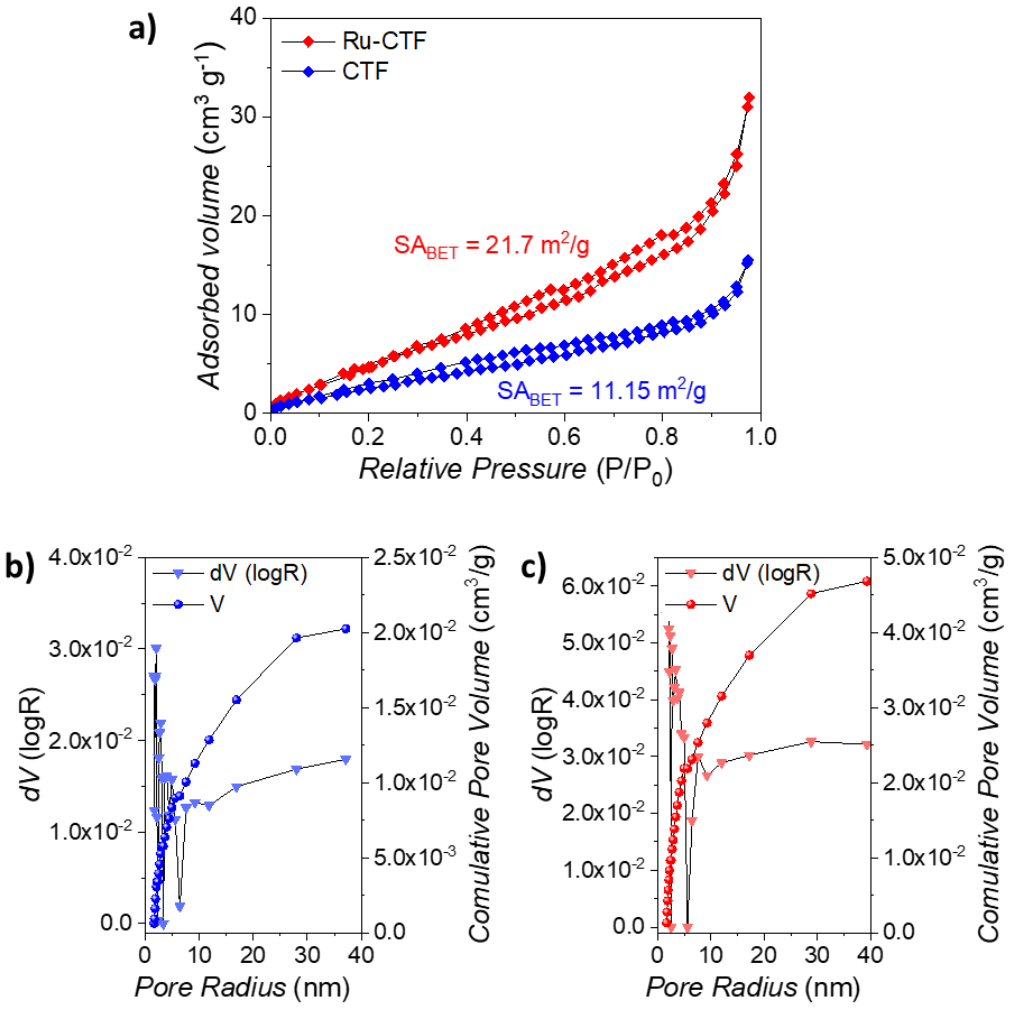

Figure S7. *N_2 adsorption-desorption isotherm (a) and pore size distribution analysis (b-c) of* ***CTF*** *(blue) and* ***Ru-CTF*** *(red).*

Microscopy

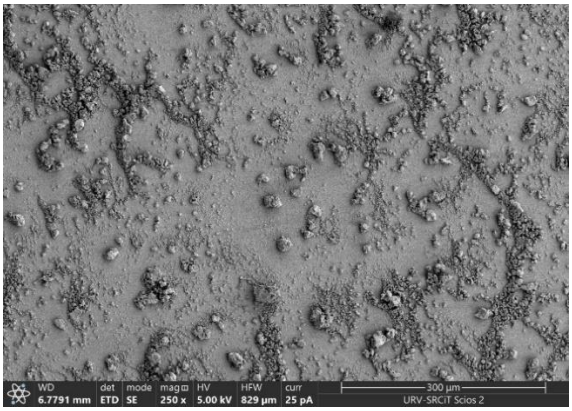

Figure S8. *SEM image of* ***CTF*** *drop-casted on top of an FTO electrode (****CTF*** *dispersion in MeOH).*

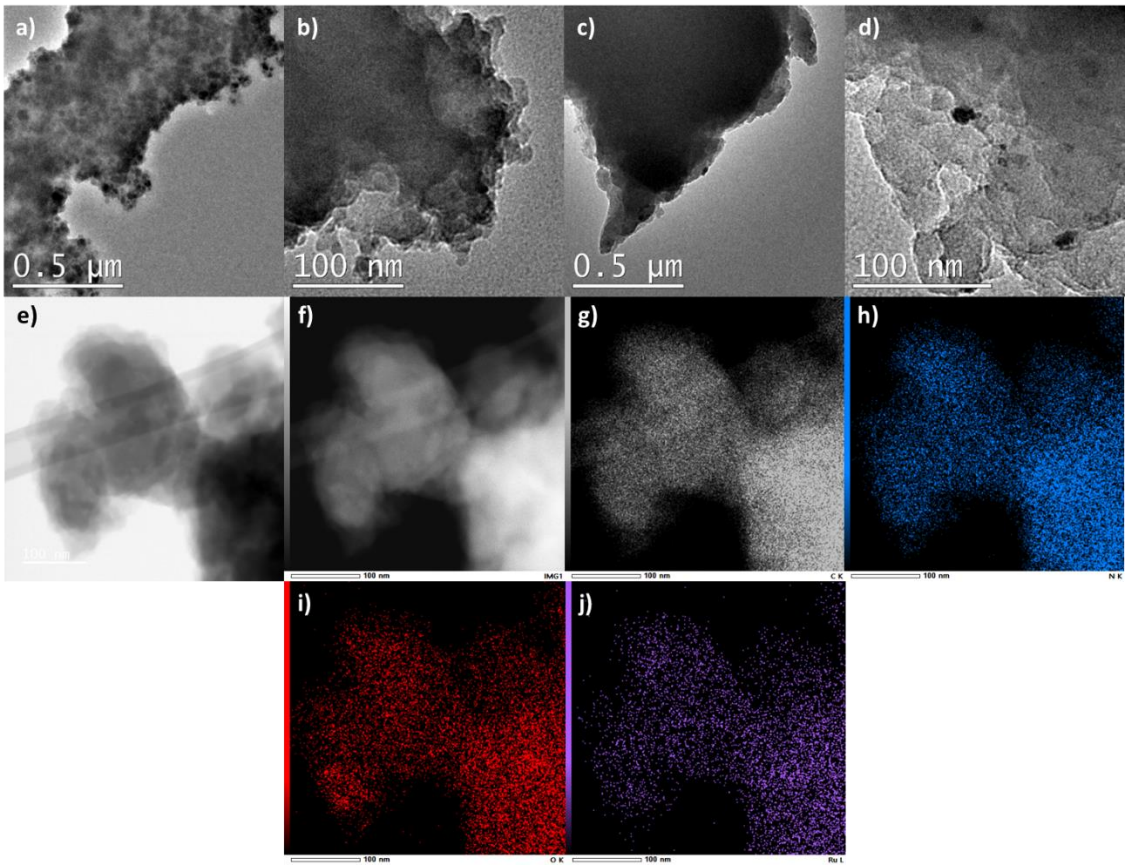

Figure S9. *TEM images of* ***CTF*** *(a, b) at 0.5 µm and 100 nm scales, and TEM images of* ***Ru-CTF*** *(c-d) at 0.5 µm and 100 nm scales. Annular dark-field (ADF) (e) and annular bright-field (ABF) (f) STEM images of* ***Ru-CTF*** *at 100 nm scale, with EDS mapping by elements: C (g), N (h), O (i) and Ru (j).*

Induced Coupled Plasma Optical Emission Spectroscopy (ICP-OES)

Table S1. *Average percentage content of Ru obtained via ICP-OES experiments performed on two samples of* ***Ru-CTF*** *(see Instrumentation section for further information).*

Sample	Weight analyzed (mg)	mol $_{Ru}$ / g $_{sample}$	g $_{Ru}$ / g $_{sample}$	Average Ru (%)
1	3.3	1.0×10^{-4}	9.8×10^{-3}	1.05%
2	2.6	1.1×10^{-4}	1.1×10^{-4}	

Electrochemistry and Impedance Spectroscopy

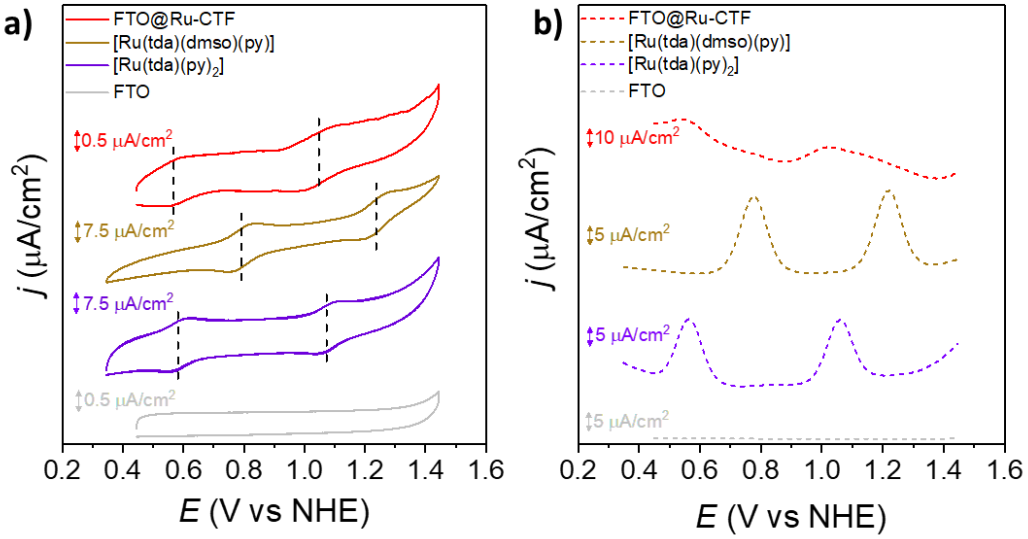

Figure S10. *Cyclic voltammetries (a) and differential pulsed voltammetries (b) of FTO@**Ru-CTF**, reference Ru complexes in solution and bare a FTO electrode in a 1 M phosphate buffer solution (pH 7), performed at a scan rate of 10 mV/s for FTO@**Ru-CTF** and FTO, at 20 mV/s for the Ru complexes.*

Table S2. *Comparison of redox potentials obtained for **Ru-CTF** with the reported values for the complexes [Ru(tda)(dmso)(py)] and [Ru(tda)(py)$_2$].*

Sample	$E_{1/2}$ ($Ru^{III/II}$) (V *vs.* NHE)	$E_{1/2}$ ($Ru^{IV/III}$) (V *vs.* NHE)	ΔE (V)
[Ru(tda)(dmso)(py)] [a]	0.80 [a]	1.24 [a]	0.06 ($Ru^{III/II}$); 0.06 ($Ru^{IV/III}$) [a]
[Ru(tda)(py)$_2$] [a]	0.59 [a]	1.08 [a]	0.06 ($Ru^{III/II}$); 0.06 ($Ru^{IV/III}$) [a]
Ru-CTF	0.58	1.05	0.06 ($Ru^{III/II}$); 0.07 ($Ru^{IV/III}$)

[a] Values of potentials reported in literature.[3]

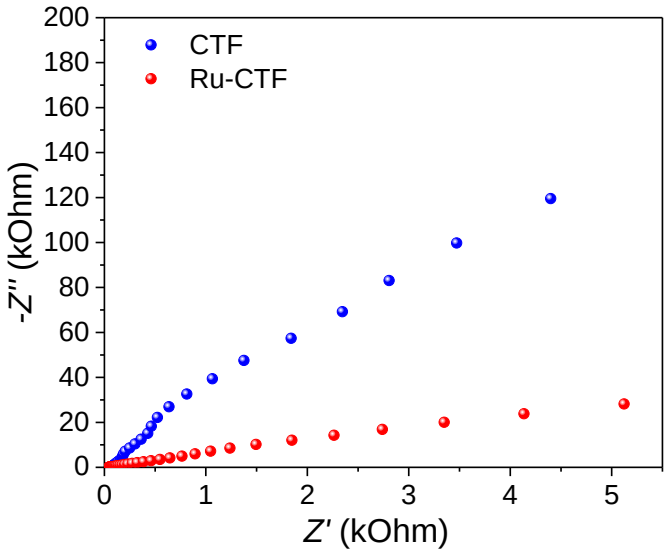

Figure S11. *Nyquist plot for* ***Ru-CTF*** *(red dots) and* ***CTF*** *(blue dots), performed at 0 V bias (open circuit potential, OCP), applying an amplitude for the sinusoidal perturbation of 5 mV and a range of frequencies between 1 Hz and 1 MHz. The Nyquist plot shows how the resistivity decreases with the addition of the catalyst, underlining the better charge transfer happening from the* ***CTF*** *through the Ru center to water for the WOR.*

UV-vis Diffuse Reflectance Spectroscopy (DRS)

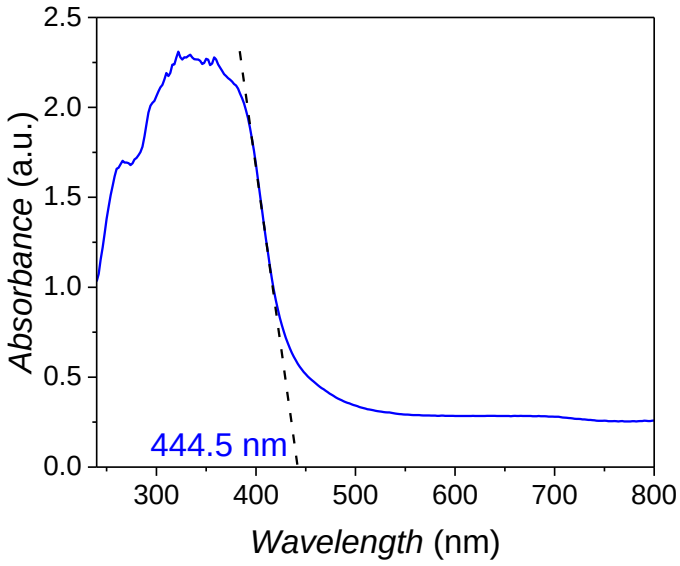

Figure S12. *UV-vis absorbance spectrum of* ***CTF****, obtained from the UV-vis DRS experiment.*

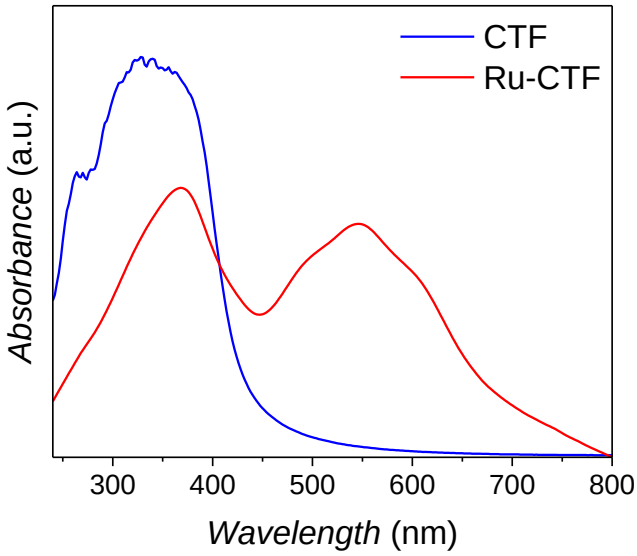

Figure S13. *UV-vis absorbance spectra (arbitrary unit) of* ***Ru-CTF*** *(red line) and* ***CTF*** *(blue line).*

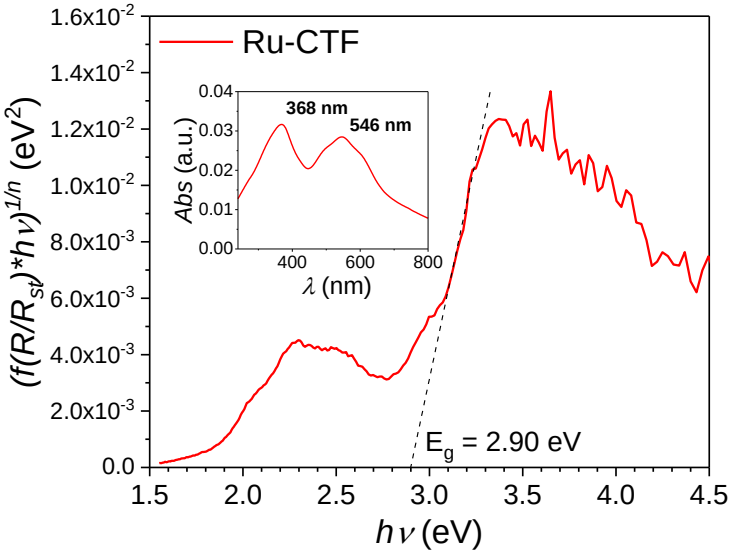

Figure S14. *Tauc plot of* ***Ru-CTF*** *compared to the absorbance spectrum (inset graph).* ***Ru-CTF*** *powder was diluted with* $BaSO_4$ *for the analysis, in order to avoid the saturation of the spectrometer in the reflectance mode.*

Photocatalytic experiments

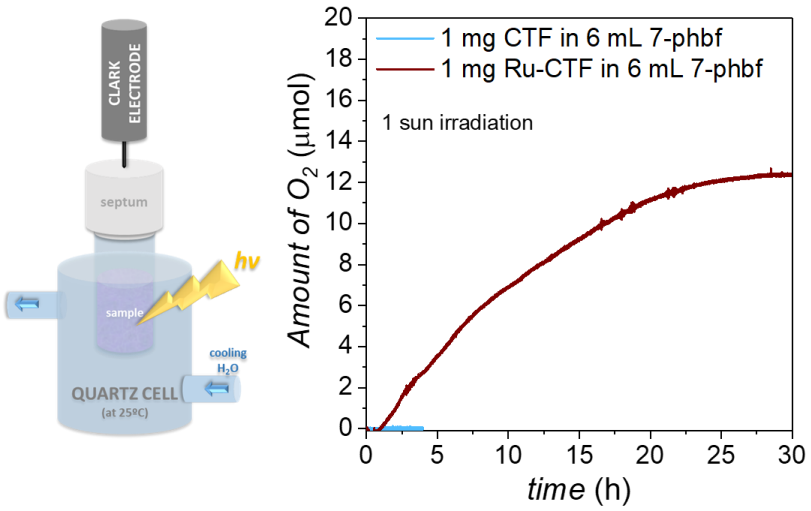

Figure S15. *On the left, schematic figure of the setup used for the photocatalysis experiments, including a thermostatic quartz cell, a septum to keep the inert atmosphere and the Clark-type electrode for oxygen detection in gas phase. On the right, an experiment of O_2 detection performed with the following conditions: 1 sun illumination, full arc, 12 mM SEA, 25 mM pH 7 phbf, using 1 mg /6 mL of* ***CTF*** *and* ***Ru-CTF*** *(light-blue and dark-red traces, respectively). See the experimental section for further details.*

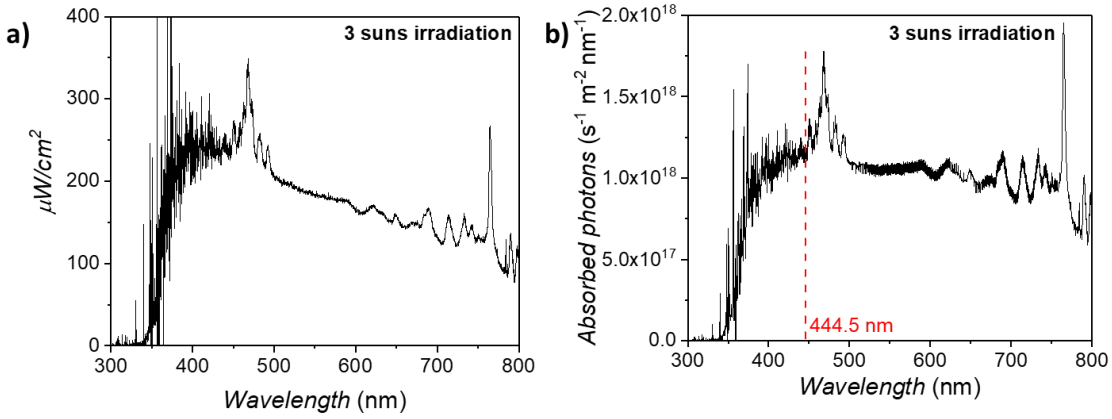

Figure S16. *(a) Solar spectrum of the Xe lamp used for the experiments at 3 suns irradiation power; (b) Photons absorbed by the dispersion calculated from the normalized solar spectrum (choosing the range of maximum absorbance of the* ***CTF****, as shown in Fig. S12).*

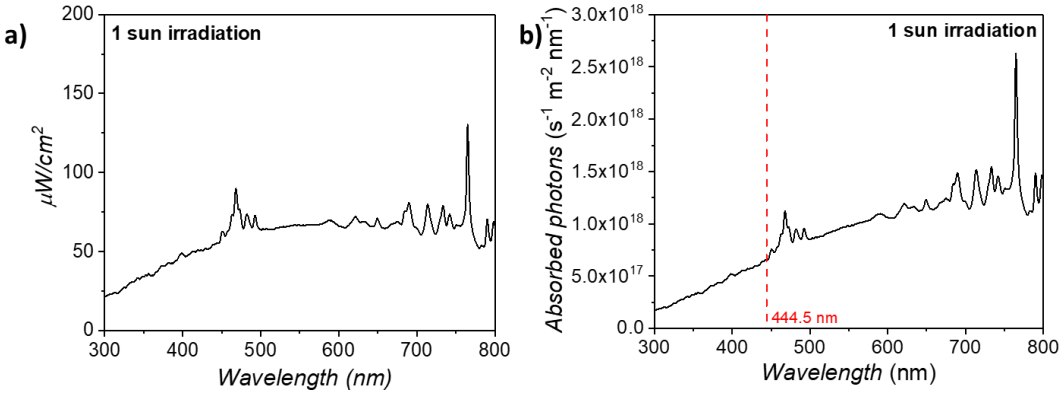

Figure S17. *(a) Solar spectrum of the Xe lamp used for the experiments at 1 suns irradiation power; (b) Photons absorbed by the dispersion calculated from the normalized solar spectrum (choosing the range of maximum absorbance of the* ***CTF****, as shown in Fig. S12).*

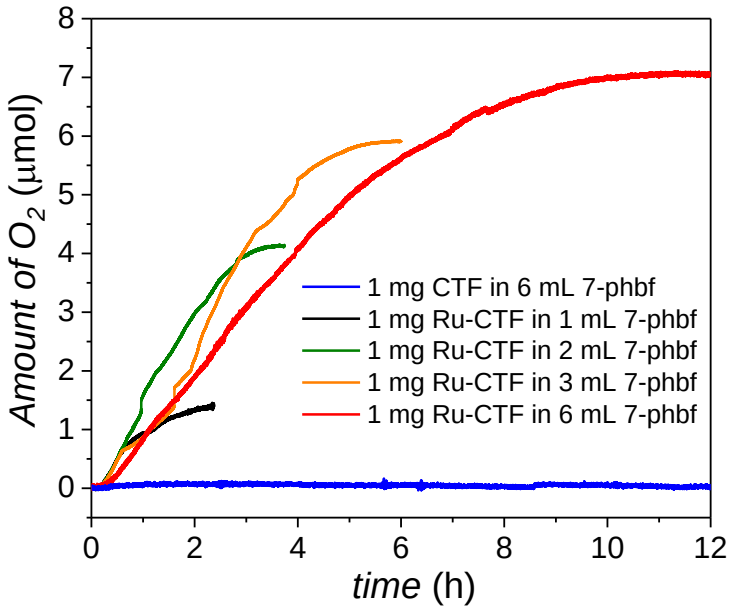

Figure S18. *Experiments of photocatalysis for O_2 production by **Ru-CTF** at different concentrations: 1 mg /1 mL (black trace), 1 mg /2 mL (green trace), 1 mg /3 mL (orange trace), 1 mg /6 mL (red trace). The compound was used under the following experimental conditions: 3 suns illumination, full arc, 10 mM SEA, 25 mM 7-phbf. A control experiment was also performed using 1 mg /6 mL **CTF** (blue trace). See the experimental section for further details.*

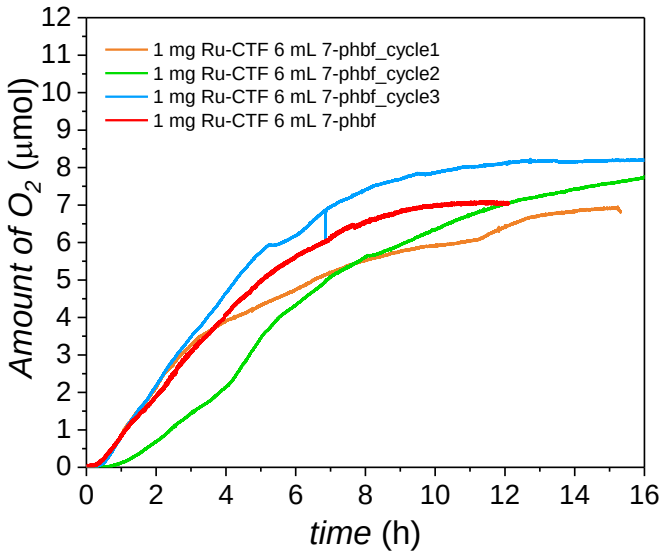

Figure S19. *Cyclic runs for O_2 production by* ***Ru-CTF****. The same compound was used three times under the following experimental conditions: 3 suns illumination, full arc, 10 mM SEA, 1 mg of* ***Ru-CTF*** *in 6 mL 7-phbf (25 mM). The experiments of cycles (cycle 1 as orange trace, cycle 2 as green trace, cycle 3 as blue trace) are compared with the reference (red line) already reported in Fig. S18. See the experimental section for further details (Photocatalysis measurements).*

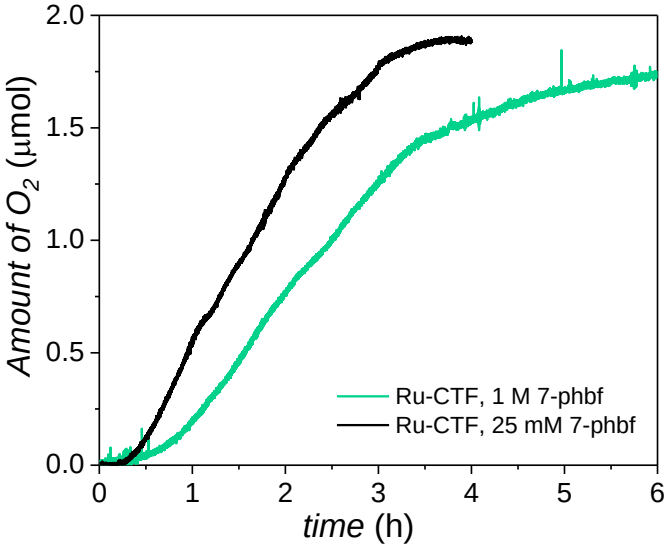

Figure S20. *Photoinduced oxygen detection experiments concerning the use of 25 mM of 7-phbf (black line) and 1 M 7-phbf (green line). 2 mg of* ***Ru-CTF*** *in 2 mL of buffer solution, 10 mM of SEA, 3 suns illumination in full arc.*

X-ray absorption spectroscopy (XAS)

As shown in the main manuscript, XAS spectroscopy shows the absence of any traces of RuO_2 after catalysis. This can be monitored by the specific peak at around 22148 eV (visualized as a minimum in the RuO_2 derivative), as well as by the absence of RuO_2 EXAFS spectrum features shown in Figure 1.

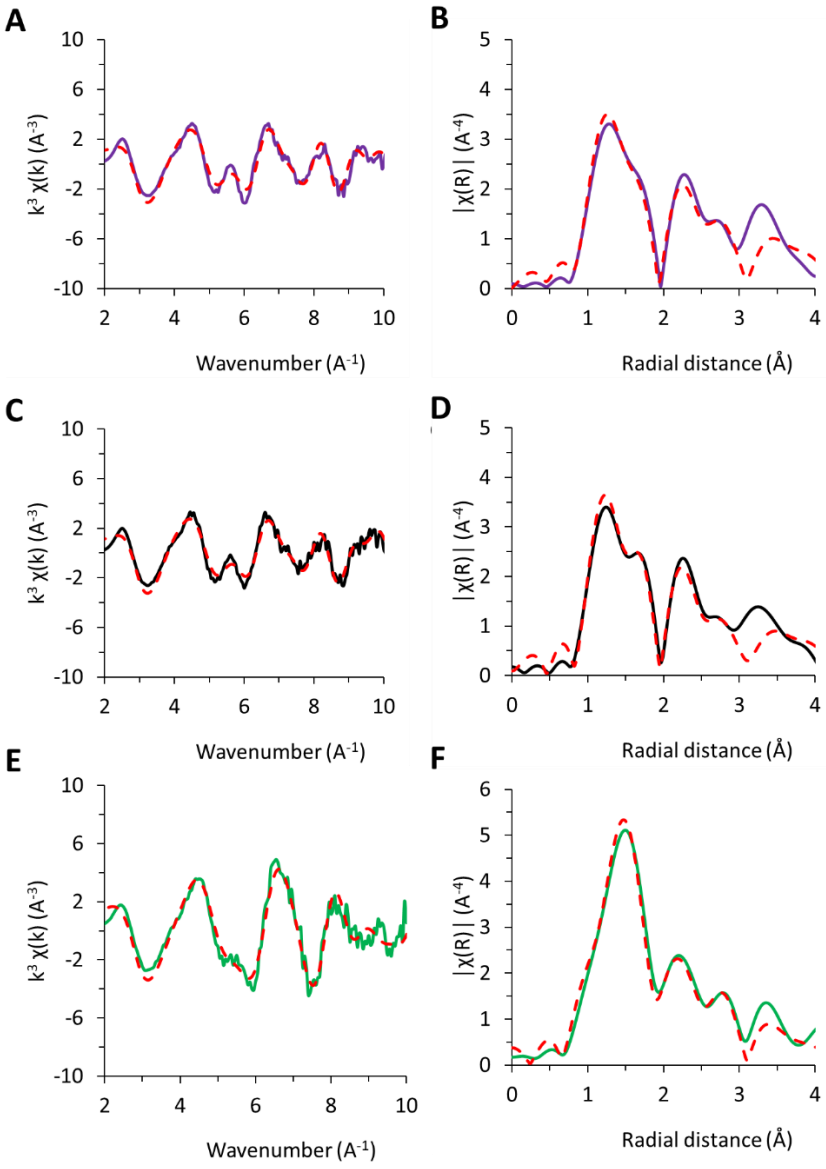

Figure S21. *Plot of the k^3-weighted Ru EXAFS and the corresponding Fourier transforms for [Ru(tda)(py)₂] (purple, a and b),* ***Ru-CTF*** *(black, c and d) and* ***Ru-CTF*** *after photocatalysis (green, e and f). Experimental data are represented as solid lines and fitted as dashed lines. Experimental spectra were fitted for over a k-range of 2–10 $Å^{-1}$.*

The spectra of the parent [Ru(tda)(py)$_2$] and the **Ru-CTF** are identical, which confirms the coordination to the pendant pyridines in the **CTF** structure and therefore the

formation of [Ru^{II}(tda-*k*-N^3O^1)$(py)_2$]. After catalysis the spectra changes due to a modification of the species (activation) as observed in previous works.[20] Particularly a rearrangement of the coordination sphere around the Ru center, with the introduction of an H_2O ligand leading to the active form of the catalyst [Ru^{II}(tda-*k*-N^3)$(py)_2(OH_2)$].[21]

Table S3. *EXAFS fitting parameters*

Sample	Region	Shell, N	Path	R, Å	σ^2 (10^{-3})	s^2	E_0,eV	R-factor	Reduced Chi-square
$[Ru^{II}(tda)(py)_2]$	k = 2 – 10	Ru-N/O, 3	Single path	1.92	1.5	0.9	-3.78	0.060	160
	R = 1 – 4	Ru-N/O, 3	Single path	2.07	1.8				
		Ru-C, 12	Single path	2.91	8.9				
		Ru-C, 24	Obt. triangle	3.12	2.6				
		Ru-C, 10	Single path	4.31	2.1				
Ru-CTF	k = 2 – 10	Ru-N/O, 3	Single path	1.92	0.3	0.9	-3.23	0.047	54
	R = 1 – 4	Ru-N/O, 3	Single path	2.08	0.4				
		Ru-C, 12	Single path	2.91	9.3				
		Ru-C, 24	Obt. triangle	3.13	4.1				
		Ru-C, 10	Single path	4.32	2.5				
Ru-CTF after catalysis	k = 2 – 10	Ru-N/O, 2	Single path	1.89	0.3	0.9	-3.84	0.026	20
	R = 1 – 4	Ru-N/O, 4	Single path	2.04	1.3				
		Ru-C, 12	Single path	2.93	5.4				
		Ru-C, 24	Obt. triangle	3.10	3.9				
		Ru-C, 10	Single path	4.39	3.4				

Dynamic Light Scattering

The experiment shown in Figure S22 shows the evolution of the particles size of **Ru-CTF** at high concentration under photocatalytic conditions over time. At the beginning, right after the preparation of the dispersion (t = 0 min, yellow dashed line), the measurement exhibits two intense distributions, centered at around 0.2 µm and 0.5 µm, apart from other two smaller signals at around 2.5 and 10 µm. After 60 minutes of irradiation (orange dashed line), the quantity of bigger particles (ranging from 2 to 30 µm) starts decreasing while the middle-size distribution is increasing (changing from 5 % to 8 % of total volume of sample detected). This means that the bigger particles got better dispersed with stirring and irradiating. At t = 120 min (green dashed line) the instrument starts detecting only one distribution from 0.4 to 1 µm, centered at 0.7 µm, indicating that under photocatalytic conditions the particles are getting aggregated. The same trend can be noted at t = 180 min (blue dashed line), confirming the aggregation of the particles during the experiment. The DLS experiment can thus suggest an aggregation phenomenon happening over time at high **Ru-CTF** concentration, resulting in a decrease of catalytic active sites and finally a slower catalytic water oxidation (see Fig. 4 and S18).

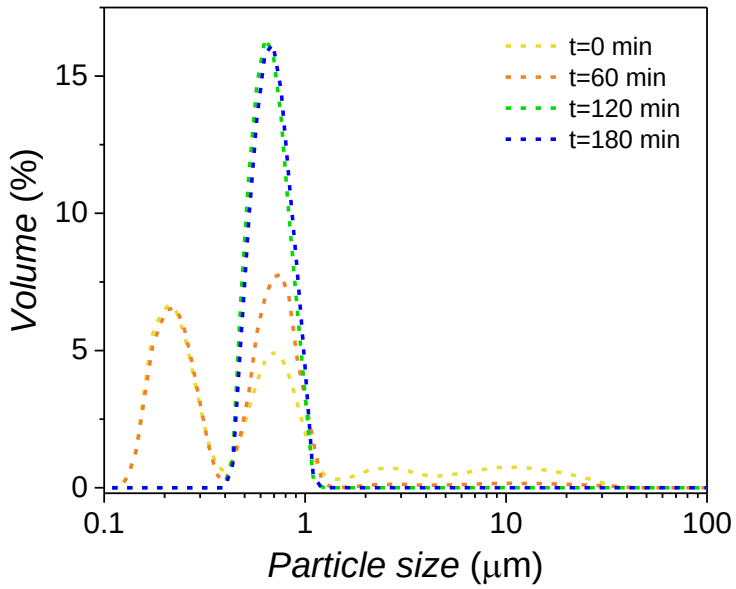

Figure S22. *Dynamic Light Scattering experiments of 0.5 mg/mL* ***Ru-CTF*** *dispersed in 20 mL of 25 mM 7-phbf solution and 10 mM SEA under 3-sun irradiation, analyzed at different irradiation times during photocatalysis. See the Instrumentation section for further information.*

Table S4. *Values (µm) of different distributions (D10, D50, D90) of the* ***Ru-CTF*** *particles at different times of analysis, got from Figure S22. The parameters D10, D50 and D90 stand for the size distribution of the 10%, the 50% and the 90% of the particles detected by the instrument.*

Analysis	D10 (µm)	D50 (µm)	D90 (µm)	Irradiation time (min)
1	0.171	0.5	6.203	0
2	0.173	0.514	0.896	60
3	0.488	0.629	0.834	120
4	0.499	0.648	0.856	180

Table S5. *Calculated values of average, standard deviation of the populations (SD) and relative standard deviation (RSD (%)) for the three distributions.*

	D10 (µm)	D50 (µm)	D90 (µm)
Average (µm)	0.3	0.6	1.9
SD	0.2	0.1	2.4
RSD (%)	58.50	12.96	124.24

Photoluminescence studies

Table S6. *Fluorescence lifetime of the* ***CTF****.*

Material [a]	τ_1 (ns)	τ_2 (ns)	τ_3 (ns)	B_1 (%)	B_2 (%)	B_3 (%)	X^2	τ_{avg} [c] (ns)
CTF	0.3	1.1	6.3	43.0	54.0	3.0	1.01	2.1
CTF, SEA 10 mM [b]	0.3	1.1	6.0	42.4	54.4	3.2	1.04	2.0
CTF, SEA 100 mM [b]	0.2	1.0	4.9	38.0	58.0	4.0	1.17	1.8

[a] PL decay measured at 450 nm upon 404 nm excitation wavelength. [b] Emission decays measured in presence of the SEA $Na_2S_2O_8$. [c] The emission decays were deconvoluted from IRF and adjusted a tri-exponential function. The average lifetime τ_{avg} was calculated as according to $\tau_{avg} = \sum_i B_i t_i^2 / \sum_i B_i t_i$.

3.6.6. Computational methods

Ru-CTF Model

Ru-CTF model has been developed by optimizing the geometry of covalent triazine-based framework (CTF) with a dangling pyridyl group connected via ethylene linker (Fig. S23a) at GFN2-xTB level of theory[22] using ORCA software package[23–25] and then adopting a subsystem of the CTF for the cluster model (Fig. S23a) with introduction of $Ru(tda)(py)_2$ complex (Fig. S23b). This subsystem of CTF together with $Ru(tda)(py)_2$ constitutes the computational **Ru-CTF** cluster model (Fig. S23b). The positions of all atoms in the CTF subsystem including the ethylene linker were kept fixed in the subsequent geometry optimization steps described below (Fig. S23b).

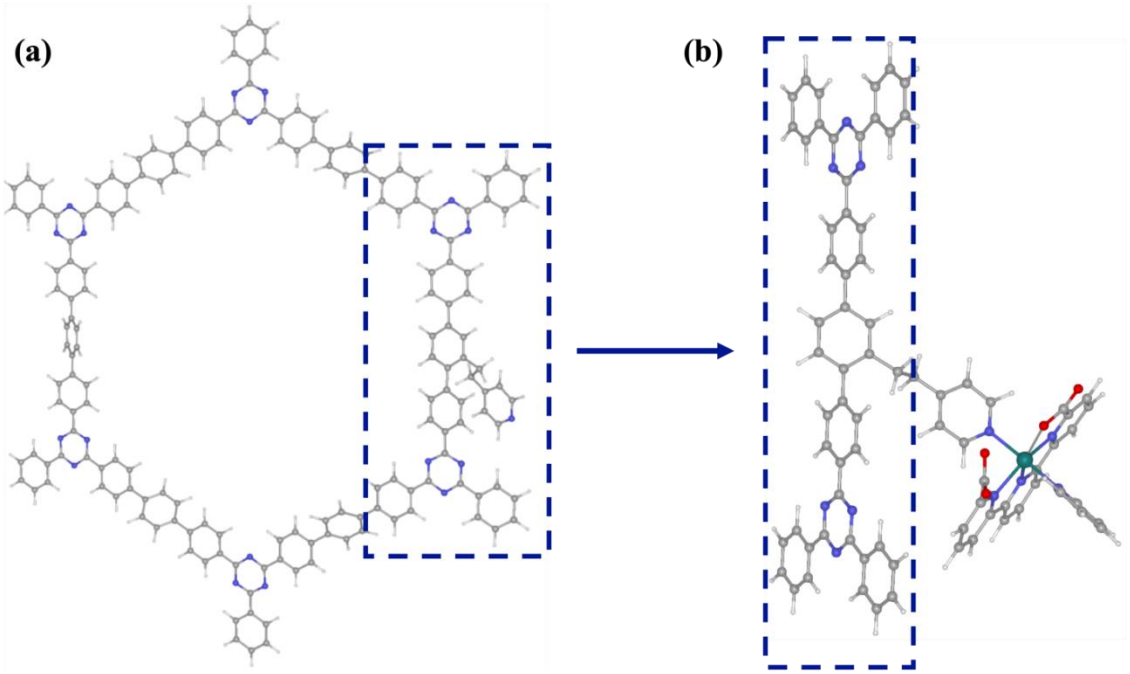

Figure S23. *(a) Optimized structure of covalent triazine-based framework (**CTF**) with a dangling pyridyl group at GFN2-xTB level and highlighted subsystem of **CTF** adopted for (b) **Ru-CTF** cluster model.*

Density functional theory

All geometries were optimized at the M06-L level of density functional theory[26] in conjunction SMD continuum solvation model[27] for water using def2-TZVP basis set[28,29] on Ru and the def2-SV(P) basis set[30] on all other atoms. Non-analytical integrals were evaluated using the integral=grid=ultrafine option as implemented in the Gaussian 16 software package.[31] The nature of all stationary points was verified by analytic

computation of vibrational frequencies, which were also used for the computation of zero-point vibrational energies and molecular partition functions. Partition functions were used in the computation of 298 K thermal contributions to the free energy employing the usual ideal-gas, rigid-rotator, harmonic oscillator approximation.[32] To avoid spurious errors for the free energy calculations, all frequencies below 50 cm^{-1} were replaced by 50 cm^{-1}. A 1 M standard state was used for all species in solution, thus, an adjustment for the 1 atm to 1 M standard-state concentration change of RT ln(24.5), (1.89 kcal/mol at 298 K) was added to the computed free energies.[32] Free-energy contributions were added to single-point MN15[33] electronic energies computed using SMD continuum solvation model for water at the optimized geometries obtained with the initial basis with the def2-TZVPP basis set on Ru and the def2-TZVP basis set on all other atoms to arrive at final, composite free energies.

Time-dependent density functional theory

Time-dependent density functional theory (TDDFT) calculations were performed, as implemented in the Gaussian 16 software package, to predict the UV/visible electronic excitations of relevant structures of **Ru-CTF** cluster model. Twenty singlet and twenty triplet excited states in the case of closed-shell electronic structures were considered. The MN15 density functional, the def2-TZVP basis set on Ru and the def2-SV(P) basis set on all other atoms were used for the TDDFT calculations. Non-equilibrium solvation effects were included *via* the linear response approximations[34] in combination with the SMD continuum solvation model for water.

Constrained density functional theory

Constrained DFT (CDFT)[35,36] calculations using spin constraints as implemented in Q-Chem 5.0 software package[37] were performed to compute the relative energies of diabatic states. CDFT calculations were performed at the MN15 level of theory with the IEFPCM continuum solvation model for water using the Sapporo-DZP basis set[38] on Ru and the 6-31G(d) basis set[39] on all other atoms. **Ru-CTF** cluster model is partitioned into two fragments at the ethylene bridge for the spin constraint CDFT calculations (Fig. S24).

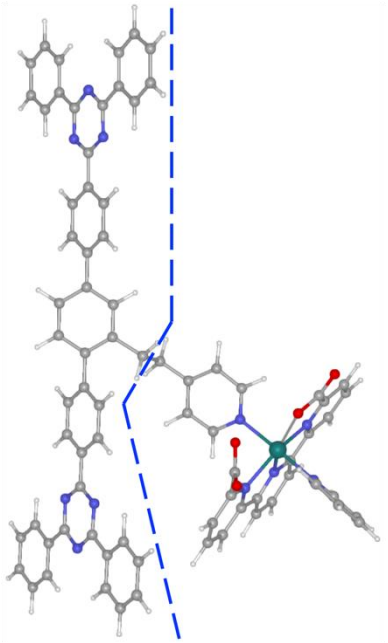

Figure S24. *Partition of* ***Ru-CTF*** *cluster model to two fragments for spin constraint CDFT calculations.*

3.6.7. Density Functional Theory Calculations

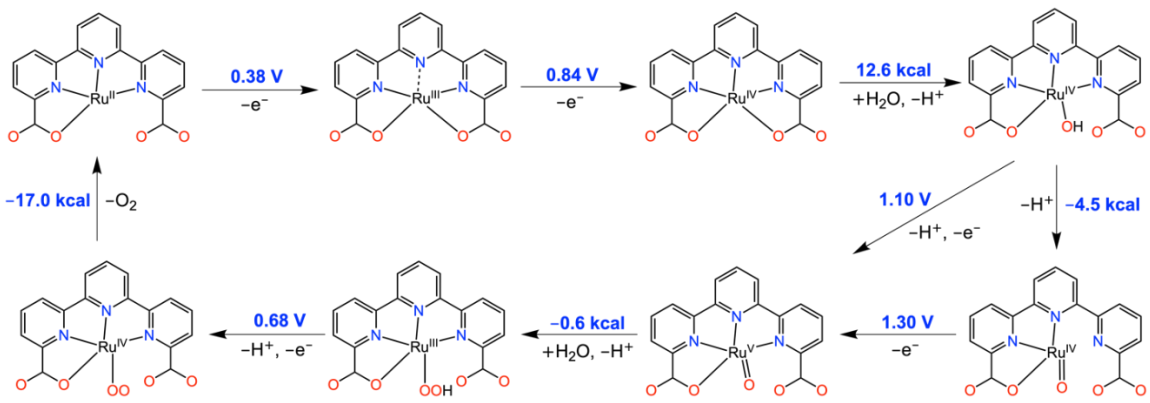

Figure S25. *Proposed water oxidation mechanism for [Ru(tda)(py)₂] catalyst. Computed oxidation potentials in units of V vs. NHE and Gibbs free energies in units of kcal/mol at MN15 level of theory at pH 7.0.*

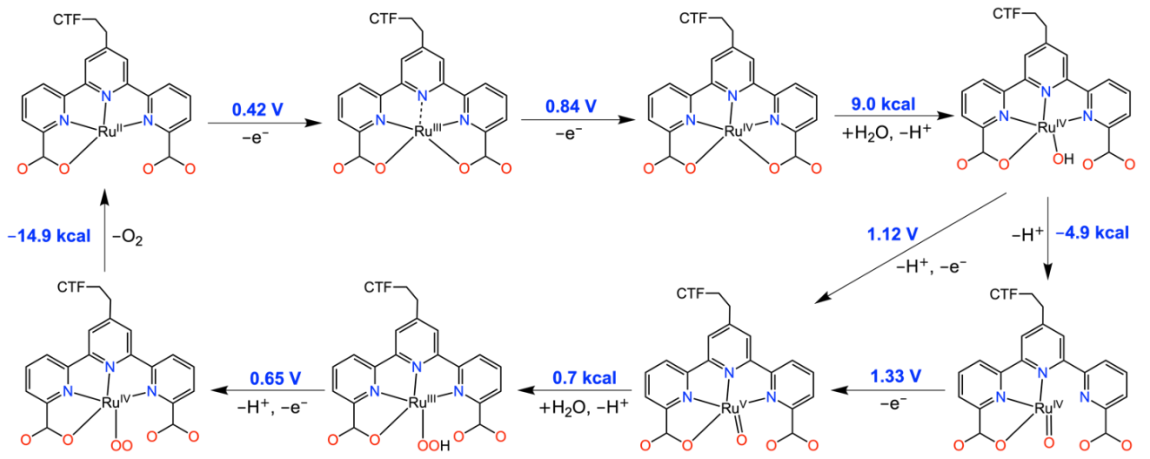

Figure S26. *Proposed water oxidation mechanism for **Ru-CTF** using cluster model. Computed oxidation potentials in units of V vs. NHE and Gibbs free energies in units of kcal/mol at MN15 level of theory at pH 7.0.*

3.6.8. Time Dependent Density Functional Theory Calculations

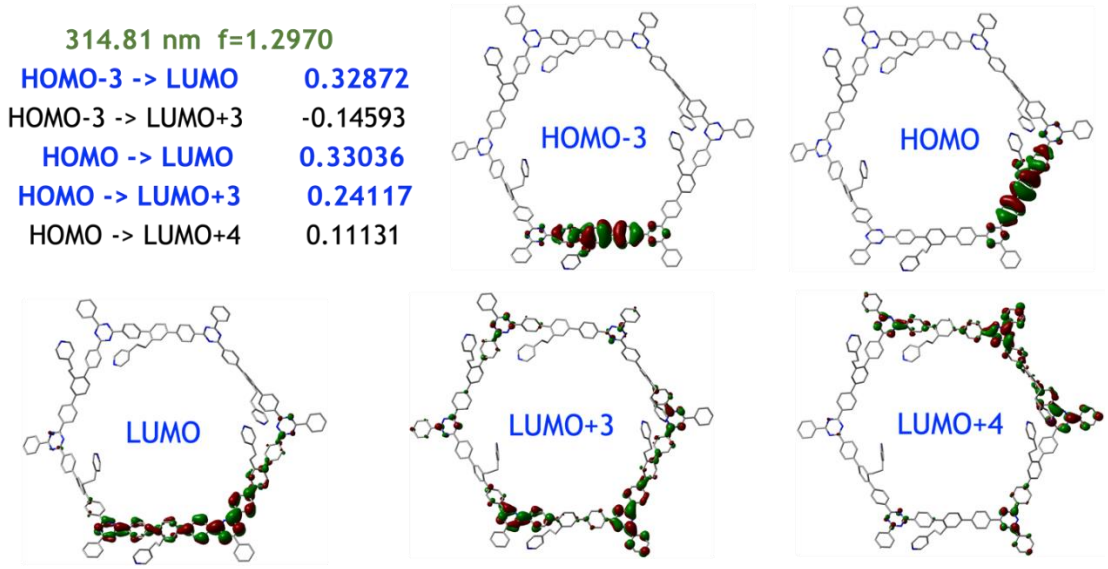

Figure S27. *First singlet electronic excitation of* ***CTF*** *model and selected set of orbitals relevant to the electronic excitation obtained via TDDFT calculations at MN15 level of theory. Wavelength of the electronic excitation (in nm) along with oscillator strength (f) and largest coefficients of configuration interaction expansion are shown.*

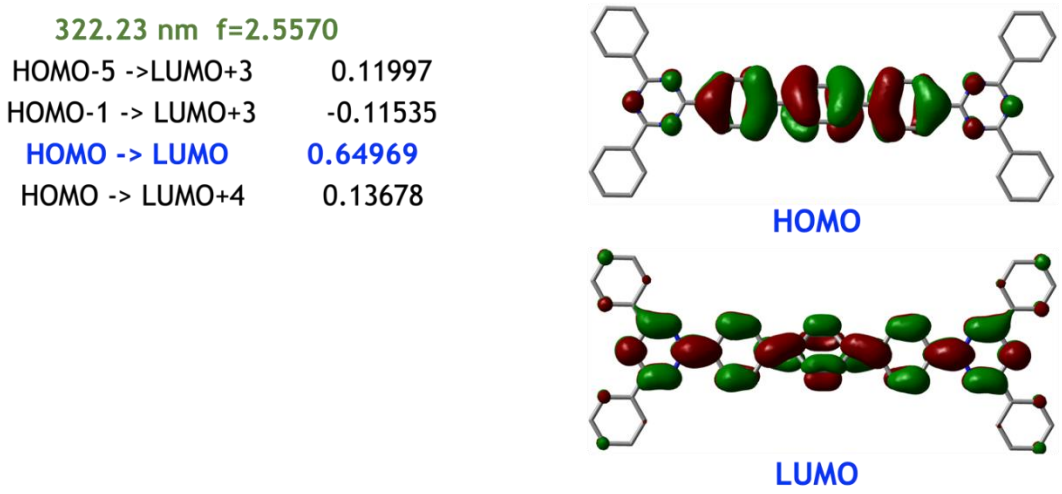

Figure S28. *First singlet electronic excitation of subsection of* ***CTF*** *model and selected set of orbitals relevant to the electronic excitation obtained via TDDFT calculations at MN15 level of theory. Wavelength of the electronic excitation (in nm) along with oscillator strength (f) and largest coefficients of configuration interaction expansion are shown.*

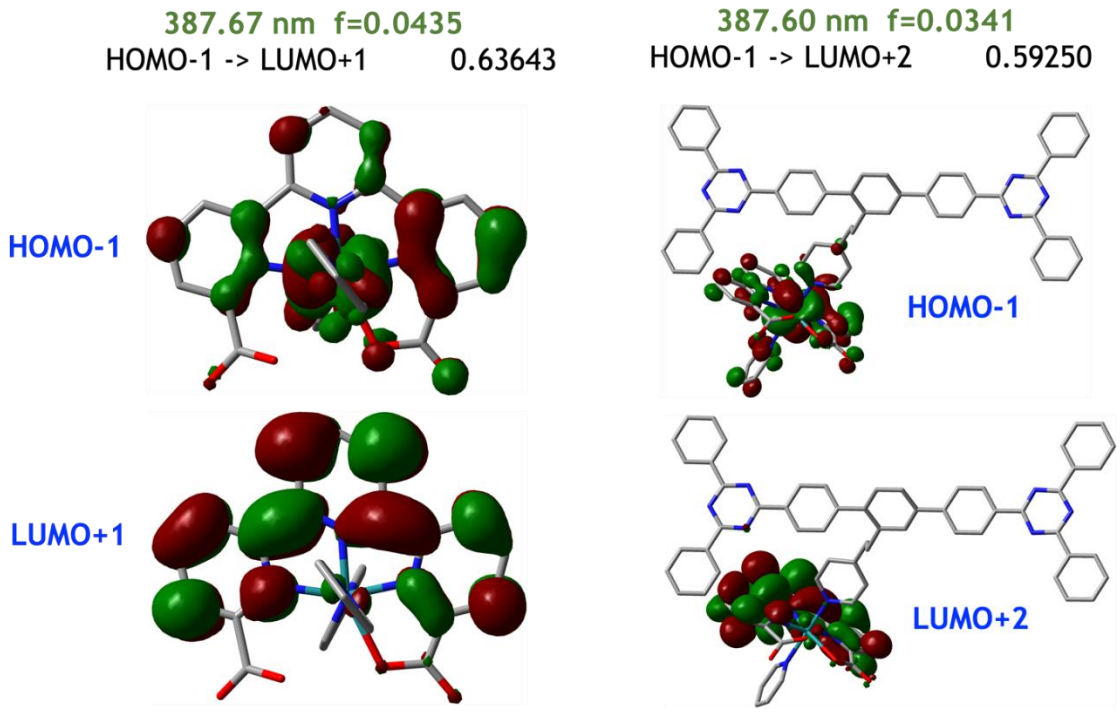

Figure S29. *Comparison of relevant singlet electronic excitations of [Ru(tda)(py)$_2$] and* ***Ru-CTF*** *cluster model, and selected set of orbitals relevant to the electronic excitation obtained via TDDFT calculations at MN15 level of theory. Wavelength of the electronic excitation (in nm) along with oscillator strength (f) and largest coefficients of configuration interaction expansion are shown.*

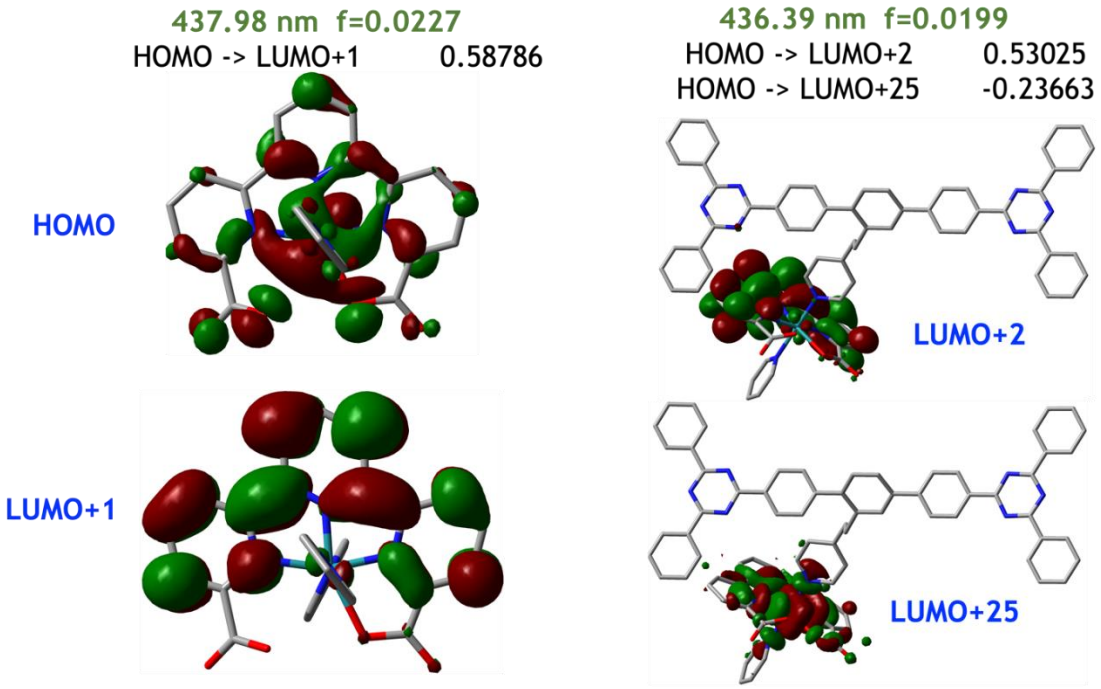

Figure S30. *Comparison of relevant singlet electronic excitations of [Ru(tda)(py)$_2$] and* ***Ru-CTF*** *cluster model, and selected set of orbitals relevant to the electronic excitation obtained via TDDFT calculations at MN15 level of theory. Wavelength of the electronic excitation (in nm) along with oscillator strength (f) and largest coefficients of configuration interaction expansion are shown (cont.).*

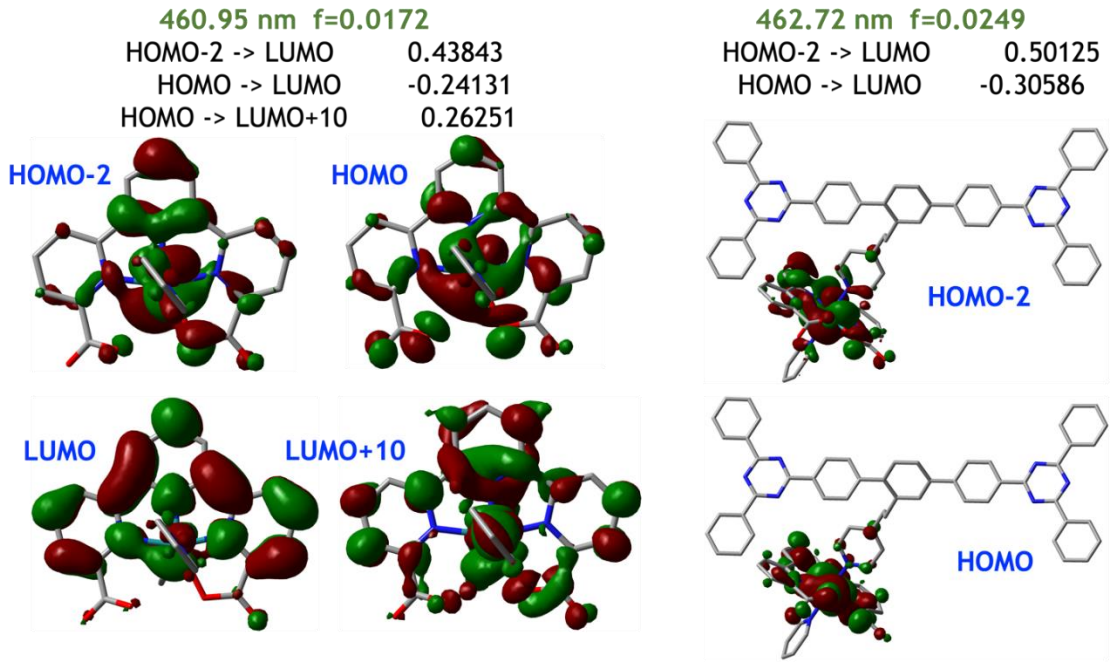

Figure S31. *Comparison of relevant singlet electronic excitations of [Ru(tda)(py)$_2$] and* ***Ru-CTF*** *cluster model, and selected set of orbitals relevant to the electronic excitation obtained via TDDFT calculations at MN15 level of theory. Wavelength of the electronic excitation (in nm) along with oscillator strength (f) and largest coefficients of configuration interaction expansion are shown (cont.).*

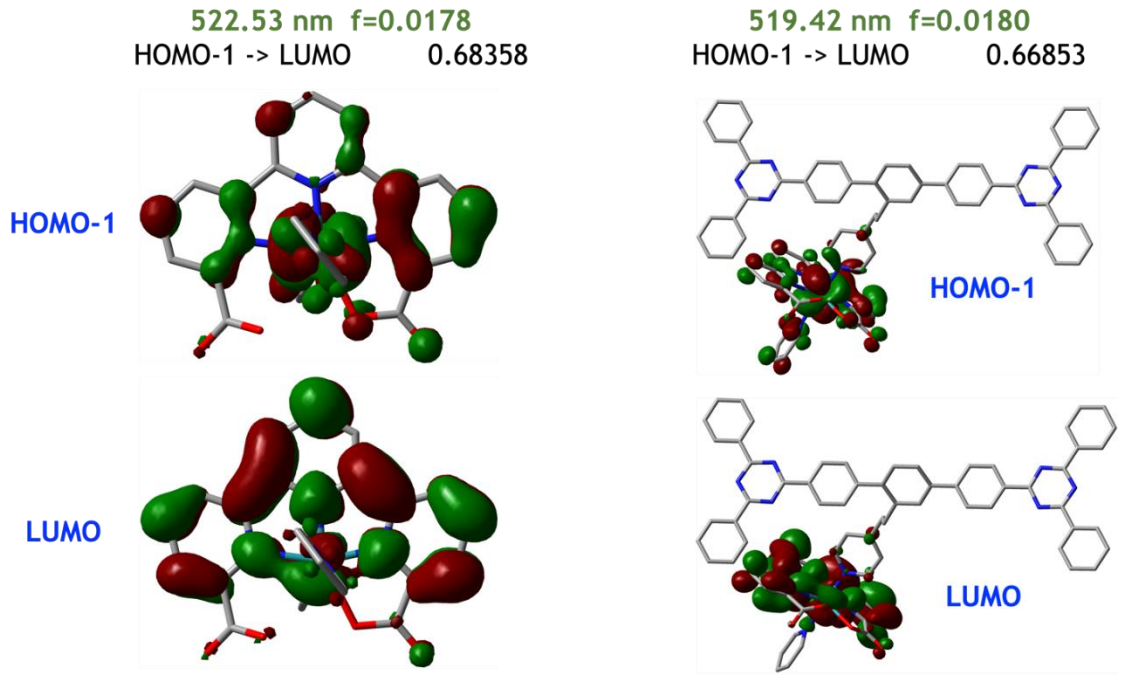

Figure S32. *Comparison of relevant singlet electronic excitations of [Ru(tda)(py)$_2$] and* ***Ru-CTF*** *cluster model, and selected set of orbitals relevant to the electronic excitation obtained via TDDFT calculations at MN15 level of theory. Wavelength of the electronic excitation (in nm) along with oscillator strength (f) and largest coefficients of configuration interaction expansion are shown (cont.).*

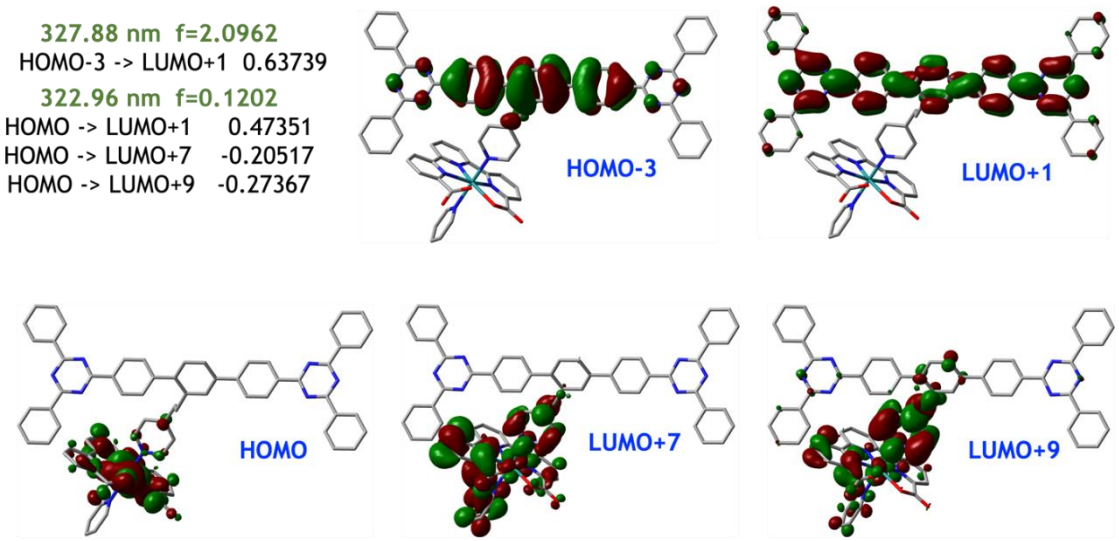

Figure S33. *Selected singlet electronic excitations of* ***Ru-CTF*** *cluster model and selected set of orbitals relevant to the electronic excitation obtained via TDDFT calculations at MN15 level of theory. Wavelength of the electronic excitation (in nm) along with oscillator strength (f) and largest coefficients of configuration interaction expansion are shown (cont.).*

Table S7. *Comparison of singlet electronic excitations of [Ru(tda)(py)$_2$] and* ***Ru-CTF*** *cluster model obtained via TDDFT calculations at MN15 level of theory. Wavelength of the electronic excitations (in nm) and oscillator strengths (f) are shown (cont.).*

Ru(tda)(py)$_2$	**Ru-CTF**
Excited State 1: 581.43 nm f=0.0013	Excited State 1: 580.17 nm f=0.0012
Excited State 2: 522.53 nm f=0.0178	Excited State 2: 519.42 nm f=0.0180
Excited State 3: 460.95 nm f=0.0172	Excited State 3: 462.72 nm f=0.0249
Excited State 4: 451.11 nm f=0.0068	Excited State 4: 448.61 nm f=0.0043
Excited State 5: 437.98 nm f=0.0227	Excited State 5: 436.39 nm f=0.0199
Excited State 6: 403.39 nm f=0.0022	Excited State 6: 403.92 nm f=0.0329
Excited State 7: 399.19 nm f=0.0315	Excited State 7: 402.49 nm f=0.0050
Excited State 8: 387.67 nm f=0.0435	Excited State 8: 387.60 nm f=0.0341
Excited State 9: 383.01 nm f=0.0166	Excited State 9: 384.61 nm f=0.0189
Excited State 10: 380.61 nm f=0.0059	Excited State 10: 379.13 nm f=0.0047
Excited State 11: 369.92 nm f=0.0066	Excited State 11: 369.04 nm f=0.0067
Excited State 12: 345.73 nm f=0.0205	Excited State 12: 347.03 nm f=0.0321
Excited State 13: 342.85 nm f=0.0268	Excited State 13: 343.05 nm f=0.0019
Excited State 14: 339.37 nm f=0.0202	Excited State 14: 339.43 nm f=0.0436
Excited State 15: 339.04 nm f=0.0212	Excited State 15: 337.24 nm f=0.0101
Excited State 16: 324.09 nm f=0.0147	Excited State 16: 327.88 nm f=2.0962
Excited State 17: 322.69 nm f=0.0056	Excited State 17: 322.96 nm f=0.1202
Excited State 18: 318.12 nm f=0.0060	Excited State 18: 320.44 nm f=0.0093
Excited State 19: 313.29 nm f=0.0444	Excited State 19: 319.02 nm f=0.0102
Excited State 20: 305.48 nm f=0.0269	Excited State 20: 316.70 nm f=0.0219

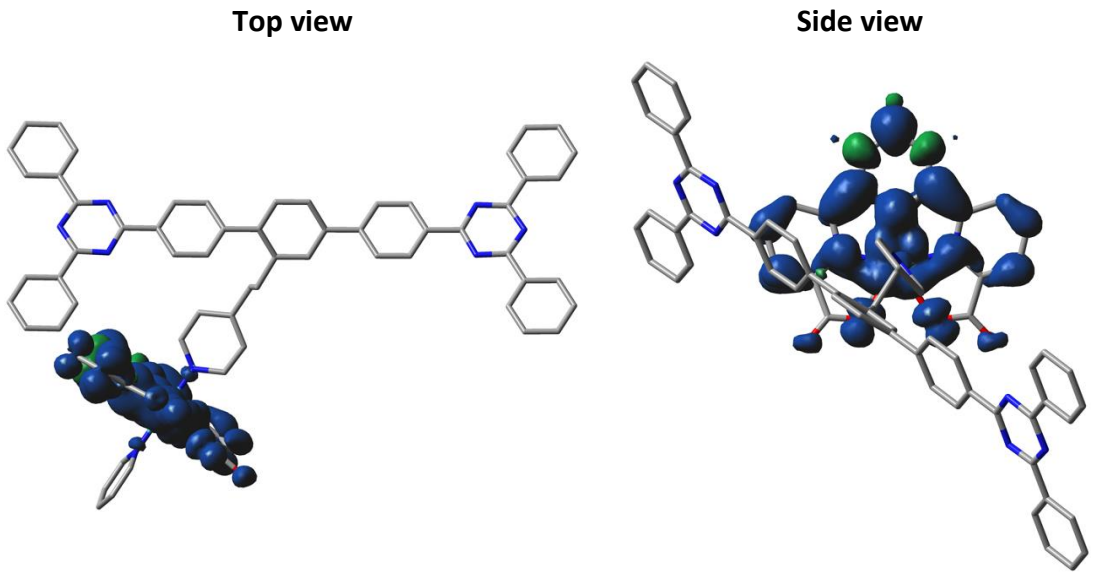

Figure S34. *Unpaired spin density plots of* ***CTF-^{3}Ru*** *state at MN15 level of theory exhibiting the d to π* charge transfer for the metal-to-ligand charge-transfer state (MLCT) of [Ru(tda)(py)$_2$].*

3.6.9. Constrained Density Functional Theory Calculations

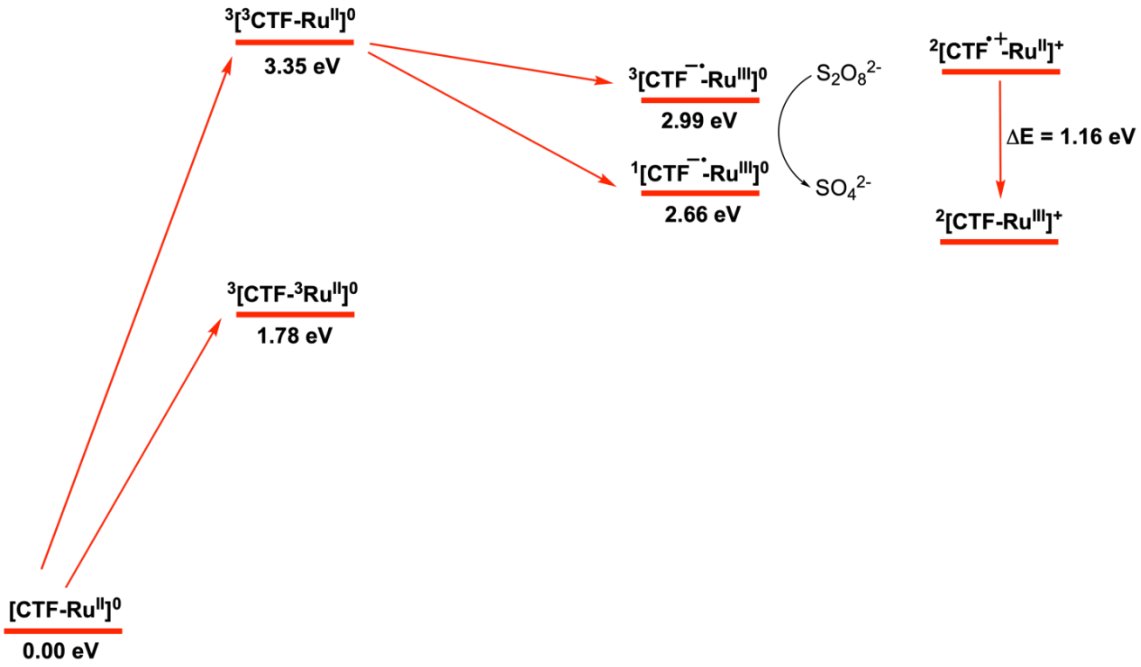

Figure S35. *Relative electronic energies (in units of eV) of diabatic states of* ***[CTF-Ru^{II}]^0*** *at MN15 level of theory (see Fig. S36 below for unpaired spin density plots).*

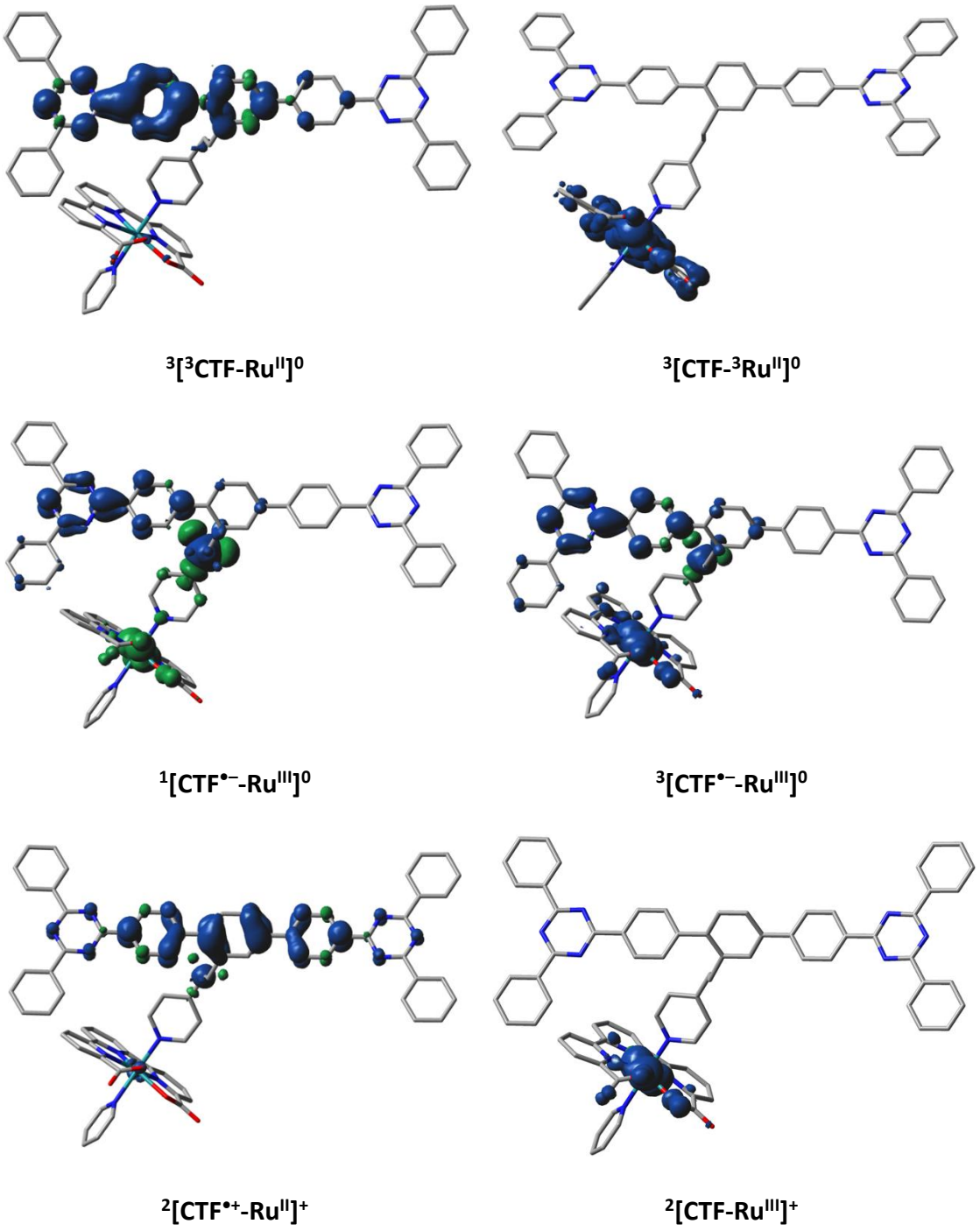

Figure S36. *Unpaired spin density plots of diabatic states of* ***[CTF-Ru^{II}]^0*** *and* ***[CTF-Ru^{III}]$^+$*** *at MN15 level of theory.*

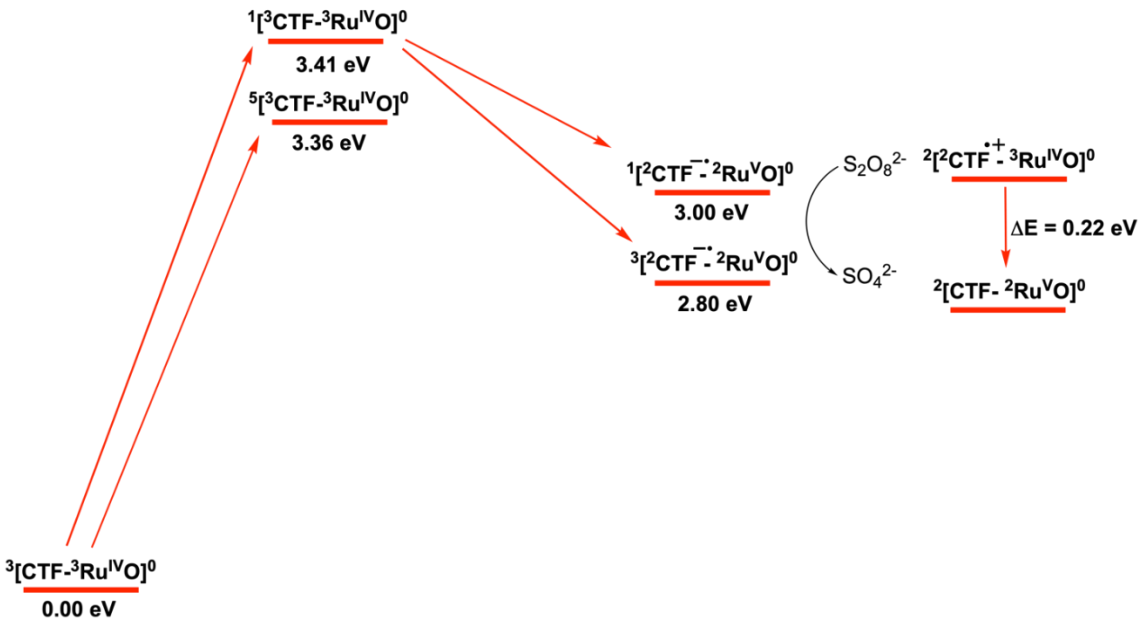

Figure S37. *Relative electronic energies (in units of eV) of diabatic states of* ***[CTF-Ru^{IV}O]^0*** *and* ***[CTF-Ru^{V}O]$^+$*** *at MN15 level of theory (see Fig. S38 below for unpaired spin density plots).*

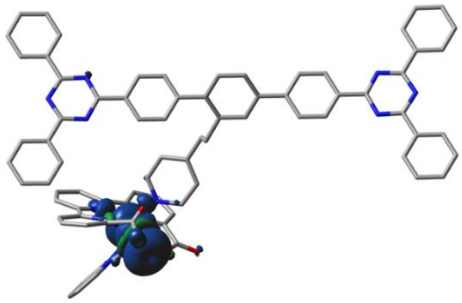

^{3}[CTF-^{3}Ru^{IV}O]^{0}

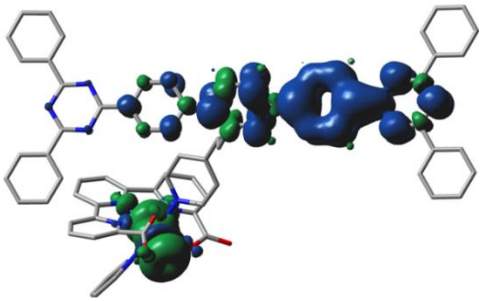

^{1}[^{3}CTF-^{3}Ru^{IV}O]^{0}

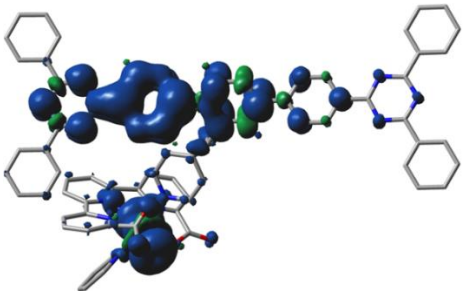

^{5}[^{3}CTF-^{3}Ru^{IV}O]^{0}

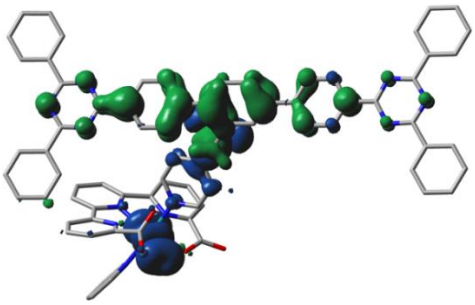

^{1}[^{2}CTF$^{\bullet-}$-^{2}Ru^{V}O]^{0}

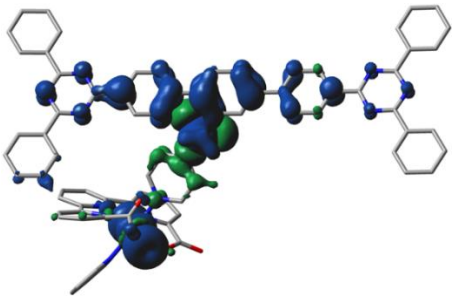

^{3}[^{2}CTF$^{\bullet-}$-^{2}Ru^{V}O]^{0}

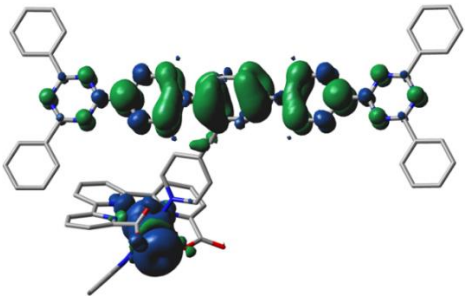

^{2}[^{2}CTF$^{\bullet+}$-^{3}Ru^{IV}O]$^{+}$

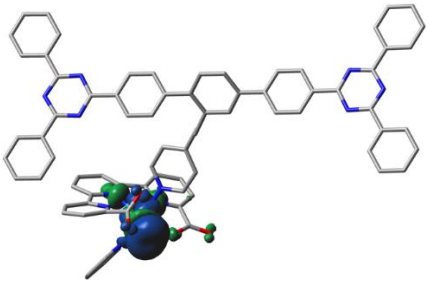

^{2}[CTF-^{2}Ru^{V}O]$^{+}$

Figure S38. *Unpaired spin density plots of diabatic states of* ***[CTF-Ru^{IV}O]^{0}*** *and* ***[CTF-Ru^{V}O]$^{+}$*** *at MN15 level of theory.*

3.6.10. References

(1) Galaup, C.; Couchet, J. M.; Bedel, S.; Tisnès, P.; Picard, C. Direct Access to Terpyridine-Containing Polyazamacrocycles as Photosensitizing Ligands for Eu(III) Luminescence in Aqueous Media. *J. Org. Chem.* **2005**, *70* (6), 2274–2284. https://doi.org/10.1021/jo0480242.

(2) Bratsos, I.; Alessio, E.; Ringenberg, M. E.; Rauchfuss, T. B. Ruthenium Complexes: Ruthenium(II)-Chlorido Complexes Of Dimethylsulfoxide. In *Inorganic Syntheses*; Rauchfuss, T. B., Ed.; Wiley-Blackwell, 2010; Vol. 35, pp 148–152. https://doi.org/10.1002/9780470651568.ch8.

(3) Matheu, R.; Benet-Buchholz, J.; Sala, X.; Llobet, A. Synthesis, Structure, and Redox Properties of a Trans-Diaqua Ru Complex That Reaches Seven-Coordination at High Oxidation States. *Inorg. Chem.* **2018**, *57* (4), 1757–1765. https://doi.org/10.1021/acs.inorgchem.7b02375.

(4) Escobedo-Morales, A.; Ruiz-López, I. I.; Ruiz-Peralta, M. de L.; Tepech-Carrillo, L.; Sánchez-Cantú, M.; Moreno-Orea, J. E. Automated Method for the Determination of the Band Gap Energy of Pure and Mixed Powder Samples Using Diffuse Reflectance Spectroscopy. *Heliyon* **2019**, *5* (4), 1–19. https://doi.org/10.1016/j.heliyon.2019.e01505.

(5) Almora, O.; Aranda, C.; Mas-Marzá, E.; Garcia-Belmonte, G. On Mott-Schottky Analysis Interpretation of Capacitance Measurements in Organometal Perovskite Solar Cells. *Appl. Phys. Lett.* **2016**, *109* (17), 173903. https://doi.org/10.1063/1.4966127.

(6) Brunauer, S.; Emmett, P. H.; Teller, E. Adsorption of Gases in Multimolecular Layers. *J. Am. Chem. Soc.* **1938**, *60* (2), 309–319. https://doi.org/10.1021/ja01269a023.

(7) Lippens, B. C.; de Boer, J. H. Studies on Pore Systems in Catalysts. V. The T Method. *J. Catal.* **1965**, *4* (3), 319–323. https://doi.org/10.1016/0021-9517(65)90307-6.

(8) Barrett, E. P.; Joyner, L. G.; Halenda, P. P. The Determination of Pore Volume and Area Distributions in Porous Substances. I. Computations from Nitrogen Isotherms. **1951**, *73*, 374–380. https://doi.org/10.1021/ja01145a126.

(9) Ravel, B.; Newville, M. ATHENA, ARTEMIS, HEPHAESTUS: Data Analysis for X-Ray Absorption Spectroscopy Using IFEFFIT. *J. Synchrotron Radiat.* **2005**, *12* (4), 537–541. https://doi.org/10.1107/S0909049505012719.

(10) Francàs, L.; Matheu, R.; Pastor, E.; Reynal, A.; Berardi, S.; Sala, X.; Llobet, A.; Durrant, J. R. Kinetic Analysis of an Efficient Molecular Light-Driven Water Oxidation System. *ACS Catal.* **2017**, *7* (8), 5142–5150. https://doi.org/10.1021/acscatal.7b01357.

(11) Bastús, N. G.; Gimbert-Suriñach, C.; Puntes, V.; Llobet, A.; Ventosa, M.; Oliveras, J. Nanocrystal–molecular Hybrids for the Photocatalytic Oxidation of Water. *ACS Appl. Energy Mater.* **2020**, *3* (10), 10008–10014. https://doi.org/10.1021/acsaem.0c01685.

(12) Meier, C. B.; Sprick, R. S.; Monti, A.; Guiglion, P.; Lee, J. S. M.; Zwijnenburg, M. A.; Cooper, A. I. Structure-Property Relationships for Covalent Triazine-Based Frameworks: The Effect of Spacer Length on Photocatalytic Hydrogen Evolution from Water. *Polymer (Guildf).* **2017**, *126*, 283–290. https://doi.org/10.1016/j.polymer.2017.04.017.

(13) Ren, S.; Bojdys, M. J.; Dawson, R.; Laybourn, A.; Khimyak, Y. Z.; Adams, D. J.; Cooper, A. I. Porous, Fluorescent, Covalent Triazine-Based Frameworks via Room-Temperature and Microwave-Assisted Synthesis. *Adv. Mater.* **2012**, *24* (17), 2357–2361. https://doi.org/10.1002/adma.201200751.

(14) Kuhn, P.; Antonietti, M.; Thomas, A. Porous, Covalent Triazine-Based Frameworks Prepared by Ionothermal Synthesis. *Angew. Chemie - Int. Ed.* **2008**, *47* (18), 3450–3453. https://doi.org/10.1002/anie.200705710.

(15) Johnson, T. J.; Aker, P. M.; Scharko, N. K.; Williams, S. D. Quantitative Infrared and near-Infrared Gas-Phase Spectra for Pyridine: Absolute Intensities and Vibrational Assignments. *J. Quant. Spectrosc. Radiat. Transf.* **2018**, *206*, 355–366. https://doi.org/10.1016/j.jqsrt.2017.11.023.

(16) Yang, Z.; Chen, H.; Wang, S.; Guo, W.; Wang, T.; Suo, X.; Jiang, D. E.; Zhu, X.; Popovs, I.; Dai, S. Transformation Strategy for Highly Crystalline Covalent Triazine Frameworks: From Staggered AB to Eclipsed AA Stacking. *J. Am. Chem. Soc.* **2020**, *142* (15), 6856–6860. https://doi.org/10.1021/jacs.0c00365.

(17) Xie, J.; Shevlin, S. A.; Ruan, Q.; Moniz, S. J. A.; Liu, Y.; Liu, X.; Li, Y.; Lau, C. C.; Guo, Z. X.; Tang, J. Efficient Visible Light-Driven Water Oxidation and Proton Reduction by an Ordered Covalent Triazine-Based Framework. *Energy Environ. Sci.* **2018**, *11* (6), 1617–1624. https://doi.org/10.1039/c7ee02981k.

(18) Wang, K.; Yang, L. M.; Wang, X.; Guo, L.; Cheng, G.; Zhang, C.; Jin, S.; Tan, B.; Cooper, A. Covalent Triazine Frameworks via a Low-Temperature Polycondensation Approach. *Angew. Chemie - Int. Ed.* **2017**, *56* (45), 14149–14153. https://doi.org/10.1002/anie.201708548.

(19) Sing, K. S. W.; Everett, D. H.; Haul, R. A. W.; Moscou, L.; Pierotti, R. A.; Rouquerol, J.; Siemienievwska, T. Reporting Physisorption Data for Gas/solid Systems. *Pure Appl. Chem.* **1985**, *57* (4), 603–619. https://doi.org/10.1351/pac198557040603.

(20) Hoque, M. A.; Gil-Sepulcre, M.; de Aguirre, A.; Elemans, J. A. A. W.; Moonshiram, D.; Matheu, R.; Shi, Y.; Benet-Buchholz, J.; Sala, X.; Malfois, M.; Solano, E.; Lim, J.; Garzón-Manjón, A.; Scheu, C.; Lanza, M.; Maseras, F.; Gimbert-Suriñach, C.; Llobet, A. Water Oxidation Electrocatalysis Using Ruthenium Coordination Oligomers Adsorbed on Multiwalled Carbon Nanotubes. *Nat. Chem.* **2020**, *12* (11), 1060–1066. https://doi.org/10.1038/s41557-020-0548-7.

(21) Matheu, R.; Ertem, M. Z.; Benet-Buchholz, J.; Coronado, E.; Batista, V. S.; Sala, X.; Llobet, A.

Intramolecular Proton Transfer Boosts Water Oxidation Catalyzed by a Ru Complex. *J. Am. Chem. Soc.* **2015**, *137* (33), 10786–10795. https://doi.org/10.1021/jacs.5b06541.

(22) Bannwarth, C.; Ehlert, S.; Grimme, S. GFN2-xTB - An Accurate and Broadly Parametrized Self-Consistent Tight-Binding Quantum Chemical Method with Multipole Electrostatics and Density-Dependent Dispersion Contributions. *J. Chem. Theory Comput.* **2019**, *15* (3), 1652–1671. https://doi.org/10.1021/acs.jctc.8b01176.

(23) Neese, F. The ORCA Program System. *Wiley Interdiscip. Rev. Comput. Mol. Sci.* **2012**, *2* (1), 73–78. https://doi.org/10.1002/wcms.81.

(24) Neese, F. Software Update: The ORCA Program System, Version 4.0. *Wiley Interdiscip. Rev. Comput. Mol. Sci.* **2018**, *8* (1), 4–9. https://doi.org/10.1002/wcms.1327.

(25) Neese, F. Software Update: The ORCA Program system—Version 5.0. *Wiley Interdiscip. Rev. Comput. Mol. Sci.* **2022**, *12* (5), 1–15. https://doi.org/10.1002/wcms.1606.

(26) Zhao, Y.; Truhlar, D. G. A New Local Density Functional for Main-Group Thermochemistry, Transition Metal Bonding, Thermochemical Kinetics, and Noncovalent Interactions. *J. Chem. Phys.* **2006**, *125* (19), 194101. https://doi.org/10.1063/1.2370993.

(27) Marenich, A. V.; Cramer, C. J.; Truhlar, D. G. Universal Solvation Model Based on Solute Electron Density and on a Continuum Model of the Solvent Defined by the Bulk Dielectric Constant and Atomic Surface Tensions. *J. Phys. Chem. B* **2009**, *113* (18), 6378–6396. https://doi.org/10.1021/jp810292n.

(28) D. Andrae, U. Häußermann, M. Dolg, H. S. & H. P. Energy-Adjustedab Initio Pseudopotentials for the Second and Third Row Transition Elements. *Theor. Chim. Acta* **1990**, *77 (2)*, 123–141. https://doi.org/https://doi.org/10.1007/BF01114537.

(29) Weigend, F.; Ahlrichs, R. Balanced Basis Sets of Split Valence, Triple Zeta Valence and Quadruple Zeta Valence Quality for H to Rn: Design and Assessment of Accuracy. *Phys. Chem. Chem. Phys.* **2005**, *7* (18), 3297–3305. https://doi.org/10.1039/b508541a.

(30) Eichkorn, K.; Weigend, F.; Treutler, O.; Ahlrichs, R. Auxiliary Basis Sets for Main Row Atoms and Transition Metals and Their Use to Approximate Coulomb Potentials. *Theor. Chem. Acc.* **1997**, *97* (1-4), 119–124. https://doi.org/10.1007/s002140050244.

(31) Frisch, M. J. T., G. W.; Schlegel, H. B.; Scuseria, G. E.; Robb, M. A.; Cheeseman, J. R.; Scalmani, G.; Barone, V.; Petersson, G. A.; Nakatsuji, H.; Li, X.; Caricato, M.; Marenich, A. V.; Bloino, J.; Janesko, B. G.; Gomperts, R.; Mennucci, B.; Hratchian, D. J. Gaussian 16, Revision A.03. *Gaussian, Inc. Wallingford CT* **2016**.

(32) Horn, A. H. C. Essentials of Computational Chemistry, Theories and Models By Christopher J.

Cramer. Wiley: Chichester, England. 2002. 562 Pp. ISBN 0-471-48551-9 (Hardcover). $110. ISBN 0-471-48552-7 (Paperback). $45. *J. Chem. Inf. Comput. Sci.* **2003**, *43* (5), 1720–1720. https://doi.org/10.1021/ci010445m.

(33) Yu, H. S.; He, X.; Li, S. L.; Truhlar, D. G. MN15: A Kohn-Sham Global-Hybrid Exchange-Correlation Density Functional with Broad Accuracy for Multi-Reference and Single-Reference Systems and Noncovalent Interactions. *Chem. Sci.* **2016**, *7* (8), 5032–5051. https://doi.org/10.1039/c6sc00705h.

(34) Scalmani, G.; Frisch, M. J.; Mennucci, B.; Tomasi, J.; Cammi, R.; Barone, V. Geometries and Properties of Excited States in the Gas Phase and in Solution: Theory and Application of a Time-Dependent Density Functional Theory Polarizable Continuum Model. *J. Chem. Phys.* **2006**, *124* (9), 094107. https://doi.org/10.1063/1.2173258.

(35) Wu, Q.; Van Voorhis, T. Direct Optimization Method to Study Constrained Systems within Density-Functional Theory. *Phys. Rev. A - At. Mol. Opt. Phys.* **2005**, *72* (2), 7–10. https://doi.org/10.1103/PhysRevA.72.024502.

(36) Kaduk, B.; Kowalczyk, T.; Van Voorhis, T. Constrained Density Functional Theory. *Chem. Rev.* **2012**, *112* (1), 321–370. https://doi.org/10.1021/cr200148b.

(37) Epifanovsky, E.; Gilbert, A. T. B.; Feng, X.; Lee, J.; Mao, Y.; Mardirossian, N.; Pokhilko, P.; White, A. F.; Coons, M. P.; Dempwolff, A. L.; Gan, Z.; Hait, D.; Horn, P. R.; Jacobson, L. D.; Kaliman, I.; Kussmann, J.; Lange, A. W.; Lao, K. U.; Levine, D. S.; Liu, J.; McKenzie, S. C.; Morrison, A. F.; Nanda, K. D.; Plasser, F.; Rehn, D. R.; Vidal, M. L.; You, Z. Q.; Zhu, Y.; Alam, B.; Albrecht, B. J.; Aldossary, A.; Alguire, E.; Andersen, J. H.; Athavale, V.; Barton, D.; Begam, K.; Behn, A.; Bellonzi, N.; Bernard, Y. A.; Berquist, E. J.; Burton, H. G. A.; Carreras, A.; Carter-Fenk, K.; Chakraborty, R.; Chien, A. D.; Closser, K. D.; Cofer-Shabica, V.; Dasgupta, S.; De Wergifosse, M.; Deng, J.; Diedenhofen, M.; Do, H.; Ehlert, S.; Fang, P. T.; Fatehi, S.; Feng, Q.; Friedhoff, T.; Gayvert, J.; Ge, Q.; Gidofalvi, G.; Goldey, M.; Gomes, J.; González-Espinoza, C. E.; Gulania, S.; Gunina, A. O.; Hanson-Heine, M. W. D.; Harbach, P. H. P.; Hauser, A.; Herbst, M. F.; Hernández Vera, M.; Hodecker, M.; Holden, Z. C.; Houck, S.; Huang, X.; Hui, K.; Huynh, B. C.; Ivanov, M.; Jász, Á.; Ji, H.; Jiang, H.; Kaduk, B.; Kähler, S.; Khistyaev, K.; Kim, J.; Kis, G.; Klunzinger, P.; Koczor-Benda, Z.; Koh, J. H.; Kosenkov, D.; Koulias, L.; Kowalczyk, T.; Krauter, C. M.; Kue, K.; Kunitsa, A.; Kus, T.; Ladjánszki, I.; Landau, A.; Lawler, K. V.; Lefrancois, D.; Lehtola, S.; Li, R. R.; Li, Y. P.; Liang, J.; Liebenthal, M.; Lin, H. H.; Lin, Y. S.; Liu, F.; Liu, K. Y.; Loipersberger, M.; Luenser, A.; Manjanath, A.; Manohar, P.; Mansoor, E.; Manzer, S. F.; Mao, S. P.; Marenich, A. V.; Markovich, T.; Mason, S.; Maurer, S. A.; McLaughlin, P. F.; Menger, M. F. S. J.; Mewes, J. M.; Mewes, S. A.; Morgante, P.; Mullinax, J. W.; Oosterbaan, K. J.; Paran, G.; Paul, A. C.; Paul, S. K.; Pavošević, F.; Pei, Z.; Prager, S.; Proynov, E. I.; Rák, Á.; Ramos-Cordoba, E.; Rana, B.; Rask, A. E.; Rettig, A.; Richard, R. M.; Rob, F.; Rossomme, E.; Scheele, T.; Scheurer, M.; Schneider, M.; Sergueev, N.; Sharada, S. M.; Skomorowski, W.; Small, D. W.; Stein, C. J.; Su, Y. C.;

Sundstrom, E. J.; Tao, Z.; Thirman, J.; Tornai, G. J.; Tsuchimochi, T.; Tubman, N. M.; Veccham, S. P.; Vydrov, O.; Wenzel, J.; Witte, J.; Yamada, A.; Yao, K.; Yeganeh, S.; Yost, S. R.; Zech, A.; Zhang, I. Y.; Zhang, X.; Zhang, Y.; Zuev, D.; Aspuru-Guzik, A.; Bell, A. T.; Besley, N. A.; Bravaya, K. B.; Brooks, B. R.; Casanova, D.; Chai, J. Da; Coriani, S.; Cramer, C. J.; Cserey, G.; Deprince, A. E.; Distasio, R. A.; Dreuw, A.; Dunietz, B. D.; Furlani, T. R.; Goddard, W. A.; Hammes-Schiffer, S.; Head-Gordon, T.; Hehre, W. J.; Hsu, C. P.; Jagau, T. C.; Jung, Y.; Klamt, A.; Kong, J.; Lambrecht, D. S.; Liang, W.; Mayhall, N. J.; McCurdy, C. W.; Neaton, J. B.; Ochsenfeld, C.; Parkhill, J. A.; Peverati, R.; Rassolov, V. A.; Shao, Y.; Slipchenko, L. V.; Stauch, T.; Steele, R. P.; Subotnik, J. E.; Thom, A. J. W.; Tkatchenko, A.; Truhlar, D. G.; Van Voorhis, T.; Wesolowski, T. A.; Whaley, K. B.; Woodcock, H. L.; Zimmerman, P. M.; Faraji, S.; Gill, P. M. W.; Head-Gordon, M.; Herbert, J. M.; Krylov, A. I. Software for the Frontiers of Quantum Chemistry: An Overview of Developments in the Q-Chem 5 Package. *J. Chem. Phys.* **2021**, *155* (8), 084801. https://doi.org/10.1063/5.0055522.

(38) Noro, T.; Sekiya, M.; Koga, T. Segmented Contracted Basis Sets for Atoms H through Xe: Sapporo-(DK)-nZP Sets (N = D, T, Q). *Theor. Chem. Acc.* **2012**, *131 (2)*, 1124. https://doi.org/10.1007/s00214-012-1124-z.

(39) Wiberg, K. B. Ab Initio Molecular Orbital Theory by W. J. Hehre, L. Radom, P. v. R. Schleyer, and J. A. Pople, John Wiley, New York, 548pp. *J. Comput. Chem.* **1986**, *7*, 379. https://doi.org/10.1002/JCC.540070314.

Chapter 4

Molecular catalyst coordinatively bonded to organic semiconductors for selective light-induced CO_2 reduction in water


4

Molecular catalyst coordinatively bonded to organic semiconductors for selective light-induced CO_2 reduction in water

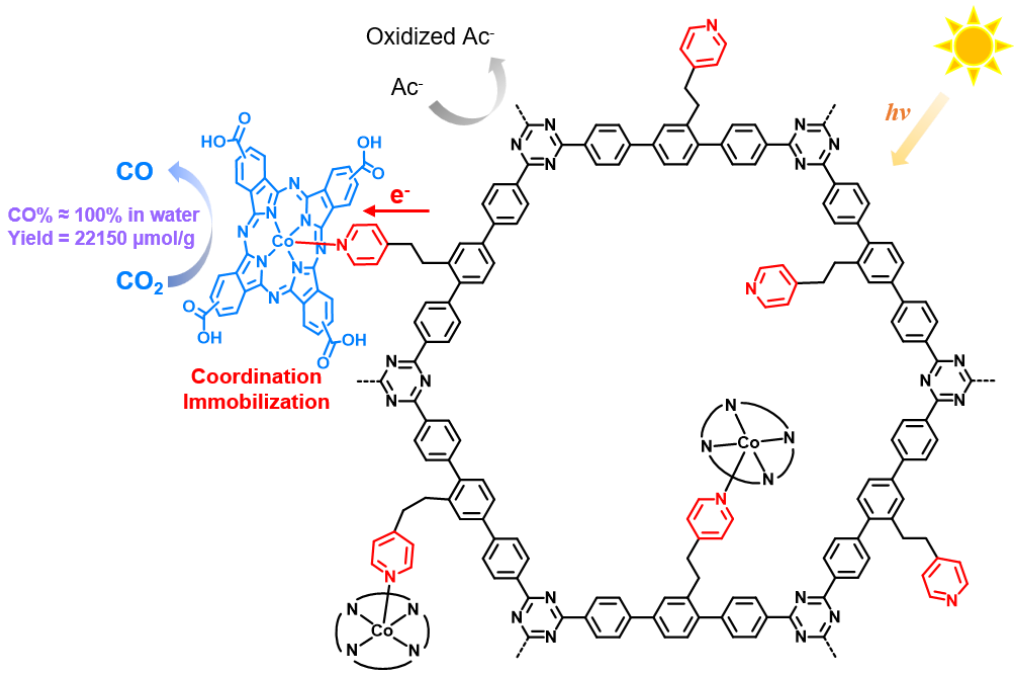

Abstract

The selective photoreduction of CO_2 in aqueous media based on earth-abundant elements only, is today a challenging topic. Here we present the anchoring of discrete molecular catalysts on organic polymeric semiconductors via covalent bonding, generating molecular hybrid materials with well-defined active sites for CO_2 photoreduction, exclusively to CO in purely aqueous media. The molecular catalysts are based on aryl substituted Co phthalocyanines that can be coordinated by dangling pyridyl attached to a polymeric covalent triazine framework that acts as a light absorber. This generates a molecular hybrid material that efficiently and selectively achieves the photoreduction of CO_2 to CO in $KHCO_3$ aqueous buffer, giving high yields in the range of 22 mmol g^{-1} (458 µmol g^{-1} h^{-1}) and turnover numbers above 550 in 48 h, with no deactivation and no detectable H_2. The electron transfer mechanism for the activation of the catalyst is proposed based on the combined results from time-resolved fluorescence spectroscopy, in situ XPS, in situ EPR and quantum chemical calculations.

Contributions:

Martina Salati synthesized the monomer for **p-CTF-py** and cooperated in the characterization and electrochemical measurements for the CTFs.

4.1. Introduction

Sunlight-driven reduction of CO_2 to carbon based products is a promising strategy to mitigate the greenhouse effect by constructing a carbon-neutral cycle, where CO_2 is utilized as a potential starting reagent for target molecules or to produce renewable energy thus replacing fossil fuels.[1–3] Because of the inert nature of CO_2 and its strong competition to H_2 evolution, extensive research efforts have been concentrated on the design of light-driven catalytic systems for CO_2 reduction in a rapid and selective manner.[4–8]

Organic polymeric semiconductors, such as carbon nitrides (CN),[9] covalent triazine frameworks (CTFs),[10] covalent organic frameworks (COFs),[11] constitute a promising type of photocatalysts, the so-called "functional materials",[12] with a broad design flexibility due to their molecular nature and their synthesis versatility. With the strategic choice and the well-defined structures, organic polymeric semiconductors can be as durable, recyclable and scalable as those inorganic ones. Further, by combining the merits of molecular and material science, new molecular hybrid materials can be prepared with superior performances.[13] Additionally, they can be based on earth-abundant and non-toxic metals which make them highly attractive for a more sustainable solar fuels production and for scalability.[9,14] In terms of CO_2 photoreduction, however, most organic polymeric semiconductors still suffer from the absence of catalytic active sites. Hence, their surface electrons will be inevitably used for direct reduction of CO_2 to $CO_2^{\cdot-}$, which demands high negative potentials up to −1.9 V *vs.* NHE under standard conditions.[15] Thus the presence of a CO_2 reduction catalyst combined with the organic semiconductor can potentially overcome the challenges of severe charge recombination and ultimately lead to high activity and selectivity.[16–18]

With these considerations in mind, free noble-metal-based molecular CO_2 reduction catalysts[19–21] based on earth-abundant elements comprehend Co macrocycles,[17] metal porphyrins,[22,23] Co/Fe quaterpyridine complexes,[24–26] some of which have been reported to achieve turnover numbers (TONs) in the range of 10^3 for selective CO_2 photoreduction to CO or even to formate. However, they mostly work in organic

solvents that are not useful for practical applications where aqueous medium is a must.[27–30]

To overcome this challenge, the judicious design of the organic polymeric photocatalyst and molecular catalysts along with their anchoring strategy is crucial. All these factors can be fine-tuned and will determine the degree of electronic communication and interfacial electron transfer kinetics that in turn will be the key for their overall performance. In this context, the molecular nature of the catalyst bonded covalently to organic semiconductors represents a step forward into the field that can lead to highly homogenous hybrid materials with very well-defined reactivity that will not suffer aggregation processes. Moreover, the easy modification of the molecular catalyst by ligand design, allowing to strategically tune both thermodynamic and kinetic properties of the catalytic reaction, gives to this type of system a high versatility to be adequately combined with organic semiconductors, thus providing systems with high quantum yields.

In this work we report a bottom-up approach to synthesize a CTF-based photocatalyst with dangling pyridine arms (**p-CTF-py**) which can provide the means for a covalent binding of cobalt macrocyclic catalysts to the semiconductor, representing the first example combining CTFs and molecular catalysts for selective CO_2 photoreduction in fully aqueous solutions. The optimal molecular hybrid photocatalyst based on **p-CTF-py** can accomplish a high CO yield of 22.1±0.8 mmol g^{-1} and a TON of 559±20 during 48 h of simulated sunlight irradiation with no H_2 evolution (~100% CO selectivity) and no deactivation.

4.2. Results and Discussion

4.2.1. Synthesis and characterization of the molecular hybrid material

The terphenyl-based monomers, [1,1':4',1''-terphenyl]-4,4''-dicarbonitrile (**M**) and 2'-(2-(pyridin-4-yl)ethyl)-[1,1':4',1''-terphenyl]-4,4''-dicarbonitrile (**M-py**) were prepared in good yields (see Scheme S2 and Experimental section for further details). Treatment of these monomers with polyphosphoric acid at 400°C under vacuum promotes their

polymerization via the formation of triazine units[31] generating the polymeric materials **p-CTF** and **p-CTF-py**, respectively (Figure 1a, Schemes S1 and S3; see SI for details).

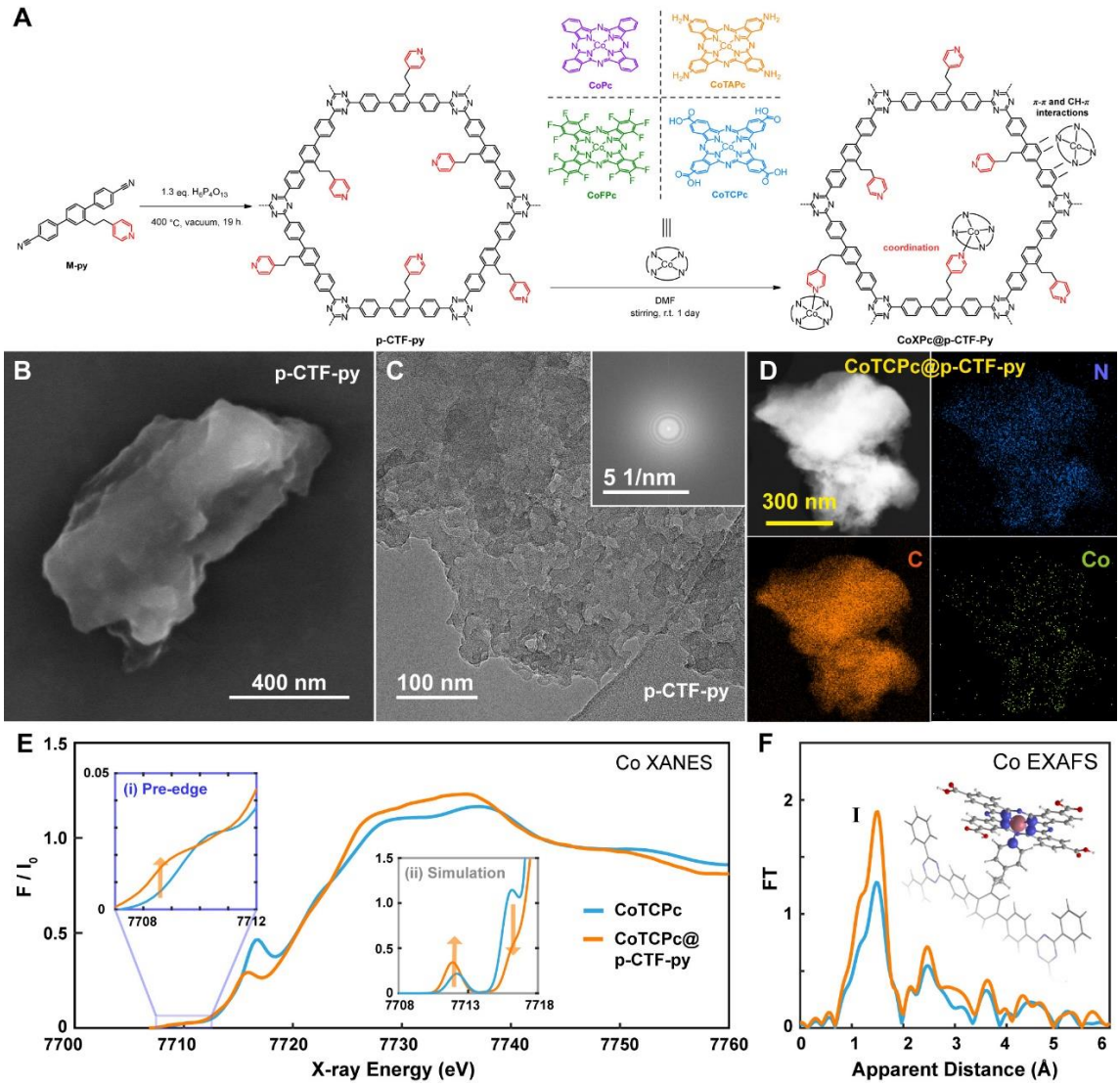

Figure 1. *(a) Synthetic scheme for* ***p-CTF-py*** *and* ***CoXPc@p-CTF-py****. (b) SEM and (c) TEM images of* ***p-CTF-py****. (d) EDS mapping of* ***CoTCPc@p-CTF-py****. (e) Normalized Co K-edge XANES and (f) Fourier transforms of k2-weighted Co EXAFS results of* ***CoTCPc*** *(blue) and* ***CoTCPc@p-CTF-py*** *(orange). Inset in (e): (i) zoom-in of the pre-edge region; (ii) simulated Co K-edge pre-edge and rising edge XANES showing the increase in the pre-edge intensity and decrease of the 1s → 4p$_z$ transition in* ***CoTCPc@p-CTF-py*** *(orange) compared to* ***CoTCPc*** *(blue). Inset in (f): DFT-calculated structure of* ***CoTCPc@p-CTF-py*** *with unpaired spin density plots.*

In contrast to the reported crystalline CTF materials synthesized via similar methods with the phenyl- or biphenyl-based monomers,[31] **p-CTF** and **p-CTF-py** are amorphous

solids as revealed by powder X-ray diffraction (Figure S1). Consequently, the real structure of the as-prepared CTF samples should be more disordered than the anticipated structure reported in Schemes S1 and S3. The chemical compositions of the two CTF-based materials were also characterized by FT-IR (Figure S2 and S3), solid-state ^{13}C NMR (Figure S4) and X-ray photoelectron spectroscopy (XPS; Figure S5 and S6), confirming the successful preparation of the polymeric CTF materials. Their morphologies were examined via scanning electron microscopy (SEM; Figure 1b and S7) and transmission electron microscopy (TEM; Figure 1c and S8), where both CTF-based materials consist of stacked, wrinkled, amorphous sheets. The uneven surface of the CTF particles possibly originates from the abundant gas release during thermal synthesis.[31] In addition, their N_2 sorption isotherms (Figure S9a) reveal nearly three times larger specific surface area of **p-CTF-py** over that of **p-CTF** (66.7 *vs*. 23.4 $cm^2\ g^{-1}$). This might be attributed to the origination of additional pores produced by the dangling pyridyl groups intercalated between the layers of **p-CTF-py**. The effects of dangling groups within the organic frameworks have been extensively utilized to tune the interlayer distances and pore volumes.[32–34] The above assumption is also consistent with a larger number of small pores of ca. 1.2 nm in the layers of **p-CTF-py** than in those of **p-CTF**, as revealed by the pore size distribution analysis (Figure S9b). Additionally, both samples possess the pores with sizes around 2.6 and 2.7 nm for **p-CTF-py** and **p-CTF** (Figure S9b), respectively, consistent with the expected hexagon channels of the CTF structures.

We also evaluated the band energies of **p-CTF-py** and **p-CTF** by UV-vis diffuse reflectance spectroscopy (UV-vis DRS; Figure S10) and Mott–Schottky plots (Figure S11), which exhibit large bandgaps (2.57 and 3.20 eV) as well as flat-band-approximated conduction band (CB) potentials of −1.15 and −1.03 V *vs.* NHE (Normal hydrogen electrode, unless otherwise stated, at pH 7.0), which have the sufficient thermodynamic driving force for the reduction of CO_2 to CO (−0.52 V).

Next, four cobalt phthalocyanine derivatives, including cobalt phthalocyanine (**CoPc**), cobalt tetra-amino phthalocyanine (**CoTAPc**), cobalt perfluorinated phthalocyanine (**CoFPc**) and cobalt tetra-carboxyl phthalocyanine (**CoTCPc;** See Figure 1a for a drawing of their structures) were immobilized on **p-CTF-py** by dispersing 10 mg of the latter in 1 mL of 1.0 mM solution of the Co catalyst and left stirring for 1 day at RT. The formed

molecular hybrid materials, **CoXPc@p-CTF-py (**X = **Ø** meaning no substitution**, F, TA, TC**) were isolated by centrifugation and washed twice with DMF and water, before freeze-drying them (Figure 1a; see SI for details). During the immobilization process, the initial solutions decolorated roughly up to 60% for X = **Ø,** F, TA and up to 85% for X= TC (Figure S12) as indicated by UV-vis spectroscopy. A similar strategy was used for the anchoring of **CoTCPc** in **p-CTF,** not containing the dangling pyridyl group, producing a decoloration of only 45%. All these results suggest that in the presence of the pyridyl group the main interaction of the molecular catalysts with the CTF absorber occurs by the formation of a covalent Co-N bond with additional supramolecular stabilization involving CH-π and π-π interactions. This is further supported by calculations at the MN15[35] level of theory (see Supplementary Information for further details) indicating that the coordination of **CoTCPc** to **p-CTF-py** is favored significantly (∆E = 10.7 kcal/mol) over adsorption via supramolecular CH-π and π-π interactions (Figure S13).

The presence of the molecular catalyst anchored on the CTF absorber was confirmed by inductively coupled plasma mass spectrometry (ICP-MS) which gives a loading in the range of 0.19-0.23% of Co per gram of material (30-40 nmols g^{-1}; Table S1) and additionally supported by IR spectroscopy (Figure S2 and S3). Further, energy dispersive X-ray spectroscopy (EDS; Figure 1d and Figure S14) shows that cobalt is homogeneously distributed on each of the CTF materials. The cross-sectional analysis of the cobalt element on **CoTCPc@p-CTF-py** further demonstrates that the Co complex is homogeneously dispersed into the CTF particles rather than mainly distributed on the surface (Figure S15). The substantial dispersion is presumably provided by the aforementioned uneven surface of the CTF particles. The TEM images (Figure S16 and S17) of both molecular hybrid photocatalysts show negligible morphological changes compared to the bare CTF materials.

The cobalt valence state of **CoTCPc** and the effect of the bonding between **CoTCPc** and the CTF materials were examined by XPS, where all the CTF-based materials display the C and N elements (Figure S5 and S6) while additional Co 2p signals can be observed for **CoTCPc@p-CTF-py** and **CoTCPc@p-CTF** (Figure S18). More importantly, the Co 2p binding energy of **CoTCPc@p-CTF-py** shows a more positive shift than that of **CoTCPc** (0.5 vs. 0.3 eV) associated with the Co-N_{pyr} covalent bond.[36]

Additional characterization of this hybrid material was carried out by X-ray absorption near edge structure (XANES) and extended X-ray absorption fine structure (EXAFS) for **CoTCPc@p-CTF-py** and for the **CoTCPc** reference (blue) (Figure 1e, 1f and S19). As shown in Figure 1e, the Co K-edge XANES of **CoTCPc** displays a pre-edge peak at 7710.4 eV with an area of 7 units (Figure 1e, inset (i), Figure S19 and Table S2) together with a prominent shoulder at 7716.7 eV which corresponds to the 1s → $4p_z$ transition and reflects the nature of the $4p_z$ orbital in its square planar environment.[37,38] In contrast, **CoTCPc@p-CTF-py** exhibits a slightly more intense pre-edge peak at 7709.0 and 7710.8 eV with an area of 8.1 units (Figure 1e inset (i), Figure S20, Table S2) as well as a weaker broadened 1s → $4p_z$ peak at 7715.7 eV. Both the increased pre-edge intensity as well as the broadened 1s → $4p_z$ peak of **CoTCPc@p-CTF-py** are due to an increase of its Co coordination number and distortion of the local geometry as supported by time-dependent DFT in XANES simulations (Figure 1e, inset (ii)). As previously reported, the features in the pre-edge region have been shown to be particularly sensitive to the geometry.[39–41] Indeed non-centrosymmetric complexes display an increased intensity in their pre-edge features due to an increase in the metal 4p mixing into the 3d orbitals contributing towards the electric dipole 1s to 4p character of this transition.[40] **CoTCPc@p-CTF-py** with its increased distorted structural conformation thus illustrates a slightly larger pre-edge than **CoTCPc**. The 1s → $4p_z$ transition, moreover, reflects the coordination environment of the Co complexes as previously elaborated.[37,38] A change in the coordination geometry of the Co center in **CoTCPc@p-CTF-py** hereby leads to a greater delocalization of the metal 4p orbitals[42,43] resulting in a less intense and broadened 1s → $4p_z$ transition feature (Figure 1e).

EXAFS studies were further carried out to extract structural information of the Co molecular catalyst before and after coordination to the CTF absorber (Figure 1f). A prominent peak **I** is observed in the EXAFS spectra corresponding to the averaged contribution of the Co-N coordination. Analysis of the EXAFS spectrum for CoTCPc reveals the best fits with four Co-N distances of 1.90 Å whereas **CoTCPc@p-CTF-py** displays an increase in the amplitude of peak **I** together with the best fit involving five Co-N distances at 1.91 Å (Figure S20 and Table S3), in agreement with their DFT optimized structures (inset of Figure 1f and Table S4).

4.2.2. Photocatalytic CO_2 Reduction

Photocatalytic experiments for the reduction of CO_2 were carried out in a home-made 4 mL quartz vessel where 0.5 mg of the molecular hybrid photocatalysts **CoXPc@p-CTF-py** were suspended in a 1.5 mL aqueous solution (0.33 g L^{-1}) of 0.1 M $KHCO_3$ containing 25 mM ascorbic acid (H_2Asc, deprotonated to $HAsc^-$ by $KHCO_3$) and degassed under 1 atm CO_2. Then the suspension was irradiated under continuous stirring with AM 1.5 G light at 300 mW cm^{-2} for 48 h.

All the molecular hybrid photocatalysts show considerable activity for CO_2 photoreduction to CO (> 99% selectivity) in water with negligible formation of hydrogen and liquid products (Figure 2, S21-S23 and Table 1, Entries 1-5), representing the first example combining CTFs and molecular catalysts for selective CO_2 photoreduction in fully aqueous solutions. The very high selectivity is mainly attributed to the excellent intrinsic performances of cobalt phthalocyanine catalysts.[44–50] Among them, **CoTCPc@p-CTF-py** exhibits the highest CO yield of 22.1±0.8 mmol g^{-1} and TON of 559±20 during 48 h, consistent with a production rate of 458±17 µmol g^{-1} h^{-1}. The best performance of **CoTCPc@p-CTF-py** can be partially attributed to the higher loading of the molecular catalyst along with increasing electron-withdrawing abilities of the functional groups[51,52] on the **CoXPc** backbone (Figure 2a, S22 and Table 1, Entries 1-4), suggesting that the carboxylic groups also contribute to the improved activity. Our previous studies[53] have demonstrated the electronic effects of the different substituents by cyclic voltammetry in homogeneous phase and theoretical calculations. We found that with increasingly electron-withdrawing groups on the Co complexes, the $Co^{II/I}$ redox potential became more positive and the calculated Hirshfeld Co atomic charges increased, mandating lower overpotentials for catalytic CO_2 reduction with **CoTCPc** being the optimal catalyst studied. This is indeed further confirmed by the parallel systems with **p-CTF** loaded with each of the four Co catalysts, where **CoTCPc@p-CTF** also displayed the highest CO yield (Figure S23 and Table 1, Entries 5-8).

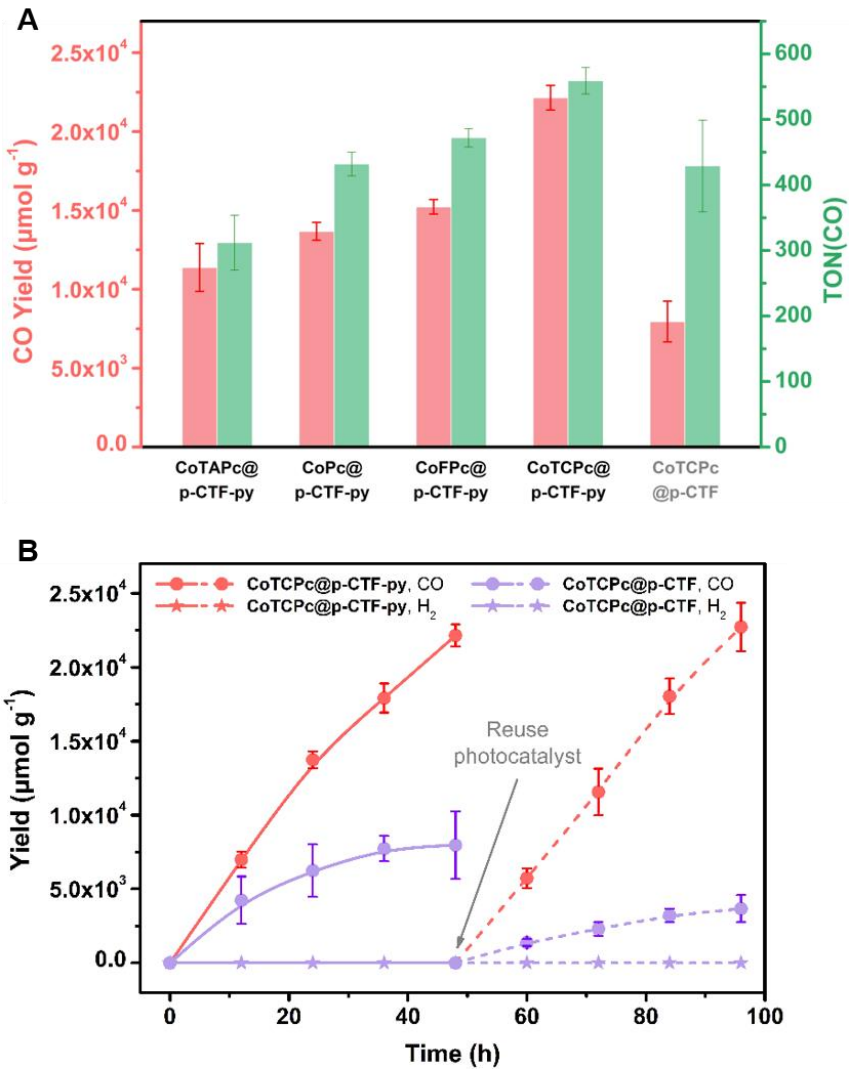

Figure 2. *CO_2 photoreduction. (a) Comparison of CO yields and TONs among the molecular hybrid photocatalysts. (b) Time profiles of photocatalytic CO (circle) and H_2 (star) formation using* ***CoTCPc@p-CTF-py*** *(red) and* ***CoTCPc@p-CTF*** *(violet). After first run of 48 h photocatalysis (solid lines), the colloidal photocatalyst was reused for the second run (dashed lines). General conditions: 0.33 g L^{-1} photocatalyst, 0.1 M $KHCO_3$, 25 mM H_2Asc, 300 mW cm^{-2} Xe lamp with AM 1.5 G filter, 1 atm CO_2, 25°C, 5 × 2 mm stir bar at 1000 rpm. The experimental error bars represent the standard deviations of three independent measurements.*

After 48 h of photocatalysis, no increment of CO could be observed in the **CoTCPc@p-CTF-py** system, which is possibly due to the substantial consumption of $HAsc^-$. We determined the chemical efficiency of $HAsc^-$ as 29.5%±1.1% by the CO yield (22.1±0.8 mmol g^{-1}) within 48 h divided by the initial amount of $HAsc^-$ versus photocatalyst (75 mmol g^{-1}). This value reflects competing reactions including back electron transfer, as

summarized in Scheme 1 and discussed thoroughly in the next section. It is also interesting to realize that these hybrid systems are also active and selective with a cut-off (> 400 nm) filter (Figure S24 and Table 1, Entry 9) and thus showing its potential in visible-light-driven CO_2 reduction to CO. The apparent quantum yield for CO production was estimated as 0.12 ± 0.02% at 405 nm (see SI for details). Moreover, the CO yield of **CoTCPc@p-CTF-py** is nearly three times of that from **CoTCPc@p-CTF** (22.1±0.8 *vs*. 8.0±1.3 mmol g^{-1}), showing the advantages of the covalent bond between CTF and the catalyst (Figure 2b). The parallel systems with other Co catalysts also show higher activity with **p-CTF-py** over **p-CTF**, further confirming facilitated photocatalysis with the appended pyridine arms (Table 1). In addition, the photocatalytic activity of **CoTCPc@p-CTF-py** remains intact in the second round of catalysis and thus achieved a cumulative TON of 1119, whereas that of **CoTCPc@p-CTF** substantially diminishes (Figure 2b and S25), underlining once again the importance of the Co-N_{pyr} covalent bond to avoid catalyst detachment. The use of bare **p-CTF-py** or **p-CTF** mixed with dissolved **CoTCPc** in the parallel systems could not initiate the formation of CO as well (Table S5), which highlights the importance of pre-installed coordinative bonding to assure effective photocatalysis and also rules out the possibility of **CoTCPc** itself serving as a semiconductor as well as the photocatalyst.

The high stability of **CoTCPc@p-CTF-py** was further confirmed by its XANES and EXAFS before and after photocatalysis (Figure S26 and Table S3), where no significant changes of the Co center were observed with retention of its molecular nature, also precluding the formation of Co-based nanoparticles as the unexpected catalyst. Although the organic polymeric semiconductors may decompose and produce CO upon irradiation,[3,54–56] such side reaction was not observed in our experiments. On one hand, the $^{13}CO_2$ isotope labelling experiments confirm that CO was dominantly generated via CO_2 photoreduction rather than the decomposition of organic material (Figure S27). On the other hand, the systematic blank experiments, especially the ones with bare CTF materials (Table S3, Entries 7 and 8), did not produce any CO product, which also excludes the possibility of the decomposed organic materials as the CO source.

Among the molecular hybrid organic photocatalysts for CO_2 photoreduction beyond CTFs, such as CN_x or COFs, most of them were operated in organic solvents[17,25,26,57–59] or

water-containing[60,61] solutions, such as various immobilizations of iron or cobalt quaterpyridine complexes with CN_x,[26,58] which afforded 10^2 to 10^3 TONs in MeCN medium (two instances in Table 1, Entries 10 and 11). Very recently, a Ni-tris-2,2'-bipyridine complex coupled with a semiconducting COF was reported to show fast CO_2 photoreduction to CO in MeCN/TEOA/H_2O (6:2:2) solutions with an overall CO yield of 2.9 mmol g^{-1},[61] nonetheless showing a moderate selectivity of 88% (Table 1, Entry 12). In contrast, the documented systems in fully aqueous solutions are quite rare. For example, besides the ones using noble-metal molecular catalysts,[21,62,63] an iron porphyrin, FeTCPP (= chloro Fe^{III} tetra(4-carboxylphenyl)porphyrin) immobilized on modified CN_x was reported[64] as a noble-metal-free system for CO_2 photoreduction to CO in aqueous TEOA solutions albeit with low selectivity (68%) and with a TON < 1 (Table 1, Entry 13). One more instance is the anchorage of a carboxyl-derived cobalt quaterpyridine catalyst on poly(triazine-imide) lithium chloride (PTI-LiCl) as a type of crystalline CN_x for photocatalytic CO_2-to-CO conversion in 0.5 M $KHCO_3$ solution with Na_2SO_3 as the sacrificial electron donor (Table 1, Entry 14).[65] This molecular hybrid affords fast CO formation rate up to 2.1 mmol g^{-1} h^{-1} with a selectivity of 96%, but only under strong UV irradiation at 390 nm rather than sunlight/visible light. The above comparisons highlight the remarkable performance and mild conditions of our **CoTCPc@p-CTF-py** system.

Table 1. *Parameters describing the performances of selected molecular catalyst anchored on organic and inorganic semiconductors, for light induced CO_2 reduction.*[a]

Entry	Catalyst	Medium	Mol Cat[b] (µmol g^{-1})	Sacrificial reagent (conc.)	CO yield (mmol g^{-1})	H_2 yield (µmol g^{-1})	TON (CO)[c]	CO%
1	**CoTCPc@p-CTF-py**	0.1 M $KHCO_3$	39.6	$HAsc^-$ (25 mM)	22.1±0.8	n.d.	1118 (559±20 in each run)	100%
2	**CoFPc@p-CTF-py**		32.2		15.2±0.5	n.d.	472±14	100%
3	**CoPc@p-CTF-py**		31.6		13.7±0.6	n.d.	432±18	100%
4	**CoTAPc@p-CTF-py**		36.6		11.4±1.5	n.d.	312±42	100%
5	**CoTCPc@p-CTF**		18.6		8.0±1.3	n.d.	429±70	100%
6	**CoFPc@p-CTF**		13.6		5.6±0.5	n.d.	403±37	100%
7	**CoPc@p-CTF**		13.8		4.2±0.2	177±32	304±14	96%
8	**CoTAPc@p-CTF**		16.2		3.9±0.3	199±30	241±18	95%
9[d]	**CoTCPc@p-CTF-py**		39.6		12.5±1.1	n.d.	316±27	100%
10[58]	**Co-qpy-Ph-COOH@CN_x**	MeCN	1.48	BIH (0.05 M)	2.28	0.07	254	97%
11[26]	**Fe-qpy-Ph-CHO@CN_x**		0.21	BIH (0.05 M), TEA (20 v%)	6.38	42.5	2554	95%
12[61]	**$Ni(bpy)_3^{2+}$@BtE-COF**	MeCN:H_2O = 3:1	550	TEOA (20 v%)	2.9	395	5.3	88%
13[64]	**FeTCPP@CN_x**	H_2O	86.4	TEOA (10 v%)	1.4×10^{-3}	0.67	0.26	68%
14[65]	**Co-qpy-Ph-COOH@PTI-LiCl**	0.5 M $KHCO_3$	9.5	Na_2SO_3 (0.2 M)	3.86	176	406	96%

[a] General conditions used: 1.5 mL aqueous solution with 0.5 mg photocatalyst hybrid material, (0.33 g L^{-1}; 39.6 µmol g^{-1} of Co catalyst), 25 mM H_2Asc (deprotonated to $HAsc^-$ by $KHCO_3$; implying 75 mmol g^{-1}) and 0.1 M $KHCO_3$ under 1 atm CO_2, under the irradiation of AM 1.5G light at 300 mW cm^{-2} for 48 h (irradiated area is ca. 2.4 cm^2). The results of blank experiments are shown in Table S5. The experimental error bars represent the standard deviations of three independent measurements. [b] Mol Cat stands for mols of catalysts per gram of sample. For the CTF samples it was calculated by ICP-MS (Table S1). [c] TON = mols of CO / mols of catalyst. [d] Light source is ≥ 400 nm cut-off light (300 mW cm^{-2}, irradiated area is ca. 2.4 cm^2).
Abbreviations: **qpy-Ph-COOH** is a quaterpyridine (qpy) ligand 4-substituted by benzoic acid; **qpy-Ph-CHO** is a qpy ligand 4-substituted by benzaldehyde; **BtE-COF** is a COF between benzotrithiophene tricarbaldehyde and 2,5-diethoxyterephthalohydrazide; **FeTCPP** is chloro Fe(III) tetra(4-carboxyl)phenyl porphyrin.

4.2.3. Electron Transfer Properties and Mechanism

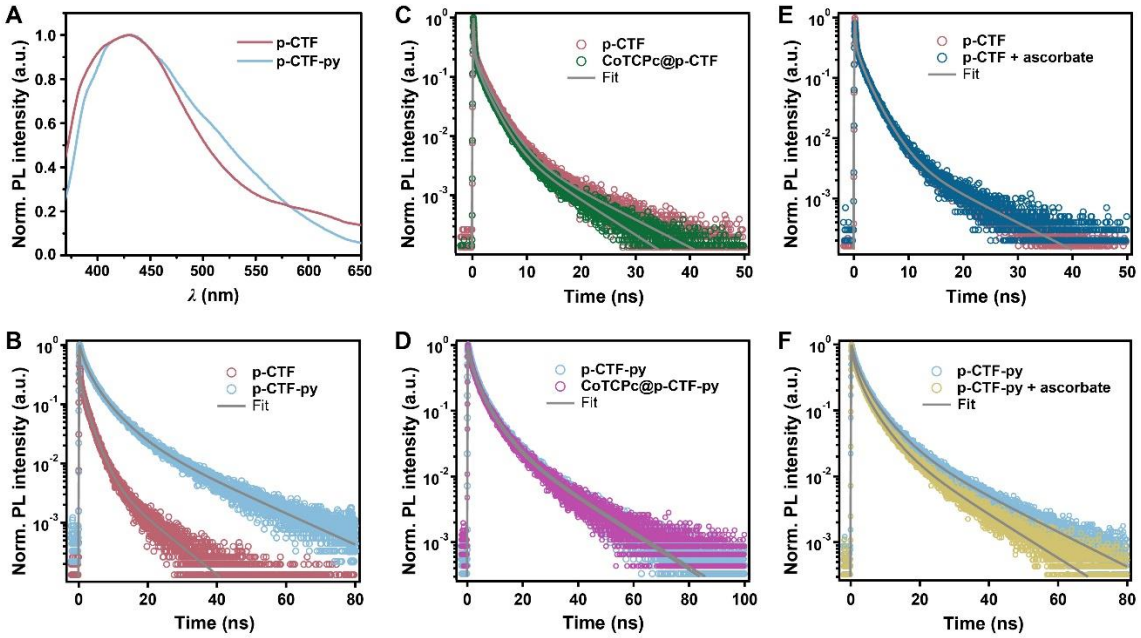

Figure 3. *(a) Intensity-normalized steady-state PL spectra of* ***p-CTF*** *and* ***p-CTF-py****. (b-e) Time-resolved PL decay traces of* ***p-CTF*** *and* ***CoTCPc@p-CTF*** *(c),* ***p-CTF-py*** *and* ***CoTCPc@p-CTF-py*** *(d),* ***p-CTF*** *without or with* $HAsc^-$ *(e),* ***p-CTF-py*** *without or with* $HAsc^-$ *(f). The solid was suspended in anhydrous DMF (0.5 g* L^{-1}*) for measurements.*

We further investigated the charge transfer process by photoluminescence (PL) spectroscopy. Figure 3a displays the steady-state PL spectra of **p-CTF** and **p-CTF-py** in colloidal systems with DMF (0.5 g L^{-1}), which forms more stable suspensions than in water. Each sample reveals a structureless emission band ranging from 370 to 650 nm upon 350 nm excitation. Further, normalized time-resolved photoluminescence (TRPL) decays of the samples from 424-496 nm were collected using time-correlated single-photon counting (TCSPC), as illustrated in Figure 3b-3f.

For both **p-CTF** and **p-CTF-py**, the best fit for the PL decay is obtained through four exponential decay functions with their parameters summarized in Table S6. The observed multi-exponential decay behavior can be ascribed to the broad distribution of electron and hole trap states. As shown in Figure 3b, for **p-CTF**, the majority of PL signal (83.8%) decays within an instrument-response-function (IRF; Figure S28) limited

timescale, giving an average PL decay lifetime of 0.43±0.06 ns. However, for **p-CTF-py**, no IRF-limited decay component is observed, exhibiting an extended average PL decay lifetime of 3.46±0.47 ns. In the charge separated states associated with the excited states of CTF materials, the negative charge is mainly located at the triazine moiety due to its strong electron acceptor nature.[66–68] Therefore, the positive charge is associated with the aromatic ring linking the triazine moieties. In the case of the **p-CTF-py**, the negative charge is also located on the triazine moiety, but now the positive charge can be at least partially located at the dangling pyridyl, represented as [$^{-}$CTF-py^{+}]*. Hence the lifetime enhancement of **p-CTF-py** can be associated with the charge separation structure at the excited state, [$^{-}$CTF-py^{+}]*, that further spatially separates the charges, as compared to **p-CTF**, and thus reduces back electron transfer probability.

The transfer of electrons or holes on the CTF-based semiconductors was further analyzed by comparing their PL decay kinetics with the **CoTCPc**-functionalized hybrid materials and in the presence of sodium ascorbate ($HAsc^{-}$), as hole scavenger. The parameters obtained are listed in Table S7.

The PL experiments in Figure 3e show that for **p-CTF** the excited state is not affected by the presence of $HAsc^{-}$ as hole scavenger, indicating that the recombination process is faster than the potential reaction of **p-CTF*** and $HAsc^{-}$. In sharp contrast, in the presence of the Co catalyst, for the **CoTCPc@p-CTF** material, the PL decay rate slightly increases with electron transfer time constant of τ_{ct} = 0.73±0.27 ns as can be observed in Figure 3c, due to the interaction between the excited CTF and the Co(II) catalyst, forming [$^{+}$CTF-Co(I)]. The latter, then, in the presence of $HAsc^{-}$ as sacrificial electron donor generates [CTF-Co(I)]. The detailed mechanisms of CO_2 reduction mediated by the immobilized Co phthalocyanines[69–71] have been well documented, where their active states are the singly reduced, formally Co(I) species in aqueous bicarbonate buffer. Consequently, the [CTF-Co(I)] can react with CO_2 and be further reduced with the second light interaction to generate CO,[72,73] completing the catalytic cycle (Scheme 1a).

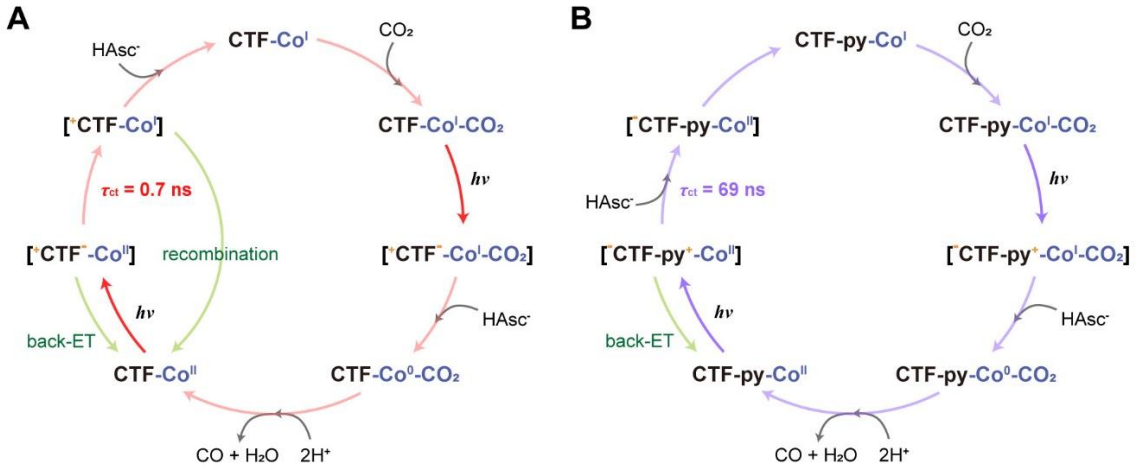

Scheme 1. *Reaction pathways followed by (a)* ***CoTCPc@p-CTF*** *(abbreviated as CTF-Co) and (b)* ***CoTCPc@p-CTF-py*** *(abbreviated as CTF-py-Co). The positive and negative charges are indicative of partial charges generated within the CTF framework induced by irradiation.*

In the case of **p-CTF-py**, the PL experiments in Figure 3d show that the excited state, [$^{-}$CTF-py^{+}-Co]*, has nearly identical lifetime as in the absence of the Co catalysts [CTF-py]* (Table S6), suggesting that the recombination is faster than electron transfer from **p-CTF-py** to the Co center. Interestingly, for the case of **p-CTF-py** the PL experiments in Figure 3f show that the excited state, [$^{-}$CTF-py^{+}]*, can be quenched by HAsc^{-} with an average hole transfer time constant of τ_{CT} = 69.2 $\pm$ 16.6 ns, in competition with the electron hole recombination process. Thus, as proposed in Scheme 1b, in the present case the catalytic process is fostered by the reaction of the excited state with HAsc^{-}, generating the [$^{-}$CTF-py-Co(II)] species that further forms the reduced species [CTF-py-Co(I)]. The Co(I) center can activate CO_2,[69,70] followed by subsequent proton-coupled electron transfer[74] by a second photon to eventually form CO thus closing the catalytic cycle.

To elucidate the nature of the charge transfer processes within **CoTCPc@p-CTF-py**, DFT and constrained DFT (CDFT) calculations at the MN15[35] level of theory were performed (see Figure 4, S29-S31 and Supplementary Information for further details). The CDFT calculations indicate that the excited state (^{4}[^{3}**CTF-**^{2}**Co^{II}**]^{0}) could be quenched by HAsc^{-} generating the reduced CTF species (^{3}[^{2}**CTF$^{\bullet-}$-**^{2}**Co^{II}**]$^{-}$), which will spontaneously (ΔE = –0.30 eV) convert to a reduced catalytic intermediate (^{1}[^{1}**CTF-**^{1}**Co^{I}**]$^{-}$) (Figure 4).

Alternatively, the excited state ($^4[^3$**CTF-^{2}Co^{II}**$]^0$) could initially evolve to a charge separated state ($^2[^2$**CTF$^{+\bullet}$-^{1}Co^I**$]^0$) by oxidation of CTF before reacting with HAsc$^-$ to generate the reduced catalytic intermediate ($^1[^1$**CTF-^{1}Co^I**$]^-$) in an exothermic step (ΔE = –0.76 eV). In the presence of high HAsc$^-$ concentration, the former pathway is expected to dominate in agreement with our proposed mechanism in Scheme 1b.

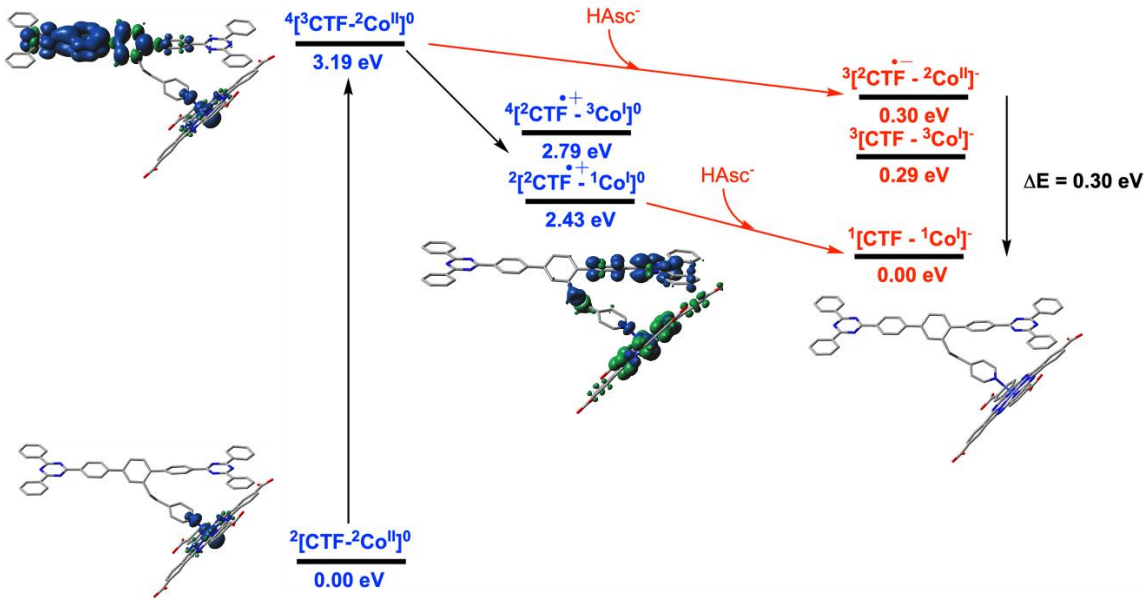

Figure 4. *Energy diagram generated via CDFT calculations for the different species involved in the light induced reactions that occur at the first reduction of* ***CoTCPc@p-CTF-py*** *cluster model. Unpaired spin density plots of key* ***CoTCPc@p-CTF-py*** *species are shown.*

To further clarify the photo-induced electron transfer processes, in-situ light-induced XPS was applied on **CoTCPc@p-CTF-py**. Under illumination (Figure 5a), all the Co binding energy values show significant negative shifts, in agreement with the Co(II)/Co(I) reduction powered by the electron injection into **CoTCPc** from the excited states of **p-CTF-py**.[52] Meanwhile, we also operated in-situ light-induced EPR on **p-CTF-py** and **CoTCPc@p-CTF-py**. The Co-free **p-CTF-py** displayed an intense *g*-signal value of 2.00, assignable to the delocalized π-electrons on the C species of the aromatic rings,[75,76] which was negligibly changed upon illumination (Figure S32). In contrast, an additional *g*-signal value of 2.17 which originates from the high-spin Co^{II} species[77] could be detected in the case of **CoTCPc@p-CTF-py** (Figure 5b). Upon illumination, this EPR signal

was weakened (Figure 5b inset), indicative of the paramagnetic Co(II) was reduced to the EPR-silent Co(I) intermediate,[57,77] consistent with the in-situ XPS results. Overall, the above in situ spectroscopic results confirm the effective Co(II)/Co(I) reduction under light excitation, supporting the mechanism proposed in Scheme 1.

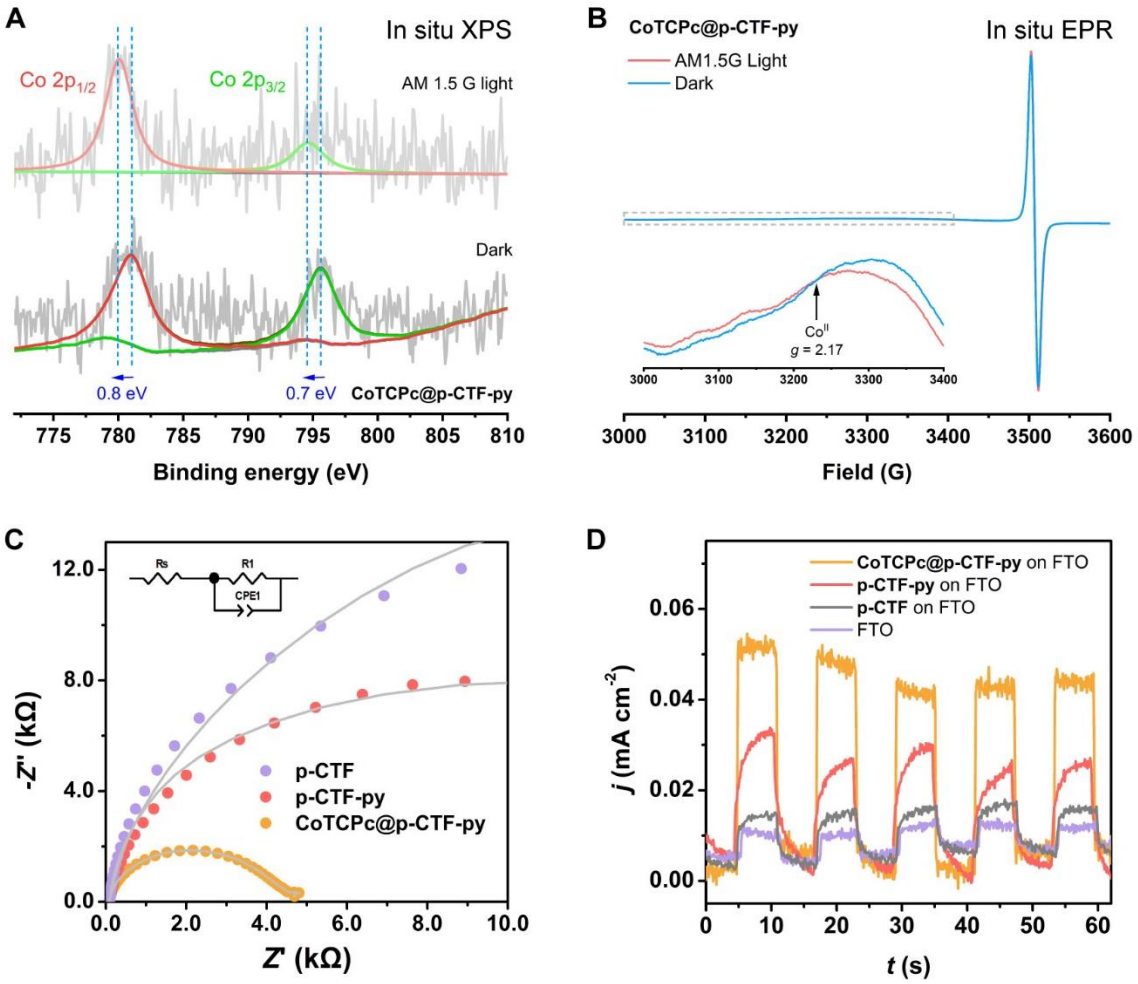

Figure 5. *(a) In situ XPS Co 2p signals of* ***CoTCPc@p-CTF-py*** *in the absence (down) and presence (up) of illumination. (b) In situ EPR signals of* ***CoTCPc@p-CTF-py*** *in the absence (blue) and presence (red) of illumination. The inset is the magnified view for the Co signals. (c) EIS spectra of* ***p-CTF*** *(violet),* ***p-CTF-py*** *(red) and* ***CoTCPc@p-CTF-py*** *(orange) on FTO electrodes carried out at E_{app} = -1.0 V vs. NHE from 20 mHz to 100 kHz in CO_2-saturated 0.1 M $KHCO_3$ solutions. The data were simulated by ZView 2.0 (grey lines) according to the circuit shown as the inset, giving charge-transfer resistance (R1) values of 30.4, 18.8, and 4.2 kΩ for* ***p-CTF****,* ***p-CTF-py*** *and* ***CoTCPc@p-CTF-py****, respectively. (d) Unbiased photocurrent response of* ***p-CTF*** *(violet),* ***p-CTF-py*** *(red) and* ***CoTCPc@p-CTF-py*** *(orange) coated on FTO slides including bare FTO (gray), in CO_2-saturated 0.1 M $KHCO_3$ aqueous solution.*

Subsequent electrochemical impedance spectroscopy (EIS) and photocurrent measurements also show consistent results to the above TRPL analysis. On one hand, **p-CTF-py** deposited on FTO slides show a smaller charge-transfer resistance than that of **p-CTF**, showing a better intrinsic charge separation (Figure 5c). This is in good agreement with the photocurrent evaluations, where the non-biased photo-current of **p-CTF-py** is markedly higher than that of **p-CTF** (Figure 5d). Further EIS outcome (Figure 5c) and photocurrent comparison (Figure 5d) also reveal the remarkably decreased charge-transfer resistance and enhanced photocurrent with immobilization of **CoTCPc** on **p-CTF-py**, respectively, demonstrating a faster charge separation rather than charge recombination with the grafted cobalt catalyst under catalytic conditions. These experiments, together with the TRPL analysis, indicate that, compared to the increased electron transfer rate, a longer-lived electron-hole lifetime plays a key role in yielding a faster CO_2 reduction reaction.

4.3. Conclusions

To sum up, we present the first couple of examples combining organic polymeric semiconductors and molecular catalysts for selective CO_2 photoreduction in fully aqueous solutions where the catalyst is solely bonded to the CTF (**p-CTF**) via covalent coordination bonding with a dangling pyridyl ligand (**p-CTF-py**). In the **p-CTF** case, the excited state is quenched intramolecularly, whereas in the **p-CTF-py** the presence of the pyridyl group favors a bimolecular quenching with $HAsc^-$. The photocatalytic hybrid material with the pyridyl pendant group axially coordinated to a carboxyl-derived Co(II) phthalocyanine (**CoTCPc@p-CTF-py**) has a charge transfer time constant that is two orders of magnitude longer than the CTF case (**CoTCPc@p-CTF**) and thus efficiently mediates the CO_2 photoreduction to CO in $KHCO_3$ aqueous buffer, achieving a high CO yield of 22.1±0.8 mmol g^{-1} (458±17 µmol g^{-1} h^{-1}) and a high turnover number of 559±20 within 48 h with no deactivation and detectable H_2 (1119 for two runs). Driven by solar/visible light, the present system displays the best performance reported so far in terms of both TONs and selectivity in water with earth abundant catalysts and organic semiconductors. Further, the covalent bonding of **p-CTF-py** with the molecular catalysts

strongly enhances the stability of the hybrid material for the photocatalytic reduction of CO_2 to CO. Systematic experiments coupled with quantum chemical calculations indicate a charge transfer mechanism significantly altered by the dangling pyridine arms, via tuning the semiconducting properties as well as the interfacial electron transfer processes.

Finally, the present **CoTCPc@p-CTF-py** molecular hybrid systems show the benefit of combining molecules and materials *via* covalent bonding and represents a sustainable alternative to those inorganic semiconductors generally featuring precious and/or heavy metals.

4.4. References

(1) Liu, Z.; Deng, Z.; He, G.; Wang, H.; Zhang, X.; Lin, J.; Qi, Y.; Liang, X. Challenges and Opportunities for Carbon Neutrality in China. *Nat. Rev. Earth Environ.* **2022**, *3* (2), 141–155. https://doi.org/10.1038/s43017-021-00244-x.

(2) Wang, J. W.; Jiang, L.; Huang, H. H.; Han, Z.; Ouyang, G. Rapid Electron Transfer via Dynamic Coordinative Interaction Boosts Quantum Efficiency for Photocatalytic CO_2 Reduction. *Nat. Commun.* **2021**, *12* (1), 1–11. https://doi.org/10.1038/s41467-021-24647-y.

(3) Bonchio, M.; Bonin, J.; Ishitani, O.; Lu, T.-B.; Morikawa, T.; Morris, A. J.; Reisner, E.; Sarkar, D.; Toma, F. M.; Robert, M. Best Practices for Experiments and Reporting in Photocatalytic CO_2 Reduction. *Nat. Catal.* **2023**, *6*, 657–665. https://doi.org/10.1038/s41929-023-00992-7.

(4) Morikawa, T.; Sato, S.; Sekizawa, K.; Suzuki, T. M.; Arai, T. Solar-Driven CO_2 Reduction Using a Semiconductor/Molecule Hybrid Photosystem: From Photocatalysts to a Monolithic Artificial Leaf. *Acc. Chem. Res.* **2022**, *55* (7), 933–943. https://doi.org/10.1021/acs.accounts.1c00564.

(5) Wang, J. W.; Ma, F.; Jin, T.; He, P.; Luo, Z. M.; Kupfer, S.; Karnahl, M.; Zhao, F.; Xu, Z.; Jin, T.; Lian, T.; Huang, Y. L.; Jiang, L.; Fu, L. Z.; Ouyang, G.; Yi, X. Y. Homoleptic Al(III) Photosensitizers for Durable CO_2 Photoreduction. *J. Am. Chem. Soc.* **2023**, *145* (1), 676–688. https://doi.org/10.1021/jacs.2c11740.

(6) Yamazaki, Y.; Takeda, H.; Ishitani, O. Photocatalytic Reduction of CO_2 Using Metal Complexes. *J. Photochem. Photobiol. C Photochem. Rev.* **2015**, *25* (4), 106–137. https://doi.org/10.1016/j.jphotochemrev.2015.09.001.

(7) Wang, J.--w.; Li, Z.; Luo, Z.--m.; Huang, Y.; Ma, F.; Kupferc, S.; Ouyang, G. Boosting CO_2

Photoreduction by π –π-Induced Preassembly between a Cu(I) Sensitizer and a Pyrene-Appended Co(II) Catalyst. *Proc. Natl. Acad. Sci.* **2023**, *120* (13), e2221219120. https://doi.org/10.1073/pnas.2221219120.

(8) Ma, F.; Luo, Z. M.; Wang, J. W.; Aramburu-Trošelj, B. M.; Ouyang, G. Earth-Abundant-Metal Complexes as Photosensitizers in Molecular Systems for Light-Driven CO_2 Reduction. *Coord. Chem. Rev.* **2024**, *500* (October 2023). https://doi.org/10.1016/j.ccr.2023.215529.

(9) Ong, W. J.; Tan, L. L.; Ng, Y. H.; Yong, S. T.; Chai, S. P. Graphitic Carbon Nitride (g-C_3N_4)-Based Photocatalysts for Artificial Photosynthesis and Environmental Remediation: Are We a Step Closer to Achieving Sustainability? *Chem. Rev.* **2016**, *116* (12), 7159–7329. https://doi.org/10.1021/acs.chemrev.6b00075.

(10) Krishnaraj, C.; Jena, H. S.; Leus, K.; Van Der Voort, P. Covalent Triazine Frameworks-a Sustainable Perspective. *Green Chem.* **2020**, *22* (4), 1038–1071. https://doi.org/10.1039/c9gc03482j.

(11) Hu, X. L.; Li, H. G.; Tan, B. E. COFs-Based Porous Materials for Photocatalytic Applications. *Chinese J. Polym. Sci. (English Ed.* **2020**, *38* (7), 673–684. https://doi.org/10.1007/s10118-020-2394-x.

(12) Thomas, A. Functional Materials: From Hard to Soft Porous Frameworks. *Angew. Chemie - Int. Ed.* **2010**, *49* (45), 8328–8344. https://doi.org/10.1002/anie.201000167.

(13) Banerjee, T.; Podjaski, F.; Kröger, J.; Biswal, B. P.; Lotsch, B. V. Polymer Photocatalysts for Solar-to-Chemical Energy Conversion. *Nat. Rev. Mater.* **2021**, *6*, 168–190. https://doi.org/10.1038/s41578-020-00254-z.

(14) Wang, Y.; Vogel, A.; Sachs, M.; Sprick, R. S.; Wilbraham, L.; Moniz, S. J. A.; Godin, R.; Zwijnenburg, M. A.; Durrant, J. R.; Cooper, A. I.; Tang, J. Current Understanding and Challenges of Solar-Driven Hydrogen Generation Using Polymeric Photocatalysts. *Nat. Energy* **2019**, *4*, 746–760. https://doi.org/10.1038/s41560-019-0456-5.

(15) Schneider, J.; Jia, H.; Muckerman, J. T.; Fujita, E. Thermodynamics and Kinetics of CO_2, CO, and H^+ Binding to the Metal Centre of CO_2 Reduction Catalysts. *Chem. Soc. Rev.* **2012**, *41* (6), 2036–2051. https://doi.org/10.1039/c1cs15278e.

(16) Chang, X.; Wang, T.; Yang, P.; Zhang, G.; Gong, J. The Development of Cocatalysts for Photoelectrochemical CO_2 Reduction. *Adv. Mater.* **2019**, *31* (31), 1–13. https://doi.org/10.1002/adma.201804710.

(17) Wang, J. W.; Gil-Sepulcre, M.; Huang, H. H.; Solano, E.; Mu, Y. F.; Llobet, A.; Ouyang, G. CH-π Interaction Boosts Photocatalytic CO_2 Reduction Activity of a Molecular Cobalt Catalyst Anchored on Carbon Nitride. *Cell Reports Phys. Sci.* **2021**, *2* (12), 100681. https://doi.org/10.1016/j.xcrp.2021.100681.

(18) Nakada, A.; Kumagai, H.; Robert, M.; Ishitani, O.; Maeda, K. Molecule/Semiconductor Hybrid Materials for Visible-Light CO_2 Reduction: Design Principles and Interfacial Engineering. *Accounts Mater. Res.* **2021**, *2* (6), 458–470. https://doi.org/10.1021/accountsmr.1c00060.

(19) Maeda, K.; Kuriki, R.; Zhang, M.; Wang, X.; Ishitani, O. The Effect of the Pore-Wall Structure of Carbon Nitride on Photocatalytic CO_2 Reduction under Visible Light. *J. Mater. Chem. A* **2014**, *2* (36), 15146–15151. https://doi.org/10.1039/c4ta03128h.

(20) Kuriki, R.; Sekizawa, K.; Ishitani, O.; Maeda, K. Visible-Light-Driven CO_2 Reduction with Carbon Nitride: Enhancing the Activity of Ruthenium Catalysts. *Angew. Chemie - Int. Ed.* **2015**, *54* (8), 2406–2409. https://doi.org/10.1002/anie.201411170.

(21) Kuriki, R.; Yamamoto, M.; Higuchi, K.; Yamamoto, Y.; Akatsuka, M.; Lu, D.; Yagi, S.; Yoshida, T.; Ishitani, O.; Maeda, K. Robust Binding between Carbon Nitride Nanosheets and a Binuclear Ruthenium(II) Complex Enabling Durable, Selective CO_2 Reduction under Visible Light in Aqueous Solution. *Angew. Chemie - Int. Ed.* **2017**, *56* (17), 4867–4871. https://doi.org/10.1002/anie.201701627.

(22) Zhao, G.; Pang, H.; Liu, G.; Li, P.; Liu, H.; Zhang, H.; Shi, L.; Ye, J. Co-Porphyrin/carbon Nitride Hybrids for Improved Photocatalytic CO_2 Reduction under Visible Light. *Appl. Catal. B Environ.* **2017**, *200*, 141–149. https://doi.org/10.1016/j.apcatb.2016.06.074.

(23) Lin, L.; Hou, C.; Zhang, X.; Wang, Y.; Chen, Y.; He, T. Highly Efficient Visible-Light Driven Photocatalytic Reduction of CO_2 over g-C_3N_4 nanosheets/tetra(4-Carboxyphenyl)porphyrin iron(III) Chloride Heterogeneous Catalysts. *Appl. Catal. B Environ.* **2018**, *221* (August 2017), 312–319. https://doi.org/10.1016/j.apcatb.2017.09.033.

(24) Tang, S.; Yin, X.; Wang, G.; Lu, X.; Lu, T. Single Titanium-Oxide Species Implanted in 2D g-C_3N_4 Matrix as a Highly Efficient Visible-Light CO_2 Reduction Photocatalyst. *Nano Res.* **2019**, *12* (2), 457–462. https://doi.org/10.1007/s12274-018-2240-4.

(25) Cometto, C.; Kuriki, R.; Chen, L.; Maeda, K.; Lau, T. C.; Ishitani, O.; Robert, M. A Carbon Nitride/Fe Quaterpyridine Catalytic System for Photostimulated CO_2-to-CO Conversion with Visible Light. *J. Am. Chem. Soc.* **2018**, *140* (24), 7437–7440. https://doi.org/10.1021/jacs.8b04007.

(26) Wei, Y.; Chen, L.; Chen, H.; Cai, L.; Tan, G.; Qiu, Y.; Xiang, Q.; Chen, G.; Lau, T. C.; Robert, M. Highly Efficient Photocatalytic Reduction of CO_2 to CO by In Situ Formation of a Hybrid Catalytic System Based on Molecular Iron Quaterpyridine Covalently Linked to Carbon Nitride. *Angew. Chemie - Int. Ed.* **2022**, *61* (11), 1–8. https://doi.org/10.1002/anie.202116832.

(27) Arcudi, F.; Dordević, L.; Nagasing, B.; Stupp, S. I.; Weiss, E. A. Quantum Dot-Sensitized Photoreduction of CO_2 in Water with Turnover Number > 80,000. *J. Am. Chem. Soc.* **2021**, *143* (43), 18131–18138. https://doi.org/10.1021/jacs.1c06961.

(28) Rodríguez-Jiménez, S.; Song, H.; Lam, E.; Wright, D.; Pannwitz, A.; Bonke, S. A.; Baumberg, J. J.; Bonnet, S.; Hammarström, L.; Reisner, E. Self-Assembled Liposomes Enhance Electron Transfer for Efficient Photocatalytic CO_2 Reduction. *J. Am. Chem. Soc.* **2022**, *144* (21), 9399–9412. https://doi.org/10.1021/jacs.2c01725.

(29) Zhang, X.; Yamauchi, K.; Sakai, K. Earth-Abundant Photocatalytic CO_2 Reduction by Multielectron Chargeable Cobalt Porphyrin Catalysts: High CO/H_2 Selectivity in Water Based on Phase Mismatch in Frontier MO Association. *ACS Catal.* **2021**, *11*, 10436–10449. https://doi.org/10.1021/acscatal.1c02475.

(30) Ma, F.; Luo, Z. M.; Wang, J. W.; Ouyang, G. Highly Efficient, Noble-Metal-Free, Fully Aqueous CO_2 Photoreduction Sensitized by a Robust Organic Dye. *J. Am. Chem. Soc.* **2024**, *146* (26), 17773–17783. https://doi.org/10.1021/jacs.4c03128.

(31) Sun, T.; Liang, Y.; Luo, W.; Zhang, L.; Cao, X.; Xu, Y. A General Strategy for Kilogram-Scale Preparation of Highly Crystal-Line Covalent Triazine Frameworks. *Angew. Chemie - Int. Ed.* **2022**, *61* (25). https://doi.org/10.1002/anie.202203327.

(32) De, A.; Haldar, S.; Michel, S.; Shupletsov, L.; Bon, V.; Lopatik, N.; Ding, L.; Eng, L. M.; Auernhammer, G. K.; Brunner, E.; Schneemann, A. Manipulation of Covalent Organic Frameworks by Side-Chain Functionalization: Toward Few Layer Nanosheets. *Chem. Mater.* **2023**, *35* (10), 3911–3922. https://doi.org/10.1021/acs.chemmater.3c00048.

(33) Pelkowski, C. E.; Natraj, A.; Malliakas, C. D.; Burke, D. W.; Bardot, M. I.; Wang, Z.; Li, H.; Dichtel, W. R. Tuning Crystallinity and Stacking of Two-Dimensional Covalent Organic Frameworks through Side-Chain Interactions. *J. Am. Chem. Soc.* **2023**, *145* (40), 21798–21806. https://doi.org/10.1021/jacs.3c03868.

(34) Wu, X.; Han, X.; Liu, Y.; Liu, Y.; Cui, Y. Control Interlayer Stacking and Chemical Stability of Two-Dimensional Covalent Organic Frameworks via Steric Tuning. *J. Am. Chem. Soc.* **2018**, *140* (47), 16124–16133. https://doi.org/10.1021/jacs.8b08452.

(35) Yu, H. S.; He, X.; Li, S. L.; Truhlar, D. G. MN15: A Kohn-Sham Global-Hybrid Exchange-Correlation Density Functional with Broad Accuracy for Multi-Reference and Single-Reference Systems and Noncovalent Interactions. *Chem. Sci.* **2016**, *7* (8), 5032–5051. https://doi.org/10.1039/c6sc00705h.

(36) Huang, Y.; Dai, H.; Moonshiram, D.; Li, Z.; Luo, Z. M.; Zhang, J. H.; Yang, W.; Shen, Y.; Wang, J. W.; Ouyang, G. Impaired Conjugation Boosts CO_2 Electroreduction by Ni(II) Macrocyclic Catalysts Immobilized on Carbon Nanotubes. *J. Mater. Chem. A* **2023**, *11* (6), 2969–2978. https://doi.org/10.1039/d2ta08781b.

(37) Hu, W.; Wang, D.; Ma, Q.; Reinhart, B. J.; Zhang, X.; Huang, J. The Impact of Axial Ligation on the

Excited State Dynamics of Cobalt(II) Phthalocyanine. *J. Photochem. Photobiol.* **2022**, *11* (June), 100132. https://doi.org/10.1016/j.jpap.2022.100132.

(38) Chandrasekaran, P.; Chiang, K. P.; Nordlund, D.; Bergmann, U.; Holland, P. L.; DeBeer, S. Sensitivity of X - Ray Core Spectroscopy to Changes in Metal Ligation : *Inorg. Chem.* **2013**, *52*, 6286–6298. https://doi.org/10.1021/ic3021723.

(39) Loeb, K. E.; Westre, T. E.; Kappock, T. J.; Mitić, N.; Glasfeld, E.; Caradonna, J. P.; Hedman, B.; Hodgson, K. O.; Solomon, E. I. Spectroscopic Characterization of the Catalytically Competent Ferrous Site of the Resting, Activated, and Substrate-Bound Forms of Phenylalanine Hydroxylase. *J. Am. Chem. Soc.* **1997**, *119* (8), 1901–1915. https://doi.org/10.1021/ja962269h.

(40) George, S. D. B.; Brant, P.; Solomon, E. I. Metal and Ligand K-Edge XAS of Organotitanium Complexes: Metal 4p and 3d Contributions to Pre-Edge Intensity and Their Contributions to Bonding. *J. Am. Chem. Soc.* **2005**, *127* (2), 667–674. https://doi.org/10.1021/ja044827v.

(41) Westre, T. E.; Kennepohl, P.; DeWitt, J. G.; Hedman, B.; Hodgson, K. O.; Solomon, E. I. A Multiplet Analysis of Fe K-Edge 1s → 3d Pre-Edge Features of Iron Complexes. *J. Am. Chem. Soc.* **1997**, *119* (27), 6297–6314. https://doi.org/10.1021/ja964352a.

(42) Moonshiram, D.; Garrido-Barros, P.; Gimbert-Suriñach, C.; Picón, A.; Liu, C.; Zhang, X.; Karnahl, M.; Llobet, A. Elucidating the Nature of the Excited State of a Heteroleptic Copper Photosensitizer by Using Time-Resolved X-Ray Absorption Spectroscopy. *Chem. - A Eur. J.* **2018**, *24* (24), 6464–6472. https://doi.org/10.1002/chem.201800330.

(43) Baker, M. L.; Mara, M. W.; Yan, J. J.; Hodgson, K. O.; Hedman, B.; Solomon, E. I. K- and L-Edge X-Ray Absorption Spectroscopy (XAS) and Resonant Inelastic X-Ray Scattering (RIXS) Determination of Differential Orbital Covalency (DOC) of Transition Metal Sites. *Coord. Chem. Rev.* **2017**, *345*, 182–208. https://doi.org/10.1016/j.ccr.2017.02.004.

(44) Lieber, C. M.; Lewis, N. S. Catalytic Reduction of Carbon Dioxide at Carbon Electrodes Modified with Cobalt Phthalocyanine. *J. Am. Chem. Soc.* **1984**, *106* (17), 5033–5034. https://doi.org/10.1021/ja00329a082.

(45) Han, N.; Wang, Y.; Ma, L.; Wen, J.; Li, J.; Zheng, H.; Nie, K.; Wang, X.; Zhao, F.; Li, Y.; Fan, J.; Zhong, J.; Wu, T.; Miller, D. J.; Lu, J.; Lee, S. T.; Li, Y. Supported Cobalt Polyphthalocyanine for High-Performance Electrocatalytic CO_2 Reduction. *Chem* **2017**, *3* (4), 652–664. https://doi.org/10.1016/j.chempr.2017.08.002.

(46) Wu, Y.; Jiang, Z.; Lu, X.; Liang, Y.; Wang, H. Domino Electroreduction of CO_2 to Methanol on a Molecular Catalyst. *Nature* **2019**, *575* (7784), 639–642. https://doi.org/10.1038/s41586-019-1760-8.

(47) Wu, Y.; Hu, G.; Rooney, C. L.; Brudvig, G. W.; Wang, H. Heterogeneous Nature of Electrocatalytic

CO/CO_2 Reduction by Cobalt Phthalocyanines. *ChemSusChem* **2020**, *13* (23), 6296–6299. https://doi.org/10.1002/cssc.202001396.

(48) Jiang, Z.; Wang, Y.; Zhang, X.; Zheng, H.; Wang, X.; Liang, Y. Revealing the Hidden Performance of Metal Phthalocyanines for CO_2 Reduction Electrocatalysis by Hybridization with Carbon Nanotubes. *Nano Res.* **2019**, *12* (9), 2330–2334. https://doi.org/10.1007/s12274-019-2455-z.

(49) Zhu, M.; Chen, J.; Guo, R.; Xu, J.; Fang, X.; Han, Y. F. Cobalt Phthalocyanine Coordinated to Pyridine-Functionalized Carbon Nanotubes with Enhanced CO_2 Electroreduction. *Appl. Catal. B Environ.* **2019**, *251* (February), 112–118. https://doi.org/10.1016/j.apcatb.2019.03.047.

(50) Wu, J. H.; Wang, J. W.; Aramburu-Trošelj, B. M.; Niu, F. J.; Guo, L. J.; Ouyang, G. Recent Progress on Nickel Phthalocyanine-Based Electrocatalysts for CO_2 Reduction. *Nanoscale* **2024**, *16* (24), 11496–11512. https://doi.org/10.1039/d4nr01269k.

(51) Li, Z.; Wang, J. W.; Huang, Y.; Ouyang, G. Enhancing CO_2 Photoreduction via the Perfluorination of Co(II) Phthalocyanine Catalysts in a Noble-Metal-Free System. *Chinese J. Catal.* **2023**, *49*, 160–167. https://doi.org/10.1016/S1872-2067(23)64433-X.

(52) Zhao, J.; Mu, Y.; Wu, L.; Luo, Z.; Velasco, L.; Sauvan, M.; Moonshiram, D.; Wang, J.; Zhang, M.; Lu, T. Directed Electron Delivery from a Pb-Free Halide Perovskite to a Co(II) Molecular Catalyst Boosts CO_2 Photoreduction Coupled with Water Oxidation . *Angew. Chemie* **2024**, *136* (21). https://doi.org/10.1002/ange.202401344.

(53) Wang, J.; Zhang, X.; Kamahl, M.; Luo, Z.-M.; Li, Z.; Huang, Y.; Yu, J.; Hu, W.; Zhang, X.; Moonshiram, D.; Ouyang, G. Photocatalytic CO_2 Reduction with a Quantum Efficiency Exceeding 60%: Time-Resolved Spectroscopic and X-Ray Studies on Cu(I) Photosensitizers in Coordinative Interaction with Co(II) Phthalocyanine Catalysts. *Res. Sq.* **2022**. https://doi.org/10.21203/rs.3.rs-1246142/v1.

(54) Zhang, Y.; Yao, D.; Xia, B.; Jaroniec, M.; Ran, J.; Qiao, S. Z. Photocatalytic CO_2 Reduction: Identification and Elimination of False-Positive Results. *ACS Energy Lett.* **2022**, *7* (5), 1611–1617. https://doi.org/10.1021/acsenergylett.2c00427.

(55) Chen, P.; Dong, X.; Huang, M.; Li, K.; Xiao, L.; Sheng, J.; Chen, S.; Zhou, Y.; Dong, F. Rapid Self-Decomposition of g-C_3N_4 During Gas-Solid Photocatalytic CO_2 Reduction and Its Effects on Performance Assessment. *ACS Catal.* **2022**, *12* (8), 4560–4570. https://doi.org/10.1021/acscatal.2c00815.

(56) Wang, S.; Jiang, B.; Henzie, J.; Xu, F.; Liu, C.; Meng, X.; Zou, S.; Song, H.; Pan, Y.; Li, H.; Yu, J.; Chen, H.; Ye, J. Designing Reliable and Accurate Isotope-Tracer Experiments for CO_2 Photoreduction. *Nat. Commun.* **2023**, *14* (1), 1–12. https://doi.org/10.1038/s41467-023-38052-0.

(57) Wang, S.; Hai, X.; Ding, X.; Jin, S.; Xiang, Y.; Wang, P.; Jiang, B.; Ichihara, F.; Oshikiri, M.; Meng, X.; Li, Y.; Matsuda, W.; Ma, J.; Seki, S.; Wang, X.; Huang, H.; Wada, Y.; Chen, H.; Ye, J. Intermolecular

Cascaded π-Conjugation Channels for Electron Delivery Powering CO_2 Photoreduction. *Nat. Commun.* **2020**, *11* (1), 1–9. https://doi.org/10.1038/s41467-020-14851-7.

(58) Ma, B.; Chen, G.; Fave, C.; Chen, L.; Kuriki, R.; Maeda, K.; Ishitani, O.; Lau, T. C.; Bonin, J.; Robert, M. Efficient Visible-Light-Driven CO_2 Reduction by a Cobalt Molecular Catalyst Covalently Linked to Mesoporous Carbon Nitride. *J. Am. Chem. Soc.* **2020**, *142* (13), 6188–6195. https://doi.org/10.1021/jacs.9b13930.

(59) Ma, B.; Blanco, M.; Calvillo, L.; Chen, L.; Chen, G.; Lau, T. C.; Dražić, G.; Bonin, J.; Robert, M.; Granozzi, G. Hybridization of Molecular and Graphene Materials for CO_2 Photocatalytic Reduction with Selectivity Control. *J. Am. Chem. Soc.* **2021**, *143* (22), 8414–8425. https://doi.org/10.1021/jacs.1c02250.

(60) Roy, S.; Reisner, E. Visible-Light-Driven CO_2 Reduction by Mesoporous Carbon Nitride Modified with Polymeric Cobalt Phthalocyanine. *Angew. Chemie - Int. Ed.* **2019**, *58* (35), 12180–12184. https://doi.org/10.1002/anie.201907082.

(61) He, Y.; Zhao, Y.; Wang, X.; Liu, Z.; Yu, Y.; Li, L. Multiple Heteroatom-Hydrogen Bonds Bridging Electron Transport in Covalent Organic Framework-Based Supramolecular System for Photoreduction of CO_2. *Angew. Chemie - Int. Ed.* **2023**, *62* (31), 1–7. https://doi.org/10.1002/anie.202307160.

(62) Kuriki, R.; Matsunaga, H.; Nakashima, T.; Wada, K.; Yamakata, A.; Ishitani, O.; Maeda, K. Nature-Inspired, Highly Durable CO_2 Reduction System Consisting of a Binuclear Ruthenium(II) Complex and an Organic Semiconductor Using Visible Light. *J. Am. Chem. Soc.* **2016**, *138* (15), 5159–5170. https://doi.org/10.1021/jacs.6b01997.

(63) Cheng, Y. Z.; Ji, W.; Hao, P. Y.; Qi, X. H.; Wu, X.; Dou, X. M.; Bian, X. Y.; Jiang, D.; Li, F. T.; Liu, X. F.; Yang, D. H.; Ding, X.; Han, B. H. A Fully Conjugated Covalent Organic Framework with Oxidative and Reductive Sites for Photocatalytic Carbon Dioxide Reduction with Water. *Angew. Chemie - Int. Ed.* **2023**, *62* (36). https://doi.org/10.1002/anie.202308523.

(64) Piercy, V. L.; Neri, G.; Manning, T. D.; Pugliese, A.; Blanc, F.; Palgrave, R. G.; Cowan, A. J.; Rosseinsky, M. J. Band Structure Engineering of Carbon Nitride Hybrid Photocatalysts for CO_2 Reduction in Aqueous Solutions. *J. Mater. Chem. A* **2023**, *11* (34), 18356–18364. https://doi.org/10.1039/d3ta02872k.

(65) McGuigan, S.; Tereniak, S. J.; Donley, C. L.; Smith, A.; Jeon, S.; Zhao, F.; Sampaio, R. N.; Pauly, M.; Keller, L.; Collins, L.; Parsons, G. N.; Lian, T.; Stach, E. A.; Maggard, P. A. Discovery of a Hybrid System for Photocatalytic CO_2 Reduction via Attachment of a Molecular Cobalt-Quaterpyridine Complex to a Crystalline Carbon Nitride. *ACS Appl. Energy Mater.* **2023**, *6* (20), 10542–10553. https://doi.org/10.1021/acsaem.3c01670.

(66) Vyas, V. S.; Lau, V. W. H.; Lotsch, B. V. Soft Photocatalysis: Organic Polymers for Solar Fuel Production. *Chem. Mater.* **2016**, *28* (15), 5191–5204. https://doi.org/10.1021/acs.chemmater.6b01894.

(67) Rath, B. B.; Krause, S.; Lotsch, B. V. Active Site Engineering in Reticular Covalent Organic Frameworks for Photocatalytic CO_2 Reduction. *Adv. Funct. Mater.* **2023**, *2309060*. https://doi.org/10.1002/adfm.202309060.

(68) Liu, X.; Qi, R.; Li, S.; Liu, W.; Yu, Y.; Wang, J.; Wu, S.; Ding, K.; Yu, Y. Triazine-Porphyrin-Based Hyperconjugated Covalent Organic Framework for High-Performance Photocatalysis. *J. Am. Chem. Soc.* **2022**, *144* (51), 23396–23404. https://doi.org/10.1021/jacs.2c09369.

(69) Liu, Y.; McCrory, C. C. L. Modulating the Mechanism of Electrocatalytic CO_2 Reduction by Cobalt Phthalocyanine through Polymer Coordination and Encapsulation. *Nat. Commun.* **2019**, *10* (1), 1–10. https://doi.org/10.1038/s41467-019-09626-8.

(70) Marianov, A. N.; Jiang, Y. Mechanism-Driven Design of Heterogeneous Molecular Electrocatalysts for CO_2 Reduction. *Accounts Mater. Res.* **2022**, *3* (6), 620–633. https://doi.org/10.1021/accountsmr.2c00041.

(71) Hutchison, P.; Smith, L. E.; Rooney, C. L.; Wang, H.; Hammes-Schiffer, S. Proton-Coupled Electron Transfer Mechanisms for CO_2 Reduction to Methanol Catalyzed by Surface-Immobilized Cobalt Phthalocyanine. *J. Am. Chem. Soc.* **2024**. https://doi.org/10.1021/jacs.4c05444.

(72) Roy, S.; Miller, M.; Warnan, J.; Leung, J. J.; Sahm, C. D.; Reisner, E. Electrocatalytic and Solar-Driven Reduction of Aqueous CO_2 with Molecular Cobalt Phthalocyanine-Metal Oxide Hybrid Materials. *ACS Catal.* **2021**, *11* (3), 1868–1876. https://doi.org/10.1021/acscatal.0c04744.

(73) Wang, J. W.; Zhang, X.; Velasco, L.; Karnahl, M.; Li, Z.; Luo, Z. M.; Huang, Y.; Yu, J.; Hu, W.; Zhang, X.; Yamauchi, K.; Sakai, K.; Moonshiram, D.; Ouyang, G. Precious-Metal-Free CO_2 Photoreduction Boosted by Dynamic Coordinative Interaction between Pyridine-Tethered Cu(I) Sensitizers and a Co(II) Catalyst. *JACS Au* **2023**, *3* (7), 1984–1997. https://doi.org/10.1021/jacsau.3c00218.

(74) Wang, J. W.; Huang, H. H.; Sun, J. K.; Ouyang, T.; Zhong, D. C.; Lu, T. B. Electrocatalytic and Photocatalytic Reduction of CO_2 to CO by Cobalt(II) Tripodal Complexes: Low Overpotentials, High Efficiency and Selectivity. *ChemSusChem* **2018**, *11* (6), 1025–1031. https://doi.org/10.1002/cssc.201702280.

(75) Lan, Z. A.; Wu, M.; Fang, Z.; Zhang, Y.; Chen, X.; Zhang, G.; Wang, X. Ionothermal Synthesis of Covalent Triazine Frameworks in a NaCl-KCl-$ZnCl_2$ Eutectic Salt for the Hydrogen Evolution Reaction. *Angew. Chemie - Int. Ed.* **2022**, *61* (18). https://doi.org/10.1002/anie.202201482.

(76) Zhang, G.; Li, G.; Heil, T.; Zafeiratos, S.; Lai, F.; Savateev, A.; Antonietti, M.; Wang, X. Tailoring the Grain Boundary Chemistry of Polymeric Carbon Nitride for Enhanced Solar Hydrogen Production

and CO_2 Reduction. *Angew. Chemie - Int. Ed.* **2019**, *58* (11), 3433–3437. https://doi.org/10.1002/anie.201811938.

(77) Wang, H.-F.; Wang, H.-J.; Zhong, D.-C.; Lu, T.-B. Unveiling the Role of Proton Concentration in Dinuclear Metal Complexes for Boosting Photocatalytic CO_2 Reduction. *Proc. Natl. Acad. Sci.* **2024**, *121* (20), e2318384121. https://doi.org/10.1073/pnas.2318384121.

4.5. Supporting information

4.5.1. Materials, instrumentation and methods

General information

All the chemicals were provided by commercial sources and used without further purification. The water used was prepared by using a Milli-Q ultrapure water purification system. Liquid-phase NMR spectra were obtained on Bruker advance III instruments (400/500 MHz). Solid-state ^{13}C NMR was conducted on a Bruker NMR machine (Ascend 400 MHz). UV–vis spectra of homogeneous solutions were collected on a Shimadzu UV-2410 spectrophotometer. UV–vis spectra of DMF suspensions were obtained on a PerkinElmer Lambda 1050 spectrophotometer with an integration sphere and a near-IR detector. FT-IR data of solid samples were acquired from a Bruker FT-IR-ATR instrument (ALPHA-E). PXRD data were collected on a Smart X-ray diffractometer (SmartLab 9 KW, Rigaku, Japan) with Cu/$K\alpha$ radiation (λ = 1.54178 Å). The evolved CO and H_2 were monitored by using an Agilent 7820A gas chromatography. The liquid phase of the reaction system was analyzed by ^1H NMR with solvent suppression mode. Electrochemical measurements were operated on a CHI660D or a CHI730C workstation. Scanning electron microscopy (SEM) images were recorded on Si wafers at a high-resolution scanning electron microscope (FEI, Scios 2). Transmission electron microscopy (TEM) and energy-dispersive X-ray spectroscopy (EDS) analyses were performed on Cu grids at a high-resolution transmission electron microscope of atomic resolution (JEOL F200) working at 200 kV with a resolution point of 1.4 Å. The Co contents were determined by ICP-MS (Agilent 7700). X-ray photoelectron spectroscopy (XPS) was operated on an ESCA LAB250 instrument (THERMO SCIENTIFIC, United Kingdom). XPS data were fitted by Thermo Avantage (v5.948) software. The

photoluminescence (PL) characterizations were collected by Horiba Scientific Fluoromax-plus spectrometer with excitation of 350 nm.

X-ray absorption spectroscopy (XAS) methods

X-ray absorption spectra were collected at Diamond Light Source at bending magnet beamline BM-18 at a storage-ring electron energy of 7 GeV and average current of 100 mA. The radiation was monochromatized by Si(111) crystal monochromators, and the XAS data were recorded in fluorescence mode. The intensity of the X-ray was monitored by three ion chambers (I_0, I_1 and I_2) filled with 70% nitrogen and 30% argon and placed before the sample (I_0) and after the sample (I_1 and I_2). Co metal was placed between ion chambers I_1 and I_2, and its absorption was recorded with each scan for energy calibration. Co XAS energy was calibrated by the first maxima in the derivative of the cobalt´s metal foil's X-ray absorption near edge structure (XANES) spectrum at 7708.20 eV. Around 15 XAS spectra were collected for the pellet and around 105 scans were collected for the hybrid complexes. Care was taken to measure at several sample positions on each sample (beam size 1000 µm (Horizontal) × 1000 µm(Vertical)) and no more than 5 scans were taken at each sample position. No damage was observed scan after scan to any samples. All samples were also protected from the X-ray beam during spectrometer movements by a shutter synchronized with the scan program.

Extended X-ray absorption fine structure (EXAFS) analysis

Athena[1] software was used for data processing. The energy scale for each scan was normalized using the cobalt metal standard. Data in energy space were pre-edge corrected, normalized, deglitched (if necessary), and background corrected. The processed data were next converted to the photoelectron wave vector (k) space and weighted by k^2. The electron wave number is defined as $k = [2m(E - E_0)/\hbar^2]^{1/2}$, E_0 is the energy origin or the threshold energy. K-space data were truncated near the zero crossings k = 2 to 14 Å^{-1} in Co EXAFS before Fourier transformation. The k-space data were transferred into the Artemis Software for curve fitting. In order to fit the data, the Fourier peaks were isolated separately, grouped together, or the entire (unfiltered) spectrum was used. The individual Fourier peaks were isolated by applying a Hanning window to the first and last 15% of the chosen range, leaving the middle 70% untouched. Curve fitting was performed using *ab initio*-calculated phases and amplitudes from the

FEFF8[2] program from the University of Washington. *Ab initio*-calculated phases and amplitudes were used in the EXAFS Equation S1.

$$\chi(k) = S_0^2 \sum_j \frac{N_j}{kR_j^2} f_{eff_j}(\pi, k, R_j) e^{-2\sigma_j^2 k^2} e^{\frac{-2R_j}{\lambda_j(k)}} \sin\left(2kR_j + \phi_{ij}(k)\right) \qquad \text{(S1)}$$

where N_j is the number of atoms in the j^{th} shell; R_j the mean distance between the absorbing atom and the atoms in the j^{th} shell; f_{eff_j} (π,*k*, R_j) is the *ab initio* amplitude function for shell *j*, and the Debye-Waller term $e^{-2\sigma_j^2 k^2}$ accounts for damping due to static and thermal disorder in absorber-back scatterer distances. The mean free path term $e^{\frac{-2R_j}{\lambda_j(k)}}$ reflects losses due to inelastic scattering, where $\lambda_j(k)$, is the electron mean free path. The oscillations in the EXAFS spectrum are reflected in the sinusoidal term $\sin\left(2kR_j + \phi_{ij}(k)\right)$, where $\phi_{ij}(k)$ is the *ab initio* phase function for shell *j*. This sinusoidal term shows the direct relation between the frequency of the EXAFS oscillations in k-space and the absorber-back scatterer distance. S_0^2 is an amplitude reduction factor.

The EXAFS equation (Equation S1) was used to fit the experimental Fourier isolated data (q-space) as well as unfiltered data (k-space) and Fourier transformed data (R-space) using *N*, S_0^2, E_0, *R*, and σ^2 as variable parameters. *N* refers to the number of coordination atoms surrounding Co for each shell. The quality of fit was evaluated by R-factor (Equation S2) and the reduced Chi^2 value. R-factor less than 2 % denotes that the fit is good enough whereas R-factor between 2 and 5 % denotes that the fit is correct within a consistently broad model. The reduced Chi^2 value is used to compare fits as more absorber-backscatter shells are included to fit the data. A smaller reduced Chi^2 value implies a better fit. Similar results were obtained from fits done in *k*, *q*, and *R*-spaces.

$$R - factor = \frac{\sum_i (difference\ between\ data\ and\ fit_i)^2}{\sum_i (data)^2} \qquad \text{(S2)}$$

The near edge fit and pre-edge peak fits were carried out with an error function, and gaussian functions respectively. The formulas for the error (erf) and Gaussian functions (gauss) are as follows:

Error function: $$A\left[erf\left(\frac{e-E_0}{w}\right)+1\right] \quad \text{(S3)}$$

Gaussian function: $$\left(\frac{A}{w\sqrt{2\pi}}\right)\exp\left[\frac{-(e-E_0)^2}{(2w^2)}\right] \quad \text{(S4)}$$

Where A corresponds to the amplitude; *w*, the width; E_0, the centroid of the pre-edge and near edge peaks and *e*, the X-ray energy. The parameters E_0, *A* and *w* used for each set of functions for the experimental and theoretical fits together with their uncertainties are tabulated below (Table S2).

The pre-edge area peaks fitting were further re-carried out in the Fityk[3] software and as previously demonstrated,[4] and the same pre-edge peak areas of 7.0 and 8.1 units were obtained for the **CoTCPc** and **CoTCPc@p-CTF-py** after catalysis thus confirming the fit procedure employed in the Athena software.[1]

Time-dependent density functional theory for XANES calculations

Time-dependent density functional theory (TDDFT) calculations for the XANES spectra of the Co complexes were carried out using previously established protocols.[5] The TDDFT XANES simulations were in this case performed with the B3LYP as functional with the def2-TZVP triple-zeta[6] basis and D3BJ dispersion correction effects with dense integration grids. The def2-TZVP/J auxiliary basis set was also employed. A broadening of 1.5 eV was applied to the calculated spectra (FWHM) with a Gaussian line shape. Up to 150 roots were calculated. The calculated XANES spectrum contains contributions from electric quadrupole, electric dipole and magnetic dipole transitions.

N_2 sorption

N_2 sorption measurement under 77 K is performed on the BSD-PM automatic specific surface and aperture analyzer. Firstly, the samples (around 50 mg) were evacuated for 2 h at room temperature, and evacuated at 120°C for 15 h to obtain the activated sample. The temperature is controlled by a liquid nitrogen bath (77 K).

Photocatalytic CO_2 reduction

Photocatalytic CO_2 reduction was conducted in a 4 mL home-made quartz reactor with water-cooling circulation system at 293±2 K. The reaction mixture was prepared in a 5 mL vessel with silicon cap, in which 0.5 mL 0.3 M $KHCO_3$ aqueous solution was mixed with 0.5 mL 0.075 M ascorbic acid (H_2Asc) aqueous solution and 0.5 mL aqueous dispersion of photocatalyst (1.0 g/L). The mass of catalyst was weighed by a hundred-thousandth analytical balance with a readability of 0.001 mg (Mettler Toledo MX5, 0.1% tolerance). After purged with CO_2 for 30 min, the photocatalysis was initiated with the irradiation of light (AM 1.5G or 400 nm cut-off filter) at 300 mW cm^{-2} (irradiated area is ca. 2.4 cm^2). The pH value was determined as 7.02±0.02. At certain time points, 0.1 mL of the gas in the headspace was collected in a syringe to gas chromatograph for detection. The liquid products in the solution phase were analyzed by ^1H NMR under solvent-suppression mode. We note that H_2Asc is deprotonated to $HAsc^-$ by $KHCO_3$, while the parallel experiments with 25 mM NaHAsc show identical performances. The error bars in the plots represent the standard deviations of three independent measurements.

Protocol for recycling reaction

After reaction, the nanoparticles were collected by a 0.20 µm PTFE membrane filter and ultrasonically re-dispersed (30 min) in a freshly prepared 1.5 mL water containing 0.1 M $KHCO_3$ and 25 mM ascorbic acid for the second run of photocatalysis.

Mott-Schottky, EIS and photocurrent tests

These measurements were conducted in a conventional three-electrode set-up using a Pt wire as the counter electrode and an Ag/AgCl (KCl sat.) electrode as the reference electrode. The working electrode is a catalyst-loaded fluorine-doped tin oxide (FTO). Prior to catalyst coating, the FTO were sonicated in ethanol and then acetone both for 15 min and dried. Then, 5 mg of solid was dispersed in 900 µL of ethanol with 100 µL of a Nafion solution (5 w%, Sigma-Aldrich) and sonicated for 30 min to obtain a colloidal suspension. Afterwards, 50 µL of the suspension was uniformly drop-casted onto the FTO. The working electrode was dried for 12 h under ambient conditions. During the measurement, the above three-electrode system was placed in a 20 mL rubber-sealed three-neck glass vessel and filled with 10 mL 0.1 M $KHCO_3$ electrolyte. The device was

purged with CO_2 for 20 min before measurement. Mott-Schottky and EIS measurements were conducted on a CHI660D electrochemical station. Photocurrent experiments were operated on a CHI730C electrochemical station under a chopped light (AM 1.5 G, 100 mW cm^{-2}) under open-circuit potentials.

Determination of apparent quantum yield for CO production

A reported method[7] was used to determine apparent quantum yield. A typical experiment employed a mixture of **CoTCPc@p-CTF-py** (0.5 g/L) and ascorbic acid (25 mM) in 1.5 mL 0.10 M $KHCO_3$ aqueous solution for evaluation. The temperature was kept at 25°C. For a simple evaluation, the light source was chosen as a LED light (λ = 405 ± 5 nm, light intensity = 100 mW·cm^{-2}, calibrated by a Newport light intensity meter, irradiated area is 0.785 cm^2). The photon flux was determined to be 2.43 × 10^{-7} Einstein/s.[8] Under these conditions, the light entering the reaction solution was considered to be fully absorbed by PS, suggesting the evaluated QE is a lower limit. The 8 h of light irradiation is consistent with the total number of photons n_p = 7.00 × 10^{-3} Einstein.

The apparent quantum yield = 2 × n (CO) / n_p was evaluated by the equation[9] for two-electron reduction of CO_2. A typical value of 0.12% ± 0.02% was determined by the measured n (CO) = 4.2 ± 0.9 µmol by GC-TCD after 4 h of irradiation.

Density functional theory calculations for XAS

Density functional theory (DFT) optimization calculations and XANES simulations were performed using the ORCA (Version 5.0) program package developed by Neese[10] and co-workers. Geometry optimizations were performed using the BP86[11] as functional with the def2-TZVP[6] triple-zeta basis sets and the D3BJ dispersion correction to account for dispersion corrections respectively. The RI[12] approximation was used to accelerate Coulomb and exchange integrals. The default GRID settings were further used for the self-consistent field iterations and for the final energy evaluation. The calculated structures were confirmed to be minima based on a check of the energies and the absence of imaginary frequencies from frequency calculations carried out on the optimized geometries.

TRPL measurements and analysis

The time-resolved photoluminescence decay (TRPL) measurement was characterized via a time-correlated single photon counting (TCSPC) method with excitation using PicoQuant Sepia II PDL 828 multichannel Picosecond Diode Laser with at 405 nm. A Nikon C2 Si confocal microscope is used to focus the laser onto the sample and collect the PL signal. The collected PL light passes through a 460±36 nm bandpass filter and detected by a PicoQuant PMA Hybrid single photon counting module. The instrument response function (IRF) was determined by measuring the solvent scattering response in the same setup. A Gaussian function is used to fit the response and a full width half maximum of 151±7 ps is calculated (Figure S27).

In bare semiconductor system, the TRPL decays of **p-CTF** and **p-CTF-py** are resulted from the charge recombination or trapping and can be analyzed with the following equation S5 as shown in Figure 3B and Table S6.

$$\mathrm{I}_{PL}(\mathrm{t}) = \sum_{i=1}^{i=4} A_i \exp\left(-\frac{t}{\tau_{rec_i}}\right) \otimes G(\Delta t) \quad \text{(S5)}$$

where $\otimes G(\Delta t)$ denotes the convolution with the instrument response function, described by a Gaussian function with a FWHM of 151±7 ps. Four exponential components are used to fit both **p-CTF** and **p-CTF-py**. The average lifetime was calculated with the following equation S6. Fitting parameters and average lifetime are summarized in Table S6.

$$< \boldsymbol{\tau} >= \frac{\sum \boldsymbol{A_i \tau_i}}{\sum \boldsymbol{A_i}} \quad \text{(S6)}$$

The charge-transfer PL quenching rate on **CoTCPc@p-CTF** (electron transfer quenching) and **p-CTF-py** with scavenger (hole transfer quenching) can be analyzed following a previous paper[13] using equation S5:

$$\mathrm{I}_{PL}(\mathrm{t}) = \sum_{i=1,j=1}^{i=4,j=2} A_i B_j \exp\left(-\frac{t}{\tau_{rec_i}} - \frac{t}{\tau_{ct_j}}\right) \otimes G(\Delta t) \quad \text{(S7)}$$

where A_i is the recombination distribution probability obtained from the unmodified **p-CTF** and **p-CTF-py** semiconductors using equation S5. B_i is the charge transfer probability due to the non-homogenous catalyst anchorage and τ_{CT_j} is the

corresponding charge transfer time constant. Initially, two types of charge transfer rate $1/\tau_{CT_j}$ are used to fit **CoTCPc@p-CTF** and **p-CTF-py** with ascorbate. On **CoTCPc@p-CTF**, an infinitely slow transfer rate can be used to describe the second charge transfer component ($1/\tau_{CT_j} \rightarrow 0$), which means that only the one charge transfer rate is responsible for the faster PL decay within the time window we studied. The results are summarized in Table S7. What worth mentioned is that in the cases of **CoTCPc@p-CTF-py** and **p-CTF** with ascorbate, only a minor charge transfer effect can be observed. Such small differences do not allow us to extract a meaningful charge transfer rate $1/\tau_{CT_j}$ using equation S7 within a reasonable fitting error range. Therefore, we only use equation S5 to fit these two TRPL decay curve as summarized in Table S6.

In-situ light induced XPS

In-situ irradiated XPS measurements were performed with the X-ray photoelectron spectrometer (ESCA LAB250, THERMO SCIENTIFIC) equipped with a 300 W Xe-lamp with an AM 1.5 G filter as a light source under vacuum. The light source was about 40 cm away from the sample supporter. XPS data were fitted by Thermo Avantage (v5.948) software.

In-situ light-induced EPR

In-situ light-induced EPR experiments were performed at room temperature on an EPR spectrometer (EXMplus6-1, Bruker). The sample powder was placed in a capillary tube and argon was purged for 10 min, followed by sealing both ends of the tube. Finally, the capillary tube was put into the test tube, and then the EPR measurements were carried out in the absence or presence illumination (Xe lamp, AM 1.5 G, 300 W), respectively.

DFT calculations to model electron transfer steps

Initially, the **CoTCPc@p-CTF-py** system has been developed by optimizing the geometry of covalent triazine-based framework with dangling pyridyl groups connected via ethylene linker at the BP86 level of theory[14,15] in conjunction with the SMD continuum solvation model for water[16] using def2-TZVP basis set[6] on Co and the def2-SV(P) basis set[6] on all other atoms (Figure S13a). Non-analytical integrals were evaluated using the integral=grid=fine option as implemented in the Gaussian 16 software package.[17] The anchoring of **CoTCPc** to **p-CTF-py** system is further investigated via both the formation

of a covalent Co-N bond (Figure S13b) and supramolecular bonding involving CH-π and π-π interactions (Figure S13c). The energetic comparison of these two configurations are assessed by performing single point electronic energy calculations at the MN15 level of theory[18] using def2-TZVP basis set on Co and the def2-SVP basis set on all other atoms using the integral=grid=ultrafine option.

Next, the **CoTCPc@p-CTF-py** cluster model is developed by adopting a subsystem of the **CoTCPc@p-CTF-py system** as shown in Figure S29. The positions of all atoms in the **p-CTF-py** subsystem including the ethylene linker were kept fixed in the subsequent geometry optimization steps described next.

All geometries were optimized at the MN15 level of density functional theory in conjunction SMD continuum solvation model for water using def2-TZVP basis set on Co and the def2-SV(P) basis set on all other atoms. Non-analytical integrals were evaluated using the integral=grid=ultrafine option as implemented in the Gaussian 16 software package.

Constrained DFT (CDFT)[19,20] calculations using spin constraints as implemented in Q-Chem 5.0 software[21] package were performed to compute the relative energies of diabatic states. CDFT calculations were performed at the MN15 level of theory with the IEFPCM continuum solvation model for water using the def2-TZVP basis set on Co and the def2-SVP basis set on all other atoms. **CoTCPc@p-CTF-py** cluster model is partitioned into two fragments at the ethylene bridge for the spin constraint CDFT calculations (Figure S30).

4.5.2. Synthetic process

Preparation of 2'-(2-(pyridin-4-yl)ethyl)-[1,1':4',1''-terphenyl]-4,4''-dicarbonitrile (M-py)

The preparation of the monomer (in this chapter named as M-py for simplicity, instead of M3-py) is already reported in the previous chapter and in a previous work,[22] following the same schematic pathway indicated with no modifications.

Preparation of p-CTF-py

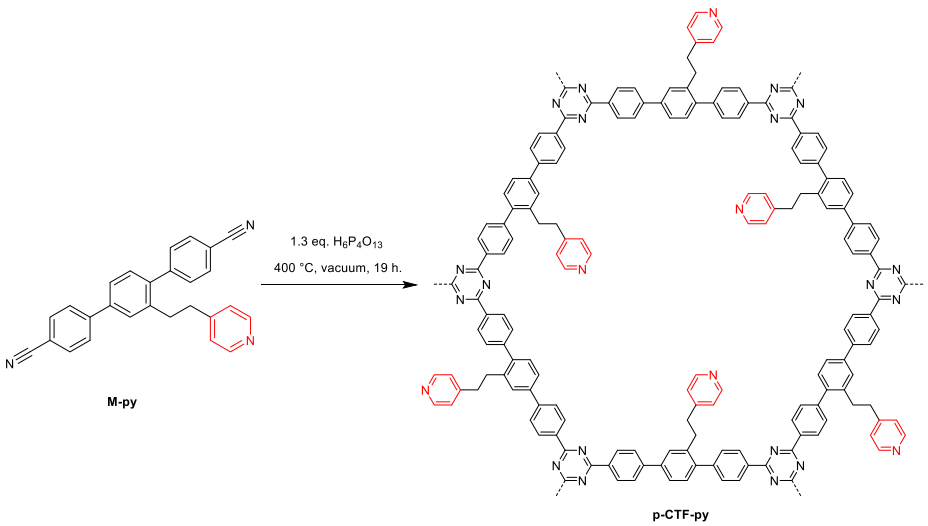

Scheme S1. *Schematic procedure for the preparation of* ***p-CTF-py****.*

The polymerization of CTF materials was modified from the reported method.[23]

Monomer **M-py** (0.5 mmol, 193 mg) and $H_6P_4O_{13}$ (115% H_3PO_4, Sigma, 0.65 mmol, 220 mg) were added into a Pyrex tube, which was flame-sealed under vacuum and placed into a muffle furnace, followed by thermal treatment at 400°C for 19 h. The elevation to 400°C took 1.5 h and the cooling was naturally done. After opening the ampule, the block product was soaked in 30% ammonia aqueous solution and exfoliated from the vessel wall with spatula. The dark flakes were isolated with filtration, which was washed with water, DMF and methanol. After drying in oven (80°C) overnight, the flakes were ball-milled (30 Hz, 60 min), then thoroughly washed by 6 M NaOH, DMF and water by sonication and isolated by centrifugation, followed by vacuum-drying to obtain a dark brown powder. Yield: 125 mg, 65%.

Preparation of CoXPc@p-CTF-py

10 mg of **p-CTF-py** powder was dispersed in 1.0 mL DMF solution containing 1.0 mM **CoXPc** (= **CoPc**, **CoTAPc**, **CoFPc** or **CoTCPc**) for 15 min sonication and then 1-d stirring in the dark. The hybrid catalyst was isolated by centrifugation, followed by washing with DMF for twice and finally with H_2O. The wet powder was subjected in freeze-drying to get dark-blue powder (ca. 8 mg, 80% yield).

Preparation of [1,1':4',1''-terphenyl]-4,4''-dicarbonitrile (M)

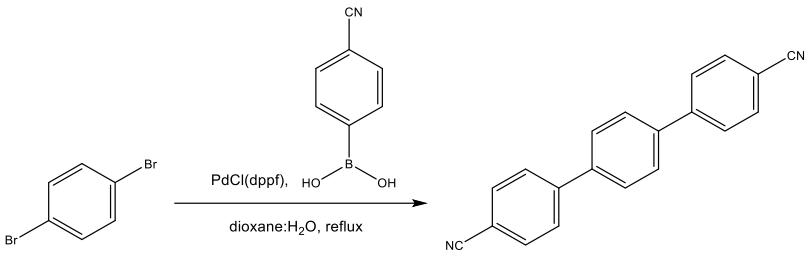

Scheme S2. *Schematic procedure for the preparation of the monomer **M**.*

In a 500 mL Schlenk flask, the Suzuki coupling between 1.8 g 1,4-dibromobenzene and 3.23 g 4-cyanoboronic acid (2 eq.) was operated with the addition of the two reagents, 6.1 g K_2CO_3 (6 eq.), and 805 mg $Pd(dppf)Cl_2$ (dppf = 1,1′-ferrocenediyl-bis(diphenylphosphine); 11 mol%), followed by degassed with N_2. Then a degassed 250 mL dioxane/H_2O (3:1) was added in the flask at reflux overnight. Upon cooling down, water (100 mL) was added, followed by extraction with dichloromethane (4 × 50 mL). The combined organic extract was dried over $MgSO_4$. The product was firstly purified by column chromatography with hexane : ethyl acetate = 3:1, which shows no fluorescence upon 366 nm UV light excitation. Some impurities were further washed by a small amount of cool ethyl acetate, affording white solid as the final product (1.0 g, 47%). ^{1}H NMR (500 MHz, CD_2Cl_2) δ 7.81 (s, 8H), 7.79 (s, 4H). ^{13}C NMR (126 MHz, CD_2Cl_2) δ 144.53, 139.31, 132.70, 127.86, 127.59, 118.73, 111.31.

Preparation of p-CTF

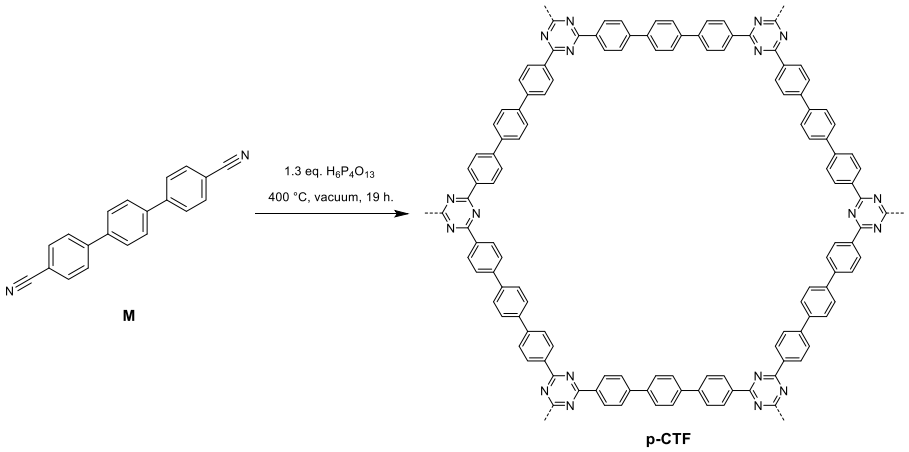

Scheme S3. *Schematic procedure for the preparation of* ***p-CTF****.*

The polymerization of **p-CTF** is analogous to that of **p-CTF-py** as follows.

Monomer **M** (0.5 mmol, 140 mg) and $H_6P_4O_{13}$ (115% H_3PO_4, Sigma, 0.65 mmol, 220 mg) were added into a Pyrex tube, which was flame-sealed under vacuum and placed into a muffle furnace, followed by thermal treatment at 400°C for 19 h. The elevation to 400°C took 1.5 h and the cooling was naturally done. After opening the ampule, the block product was soaked in 30% ammonia aqueous solution and exfoliated from the vessel wall with spatula. The dark-brown flakes were isolated with filtration, which was washed with water, DMF and methanol. After drying in oven (80°C) overnight, the flakes were ball-milled (30 Hz, 60 min) and then thoroughly washed by 6 M NaOH, DMF and water by sonication and isolated by centrifugation, followed by vacuum-drying to obtain a brown powder. Yield: 56 mg, 40%.

Preparation of CoTCPc@p-CTF

10 mg of **p-CTF** powder was dispersed in 1.0 mL 1.0 mM DMF **CoTCPc** solution for 15 min sonication and then 1-d stirring in the dark. The hybrid catalyst was isolated by centrifugation, followed by washing with DMF for twice and finally with H_2O. The wet powder was subjected in freeze-drying to get green powder (8.5 mg, 85% yield).

4.5.3. Results

Characterization of the hybrid materials

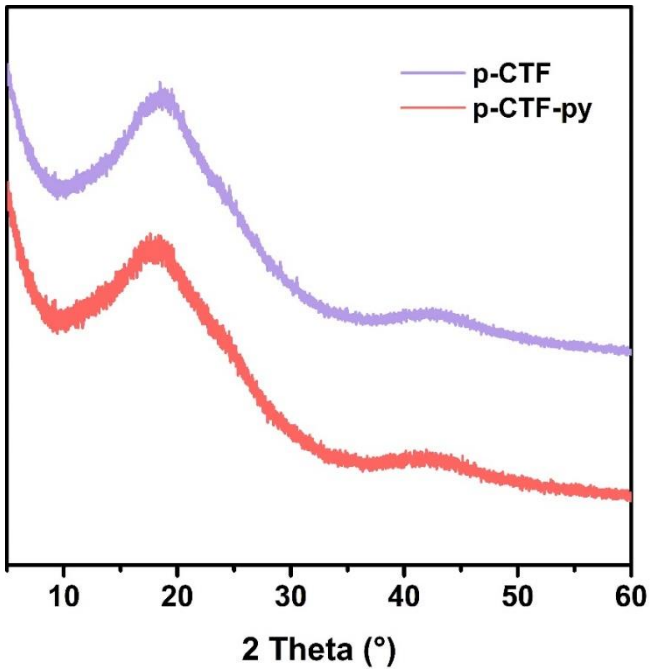

Figure S1. *PXRD patterns of* ***p-CTF-py*** *(red) and* ***p-CTF*** *(violet).*

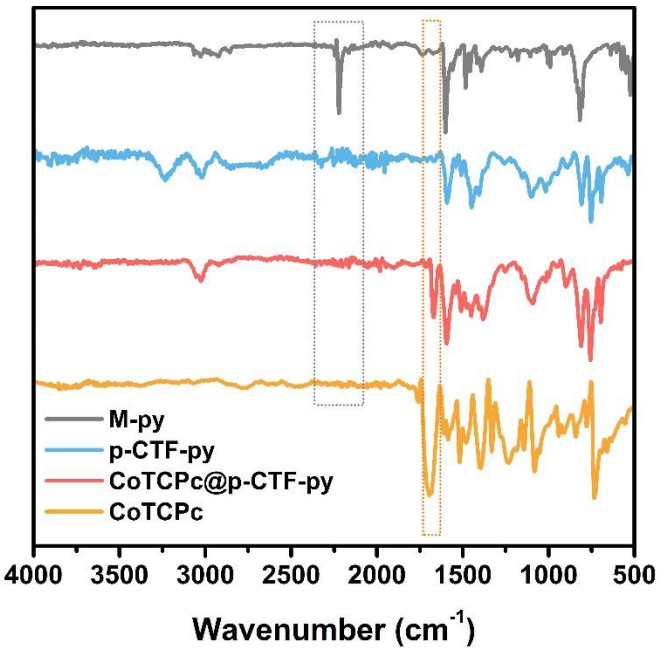

Figure S2. *IR spectra of* ***M-py*** *(grey),* ***p-CTF-py*** *(blue),* ***CoTCPc@p-CTF-py*** *(red) and* ***CoTCPc*** *(orange). The C≡N signal (ca. 2200 cm^{-1}, grey box) and the characteristic signal of* ***CoTCPc*** *(ca. 1700 cm^{-1}, orange box) are highlighted. The disappearance of C≡N signal in CTF-based samples indicate the successful polymerization of the monomer.*

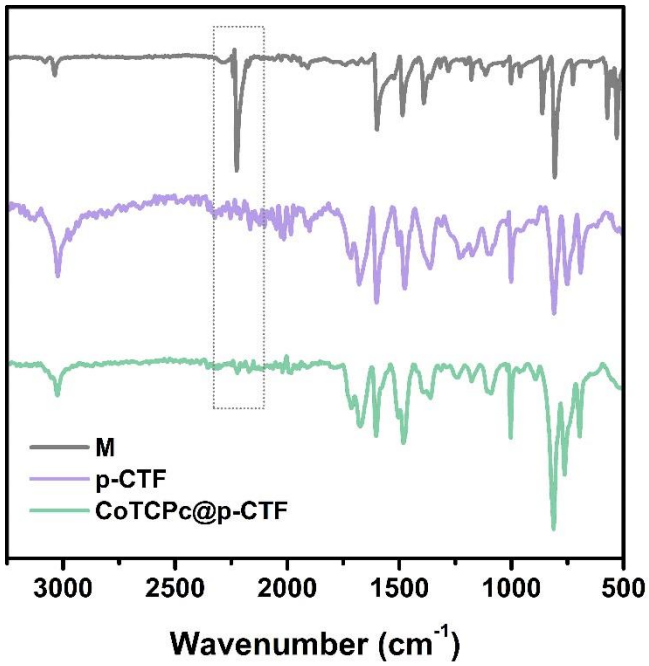

Figure S3. *IR spectra of **M** (grey), **p-CTF** (violet) and **CoTCPc@p-CTF** (green). The C≡N signal (approx. 2200 cm^{-1}, grey box) is highlighted. The disappearance of C≡N signal in CTF-based samples indicate the successful polymerization of the monomer. Negligible difference was noticed between **p-CTF** and **CoTCPc@p-CTF-py**, indicating the low catalyst loading.*

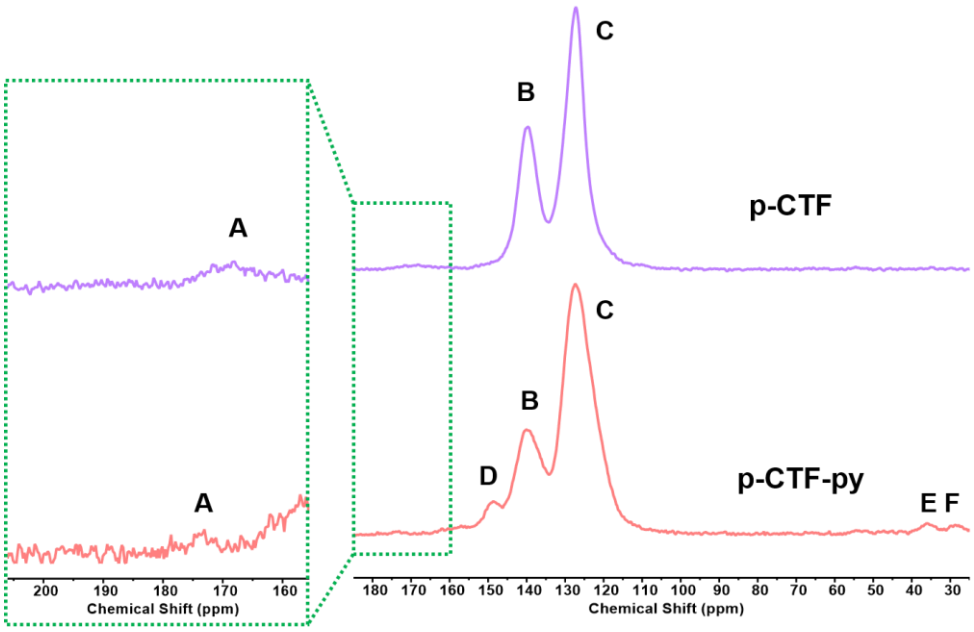

Figure S4. *Solid-state ^{13}C NMR analysis on **p-CTF** (violet) and **p-CTF-py** (red). The relatively week signals of A (triazine carbon), D (pyridyl carbon), E/F (methylene carbon) species were induced by the very strong signals of B/C (phenyl carbon).*

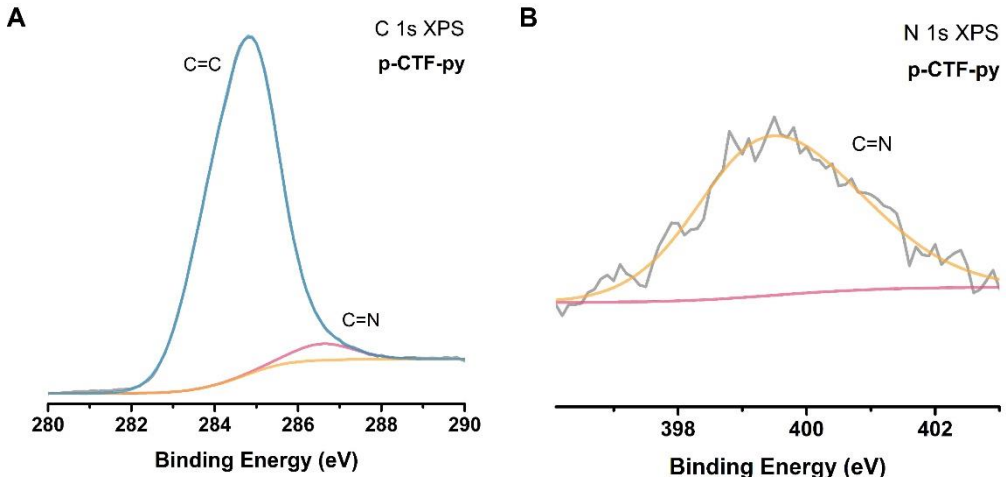

Figure S5. *(a) C 1s and (b) N 1s XPS results of* ***p-CTF-py****.*

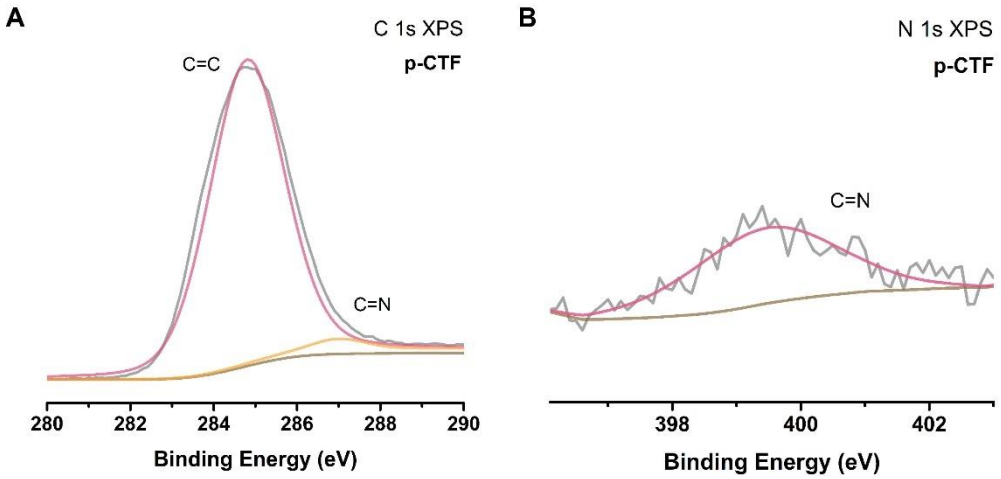

Figure S6. *(a) C 1s and (b) N 1s XPS results of* ***p-CTF****.*

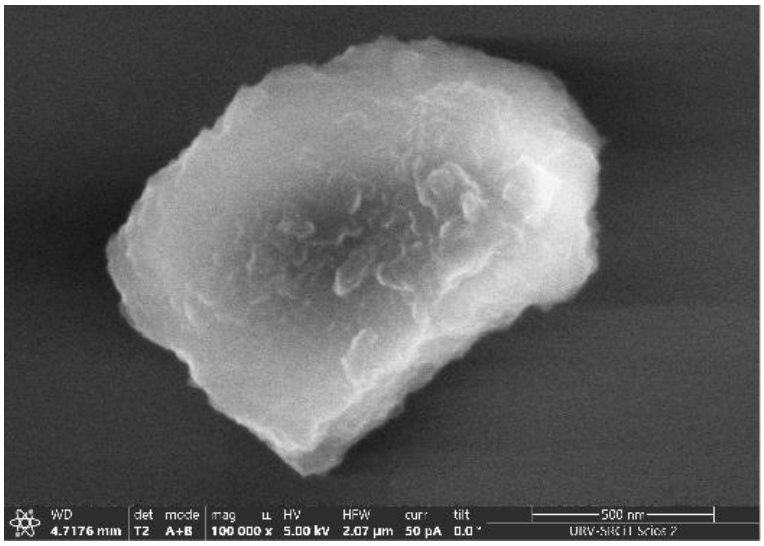

Figure S7. *SEM image of* ***p-CTF****.*

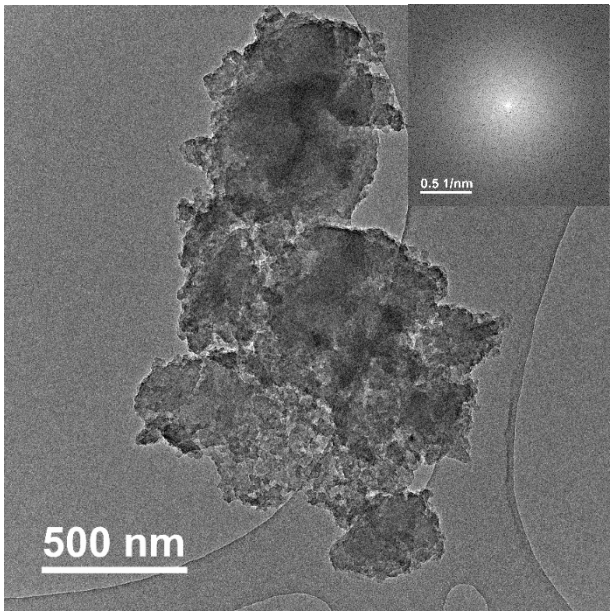

Figure S8. *HRTEM image of* ***p-CTF*** *with FFT results.*

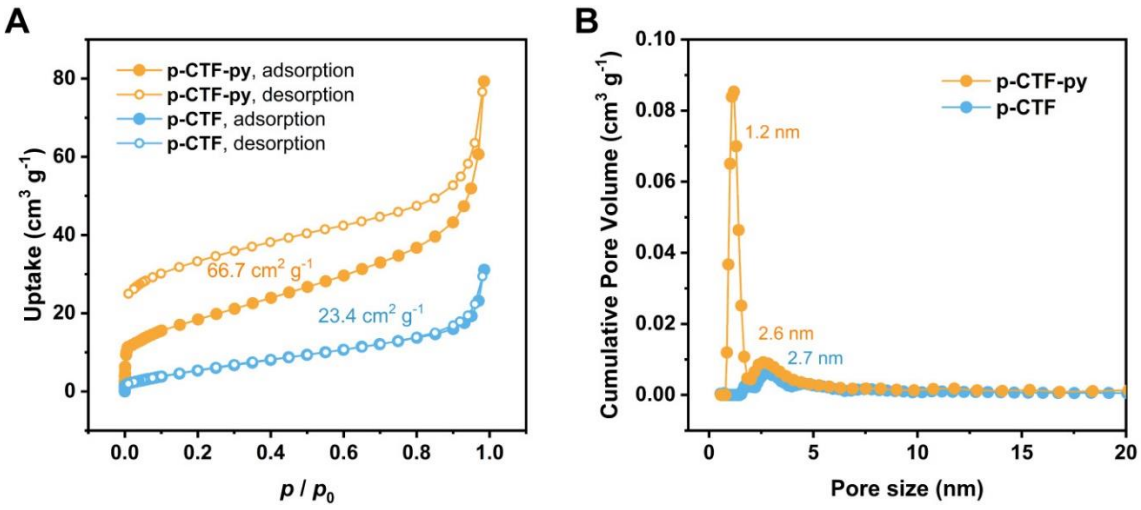

Figure S9. *(a) N_2 sorption isotherms at 77 K and (b) pore size distributions of* ***p-CTF-py*** *and* ***p-CTF****.*

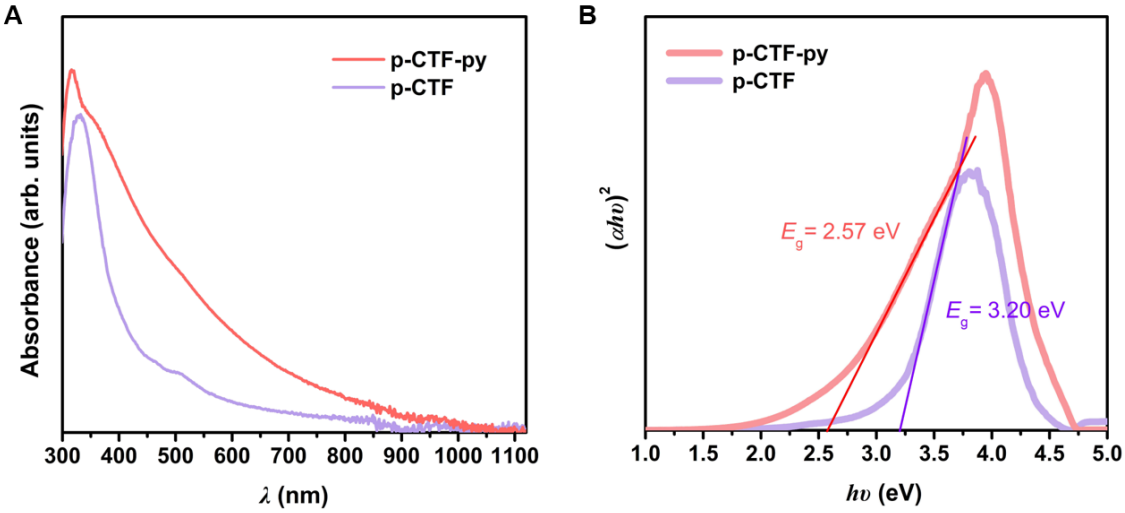

Figure S10. *(a) DRS spectra of* ***p-CTF-py*** *(red) and* ***p-CTF*** *(violet) in 0.5 g L^{-1} DMF suspension measured from the UV-vis to the NIR region. (b) Tauc plots from DRS results.*

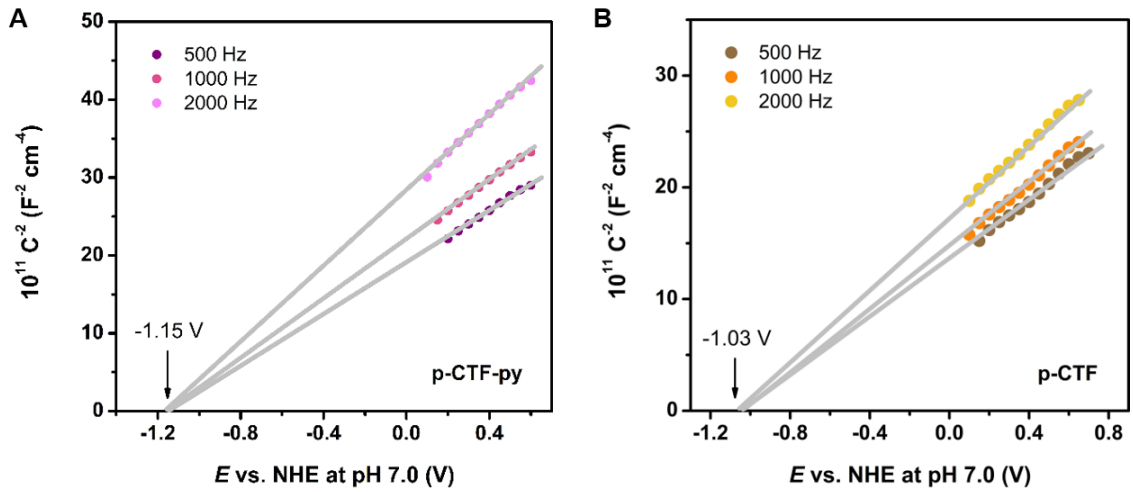

Figure S11. *Mott–Schottky plots of (a)* ***p-CTF-py*** *and (b)* ***p-CTF****.*

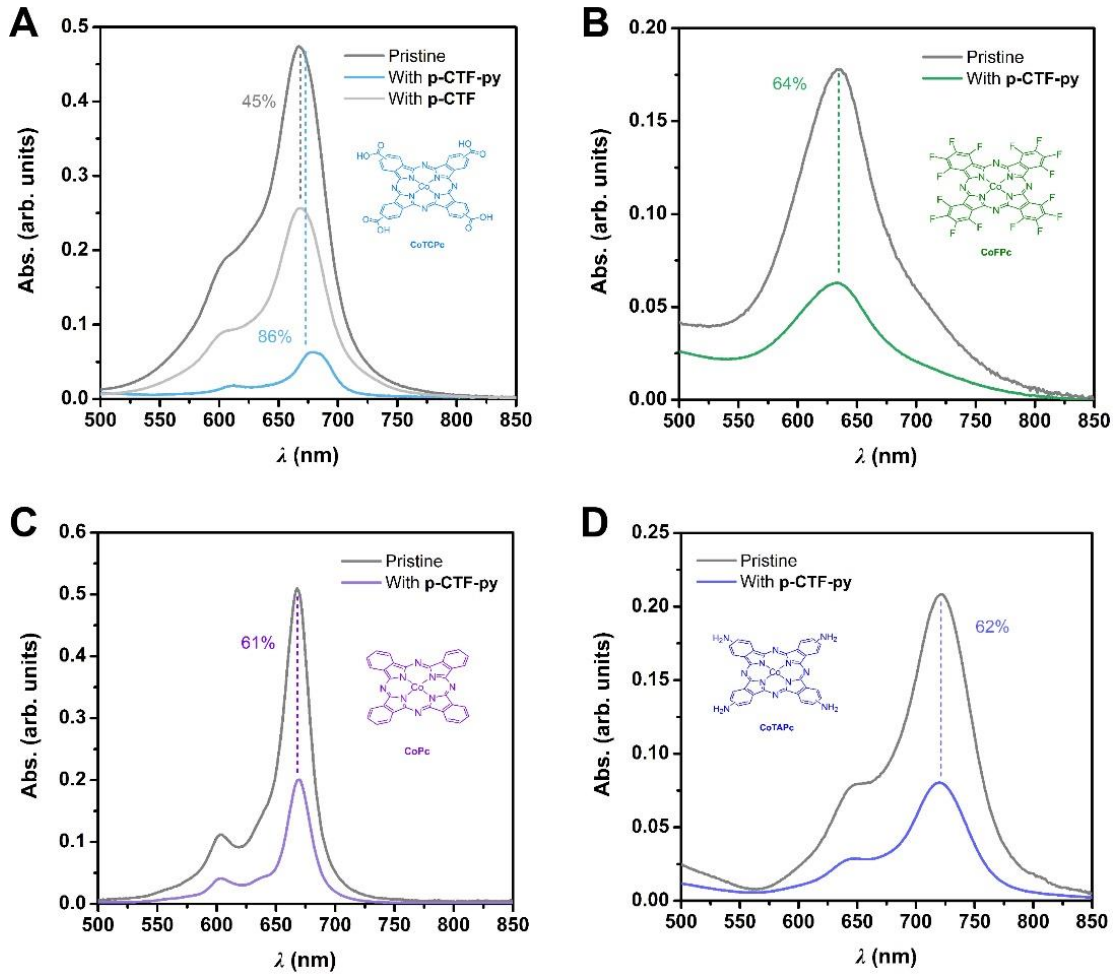

Figure S12. *UV-vis absorption spectra of 1.0 mM DMF solution of (a)* ***CoTCPc****, (b)* ***CoFPc****, (c)* ***CoPc*** *and (d)* ***CoTAPc*** *and the first centrifuge supernatant after immobilization on* ***p-CTF-py****. The parallel experiment result with* ***CoTCPc*** *mixing with* ***p-CTF*** *is shown in (a) for comparison (grey lines).*

Table S1. *ICP-MS results on the Co-based materials (errors from two independent measurements are within 5%).*

Sample	Co wt.%	[Co] (nmol mg^{-1})
CoPc@p-CTF-py	0.1867%	31.64
CoTAPc@p-CTF-py	0.2157%	36.56
CoFPc@p-CTF-py	0.1905%	32.29
CoTCPc@p-CTF-py	0.2339%	39.64
CoTCPc@p-CTF	0.1095%	18.56
CoPc@p-CTF	0.0717%	12.15
CoTAPc@p-CTF	0.0957%	16.22
CoFPc@p-CTF	0.0705%	11.95

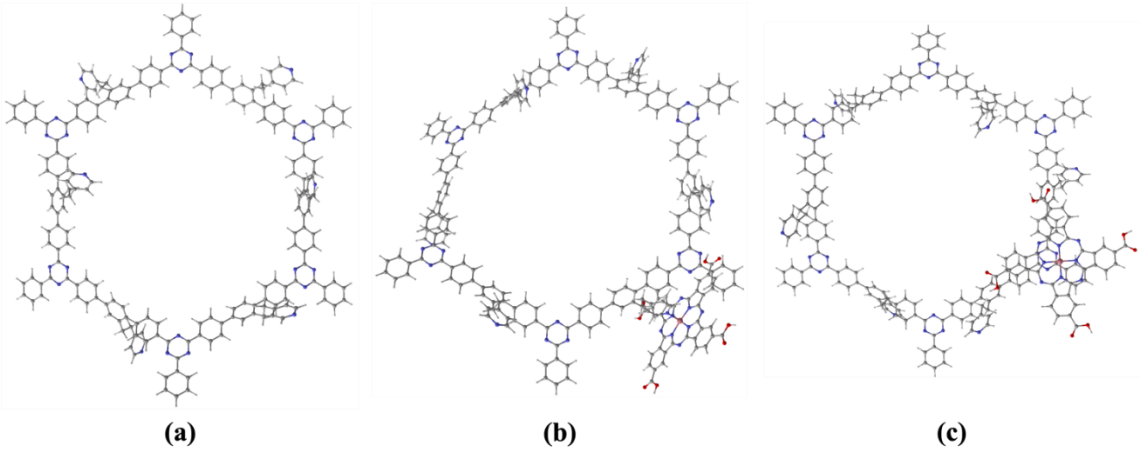

Figure S13. *Optimized structures of (a)* ***p-CTF-py****; (b)* ***CoTCPc*** *anchored to* ***p-CTF-py*** *via formation of a covalent Co-N bond and (c)* ***CoTCPc*** *anchored to* ***p-CTF-py*** *via supramolecular bonding involving CH-π and π-π interactions at the BP86 level of theory.*

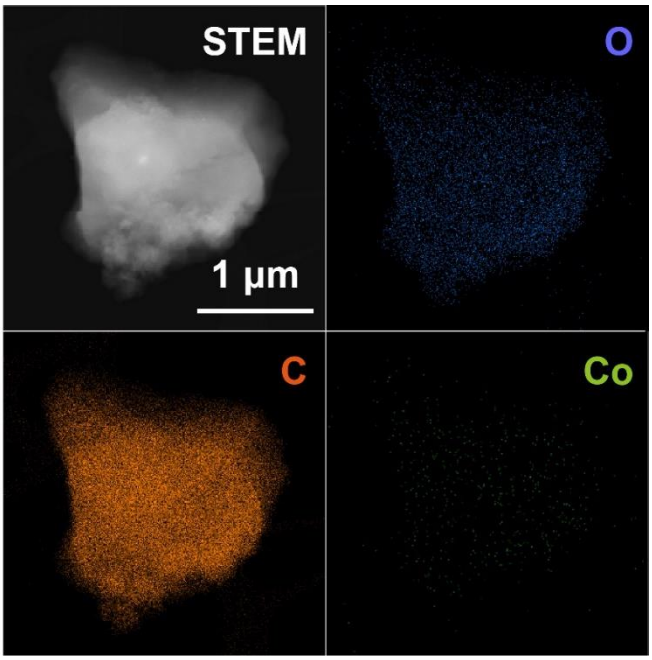

Figure S14. *EDS mapping results of* ***CoTCPc@p-CTF****.*

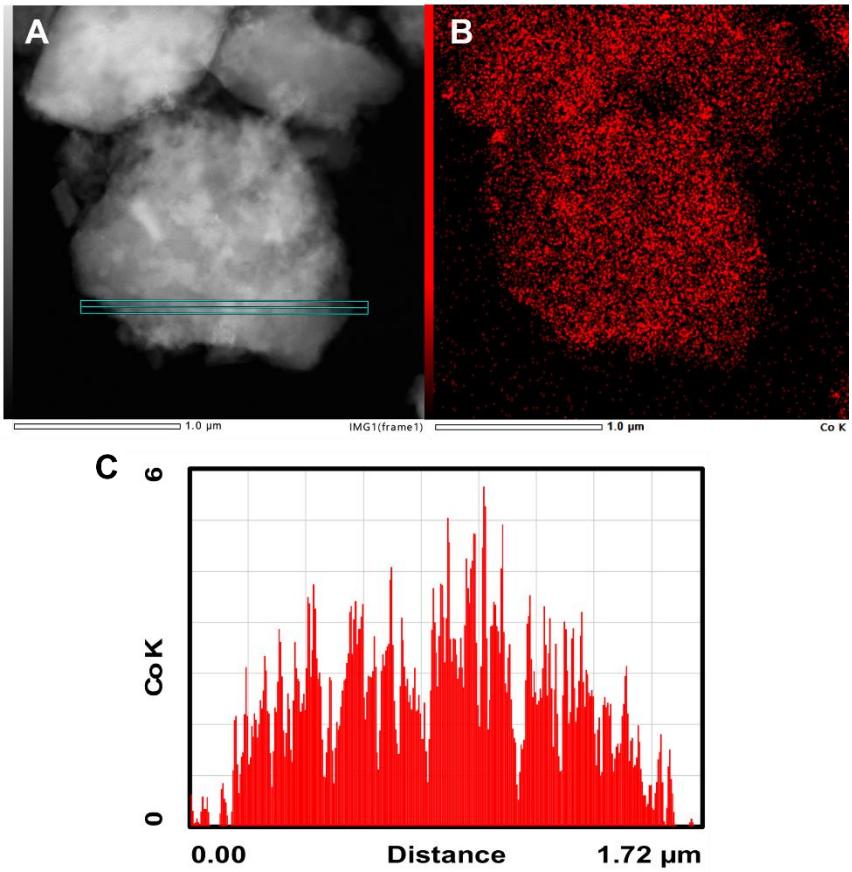

Figure S15. *(a) TEM image, (b) cobalt elemental mapping and (c) cross-sectional cobalt distribution of one particle of* ***CoTCPc@p-CTF-py****.*

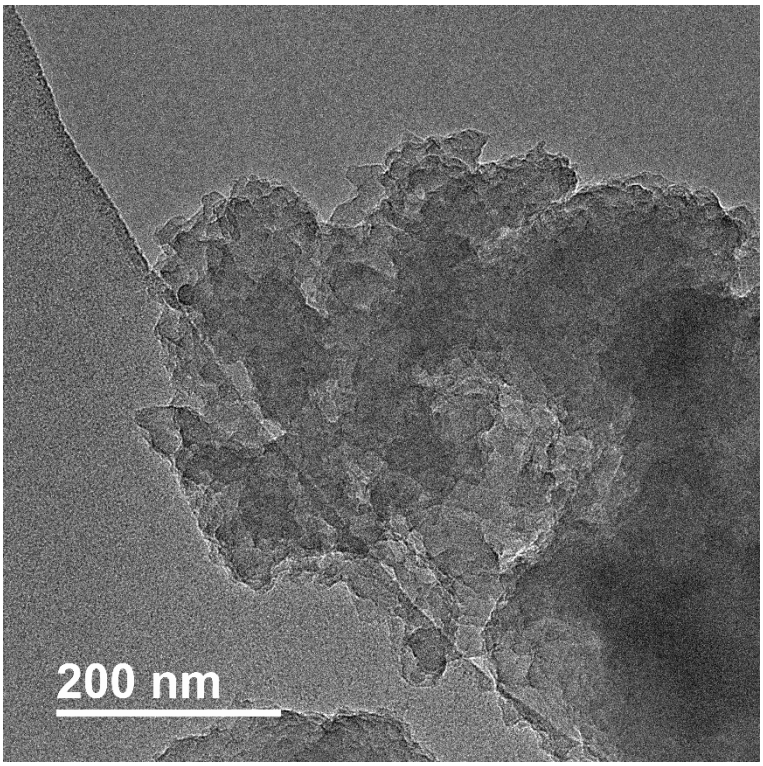

Figure S16. *HRTEM image of* ***CoTCPc@p-CTF-py****.*

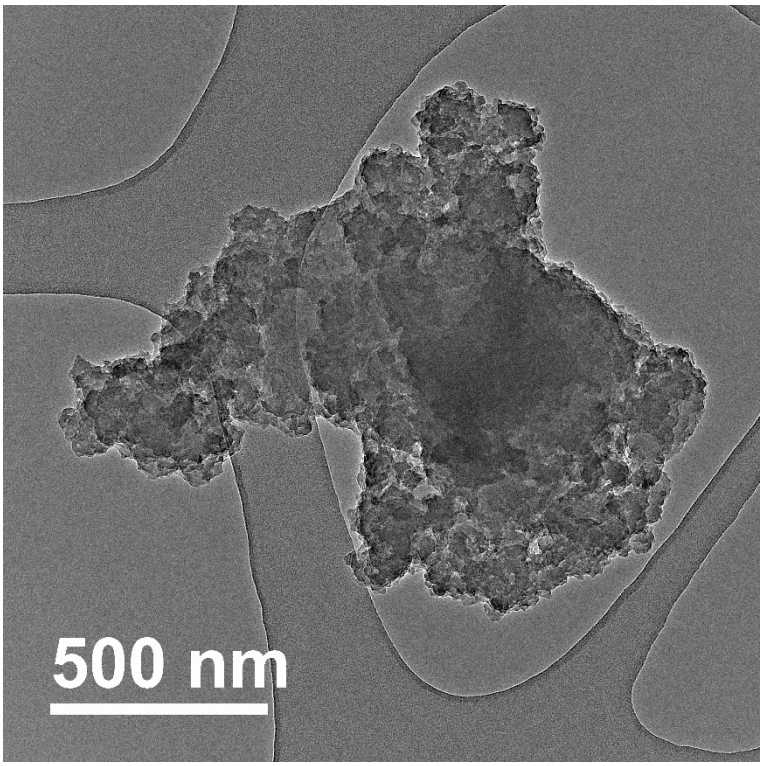

Figure S17. *HRTEM image of* ***CoTCPc@p-CTF****.*

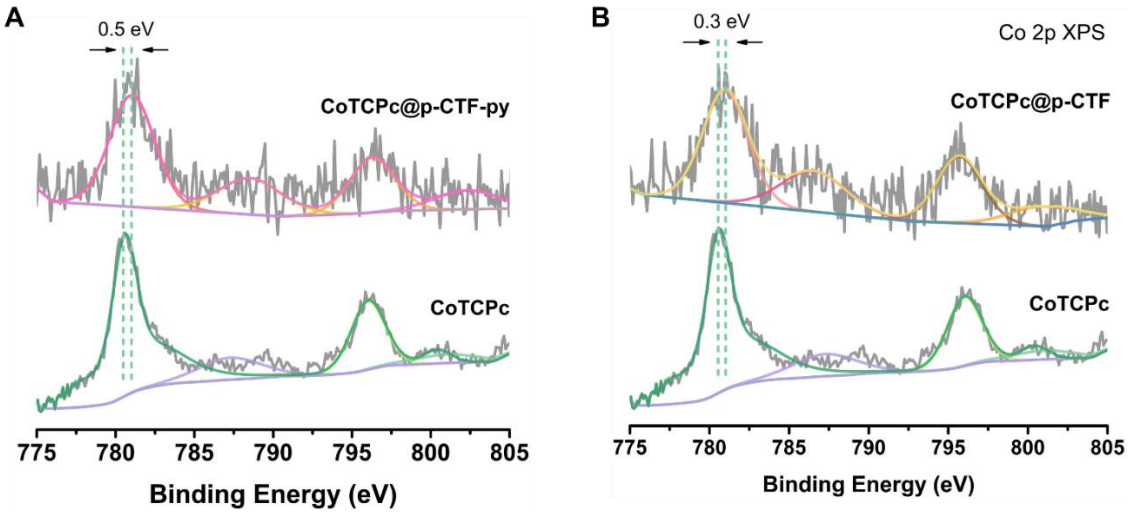

Figure S18. *(a) Co 2p XPS spectra of* ***CoTCPc*** *(down) and* ***CoTCPc@p-CTF-py*** *(up). (b) Co 2p XPS spectra of* ***CoTCPc*** *(down) and* ***CoTCPc@p-CTF*** *(up).*

XAS measurements

Table S2*. Pre-edge parameter fits for* ***CoTCPc*** *and* ***CoTCPc@p-CTF-py*** *after catalysis.*

CoTCPc			
Function	Centroid (eV)	Amplitude	Width
Erf	7713.50 eV	0.09	2.00
Gauss	7710.43 eV	0.07	1.10
Pre-edge area		7.0 units	
CoTCPc@p-CTF-py after catalysis			
Function	Centroid (eV)	Amplitude	Width
Erf	7713.50	0.09	2.00
Gauss	7709.00	0.033	0.800
Gauss	7710.77	0.048	0.850
Pre-edge area		8.1 units	

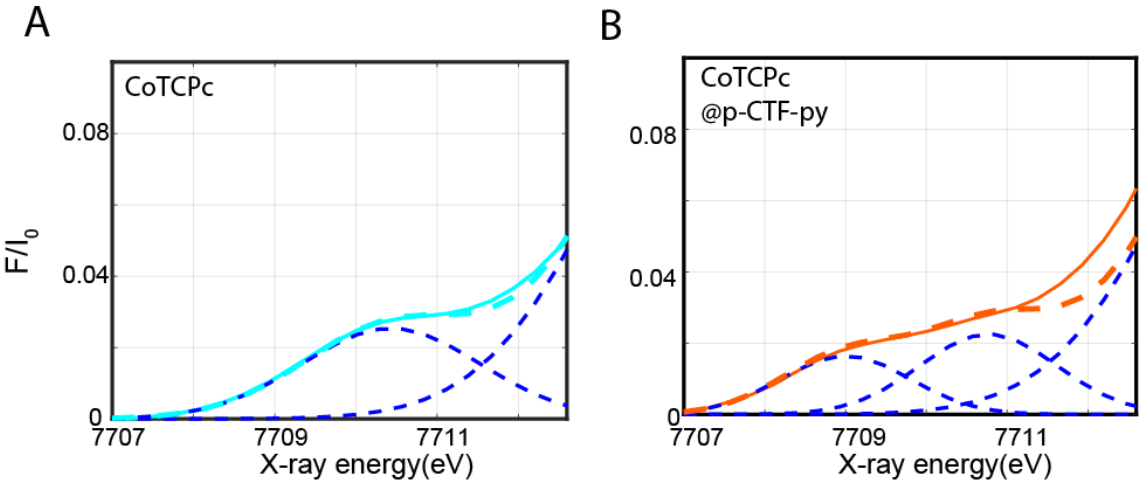

Figure S19. *Zoom-in of the pre-edge regions of (a)* ***CoTCPc*** *or (b)* ***CoTCPc@p-CTF-py*** *after catalysis together with the respective fits shown in cyan and orange dashed lines, respectively. The blue lines correspond to the step and gaussian functions used to fit the pre-edge peak as elaborated in Table S2.*

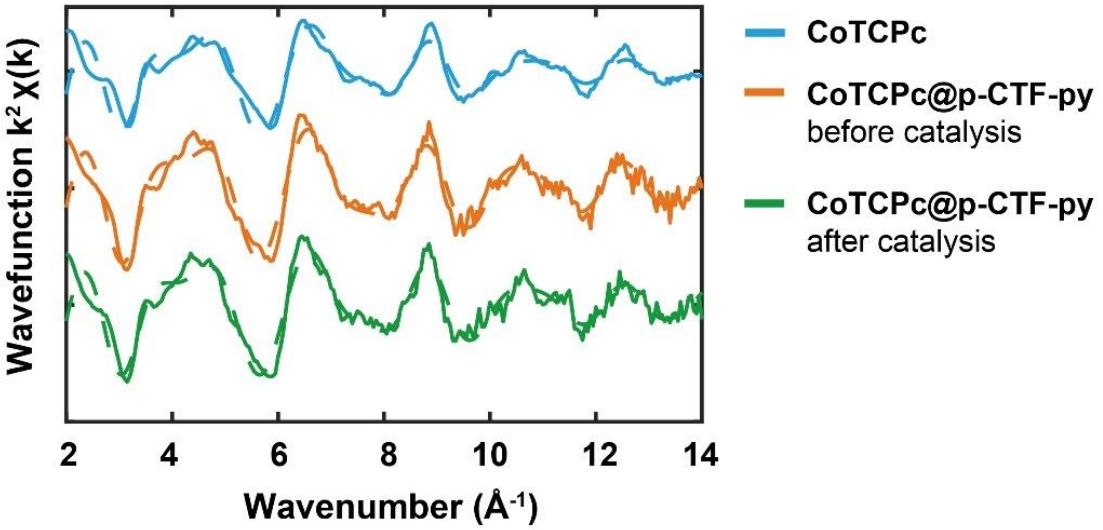

Figure S20. *Back Fourier transformed experimental (solid) and fitted (dashed) $k_2[\chi(k)]$ of* ***CoTCPc*** *(Fit 2, Table S3, in blue), as well as* ***CoTCPc@p-CTF-py*** *before (Fit 6, Table S3, in orange) and after (Fit 9, Table S3, in green) 48 h of photocatalysis.*

Table S3. *Overview of the applied EXAFS Fits parameters for the Co^{III} based complexes.*

Complex	Fit	Region	Shell, N	R, Å	E_0	ss.^{2} (10^{-3})	R-factor	Reduced Chi-square
CoTCPc	1	I	Co-N, 4	1.89	4.1	3.6	0.0317	1300
	2	All	Co-N, 4 Co-C, 8	1.90 2.92	7.4	3.4 6.4	0.0384	788
	3	All	Co-N,5 Co-C,8	1.90 2.92	6.8	5.8 5.6	0.05	1048
CoTCPc@ p-CTF-py	4	I	Co-N, 4	1.91	6.5	1.0	0.0061	42
	5	All	Co-N, 4 Co-C,8	1.91 2.93	8.3	0.9 4.5	0.0189	46
	6	All	Co-N, 5 Co-C,8	1.91 2.93	7.7	2.4 4.0	0.0172	42
CoTCPc@ p-CTF-py after catalysis	7	I	Co-N, 4	1.90	5.3	1.6	0.0076	47
	8	All	Co-N, 4 Co-C,8	1.91 2.93	7.4	1.4 5.1	0.0191	43
	9	All	Co-N, 5 Co-C,8	1.90 2.92	6.8	3.0 4.5	0.0184	41

***** Region **I** corresponds to the fit between 1.1- 2.0 Å, in apparent distance scale and Region **II** to the fit between1.1-2.7 Å .

Table S4. *Overview of the DFT calculated parameters of* ***CoTCPc*** *and* ***CoTCPc@p-CTF-py****.*

Complex	Axial positions	Co-N_1	Co-N_2	Co-N_3	Co-N_4
CoTCPc	None	1.92536	1.92536	1.92536	1.92536
CoTCPc@p-CTF-py	Co-N_{py}, 2.19785	1.94247	1.94211	1.94045	1.94054

Photocatalysis for CO_2 reduction

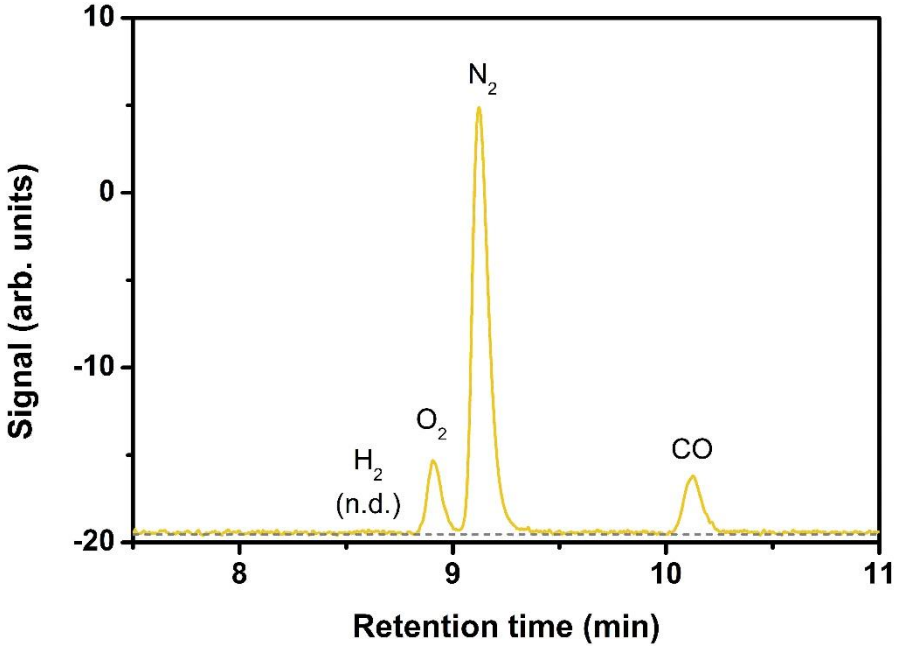

Figure S21. *GC-TCD trace for the gaseous products from the 12-h photocatalysis with 0.5 mg* ***CoTCPc@p-CTF-py****.*

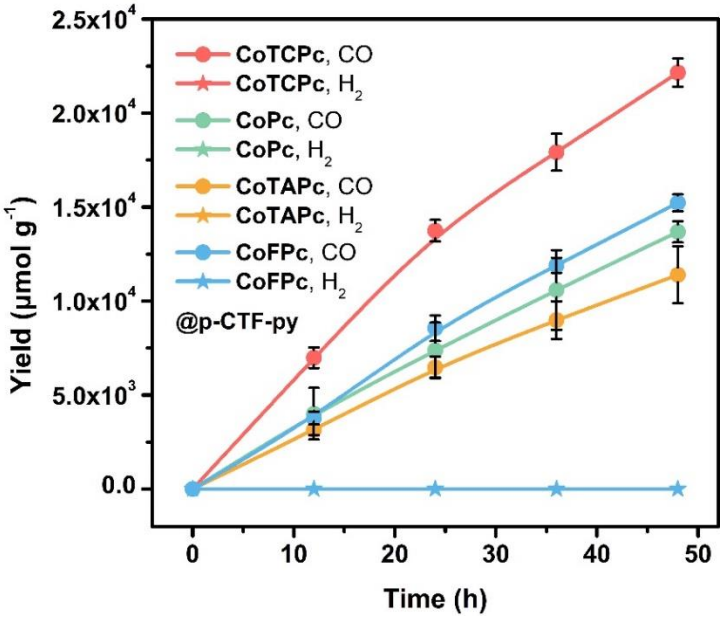

Figure S22. *CO_2 photoreduction. Time profiles of photocatalytic CO (circle) and H_2 (star) formation with* ***CoTCPc@p-CTF-py*** *(red),* ***CoPc@p-CTF-py*** *(green),* ***CoTAPc@p-CTF-py*** *(orange) or* ***CoFPc@p-CTF-py*** *(blue). General conditions: 0.33 g L^{-1} photocatalyst, 0.1 M $KHCO_3$, 25 mM ascorbic acid, 300 mW cm^{-2} Xe lamp with AM 1.5 G filter, 1 atm CO_2, 25°C, 5 × 2 mm stir bar at 1000 rpm. The experimental error bars represent the standard deviations of three independent measurements.*

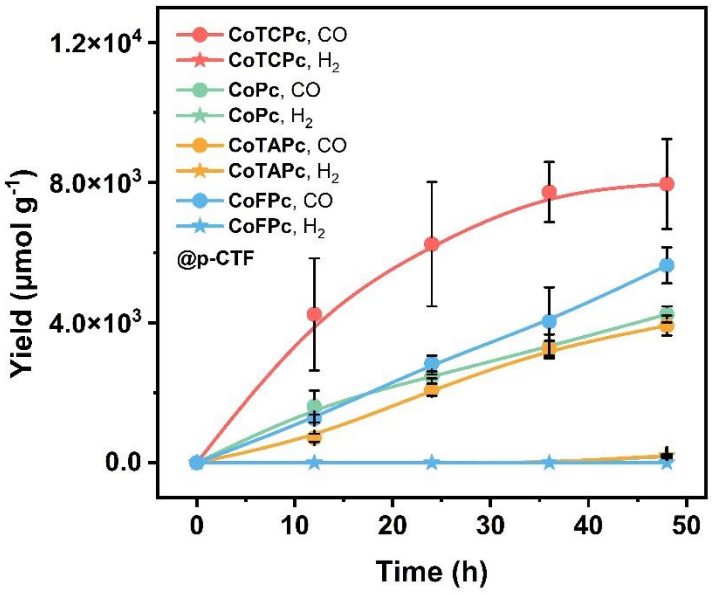

Figure S23. *CO_2 photoreduction. Time profiles of photocatalytic CO (circle) and H_2 (star) formation with* ***CoTCPc@p-CTF*** *(red),* ***CoPc@p-CTF*** *(green),* ***CoTAPc@p-CTF*** *(orange) or* ***CoFPc@p-CTF*** *(blue). General conditions: 0.33 g L^{-1} photocatalyst, 0.1 M $KHCO_3$, 25 mM ascorbic acid, 300 mW cm^{-2} Xe lamp with AM 1.5 G filter, 1 atm CO_2, 25°C, 5 × 2 mm stir bar at 1000 rpm. The experimental error bars represent the standard deviations of three independent measurements.*

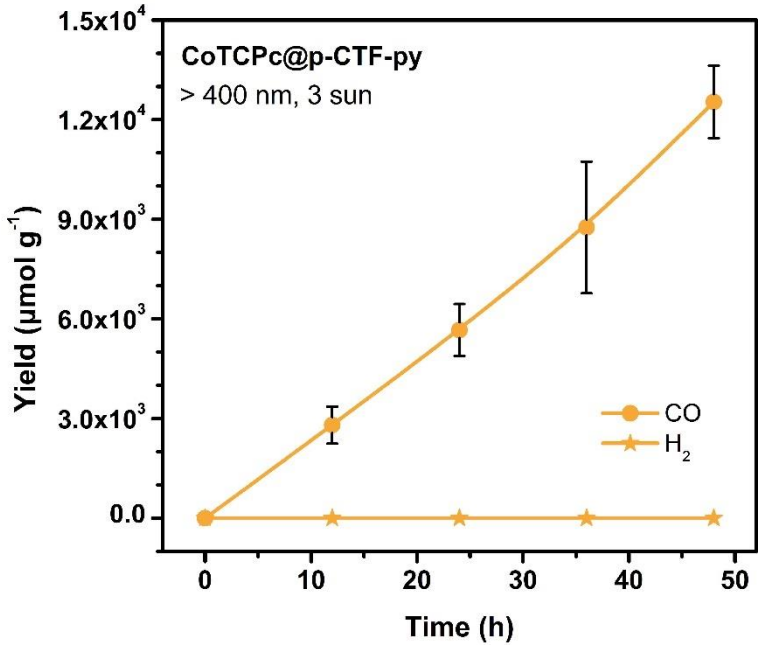

Figure S24. *CO_2 photoreduction. Time profiles of photocatalytic CO (circle) and H_2 (star) formation using 0.5 mg* ***CoTCPc@p-CTF-py*** *under >400 nm light (300 mW cm^{-2}). General conditions: 0.33 g L^{-1} photocatalyst, 0.1 M $KHCO_3$, 25 mM ascorbic acid, 300 mW cm^{-2} Xe lamp with a >400 nm cut-off filter, 1 atm CO_2, 25°C, 5 × 2 mm stir bar at 1000 rpm. The experimental error bars represent the standard deviations of three independent measurements.*

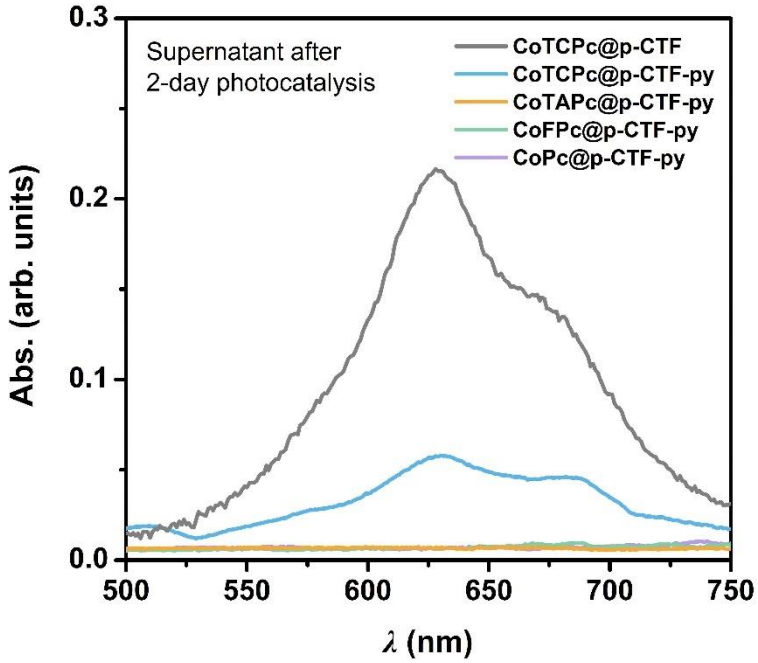

Figure S25. *UV-vis absorption spectra of the supernatants after 2-day photocatalysis with* ***CoTCPc@p-CTF*** *(gray),* ***CoTCPc@p-CTF-py*** *(blue),* ***CoTAPc@p-CTF-py*** *(orange),* ***CoFPc@p-CTF-py*** *(green) and* ***CoPc@p-CTF-py*** *(violet). We noticed that the supernatant of the colloidal systems with* ***CoTCPc*** *became pale blue after photocatalysis. This observation can be attributed to the detachment of a part of* ***CoTCPc*** *molecules which bind to CTF-based surfaces via non-covalent interactions. More importantly, the dissolved* ***CoTCPc*** *was much less in the system with* ***p-CTF-py*** *than the one with* ***p-CTF****, consistent with the above stable performance and clearly demonstrating the merit of covalent coordination in strengthening the immobilized molecular catalysts via the pyridine linkages.*

Table S5. *Blank experiments for CO_2 photoreduction in aqueous systems.*

Entry	Altered Conditions	CO yield (μmol g^{-1})	H_2 yield (μmol g^{-1})
1	Standard conditions with **CoTCPc@p-CTF-py** [a]	22150±780	n.d.
2	With $CoCl_2$	n.d.	n.d.
3	No light	n.d.	n.d.
4	No CO_2	n.d.	n.d.
5	No $KHCO_3$	n.d.	n.d.
6	No polymeric photocatalyst, with 5 μM **CoTCPc** in solution	n.d.	n.d.
7	No cobalt complex, with bare **p-CTF-py**	n.d.	n.d.
8	No cobalt complex, with bare **p-CTF**	n.d.	n.d.
9	bare **p-CTF-py** mixed with 5 μM **CoTCPc** in solution	n.d.	n.d.
10	bare **p-CTF** mixed with 5 μM **CoTCPc** in solution	n.d.	n.d.

[a] Standard conditions: 1.5 mL aqueous solution with 0.5 mg **CoTCPc@p-CTF-py**, 25 mM ascorbic acid and 0.1 M $KHCO_3$ under 1 atm CO_2, under the irradiation of AM 1.5 G light at 300 mW cm^{-2} for 48 h (irradiated area is ca. 2.4 cm^2). The experimental error bars represent the standard deviations of three independent measurements.

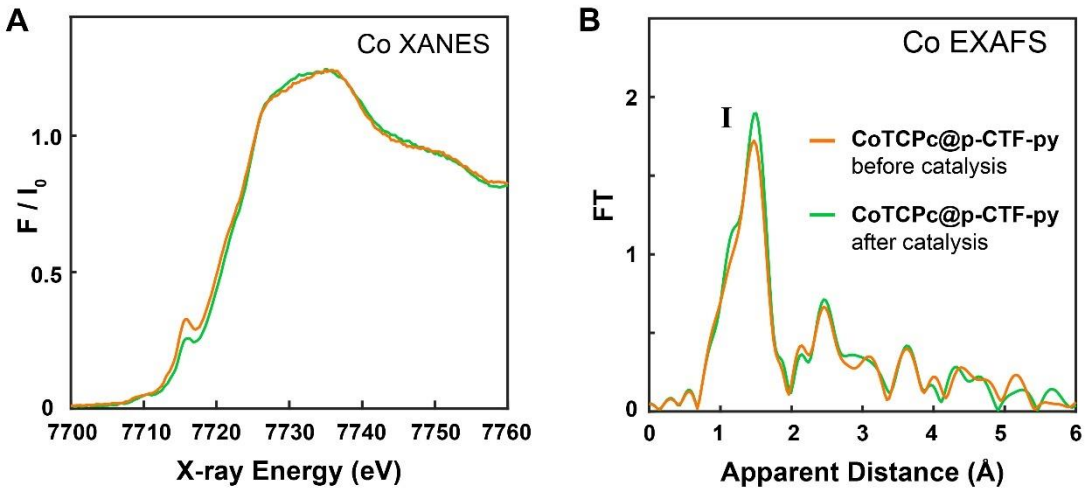

Figure S26. *(a) Normalized Co K-edge XANES spectra and (b) Fourier transforms of k^2-weighted Co EXAFS of **CoTCPc@p-CTF-py** before (orange) and after (green) 48 h of photocatalysis.*

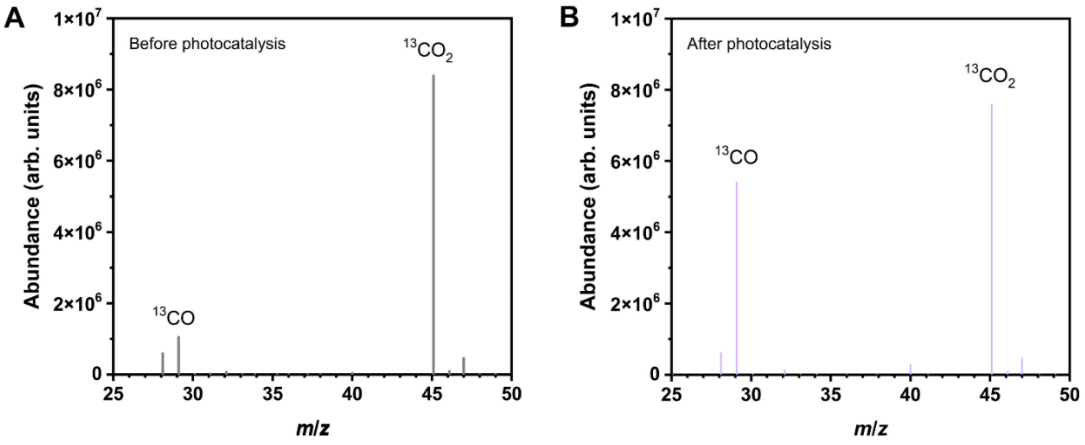

Figure S27. *^{13}C isotope experiments (a) with the initial $^{13}CO_2$ gas and (b) from the 12-h photocatalysis with 0.5 mg* ***CoTCPc@p-CTF-py*** *under 1 atm $^{13}CO_2$. As shown in (a), a weak, fragmental signal of ^{13}CO at m/z = 29 appeared while its abundance is much lower than the one after photocatalysis. Meanwhile, the signals of ^{12}CO (overlapped with N_2) at m/z = 28 were negligibly changed before and after photocatalysis. Both observations clearly demonstrate that the detected CO should originate from CO_2 rather than the organic components during photocatalysis. We note that the abundance values in these measurements are semi-quantitative.*

TRPL measurements

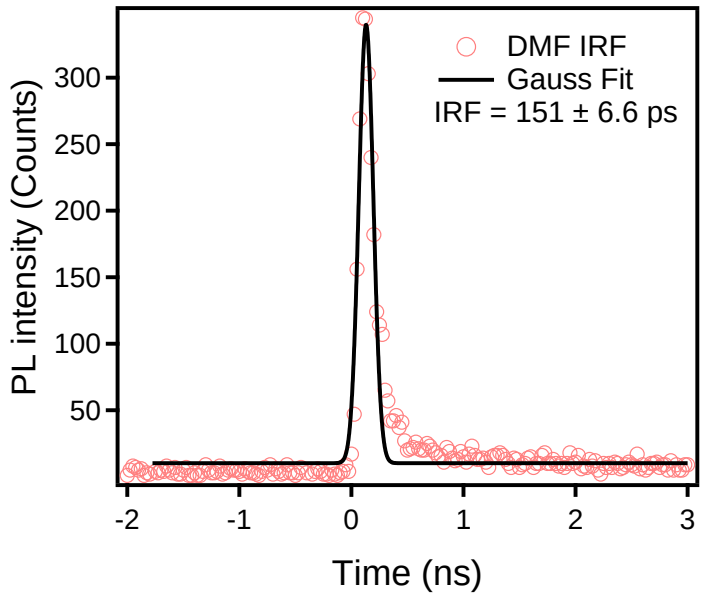

Figure S28. *Instrument response function (IRF) of TCSPC setup measured with DMF solvent photon scattering. The experimental error bars represent the standard deviations of three independent measurements.*

Table S6. *TRPL decay kinetics of* ***p-CTF****,* ***p-CTF*** *with ascorbate,* ***p-CTF-py****, and* ***CoTCPc@p-CTF-py****. The experimental error bars represent the standard deviations of three independent measurements.*

	p-CTF	**p-CTF** + ascorbate	**p-CTF-py**	**CoTCPc@p-CTF-py**
A_1 (%)	83.8 ± 0.3		27.8 ± 0.3	
τ_1 (ps)	108 ± 0.2		819 ± 7	332 ± 4
A_2 (%)	6.1 ± 0.2		38.0 ± 0.7	
τ_2 (ns)	0.96 ± 0.02		2.19 ± 0.02	1.92 ± 0.03
A_3 (%)	9.6 ± 0.2		29.3 ± 0.7	
τ_3 (ns)	2.43 ± 0.04		5.41 ± 0.09	5.08 ± 0.09
A_4 (%)	0.5 ± 0.03		4.9 ± 0.2	
τ_4 (ns)	9.28 ± 0.33		16.48 ± 0.32	16.1 ± 0.3
τ_{ave} (ns)	0.43 ± 0.06		3.46 ± 0.47	3.10 ± 0.44
IRF (ps)	151 ± 7			

Table S7. *Extracted electron quenching between* ***CoTCPc*** *and* ***p-CTF*** *and hole quenching rate between* ***CoTCPc*** *and* ***p-CTF-py*** *from TRPL data Figure 3b using equation S5. The experimental error bars represent the standard deviations of three independent measurements.*

	CoTCPc@p-CTF	**p-CTF-py** + ascorbate
B_1 (%)	26.4 ± 4.5	23.2 ± 0.8
τ_{CT1} (ns)	0.73 ± 0.27	0.29 ± 0.3
B_2 (%)	73.6 ± 4.4	76.8 ± 0.8
τ_{CT2} (ns)	∞	90 ± 21.6
τ_{CT} (ns)*	0.73 ± 0.27	69.2 ± 16.6

*Averaged values.

Computational studies

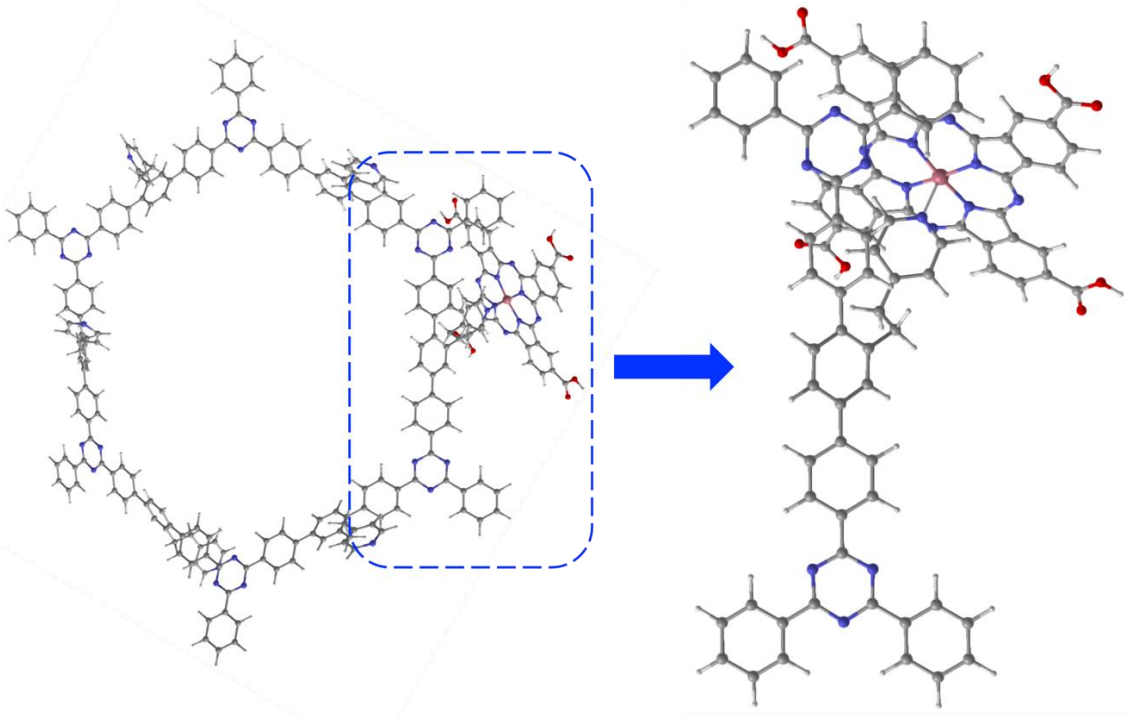

Figure S29. *Optimized structure of* ***CoTCPc*** *anchored to* ***p-CTF-py*** *via formation of a covalent Co-N bond (left) and highlighted subsystem adopted for* ***CoTCPc@p-CTF-py*** *cluster model (right).*

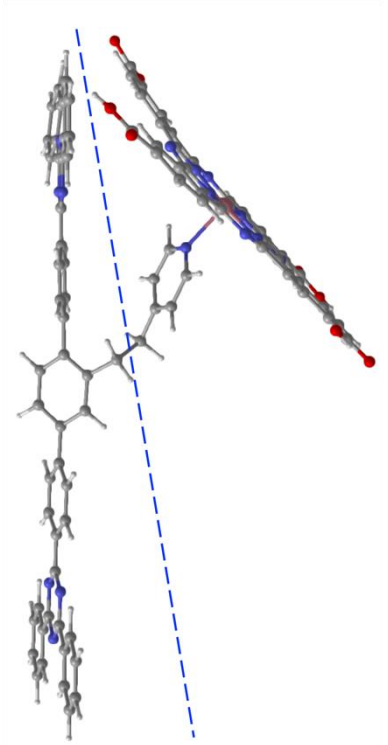

Figure S30. *Partition of* ***CoTCPc@p-CTF-py*** *cluster model to two fragments for spin constraint CDFT calculations.*

$^{2}[CTF\text{-}^{2}Co^{II}]^{0}$

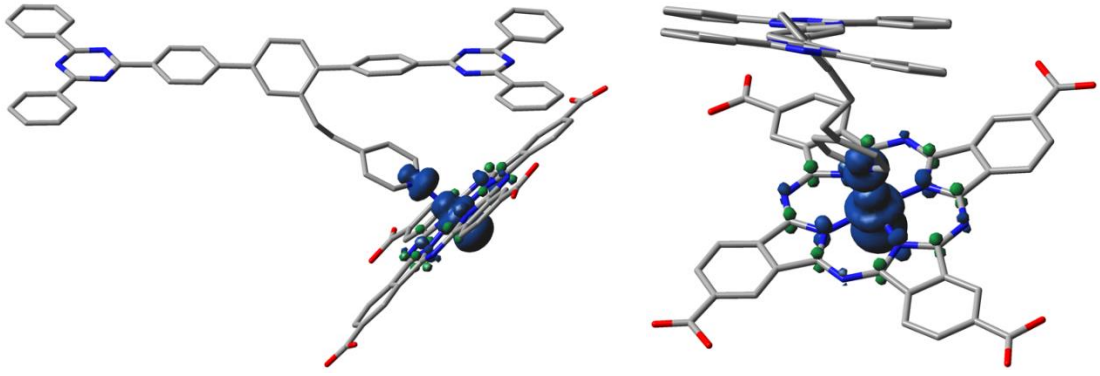

$^{4}[^{3}CTF\text{-}^{2}Co^{II}]^{0}$

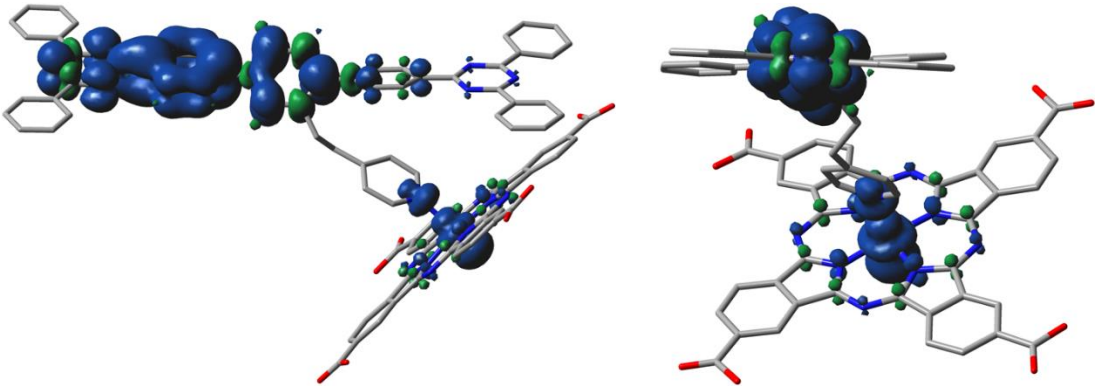

$^{3}[^{2}CTF^{\bullet-}\text{-}^{2}Co^{II}]^{-}$

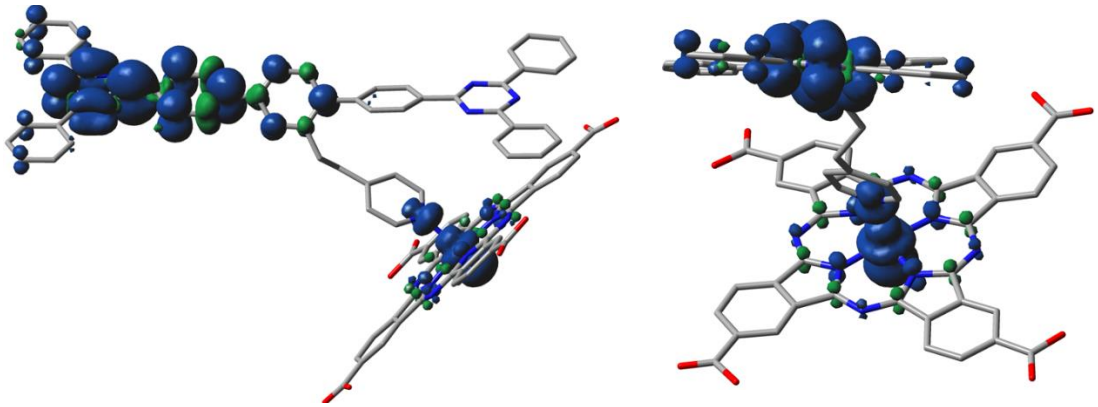

$^{4}[^{2}CTF^{\bullet+}\text{-}^{3}Co^{I}]^{0}$

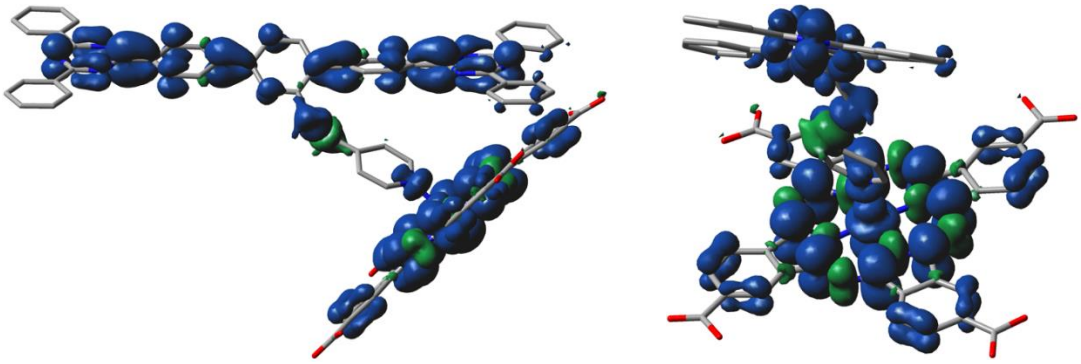

$^{2}[^{2}CTF^{\bullet+}\text{-}^{1}Co^{I}]^{0}$

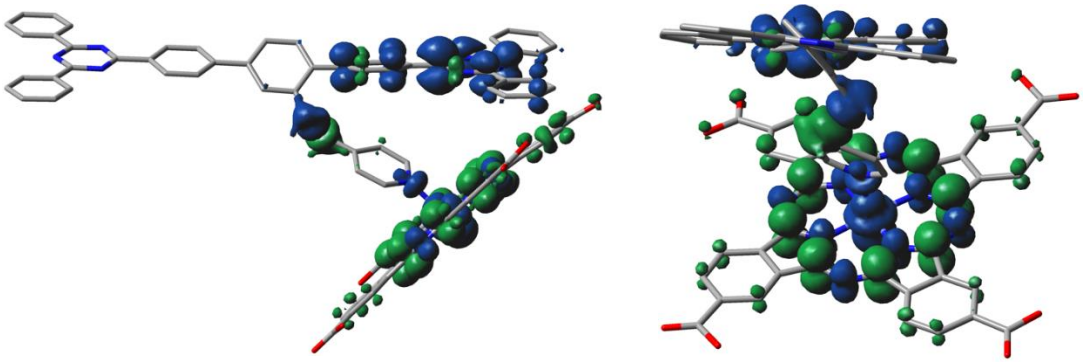

$^{3}[CTF\text{-}^{3}Co^{I}]^{-}$

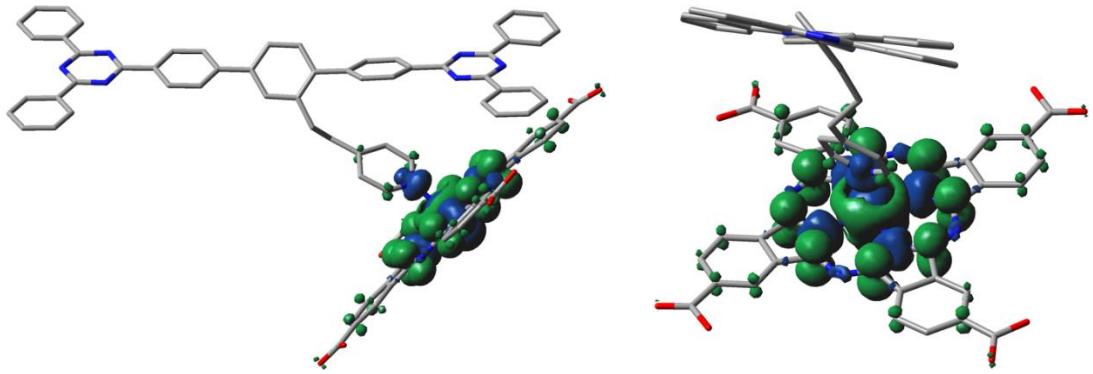

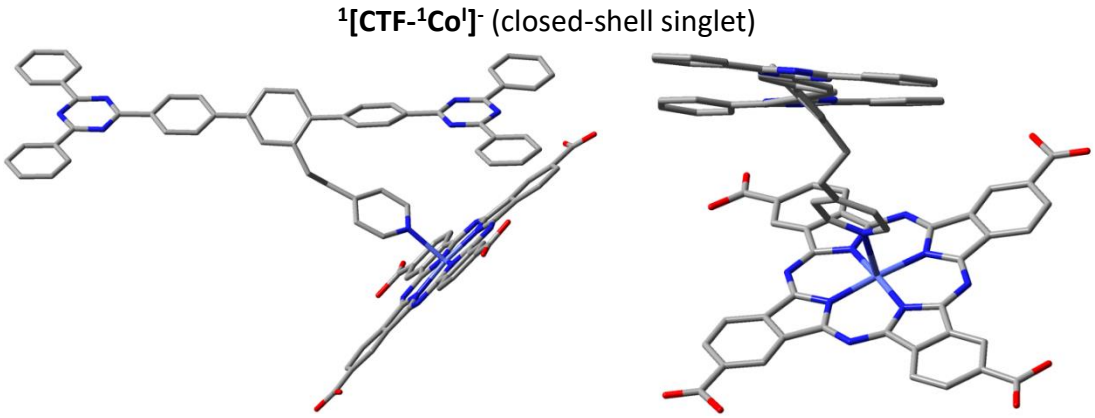

Figure S31. *Unpaired spin density plots of* ***CoTCPc@p-CTF-py*** *species in energy diagram in Figure 4 generated via CDFT calculations.*

EPR measurements

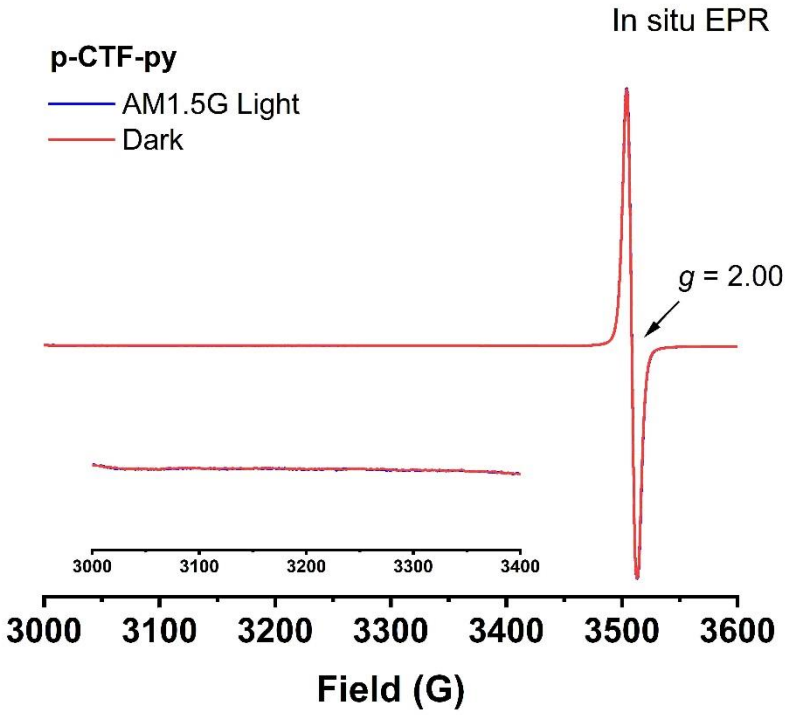

Figure S32. *In situ EPR signals of* ***p-CTF-py*** *in the absence (blue) and presence (red) of illumination.*

4.5.4. References

(1) Ravel, B.; Newville, M. ATHENA, ARTEMIS, HEPHAESTUS: Data Analysis for X-Ray Absorption Spectroscopy Using IFEFFIT. *J. Synchrotron Radiat.* **2005**, *12* (4), 537–541. https://doi.org/10.1107/S0909049505012719.

(2) Rehr, J. J.; Albers, R. C. Theoretical Approaches to X-Ray Absorption Fine Structure. *Rev. Mod. Phys.* **2000**, *72* (3), 621–654. https://doi.org/10.1103/RevModPhys.72.621.

(3) Wojdyr, M. Fityk: A General-Purpose Peak Fitting Program. *J. Appl. Crystallogr.* **2010**, *43* (5 PART 1), 1126–1128. https://doi.org/10.1107/S0021889810030499.

(4) Pattanayak, S.; Jasniewski, A. J.; Rana, A.; Draksharapu, A.; Singh, K. K.; Weitz, A.; Hendrich, M.; Que, L.; Dey, A.; Sen Gupta, S. Spectroscopic and Reactivity Comparisons of a Pair of bTAML Complexes with FeV=O and FeIV=O Units. *Inorg. Chem.* **2017**, *56* (11), 6352–6361. https://doi.org/10.1021/acs.inorgchem.7b00448.

(5) DeBeer George, S.; Petrenko, T.; Neese, F. Prediction of Iron K-Edge Absorption Spectra Using Time-Dependent Density Functional Theory. *J. Phys. Chem. A* **2008**, *112* (50), 12936–12943. https://doi.org/10.1021/jp803174m.

(6) Weigend, F.; Ahlrichs, R. Balanced Basis Sets of Split Valence, Triple Zeta Valence and Quadruple Zeta Valence Quality for H to Rn: Design and Assessment of Accuracy. *Phys. Chem. Chem. Phys.* **2005**, *7* (18), 3297–3305. https://doi.org/10.1039/b508541a.

(7) Guo, Z.; Chen, G.; Cometto, C.; Ma, B.; Zhao, H.; Groizard, T.; Chen, L.; Fan, H.; Man, W.-L.; Yiu, S.-M.; Lau, K.-C.; Lau, T.-C.; Robert, M. Selectivity Control of CO versus HCOO− Production in the Visible-Light-Driven Catalytic Reduction of CO_2 with Two Cooperative Metal Sites. *Nat. Catal.* **2019**, *2*, 801–808. https://doi.org/10.1038/s41929-019-0331-6.

(8) Kuhn, H. J.; Braslavsky, S. E.; Schmidt, R. Chemical Actinometry (IUPAC Technical Report). *Pure Appl. Chem.* **2004**, *76* (12), 2105–2146. https://doi.org/10.1351/pac200476122105.

(9) Thoi, V. S.; Kornienko, N.; Margarit, C. G.; Yang, P.; Chang, C. J. Visible-Light Photoredox Catalysis: Selective Reduction of Carbon Dioxide to Carbon Monoxide by a Nickel N-Heterocyclic Carbene-Isoquinoline Complex. *J. Am. Chem. Soc.* **2013**, *135* (38), 14413–14424. https://doi.org/10.1021/ja4074003.

(10) Neese, F. The ORCA Program System. *Wiley Interdiscip. Rev. Comput. Mol. Sci.* **2012**, *2* (1), 73–78. https://doi.org/10.1002/wcms.81.

(11) Stephens, P. J.; Devlin, F. J.; Chabalowski, C. F.; Frisch, M. J. Ab Initio Calculation of Vibrational Absorption and Circular Dichroism Spectra Using Density Functional Force Fields. *J. Phys. Chem.* **1994**, *98* (45), 11623–11627. https://doi.org/10.1021/j100096a001.

(12) Kossmann, S.; Neese, F. Efficient Structure Optimization with Second-Order Many-Body Perturbation Theory: The RIJCOSX-MP2 Method. *J. Chem. Theory Comput.* **2010**, *6* (8), 2325–2338. https://doi.org/10.1021/ct100199k.

(13) Choi, C.; Zhao, F.; Hart, J. L.; Gao, Y.; Menges, F.; Rooney, C. L.; Harmon, N. J.; Shang, B.; Xu, Z.; Suo, S.; Sam, Q.; Cha, J. J.; Lian, T.; Wang, H. Synergizing Electron and Heat Flows in Photocatalyst for Direct Conversion of Captured CO_2. *Angew. Chemie - Int. Ed.* **2023**, *62* (23), 1–9. https://doi.org/10.1002/anie.202302152.

(14) Perdew, J. P.; Yue, W. Accurate and Simple Density Functional for the Electronic Exchange Energy: Generalized Gradient Approximation. *Phys. Rev. B* **1986**, *33* (12), 8800. https://doi.org/10.1103/PhysRevB.33.8800.

(15) Becke, A. D. Density-Functional Exchange-Energy Approximation with Correct Asymptotic Behavior. *Phys. Rev. A* **1988**, *38* (6), 3098. https://doi.org/10.1103/PhysRevA.38.3098.

(16) Marenich, A. V.; Cramer, C. J.; Truhlar, D. G. Universal Solvation Model Based on Solute Electron Density and on a Continuum Model of the Solvent Defined by the Bulk Dielectric Constant and Atomic Surface Tensions. *J. Phys. Chem. B* **2009**, *113* (18), 6378–6396. https://doi.org/10.1021/jp810292n.

(17) Frisch, M. J. T., G. W.; Schlegel, H. B.; Scuseria, G. E.; Robb, M. A.; Cheeseman, J. R.; Scalmani, G.; Barone, V.; Petersson, G. A.; Nakatsuji, H.; Li, X.; Caricato, M.; Marenich, A. V.; Bloino, J.; Janesko, B. G.; Gomperts, R.; Mennucci, B.; Hratchian, D. J. Gaussian 16, Revision A.03. *Gaussian, Inc. Wallingford CT* **2016**.

(18) Yu, H. S.; He, X.; Li, S. L.; Truhlar, D. G. MN15: A Kohn-Sham Global-Hybrid Exchange-Correlation Density Functional with Broad Accuracy for Multi-Reference and Single-Reference Systems and Noncovalent Interactions. *Chem. Sci.* **2016**, *7* (8), 5032–5051. https://doi.org/10.1039/c6sc00705h.

(19) Wu, Q.; Van Voorhis, T. Direct Optimization Method to Study Constrained Systems within Density-Functional Theory. *Phys. Rev. A - At. Mol. Opt. Phys.* **2005**, *72* (2), 7–10. https://doi.org/10.1103/PhysRevA.72.024502.

(20) Kaduk, B.; Kowalczyk, T.; Van Voorhis, T. Constrained Density Functional Theory. *Chem. Rev.* **2012**, *112* (1), 321–370. https://doi.org/10.1021/cr200148b.

(21) Epifanovsky, E.; Gilbert, A. T. B.; Feng, X.; Lee, J.; Mao, Y.; Mardirossian, N.; Pokhilko, P.; White, A. F.; Coons, M. P.; Dempwolff, A. L.; Gan, Z.; Hait, D.; Horn, P. R.; Jacobson, L. D.; Kaliman, I.; Kussmann, J.; Lange, A. W.; Lao, K. U.; Levine, D. S.; Liu, J.; McKenzie, S. C.; Morrison, A. F.; Nanda, K. D.; Plasser, F.; Rehn, D. R.; Vidal, M. L.; You, Z. Q.; Zhu, Y.; Alam, B.; Albrecht, B. J.; Aldossary, A.; Alguire, E.; Andersen, J. H.; Athavale, V.; Barton, D.; Begam, K.; Behn, A.; Bellonzi, N.; Bernard,

Y. A.; Berquist, E. J.; Burton, H. G. A.; Carreras, A.; Carter-Fenk, K.; Chakraborty, R.; Chien, A. D.; Closser, K. D.; Cofer-Shabica, V.; Dasgupta, S.; De Wergifosse, M.; Deng, J.; Diedenhofen, M.; Do, H.; Ehlert, S.; Fang, P. T.; Fatehi, S.; Feng, Q.; Friedhoff, T.; Gayvert, J.; Ge, Q.; Gidofalvi, G.; Goldey, M.; Gomes, J.; González-Espinoza, C. E.; Gulania, S.; Gunina, A. O.; Hanson-Heine, M. W. D.; Harbach, P. H. P.; Hauser, A.; Herbst, M. F.; Hernández Vera, M.; Hodecker, M.; Holden, Z. C.; Houck, S.; Huang, X.; Hui, K.; Huynh, B. C.; Ivanov, M.; Jász, Á.; Ji, H.; Jiang, H.; Kaduk, B.; Kähler, S.; Khistyaev, K.; Kim, J.; Kis, G.; Klunzinger, P.; Koczor-Benda, Z.; Koh, J. H.; Kosenkov, D.; Koulias, L.; Kowalczyk, T.; Krauter, C. M.; Kue, K.; Kunitsa, A.; Kus, T.; Ladjánszki, I.; Landau, A.; Lawler, K. V.; Lefrancois, D.; Lehtola, S.; Li, R. R.; Li, Y. P.; Liang, J.; Liebenthal, M.; Lin, H. H.; Lin, Y. S.; Liu, F.; Liu, K. Y.; Loipersberger, M.; Luenser, A.; Manjanath, A.; Manohar, P.; Mansoor, E.; Manzer, S. F.; Mao, S. P.; Marenich, A. V.; Markovich, T.; Mason, S.; Maurer, S. A.; McLaughlin, P. F.; Menger, M. F. S. J.; Mewes, J. M.; Mewes, S. A.; Morgante, P.; Mullinax, J. W.; Oosterbaan, K. J.; Paran, G.; Paul, A. C.; Paul, S. K.; Pavošević, F.; Pei, Z.; Prager, S.; Proynov, E. I.; Rák, Á.; Ramos-Cordoba, E.; Rana, B.; Rask, A. E.; Rettig, A.; Richard, R. M.; Rob, F.; Rossomme, E.; Scheele, T.; Scheurer, M.; Schneider, M.; Sergueev, N.; Sharada, S. M.; Skomorowski, W.; Small, D. W.; Stein, C. J.; Su, Y. C.; Sundstrom, E. J.; Tao, Z.; Thirman, J.; Tornai, G. J.; Tsuchimochi, T.; Tubman, N. M.; Veccham, S. P.; Vydrov, O.; Wenzel, J.; Witte, J.; Yamada, A.; Yao, K.; Yeganeh, S.; Yost, S. R.; Zech, A.; Zhang, I. Y.; Zhang, X.; Zhang, Y.; Zuev, D.; Aspuru-Guzik, A.; Bell, A. T.; Besley, N. A.; Bravaya, K. B.; Brooks, B. R.; Casanova, D.; Chai, J. Da; Coriani, S.; Cramer, C. J.; Cserey, G.; Deprince, A. E.; Distasio, R. A.; Dreuw, A.; Dunietz, B. D.; Furlani, T. R.; Goddard, W. A.; Hammes-Schiffer, S.; Head-Gordon, T.; Hehre, W. J.; Hsu, C. P.; Jagau, T. C.; Jung, Y.; Klamt, A.; Kong, J.; Lambrecht, D. S.; Liang, W.; Mayhall, N. J.; McCurdy, C. W.; Neaton, J. B.; Ochsenfeld, C.; Parkhill, J. A.; Peverati, R.; Rassolov, V. A.; Shao, Y.; Slipchenko, L. V.; Stauch, T.; Steele, R. P.; Subotnik, J. E.; Thom, A. J. W.; Tkatchenko, A.; Truhlar, D. G.; Van Voorhis, T.; Wesolowski, T. A.; Whaley, K. B.; Woodcock, H. L.; Zimmerman, P. M.; Faraji, S.; Gill, P. M. W.; Head-Gordon, M.; Herbert, J. M.; Krylov, A. I. Software for the Frontiers of Quantum Chemistry: An Overview of Developments in the Q-Chem 5 Package. *J. Chem. Phys.* **2021**, *155* (8), 084801. https://doi.org/10.1063/5.0055522.

(22) Salati, M.; Dorchies, F.; Wang, J.-W.; Ventosa, M.; González-Carrero, S.; Bozal-Ginesta, C.; Holub, J.; Rüdiger, O.; DeBeer, S.; Gimbert-Suriñach, C.; Durrant, J. R.; Ertem, M. Z.; Gil-Sepulcre, M.; Llobet, A. Covalent Triazine-Based Frameworks with Covalently Anchored Ru-Tda Based Catalyst for Photoinduced Water Oxidation. *Small* **2024**, 2406375, 1-9. https://doi.org/10.1002/smll.202406375.

(23) Sun, T.; Liang, Y.; Luo, W.; Zhang, L.; Cao, X.; Xu, Y. A General Strategy for Kilogram-Scale Preparation of Highly Crystal-Line Covalent Triazine Frameworks. *Angew. Chemie - Int. Ed.* **2022**, *61* (25). https://doi.org/10.1002/anie.202203327.


4

Chapter 5

Supramolecular interaction of molecular catalyst on a polymeric carbon nitride photoanode enhances PEC activity and stability at neutral pH


5

Supramolecular interaction of molecular catalyst on a polymeric carbon nitride photoanode enhances PEC activity and stability at neutral pH

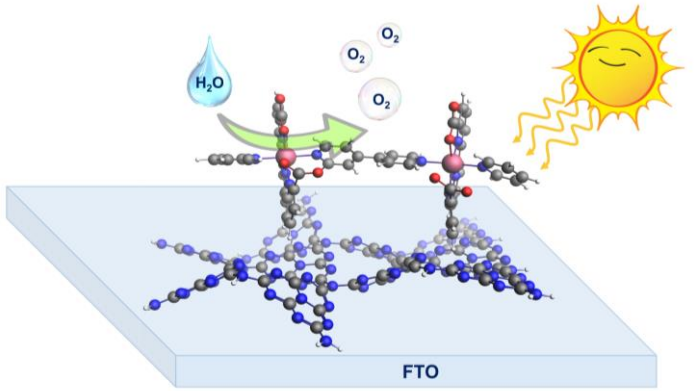

Abstract

Polymeric carbon nitride (CN) emerged as an alternative, metal-free photoanode material in water-splitting photoelectrochemical cells (PEC). However, the performance of CN photoanodes is limited due to the slow charge separation and water oxidation kinetics as a consequence of a poor interaction with water oxidation catalysts (WOCs). Moreover, operation under benign, neutral pH conditions is rarely reported. Here, we designed a porous CN photoanode connected to a highly active molecular Ru-based WOC, which also acts as an additional photo-absorber. We show that the strong interaction between the π-system of the heptazine units within the CN to the CH groups of the WOC's equatorial ligand enables a strong connection between them and an efficient electronic communication path. The optimized photoanode exhibits a photocurrent density of 180 ± 10 μA cm^{-2} at 1.23 V *vs.* reversible hydrogen electrode (RHE) with 89% Faradaic efficiency for oxygen evolution with turnover numbers (TONs) in the range of 3300 and turnover frequency (TOF) of 0.4 s^{-1}, low onset potential, extended incident photon to current conversion, and good stability up to 5 h. This study may lead to the integration of molecular catalysts and polymeric organic absorbers using supramolecular interactions.

Contributions:

Martina Salati synthesized [Ru(tda)(4,4'-bpy)]$_{15}$(4,4'-bpy) (**Ru$_{15}$**) and precursors, optimized the anchoring strategy and the photoelectrochemical experiments.

5.1. Introduction

Polymeric carbon nitride (CN) has gained significant interest as a low-cost and benign photoanodic material for water-splitting photoelectrochemical cells (PEC).[1–6] However, low charge separation and transfer efficiency and slow water oxidation kinetics hinder the photoactivity and PEC performance of CN photoanodes.[7–11] Moreover, a pristine CN photoanode is prone to degradation due to the moderate oxygen evolution reaction (OER), which leads to hole accumulation and self-oxidation of the CN layer.[7,12,13] Therefore, low Faradaic efficiencies (FE) towards molecular oxygen and poor stabilities are usually observed. A common approach to overcome the sluggish OER kinetics in PEC is introducing a co-catalyst, which acts as hole sink and catalytic site for OER.[14] In recent years, only few reports have shown that heterogenous metal oxide-based co-catalysts can improve the CN photoanode activity towards OER.[14–17] Unlike metal oxide-based photoanodes ($BiVO_4$, Fe_2O_3), most known co-catalyst deposition methods did not lead to a successful enhanced oxygen production on a CN-based photoanode.[18–22] The poor hole transfer from the CN to the co-catalyst may stem from the insufficient interaction between the materials although it is still not fully understood. Moreover, CN and many heterogeneous OER electrocatalysts based on oxides work efficiently only in alkaline conditions.[7,14] Consequently, the performance of CN photoanodes in a neutral electrolyte medium is relatively poor.[23,24] There is an allure in achieving water-splitting PEC under neutral conditions as it offers gentler operating conditions compared to alkaline or acidic environments.

Highly performant and robust molecular catalysts have been developed recently for the water oxidation reaction, mainly based on Ru complexes containing the so-called FAME (flexible, adaptable, multidentate, equatorial) ligands that achieve high turnover numbers (TONs) and turnover frequencies (TOFs), with the $[Ru^{II}(tda\text{-}\kappa\text{-}N^3O)(py)_2]$ (Ru-tda, where tda^{2-} is [2,2':6',2"-terpyridine]-6,6"-dicarboxylate and py is pyridine) being one of the best examples.[25–27] The well-defined nature of these molecular catalysts, together with the capacity to spectroscopically characterize intermediates, has prompted a remarkable development of water oxidation catalysts (WOCs).[28] In addition, the capacity to functionalize the ligands that are bonding the metal center, offer a wide variety of anchoring strategies.[29–33] Recently, we have developed the oligomeric

derivative of the Ru-tda catalysts, using 4,4'-bpy as bridging ligands to form [Ru(tda)(4,4'-bpy)]$_{15}$(4,4'-bpy) (**Ru$_{15}$**).[32] The latter has the capacity to generate a large number of CH–π interactions with graphitic surfaces, generating robust hybrid materials for the efficient oxidation of water in heterogeneous phase.

In the present work, we explore the capacity of **Ru$_{15}$** catalyst to interact with the π system of the heptazines, constituting the repeating unit of the CN material, *via* the CH groups of the tda ligand and generating a monolayer of well-defined molecular catalyst on top of the CN surface. The CN synthetic procedure is chosen to form a porous layer with good adhesion to the conductive substrate (i.e., fluorine-doped tin oxide, FTO), allowing exploration of the co-catalyst role on an FTO/CN/**Ru$_{15}$** photoanode. This should provide the needed electronic communication between the co-catalyst and the light absorbing material, leading to a superior performance of the hybrid material constituted by **Ru$_{15}$** and the CN.

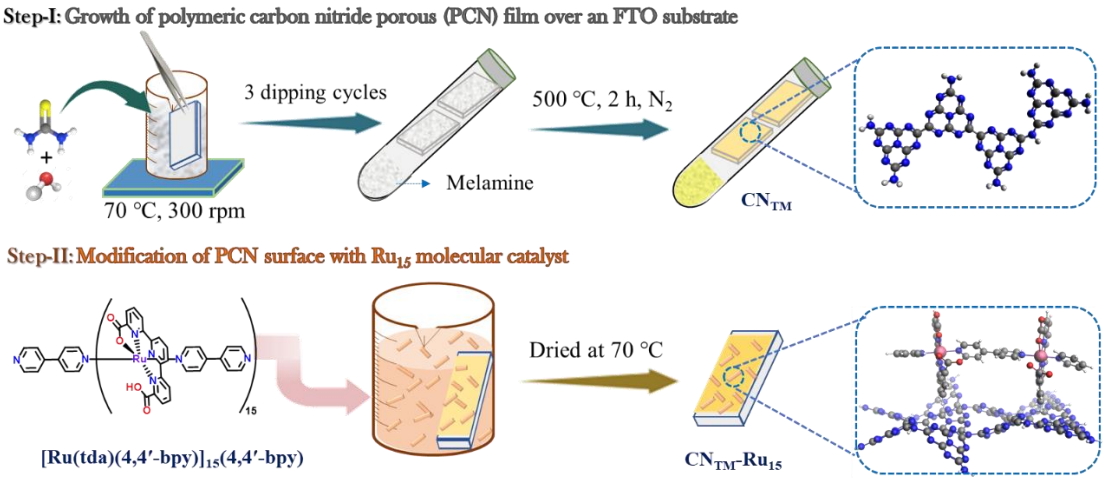

Scheme 1. *Procedure for the preparation of* ***CN$_{TM}$*** *film and the anchoring of the* ***Ru$_{15}$*** *oligomer to generate the hybrid material* ***CN$_{TM}$–Ru$_{15}$****.*

5.2. Results and discussion

The fabrication process of a porous CN film over FTO-coated glass as the substrate is illustrated in Scheme 1. Thiourea and melamine were used to prepare **CN$_{TM}$** photoanodes using a two-step method involving dipping and thermal treatment. The

anchoring of the **Ru_{15}** oligomer into the **CN_{TM}** film was performed by dipping the **CN_{TM}** electrode in a solution containing 1 mg of **Ru_{15}** in 10 mL of 2,2,2-trifluoroethanol (TFE), for 20 min. Afterwards the electrode was removed from the solution and rinsed with TFE to generate the hybrid material, **CN_{TM}-Ru_{15}**. Further experimental details are given in the Supporting Information. The interaction of the **Ru_{15}** oligomeric water oxidation catalyst with the surface of the CN film occurs via CH–π interaction as we have previously described in the case of graphitic surfaces.[32–34] In order to further characterize this interaction and visualize it, we have carried out DFT calculations with a low molecular weight model system that involves a 10 heptazine units (164 atoms: 60 C, 86 N, and 18 H) molecule for the carbon nitride, labelled as **CN_{Red}**, and a dinuclear Ru complex {[Ru(tda)(py)]$_2$(μ-4,4'-bpy)]} labeled as **Ru_2**, to form **CN_{Red}-Ru_2** (see Figures 1, S14–S22 and Tables S4–S7). Structural combinations of the two units were explored including aqueous solvent effects, yielding for the most favorable case a stabilization energy of 12.7 kcal mol^{-1} per Ru center, that would imply 190.5 kcal mol^{-1} for the entire **Ru_{15}** oligomer with **CN_{TM}**. This large stabilization energy is due to CH–π interactions between the CH aromatic groups of the tda ligands bonded to the Ru center and the π -system of the **CN_{Red}** surface.

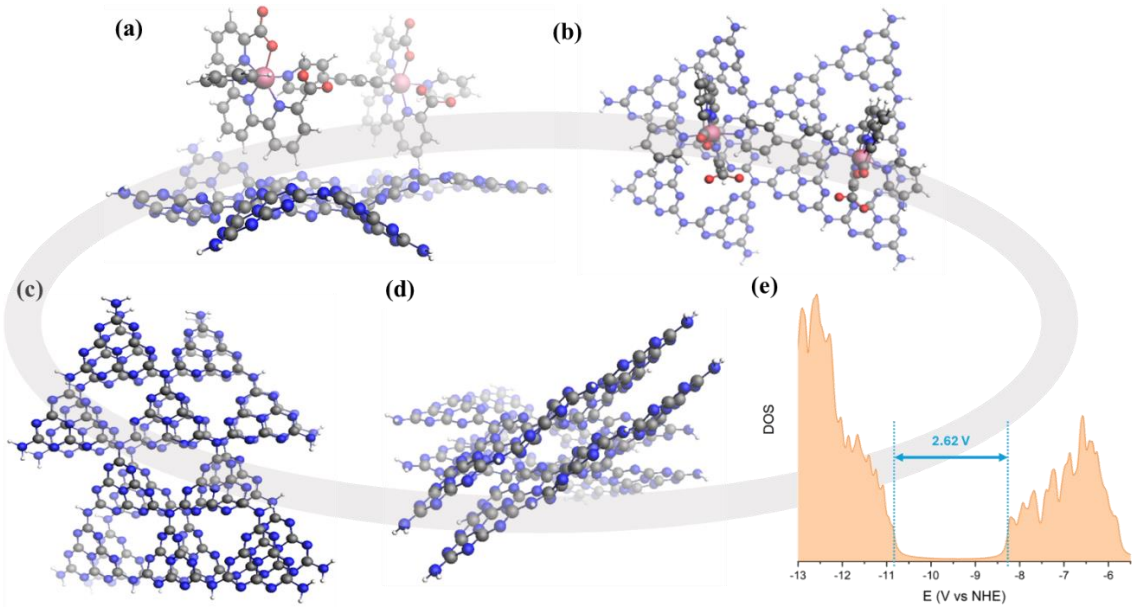

Figure 1. *(a) Side and (b) top views of the DFT calculated model of* ***CN_{Red}-Ru_2****. (c) Top and (d) side views of optimized structure consisting of two layers of heptazine units* ***$(CN_{Red})_2$*** *interacting via π–π stacking interactions. (e) Density of States diagram for* ***$(CN_{Red})_2$****.*

PXRD (Powder X-ray diffraction) and FTIR (Fourier-transform infrared) spectroscopy were used to investigate the structural and functional properties of the films. The **CN_{TM}** material exhibits two characteristic diffraction signals at 13.0° and 27.4°, which can be assigned to (100) and (002) planes, respectively, representative of the interplanar spacing and the conjugated aromatic system (Figure 2a) in a heptazine-based CN.[35,36] Upon the incorporation of the **Ru_{15}** oligomeric catalyst, the XRD pattern remains unchanged, underlining the structural stability of **CN_{TM}** films. The FTIR spectra of **CN_{TM}** and **CN_{TM}-Ru_{15}** films show the typical peak at 805 cm^{-1}, which corresponds to the breathing mode of triazine units present in the sample (Figure 2b). Additionally, the stretching modes of CN heterocycles were observed between 1200 to 1600 cm^{-1}, with specific vibrations at 1400 and 1633 cm^{-1} in the **CN_{TM}** film. Upon loading of the **Ru_{15}** catalyst onto the **CN_{TM}** film, the stretching modes of the CN heterocycles are found to be 1394 and 1625 cm^{-1}. The broad band observed between 2980 and 3500 cm^{-1} in the spectra is attributed to either NH_2 groups or surface-adsorbed water molecules.[36] Additionally, ^1H NMR, XRD and FTIR data of the **Ru_{15}** oligomer are provided in Figure S1.

The modification of the **CN_{TM}** film with the **Ru_{15}** oligomer has caused a visual change in the electrodes (Figure 2c), which translates into the presence of a new broad band at approximately 480–550 nm, associated with metal to ligand charge transfer (MLCT) band for the Ru complex, as can be observed in the diffuse reflectance spectrum (DRS) in Figure 2d, and is comparable to the one visible in the UV–vis spectrum of **Ru_{15}** (Figure S2).

The direct optical bandgaps (E_g) of the **CN_{TM}** and **CN_{TM}–Ru_{15}** films are 2.61 and 2.50 eV, respectively (Figure S3). Valence band X-ray photoelectron spectroscopy (VB-XPS) discloses a more positive VB energy (E_{VB}) position for the **CN_{TM}–Ru_{15}** films of 2.17 V *vs.* NHE with regard to that of bare **CN_{TM}**, which gives a value of 1.97 V *vs.* NHE and thus a better thermodynamic driving force for the former (Figure S4).[9,36] Finally, the corresponding conduction band energy (E_{CB}) of the **CN_{TM}** and **CN_{TM}–Ru_{15}** films is –0.64 and –0.33 V *vs.* NHE, respectively (inset of Figure 2d for the energy diagram).

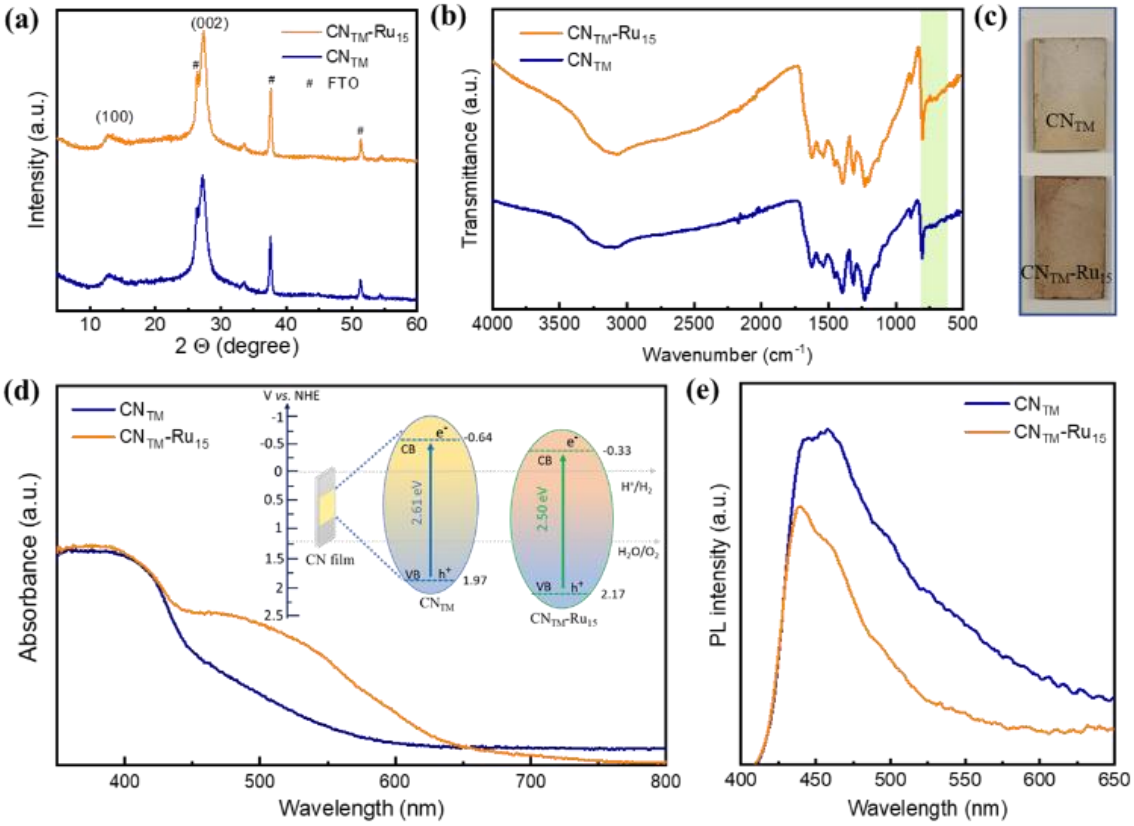

Figure 2. *(a) XRD of* ***CN$_{TM}$*** *and* ***CN$_{TM}$-Ru$_{15}$*** *films. (b) FTIR spectra of* ***CN$_{TM}$*** *and* ***CN$_{TM}$-Ru$_{15}$*** *films. Spectra are vertically offset for clarity. (c) Digital photographs of* ***CN$_{TM}$*** *and* ***CN$_{TM}$-Ru$_{15}$*** *photoelectrodes on FTO. (d) UV–vis DRS of* ***CN$_{TM}$*** *and* ***CN$_{TM}$-Ru$_{15}$*** *films. Inset is the schematic representation of the electronic band structure of* ***CN$_{TM}$*** *and* ***CN$_{TM}$-Ru$_{15}$*** *(on the normal hydrogen electrode (NHE) scale) determined using the XPS-VB position and the optical E_g calculation. (e) Photoluminescence emission spectra (excitation wavelength 370 nm) of* ***CN$_{TM}$*** *and* ***CN$_{TM}$–Ru$_{15}$*** *films.*

The electronic properties of the **CN$_{TM}$** material were also analyzed based on TD-DFT calculations. A single sheet of **CN$_{Red}$** made out of 10 heptazine units gave a band gap of 3.25 eV. Interestingly, a two-layer of heptazine units (**CN$_{Red}$**)$_2$ interacting via π–π stacking, as shown in Figure 1, gives a band gap of 2.62 eV closely matching the experimental value (2.61 eV), thus manifesting the importance of the delocalization of the electron density on the 2D network along with the π–π stacking interactions among the different layers to properly describe carbon nitride type of materials.

Photoluminescence (PL) spectra are significantly different in the presence and absence of the **Ru$_{15}$**, as can be observed in Figure 2e, where the intensity of the prominent

emission peak at 450 nm in the **CN_{TM}–Ru_{15}** is partially quenched compared to pristine **CN_{TM}**, suggesting the presence of an alternative non-radiative recombination path.[37,38]

The SEM images of the **CN_{TM}** (Figures 3a-c) indicate a porous sheet-like morphology with good adhesion to the FTO substrate with a thickness of 40–50 µm. The **CN_{TM}–Ru_{15}** film images (Figures 3d–f) suggest the preservation of the porous sheet-like morphology, with a rough surface. Cross-section analysis (Figures 3g–h) indicates an intimate contact between the film and substrate with similar film thickness to the **CN_{TM}** film. Energy dispersive X-ray spectroscopy (EDS) confirms the presence of Ru in the **CN_{TM}–Ru_{15}** film (Figure S5).

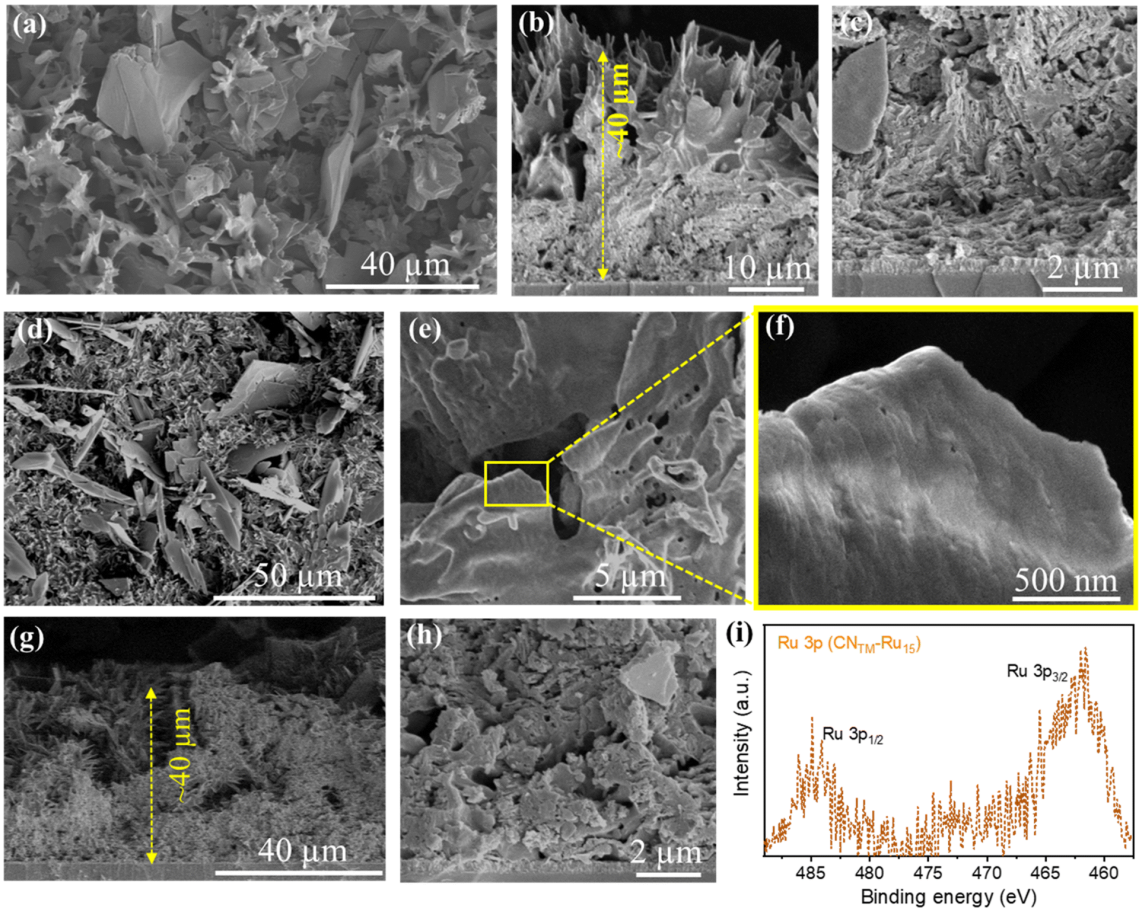

Figure 3. *(a) SEM image showing the morphology of the upper surface of the **CN_{TM}** electrode. (b, c) Cross-sectional SEM images of **CN_{TM}** electrodes at different magnifications. (d, e, f) Top-view of **CN_{TM}–Ru_{15}** at different magnifications. (g, h) Cross-sectional SEM images of **CN_{TM}–Ru_{15}** electrodes at different magnifications. (i) High-resolution Ru 3p XPS spectra of **CN_{TM}-Ru_{15}** film.*

Moreover, the morphology of the **CN_{TM}–Ru_{15}** sample was examined using a high-angle annular dark-field scanning transmission electron microscope (HAADF-STEM), revealing the layered structure of CN (see Figure S6). EDS mapping further confirms the presence and distribution of the **Ru_{15}** oligomer over the CN surface (Figure S7).

X-ray photoelectron spectroscopy (XPS) confirms the successful loading of **Ru_{15}** on **CN_{TM}** film showing the presence of C, N, and Ru in the **CN_{TM}–Ru_{15}** film (Figure S8a). The high-resolution XPS C 1s spectrum of **CN_{TM}** film (Figure S8b) exhibits two peaks centered around 284.7 and 288.3 eV, assigned to C=O groups, sp^2 C–C bonding and N–C=N bonding in the triazine-units of carbon nitride, respectively. The high-resolution N 1s XPS curve shows three deconvoluted peaks attributed to C–N=C, N–$(C)_3$, and C–N–H_x bond, respectively (Figure S8c).[37,39,40] The deconvolution of the C 1s spectrum of the **CN_{TM}–Ru_{15}** sample reveals six peaks. The additional three peaks are ascribed to C–C=C (sp^2), N(sp^2)–C, and Ru $3d_{3/2}$ (overlapping with C 1s), respectively, originating from the Ru-oligomer (Figure S8b). The N 1s spectrum of **CN_{TM}–Ru_{15}** shows five deconvoluted peaks, where two additional peaks centered at 397.4 and 399.2 eV and originate from the Ru-oligomer (Figure S8c). The high-resolution S 2p spectrum (Figure S8d) shows peaks centered at 167.9 and 169.6 eV, ascribed to an S-H bond (S $2p_{3/2}$ and S $2p_{1/2}$, respectively) in the CN film, which was prepared using a thiourea precursor as the S source.

It is noteworthy that the peaks related to C–N=C, N–$(C)_3$, and C–N–H_x bonds stemming from the carbon nitride have shifted to higher binding energies after modification with **Ru_{15}** due to the Ru oligomer/carbon nitride interaction. The high-resolution XPS Ru 3p spectrum of **CN_{TM}–Ru_{15}** film displays a peak in the 485-460 eV range, attributed to the presence of Ru(II) species (Figure 3i).[41] Finally, inductively-coupled plasma optical emission spectroscopy (ICP-OES) elemental analysis for the **CN_{TM}–Ru_{15}** samples gives 6.5 µg of Ru per g of sample, that implies 64.3 nmols of Ru per g of **CN_{TM}–Ru_{15}** (see Table S1).

PEC measurements of **CN_{TM}** and **CN_{TM}–Ru_{15}** films were performed in a three-electrode system under simulated 1 sun illumination in a NaH_2PO_4/Na_2HPO_4 buffer solution (pH 7, ionic strength 0.1 M) as a supporting electrolyte. The linear sweep voltammetry (LSV) curves (Figure 4a) of **CN_{TM}** and **CN_{TM}–Ru_{15}** films demonstrate a typical PEC behavior, with an onset potential of 0.55 V *vs.* RHE. Chronoamperometry measurements at 1.23 V *vs.*

RHE (Figure 4b) reveal that the incorporation of **Ru_{15}** leads to an improvement in the photocurrent densities of about 40%, from 130 ± 8 µA cm^{-2} for the **CN_{TM}** film to 180 ± 10 µA cm^{-2} for the **CN_{TM}–Ru_{15}** film both at an E_{app} = 1.23 V *vs.* RHE. This improvement is attributed to the synergy between the **CN_{TM}** and **Ru_{15}** anchored on the surface by CH–π interactions, facilitating charge transfer and separation and the additional capacity of **Ru_{15}** to efficiently catalyze the water oxidation reaction.

The measured incident photon-to-current conversion efficiency (IPCE) of **CN_{TM}** and **CN_{TM}–Ru_{15}** films at several illumination wavelengths ranging from 280 to 650 nm is displayed in Figure 4c. The IPCE values are in good agreement with the absorption spectra of the films. The IPCE value of **CN_{TM}–Ru_{15}** film (6.7%) is higher than that of the **CN_{TM}** film (5.8%) at 370 nm. In addition, the IPCE measurement reveals that **CN_{TM}-Ru_{15}** film is photoactive at longer wavelengths, up to ~550 nm (inset of Figure 4c), mainly due to the contribution of the **Ru_{15}** oligomer (Figure S2).

Notably, the incorporation of **Ru_{15}** into the **CN_{TM}** film significantly enhances the long-term stability. As shown in Figure 4d, **CN_{TM}–Ru_{15}** films in a neutral pH medium retain ~35% photocurrent density even after 5.5 h. In sharp contrast, the **CN_{TM}** film completely loses its photocurrent density (~96%) within 2 hours. Importantly, O_2 measurements indicate that most of the current is attributed to oxygen evolution and not to self-oxidation of the CN layer. **CN_{TM}–Ru_{15}** generates O_2 at a rate of 0.014 µmol cm^{-2} min^{-1} (Figure S9) with Faradaic efficiency (FE) of up to 89% after 20 min. Overall, this implies a TON over 3000 after 5 h and a TOF of 0.4 s^{-1} (Table S2).

A comparison table for the PEC performance using metal oxides as WOCs co-catalyst with CN-based film is given in Table S3. It is worth mentioning that the molecular hybrid material is superior in terms of FE for O_2 generation. It is also important to mention here that the amount of used Ru is in the range of micrograms of Ru per g of sample. This generally implies a loading of catalyst 4 to 6 orders of magnitude lower[32,33] than related examples using Co, Ni, or Fe oxides.[42,43]

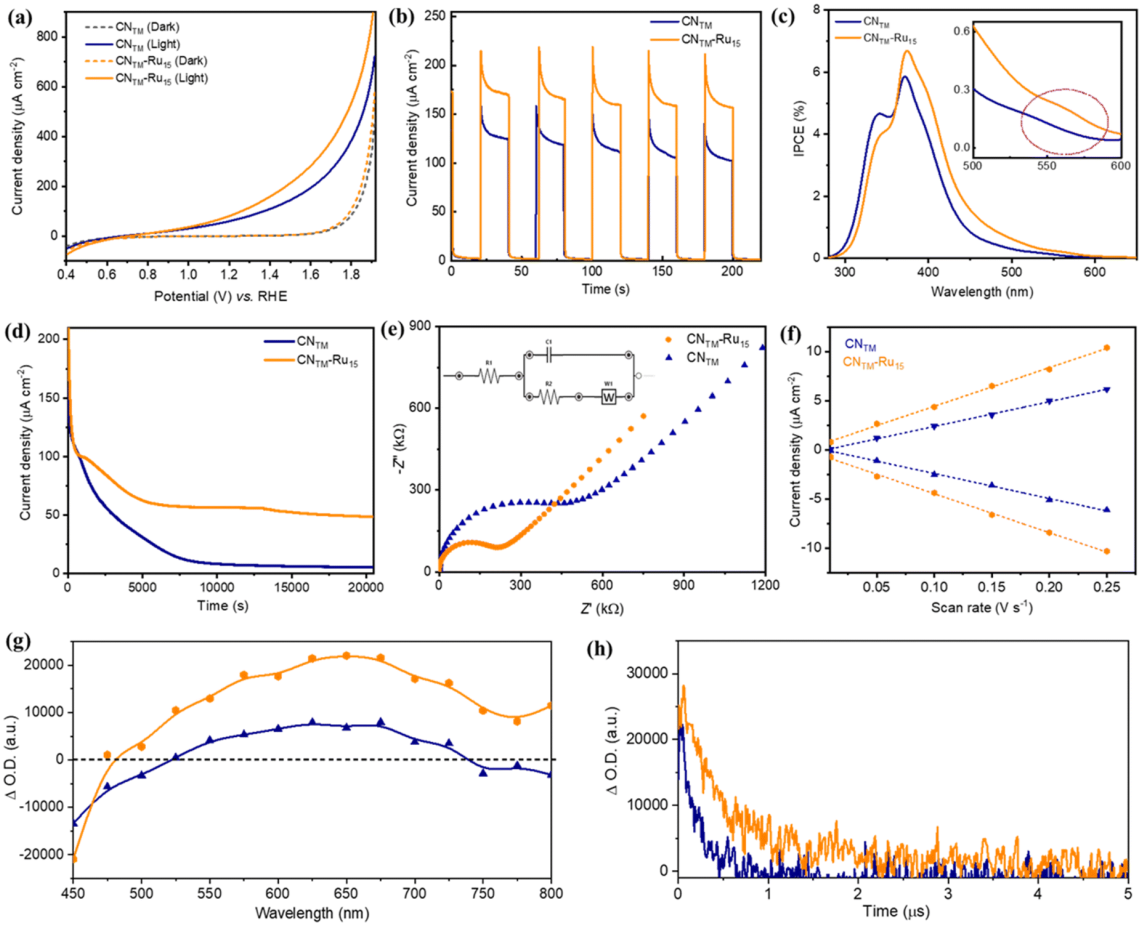

Figure 4. *(a) Linear sweep voltammetry (LSV) of* ***CN_{TM}*** *and* ***CN_{TM}–Ru_{15}*** *electrodes (phosphate buffer, pH 7) in the dark and under 1 sun illumination. (b) Chronoamperometry (current densities vs. time) of* ***CN_{TM}*** *and* ***CN_{TM}–Ru_{15}*** *electrodes in phosphate buffer (pH 7) at 1.23 VRHE upon on/off 1 sun illumination. (c) Incident photon-to-current conversion efficiency (IPCE) of the* ***CN_{TM}*** *and* ***CN_{TM}–Ru_{15}*** *film at different wavelengths (280–650 nm) in a phosphate buffer solution (pH 7) at 1.23 VRHE. (d) Stability measurement (current density under continuous 1 sun illumination) of* ***CN_{TM}*** *and* ***CN_{TM}–Ru_{15}*** *electrodes in phosphate buffer (pH 7). (e) Nyquist plot of* ***CN_{TM}*** *and* ***CN_{TM}–Ru_{15}*** *films (fitted data). Inset is the equivalent circuit that was used for fitting: the R_{CT} value was obtained by fitting the semicircles of the Nyquist plots. (f) Cathodic and anodic charging current densities of CN films at 0 V vs. Ag/AgCl as a function of scan rate. (g) Transient absorption spectra of* ***CN_{TM}*** *(blue triangles) and* ***CN_{TM}–Ru_{15}*** *(orange hexagons) dispersions in MeCN and acquired at 250 ns. (h) Transient absorption decays of* ***CN_{TM}*** *(blue) and* ***CN_{TM}–Ru_{15}*** *(orange) dispersions in MeCN, monitored at 650 nm. The measurements were performed upon laser excitation at 355 nm under N_2 atmosphere. The* ***CN_{TM}*** *and* ***CN_{TM}-Ru_{15}*** *dispersion's UV–vis absorption was adjusted at identical values at the excitation wavelength (355 nm).*

The **CN_{TM}–Ru_{15}** film after the stability experiment was examined using PXRD, XPS and SEM (Figure S10), revealing minimal alterations in the film's structure and morphology. The improved durability of the **CN_{TM}–Ru_{15}** film is associated with better charge

separation and the high OER catalytic activity of the **Ru_{15}**. We analyzed the charge transfer kinetics behavior of **CN_{TM}** and **CN_{TM}–Ru_{15}** films using electrochemical impedance spectroscopy (EIS) and transient absorption spectroscopy (TAS) to elucidate the activity improvement. The EIS experiments (Figures 4e and S11) disclosed lower charge transfer resistance (R_{CT}=250 kΩ) for **CN_{TM}–Ru_{15}** film than for **CN_{TM}** alone (R_{CT} =470 kΩ), implying better hole transfer to the solution. An increased electrochemically active surface area (ECSA) is shown in Figures 4f and S12, indicating more active sites for the water oxidation after modification with **Ru_{15}** oligomer.

TAS measurements of **CN_{TM}** and **CN_{TM}–Ru_{15}** dispersions in MeCN upon 355 nm laser excitation further confirmed the improved photo-induced charge transfer kinetics in the presence of the **Ru_{15}**. The TA spectrum of **CN_{TM}** (Figure 4g) exhibits a negative feature up to ca. 525 nm, due to the bleaching of the ground state absorption of **CN_{TM}**. The detected positive signal from 525 to 750 nm indicates the presence of excited states absorbing in the visible region, as previously reported for related CN materials. The TA spectrum of **CN_{TM}–Ru_{15}** presents similar features with higher signal intensity. Still, it exhibits extended transient absorption in the NIR region (750–800 nm) due to the **Ru_{15}** incorporation. It is worth noticing that the increase in the positive signal intensity for **CN_{TM}–Ru_{15}** is proportional to an enhancement in photo-induced charge carriers, in good agreement with the photocurrent and IPCE measurements, indicating a more efficient charge separation in **CN_{TM}–Ru_{15}** compared to **CN_{TM}**. These positive signals are attributed to photo-generated electrons in **CN_{TM}** and **CN_{TM}–Ru_{15}**. Hole quenching experiments using MeOH as a sacrificial electron donor (Figure S13) confirm that the electrons are the main charge carriers detected in these experimental conditions.

The TA decays of **CN_{TM}** and **CN_{TM}–Ru_{15}** at 650 nm (Figure 4h) reveal an almost one magnitude order longer electron half-lifetime of the **CN_{TM}–Ru_{15}** (1.60 μs) *vs.* **CN_{TM}** (0.24 μs) thanks to a better charge separation and thus lower recombination rates. This agrees with the mechanism proposed in Equations 1–3:

[CN_{TM}–Ru_{15}] + $h\nu$ → **[CN_{TM}-Ru_{15}]*** (excited state) (1)

[CN_{TM}–Ru_{15}]* → [$^-CN_{TM}$-Ru_{15}^+] (charge separated state) (2)

4[$^-CN_{TM}$–Ru_{15}^+] + 2 H_2O → **4[CN_{TM}-Ru_{15}] +** $O_2 + 4H^+ + 4e^-$ (WOR) (3)

where the introduction of supramolecularly bonded **Ru_{15}** on the **CN_{TM}** layer results in enhanced charge separated state (Equation 2), mainly thanks to fast hole extraction from the **CN_{TM}** to the **Ru_{15}**, followed by water oxidation reaction (WOR) (Equation 3). The final assembly is thus overall leading to better photoactivity at longer wavelengths and better electron collection.

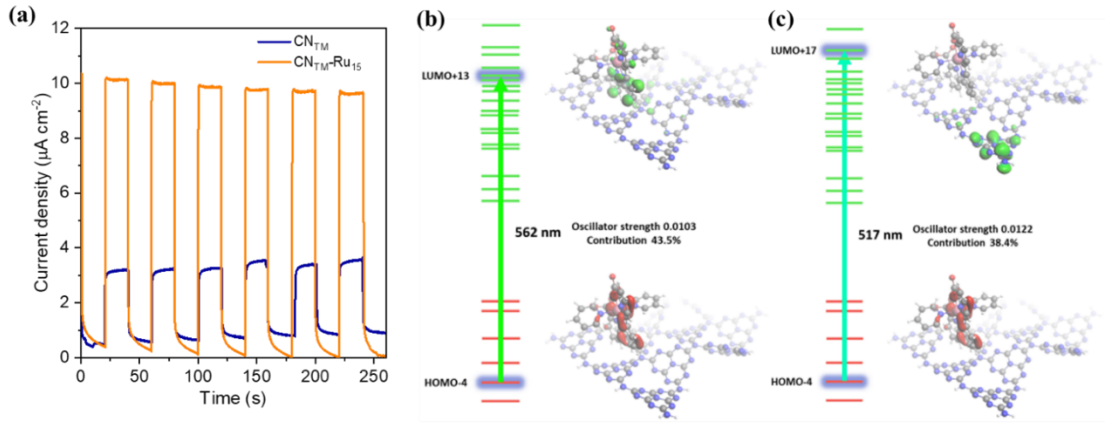

Figure 5. *(a) Chronoamperometry (current densities vs. time) of* ***CN_{TM}*** *and* ***CN_{TM}–Ru_{15}*** *electrodes in phosphate buffer (pH 7) at 1.23 V vs. RHE under illumination using 510 nm band-pass filter (FWHM 10 nm). Calculated major contributions for electronic transition.*

Furthermore, additional photocurrent measurements were performed using 510 nm band-pass filter (FWHM 10 nm) for both the electrodes as presented in Figure 5a, showing a photocurrent enhancement of approx. 3.2 times higher in the case of **CN_{TM}–Ru_{15}** compared to **CN_{TM}** due to the presence of the molecular catalyst. This points out the behavior of **Ru_{15}** as both a light absorber and a catalyst.[44] To gain some insights on the processes occurring upon light excitation of the system, we computed the absorption spectra by means of TD-DFT of the model hybrid **CN_{Red}–Ru_2**, and the results are shown in Figure 5 and Figures S14–S22. Two transitions are displayed, one at 562 nm (Figure 5b) that is mainly intramolecular involving the Ru catalyst, which later can further transfer an electron to the valence band of the **CN_{Red}** moiety, resembling the typical Grätzel's dye-sensitized solar cells based on TiO_2 and $[Ru(bpy)_3]^{2+}$.[45,46] A second excitation at 517 nm, shown in Figure 5c, would involve a direct charge transfer from the Ru center to the valence band of **CN_{Red}**.

5.3. Conclusions

In this work, we introduced a new molecular hybrid material **CN_{TM}–Ru_{15}** based on the anchoring of a highly active molecular water oxidation catalyst on **CN_{TM}** photoanode. The successful deposition of **Ru_{15}** oligomer on polymeric carbon nitride photoanodes (**CN_{TM}**) through CH–π interactions enables good photoelectrochemical water-splitting activity at neutral pH, enhanced long-term stability and high FE (> 89%) for oxygen production. Detailed structural, photoelectrochemical, and mechanistic studies reveal that the **Ru_{15}** markedly improves charge separation and hole extraction kinetics, enabling efficient water oxidation. Furthermore, the **Ru_{15}** oligomer leads to better light harvesting, higher electrochemical surface area, and improved electronic conductivity. The optimized **CN_{TM}–Ru_{15}** film demonstrates a photocurrent density of 180 ± 10 μA cm^{-2} with 89% FE for oxygen evolution, good stability up to 5 h, and IPCE values up to 6.7%. The amount of Ru-based catalyst loaded on the surface that represents only 6.5 ppm of the electrode composition and leads to TONs in the range of 3300 and a TOF of 0.4 s^{-1}. Furthermore, we have also shown that in the **CN_{TM}–Ru_{15}** hybrid material the Ru centers act both as catalyst and as photoabsorber.

Finally, the present work is an example of the positive synergy that can be obtained with the proper utilization of a molecular-based catalyst and a polymeric organic absorber.

5.4. References

(1) Volokh, M.; Peng, G.; Barrio, J.; Shalom, M. Carbon Nitride Materials for Water Splitting Photoelectrochemical Cells. *Angew. Chemie - Int. Ed.* **2019**, *58* (19), 6138–6151. https://doi.org/10.1002/anie.201806514.

(2) Dharmarajan, N. P.; Vidyasagar, D.; Yang, J. H.; Talapaneni, S. N.; Lee, J.; Ramadass, K.; Singh, G.; Fawaz, M.; Kumar, P.; Vinu, A. Bio-Inspired Supramolecular Self-Assembled Carbon Nitride Nanostructures for Photocatalytic Water Splitting. *Adv. Mater.* **2024**, *36* (2). https://doi.org/10.1002/adma.202306895.

(3) Fan, X.; Wang, Z.; Lin, T.; Du, D.; Xiao, M.; Chen, P.; Monny, S. A.; Huang, H.; Lyu, M.; Lu, M.; Wang, L. Coordination Chemistry Engineered Polymeric Carbon Nitride Photoanode with Ultralow Onset Potential for Water Splitting. *Angew. Chemie - Int. Ed.* **2022**, *61* (32), 1–6. https://doi.org/10.1002/anie.202204407.

(4) Peng, G.; Albero, J.; Garcia, H.; Shalom, M. A Water-Splitting Carbon Nitride Photoelectrochemical Cell with Efficient Charge Separation and Remarkably Low Onset Potential. *Angew. Chemie - Int. Ed.* **2018**, *57* (48), 15807–15811. https://doi.org/10.1002/anie.201810225.

(5) Zhang, J.; Zhang, J.; Dong, C.; Xia, Y.; Jiang, L.; Wang, G.; Wang, R.; Chen, J. Direct Growth of Polymeric Carbon Nitride Nanosheet Photoanode for Greatly Efficient Photoelectrochemical Water-Splitting. *Small* **2023**, *19* (34), 1–7. https://doi.org/10.1002/smll.202208049.

(6) Jeon, T. H.; Park, C.; Kang, U.; Moon, G. hee; Kim, W.; Park, H.; Choi, W. Photoelectrochemical Water Oxidation Using Hematite Modified with Metal-Incorporated Graphitic Carbon Nitride Film as a Surface Passivation and Hole Transfer Overlayer. *Appl. Catal. B Environ.* **2024**, *340* (June 2023), 123167. https://doi.org/10.1016/j.apcatb.2023.123167.

(7) Qin, J.; Barrio, J.; Peng, G.; Tzadikov, J.; Abisdris, L.; Volokh, M.; Shalom, M. Direct Growth of Uniform Carbon Nitride Layers with Extended Optical Absorption towards Efficient Water-Splitting Photoanodes. *Nat. Commun.* **2020**, *11* (1), 1–9. https://doi.org/10.1038/s41467-020-18535-0.

(8) Jiang, L.; Yuan, X.; Pan, Y.; Liang, J.; Zeng, G.; Wu, Z.; Wang, H. Doping of Graphitic Carbon Nitride for Photocatalysis: A Reveiw. *Appl. Catal. B Environ.* **2017**, *217*, 388–406. https://doi.org/10.1016/j.apcatb.2017.06.003.

(9) Mondal, S.; Mark, G.; Abisdris, L.; Li, J.; Shmila, T.; Tzadikov, J.; Volokh, M.; Xing, L.; Shalom, M. Developing Extended Visible Light Responsive Polymeric Carbon Nitrides for Photocatalytic and Photoelectrocatalytic Applications. *Mater. Horizons* **2023**, *10* (4), 1363–1372. https://doi.org/10.1039/d3mh00016h.

(10) Yang, Y.; Wang, S.; Jiao, Y.; Wang, Z.; Xiao, M.; Du, A.; Li, Y.; Wang, J.; Wang, L. An Unusual Red Carbon Nitride to Boost the Photoelectrochemical Performance of Wide Bandgap Photoanodes. *Adv. Funct. Mater.* **2018**, *28* (47), 1–10. https://doi.org/10.1002/adfm.201805698.

(11) Mondal, S.; Mark, G.; Tashakory, A.; Volokh, M.; Shalom, M. Porous Carbon Nitride Rods as an Efficient Photoanode for Water Splitting and Benzylamine Oxidation. *J. Mater. Chem. A* **2024**, *12* (19), 11502–11510. https://doi.org/10.1039/d4ta00237g.

(12) Shmila, T.; Mondal, S.; Barzilai, S.; Karjule, N.; Volokh, M.; Shalom, M. Boron and Sodium Doping of Polymeric Carbon Nitride Photoanodes for Photoelectrochemical Water Splitting. *Small* **2023**, *19* (42), 1–10. https://doi.org/10.1002/smll.202303602.

(13) Li, F.; Yue, X.; Liao, Y.; Qiao, L.; Lv, K.; Xiang, Q. Understanding the Unique S-Scheme Charge Migration in Triazine/heptazine Crystalline Carbon Nitride Homojunction. *Nat. Commun.* **2023**, *14* (1). https://doi.org/10.1038/s41467-023-39578-z.

(14) Karjule, N.; Singh, C.; Barrio, J.; Tzadikov, J.; Liberman, I.; Volokh, M.; Palomares, E.; Hod, I.; Shalom, M. Carbon Nitride-Based Photoanode with Enhanced Photostability and Water Oxidation

Kinetics. *Adv. Funct. Mater.* **2021**, *31* (25), 1–10. https://doi.org/10.1002/adfm.202101724.

(15) Hou, Y.; Zuo, F.; Dagg, A. P.; Liu, J.; Feng, P. Branched WO3 Nanosheet Array with Layered C3N 4 Heterojunctions and CoO_x Nanoparticles as a Flexible Photoanode for Efficient Photoelectrochemical Water Oxidation. *Adv. Mater.* **2014**, *26* (29), 5043–5049. https://doi.org/10.1002/adma.201401032.

(16) Zhang, W.; Albero, J.; Xi, L.; Lange, K. M.; Garcia, H.; Wang, X.; Shalom, M. One-Pot Synthesis of Nickel-Modified Carbon Nitride Layers Toward Efficient Photoelectrochemical Cells. *ACS Appl. Mater. Interfaces* **2017**, *9* (38), 32667–32677. https://doi.org/10.1021/acsami.7b08022.

(17) Gong, R.; Mitoraj, D.; Gao, D.; Mundszinger, M.; Sorsche, D.; Kaiser, U.; Streb, C.; Beranek, R.; Rau, S. A Triad Photoanode for Visible Light-Driven Water Oxidation via Immobilization of Molecular Polyoxometalate on Polymeric Carbon Nitride. *Adv. Sustain. Syst.* **2022**, *6* (5), 34–41. https://doi.org/10.1002/adsu.202100473.

(18) Cesar, I.; Kay, A.; Martinez, J. A. G.; Grätzel, M. Translucent Thin Film Fe_2O_3 Photoanodes for Efficient Water Splitting by Sunlight: Nanostructure-Directing Effect of Si-Doping. *J. Am. Chem. Soc.* **2006**, *128* (14), 4582–4583. https://doi.org/10.1021/ja060292p.

(19) Wang, Z.; Gu, Y.; Zheng, L.; Hou, J.; Zheng, H.; Sun, S.; Wang, L. Machine Learning Guided Dopant Selection for Metal Oxide-Based Photoelectrochemical Water Splitting: The Case Study of Fe_2O_3 and CuO. *Adv. Mater.* **2022**, *34* (10), 1–7. https://doi.org/10.1002/adma.202106776.

(20) Liu, J.; Luo, Z.; Mao, X.; Dong, Y.; Peng, L.; Sun-Waterhouse, D.; Kennedy, J. V.; Waterhouse, G. I. N. Recent Advances in Self-Supported Semiconductor Heterojunction Nanoarrays as Efficient Photoanodes for Photoelectrochemical Water Splitting. *Small* **2022**, *18* (48), 1–26. https://doi.org/10.1002/smll.202204553.

(21) Liu, B.; Wang, X.; Zhang, Y.; Xu, L.; Wang, T.; Xiao, X.; Wang, S.; Wang, L.; Huang, W. A $BiVO_4$ Photoanode with a VO_X Layer Bearing Oxygen Vacancies Offers Improved Charge Transfer and Oxygen Evolution Kinetics in Photoelectrochemical Water Splitting . *Angew. Chemie* **2023**, *135* (10). https://doi.org/10.1002/ange.202217346.

(22) Zhang, Z.; Huang, X.; Zhang, B.; Bi, Y. High-Performance and Stable $BiVO_4$ Photoanodes for Solar Water Splitting via Phosphorus-Oxygen Bonded FeNi Catalysts. *Energy Environ. Sci.* **2022**, *15* (7), 2867–2873. https://doi.org/10.1039/d2ee00936f.

(23) Tashakory, A.; Karjule, N.; Abisdris, L.; Volokh, M.; Shalom, M. Mediated Growth of Carbon Nitride Films via Spray-Coated Seeding Layers for Photoelectrochemical Applications. *Adv. Sustain. Syst.* **2021**, *5* (11), 1–7. https://doi.org/10.1002/adsu.202100005.

(24) Xia, J.; Karjule, N.; Abisdris, L.; Volokh, M.; Shalom, M. Controllable Synthesis of Carbon Nitride Films with Type-II Heterojunction for Efficient Photoelectrochemical Cells. *Chem. Mater.* **2020**, *32*

(13), 5845–5853. https://doi.org/10.1021/acs.chemmater.0c01856.

(25) Gil-Sepulcre, M.; Llobet, A. Molecular Water Oxidation Catalysts Based on First-Row Transition Metal Complexes. *Nat. Catal.* **2022**, *5*, 79–82. https://doi.org/10.1038/s41929-022-00750-1.

(26) Vereshchuk, N.; Gil-Sepulcre, M.; Ghaderian, A.; Holub, J.; Gimbert-Suriñach, C.; Llobet, A. Metamorphic Oxygen-Evolving Molecular Ru and Ir Catalysts. *Chem. Soc. Rev.* **2022**, *52* (1), 196–211. https://doi.org/10.1039/d2cs00463a.

(27) Garrido-Barros, P.; Gimbert-Suriñach, C.; Matheu, R.; Sala, X.; Llobet, A. How to Make an Efficient and Robust Molecular Catalyst for Water Oxidation. *Chem. Soc. Rev.* **2017**, *46* (20), 6088–6098. https://doi.org/10.1039/c7cs00248c.

(28) Matheu, R.; Ertem, M. Z.; Benet-Buchholz, J.; Coronado, E.; Batista, V. S.; Sala, X.; Llobet, A. Intramolecular Proton Transfer Boosts Water Oxidation Catalyzed by a Ru Complex. *J. Am. Chem. Soc.* **2015**, *137* (33), 10786–10795. https://doi.org/10.1021/jacs.5b06541.

(29) Matheu, R.; Moreno-Hernandez, I. A.; Sala, X.; Gray, H. B.; Brunschwig, B. S.; Llobet, A.; Lewis, N. S. Photoelectrochemical Behavior of a Molecular Ru-Based Water-Oxidation Catalyst Bound to TiO_2-Protected Si Photoanodes. *J. Am. Chem. Soc.* **2017**, *139* (33), 11345–11348. https://doi.org/10.1021/jacs.7b06800.

(30) Grau, S.; Berardi, S.; Moya, A.; Matheu, R.; Cristino, V.; Vilatela, J. J.; Bignozzi, C. A.; Caramori, S.; Gimbert-Suriñach, C.; Llobet, A. A Hybrid Molecular Photoanode for Efficient Light-Induced Water Oxidation. *Sustain. Energy Fuels* **2018**, *2* (9), 1979–1985. https://doi.org/10.1039/c8se00146d.

(31) Creus, J.; Matheu, R.; Peñafiel, I.; Moonshiram, D.; Blondeau, P.; Benet-Buchholz, J.; García-Antón, J.; Sala, X.; Godard, C.; Llobet, A. A Million Turnover Molecular Anode for Catalytic Water Oxidation. *Angew. Chemie - Int. Ed.* **2016**, *55* (49), 15382–15386. https://doi.org/10.1002/anie.201609167.

(32) Hoque, M. A.; Gil-Sepulcre, M.; de Aguirre, A.; Elemans, J. A. A. W.; Moonshiram, D.; Matheu, R.; Shi, Y.; Benet-Buchholz, J.; Sala, X.; Malfois, M.; Solano, E.; Lim, J.; Garzón-Manjón, A.; Scheu, C.; Lanza, M.; Maseras, F.; Gimbert-Suriñach, C.; Llobet, A. Water Oxidation Electrocatalysis Using Ruthenium Coordination Oligomers Adsorbed on Multiwalled Carbon Nanotubes. *Nat. Chem.* **2020**, *12* (11), 1060–1066. https://doi.org/10.1038/s41557-020-0548-7.

(33) Gil-Sepulcre, M.; Lindner, J. O.; Schindler, D.; Velasco, L.; Moonshiram, D.; Rüdiger, O.; Debeer, S.; Stepanenko, V.; Solano, E.; Würthner, F.; Llobet, A. Surface-Promoted Evolution of Ru-Bda Coordination Oligomers Boosts the Efficiency of Water Oxidation Molecular Anodes. *J. Am. Chem. Soc.* **2021**, *143* (30), 11651–11661. https://doi.org/10.1021/jacs.1c04738.

(34) Schindler, D.; Gil-Sepulcre, M.; Lindner, J. O.; Stepanenko, V.; Moonshiram, D.; Llobet, A.; Würthner, F. Efficient Electrochemical Water Oxidation by a Trinuclear Ru(bda) Macrocycle

Immobilized on Multi-Walled Carbon Nanotube Electrodes. *Adv. Energy Mater.* **2020**, *10* (43), 1–7. https://doi.org/10.1002/aenm.202002329.

(35) Roy, R. S.; Mondal, S.; Mishra, S.; Banoo, M.; Sahoo, L.; Kumar, A.; Vinod, C. P.; De, A. K.; Gautam, U. K. Covalently Interconnected Layers in g-C_3N_4: Toward High Mechanical Stability, Catalytic Efficiency and Sustainability. *Appl. Catal. B Environ.* **2023**, *322* (September 2022), 122069. https://doi.org/10.1016/j.apcatb.2022.122069.

(36) Mark, G.; Mondal, S.; Volokh, M.; Xia, J.; Shalom, M. Halogen–Hydrogen Bonding for the Synthesis of Efficient Polymeric Carbon-Nitride Photocatalysts. *Sol. RRL* **2022**, *6* (12), 1–9. https://doi.org/10.1002/solr.202200834.

(37) Mondal, S.; Sahoo, L.; Vaishnav, Y.; Mishra, S.; Roy, R. S.; Vinod, C. P.; De, A. K.; Gautam, U. K. Wavelength Dependent Luminescence Decay Kinetics in "Quantum-Confined" g-C_3N_4 nanosheets Exhibiting High Photocatalytic Efficiency upon Plasmonic Coupling. *J. Mater. Chem. A* **2020**, *8* (39), 20581–20592. https://doi.org/10.1039/d0ta08001b.

(38) Karjule, N.; Barrio, J.; Xing, L.; Volokh, M.; Shalom, M. Highly Efficient Polymeric Carbon Nitride Photoanode with Excellent Electron Diffusion Length and Hole Extraction Properties. *Nano Lett.* **2020**, *20* (6), 4618–4624. https://doi.org/10.1021/acs.nanolett.0c01484.

(39) Hou, Y.; Zhu, Y.; Xu, Y.; Wang, X. Photocatalytic Hydrogen Production over Carbon Nitride Loaded with WS_2 as Cocatalyst under Visible Light. *Appl. Catal. B Environ.* **2014**, *156-157*, 122–127. https://doi.org/10.1016/j.apcatb.2014.03.002.

(40) Zhang, Q.; Chen, X.; Yang, Z.; Yu, T.; Liu, L.; Ye, J. Precisely Tailoring Nitrogen Defects in Carbon Nitride for Efficient Photocatalytic Overall Water Splitting. *ACS Appl. Mater. Interfaces* **2022**, *14* (3), 3970–3979. https://doi.org/10.1021/acsami.1c19638.

(41) Awasthi, M. K.; Rai, R. K.; Behrens, S.; Singh, S. K. Low-Temperature Hydrogen Production from Methanol over a Ruthenium Catalyst in Water. *Catal. Sci. Technol.* **2021**, *11* (1), 136–142. https://doi.org/10.1039/d0cy01470b.

(42) Ma, J.; Bai, X.; He, W.; Wang, S.; Li, L.; Chen, H.; Wang, T.; Zhang, X.; Li, Y.; Zhang, L.; Chen, J.; Meng, F.; Fu, Y. Amorphous FeNi-Bimetallic Infinite Coordination Polymers as Advanced Electrocatalysts for the Oxygen Evolution Reaction. *Chem. Commun.* **2019**, *55* (83), 12567–12570. https://doi.org/10.1039/c9cc06109f.

(43) Volokh, M.; Shalom, M. Polymeric Carbon Nitride as a Platform for Photoelectrochemical Water-Splitting Cells. *Ann. N. Y. Acad. Sci.* **2023**, *1521* (1), 5–13. https://doi.org/10.1111/nyas.14963.

(44) Cloward, I. N.; Liu, T.; Rose, J.; Jurado, T.; Bonn, A. G.; Chambers, M. B.; Pitman, C. L.; Horst, M. A. ter; Miller, A. J. M. Catalyst Self-Assembly Accelerates Bimetallic Light-Driven Electrocatalytic H_2 Evolution in Water. *Nat. Chem.* **2024**, *16*, 709–716. https://doi.org/10.1038/s41557-024-01483-

3.

(45) Li, G.; Yella, A.; Brown, D. G.; Gorelsky, S. I.; Nazeeruddin, M. K.; Grätzel, M.; Berlinguette, C. P.; Shatruk, M. Near-IR Photoresponse of Ruthenium Dipyrrinate Terpyridine Sensitizers in the Dye-Sensitized Solar Cells. *Inorg. Chem.* **2014**, *53* (11), 5417–5419. https://doi.org/10.1021/ic5006538.

(46) Grätzel, M. Recent Advances in Sensitized Mesoscopic Solar Cells. *Acc. Chem. Res.* **2009**, *42* (11), 1788–1798. https://doi.org/10.1021/ar900141y.

5.5. Supporting information

5.5.1. Materials

All mentioned chemicals were purchased from commercial sources and used directly without further purification. Thiourea (99%) was brought from Acros Organics. Sodium sulphate anhydrous (Na_2SO_4, 99%) was purchased from Loba Chemie, India. Melamine (99%) and 2,2,2-trifluoroethanol (TFE, 99%) were brought from Sigma-Aldrich. Disodium phosphate (Na_2HPO_4 ,98+%) and sodium dihydrogen phosphate (NaH_2PO_4, 96%) were purchased from Alfa Aesar. Ethanol (≥99%), and acetone (≥99%) were brought from Bio-Lab Ltd, Israel. For the synthesis of Ru based complexes, all the chemicals used in this work were provided by Sigma Aldrich, unless explicitly indicated. $RuCl_3{\cdot}xH_2O$ was purchased from Alfa Aesar. The precursor complexes $[RuCl_2(dmso)_4]$ and $[Ru(tda)(dmso)(H_2O)]$ and also 6,6'-dicarboxylic acid-[2,2':6',2''-terpyridyl] (H_2tda) were prepared according to a reported procedure.[1] Fluorine-doped tin oxide (FTO)-coated glass (12–14 Ω sq^{-1}) was purchased from Xop Glass company, Spain. deionized water using Millipore Milli Q Direct 3 purification system (18.2 MΩ cm resistivity at room temperature) was used for all the experiments.

5.5.2. Characterization

NMR spectroscopy

Bruker Avance 500 MHz instruments were used to carry out NMR spectroscopy.

Powder-XRD

The structural analysis of synthesized films was carried out using X-ray diffraction patterns (XRD), using a PANalytical's Empyrean diffractometer equipped with a position

sensitive detector X'Celerator. XRD data was recorded with a scanning time of ~7 min for 2ϑ ranging from 5° to 60° using Cu Kα radiation (λ = 1.54178 Å, 40 kV, 30 mA).

FT-IR

Fourier-transform infrared spectroscopy (FTIR, Thermo Scientific Nicolet iS5 FTIR spectrometer equipped with a Si ATR) was used to study the materials' functional groups.

SEM, TEM and EDS

Morphology of the CN films were characterized by scanning electron microscopy (SEM) using a FEI Verios high-resolution SEM, which is equipped with a FEG source and a through-lens detector (secondary electrons) operated at U_0 = 3.5 kV and I = 25 pA. Energy dispersive X-ray spectrometry (EDS) data were obtained using a FEI Verios 460L high resolution SEM equipped with a FEG source and operated at U_0 = 20 kV. HAADF-STEM images were recorded using S/TEM Spectra 200 microscope.

UV-vis diffuse reflectance spectroscopy

UV–vis diffuse reflectance spectroscopy (Cary 100 spectrophotometer, equipped with a diffuse reflectance accessory) and photoluminescence spectroscopy (Horiba Scientific FluroMax 4 spectrofluorometer) were performed to study the optical properties. The excitation wavelength (λ_{ex}) was 370 nm and the emission wavelength (λ_{em}) was 460 nm.

XPS and UPS

X-ray photoelectron spectroscopic (XPS) data were obtained from an X-ray photoelectron spectrometer ESCALAB 250 ultrahigh vacuum (1×10^{-9} bar) device with an Al Kα X-ray source and a monochromator. The X-ray beam size was 500 µm. All spectra were calibrated relative to a carbon C 1s peak, positioned at 284.8 eV, to correct the charging effect.

ICP-OES

20 mg of powder of **CN_{TM}–Ru_{15}** sample (corresponding to 1 cm^2 area) were digested in 10 mL of aqueous solution with 7% HCl and analyzed at the ICP-OES using a Spectro ARCOS ICP-OES, FHX22 Multi-View Plasma instrument. The analysis was repeated three times.

TAS measurements

Transient absorption experiments were performed using an OPO System Ekspla (EKS-NT342C-10) coupled with an UV extension (EKS-NT342C-SH-SFG) as the excitation source and an Edinburgh Instruments detection system (LP980) coupled with an ICCD camera (Andor iStar CCD 320T). Optically diluted samples (*A* ca. 0.7 at excitation wavelength) in acetonitrile were used. Information on the excitation wavelengths is included in the main text. All measurements were done in quartz cuvettes (1 cm optical pathlength) and at room temperature (23 °C).

5.5.3. PEC and electrochemical measurements

Photoelectrochemical experiments

All the photoelectrochemical measurements were performed using a three-electrode configuration system on a PalmSens3 potentiostat. A Pt foil (1.0 cm^2) and Ag/AgCl (saturated KCl) were used as the counter- and reference-electrode, respectively. Phosphate buffer solution, (pH ~7) 0.1 M was used as the electrolyte for the photocurrent measurements. The photoanode was dipped into electrolyte medium in a custom-made Teflon cell. The obtained potentials were converted to the reversible hydrogen electrode (RHE) scale using Equation S1 below reported:

$$V_{RHE} = V_{Ag/AgCl} + (0.0591 \times pH) + 0.197 \quad \text{(S1)}$$

Photocurrents were recorded at bias 1.23 V *vs.* RHE using illumination from a solar simulator (Newport 300 W ozone-free Xe arc lamp, equipped with water and air mass AM 1.5G filters). 1 sun illumination was calibrated by means of a silicon photodiode (Newport power meter model 919-P) providing total light of 100 $mW \cdot cm^2$ to the photoelectrode.

IPCE

For incident photon-to-current conversion efficiency (IPCE) measurement a Zahner CIMPS-QE/IPCE photoelectrochemical workstation coupled with a TLS03 tunable light source controlled by a PP211 potentiostat (Zahner-Elektrik, Germany) in a dedicated three-electrode photoelectrochemical cell (PEEC-2) using an Ag/AgCl (sat. KCl) reference electrode and Pt coil as the counter electrode. For the measurements, the following Equation S2 was used:

$$\text{IPCE}\ (\%) = \frac{J\left(\text{mA cm}^{-2}\right) \cdot 1240\ (\text{V nm})}{\lambda(\text{nm}) \cdot I_{\text{incident}}(\text{mW cm}^{-2})} \times 100\% \quad \text{(S2)}$$

Where j is the photocurrent density, λ is the illumination wavelength, I_{incident} (calibrated to illumination spot of 8 mm in diameter) is the incident illumination power, and 1240 is the unit conversion factor. The calculation was performed by the coupled ThalesXT software.

EIS and Mott-Schottky experiments

All electrochemical measurements were performed using a three-electrode system on an Autolab potentiostat (Metrohm, PGSTAT302N). 0.5 M Na_2SO_4 aqueous solution was used for impedance spectroscopy measurement. Nyquist plots of the films were measured at an applied potential of 1.23 V vs. RHE with a frequency range from 40 kHz to 100 mHz and a 5 mV amplitude of the sinusoidal perturbation.

O_2 detection experiments

The O_2 production for **CN_{TM}** and **CN_{TM}–Ru_{15}** film in phosphate buffer solution (pH~7) was detected using a fiber optic oxygen meter under chronoamperometric condition (1.23 V vs. RHE, 1 sun illumination). A two-compartment cell (H-cell) was used and tightly sealed with a rubber septum for each chamber and parafilm to avoid any gas leakage. The electrolyte solution was purged with Ar for 30 min before the experiments. The O_2 quantification was performed for the duration of 1 hour, as shown in Fig. S6. FE was calculated using Equations S3 and S4:

$$n = \frac{I \cdot t}{z \cdot F} \quad \text{(S3)}$$

$$\text{FE}(\%) = \frac{\text{Experimental } \mu\text{mol of } O_2}{\text{Theoretical } \mu\text{mol of } O_2} \times 100\% \quad \text{(S4)}$$

Where n is the O_2 amount (measured in mol), I stands for the current (A), z is the number of transferred electrons (for O_2 evolution, z = 4), t is the time (s), and F is the Faraday constant (96485 C mol^{-1}).

5.5.4. Synthetic procedures

CN_{TM} film preparation

CN films were prepared using an adapted procedure,[2,3] using thiourea as the precursor material. Typically, 40 g thiourea was dissolved in a 100 mL glass beaker containing 40 mL DI water, and this solution was heated and stirred for 1 h at 85°C at a constant stirring rate of 300 rpm using a PTFE-coated magnetic stir bar to reach finally a saturated aqueous thiourea solution. In the next step, a clean FTO was dipped for 1 second into the hot saturated thiourea solution, resulting in a uniform precursor film layer on FTO after the remaining attached solution is left to dry. This dip-dry process was repeated for three times to increase the thickness. Next, thiourea-coated FTOs were dried at 70°C for 1 h on a hot plate and transferred into a glass test-tube containing 1 g of melamine powder at its bottom. The test-tubes were wrapped tightly with aluminum foil and calcined at the target temperature of 500°C for 2 h under nitrogen (N_2) atmosphere in a tube furnace (heating ramp from room temperature to 500°C was 5°C min^{-1}).

Synthesis of [Ru(tda)(4,4'-bpy)]$_{15}$(4,4'-bpy) oligomer (Ru_{15})

The final [Ru(tda)(4,4'-bpy)]$_{15}$(4,4'-bpy) oligomer, as well as the ligand 6,6'-dicarboxylic acid-[2,2':6',2"-terpyridyl] (H_2tda) and the precursor complexes [$RuCl_2(dmso)_4$] and [Ru(tda)(dmso)(H_2O)], were synthesized according to the literature.[1,4]

Supramolecular loading of [Ru(tda)(4,4'-bpy)]$_{15}$(4,4'-bpy) oligomer on CN photoelectrodes (CN_{TM}-Ru_{15})

For the loading of the [Ru(tda)(4,4'-bpy)]$_{15}$(4,4'-bpy) oligomer onto the **CN_{TM}** electrodes surface, 1 mg of the **Ru_{15}** was dissolved in 10 mL TFE solvent and CN photoanodes were thus completely soaked in the orange-reddish oligomer solution for 20 minutes, and afterwards rinsed with clean TFE solvent to remove the excess Ru-complex which does not interact with the CN. The modified CN electrodes (labelled as **CN_{TM}–Ru_{15}**) were finally dried at 70°C on a hot plate for 60 min, before using them for photoelectrochemical experiments.

5.5.5. Computational details

The geometric parameters of all molecular structures were fully optimized at a density functional theory (DFT) level using the software package AMS2021.[5] The molecular geometries were computed using the BP86-D3 density functional combined method

(Becke exchange functional[6] with gradient correction provided by the Perdew expression,[7] plus Grimme's D3 empirical dispersion correction).[8] Slater type DZP basis set for elements H, C, N, and O, and TZP basis set for the Ru were used as provided in the ADF library. ZORA[9,10] scalar relativistic corrections were also included. The COSMO[11,12] implicit solvation model was selected to simulate the aqueous solvation effects. The band gap was finally evaluated through single point calculations with the HSE06 functional.[13] The electron absorption energies were computed by using TD-DFT with the statistical average of orbital potentials (SAOP)[14,15] exchange-correlation functional. The spectra were simulated using a gaussian sum with 35 nm, 150 nm, and 150 nm bandwidth for Ru oligomer, carbon nitride, and the anchored system, respectively. The number of excitations included in the TD-DFT calculation was 150 for Ru oligomer and carbon nitride, and 500 for the anchored system. All the structures and output files were uploaded to the ioChem-BD database[16] and are openly accessible.

5.5.6. Experimental results

Spectroscopic characterization

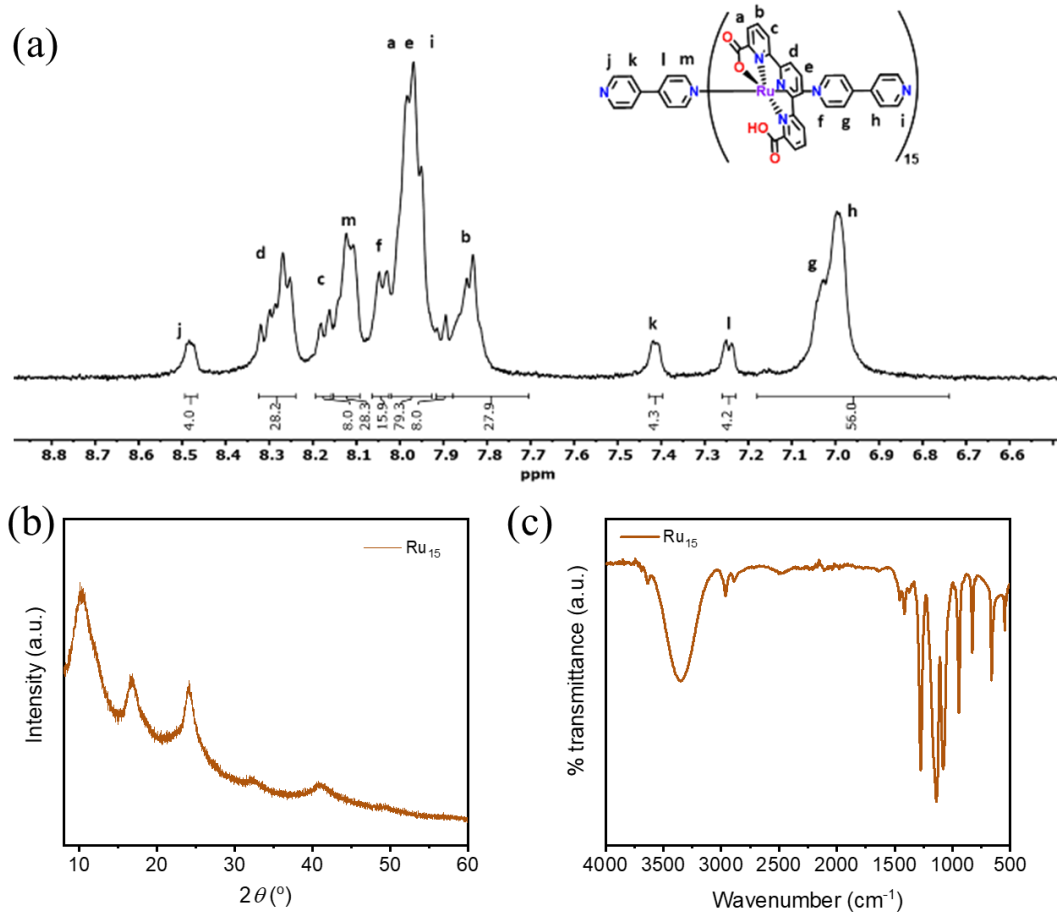

Figure S1. *(a) ^{1}H NMR spectrum (500 MHz, 298 K, [d_2]-DCM/[d_3]-TFE (4:1)) of* ***Ru$_{15}$*** *oligomer. (b) XRD patten of* ***Ru$_{15}$*** *oligomer. (c) FTIR spectrum of* ***Ru$_{15}$*** *oligomer.*

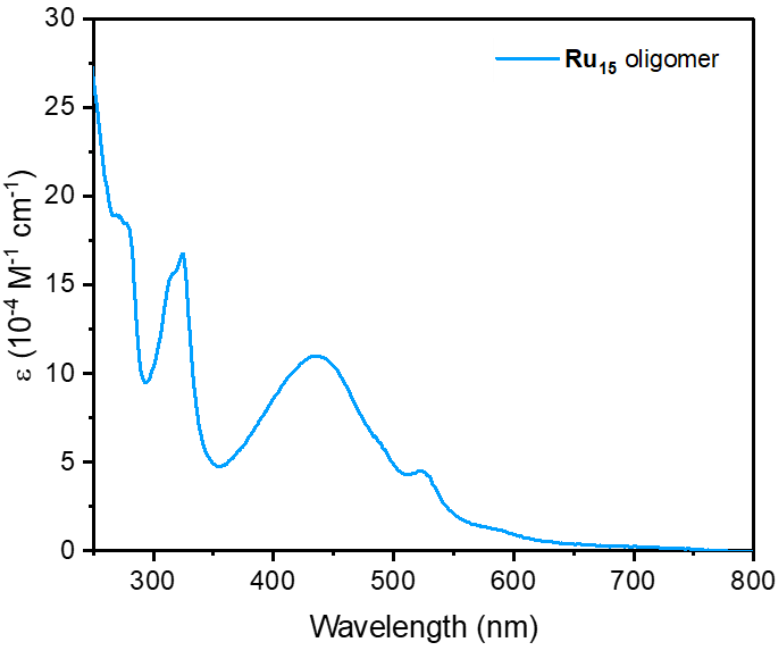

Figure S2. *UV–vis absorption spectrum of* ***Ru₁₅*** *oligomer (2 mM in TFE).*

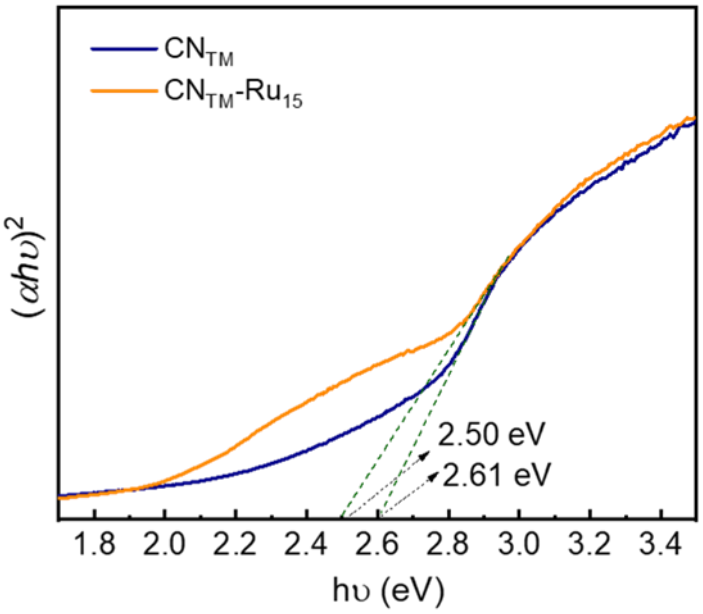

Figure S3. *Tauc plot calculation, using UV–vis diffuse reflectance spectra of* ***CN_{TM}*** *and* ***CN_{TM}–Ru₁₅*** *films, with the respective energy band gap (E_g), assuming a direct E_g.*

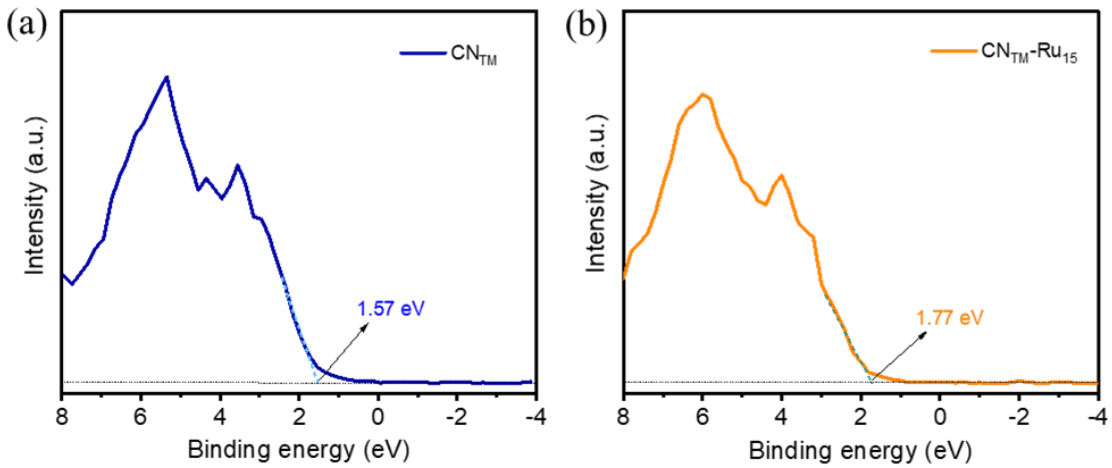

Figure S4. *Valence band (VB) XPS spectra of (a)* ***CN$_{TM}$****, (b)* ***CN$_{TM}$–Ru$_{15}$*** *films, respectively.*

To convert the measured XPS VB values of the photoanodes to the normal hydrogen electrode (NHE) scale, the following calculation was performed (Eq. S5):

$$E_{NHE}\,(\mathrm{V}) = \Phi + E_{VB\text{-}XPS} - 4.44 \qquad \text{(S5)}$$

Where Φ is the work function of the instrument (Φ = 4.84 eV), $E_{VB\text{-}XPS}$ is the measured valence band maximum energy value, and 4.44 eV is the vacuum level.[17]

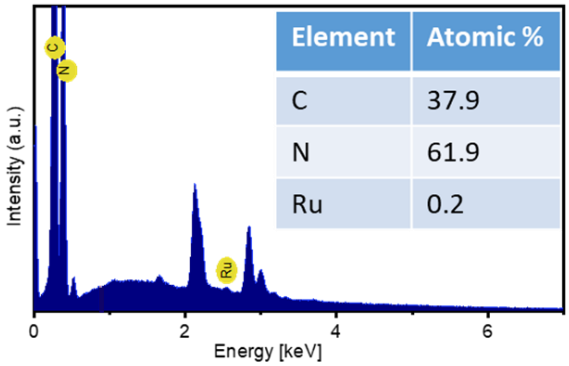

Figure S5. *Energy-dispersive X-ray spectroscopy (EDS) of* ***CN$_{TM}$–Ru$_{15}$*** *film. The EDS was carried out using SEM instrument, operated at U_0 = 10 kV on a film without sputtering.*

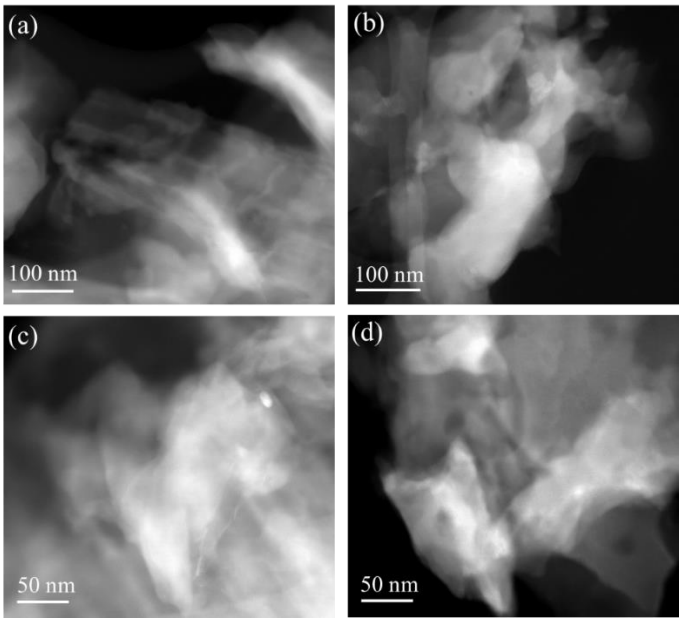

Fig. S6. *HAADF-TEM images of the* ***CN_{TM}-Ru_{15}*** *sample.*

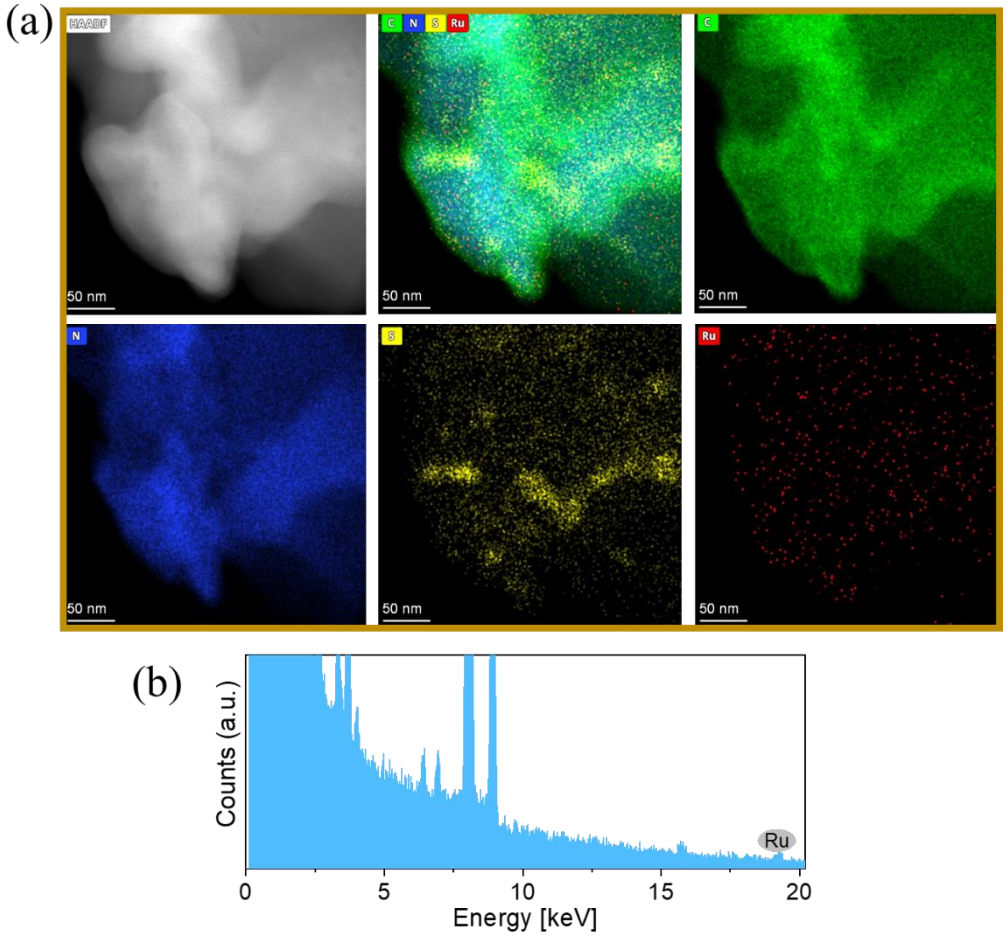

Fig. S7. *(a) TEM-EDS mapping of the* ***CN_{TM}-Ru_{15}*** *sample. (b) EDS spectrum of* ***CN_{TM}-Ru_{15}*** *sample.*

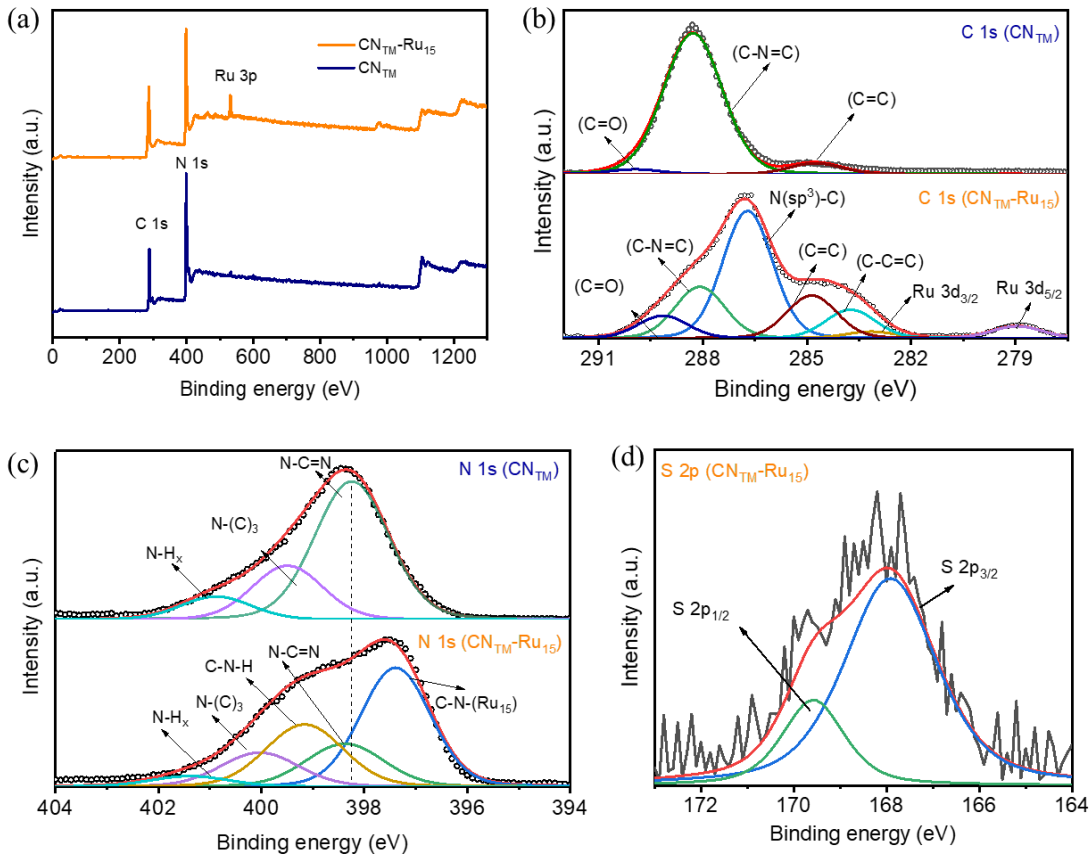

Figure S8. *XPS analysis of* ***CN_{TM}*** *and* ***CN_{TM}–Ru_{15}*** *films. (a) XPS survey spectra. (b) High-resolution C 1s XPS spectra. (c) High-resolution N 1s XPS spectra. (d) High-resolution S 2p XPS spectrum of* ***CN_{TM}-Ru_{15}*** *film.*

Oxygen evolution experiments

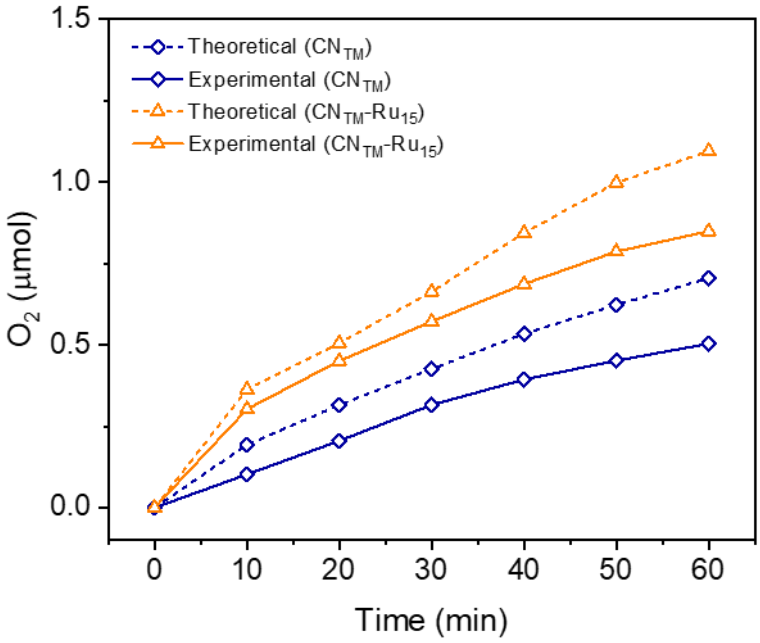

Figure S9. *Amount of O_2 produced over time using **CN_{TM}–Ru_{15}** electrode (orange solid line) in phosphate buffer (pH 7, 0.1 M) at 1.23 V_{RHE} under 1 sun illumination with respect to **CN_{TM}** blank (blue solid line). The theoretical amount of O_2 for **CN_{TM}** (blue dotted line) and **CN_{TM}–Ru_{15}** (orange dotted line) is also shown, calculated from Equation S3 (Supporting Information, section* PEC and electrochemical measurements*).*

Table S1. *Amount of Ru metal found by ICP-OES in **CN_{TM}–Ru_{15}** samples.*

Amount sample analyzed (mg) [a]	Amount Ru obtained (mg L^{-1})	µg (Ru) g^{-1} (sample) [b]	% Ru	nmol (Ru) g^{-1} (sample)
20	0.013	6.5	6.5×10^{-4}	64.3

[a] The amount of sample analyzed (20 mg) corresponds to the area irradiated of the electrode (1 cm^2). [b] The transformation from mg L^{-1} to µg Ru g^{-1} sample was performed considering the amount of sample analyzed and the volume of digested solution injected (10 mL).

Table S2. *Calculated TON and TOF from the O_2 evolution experiments.*

	µmol O_2 cm^{-2} min^{-1}	Time (min)	Total O_2 amount (µmol)	FE (%)[a]	TON[b]	TOF (h^{-1})[c]
CN_{TM}	8.4×10^{-3}	60	0.5	74	—	—
CN_{TM}-Ru_{15}	0.014	60	0.85	89.3	660	1409

[a] The Faradaic efficiency reported was calculated after 20 min of experiment, representing the maximum value that was reached during the measurement, comparing experimental and theoretical data. [b] The value of TON was calculated considering the total amount of O_2 produced in mol, divided by the mol of Ru found through ICP-OES. [c] The value of TOF was calculated considering the total amount of O_2 produced in mol, divided by the mol of Ru found through ICP-OES and the time (in hours) when the rate of O_2 production is faster (10 min).

Table S3. *Comparison of different CN photoanodes used with water oxidation catalysts for OER.*

Entry	Material	Electrolyte	Photocurrent (µA cm^{-2}) at 1.23 V vs RHE	Faradaic efficiency (%)	Light intensity	Ref.
1	**CN_{TM}**	0.1 M Na_2HPO_4/NaH_2PO_4, pH 7	130 ± 10	74	100 mW cm^{-2} AM 1.5 G	This work
2	**CN_{TM}–Ru_{15}**	0.1 M Na_2HPO_4/NaH_2PO_4, pH 7	180 ± 10	89.3	100 mW cm^{-2} AM 1.5 G	This work
3	CN-MR /$NiFeO_xH_y$	0.1 M KOH, pH 13	320 ± 28	43.8	100 mW cm^{-2} AM 1.5 G	18
4	CoPOM-PEI-CN_x-TiO_2	0.1 M borate solution, pH 8	230	15 ±4	λ > 420 nm, 150 mW cm^{-2}	19
5	Ni-CN_x	0.1 M aqueous KOH, pH ~ 13	69.8	—	100 mW cm^{-2} AM 1.5 G	20
6	3DB WO_3-NA/C_3N_4-NS//CoO_x	0.01 M Na_2SO_4	1.5×10^3	82.8	150 mW cm^{-2} AM 1.5 G	21

Characterization after catalysis

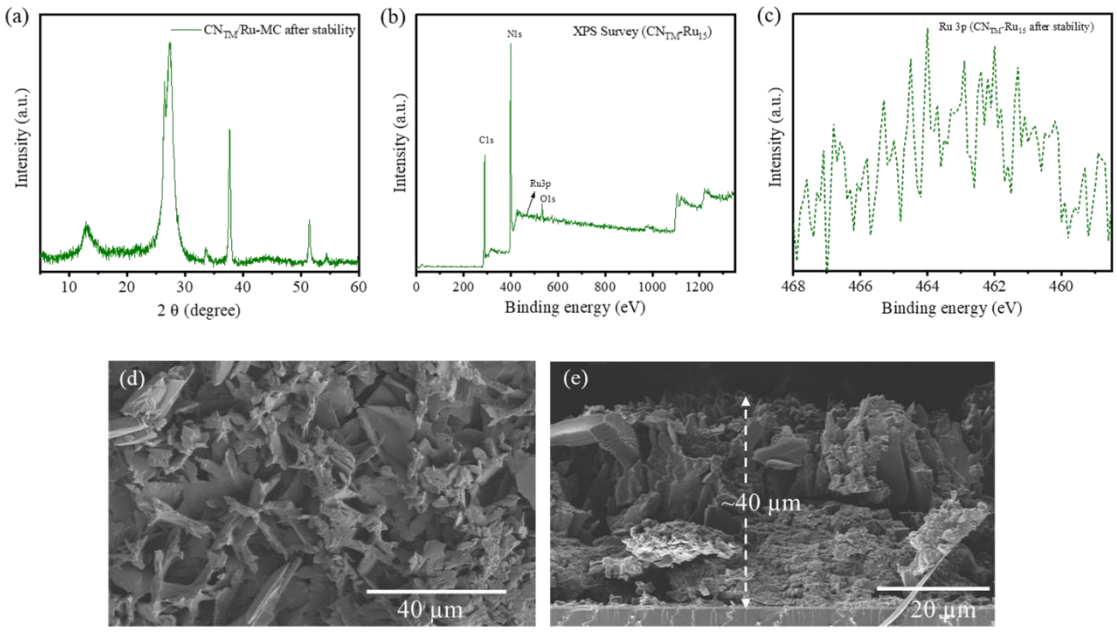

Figure S10. *Characterization of* ***CN_{TM}–Ru_{15}*** *films after the stability measurement. (a) XRD, (b) XPS survey spectrum, (c) High-resolution Ru 3p XPS spectrum, and SEM images: (d) Top-view and (e) cross-section.*

Electrochemical measurements

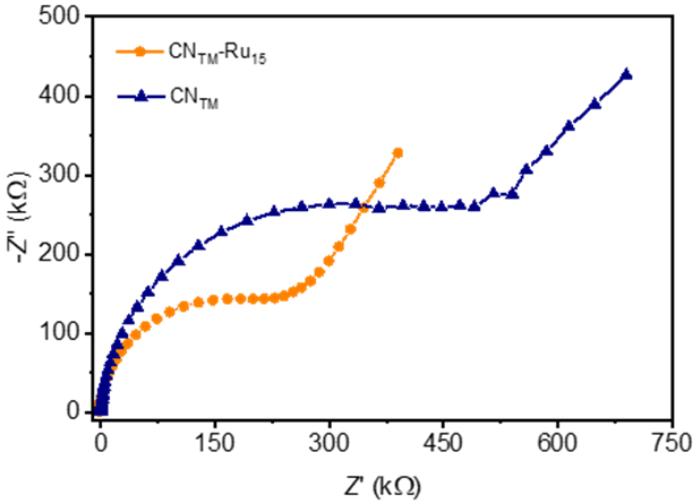

Figure S11. *Nyquist plot (raw data) from EIS measurement of* ***CN_{TM}*** *and* ***CN_{TM}–Ru_{15}*** *films.*

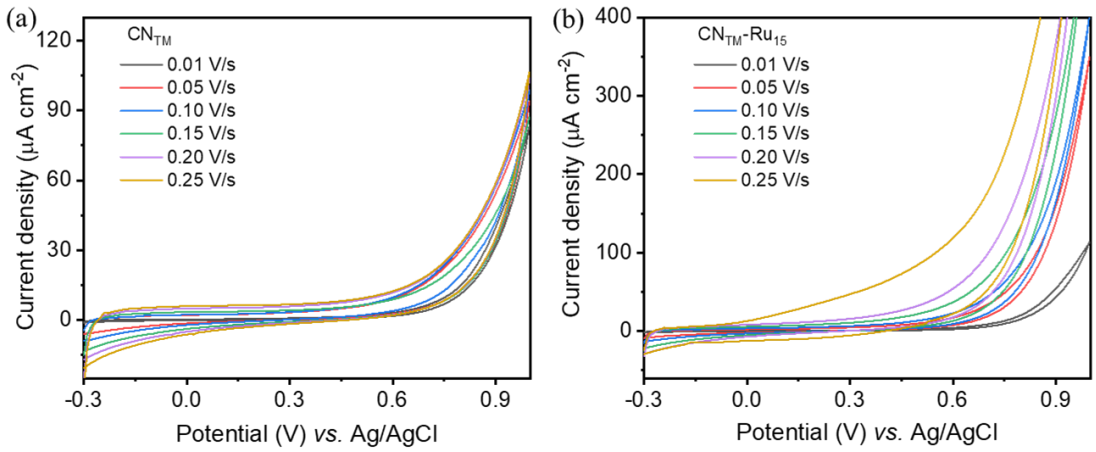

Figure S12. *Cyclic voltammetry test of the* ***CN$_{TM}$*** *and* ***CN$_{TM}$–Ru$_{15}$*** *films as a function of scan rate.*

TAS measurements

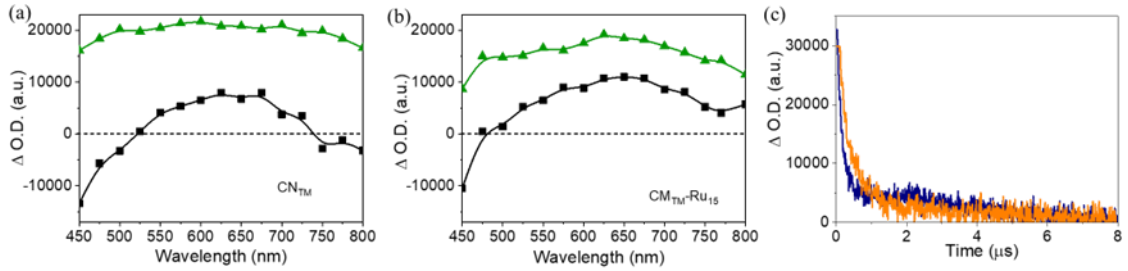

Figure S13. *Transient absorption spectra of (a)* ***CN$_{TM}$*** *and (b)* ***CN$_{TM}$–Ru$_{15}$*** *dispersions in acetonitrile (black squares) or 2:1 v/v acetonitrile:MeOH mixture (green triangles) acquired at 250 ns under N_2 atmosphere upon 355 nm laser excitation. (c) Transient absorption decay of* ***CN$_{TM}$*** *(blue) and* ***CN$_{TM}$–Ru$_{15}$*** *(orange) dispersions in 7:3 v/v acetonitrile:MeOH mixture, monitored at 650 nm under N_2 atmosphere upon 355 nm laser excitation.*

5.5.7 Computational results

Structure optimization and anchoring

A dimer of Ru(tda) connected by a 4,4'-bpy and a carbon nitride of 164 atoms (60 C, 86 N, 18 H) were used to study the oligomer attachment onto the surface. Initially, the geometries of carbon nitride and dimer were optimized separately. These structures were later used for the anchoring analysis.

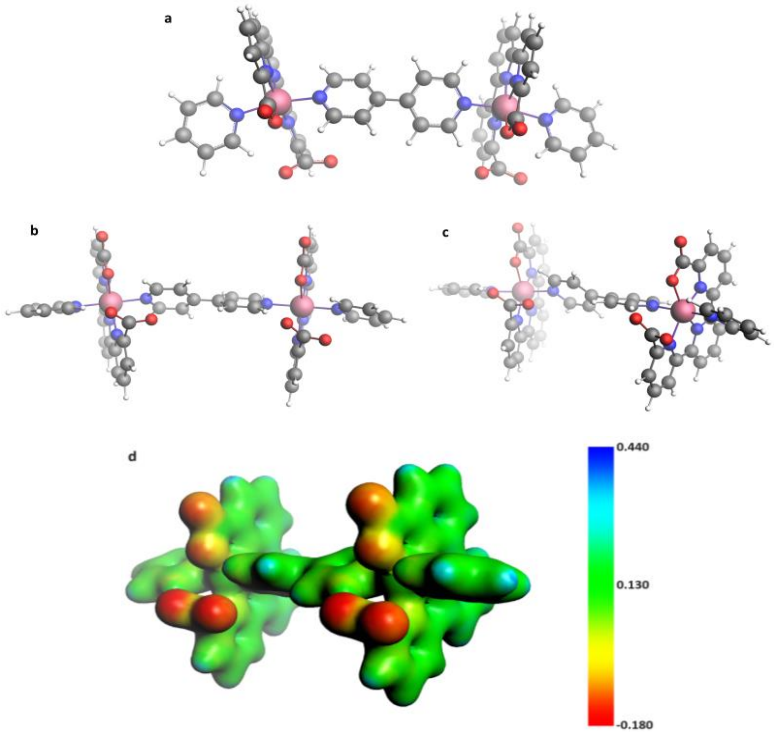

Figure S14. *Optimized molecular structures of Ru(tda)py$_2$ dimer; (a) top view, (b) front view, (c) side view, (d) molecular electrostatic potential map (a.u.).*

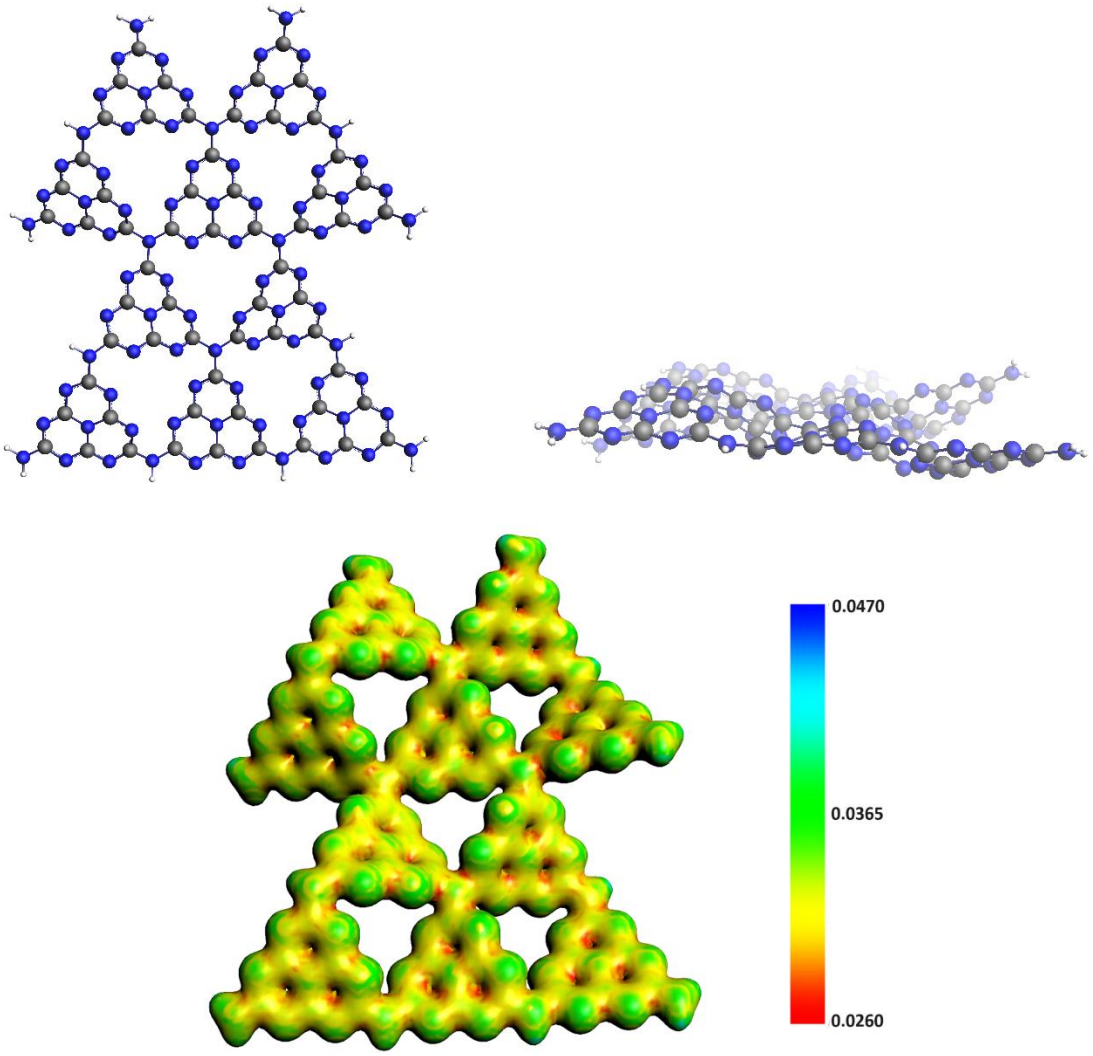

Figure S15. *Optimized structure of carbon nitride surface model; top view (top left), side view (top right), and molecular electrostatic potential map (a.u., bottom).*

The optimized structure of the carbon nitride model results to be non-planar as previous studies have suggested by comparing experimental and computational data.[22,23] Further details regarding the carbon nitride structure are presented in the section *Carbon nitride structure insights.*

Moreover, the band gap of the material was determined using the HSE06 functional, which yields more suitable outcomes for computing such electronic properties.[24,25] A larger model consisting of a two-layer carbon nitride was required to replicate the electronic structure of the real world solid (see Figure 1). The resulting computed value of 2.62 eV agrees with the measured value (2.61 eV).

In this study, the metal complex and the carbon nitride surface were assembled with different relative orientations and the different starting geometries were left to adjust to their energy minima. This method permitted obtaining five different stable attachments. The five geometries were labeled considering the amount of H atoms forming CH–π interactions and the type of carboxylate closer to the surface. By counting the number of CH–π interactions, three types of structures can be distinguished, namely 0 H (relying only on anion–π interactions), 2 H, and 4 H. The carboxylate groups were sorted according to the presence of an O–Ru bond, or the presence of a negative charge (O^-). The molecular structures and their respective energy values were reported in Figure S16 and Table S4.

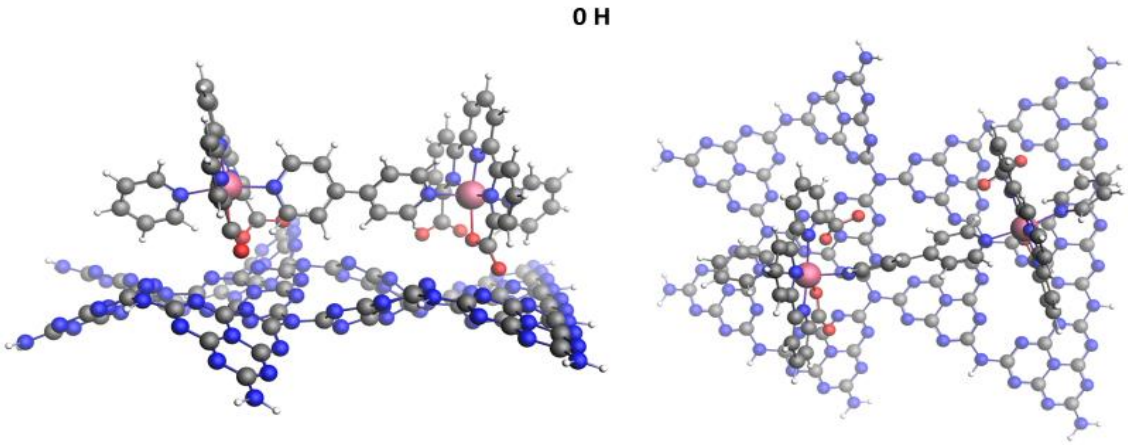

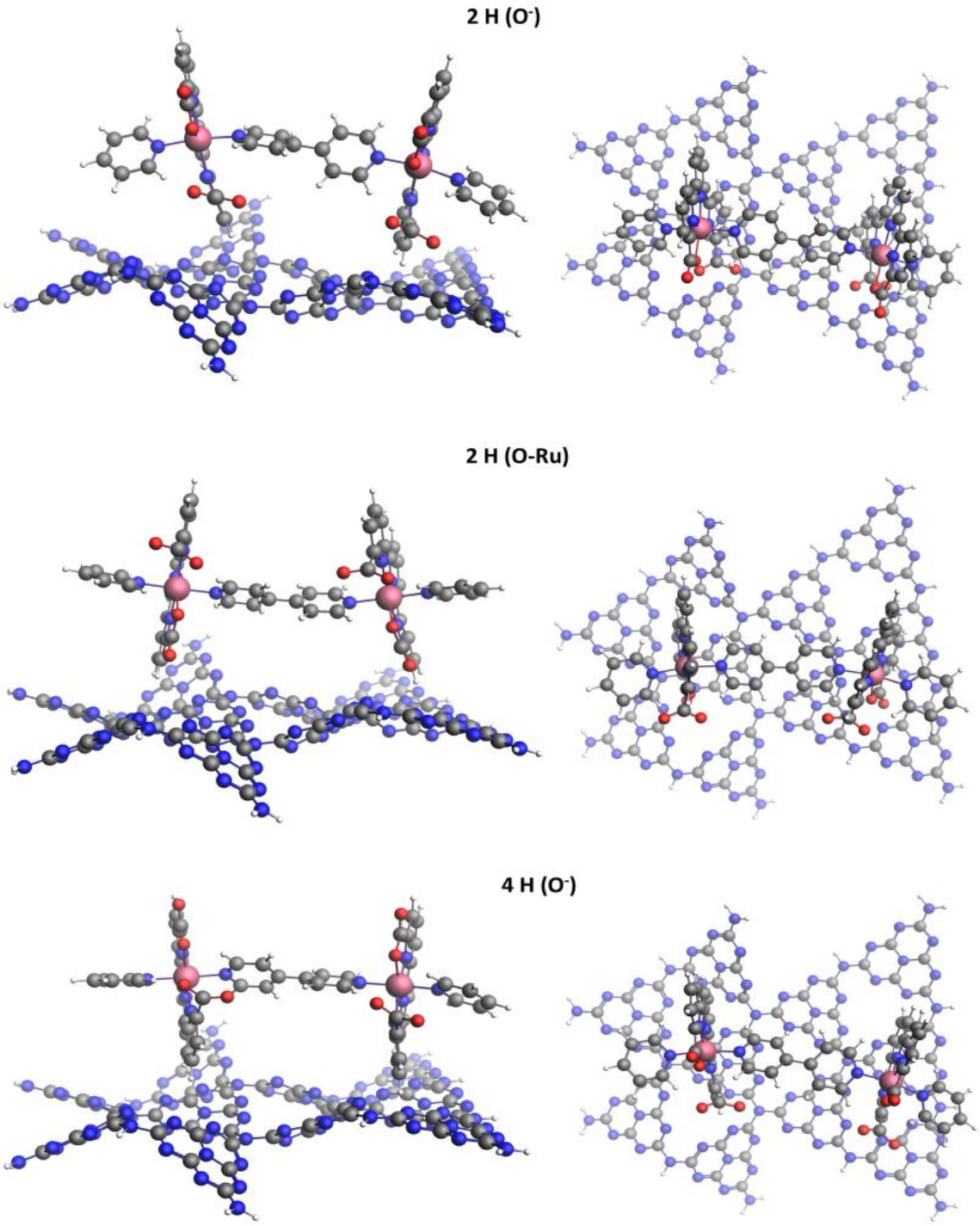
2 H (O-)
2 H (O-Ru)
4 H (O-)

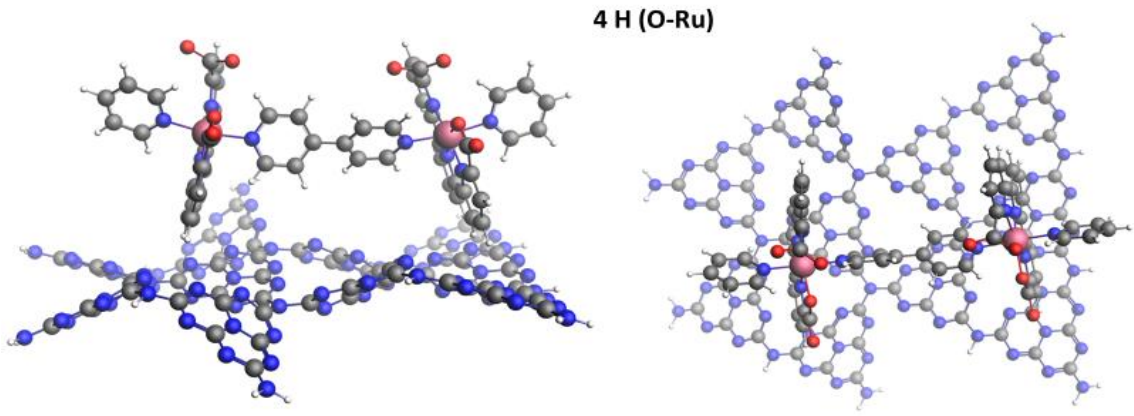

Figure S16. *Possible anchoring of* ***Ru_2*** *on carbon nitride surface; (left) side views, (right) top views.*

Table S4. *Anchoring energies and Boltzmann distribution of the possible interacting geometries in water.*

Attachment type	$E_{anchoring}$ (kcal mol^{-1})	E_{rel} (kcal mol^{-1})	Probability
0 H	–8.8	3.9	1.9×10^{-6}
2 H (O^-)	–4.1	8.6	2.9×10^{-13}
2 H (O–Ru)	–3.5	9.1	4.1×10^{-14}
4 H (O^-)	–12.7	0.0	1
4 H (O–Ru)	–10.8	1.9	1.5×10^{-3}

Table S5. *Anchoring energies and Boltzmann distribution of the possible interacting geometries in gas phase.*

Attachment type	$E_{anchoring}$ (kcal mol^{-1})	E_{rel} (kcal mol^{-1})	Probability
0 H	–29.6	0.0	1
2 H (O^-)	–14.1	15.5	2.0×10^{-23}
2 H (O–Ru)	–9.9	19.7	1.3×10^{-29}
4 H (O^-)	–20.7	8.9	1.0×10^{-13}
4 H (O–Ru)	–19.9	9.7	6.5×10^{-15}

The inversion of the most stabilizing interaction becomes apparent when comparing the anchoring energies in solution with those in the gas phase. Indeed, when the system is not in solvent, the most stable interaction is the 0 H due to the formation of strong anion–π interactions with the surface. When water is taken into account implicitly, the electrostatic effect on the carboxylic groups leads to a diminishment of anion–π strength, bringing the four CH–π interactions of the 4 H (O^-) structure (with the additional stabilization of the carboxylic groups by the solvent) to be the most stable. It is worth noticing that a more accurate model using explicit water molecules would probably enhance the stability of system 4 H (O^-) due to the additional formation of hydrogen bonds with the solvent. The action of hydrophobic effect is to exclude because of the lower anchoring energies when the solvent is considered part of the system.

Besides this inversion for the most stabilizing interaction, two other trends are visible from our data. First of all, the anchoring via four CH–π interactions always leads to higher stability. Secondly, the anchoring via a structure with the dangling carboxylate closer to the surface is always to prefer over structures with the O–Ru carboxylate closer. Even though the former claim is intuitive, the latter is not and deserves an explanation. The cause lies in the closer position of the pyridine to the dangling carboxylate when the dangling carboxylate is closer to the surface.

The CH–π distances in water phase of structure 4 H (O^-) are 2.36 and 3.26 Å for tda(1), and 2.85 and 3.08 Å for tda(2).

The anchoring energy for each dimeric structure considered ($E_{anchoring\ dimer}$) were calculated by the formula:

$$E_{\text{anchoring dimer}} = E_{\text{dimer on CN}} - (E_{\text{dimer}} + E_{\text{CN}}) \quad \text{(S6)}$$

Where $E_{dimer\ on\ CN}$ is the energy of the assembled system, and E_{dimer} and E_{CN} are the energies of the isolated dimer and surface, respectively.

These values were divided by two to determine the anchoring energy of each single $Ru(tda)py_2$ unit:

$$E_{\text{anchoring}} = \frac{E_{\text{anchoring dimer}}}{2} \quad \text{(S7)}$$

The relative energies (E_{rel}) were calculated as energy differences to the most stable anchoring ($E_{4\,H\,(O-)}$) employing the Equation S8 for aqueous phase, or S9 for gas phase:

$$E_{\mathrm{rel}} = E_i - E_{4\,\mathrm{H\,O^-}} \quad \text{(S8)}$$

$$E_{\mathrm{rel}} = E_i - E_{0\,\mathrm{H}} \quad \text{(S9)}$$

Where in both cases, E_i is the energy of the anchoring to compare.

The Boltzmann distribution was obtained by Equation S10:

$$p_i = \frac{\exp\left(-\varepsilon_i/(k_{\mathrm{B}}T)\right)}{\sum \exp\left(-\varepsilon_j/(k_{\mathrm{B}}T)\right)} \quad \text{(S10)}$$

Where p_i is the probability of i^{th} interaction to take place, ε_i is the anchoring energy of the geometry under examination and ε_j are all the anchoring energies. The temperature was considered constant at 298.15 K.

The anchoring energy of an oligomer of 15 units of Ru(tda) was obtained multiplying the number of units (*n* units) times the anchoring energy of a single monomer ($E_{anchoring}$) using Equation S11:

$$E_{\mathrm{anchoring\ oligomer\ 15}} = 15 \cdot E_{\mathrm{anchoring}} \quad \text{(S11)}$$

Carbon nitride structure insights

The structure of carbon nitride has long been debated. Many examples available in the literature overlook the true structural nature of carbon nitride and just consider it a planar surface.[25–27] However, recent studies aimed to clarify the topology of this material showed that the most stable conformer possesses a certain degree of rugosity.[22,23,28–30] Here we want to provide some insights emerging from our calculations.

In our study we optimized a molecular model of carbon nitride (CN10) by (i) leaving it able to adjust to its minimum energy and (ii) imposing a planar structure. The optimization lacking constraints led to a corrugated structure (in agreement with previous works)[22,23,28–30] being 154.6 kcal mol^{-1} more stable than its planar analog.

The lack of planarity was analyzed by measuring the dihedral angles of the N atoms connecting the heptazine units. A dihedral angle is the angle between two intersecting planes. In this case the planes are defined according to the atoms bound to the out-of-heptazines nitrogen, three types of nitrogen atoms can be distinguished, namely $ArNH_2$, Ar_2NH, and Ar_3N (see Figure S17). The values of the dihedral angles are reported in Tables S5, S6, and S7.

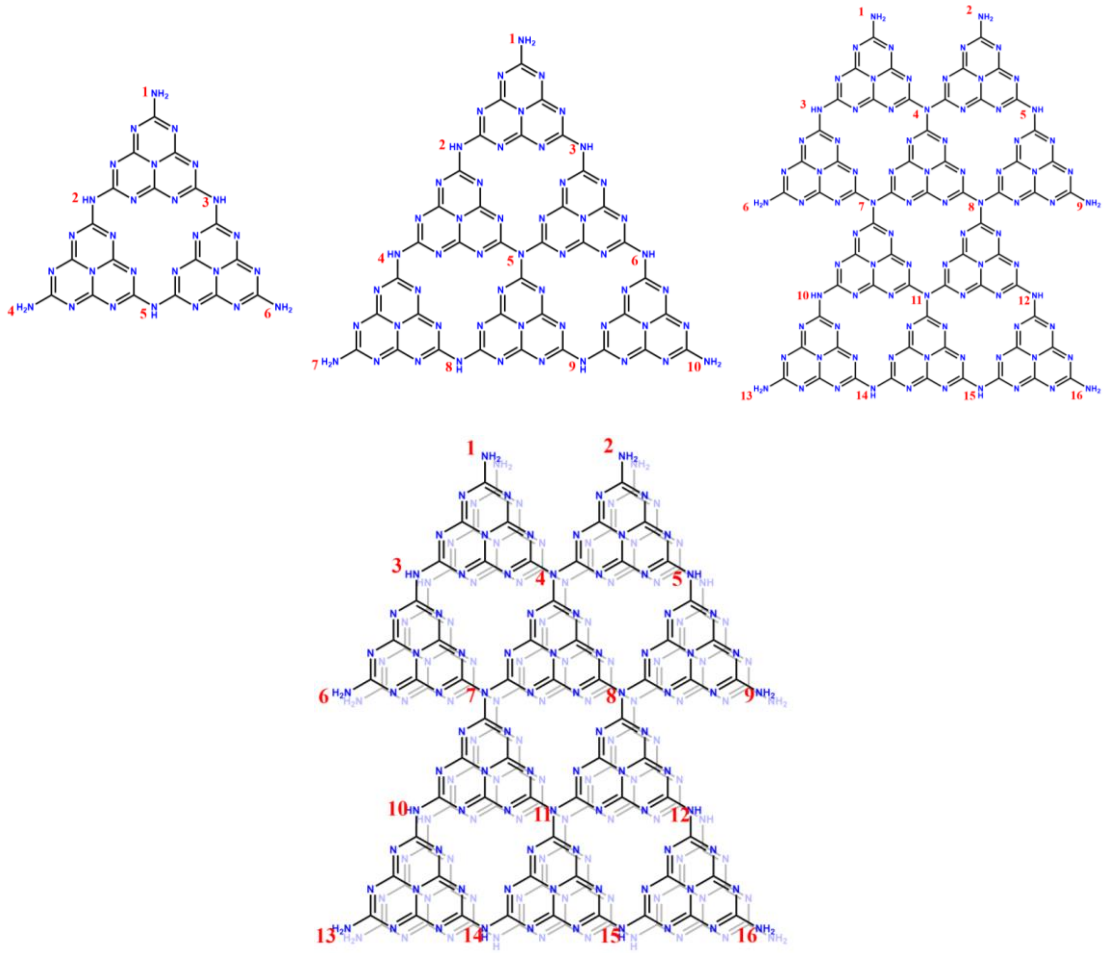

Figure S17. *Schematic representation of the carbon nitride models considered in this study CN3 (top left), CN6 (top center), CN10 (top right), and CN10 2 layers (bottom) with labeled N bridging atoms.*

Table S6. *Dihedral angles in the optimized structure of CN3.*

$ArNH_2$	Dihedral angle
1	179.9°
4	156.6°
6	156.3°
Ar_2NH	Dihedral angle
2	192.5°
3	193.9°
5	180.6°

Table S7. *Dihedral angles in the optimized structure of CN6.*

$ArNH_2$	Dihedral angle
1	179.7°
7	180.0°
10	179.9°
Ar_2NH	Dihedral angle
2	167.3°
3	165.9°
4	153.6°
6	153.3°
8	177.7°
9	178.8°
Ar_3N	Dihedral angle
5	180.6°

Table S8. *Dihedral angles in the optimized structure of CN10.*

$ArNH_2$	**Dihedral angle**
1	174.2°
2	174.7°
6	177.1°
9	176.6°
13	178.0°
16	177.8°
Ar_2NH	**Dihedral angle**
3	139.2°
5	139.3°
10	151.7°
12	152.5°
14	178.3°
15	176.9°
Ar_3N	**Dihedral angle**
4	180.2°
7	167.2°
8	166.6°
11	177.7°

Table S9. *Dihedral angles in the optimized structure of CN10 2 layers.*

$ArNH_2$	**Dihedral angle**
1’	147.9°
2’	150.1°
6’	145.4°
9’	162.3°

13’	148.8°
16’	155.0°
1’’	147.9°
2’’	150.0°
6’’	153.3°
9’’	148.0°
13’’	148.6°
16’’	154.8°
Ar_2NH	**Dihedral angle**
3’	172.8°
5’	165.5°
10’	175.7°
12’	175.8°
14’	176.8°
15’	178.5°
3’’	169.5°
5’’	169.3°
10’’	175.7°
12’’	175.4°
14’’	178.7°
15’’	177.0°
Ar_3N	**Dihedral angle**
4’	175.9°
7’	175.0°
8’	175.5°
11’	173.6°
4’’	178.4°
7’’	176.5°
8’’	175.9°

11''	175.4°

The distortion from planarity was defined by the Equation S12:

$$\text{deviation from planarity (°)} = 180\ ° - \text{dihedral angle (°)} \qquad \text{(S12)}$$

Where the dihedral angles considered are the angles formed by the bridging N atoms.

It is noteworthy that the average deviation for Ar_3N in CN10 is 7.2°, while this value decreases to 5° and 3.5° for the two layers of CN10 2 layers. This data clearly shows that the interlayer π–π stacking helps the planarity of the system and that the distortion present in the CN10 model is slightly exaggerated by the lack of additional layers.

In the bridging N surrounded exclusively by aromatic systems, the maximum distortion from planarity is produced in CN10 2 layers with a value of 173.6° (180° –173.6° = 6.4°) (see Figure S18). In both cases, the deviation from planarity is modest and allows a π-conjugation over the entire surface, in agreement with a previous report.[31]

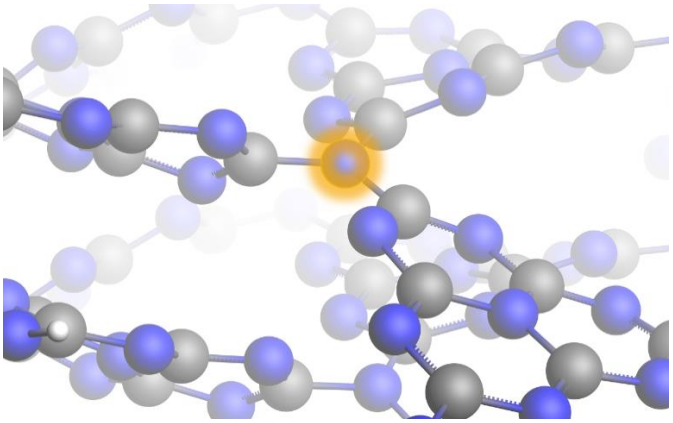

Figure S18. *View of a bridging N atom in CN10 2 layers.*

Even though these conclusions might appear contradictory to the hypothesis of a planar material, the partial sp^3 character of the bridging N is not the main reason for the lack of planarity. The fundamental cause for the non-planarity of the carbon nitride is attributed to the repulsion produced between the neighboring N atoms belonging to the different heptazine units, leading to a distortion to alleviate the tension. A graphical description of these repulsive forces is reported in Figure S19.

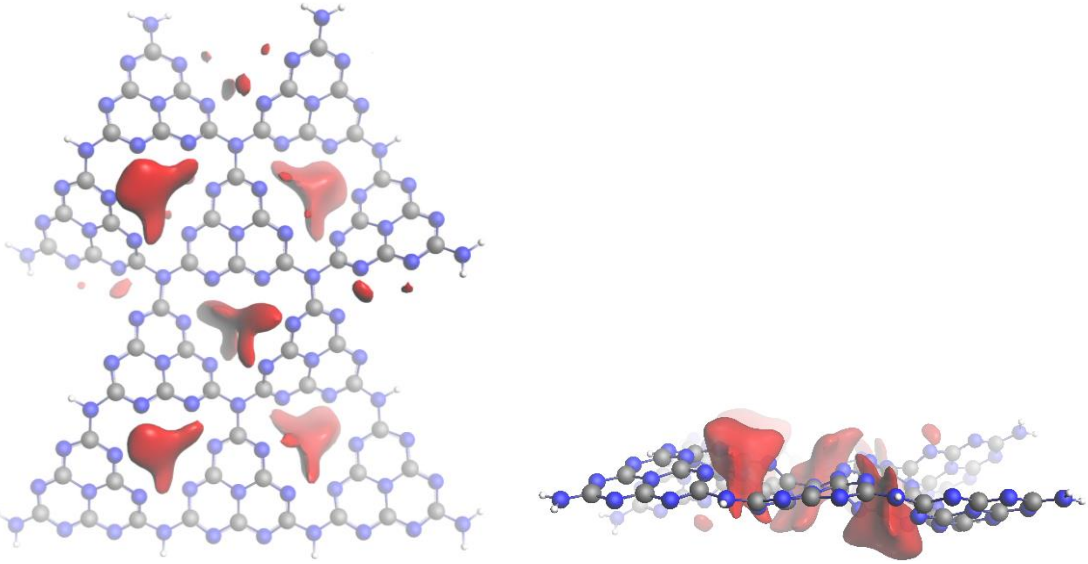

Figure S19. *Coulombic potential SCF (in red) in CN10: (left) top view, (right) side view.*

Photoexcitations

To gain some insights on the processes occurring upon light excitation of the system, we computed the absorption spectra by means of TD-DFT. Figure S20 reports the spectra of the two separate species, namely the surface (CN_{Red}) and the oligomer, and of the assembled system. It is worth noting that the band emerging in the assembled system at 500–650 nm does not derive from the overlap of absorption of its components, but it is rather a consequence of the assembly. The only possible reason for this new band to emerge is the direct electron excitation from one component to another. This mechanism differs from the more common electron transfer mechanism in which the electron gets promoted to the excited state of the photosensitizer and subsequently undergoes electron transfer to the acceptor.

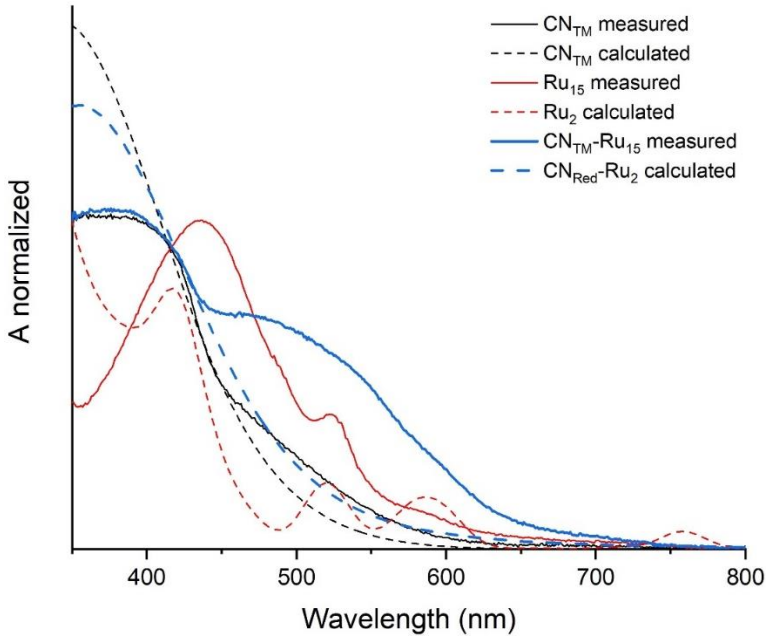

Figure S20. *Measured (solid lines) and calculated (dashed lines) UV–vis spectra.*

The plateau reached near 400 nm in the measured spectra of **CN_{TM}** and **CN_{TM}-Ru_{15}** represents the saturation due to the absorption of all incident photons. This effect is not observed in the simulated spectra as the excitation method cannot produce saturation.

To better comprehend the nature of the newly emerged band (500–650 nm), the orbitals involved in its main transitions are shown in Figure S21. All these transitions describe the excitation of an electron localized on the Ru(tda) unit to the carbon nitride, indicating a complex-to-surface electron transfer. These results are in agreement with the arising of the new band.

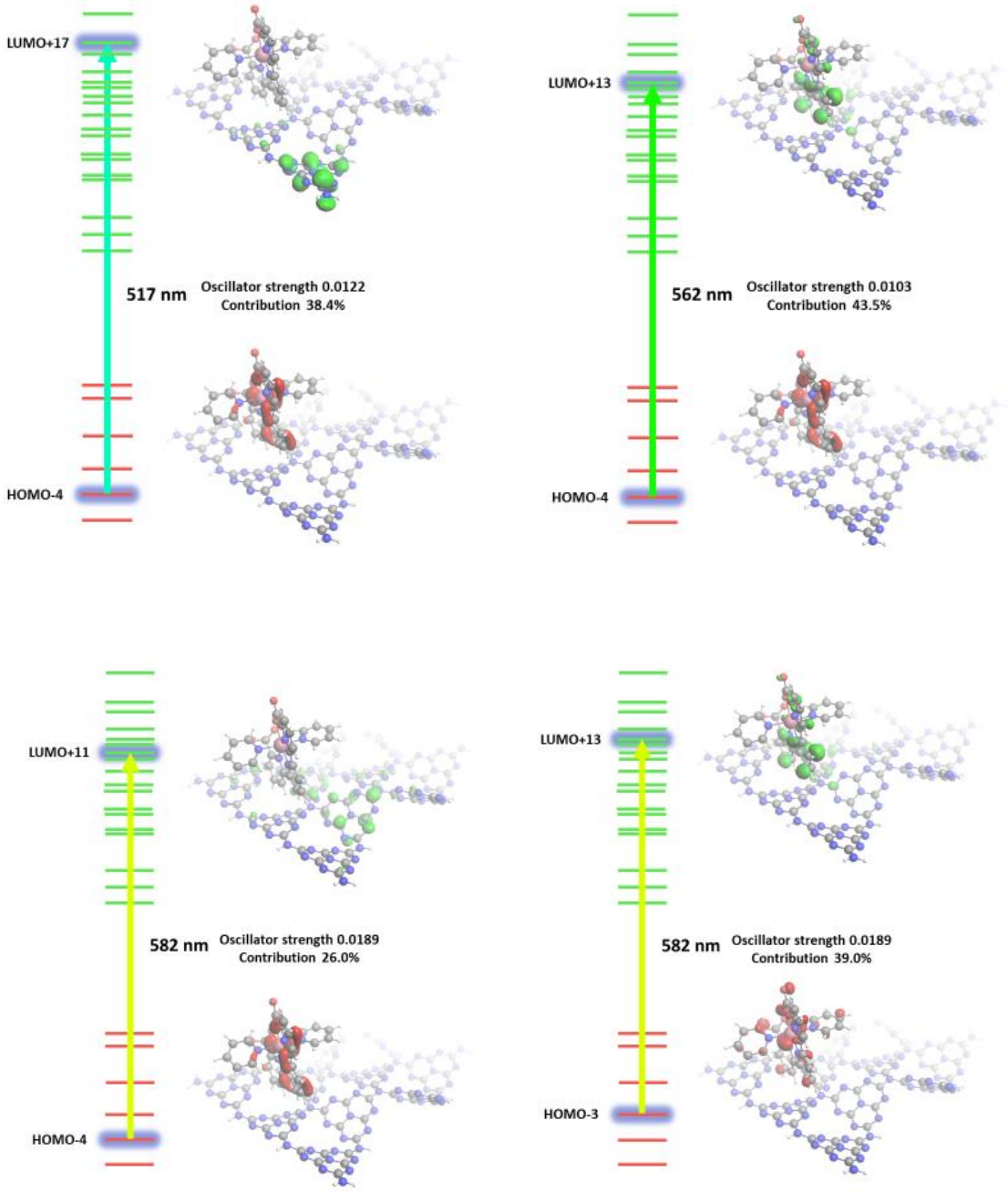

Figure S21. *Major contributions for the transition at 517 nm, 562 nm, and 582 nm. The orbitals and energy levels are depicted in red (populated) and green (excited).*

Moreover, the measured and simulated UV–vis spectra of **CN_{TM}** and the oligomer of ruthenium were plotted individually to provide more details on the separated systems (Figure S22). All the spectra were normalized to provide a good fitting of the calculated oscillator strength with the measured absorbance.

In the case of **CN_{TM}**, the simulation follows the trend of the measured spectrum. However, the theoretical and experimental spectra diverge in the region below 400 nm. The experimental spectrum shows saturation caused by the absorption of all the incident photons. On the other hand, the calculations cannot reach a saturation state, then in this region the intensity is remarkably enhanced due to all the high energy transitions.

The absorption of the oligomer (**Ru_{15}**) was described using a dimeric model (**Ru_2**). The simulated trend of **Ru_2** fits the experimental spectrum of the 15 units oligomer. It is noteworthy that the peak at 437 nm of **Ru_{15}** is the blue shifted in the Ru_2 model at 417 nm. This difference is not the consequence of an inappropriate model but the fruit of a constant red-shift taking place from the monomer to the pentadecamer, already described in a previous work.[4]

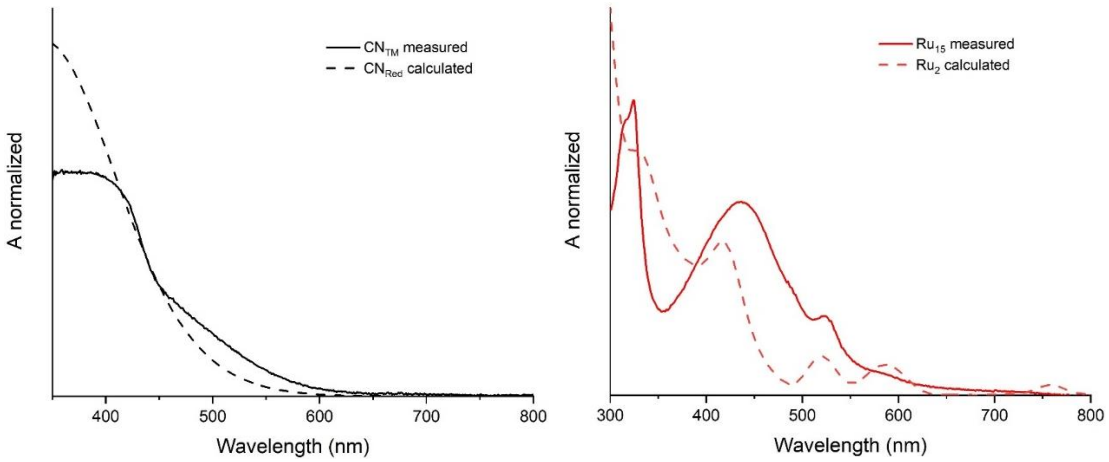

Figure S22. *Measured (solid line) and calculated (dashed line) UV–vis spectra of CN (left) and Ru oligomer (right).*

5.5.8. References

(1) Matheu, R.; Benet-Buchholz, J.; Sala, X.; Llobet, A. Synthesis, Structure, and Redox Properties of a Trans-Diaqua Ru Complex That Reaches Seven-Coordination at High Oxidation States. *Inorg. Chem.* **2018**, *57* (4), 1757–1765. https://doi.org/10.1021/acs.inorgchem.7b02375.

(2) Shmila, T.; Mondal, S.; Barzilai, S.; Karjule, N.; Volokh, M.; Shalom, M. Boron and Sodium Doping of Polymeric Carbon Nitride Photoanodes for Photoelectrochemical Water Splitting. *Small* **2023**, *19* (42), 1–10. https://doi.org/10.1002/smll.202303602.

(3) Qin, J.; Barrio, J.; Peng, G.; Tzadikov, J.; Abisdris, L.; Volokh, M.; Shalom, M. Direct Growth of Uniform Carbon Nitride Layers with Extended Optical Absorption towards Efficient Water-Splitting Photoanodes. *Nat. Commun.* **2020**, *11* (1), 1–9. https://doi.org/10.1038/s41467-020-18535-0.

(4) Hoque, M. A.; Gil-Sepulcre, M.; de Aguirre, A.; Elemans, J. A. A. W.; Moonshiram, D.; Matheu, R.; Shi, Y.; Benet-Buchholz, J.; Sala, X.; Malfois, M.; Solano, E.; Lim, J.; Garzón-Manjón, A.; Scheu, C.; Lanza, M.; Maseras, F.; Gimbert-Suriñach, C.; Llobet, A. Water Oxidation Electrocatalysis Using Ruthenium Coordination Oligomers Adsorbed on Multiwalled Carbon Nanotubes. *Nat. Chem.* **2020**, *12* (11), 1060–1066. https://doi.org/10.1038/s41557-020-0548-7.

(5) Te Velde, G. t; Bickelhaupt, F. M.; Baerends, E. J.; Fonseca Guerra, C.; van Gisbergen, S. J. A.; Snijders, J. G.; Ziegler, T. Chemistry with ADF. *J. Comput. Chem.* **2001**, *22* (9), 931–967. https://doi.org/10.1002/jcc.1056

(6) Becke, A. D. Density-Functional Exchange-Energy Approximation with Correct Asymptotic Behavior. *Phys. Rev. A* **1988**, *38* (6), 3098. https://doi.org/10.1103/PhysRevA.38.3098

(7) Perdew, J. P.; Yue, W. Accurate and Simple Density Functional for the Electronic Exchange Energy: Generalized Gradient Approximation. *Phys. Rev. B* **1986**, *33* (12), 8800. https://doi.org/10.1103/PhysRevB.33.8800

(8) Caldeweyher, E.; Ehlert, S.; Hansen, A.; Neugebauer, H.; Spicher, S.; Bannwarth, Christoph Grimme, S. A Generally Applicable Atomic-Charge Dependent London Dispersion Correction. *J. Chem. Phys.* **2019**, *150(15)*, 154122. https://doi.org/10.1063/1.5090222

(9) Lenthe, E. van; Baerends, E.-J.; Snijders, J. G. Relativistic Regular Two-component Hamiltonians. *J. Chem. Phys.* **1993**, *99* (6), 4597–4610. https://doi.org/10.1063/1.466059

(10) Van Lenthe, E.; Ehlers, A. W.; Baerends, E. J. Geometry Optimizations in the Zero Order Regular Approximation for Relativistic Effects. *J. Chem. Phys.* **1999**, *110*, 8943–8953. https://doi.org/10.1063/1.478813

(11) Klamt, A. Conductor-like Screening Model for Real Solvents: A New Approach to the Quantitative Calculation of Solvation Phenomena. *J. Phys. Chem.* **1995**, *99* (7), 2224–2235. https://doi.org/10.1021/j100007a062

(12) Pye, C. C.; Ziegler, T. An Implementation of the Conductor-like Screening Model of Solvation within the Amsterdam Density Functional Package. *Theor. Chem. Acc.* **1999**, *101*, 396–408. https://doi.org/10.1007/s002140050457

(13) Heyd, J.; Scuseria, G. E.; Ernzerhof, M. Hybrid Functionals Based on a Screened Coulomb Potential. *J. Chem. Phys.* **2003**, *118* (18), 8207–8215. https://doi.org/10.1063/1.1564060

(14) Schipper, P. R. T.; Gritsenko, O. V; van Gisbergen, S. J. A.; Baerends, E. J. Molecular Calculations of Excitation Energies and (Hyper) Polarizabilities with a Statistical Average of Orbital Model Exchange-Correlation Potentials. *J. Chem. Phys.* **2000**, *112* (3), 1344–1352. https://doi.org/10.1063/1.480688

(15) Gritsenko, O. V; Schipper, P. R. T.; Baerends, E. J. Approximation of the Exchange-Correlation Kohn–Sham Potential with a Statistical Average of Different Orbital Model Potentials. *Chem. Phys. Lett.* **1999**, *302* (3-4), 199–207. https://doi.org/10.1016/S0009-2614(99)00128-1

(16) Álvarez-Moreno, M.; de Graaf, C.; Lopez, N.; Maseras, F.; Poblet, J. M.; Bo, C. Managing the Computational Chemistry Big Data Problem: The ioChem-BD Platform. *J. Chem. Inf. Model.* **2015**, *55* (1), 95–103. https://doi.org/10.1021/ci500593j

(17) Li, J.; Wang, X.; Huang, L.; Tian, L.; Shalom, M.; Xiong, C.; Zhang, H.; Jia, Q.; Zhang, S.; Liang, F. Ultrathin Mesoporous Graphitic Carbon Nitride Nanosheets with Functional Cyano Group Decoration and Nitrogen-Vacancy Defects for an Efficient Selective CO_2 Photoreduction. *Nanoscale* **2021**, *13* (29), 12634–12641. https://doi.org/10.1039/D1NR02639A

(18) Karjule, N.; Singh, C.; Barrio, J.; Tzadikov, J.; Liberman, I.; Volokh, M.; Palomares, E.; Hod, I.; Shalom, M. Carbon Nitride-Based Photoanode with Enhanced Photostability and Water Oxidation Kinetics. *Adv. Funct. Mater.* **2021**, *31* (25). https://doi.org/10.1002/adfm.202101724.

(19) Gong, R.; Mitoraj, D.; Gao, D.; Mundszinger, M.; Sorsche, D.; Kaiser, U.; Streb, C.; Beranek, R.; Rau, S. A Triad Photoanode for Visible Light-Driven Water Oxidation via Immobilization of Molecular Polyoxometalate on Polymeric Carbon Nitride. *Adv. Sustain. Syst.* **2022**, *6* (5), 34–41. https://doi.org/10.1002/adsu.202100473.

(20) Zhang, W.; Albero, J.; Xi, L.; Lange, K. M.; Garcia, H.; Wang, X.; Shalom, M. One-Pot Synthesis of Nickel-Modified Carbon Nitride Layers Toward Efficient Photoelectrochemical Cells. *ACS Appl. Mater. Interfaces* **2017**, *9* (38), 32667–32677. https://doi.org/10.1021/acsami.7b08022.

(21) Hou, Y.; Zuo, F.; Dagg, A. P.; Liu, J.; Feng, P. Branched WO3 Nanosheet Array with Layered C_3N_4 Heterojunctions and CoO_x Nanoparticles as a Flexible Photoanode for Efficient Photoelectrochemical Water Oxidation. *Adv. Mater.* **2014**, *26* (29), 5043–5049. https://doi.org/10.1002/adma.201401032.

(22) Sehnert, J.; Baerwinkel, K.; Senker, J. Ab Initio Calculation of Solid-State NMR Spectra for Different

Triazine and Heptazine Based Structure Proposals of g-C_3N_4. *J. Phys. Chem. B* **2007**, *111* (36), 10671–10680. https://doi.org/10.1021/jp072001k.

(23) Wang, J.; Hao, D.; Ye, J.; Umezawa, N. Determination of Crystal Structure of Graphitic Carbon Nitride: Ab Initio Evolutionary Search and Experimental Validation. *Chem. Mater.* **2017**, *29* (7), 2694–2707. https://doi.org/10.1021/acs.chemmater.6b02969.

(24) Galushchinskiy, A.; Zou, Y.; Odutola, J.; Nikačević, P.; Shi, J.; Tkachenko, N.; López, N.; Farràs, P.; Savateev, O. Insights into the Role of Graphitic Carbon Nitride as a Photobase in Proton-Coupled Electron Transfer in (sp3) C−H Oxygenation of Oxazolidinones. *Angew. Chemie Int. Ed.* **2023**, *62* (18), e202301815. https://doi.org/10.1002/anie.202301815.

(25) Wang, X.; Ma, J.; Fan, J.; Zhu, H.; Liu, X.; Xia, H.; Liu, Y. Characterization of Type I/II g-C_3N_4/MoS_2 van Der Waals Heterostructures: A New Theoretical Insight. *J. Chem. Inf. Model.* **2023**, *63* (15), 4708–4715. https://doi.org/10.1021/acs.jcim.3c01089.

(26) Wang, X.; Blechert, S.; Antonietti, M. Polymeric Graphitic Carbon Nitride for Heterogeneous Photocatalysis. *Acs Catal.* **2012**, *2* (8), 1596–1606. https://doi.org/10.1021/cs300240x.

(27) Wu, H.-Z.; Liu, L.-M.; Zhao, S.-J. The Effect of Water on the Structural, Electronic and Photocatalytic Properties of Graphitic Carbon Nitride. *Phys. Chem. Chem. Phys.* **2014**, *16* (7), 3299–3304. https://doi.org/10.1039/C3CP54333A.

(28) Azofra, L. M.; MacFarlane, D. R.; Sun, C. A DFT Study of Planar vs. Corrugated Graphene-like Carbon Nitride (g-C_3N_4) and Its Role in the Catalytic Performance of CO_2 Conversion. *Phys. Chem. Chem. Phys.* **2016**, *18* (27), 18507–18514. https://doi.org/10.1039/C6CP02453J.

(29) Asif, K.; Perveen, M.; Khera, R. A.; Nazir, S.; Ayub, A. R.; Asif, T.; Shabbir, M.; Iqbal, J. Computational and Theoretical Study of Graphitic Carbon Nitride (g-C_3N_4) as a Drug Delivery Carrier for Lonidamine Drug to Treat Cancer. *Comput. Theor. Chem.* **2021**, *1206*, 113459. https://doi.org/10.1016/j.comptc.2021.113459.

(30) Melissen, S.; Le Bahers, T.; Steinmann, S. N.; Sautet, P. Relationship between Carbon Nitride Structure and Exciton Binding Energies: A DFT Perspective. *J. Phys. Chem. C* **2015**, *119* (45), 25188–25196. https://doi.org/10.1021/acs.jpcc.5b07059.

(31) Cao, S.; Low, J.; Yu, J.; Jaroniec, M. Polymeric Photocatalysts Based on Graphitic Carbon Nitride. *Adv. Mater.* **2015**, *27* (13), 2150–2176. https://doi.org/10.1002/adma.201500033.

Chapter 6

Strategic functionalization of carbon nitride photoanodes for improved charge separation in the water oxidation process


6

Strategic functionalization of carbon nitride photoanodes for improved charge separation in the water oxidation process

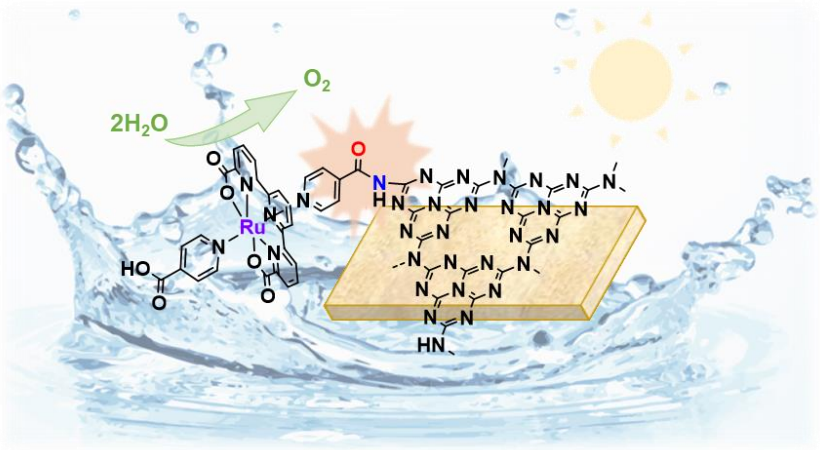

Abstract

In this work, we have successfully synthesized a molecular hybrid material with the inclusion of a Ru(tda) based catalyst onto carbon nitride (CN) through covalent grafting *via* amidation reaction. The formation of the amide bridging linkage between the catalyst's axial ligand and the terminal amino groups of the organic semiconductor yielded the newly prepared **CN_{TM}@Ru** photoactive material, which was studied through different spectroscopic, optical and photoelectrochemical techniques. The capability to behave as photoelectrocatalyst to oxidize water to dioxygen was studied under 1 sun irradiation at pH 7, improving the performance in terms of current, stability and Faradaic efficiency compared to the **CN_{TM}** and also to the previously reported **CN_{TM}-Ru_{15}** photoanode. The photophysical characterization revealed an improved charge separation and transfer kinetics with respect to the bare material, and confirmed the efficiency of the catalyst to promote the multielectron water oxidation process. The current Chapter presents thus a valid alternative to the supramolecular interaction methodology presented in Chapter 5 and a promising potential to further improve the efficiency of CN-based systems.

Contributions:

Martina Salati synthesized the [Ru(tda)(pyCOOH)$_2$] catalyst and precursors, **CN$_{TM}$** films and **CN$_{TM}$@Ru** functionalized photoanodes, as well as performed all the characterization measurements for the materials and the photoelectrochemical experiments.

6.1. Introduction

In order to address the increasing energy demand and the derived climate change produced by the combustion of fossil fuels, the production of the so-called solar fuels has emerged as promising alternative to traditional energy sources.[1,2] One example of green solar fuel is the hydrogen obtained *via* light-driven water splitting (*hv*-WS), a well-known process where, at the anode, molecular oxygen is produced as subproduct, together with electrons and protons, through the water oxidation reaction (WOR), while at the cathode protons are reduced to yield H_2 as the main fuel.[3,4] However, due to the high thermodynamic potential for this transformation and the sluggish reaction of oxygen evolution (OER), the process requires the use of energy, sunlight in this case, as well as the use of effective materials and catalysts to boost the WS.[5] Within this context, efforts have been focused on developing efficient and robust water oxidation catalysts (WOCs), which are typically based on transition-metals and can be grouped in molecular complexes[6–8] and metal oxides.[9,10]

From the molecular perspective, Ru-based complexes are certainly among the most efficient WOCs described in the literature, where the [Ru(tda)py_2] (where tda^{2-} is [2,2′:6′,2″-terpyridine]-6,6″-dicarboxylate and py is pyridine) achieves turnover frequencies (TOF) of 8 000 s^{-1} at neutral pH values.[11,12] Thus, the anchoring of molecular WOCs within semiconductor materials provides the possibility to perform heterogeneous catalysis and potentially increase the system efficiency and stability towards water oxidation, even in the presence of light.[13–16] Particularly, [Ru(tda)$(py)_2$] type of complexes provide versatile platform to functionalize the semiconductor materials through the existing well-controlled anchoring strategies. These can be performed *via* different pathways: (i) by supramolecular interactions, such as π-π or CH-π; (ii) by covalent bonding, which includes the inclusion of the catalyst inside the material structure, such as the synthesis of metal-organic frameworks, and the anchoring to the material's terminal groups. [8,17,18] In the latter case, the molecular catalysts grafted on the material surface could show unique advantages such as efficient intramolecular charge transfer and improved catalytic activity.

Within the range of materials studied, polymeric carbon nitride (CN) is an organic-based semiconductor which has gained particular attention because of its great robustness and tunability of electronical and structural properties following the different thermal and chemical synthetic conditions used.[19,20] This has been deeply studied in the field of water splitting, especially for hydrogen production in photocatalysis (PC) and photoelectrochemical cells (PEC).[21–23] From the anodic perspective, CN materials have shown minimal charge separation and transfer efficiencies, which led to slow kinetics for the water oxidation half-reaction. Thus, achieving a low photoactivity, in terms of photocurrents, and limited stabilities, especially in neutral medium. It is thus pivotal the inclusion of a catalyst in the system to improve the charge separation and electron transfer kinetics. Typically, researchers have studied these systems with the use of metal-oxides as catalysts[24–26] and the employment of highly basic or acidic conditions such as KOH or H_2SO_4 in order to prompt the oxidation process.[27–30] Considering that the covalent grafting of molecular metal-based catalysts onto the surface can ideally improve the efficiency of the hybrid system, few cases have been developed following this methodology.[31,32] In this context, Maeda[33,34] reported several ways to anchor Ru-based molecular catalysts to the CN surface *via* different terminal groups (i.e. -COOH, -PO_3H_2, -CH_2PO_3H), in order to study the mechanism of intramolecular charge transfer for the CO_2 reduction. As well, Robert, Ishitani and coworkers[35] described the covalent grafting of a cobalt–quaterpyridine molecular complex (Coqpy-Ph-COOH) to CN semiconductor through an amide linkage for the reaction. On the other side, one of the few examples for OER was reported by Feng *et al.*,[30] where a Ru-based molecular catalyst was prepared *in situ* onto CN powder through the formation of an amide as bridging group. However, considering the different cases studied for the reduction half-reaction and the rarely described systems with covalent linkage for oxygen evolution,[30,36] no example of this particular methodology was ever reported in a CN-based PEC device. Additionally, only one case (explained in Chapter 5) described an efficient molecular hybrid CN-based material for light-driven OER working in neutral pH medium.[37]

Hence, taking inspiration from previous works and Chapters 3 to 5 of this thesis, we prepared and characterized a CN photoanode (**CN_{TM}**) functionalized with a [Ru(tda)$(py)_2$]

type of molecular catalyst *via* covalent bonding to the surface. This material was strategically designed to ensure an optimal electronic connectivity between the semiconductor and the catalyst, promoting an efficient hole extraction by the metal center and avoiding undesired secondary reactions at the surface, such as self-oxidation of the material and degradation.[30,35] The photoelectrocatalytic performance of the new hybrid construct, namely **CN_{TM}@Ru**, was investigated for WOR in complete neutral medium, achieving photocurrent stabilities of more than 15 hours, higher catalytic activities (*J* of 480 μA/cm^2) and improved charge transfer kinetics compared to the bare CN electrode.

6.2. Results and discussion

6.2.1. Fabrication and characterization of the photoanodes

For the fabrication of the **CN_{TM}** films, thiourea and melamine were employed using a two-step method involving dipping and thermal treatment using FTO as supporting conductive layer (see Materials and Characterization sections in the SI). The functionalization of **CN_{TM}** with the $[Ru(tda)(pyCOOH)_2]$[14] (where pyCOOH is isonicotinic acid) molecular catalyst (see SI for further details) was performed following an amidation reaction at room temperature, based on a procedure for CN powders reported by Robert, Ishitani and coworkers,[35] to obtain the molecular hybrid material, namely **CN_{TM}@Ru**, with the catalyst covalently bonded to the organic electrode (Figure 1a, Schemes S3, S4). The prepared materials were characterized by PXRD (powder X-ray diffraction) and FTIR (Fourier-transform infrared) spectroscopy to investigate the structural and functional properties of the films. The bare **CN_{TM}** exhibits two characteristic diffraction signals at 12.5° and 24.5°, which can be assigned to (100) and (002) planes, respectively, representative of the interplanar spacing between the different CN layers and the conjugated aromatic system (Figure 1b).[38,39] Upon functionalization of the electrodes with the catalyst, the XRD pattern remains unchanged, underlining the structural stability of **CN_{TM}** films, and points out to a low amount of loaded catalyst onto the CN surface (see further in this section for better discussion).

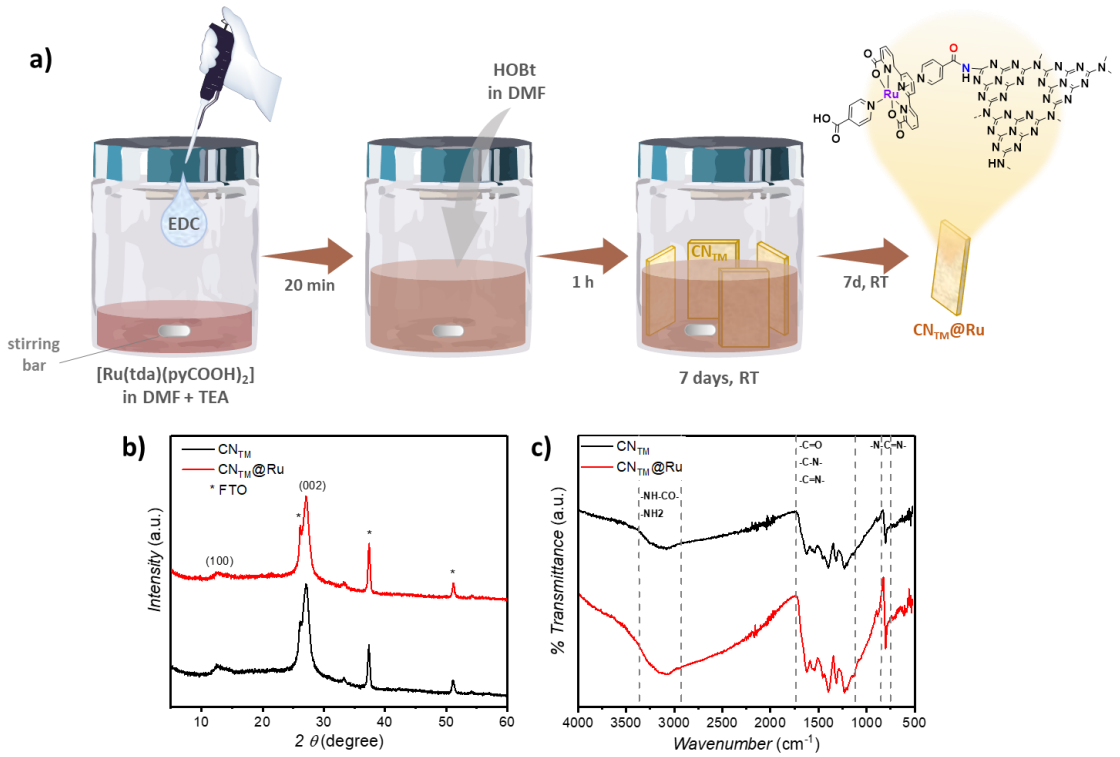

Figure 1. *(a) Schematic synthetic process for the functionalization through covalent bonding of the* ***CN$_{TM}$*** *films, described in details in the Supporting Information. (b) PXRD spectra of* ***CN$_{TM}$*** *(black line) and* ***CN$_{TM}$@Ru*** *(red line). (c) FT-IR spectra for* ***CN$_{TM}$*** *(black) and* ***CN$_{TM}$@Ru*** *(red), with the corresponding stretching/bending modes.*

The FTIR spectrum of **CN$_{TM}$** shows a peak at 805 cm^{-1}, which corresponds to the breathing mode of triazine units present in the sample (Figure 1c). Additionally, stretching modes of CN heterocycles were observed between 1200 to 1700 cm^{-1}, while no peak related to the C-S stretching of the thiourea precursor was shown in the area 1000-1200 cm^{-1}, which confirmed the successful polymerization of carbon nitrides.[40,41] The broad band observed between 2900 and 3350 cm^{-1} in the spectra is attributed to the -NH$_2$ terminal groups of CN films.[35] Upon covalent bridging of the molecular catalyst onto **CN$_{TM}$** to form the **CN$_{TM}$@Ru**, a higher intensity of the latter band was detected, especially for the stretching modes at around 3080 and 3150 cm^{-1}, which was attributed to the formation of the new amide group (with the -NH-CO- stretching), (Figure S2a-c).[35] No significant band shifts were detected for **CN$_{TM}$@Ru** compared to the bare **CN$_{TM}$**, likely due to the small amount of catalyst present on the electrode surface and the overlap of the peaks of the catalyst with those of CN in most cases. The exception was the

stretching at 3080 cm^{-1}, which slightly shifted to 3065 cm^{-1} for **CN_{TM}@Ru** (see Figure S2b-c in the SI).

Scanning electron microscopy (SEM) images of **CN_{TM}** (Figure S3) indicate a porous sheet-like morphology, with sharp rods displayed on the surface as a result of the last step of the synthetic approach.[38] After the functionalization with Ru complex, the SEM images suggest that the morphology is preserved, as discussed above for the XRD and FT-IR descriptions (Figure 1b, 1c and S2).

X-ray photoelectron spectroscopy (XPS) confirms the successful loading of Ru catalyst on **CN_{TM}** film (Figure S4). In Fig. 2a, the high-resolution C 1s spectrum of **CN_{TM}** film exhibits two peaks centered at around 284.7 and 288.3 eV, assigned to sp^2 C-C bonding and N-C=N bonding in the triazine-units of carbon nitride, respectively.[30,35,42,43] A less intense peak located at 286.2 eV appears in the C-O/C-NH_x (x = 1, 2) region, which is tentatively attributed to the C-NH-C bonding and the C-NH_2 terminal groups, or to C-O bonding due to potential water molecules adsorbed on the CN surface.[27,44,45] The high-resolution N 1s XPS spectrum for CN_{TM} shows four deconvoluted peaks attributed to C-N=C, N-$(C)_3$, C-N-H and C-NH_2 bonds (or oxidized N), respectively (Figure 2b).[30,42] The deconvolution of the C 1s spectrum of the **CN_{TM}@Ru** sample in Fig. 2c shows the relative increase of the peak at 286.2 eV compared to the other peaks, attributed to the inclusion of the catalyst, rich in carboxylic groups. The N 1s spectrum (Figure 2d) for **CN_{TM}@Ru** presents an increment of the signal intensity of N bonded in a C-N=C fashion with respect to **CN_{TM}** and an almost equal intensity for the peaks corresponding to the N-$(C)_3$ and C-N-H bonds, considering that the signals in the C 1s spectra present almost the same intensity. On contrast, the peak for C-NH_2 bonds seems to have disappeared, a determining sign that the terminal -NH_2 have been successfully replaced for amide groups, meanwhile a weak broad peak centered at 404.1 eV reveals the presence of a π-excitation or charging effect localized on the heterocycles.[46,47] Interestingly, after modification of the electrodes with the catalyst, we can also observe a small shift to lower binding energies (around 0.3 eV) of the peaks in the spectra N 1s and C 1s. The high-resolution Ru 3p spectrum of **CN_{TM}@Ru** film displays a peak at 461.2 eV, which further confirms the anchoring of the Ru molecular system as a Ru^{2+} species (Figure S4).[48,49] Finally, **CN_{TM}@Ru** films were analyzed through inductively-coupled plasma mass

spectrometry (ICP-MS) to obtain the average value of 19 µg of Ru per g of sample, which implies 0.19 µmols of Ru per g of **CN_{TM}@Ru** (see Table S1).

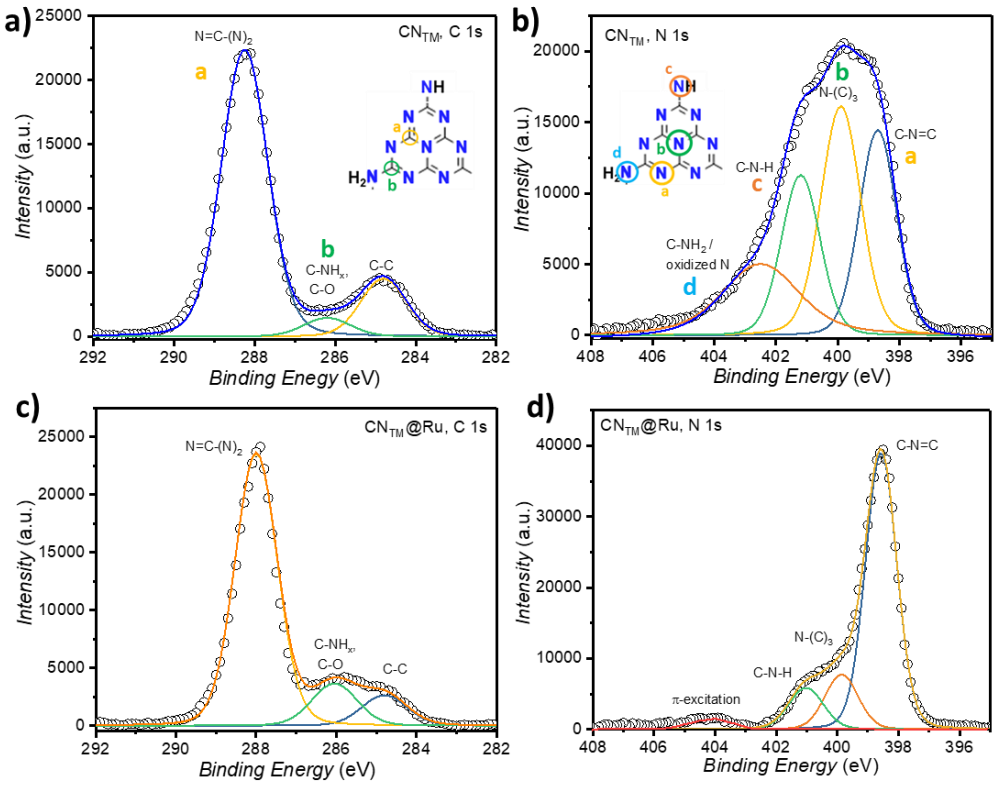

***Figure 2**. High-resolution XPS spectra of **CN_{TM}**, with deconvoluted curves for C 1s (a) and N 1s (b) spectra; High-resolution XPS spectra of **CN_{TM}@Ru**, with deconvoluted curves for C 1s (c) and N 1s (d) spectra.*

To gain further insights into the optical and electrochemical properties of the system, UV-vis diffuse reflectance spectroscopy (DRS), Mott-Schottky measurements (M-S) and ultraviolet photoelectron spectroscopy (UPS) were performed for both **CN_{TM}** and **CN_{TM}@Ru**. The modification of **CN_{TM}** with the Ru catalyst causes a slight change in the color of the film from pale yellow to saffron and the appearance of a new broad band absorbing between 450 and 650 nm (Figure S5), coincident with the MLCT band of the catalyst (Figure S6).[11,13] The direct optical bandgaps (E_g) of **CN_{TM}** and **CN_{TM}@Ru** electrodes were calculated from the Tauc plot obtained through DRS measurements, to be as 2.89 and 2.83 eV, respectively (Figure 1a), consistent with other examples

reported.[41] The modest change in bandgap after functionalization was detected also for the molecular hybrid system **CN_{TM}-Ru_{15}** examined in Chapter 5,[37] and it can be attributed to a low catalyst amount loaded. The conduction band energy (E_{CB}) for **CN_{TM}** and **CN_{TM}@Ru**, calculated from the Mott-Schottky plot, are found to be –0.28 and –0.02 V *vs.* NHE at pH 0, respectively (Figures 1b and S7), with the valence band energies for both systems obtained through the Equation S4, which are calculated as 2.61 V and 2.81 V *vs.* RHE, respectively, for **CN_{TM}** and **CN_{TM}@Ru**, meaning that the covalent anchorage of the catalyst on the surface can partially improve the driving force for O_2 evolution (Figure 1c).

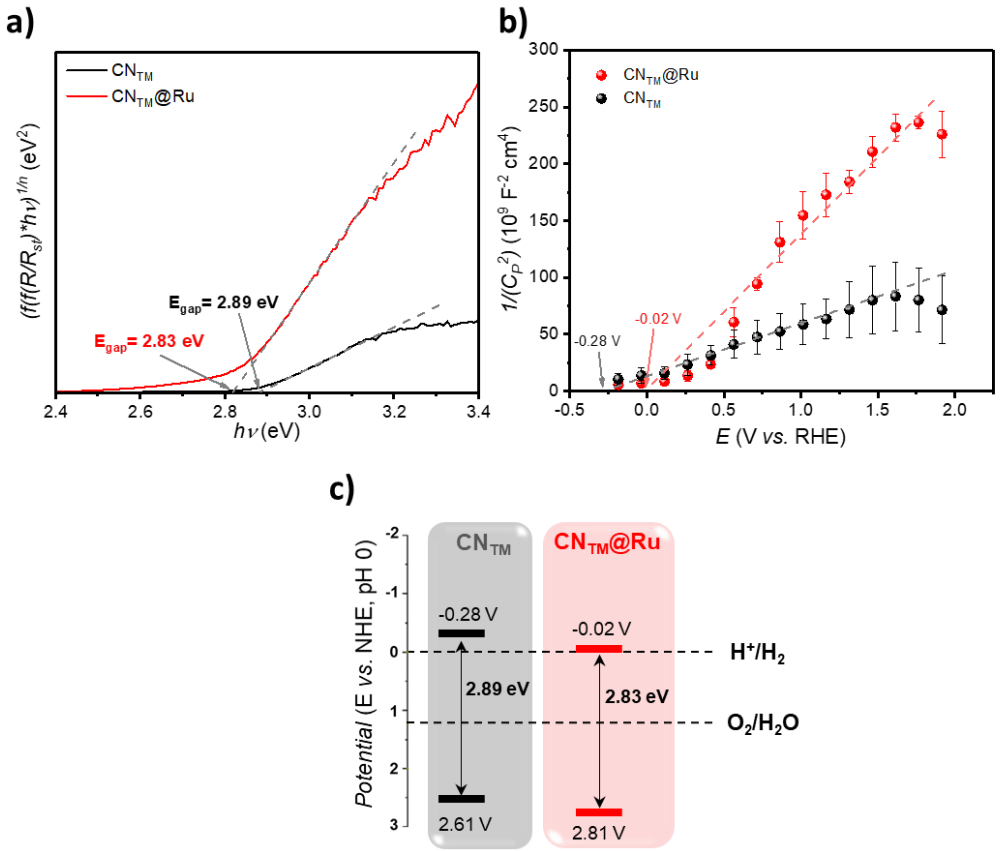

Figure 3. *(a) Tauc plot of **CN_{TM}** and **CN_{TM}@Ru** films obtained through diffuse reflectance spectroscopy (DRS). (b) Mott-Schottky average curves for **CN_{TM}** and **CN_{TM}@Ru** films, obtained using frequencies of 500, 1000 and 2000 Hz with the following electrochemical conditions: **CN_{TM}** and **CN_{TM}@Ru** as working electrodes, Ag/AgCl (sat. KCl) as reference electrode and Platinum plate (1 cm^2 of area) as counter electrode, phosphate buffer solution (pH 7, 0.1 M ionic strength) as electrolyte, dark (see Figure S7 for complete plot). (c) Energy diagram for the three systems calculated from the Tauc plot and the UPS experiments.*

To confirm the energy values obtained, we performed also UPS analyses (Figure S8), which discloses similar data to the one calculated from the M-S plots (2.6 V *vs.* NHE for **CN_{TM}** and 2.71 V *vs.* NHE for the **CN_{TM}@Ru** system).

6.2.2. Photo-electrochemical performances

Photoelectrochemical measurements of **CN_{TM}** and **CN_{TM}@Ru** samples were investigated in a three-electrode system under 1 sun illumination using sodium phosphate buffer (pH 7, 0.1 M) as electrolyte (see SI for further details). Linear sweep voltammetry (LSV) and chronoamperometry analysis were performed to study the PEC properties. LSV curves (Figure S9a) of **CN_{TM}** and **CN_{TM}@Ru** films show a low onset potential (-0.1 V *vs.* RHE) and an increase in photocurrent density for **CN_{TM}@Ru** compared to **CN_{TM}**, with around 0.45 mA/cm^2 vs. 0.1 mA/cm^2 at 1.23 V *vs.* RHE, respectively. This behavior is due to the incorporation of Ru catalyst into the **CN_{TM}** film, which leads, indeed, to a more efficient system for water oxidation to dioxygen with respect to the bare CN. The photocurrent densities of **CN_{TM}** and **CN_{TM}@Ru** were additionally compared by chronoamperometry technique with chopped light at an applied potential of 1.23 V *vs.* RHE using back-side illumination, as shown in Figure 4a. Under on-off illumination over time, the **CN_{TM}@Ru** electrodes show an increased current density of 480 μA cm^{-2} compared to 280 μA cm^{-2} for the **CN_{TM}** film, underlining the synergy between the **CN_{TM}** and Ru catalyst covalently bonded to the surface. The reproducibility of the results was confirmed by analyzing replicates of **CN_{TM}@Ru** samples, as it can be seen in Fig. S9b. The long-term stability for **CN_{TM}@Ru** is shown in Figure 4b, where under continuous irradiation the system reaches 42 μA/cm^2 of photocurrent after 2.5 hours, remaining constant for 13 hours. **CN_{TM}** film, meanwhile, loses its photocurrent density down to one order of magnitude lower (3.9 μA/cm^2) in ca. 2 hours. Even though there is a first drop in photocurrent assigned to a minimal detachment of the CN material from the electrode surface under working conditions (*vide infra*), the activity of **CN_{TM}@Ru** remains remarkably stable for more than 14 hours. Within this context, bare CN-based materials are normally reported to be unstable in neutral pH electrolytes, as observed for **CN_{TM}** (see Figure 4b, inset). For a better understanding of the existing charge transfer processes, electrochemical impedance spectroscopy (EIS) was performed under dark conditions. The Nyquist plot is presented in Figure S10a, where the arc radius for **CN_{TM}@Ru** film is visually smaller

compared to that for **CN_{TM}**, resulting in resistance to charge transfer (R_{CT}) calculated values of 1.67 x 10^4 Ohm and 1.9 x 10^4 Ohm, respectively, at 1.23 V *vs.* RHE (Figure S10b). This suggests that the incorporation of Ru catalyst through covalent anchorage provides a more efficient charge transfer and facilitates the separation and migration of excitons, resulting in higher photocurrent and improved stability.

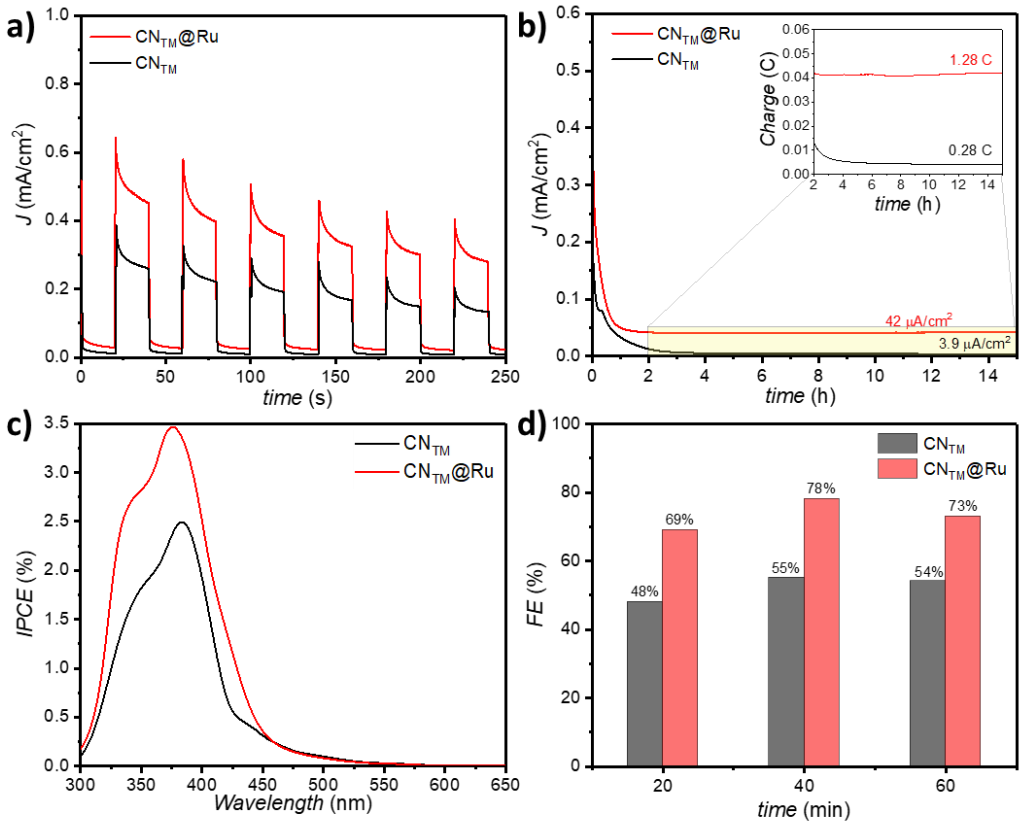

Figure 4. *(a) Chronoamperometry (current densities vs. time) of* ***CN_{TM}****,* ***CN_{TM}@Ru*** *and* ***CN_{TM}/Ru*** *electrodes in phosphate buffer (pH 7, I = 0.1 M) at 1.23 V_{RHE} upon on/off 1 sun illumination. (b) Long-term stability measurement (current density under continuous 1 sun illumination) of* ***CN_{TM}*** *and* ***CN_{TM}@Ru*** *electrodes in phosphate buffer (pH 7); Inset: charges transferred over time by the two systems, obtained by applying the formula* Q = J/t *(where* Q *is charge in coulomb (C),* J *is photocurrent density (A/m^2) and* t *is time (s)). (c) Incident photon-to-current conversion efficiency (IPCE) of the* ***CN_{TM}*** *(black dotted line) and* ***CN_{TM}@Ru*** *(red dotted line) films at different wavelengths (300–650 nm) in a phosphate buffer solution (pH 7) at 1.23 V_{RHE}, compared to the UV-vis absorption spectra for both* ***CN_{TM}*** *(black continuous line) and* ***CN_{TM}@Ru*** *(red continuous line). (d) Faradaic efficiencies calculated from the different acquired measurements of O_2 over time, detected at every 20 minutes, using Equations S5 and S6 reported in the Characterization section; conditions used: phosphate buffer (pH 7, I = 0.1 M) at 1.23 V_{RHE} upon continuous 1 sun illumination.*

The measured incident photon-to-current conversion efficiency (IPCE) of **CN_{TM}** and **CN_{TM}@Ru** films is displayed in Figure 4c. The IPCE values were measured at several illumination wavelengths ranging from 300 to 650 nm and were found to be in good agreement with the UV-vis DRS results of the films. It can be observed that the IPCE (%) for **CN_{TM}@Ru** film presents an increment of intensity of 40% respect to **CN_{TM}** film in the maximum absorption range (3.5% and 2.5%, respectively), until the intensities become equal from around 450 nm to higher wavelengths. The increased efficiency is attributed to the improved charge transfer facilitated by the presence of Ru complex anchored. Moreover, the maximum absorption value slightly shifted from 384 to 375 nm, which could happen potentially due to the oxidation of the Ru(tda) molecular complex, whose spectrum shifts to higher energies when higher oxidation states than Ru^{II} are reached.[11]

Finally, the oxygen evolution for both films over time was investigated, using the same experimental conditions as in previous measurements (chronoamperometry for 1 hour with applied potential 1.23 V *vs.* RHE under 1 sun irradiation, phosphate buffer at pH 7). The experiment reported in Figure 4a shows the capability of **CN_{TM}@Ru** to generate oxygen in an almost double amount compared to the bare CN electrode, reaching 78% of Faradaic efficiency after 40 minutes with respect to the 55% of **CN_{TM}** (Figure 4d and Table S2). Considering the Ru amount detected by ICP-MS, an overall calculation of the TONs and TOFs for **CN_{TM}@Ru** gave the values of 2.4×10^4 over 15 hours and 0.6 s^{-1}, respectively (Table S2). The high performance of the hybrid material highlights the potentiality of the anchoring strategy through amidation reaction, which greatly equalizes, and even overcome, the efficiency of the previously reported **CN_{TM}-Ru_{15}** (see Chapter 5).

To further study the stability of the photoanodes after 15 hours of catalysis, the morphology and structure integrity of the electrodes were investigated by microscopic and spectroscopic techniques. The PXRD analysis and the SEM top-view measurements for **CN_{TM}@Ru** after catalysis showed a negligible change in the structure and in the morphology, underlining that the CN structure remains basically unaltered under catalytic conditions (Figure S12, S13). A change of the thickness for the **CN_{TM}@Ru** film was shown by SEM cross-section images (from ca. 51 µm before catalysis to ca. 34 µm after catalysis, Figures S3h and S13d), indicating partial detachment of the hybrid

material from the photoanode. Further analysis of the XPS spectra for **CN_{TM}@Ru** after catalysis (Figure S14) reveals the decrease of the C-O peak at 286.5 eV compared to the N=C-N peak in the C 1s spectrum and the reappearance of the -NH_2 peak in the N 1s spectrum (or corresponding to oxidized N). This, along with the partial decrease of the peak corresponding to the Ru^{2+} species in the Ru 3p spectrum (Figure S14d), can be correlated to the detachment of the Ru(tda) catalyst with the CN material from the electrode surface, possibly due to the photoelectrochemical conditions applied, corroborated by the initial partial loss of photocurrent in the long-term stability (Figure 4b). To confirm the detachment of Ru catalyst from the CN surface, ICP-MS analysis was finally performed for **CN_{TM}@Ru** after catalysis, obtaining a loss of 32% of the metal (13 $\mu g/g_{sample}$ *vs.* the initial 19 $\mu g/g_{sample}$; see Table S1).

6.2.3. Mechanistic studies

To better understand the charge separation and electron transfer processes occurring in the hybrid system during the water oxidation process, we analyzed **CN_{TM}** and **CN_{TM}@Ru** using photoluminescence (PL) and transient absorption spectroscopy (TAS) measurements. The PL spectra (Figure 5a) show that in the **CN_{TM}@Ru** system, after a first excitation at 380 nm, the intensity of the prominent emission peak at 450 nm characteristic of the CN-based materials is quenched up to 51% compared to pristine **CN_{TM}**, suggesting an alternative non-radiative recombination path and thus a better electron transfer with the Ru(tda) catalyst, which is confirmed by the reported photocurrent (Figure 4). Transient absorption spectroscopy experiments of **CN_{TM}** and **CN_{TM}@Ru** dispersed in MeCN after laser excitation at 300 nm are reported in Figures 5 (see also Figures S16 and S17). The TA spectrum for **CN_{TM}** (Fig. 5b, black and grey traces) under N_2 atmosphere shows a fast charge recombination at all the wavelengths in the range from 350 to 800 nm, which is completed after around 400 ns, as visible in Figures 5c and S16. Indeed, for the TA signal at 425 nm and 650 nm reported in Figures 5c and S16, the lifetime (τ_{CN}) of the charge separated states for **CN_{TM}** are 95 ns and 83 ns, respectively, and no emission signal is observed at 1500 ns after the excitation. Instead, when we analyze the **CN_{TM}@Ru** film (Figure 5b, red and light-red traces), the spectrum presents higher signal amplitude, indicating longer living separated charges compared to the bare electrode. Moreover, in the region of 350-550 nm (Figures 5b and 5c), kinetic

traces show two components, a faster one with slightly slower lifetime than CN ($\tau^1_{CN\text{-}Ru}$ = 131 ns at 425 nm) and, a slower component ($\tau^2_{CN\text{-}Ru}$) which extends to the microsecond time scale, not determinable from our instruments.

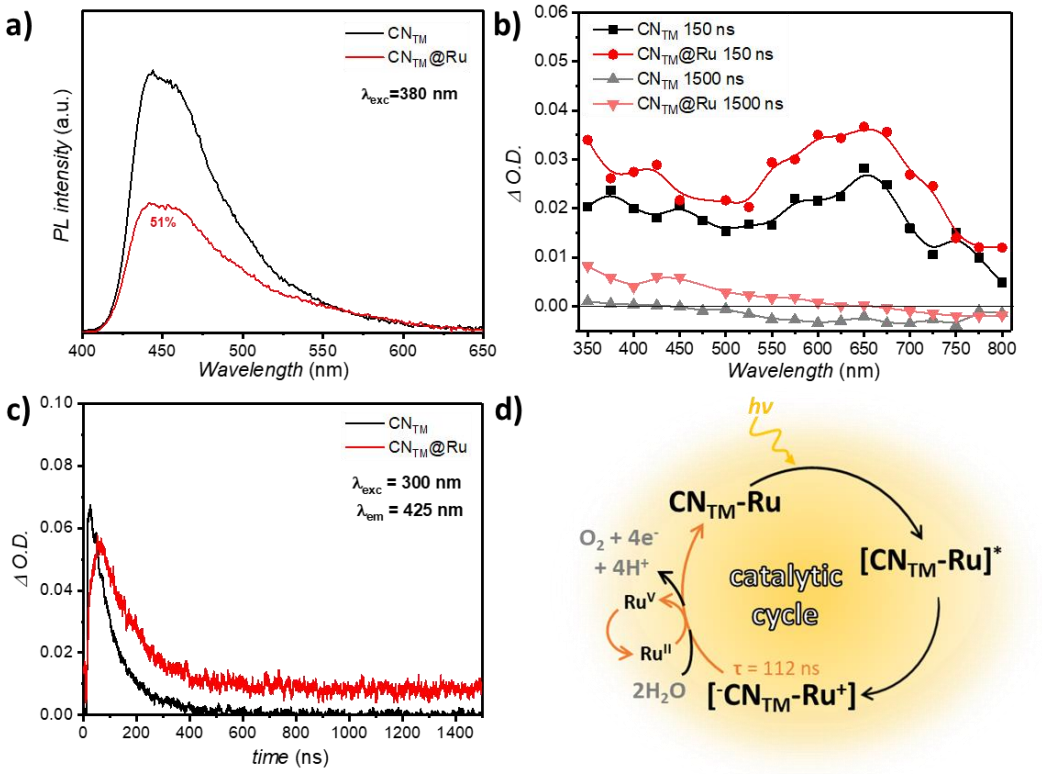

Figure 4. *(a) Photoluminescence (PL) spectra for* ***CN$_{TM}$*** *(black) and* ***CN$_{TM}$@Ru*** *(red) in solid state, after excitation at 380 nm. (b) Transient absorption spectra (plotted in difference of optical density, ΔOD) for* ***CN$_{TM}$*** *(black and grey traces) and* ***CN$_{TM}$@Ru*** *(red and light-red traces) dispersions in MeCN acquired at 150 ns and 1500 ns. (c) Transient absorption decays of* ***CN$_{TM}$*** *(black) and* ***CN$_{TM}$@Ru*** *(red) dispersions in MeCN, monitored at 425 nm (the measurements reported in (b) and (c) were performed upon laser excitation at 300 nm under N_2 atmosphere). (d) Proposed catalytic cycle for* ***CN$_{TM}$@Ru****, on the basis of the TAS experiments performed: after irradiation (hν),* ***CN$_{TM}$@Ru*** *(here described as CN$_{TM}$-Ru for simplicity) gets excited forming [CN$_{TM}$-Ru]* and the charges get separated between the CN material and the catalyst (charge-separated state [$^-$CN$_{TM}$-Ru$^+$]), with the accumulation of holes on the Ru, oxidized from Ru^{II} to Ru^V; the final step presents the oxidation of the hole scavenger (in this case water to oxygen) and the restoring of the initial CN$_{TM}$-Ru state. The lifetime (τ) reported correspond to the measured values in the presence of MeOH as sacrificial electron donor.*

Considering, instead, the region from 550 nm to 800 nm (Figures 5b and S16), the kinetic trace of **CN$_{TM}$@Ru** presents only one component ($\tau_{CN\text{-}Ru}$ = 120 ns at 650 nm), that is

similar to $\tau^1_{CN\text{-}Ru}$ at 425 nm and τ_{CN}. Given the typical higher energy onset detected in the UV-vis absorption spectra of the $[Ru^{III}(tda)(py)_2]^+$ and $[Ru^{IV}(tda)(py)_2]^{2+}$ complexes compared to the Ru^{II} species,[11] this can be indicative of the formation of a long-lived charge separated state involving highly-oxidized Ru catalysts.

Additionally, hole-quenching experiments were carried out in presence of O_2 and MeOH (Fig. S17). In the case of **CN_{TM}** film (Figure S17a), no visible difference was detected in 150 ns after the excitation, indicating that the quenchers are not influencing the charge separation lifetime, and no excited triplet states are formed upon light irradiation. With regard to **CN_{TM}@Ru** the absence of triple states was also confirmed, since no difference is shown when adding O_2 compared to the spectra under N_2 (Figures S17c and S17d). However, upon MeOH addition we see a partial quenching of the signal after 150 ns ($\tau_{CN\text{-}Ru}$ = 112 ns at 425 nm) and subsequently a complete quenching after 1500 ns, indicating that MeOH is working as a sacrificial electron donor, reducing the oxidizing Ru metal back to its Ru^{II} oxidation state (Figures S17b, S17c, S17d).

From these results we can finally hypothesize the catalytic cycle for **CN_{TM}@Ru** (Figure 5d). Upon light irradiation, the molecular hybrid material passes to its excited state **[CN_{TM}-Ru]***, and consequently to the charge separated state **[$^-CN_{TM}$-Ru^+]**, which possesses a longer lifetime ($\tau_{CN\text{-}Ru}$ = 131 ns) compared to the system **CN_{TM}** (τ_{CN} = 95 ns), where instead the charges recombine faster. However, when a hole scavenger like MeOH is added, we experience a decrease of the charge separated lifetime ($\tau_{CN\text{-}Ru}$ = 112 ns), since MeOH extracts the holes accumulated on the Ru center and the electrons remain delocalized on the CN polymer, making recombination more difficult to take place. This process can be ideally considered as well for water oxidation to dioxygen, providing a good explanation for the enhanced photocurrent obtained with the molecule hybrid system **CN_{TM}@Ru**.

6.3. Conclusions

In summary, we have covalently anchored the $[Ru(tda)(pyCOOH)_2]$ molecular complex on carbon-nitride photoanodes, yielding **CN_{TM}@Ru** by a simple protocol at room temperature. The strategic functionalization of the CN terminal groups allows the enhancement of charge separation between the two components and introduces the

WOC in the material. Spectroscopic, optical and electrochemical techniques were used to fully characterize the hybrid system, which presents similarities with the newly reported **CN_{TM}-Ru_{15}**. This functionalization does not impact the overall morphology and structure of the carbon nitride, and at the same time the optical properties were visibly improved, leading to an increased driving force for oxygen evolution. Under photoelectrochemical conditions, the photocurrent increases of more than 40% for **CN_{TM}@Ru** compared to the bare **CN_{TM}** (*J* of 480 μA cm^{-2} *vs.* 280 μA cm^{-2}, respectively) using 1 sun irradiation at the thermodynamic OER potential, doubling the reported photocurrent densities for **CN_{TM}-Ru_{15}** and underlining a better catalyst-material connection and improved charge transfer. The production of oxygen is fairly stable for over 15 hours and the Faradaic efficiency is nearly 80% for **CN_{TM}@Ru** with respect to 55% for **CN_{TM}**, with its low stability of less than 2 h. The values of TON and TOF obtained, 2 x 10^4 and 0.6 s^{-1}, also highlight the increased efficiency of the newly synthetized **CN_{TM}@Ru** compared to the previously reported **CN_{TM}-Ru_{15}**. Thus, we report **CN_{TM}@Ru** as the first case of Ru catalyst-carbon nitride bridged photoanode performing for water oxidation reaction at neutral pH values. Further, photophysical experiments indicate that a fast charge separation and transfer between the material and the anchored Ru-catalyst takes place, which improves with the addition of water as hole scavenger for the following generation of oxygen. The strategic integration of a molecular-based catalyst within CN photoelectrodes represents thus a valid alternative to the supramolecular interaction methodology and a promising potential for further improving CN-based systems in terms of light absorbance, charge separation and stability in neutral medium, giving higher advantages to the hybrid system to be further employed in different environments.

6.4. References

(1) Armaroli, N.; Balzani, V. The Future of Energy Supply: Challenges and Opportunities. *Angew. Chemie - Int. Ed.* **2007**, *46* (1-2), 52–66. https://doi.org/10.1002/anie.200602373.

(2) Nocera, D. G. Solar Fuels and Solar Chemicals Industry. *Acc. Chem. Res.* **2017**, *50* (3), 616–619. https://doi.org/10.1021/acs.accounts.6b00615.

(3) Nocera, D. G. The Artificial Leaf. *Acc. Chem. Res.* **2012**, *45* (5), 767–776.

https://doi.org/10.1021/ar2003013.

(4) Armaroli, N.; Balzani, V. The Hydrogen Issue. *ChemSusChem* **2011**, *4* (1), 21–36. https://doi.org/10.1002/cssc.201000182.

(5) Millet, P. Fundamentals of Water Electrolysis. In *Hydrogen Production: By Electrolysis*; Godula-Jopek, A., Ed.; Wiley-VCH verlag GmbH & Co. KGaA, 2015; pp 33–62. https://doi.org/10.1002/9783527676507.ch2.

(6) Matheu, R.; Garrido-Barros, P.; Gil-Sepulcre, M.; Ertem, M. Z.; Sala, X.; Gimbert-Suriñach, C.; Llobet, A. The Development of Molecular Water Oxidation Catalysts. *Nat. Rev. Chem.* **2019**, *3* (5), 331–341. https://doi.org/10.1038/s41570-019-0096-0.

(7) Garrido-Barros, P.; Gimbert-Suriñach, C.; Matheu, R.; Sala, X.; Llobet, A. How to Make an Efficient and Robust Molecular Catalyst for Water Oxidation. *Chem. Soc. Rev.* **2017**, *46* (20), 6088–6098. https://doi.org/10.1039/c7cs00248c.

(8) Berardi, S.; Drouet, S.; Francàs, L.; Gimbert-Suriñach, C.; Guttentag, M.; Richmond, C.; Stoll, T.; Llobet, A. Molecular Artificial Photosynthesis. *Chem. Soc. Rev.* **2014**, *43* (22), 7501–7519. https://doi.org/10.1039/c3cs60405e.

(9) Dong, G.; Yan, L.; Bi, Y. Advanced Oxygen Evolution Reaction Catalysts for Solar-Driven Photoelectrochemical Water Splitting. *J. Mater. Chem. A* **2023**, *11* (8), 3888–3903. https://doi.org/10.1039/d2ta09479g.

(10) Gunawan, D.; Zhang, J.; Li, Q.; Toe, C. Y.; Scott, J.; Antonietti, M.; Guo, J.; Amal, R. Materials Advances in Photocatalytic Solar Hydrogen Production: Integrating Systems and Economics for a Sustainable Future. *Adv. Mater.* **2024**, *2404618*, 1–37. https://doi.org/10.1002/adma.202404618.

(11) Matheu, R.; Ertem, M. Z.; Benet-Buchholz, J.; Coronado, E.; Batista, V. S.; Sala, X.; Llobet, A. Intramolecular Proton Transfer Boosts Water Oxidation Catalyzed by a Ru Complex. *J. Am. Chem. Soc.* **2015**, *137* (33), 10786–10795. https://doi.org/10.1021/jacs.5b06541.

(12) Creus, J.; Matheu, R.; Peñafiel, I.; Moonshiram, D.; Blondeau, P.; Benet-Buchholz, J.; García-Antón, J.; Sala, X.; Godard, C.; Llobet, A. A Million Turnover Molecular Anode for Catalytic Water Oxidation. *Angew. Chemie - Int. Ed.* **2016**, *55* (49), 15382–15386. https://doi.org/10.1002/anie.201609167.

(13) Hoque, M. A.; Gil-Sepulcre, M.; de Aguirre, A.; Elemans, J. A. A. W.; Moonshiram, D.; Matheu, R.; Shi, Y.; Benet-Buchholz, J.; Sala, X.; Malfois, M.; Solano, E.; Lim, J.; Garzón-Manjón, A.; Scheu, C.; Lanza, M.; Maseras, F.; Gimbert-Suriñach, C.; Llobet, A. Water Oxidation Electrocatalysis Using Ruthenium Coordination Oligomers Adsorbed on Multiwalled Carbon Nanotubes. *Nat. Chem.* **2020**, *12* (11), 1060–1066. https://doi.org/10.1038/s41557-020-0548-7.

(14) Liseev, T.; Howe, A.; Hoque, M. A.; Gimbert-Suriñach, C.; Llobet, A.; Ott, S. Synthetic Strategies to Incorporate Ru-Terpyridyl Water Oxidation Catalysts into MOFs: Direct Synthesis: Vs. Post-Synthetic Approach. *Dalt. Trans.* **2020**, *49* (39), 13753–13759. https://doi.org/10.1039/d0dt01890b.

(15) Grau, S.; Berardi, S.; Moya, A.; Matheu, R.; Cristino, V.; Vilatela, J. J.; Bignozzi, C. A.; Caramori, S.; Gimbert-Suriñach, C.; Llobet, A. A Hybrid Molecular Photoanode for Efficient Light-Induced Water Oxidation. *Sustain. Energy Fuels* **2018**, *2* (9), 1979–1985. https://doi.org/10.1039/c8se00146d.

(16) Matheu, R.; Moreno-Hernandez, I. A.; Sala, X.; Gray, H. B.; Brunschwig, B. S.; Llobet, A.; Lewis, N. S. Photoelectrochemical Behavior of a Molecular Ru-Based Water-Oxidation Catalyst Bound to TiO_2-Protected Si Photoanodes. *J. Am. Chem. Soc.* **2017**, *139* (33), 11345–11348. https://doi.org/10.1021/jacs.7b06800.

(17) Schreier, M.; Luo, J.; Gao, P.; Moehl, T.; Mayer, M. T.; Grätzel, M. Covalent Immobilization of a Molecular Catalyst on Cu_2O Photocathodes for CO_2 Reduction. *J. Am. Chem. Soc.* **2016**, *138* (6), 1938–1946. https://doi.org/10.1021/jacs.5b12157.

(18) Habisreutinger, S. N.; Schmidt-Mende, L.; Stolarczyk, J. K. Photocatalytic Reduction of CO_2 on TiO_2 and Other Semiconductors. *Angew. Chemie - Int. Ed.* **2013**, *52* (29), 7372–7408. https://doi.org/10.1002/anie.201207199.

(19) Wang, X.; Blechert, S.; Antonietti, M. Polymeric Graphitic Carbon Nitride for Heterogeneous Photocatalysis. *Acs Catal.* **2012**, *2* (8), 1596–1606.

(20) Thomas, A.; Fischer, A.; Goettmann, F.; Antonietti, M.; Müller, J. O.; Schlögl, R.; Carlsson, J. M. Graphitic Carbon Nitride Materials: Variation of Structure and Morphology and Their Use as Metal-Free Catalysts. *J. Mater. Chem.* **2008**, *18* (41), 4893–4908. https://doi.org/10.1039/b800274f.

(21) Thangamuthu, M.; Ruan, Q.; Ohemeng, P. O.; Luo, B.; Jing, D.; Godin, R.; Tang, J. Polymer Photoelectrodes for Solar Fuel Production: Progress and Challenges. *Chem. Rev.* **2022**, *122* (13), 11778–11829. https://doi.org/10.1021/acs.chemrev.1c00971.

(22) Volokh, M.; Peng, G.; Barrio, J.; Shalom, M. Carbon Nitride Materials for Water Splitting Photoelectrochemical Cells. *Angew. Chemie - Int. Ed.* **2019**, *58* (19), 6138–6151. https://doi.org/10.1002/anie.201806514.

(23) Barrio, J.; Volokh, M.; Shalom, M. Polymeric Carbon Nitrides and Related Metal-Free Materials for Energy and Environmental Applications. *J. Mater. Chem. A* **2020**, *8* (22), 11075–11116. https://doi.org/10.1039/d0ta01973a.

(24) Zhen, W.; Xue, C. Atomic- and Molecular-Level Functionalizations of Polymeric Carbon Nitride for Solar Fuel Production. *Sol. RRL* **2021**, *5* (2), 1–28. https://doi.org/10.1002/solr.202000440.

(25) Wang, Y.; Liu, L.; Ma, T.; Zhang, Y.; Huang, H. 2D Graphitic Carbon Nitride for Energy Conversion and Storage. *Adv. Funct. Mater.* **2021**, *31* (34), 1–36. https://doi.org/10.1002/adfm.202102540.

(26) Bai, X.; Zhang, X.; Sun, Y.; Huang, M.; Fan, J.; Xu, S.; Li, H. Low Ruthenium Content Confined on Boron Carbon Nitride as an Efficient and Stable Electrocatalyst for Acidic Oxygen Evolution Reaction. *Angew. Chemie - Int. Ed.* **2023**, *62* (38). https://doi.org/10.1002/anie.202308704.

(27) Karjule, N.; Singh, C.; Barrio, J.; Tzadikov, J.; Liberman, I.; Volokh, M.; Palomares, E.; Hod, I.; Shalom, M. Carbon Nitride-Based Photoanode with Enhanced Photostability and Water Oxidation Kinetics. *Adv. Funct. Mater.* **2021**, *31* (25). https://doi.org/10.1002/adfm.202101724.

(28) Karjule, N.; Barrio, J.; Xing, L.; Volokh, M.; Shalom, M. Highly Efficient Polymeric Carbon Nitride Photoanode with Excellent Electron Diffusion Length and Hole Extraction Properties. *Nano Lett.* **2020**, *20* (6), 4618–4624. https://doi.org/10.1021/acs.nanolett.0c01484.

(29) Wen, F.; Pang, L.; Zhang, T.; Huang, X.; Xu, Y.; Li, Y. Fe Doped NiS_2 Derived from Metal-Organic Framework Embedded into g-C_3N_4 for Efficiently Oxygen Evolution Reaction. *Int. J. Hydrogen Energy* **2023**, *48* (86), 33525–33536. https://doi.org/10.1016/j.ijhydene.2023.05.053.

(30) Feng, Y.; Sun, W.; Liang, X.; Dong, X.; Yang, X.; Hu, C.; Li, B.; Yang, J.; Ma, B.; Ding, Y. Mononuclear Ruthenium (II) Complex Covalently Anchored on Melem and g-C_3N_4 as Efficient Heterogeneous Catalysts for Chemical Water Oxidation. *J. Colloid Interface Sci.* **2023**, *643* (December 2022), 480–488. https://doi.org/10.1016/j.jcis.2023.04.053.

(31) Gadolini, S.; Kerber, R. N.; Seljamäe-Green, R. T.; Tong, W.; Farràs, P.; Corbos, E. C. Covalently Anchored Molecular Catalyst onto a Graphitic Carbon Nitride Surface for Photocatalytic Epoxidation of Olefins. *ACS Catal.* **2024**, 14639–14651. https://doi.org/10.1021/acscatal.4c04187.

(32) Salati, M.; Dorchies, F.; Wang, J. W.; Ventosa, M.; González-Carrero, S.; Bozal-Ginesta, C.; Holub, J.; Rüdiger, O.; DeBeer, S.; Gimbert-Suriñach, C.; Durrant, J. R.; Ertem, M. Z.; Gil-Sepulcre, M.; Llobet, A. Covalent Triazine-Based Frameworks with Ru-Tda Based Catalyst Anchored via Coordination Bond for Photoinduced Water Oxidation. *Small* **2024**, *2406375*, 1–9. https://doi.org/10.1002/smll.202406375.

(33) Maeda, K.; Kuriki, R.; Zhang, M.; Wang, X.; Ishitani, O. The Effect of the Pore-Wall Structure of Carbon Nitride on Photocatalytic CO_2 Reduction under Visible Light. *J. Mater. Chem. A* **2014**, *2* (36), 15146–15151. https://doi.org/10.1039/c4ta03128h.

(34) Kuriki, R.; Maeda, K. Development of Hybrid Photocatalysts Constructed with a Metal Complex and Graphitic Carbon Nitride for Visible-Light-Driven CO_2 Reduction. *Phys. Chem. Chem. Phys.* **2017**, *19* (7), 4938–4950. https://doi.org/10.1039/c6cp07973c.

(35) Ma, B.; Chen, G.; Fave, C.; Chen, L.; Kuriki, R.; Maeda, K.; Ishitani, O.; Lau, T. C.; Bonin, J.; Robert, M. Efficient Visible-Light-Driven CO_2 Reduction by a Cobalt Molecular Catalyst Covalently Linked

to Mesoporous Carbon Nitride. *J. Am. Chem. Soc.* **2020**, *142* (13), 6188–6195. https://doi.org/10.1021/jacs.9b13930.

(36) Zhen, W.; Yuan, X.; Shi, X.; Xue, C. Grafting Molecular Cobalt-Oxo Cubane Catalyst on Polymeric Carbon Nitride for Efficient Photocatalytic Water Oxidation. *Chem. - An Asian J.* **2020**, *15* (16), 2480–2486. https://doi.org/10.1002/asia.202000583.

(37) Mondal, S.; Salati, M.; Nicaso, M.; Alber, J.; Segado-Centellas, M.; Volokh, M.; Bo, C.; García, H.; Gil-Sepulcre, M.; Llobet, A.; Shalom, M. Supramolecular Interaction of a Molecular Catalyst with a Polymeric Carbon Nitride Photoanode Enhances Photoelectrochemical Activity and Stability at Neutral pH. *Chem. Sci.* **2024**. https://doi.org/10.1039/d4sc04678a.

(38) Qin, J.; Barrio, J.; Peng, G.; Tzadikov, J.; Abisdris, L.; Volokh, M.; Shalom, M. Direct Growth of Uniform Carbon Nitride Layers with Extended Optical Absorption towards Efficient Water-Splitting Photoanodes. *Nat. Commun.* **2020**, *11* (1), 1–9. https://doi.org/10.1038/s41467-020-18535-0.

(39) Mondal, S.; Sahoo, L.; Banoo, M.; Vaishnav, Y.; Prabhakaran Vinod, C.; Gautam, U. K. Enhancing the Catalytic Activity of Pd Nanocrystals towards Suzuki Cross-Coupling by g-C_3N_4 Photosensitization. *ChemNanoMat* **2024**, *10* (1), 1–11. https://doi.org/10.1002/cnma.202300451.

(40) Ong, W. J.; Tan, L. L.; Chai, S. P.; Yong, S. T.; Mohamed, A. R. Surface Charge Modification via Protonation of Graphitic Carbon Nitride (g-C_3N_4) for Electrostatic Self-Assembly Construction of 2D/2D Reduced Graphene Oxide (rGO)/g-C_3N_4 Nanostructures toward Enhanced Photocatalytic Reduction of Carbon Dioxide to Methane. *Nano Energy* **2015**, *13*, 757–770. https://doi.org/10.1016/j.nanoen.2015.03.014.

(41) Mark, G.; Mondal, S.; Volokh, M.; Xia, J.; Shalom, M. Halogen–Hydrogen Bonding for the Synthesis of Efficient Polymeric Carbon-Nitride Photocatalysts. *Sol. RRL* **2022**, *6* (12), 1–9. https://doi.org/10.1002/solr.202200834.

(42) Zhang, Q.; Chen, X.; Yang, Z.; Yu, T.; Liu, L.; Ye, J. Precisely Tailoring Nitrogen Defects in Carbon Nitride for Efficient Photocatalytic Overall Water Splitting. *ACS Appl. Mater. Interfaces* **2022**, *14* (3), 3970–3979. https://doi.org/10.1021/acsami.1c19638.

(43) Akaike, K.; Aoyama, K.; Dekubo, S.; Onishi, A.; Kanai, K. Characterizing Electronic Structure near the Energy Gap of Graphitic Carbon Nitride Based on Rational Interpretation of Chemical Analysis. *Chem. Mater.* **2018**, *30* (7), 2341–2352. https://doi.org/10.1021/acs.chemmater.7b05316.

(44) Lv, H.; Huang, Y.; Koodali, R. T.; Liu, G.; Zeng, Y.; Meng, Q.; Yuan, M. Synthesis of Sulfur-Doped 2D Graphitic Carbon Nitride Nanosheets for Efficient Photocatalytic Degradation of Phenol and Hydrogen Evolution. *ACS Appl. Mater. Interfaces* **2020**, *12* (11), 12656–12667. https://doi.org/10.1021/acsami.9b19057.

(45) Zhang, J.; Zhang, J.; Dong, C.; Xia, Y.; Jiang, L.; Wang, G.; Wang, R.; Chen, J. Direct Growth of

Polymeric Carbon Nitride Nanosheet Photoanode for Greatly Efficient Photoelectrochemical Water-Splitting. *Small* **2023**, *19* (34), 1–7. https://doi.org/10.1002/smll.202208049.

(46) Zhang, G.; Zhang, J.; Zhang, M.; Wang, X. Polycondensation of Thiourea into Carbon Nitride Semiconductors as Visible Light Photocatalysts. *J. Mater. Chem.* **2012**, *22* (16), 8083–8091. https://doi.org/10.1039/c2jm00097k.

(47) Yu, J.; Wang, K.; Xiao, W.; Cheng, B. Photocatalytic Reduction of CO_2 into Hydrocarbon Solar Fuels over g-C_3N_4-Pt Nanocomposite Photocatalysts. *Phys. Chem. Chem. Phys.* **2014**, *16* (23), 11492–11501. https://doi.org/10.1039/c4cp00133h.

(48) Morgan, D. J. Resolving Ruthenium: XPS Studies of Common Ruthenium Materials. *Surf. Interface Anal.* **2015**, *47* (11), 1072–1079. https://doi.org/10.1002/sia.5852.

(49) Awasthi, M. K.; Rai, R. K.; Behrens, S.; Singh, S. K. Low-Temperature Hydrogen Production from Methanol over a Ruthenium Catalyst in Water. *Catal. Sci. Technol.* **2021**, *11* (1), 136–142. https://doi.org/10.1039/d0cy01470b.

6.5. Supporting information

6.5.1. Materials

All mentioned chemicals were purchased from commercial sources and used directly without further purification. Thiourea (99%) was bought from Acros Organics. Sodium sulphate anhydrous (Na_2SO_4, 99%) was purchased from Loba Chemie, India. Melamine (99%) and 2,2,2-trifluoroethanol (TFE, 99%) were bought from Sigma-Aldrich. Disodium phosphate (Na_2HPO_4 ,98+%) and sodium dihydrogen phosphate (NaH_2PO_4, 96%) were purchased from Alfa Aesar. For the synthesis of Ru based complexes, all the chemicals used in this work were provided by Sigma Aldrich, unless explicitly indicated. $RuCl_3 \cdot xH_2O$ was purchased from Alfa Aesar. The precursor complexes $[RuCl_2(dmso)_4]$ and $[Ru(tda)(dmso)(H_2O)]$ and the equatorial ligand 6,6′-dicarboxylic acid-[2,2′:6′,2′′-terpyridyl] (H_2tda) were prepared according to a reported procedure.[1] All the reagents used for the synthesis of the hybrid photoanodes were bought from Sigma Aldrich, unless otherwise stated. *N*-(3-Dimethylaminopropyl)-*N*′-ethylcarbodiimide (EDC, 97%) was purchased from ThermoFischer Scientific. Fluorine-doped tin oxide (FTO)-coated glass (12–14 Ω sq^{-1}) was purchased from Xop Glass company, Spain. Deionized water

using Millipore Milli Q Direct 3 purification system (18.2 MΩ cm resistivity at room temperature) was used for all the experiments.

6.5.2. Characterization

Powder-XRD

The structural analysis of synthesized films was carried out using X-ray diffraction patterns (XRD), using a PANalytical's Empyrean diffractometer equipped with a position sensitive detector X'Celerator. XRD data was recorded with a scanning time of ~7 min for 2ϑ ranging from 5° to 60° using Cu Kα radiation (λ = 1.54178 Å, 40 kV, 30 mA).

FT-IR

To study the materials' functional groups, Fourier-transform infrared spectroscopy (FTIR, Thermo Scientific Nicolet iS5 FTIR spectrometer equipped with a Si ATR) was used.

SEM

Morphology of the CN films were characterized by scanning electron microscopy (SEM) using a FEI Verios high-resolution SEM, which is equipped with a FEG source and a through-lens detector (secondary electrons) operated at U_0 = 3.5 kV and I = 25 pA.

UV-vis diffuse reflectance spectroscopy

UV–vis diffuse reflectance spectroscopy (Cary 100 spectrophotometer, equipped with a diffuse reflectance accessory) and photoluminescence spectroscopy (Horiba Scientific FluroMax 4 spectrofluorometer) were performed to study the optical properties. The excitation wavelength (λ_{ex}) was 355 nm and the emission wavelength (λ_{em}) was 460 nm.

XPS and UPS

X-ray photoelectron spectroscopic (XPS) data were obtained from an X-ray photoelectron spectrometer ESCALAB 250 ultrahigh vacuum (1×10^{-9} bar) device with an Al Kα X-ray source and a monochromator. The X-ray beam size was 500 µm. All spectra were calibrated relative to a carbon C 1s peak, positioned at 284.8 eV, to correct the charging effect. The deconvolution of the XPS curves was performed through Voigt function with *Fityk* (version 1.3.1) software. For the E_{VB} calculation, 20.82 eV was considered as the He(I) ionization energy, 4.44 eV as the conversion value from absolute vacuum scale to normal hydrogen electrode (NHE) at pH 0,[2] and the first and last

electron excitations ($E_{B,i}$ and $E_{B,f}$ of the spectra) were taken from the plotted data. The conversion equation is the following (Equation S1):

$$E_{VB} \text{ (V } vs\text{. NHE, pH 0)} = [20.82 \text{ eV} - (E_{B,f} - E_{B,i})] - 4.44 \quad \text{(S1)}$$

ICP-MS

The determination of Ru in solids was made by Induced coupled plasma-mass spectrometry (ICP-MS), using Agilent instrument, model 7900. A quantity between 1 and 5 mg of **CN_{TM}@Ru** sample were weighted with a Microbalance MX5 from Mettler Toledo, and later digested, as duplicates, in a microwave digestor Milestone, model Ultrawave, with a mixture of HNO_3 and HCl concentrated, analyzing blanks in parallel.

TAS measurements

Transient absorption experiments were performed using an OPO System Ekspla (EKS-NT342C-10) coupled with an UV extension (EKS-NT342C-SH-SFG) as the excitation source and an Edinburgh Instruments detection system (LP980) coupled with an ICCD camera (Andor iStar CCD 320T). Optically diluted samples (*A* ca. 0.7 at excitation wavelength) in acetonitrile were used. All measurements were done upon laser excitation at 300 nm in quartz cuvettes (1 cm optical pathlength) and at room temperature (25 °C), in the presence of N_2, O_2 or MeOH.

6.5.3. PEC and electrochemical measurements

Photoelectrochemical experiments

All the photoelectrochemical measurements were performed using a three-electrode configuration system on a PalmSens3 potentiostat. A Pt foil (1.0 cm^2) and Ag/AgCl (saturated KCl) were used as the counter- and reference-electrode, respectively. Phosphate buffer solution, (0.1 M, pH 7) was used as the electrolyte for the photoelectrochemical experiments. The photoanode was dipped into electrolyte medium in a custom-made Teflon cell. The obtained potentials were converted to the reversible hydrogen electrode (RHE) scale using Equation S2 below reported:

$$V_{RHE} = V_{Ag/AgCl} + (0.0591 \times \text{pH}) + 0.197 \quad \text{(S2)}$$

Photocurrents were recorded at bias 1.23 V *vs.* RHE using illumination from a solar simulator (Newport 300 W ozone-free Xe arc lamp, equipped with water and air mass

AM 1.5 G filters). 1 sun illumination was calibrated by means of a silicon photodiode (Newport power meter model 919-P) providing total light of 100 mW·cm^2 to the photoelectrode.

Incident photon-to-current conversion efficiency (IPCE)

For IPCE measurement, the following Equation S3 was used:

$$\mathrm{IPCE}\ (\%) = \frac{J\left(\mathrm{mA\ cm^{-2}}\right) \cdot 1240}{\lambda(\mathrm{nm}) \cdot I_{\mathrm{incident}}(\mathrm{mW\ cm^{-2}})} \times 100\% \quad \text{(S3)}$$

where J is the measured photocurrent density, I_{incident} is the incident illuminating power density, and λ is the wavelength of the incident monochromic light.

Electrochemical impedance spectroscopy (EIS) and Mott-Schottky experiments

EIS and Mott-Schottky measurements were performed using a three-electrode system on an Autolab potentiostat (Metrohm, PGSTAT302N). NaH_2PO_4/Na_2HPO_4 aqueous solution (pH 7, I = 0.1 M) was used for impedance measurement. Nyquist plots of the films were measured at an applied potential of 1.23 V *vs.* RHE with frequency range from 40 kHz to 100 mHz and 5 mV amplitude of the sinusoidal perturbation. Mott-Schottky measurements were conducted at 500, 1000 and 2000 Hz frequencies in a range from -0.2 V to 1.8 V *vs.* RHE.

For the subsequent calculation of the valence band, Equation S4 was used:

$$E_{VB}\ (\mathrm{V}\ vs.\ \mathrm{NHE,\ pH\ 0}) = E_{CB} - E_{gap} \quad \text{(S4)}$$

O_2 detection experiments

The O_2 production for **CN_{TM}** and **CN_{TM}@Ru** films in phosphate buffer solution (pH 7, I = 0.1 M) was detected using a fiber optic oxygen meter under chronoamperometric condition (1.23 V vs. RHE, 1 sun illumination). A two-compartment cell (H-cell) was used and tightly sealed with a rubber septum for each chamber and parafilm to avoid any gas leakage. The electrolyte solution was purged with Ar for 30 min before the experiments. The O_2 quantification was performed for the duration of 1 hour, as shown in Fig. S6. FE was calculated using Equations S5 and S6:

$$n = \frac{I \cdot t}{z \cdot F} \quad \text{(S5)}$$

$$\mathrm{FE}(\%) = \frac{\text{Experimental } \mu\text{mol of } O_2}{\text{Theoretical } \mu\text{mol of } O_2} \times 100\% \quad \text{(S6)}$$

Where *n* is the O_2 amount (measured in mol), *I* stands for the current (A), *z* is the number of transferred electrons (for O_2 evolution, *z* = 4), *t* is the time (s), and *F* is the Faraday constant (96485 C mol^{-1}).

6.5.4. Synthetic procedures

CN_{TM} films fabrication

The film fabrication used follows almost entirely the procedure reported in the last Chapter 5 (see supporting information, *section 5.5.4*).

CN_{TM}: 40 g of thiourea were firstly grinded in a mortar (to give good homogeneity to the samples) and later dissolved in 40 mL of MilliQ water heated up to 85°C for 1 h (stirring at 250 rpm), until complete saturation of the solution. The FTO electrodes were then rapidly dipped inside the saturated solution (1 second), after blowing on the surface to get the film forming on top redissolved. The process was repeated 3 times, letting the electrodes dry for 5 minutes after each deposition. The electrodes were finally placed in the oven (70°C for 1 h) and then in the furnace for annealing.[3]

For the annealing procedure, 1 g of melamine powder was added at the bottom surface of each tube (during annealing the melamine evaporates and diffuses onto the surface of the electrodes). The electrodes were then placed inside, near to the outlet of the tube, which were then sealed with aluminum foil. The tubes are placed in the furnace, where N_2 is flowed at 160 mL/min. Conditions of method: (i) ramp from 50°C to 120°C in 1 hour; (ii) ramp to 500°C in 76 minutes; (iii) isotherm at 500°C for 2 hours; (iv) ramp to 40°C in 1 hour.

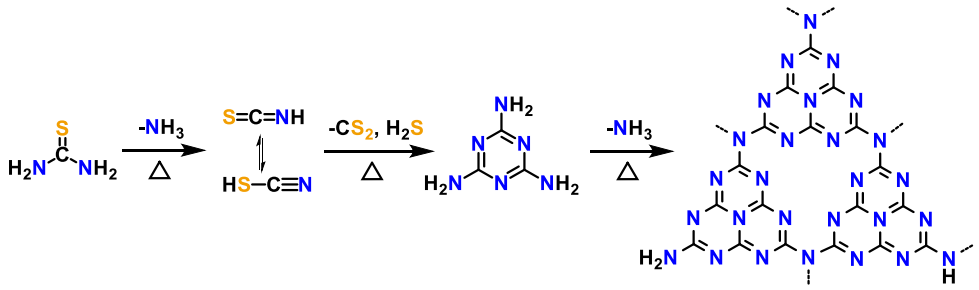

***Scheme S1**. Simplified reaction pathway for the carbon nitride formation starting from thiourea.*[4]

Synthesis of the [Ru(tda)(pyCOOH)$_2$] catalyst

The ligand 6,6'-Dicarboxylic acid-[2,2':6',2"-terpyridyl] (H_2tda) and the precursor complexes [$RuCl_2(dmso)_4$] and [Ru(tda)(dmso)(H_2O)] were synthesized according to the literature.[1,5] The synthesis of the [Ru(tda)(pyCOOH)$_2$] catalyst was later performed following the reported procedure by Liseev *et al.* (Scheme S2).[6]

[Ru(tda)(pyCOOH)$_2$]: In a 25 mL flask, 30 mg [Ru(tda)(dmso)(H_2O)] (0.06 mmol) and 22.2 mg of isonicotinic acid (0.18 mmol, 3 eq.) were degassed, before adding 6 mL of degassed water. The reaction was left stirring under reflux in N_2 atmosphere for 1 day. After stopping the reaction, the solution (already some precipitate appeared) was left overnight in the fridge, and the precipitate obtained was immediately filtered and washed with cold water. The solid was then washed with acetone and Et_2O, dried and finally analyzed (20 mg obtained, 60% yield).

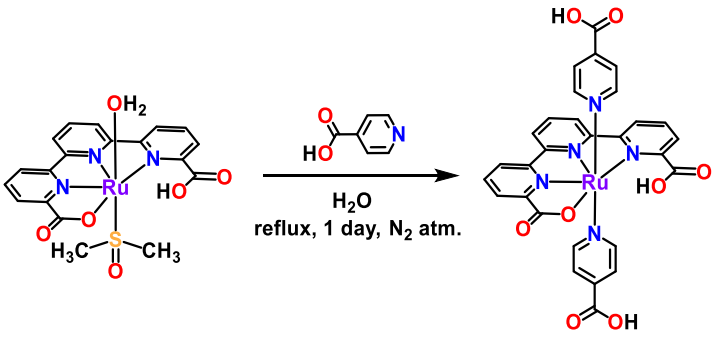

***Scheme S2**. Synthetic reaction for [Ru(tda)(pyCOOH)$_2$].*

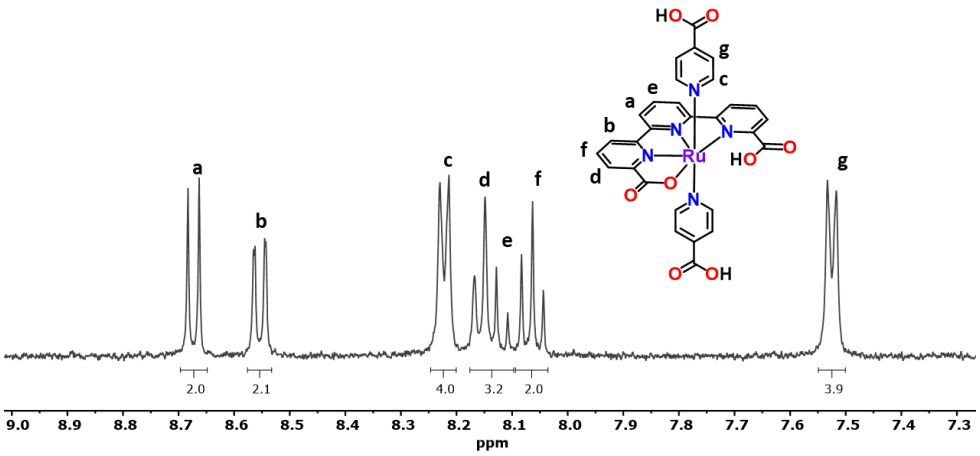

***Figure S1.** ^{1}H NMR (CD_3OD, 300 MHz) of [Ru(tda)(pyCOOH)$_2$].*

Functionalization of CN films with [Ru(tda)(pyCOOH)$_2$]: covalent anchoring

For the synthesis of the hybrid electrodes through covalent bonding (namely **CN$_{TM}$@Ru**), an amidation reaction was performed, following and adapting the strategy used by Ma *et al.* (Schemes S3-S4).[7]

CN$_{TM}$@Ru: 1.2 mg of [Ru(tda)(pyCOOH)$_2$] (1.8 umol) were dissolved in 10 mL of DMF with 3 µL of triethylamine (TEA, 12 eq.), and 3 µL of 1-ethyl-3-(3-dimethylaminopropyl)carbodiimide (EDC, 12 eq.) were added to the solution. After 20 minutes stirring at RT, 3 mg of 1-hydroxybenzotriazole hydrate (HOBt, 12 eq.) were dissolved in 10 mL of DMF and added to the solution. The solution was then left under stirring at RT for 1 hour. Finally, CN$_{TM}$ electrodes (4 in total) were introduced in the solution, placing them close to the walls, and the stirring was kept for 7 days at RT, covering the flask with aluminum foil. The electrodes were then removed from the solution and rinsed with DMF and deionized water. Finally, they were dried at 60°C for 2 h and under vacuum overnight.

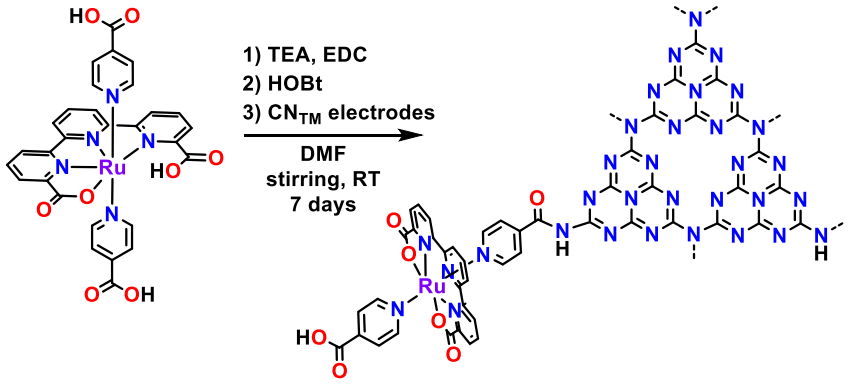

Scheme S3. *Amidation reaction between **CN$_{TM}$** and Ru(tda) complex through EDC/HOBt addition, normally used for peptides formation.*[7]

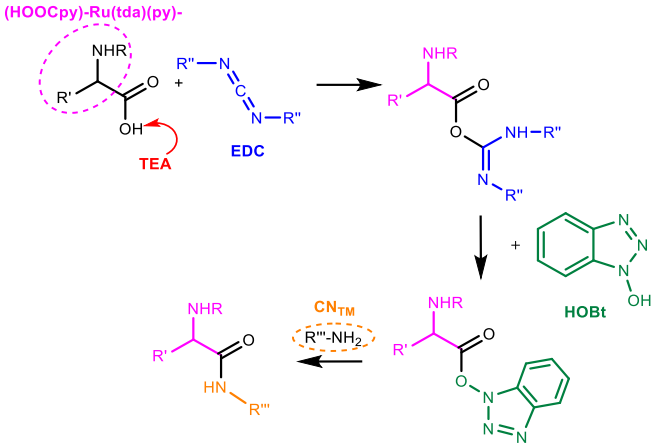

Scheme S4. *Reaction mechanism for amidation through coupling process with EDC and HOBt.*

6.5.5. Experimental results

Spectroscopic and optical characterization and microscopy

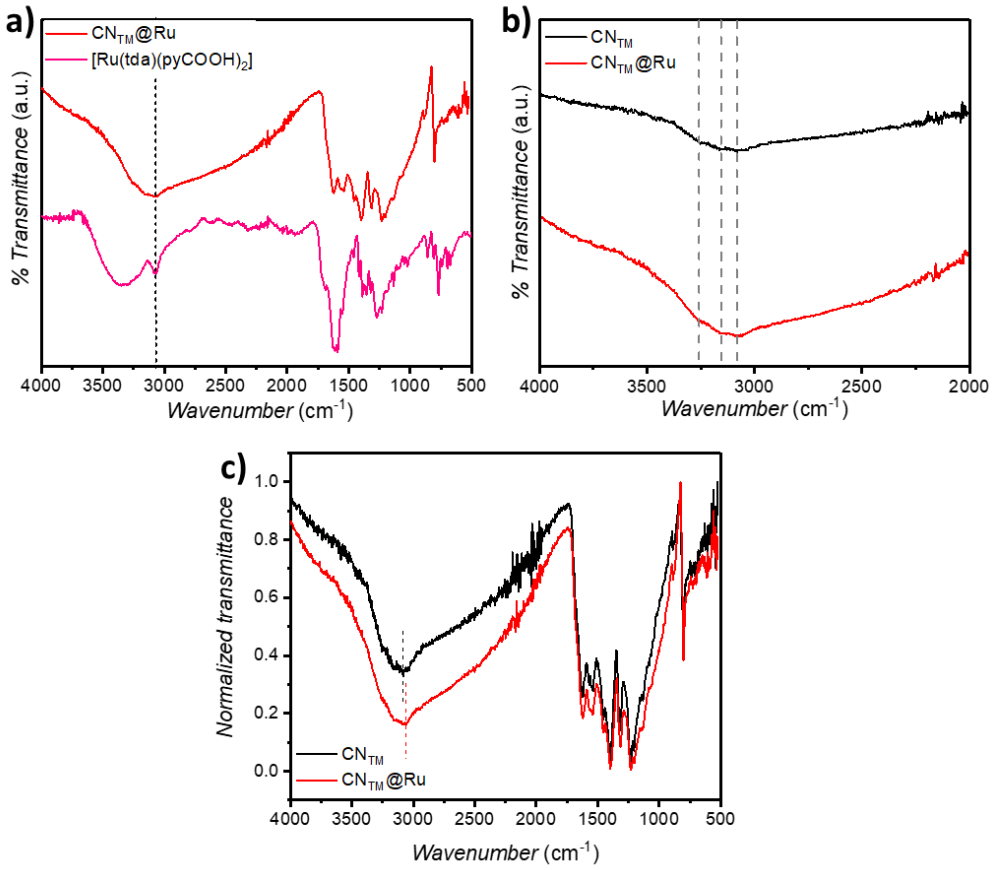

Figure S2. *(a) FT-IR spectra of* ***CN$_{TM}$@Ru*** *(red) and [Ru(tda)(pyCOOH)$_2$] (pink); (b) enlargement of the FT-IR spectra for* ***CN$_{TM}$*** *(black) and* ***CN$_{TM}$@Ru*** *(red) of Figure 1c, in the region 4000-2000 cm^{-1}.*

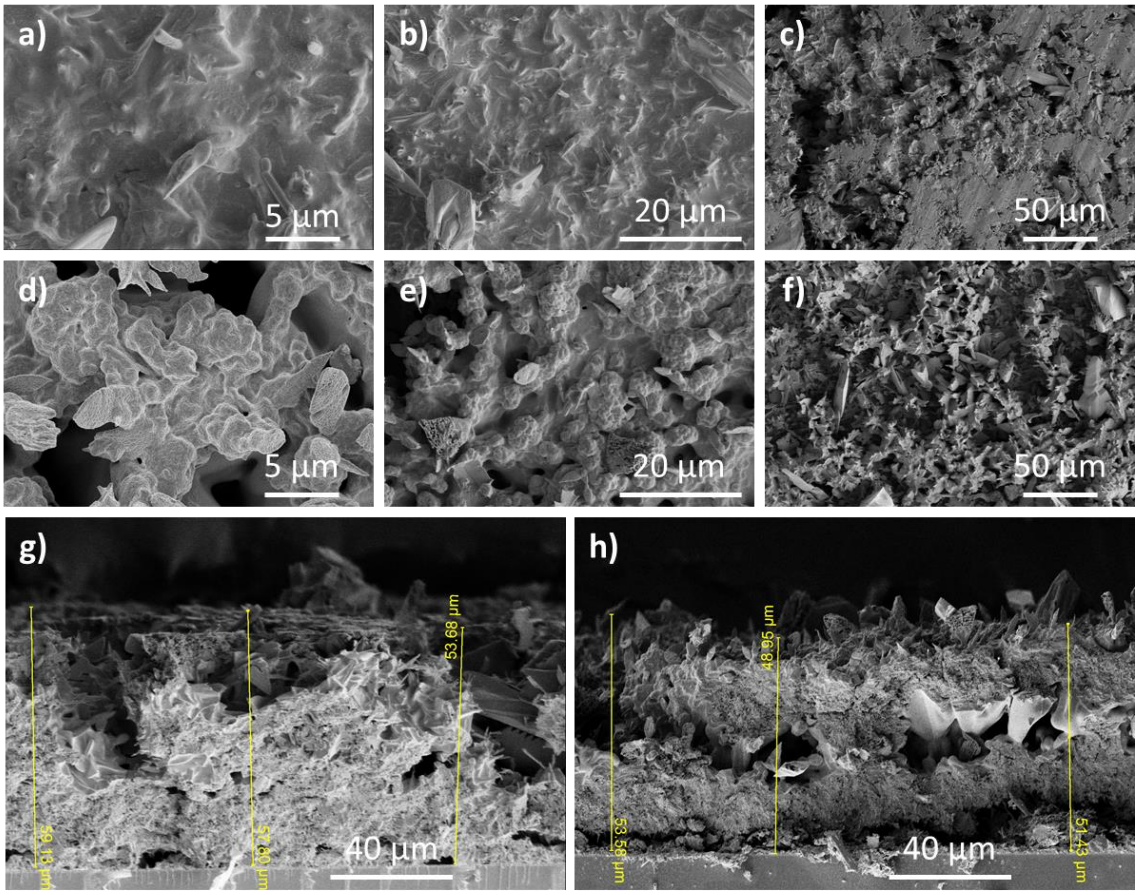

Figure S3. *SEM top-view images of* ***CN$_{TM}$*** *(a,b,c) and* ***CN$_{TM}$@Ru*** *(d,e,f) at a magnification of 5 µm (a,d), 20 µm (b,e) and 50 µm (c,f). SEM cross-section images of* ***CN$_{TM}$*** *(g) and* ***CN$_{TM}$@Ru*** *(h).*

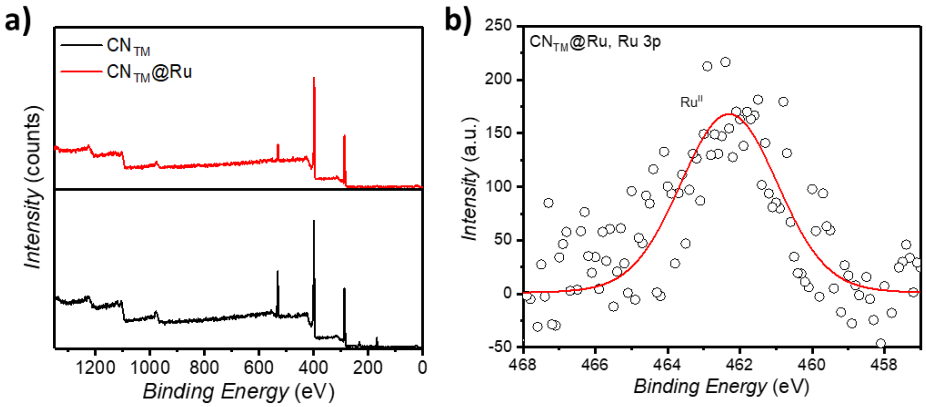

Figure S4. *(a) Survey XPS spectra for* ***CN$_{TM}$*** *and* ***CN$_{TM}$@Ru****. (b) High-resolution Ru 3p XPS spectrum for* ***CN$_{TM}$@Ru****.*

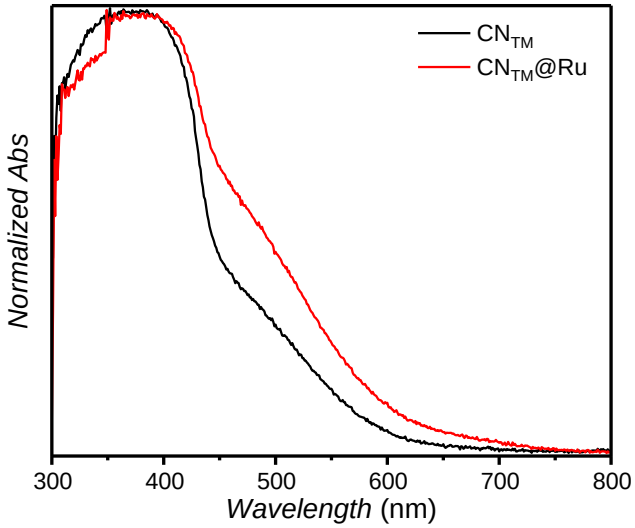

Figure S5. *UV-vis absorption spectra, obtained through DRS spectra after normalization of the signal, for* ***CN$_{TM}$*** *(black) and* ***CN$_{TM}$@Ru*** *(red).*

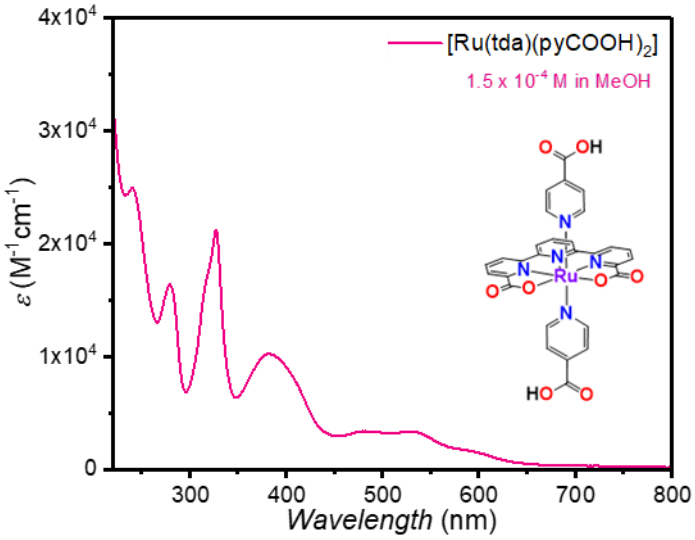

Figure S6. *UV-vis absorption spectrum of [Ru(tda)(pyCOOH)$_2$] catalyst (1.5 x 10^{-4} M in MeOH).*

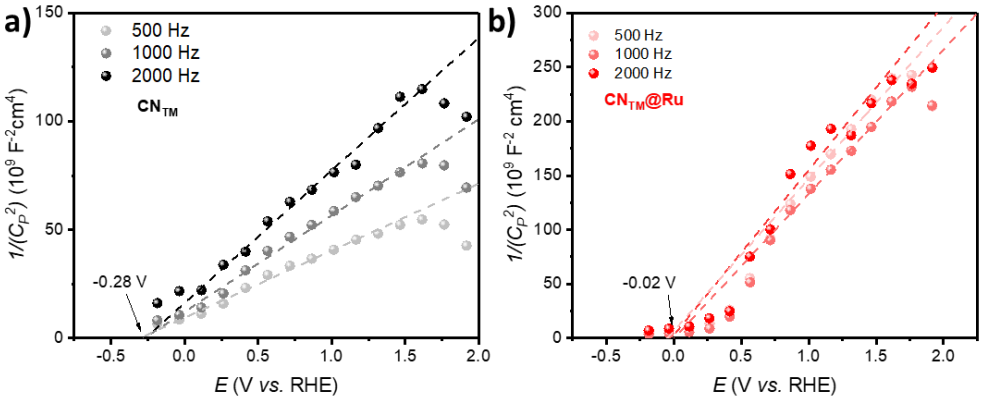

Figure S7. *Mott-Schottky plot for* ***CN$_{TM}$*** *(a) and* ***CN$_{TM}$@Ru*** *(b). Conditions of measurements:* ***CN$_{TM}$*** *and* ***CN$_{TM}$@Ru*** *as working electrodes, Ag/AgCl (sat. KCl) as reference electrode and Platinum plate (1 cm^2 of area) as counter electrodes, phosphate buffer solution (pH 7, 0.1 M ionic strength) as electrolyte, dark conditions.*

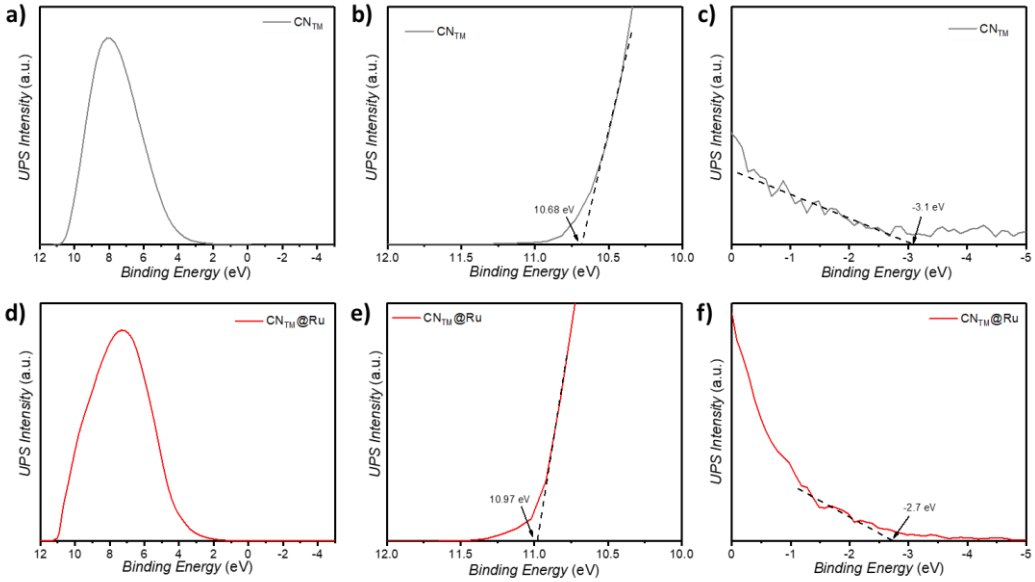

Figure S8. *UPS spectra of* ***CN$_{TM}$*** *(a-c) and* ***CN$_{TM}$@Ru*** *(d-f). Spectra (a,d) show the full UPS spectra in the range from -5 to 12 eV; spectra (b,e) show the enlargement of the corresponding spectra for the last electron excitation (extrapolation of E_{Bf}); spectra (c,f) show the enlargement of the corresponding spectra for the first electron excitation (extrapolation of E_{Bi}).*

Electrochemical and photoelectrochemical characterization

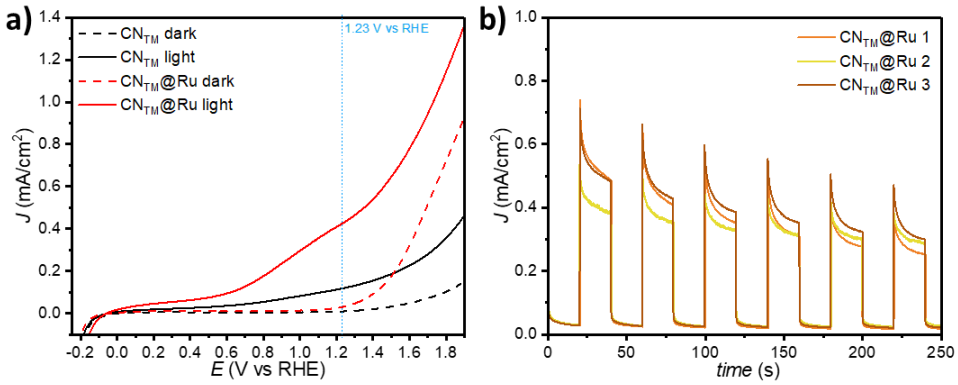

***Figure S9**. (a) Linear sweep voltammetry (LSV) of **CN$_{TM}$** and **CN$_{TM}$@Ru** electrodes (phosphate buffer, pH 7) in the dark and under 1 sun illumination, 20 mV/s of scan rate. (b) Chronoamperometry (current densities vs. time) of **CN$_{TM}$@Ru** film replicates in phosphate buffer (pH 7, I = 0.1 M) at 1.23 V$_{RHE}$ upon on/off 1 sun illumination.*

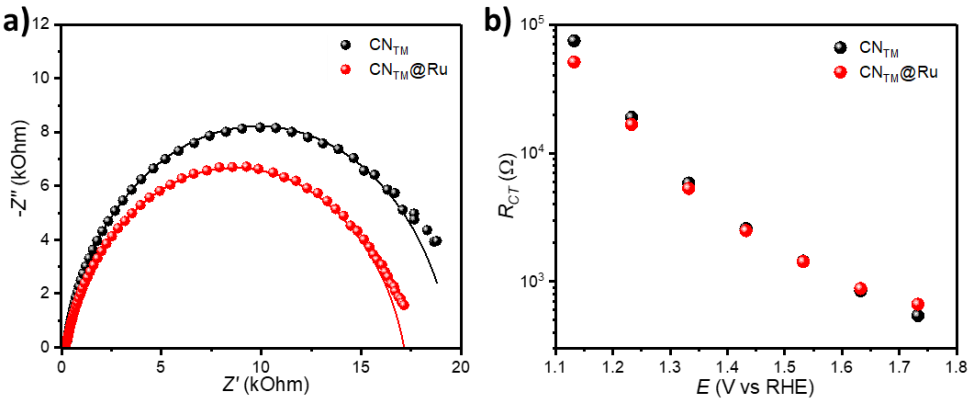

***Figure S10**. (a) Nyquist plot of **CN$_{TM}$** (black dots) and **CN$_{TM}$@Ru** (red dots) films at 1.23 V vs. RHE (the lines represent the fitted data); (b) Charge transfer resistance (R$_{CT}$) of **CN$_{TM}$** (black dots) and **CN$_{TM}$@Ru** (red dots) electrodes at different applied potentials.*

Oxygen evolution experiments

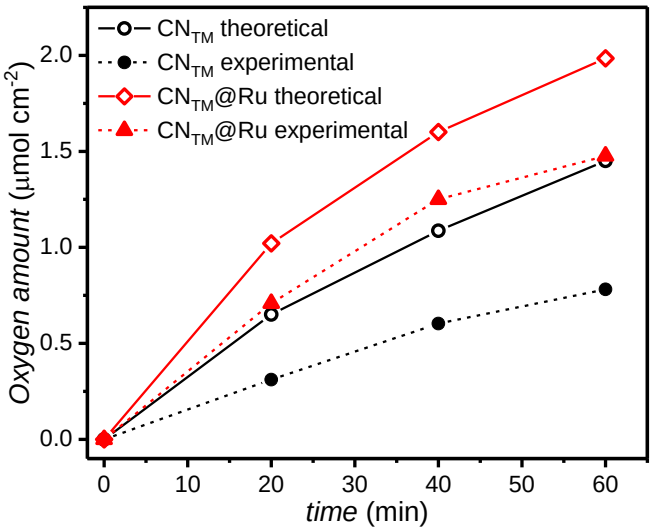

Figure S11. *Amount of O_2 produced over time using* ***CN_{TM}@Ru*** *(red solid line) and* ***CN_{TM}*** *(black solid line) electrodes in phosphate buffer (pH 7, 0.1 M) at 1.23 V_{RHE} under 1 sun illumination, compared to the theoretical amount of O_2 for* ***CN_{TM}*** *(black dotted line) and* ***CN_{TM}@Ru*** *(red dotted line).*

Table S1. *Average content of Ru metal found by ICP-MS in* ***CN_{TM}@Ru*** *samples.*

	Amount sample analyzed (mg)	µg (Ru) g^{-1} (sample)	% Ru	µmol (Ru) g^{-1} (sample)
CN_{TM}@Ru	5	19	1.9×10^{-3}	0.19
CN_{TM}@Ru after catalysis	5	13	1.3×10^{-3}	0.13

Table S2. *Calculated TON and TOF from the O_2 amount detected over 1 hour, photoelectrocatalysis at 1.23 V vs. RHE as applied potential and 1 sun of irradiation intensity, in 7-phbf as electrolyte.*

	Time (min)	µmol O_2 cm^{-2}	FE (%)[a]	TON[b]	TOF (h^{-1})[c]
CN_{TM}	60	0.78	55	—	—
CN_{TM}@Ru	60	1.48	78	1571	2262

[a] The Faradaic efficiency reported was calculated after 40 min of experiment, representing the maximum value that was reached during the measurement, comparing experimental and theoretical data. [b] The value of TON was calculated considering the total amount of O_2 produced in mol, divided by the mol of Ru found through ICP-MS. [c] The value of TOF was calculated considering the total amount of O_2 produced in mol, divided by the mol of Ru found through ICP-MS and the time (in hours) when the rate of O_2 production is faster (20 min).

Characterization after catalysis

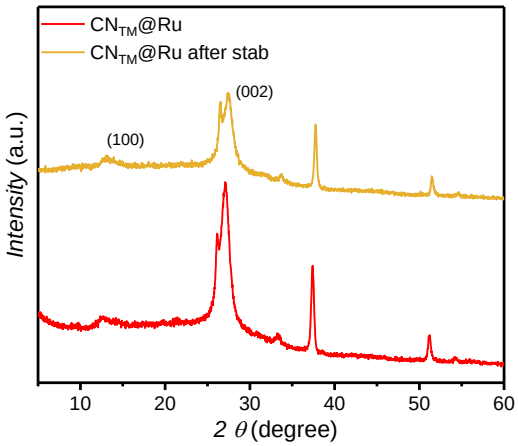

Figure S12. *PXRD spectra of **CN_{TM}@Ru** (red) compared to **CN_{TM}@Ru** after catalysis (orange).*

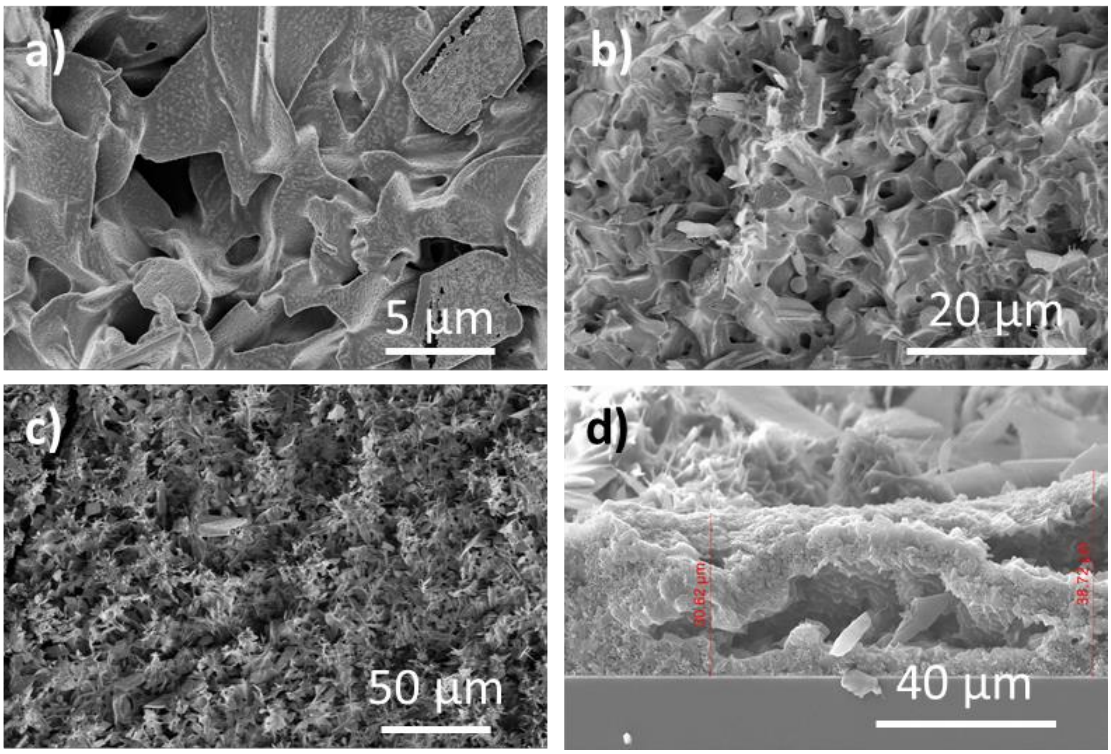

Figure S13. *SEM top-view images of* ***CN_{TM}@Ru*** *after catalysis at a magnification of 5 µm (a), 20 µm (b) and 50 µm (c). SEM cross-section image of* ***CN_{TM}@Ru*** *after catalysis (d).*

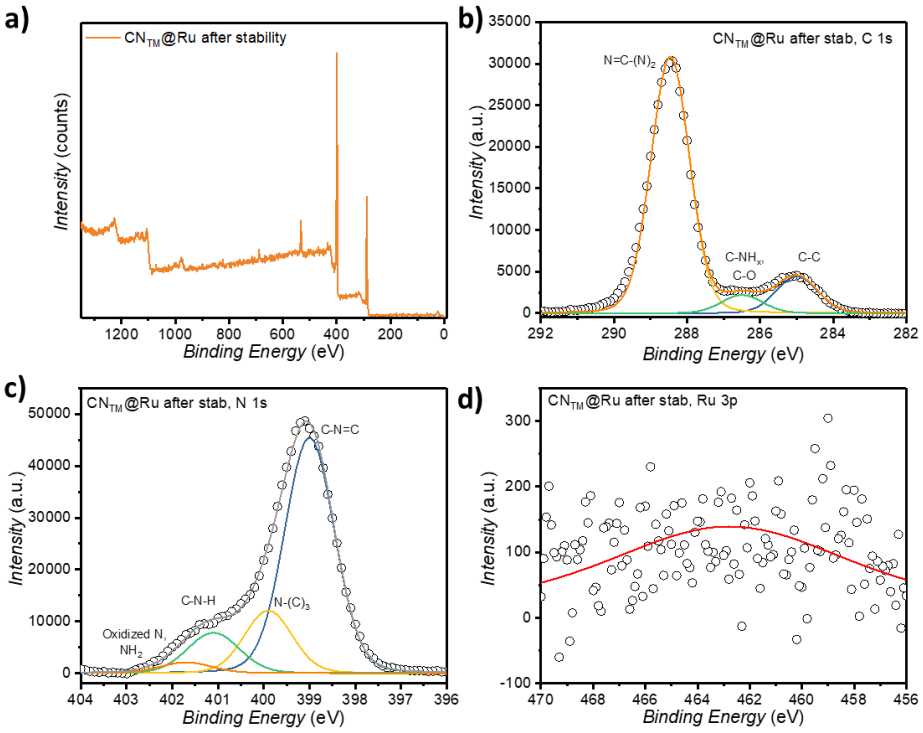

***Figure S15**. XPS survey spectrum (a) and high-resolution C 1s (b), N 1s (c) and Ru 3p (d) XPS spectra for **CN_{TM}@Ru** after catalysis.*

TAS measurements

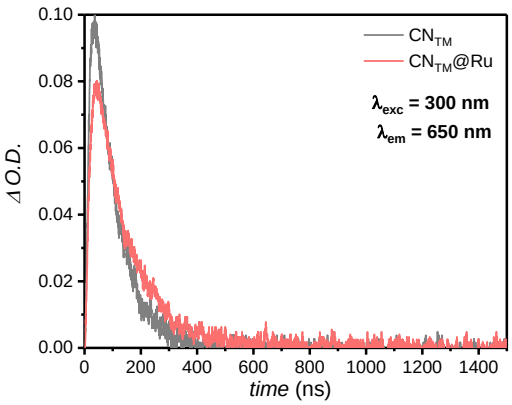

***Figure S16.** Transient absorption decays (plotted in difference of optical density, ΔOD) for **CN_{TM}** (grey) and **CN_{TM}–Ru_{15}** (light-red) dispersions in MeCN, monitored at 650 nm under N_2 atmosphere, upon laser excitation at 300 nm.*

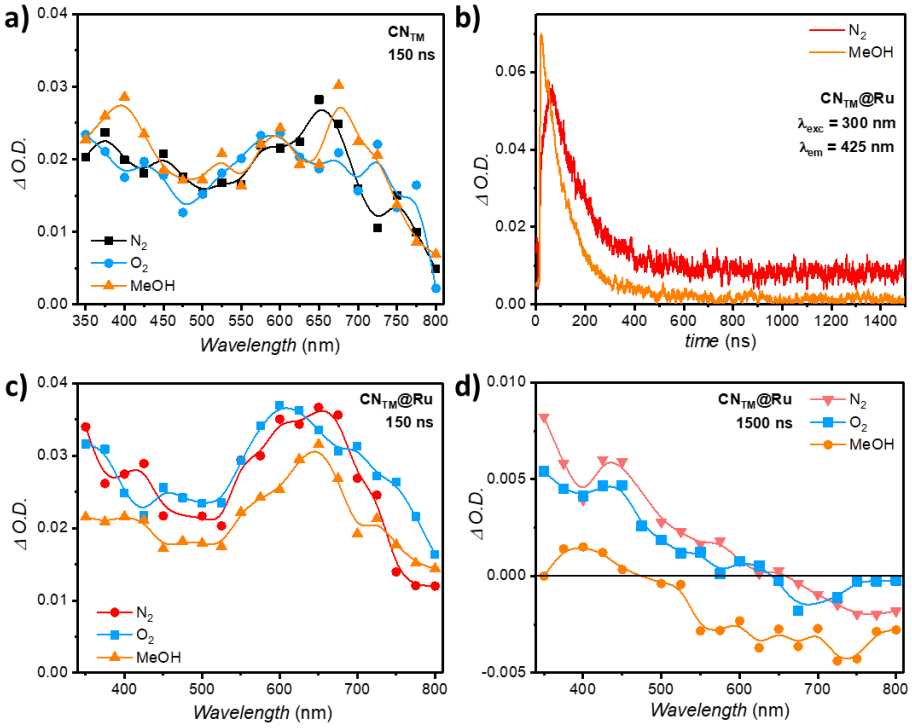

Figure S17. *(a) Transient absorption spectra of* ***CN$_{TM}$*** *dispersion in MeCN acquired at 150 ns in N_2 atmosphere (black squares), with O_2 (light-blue circles) and with MeOH (orange triangles). (b) Transient absorption decays of* ***CN$_{TM}$@Ru*** *dispersions in MeCN, monitored at 425 nm upon laser excitation at 300 nm, under N_2 atmosphere (red) and with MeOH (orange). (c) Transient absorption spectra of* ***CN$_{TM}$@Ru*** *dispersion in MeCN acquired at 150 ns in N_2 atmosphere (red circles), with O_2 (light-blue squares) and with MeOH (orange triangles). (d) Transient absorption spectra of* ***CN$_{TM}$@Ru*** *dispersion in MeCN acquired at 1500 ns in N_2 atmosphere (light-red triangles), with O_2 (light-blue squares) and with MeOH (orange circles).*

Table S3. *Lifetime of the charge separated states calculated for* ***CN$_{TM}$*** *and* ***CN$_{TM}$@Ru*** *in different conditions.*

Emission wavelength	τ CN$_{TM}$ (N_2) (ns) [a]	τ CN$_{TM}$@Ru (N_2) (ns) [a]	τ CN$_{TM}$@Ru (MeOH) [a]
425 nm	95	131 (1); > 1500 (2)	112
650 nm	83	120	-

[a] The charge separated states lifetime was calculated through exponential fitting of the curves obtained, using the following equation: $A = A_0\, e^{-t/\tau}$, where A is the final signal, A_0 is the signal at t_0 after excitation, t is the time of the experiment after excitation and τ is the lifetime of charge separated states.

6.5.6. References

(1) Matheu, R.; Benet-Buchholz, J.; Sala, X.; Llobet, A. Synthesis, Structure, and Redox Properties of a Trans-Diaqua Ru Complex That Reaches Seven-Coordination at High Oxidation States. *Inorg. Chem.* **2018**, *57* (4), 1757–1765. https://doi.org/10.1021/acs.inorgchem.7b02375.

(2) Tsiplakides, D.; Vayenas, C. G. The Absolute Potential Scale in Solid State Electrochemistry. *Solid State Ionics* **2002**, *152-153*, 625–639. https://doi.org/10.1016/S0167-2738(02)00396-X.

(3) Qin, J.; Barrio, J.; Peng, G.; Tzadikov, J.; Abisdris, L.; Volokh, M.; Shalom, M. Direct Growth of Uniform Carbon Nitride Layers with Extended Optical Absorption towards Efficient Water-Splitting Photoanodes. *Nat. Commun.* **2020**, *11* (1), 1–9. https://doi.org/10.1038/s41467-020-18535-0.

(4) Zhang, G.; Zhang, J.; Zhang, M.; Wang, X. Polycondensation of Thiourea into Carbon Nitride Semiconductors as Visible Light Photocatalysts. *J. Mater. Chem.* **2012**, *22* (16), 8083–8091. https://doi.org/10.1039/c2jm00097k.

(5) Hoque, M. A.; Gil-Sepulcre, M.; de Aguirre, A.; Elemans, J. A. A. W.; Moonshiram, D.; Matheu, R.; Shi, Y.; Benet-Buchholz, J.; Sala, X.; Malfois, M.; Solano, E.; Lim, J.; Garzón-Manjón, A.; Scheu, C.; Lanza, M.; Maseras, F.; Gimbert-Suriñach, C.; Llobet, A. Water Oxidation Electrocatalysis Using Ruthenium Coordination Oligomers Adsorbed on Multiwalled Carbon Nanotubes. *Nat. Chem.* **2020**, *12* (11), 1060–1066. https://doi.org/10.1038/s41557-020-0548-7.

(6) Liseev, T.; Howe, A.; Hoque, M. A.; Gimbert-Suriñach, C.; Llobet, A.; Ott, S. Synthetic Strategies to Incorporate Ru-Terpyridyl Water Oxidation Catalysts into MOFs: Direct Synthesis: Vs. Post-Synthetic Approach. *Dalt. Trans.* **2020**, *49* (39), 13753–13759. https://doi.org/10.1039/d0dt01890b.

(7) Ma, B.; Chen, G.; Fave, C.; Chen, L.; Kuriki, R.; Maeda, K.; Ishitani, O.; Lau, T. C.; Bonin, J.; Robert, M. Efficient Visible-Light-Driven CO_2 Reduction by a Cobalt Molecular Catalyst Covalently Linked to Mesoporous Carbon Nitride. *J. Am. Chem. Soc.* **2020**, *142* (13), 6188–6195. https://doi.org/10.1021/jacs.9b13930.


6

Chapter 7

General conclusions


7

In the current thesis, the work of four different projects based on photocatalytic (PC) and photoelectrochemical (PEC) solar fuel generation has been presented in four experimental chapters. Chapters 3 and 4 focused on the implementation of covalent triazine frameworks (CTF) with molecular catalysts covalently anchored for the water oxidation and CO_2 reduction half-reactions. Chapters 4 and 5 analyzed the different functionalization of carbon nitride photoanode with molecular and oligomeric catalysts for light-induced water oxidation, to understand the role of the catalyst on the surface and its effect on the overall efficiency of the photoanode. Considering the objectives proposed in Chapter 2 of the present thesis and according to the experimental results presented above, the conclusions and the outlook for each of the systems are summarized here below.

Chapter 3:

- A novel CTF with a dangling pyridyl group has been successfully synthesized, employing a room temperature procedure to avoid the material carbonization. The bare CTF has been then functionalized *via* covalent anchoring with the [Ru(tda)(py)$_2$] molecular catalyst (where *tda*$^{2-}$ is [2,2':6',2''-terpyridine]-6,6''-dicarboxylate and *py* is pyridine), yielding the named **Ru-CTF** hybrid material.
- The full spectroscopic characterization of the molecular precursors of the new **CTF** has been reported and the optical, structural and morphological properties of **CTF** and **Ru-CTF** have been analyzed, indicating **Ru-CTF** as an optimal molecular hybrid system for light-induced water oxidation (WO). The content of Ru metal has also been measured, confirming a 14% functionalization of the pyridyl groups.
- The photocatalysis experiments were performed using **Ru-CTF** suspended in pH 7 phosphate buffer solution in the presence of sodium persulfate as sacrificial agent and 300 mW/cm^2 light intensity. The measurements of oxygen produced by **Ru-CTF** provided with TONs and TOFs of 220 and 17 h^{-1}, respectively, outperforming the best CTF materials reported so far. In the same conditions, blank experiments with **CTF** were carried out, confirming the high efficiency of the hybrid material thanks to the Ru-based catalyst included in the structure.

- Photophysical studies proved the enhancement of the charge separation for **Ru-CTF** compared to the bare **CTF**, providing an almost unitary quenching of the emission spectrum and providing with lower recombination rates for **Ru-CTF**. Further computational studies confirmed the formation upon light excitation of a long-lived charge separated state, where the positive charge is located on the Ru center and the negative charge on the CTF moiety.

Chapter 4:

- A novel synthesis of the CTF described in Chapter 3 was performed via trimerization, using two different monomers to obtain **p-CTF** and **p-CTF-py**, the second one maintaining the dangling pyridyl group in the structure. The combination of the two organic polymers with four different Co-based molecular catalysts (cobalt phthalocyanine, **CoPc**; cobalt tetra-amino phthalocyanine, **CoTAPc**; cobalt perfluorinated phthalocyanine, **CoFPc**; cobalt tetra-carboxyl phthalocyanine, **CoTCPc**) was then carried out, to obtain **CoPc@p-CTF-py**, **CoTAPc@p-CTF-py**, **CoFPc@p-CTF-py**, **CoTCPc@p-CTF-py** and **CoTCPc@p-CTF**.
- The optical, morphological and spectroscopic characterization was performed for all the hybrid systems and the coordination of the Co catalysts to the pyridyl group of **p-CTF-py** was studied through the charge separation effect. For the case of **CoTCPc@p-CTF**, the catalyst was determined as supramolecularly interacting with the material (CH-π or π-π), while in **CoTCPc@p-CTF** system, the Co complex is mainly anchored *via* covalent bonding .
- The improved charge separation obtained in **CoTCPc@p-CTF-py** system provided with efficient and extremely selective CO_2 photoreduction to CO in $KHCO_3$ aqueous buffer, achieving a yield of around 460 µmol g^{-1} h^{-1} and a high TON of 560 within 48 h with no deactivation or detectable H_2. The molecular hybrid colloid represents the most performant example reported so far for CO_2 reduction in water with earth abundant elements only.

Chapter 5:

- The design of a porous carbon nitride photoanode connected to the highly active **Ru_{15}** catalyst ($[Ru(tda)(4,4'\text{-bpy})]_{15}(4,4'\text{-bpy})$, where *bpy* is bipyridyne) through CH-π interactions was performed by a simply dipping method at room temperature. The resulting **CN_{TM}-Ru_{15}** and the bare **CN_{TM}** films were successfully characterized through spectroscopic, optical and morphological techniques.
- Photoelectrochemical experiments performed in neutral pH at 1 sun irradiation and at the thermodynamic WO potential showed an increased photocurrent in the presence of the Ru catalyst, reaching 180 $\mu A/cm^2$ for **CN_{TM}-Ru_{15}** *vs.* 130 $\mu A/cm^2$ for **CN_{TM}**. The oxygen detection measurements under continuous illumination provided with 89% Faradaic efficiency with TONs in the range of 3300 and TOFs of 0.4 s^{-1}, with a great stability for over 5 hours.
- The good electronic communication was detected electrochemically and photophysically, with Ru catalyst contributing for a better charge transfer and lower recombination, underlining the supramolecular interactions as a strong connection to the material.
- The role of the oligomeric Ru catalyst on the CN surface was further analyzed photoelectrochemically and computationally. The potential and additional photoabsorbing behavior of the same Ru-catalyst on the material surface in the metal-to-ligand-charge-transfer (MLCT) region confirmed the positive synergy within the molecular hybrid **CN_{TM}-Ru_{15}**.

Chapter 6:

- The anchoring of the $[Ru(tda)(pyCOOH)_2]$ molecular complex (where *pyCOOH* is iso-nicotinic acid) onto the **CN_{TM}** photoanode, similarly synthetized as in Chapter 5, was successfully achieved through covalent grafting *via* amidation reaction. The formation of the amide bridging linkage between the catalyst and the organic semiconductor yielded the **CN_{TM}@Ru** hybrid material, which was studied through different spectroscopic, optical and morphological techniques.

- The optical and electrochemical properties were analyzed and compared to the previously reported **CN_{TM}-Ru_{15}**, showing similar bandgap energy and good electronic connectivity with the CN material.
- The photoelectrochemical characterization was performed under 1 sun irradiation in a pH 7 buffer solution, achieving high activity towards water oxidation, with nearly 80% Faradaic efficiency, and a good stability for over 15 hours in a neutral medium. Because of the low content of Ru in the samples (19 $\mu g/g_{sample}$), **CN_{TM}@Ru** achieved TONs and TOFs of 2 x 10^4 and 0.6 s^{-1}, highlighting the increased efficiency of the newly synthetized **CN_{TM}@Ru** compared to the previously reported **CN_{TM}-Ru_{15}**.
- The photophysical characterization revealed an improved charge separation and transfer kinetics of **CN_{TM}@Ru** compared to the bare electrode, and comparable values to **CN_{TM}-Ru_{15}**. The catalytic cycle was finally provided with the information collected, confirming the strategic integration of a molecular-based catalyst within CN photoelectrodes as a valid alternative to the supramolecular interaction methodology.

UNIVERSITAT ROVIRA I VIRGILI
Molecular-based hybrid materials for artificial photosynthesis: Exploring new horizons in sustainable energy solutions
Martina Salati

UNIVERSITAT ROVIRA I VIRGILI
Molecular-based hybrid materials for artificial photosynthesis: Exploring new horizons in sustainable energy solutions
Martina Salati

UNIVERSITAT ROVIRA I VIRGILI
Molecular-based hybrid materials for artificial photosynthesis: Exploring new horizons in sustainable energy solutions
Martina Salati